

ISUD 6

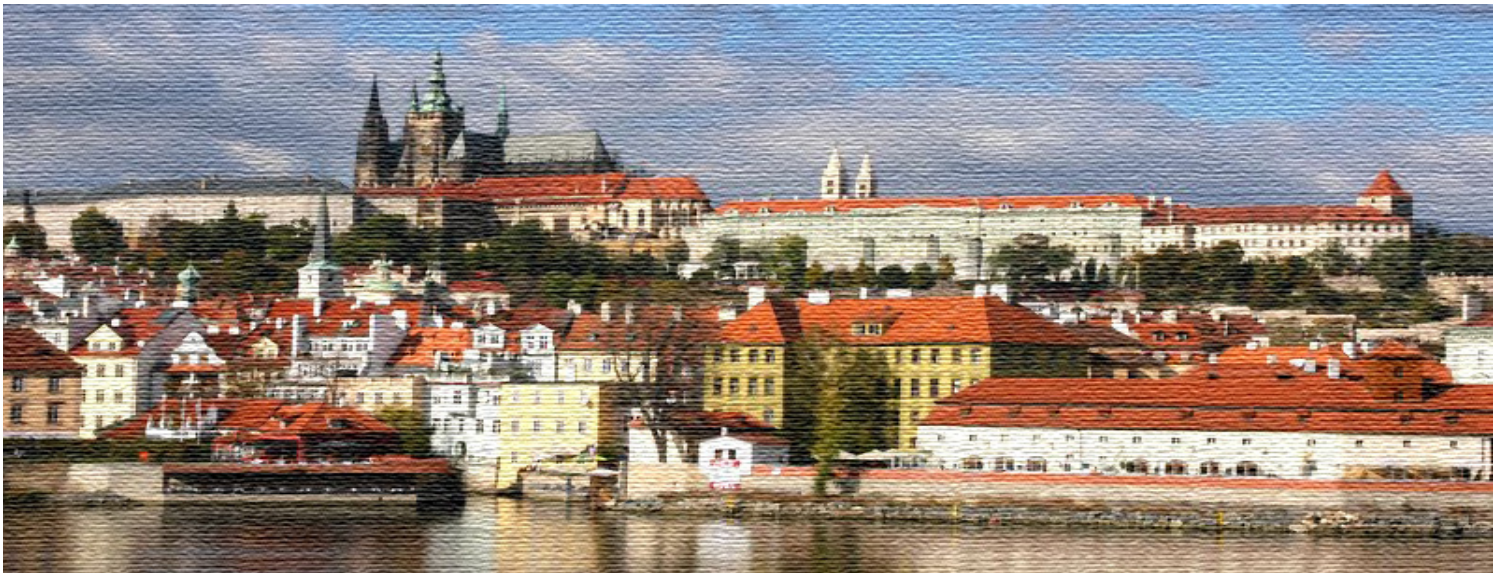
Proceedings of the 6th International Symposium on Ultrasonic Doppler Method for Fluid Mechanics and Fluid Engineering

9-11 September 2008, Prague, Czech Republic

Editors:

Zdenek Chara

Vojtech Bares



**Institute of Hydrodynamics,
Academy of Sciences of the
Czech Republic, v. v. i.**



**Czech Technical University in Prague
Faculty of Civil Engineering**

Proceedings of the Sixth International Symposium on Ultrasonic Doppler Methods for Fluid Mechanics and Fluid Engineering

9-11 September 2008, Prague, Czech Republic,

Editors:

Zdenek Chara

Vojtech Bares

Institute of Hydrodynamics AS CR, v. v. i.

Czech Technical University in Prague

Faculty of Civil Engineering

Department of Sanitary and Ecological Engineering

Scientific Committee:

Prof. Dr. M. Aritomi, Tokyo Institute of Technology, Fluid/Nuclear

Dr. G. De Cesare, EPF Lausanne, Hydraulics

Prof. Dr. J. A. Jensen, Technical University of Denmark, Medical Signal Processing

Dr. G. King, Warwick University, Physics

Dr. M. Mori, TEPCO, Industrial Applications

Prof. J. Pollert, CTU, Department of Sanitary and Ecological Engineering

Dr. C. Rennie, University of Ottawa/HIS IAHR, Environmental Hydraulics

Prof. Dr. Y. Takeda, Hokkaido University, Fluid Engineering/Mechanics

Prof. Dr. A. Tokuhiro, University of Missouri, Nuclear Engineering

Prof. Dr. E.J. Windhab, ETHZ, Food Process/Fluid Engineering

Organizing Committee:

Dr. V. Bares

Dr. Z. Chara

Prof. J. Pollert

Prof. Dr. Y. Takeda

Copyright © 2008

**Czech Technical University in Prague
Faculty of Civil Engineering
Thakurova 7
166 29 Prague 6
Czech Republic**

**Institute of Hydrodynamics AS CR, v. v. i.
Pod Patankou 5
166 12 Prague 6
Czech Republic**

ISBN: 978-80-87117-05-7

Table of Contents

Keynote Lectures

Velocity measurements in liquid metal flows using the Ultrasonic Doppler Method: examples and perspectives Sven Eckert, G. Gerbeth	<u>1</u>
Ultrasonic velocimetry and the rheological investigation of complex fluids Sébastien Manneville	<u>7</u>
Series of calibration tests at national standard loops and industrial applications of new type flow-metering system with Ultrasonic Pulse- Doppler Profile-Velocimetry for power plants Michitsugu Mori	<u>13</u>

Papers

Single-shot Doppler Velocity Estimation using double chirp pulse compression Farès Abda, Philippe Schmitt	<u>21</u>
Open-channel discharge measurement based on Ultrasonic Doppler Velocity Profiling – laboratory experiments Vojtech Bares1, Jan KrajdI, Jaroslav Pollert	<u>25</u>
How can computational fluid dynamics improve measuring in real sewers? Hossein Bonakdari, Ali Akbar Zinatizadeh	<u>29</u>
Comparative study of ADV and LDA measuring techniques Zdenek Chara, Vaclav Matousek	<u>33</u>
Flood discharge measurement using ADCP Yen-Chang Chen, Su-Pai Kao, Sheng-Reng Yu	<u>37</u>
Experiments on turbidity currents influenced by solid and permeable obstacles and water jet screens Giovanni De Cesare, Christoph D. Oehy, Anton J. Schleiss	<u>41</u>
ADCP measurements in a reservoir of a run-of-river hydro power plant Clemens Dorfmann, Helmut Knoblauch	<u>45</u>

Influence of bank roughness and inclination on straight channel flows	
Alexandre Duarte, Koen Blanckaert, Anton J. Schleiss	<u>49</u>
Velocity gauging with ADCP in rivers with bedload and sediment transport	
Katharina Fiedler, Theodor Strobl, Franz Zunic, Horst Matthes	<u>53</u>
Development of Rheometry based on UVP for visco-elastic liquid	
Naoki Furuya, Yuji Tasaka, Yuichi Murai, Yasushi Takeda	<u>57</u>
Development of a multiphase flow meter by means of multiple ultrasonic velocity profile measurements	
S. Roberto Gonzalez A., Yuichi Murai, Yuji Tasaka, Yasushi Takeda	<u>61</u>
Liquid metal Taylor-Couette experiment on the magnetorotational instability	
Thomas Gundrum, Frank Stefani, Gunter Gerbeth, Jacek Szklarski, Günther Rüdiger, Rainer Hollerbach	<u>65</u>
Instantaneous three-dimensional flow structure in a suction sump by 3D-PTV and UVP measurements	
Katsuya Hirata, Yuki Nakatani, Katsuhisa Inagaki, Jiro Funaki	<u>69</u>
A comparative study on near-field flow structures in a circular free jet and a square free jet	
Yoshihiro Inoue, Kunikazu Kondo, Shintaro Yamashita	<u>73</u>
Study on ultrasonic velocity profile measurement in vapor-water two-phase flow	
Daisuke Ito, Hiroshige Kikura, Masanori Aritomi, Michitsugu Mori	<u>77</u>
Effect of standing baffle on the structure of flow in a rectangular open channel	
Hamidreza Jamshidnia, Yasushi Takeda	<u>81</u>
Application of acoustic Doppler Velocimetry in microbubble containing water	
Lennart Jönsson	<u>85</u>
Application of linear ultrasonic array transducer to two-phase flow measurements	
Hiroshige Kikura, Takuya Hayashida, Daisuke Ito, Masanori Aritomi, Michitsugu Mori	<u>91</u>
Development of ultrasonic streamflow monitoring system using an existing low head broad-crested agricultural small dam	
Donggu Kim, Chanjoo Lee, Won Kim	<u>95</u>

Rheological characterisation of highly concentrated mineral suspensions using an ultrasonic velocity profiler Reinhardt Kotzé, Rainer Haldenwang, Paul Slatter	<u>99</u>
Numerical prediction of compound channel flow in comparison with ultrasonic Doppler method measurement Jan Krupicka, Vojtech Bares, Jakub Jirak, Petr Sklenar	<u>103</u>
Suspended solids and attenuation of ultrasonic beams Frédérique Larrarte, Pierre François	<u>107</u>
Discharge estimation using partially measured ADV data Chanjoo Lee, Won Kim, Chiyoung Kim, Donggu Kim	<u>111</u>
Turbulence and free surface flow at relevant Froude number Sandro Longo	<u>115</u>
Vortices at intake works of pump-storage schemes Rémi Martinerie, Michael Müller, Giovanni De Cesare, Jean-Louis Boillat	<u>119</u>
Flume flows between boundaries of very different roughness: evaluation of friction using ADV measurements Vaclav Matousek, Tomas Picek	<u>123</u>
Contact measurement of turbulent intensity of the pipe flow using UVP Hisato Minagawa, Tomoki Ishida, Takahiro Yasuda	<u>127</u>
Non-Newtonian fluid flow in elastic tubes S. Nahar, B.H. Birkhofer, S.A.K. Jeelani, E.J. Windhab	<u>131</u>
Experimental study for thermal striping in LBE loop by using UVP with high-temperature ultrasonic transducer Hironari Obayashi, Kenji Kikuchi	<u>135</u>
Boundary layer measurement of a vessel sailing over the sea Shoko Ohta, Akinari Shigetomi, Yuji Tasaka, Yuichi Murai, Yasushi Takeda, Munehiko Hinatsu, Yoshiaki Kodoma	<u>139</u>
Application of the Ultrasound Doppler method for velocity measurements in an electromagnetically-stirred liquid metal Dirk Rübiger, Sven Eckert, G. Gerbeth	<u>143</u>
Uncertainty of ADCP spatial velocity distributions Colin D. Rennie	<u>147</u>
Instrumental development and characterization for loaded liquid flow measurement Philippe Schmitt, Farès Abda, Anne Pallarès, Stéphane Fischer, Denis Ensminger, Pierre François	<u>151</u>

A basic study on sound-field characteristics around an ultrasonic oscillator and acoustic streaming Hirochika Tanigawa, Hiroaki Takeda, Jiro Funaki, Katsuya Hirata	<u>155</u>
Ultrasonic investigation of flow transition in surface switching of rotating fluid Yuji Tasaka, Kanako Yano, Makoto Ima	<u>159</u>
Acoustic Doppler Velocity Profiler for velocity and turbulence measurements in a large amplitude meandering flume Donatella Termini, Mafalda Piraino	<u>163</u>
Cross Correlation – the better Ultra Sonic Doppler – technique Michael Teufel, Milan Suchánek	<u>167</u>
Near wall studies of pulp suspension flow Johan Wiklund, Helena Fock, Anders Rasmuson, Mats Stading	<u>171</u>
Measurement of turbulent thermal convection in liquid metal under uniform magnetic field Takatoshi Yanagisawa, Yasuko Yamagishi, Aataru Sakuraba, Yuji Tasaka, Kanako Yano, Yasushi Takeda, Yozo Hamano	<u>175</u>
Ultrasonic investigation on coupling of flows between liquid and liquid metal layers Kanako Yano, Yuji Tasaka, Yuichi Murai, Yasushi Takeda, Takatoshi Yanagisawa	<u>179</u>

Author Index

Abda F.	21 , 151	Martinerie R.	119
Aritomi M.	77 , 91	Matousek V.	33 , 123
Bares V.	25 , 103	Matthes H.	53
Birkhofer B.H.	131	Minagawa H.	127
Blanckaert K.	49	Mori M.	13 , 77 , 91
Boillat J.-L.	119	Müller M.	119
Bonakdari H.	29	Murai Y.	57 , 61 , 139 , 179
Chara Z.	33	Nahar S.	131
Chen Y.-Ch.	37	Nakatani Y.	69
De Cesare G.	41 , 119	Obayashi H.	135
Dorfmann C.	45	Oehy Ch.D.	41
Duarte A.	49	Ohta S.	139
Eckert S.	1 , 143	Pallarès A.	151
Ensminger D.	151	Picek T.	123
Fiedler K.	53	Piraino M.	163
Fischer S.	151	Pollert J.	25
Fock H.	171	Räbiger D.	143
François P.	107 , 151	Rasmuson A.	171
Funaki J.	69 , 155	Rennie C.D.	147
Furuya N.	57	Rüdiger G.	65
Gerbeth G.	1 , 65 , 143	Sakuraba A.	175
Gonzalez A.S.R.	61	Shigetomi A.	139
Gundrum T.	65	Schleiss A.J.	41 , 49
Haldenwang R.	99	Schmitt P.	21 , 151
Hamano Y.	175	Sklenar P.	103
Hayashida T.	91	Slatter P.	99
Hinatsu M.	139	Stading M.	171
Hirata K.	69 , 155	Stefani F.	65
Hollerbach R.	65	Strobl T.	53
Iima M.	159	Suchánek M.	167
Inagaki K.	69	Szklarski J.	65
Inoue Y.	73	Takeda H.	155
Ishida T.	127	Takeda Y.	57 , 61 , 81 , 139 , 175 , 179
Ito D.	77 , 91	Tanigawa H.	155
Jamshidnia H.	81	Tasaka Y.	57 , 61 , 139 , 159 , 175 , 179
Jeelani S.A.K.	131	Termini D.	163
Jirak J.	103	Teufel M.	167
Jönsson L.	85	Wiklund J.	171
Kao S.-P.	37	Windhab E.J.	131
Kikuchi K.	135	Yamagishi Y.	175
Kikura H.	77 , 91	Yamashita S.	73
Kim D.	95 , 111	Yanagisawa T.	175 , 179
Kim Ch.	111	Yano K.	159 , 175 , 179
Kim W.	95 , 111	Yasuda T.	127
Knoblauch H.	45	Yu S.-R.	37
Kodoma Y.	139	Zinatizadeh A.A.	29
Kondo K.	73	Zunic F.	53
Kotzé R.	99		
Krajdl J.	25		
Krupicka J.	103		
Larrarte F.	107		
Lee Ch.	95 , 111		
Longo S.	115		
Manneville S.	7		

Velocity measurements in liquid metal flows using the Ultrasonic Doppler Method: examples and perspectives

Sven Eckert* and G. Gerbeth

Forschungszentrum Dresden-Rossendorf (FZD), MHD Department, P.O: Box 510119, 01314 Dresden, Germany (*Corresponding author, e-mail: s.eckert@fzd.de).

The Ultrasound Doppler Method (UDM) can be considered as an attractive technique to obtain velocity data from opaque flows. In this presentation various applications of UDM in liquid metal flows will be shown to demonstrate the capabilities and current restrictions of this technique. For instance, we consider flow fields arising from an electromagnetic stirring, discuss the application of UDM for measurements in liquid metal two-phase flows and present velocity measurements obtained during the solidification of metallic alloys. Besides the determination of velocity profiles in a solidifying melt the UDM data allow for an assessment of the current position of the solidification front, too. Specific problems arising in the context of UDM measurements in liquid metal experiments will be discussed. To extend the application range towards higher temperatures and abrasive liquids a new integrated ultrasonic sensor with an acoustic wave guide has been designed. For instance, successful measurements have been reported for liquid aluminium at temperatures of about 750°C.

Keywords: Liquid metal, Ultrasound Doppler method, High temperature sensor, electromagnetic stirring, solidification

1 INTRODUCTION

Considerable expenditure is permanently focussed on the optimisation of methods and facilities for material processing technologies like melting, refining or casting of metals and alloys. The main goals are an improvement of the final product quality, an enhancement of the process efficiency and an economical consumption of resources and energy. In processes involving electrically conducting liquids, the application of an external magnetic field offers efficient opportunities for a contact-less flow control and fluid handling. Further developments require a better knowledge about the details of the flow structure, the heat and mass transfer properties of the flow especially during phase transitions like melting or solidification. Numerical simulations could provide a better understanding of such processes, but experimental data of the velocity field are indispensable for validation of the CFD codes.

The instrumentation of liquid metal flows for obtaining flow quantities like velocity, pressure, void fraction, properties of a dispersed phase etc. has to be considered as very difficult issue. No matter what diagnostic method is chosen, some serious restrictions always exist with respect to the particular sensors, for instance, the material properties of the liquid metal, the amount of impurities, the velocity range, the accuracy of the method, or the presence of electromagnetic fields. Considerable problems arise from the opaqueness of the liquid, the high temperatures or the corrosiveness of the fluid. As a consequence, there is a very constrained choice of commercially

available techniques to measure the velocity structure in metallic melts at high temperatures.

During the last 20 years the ultrasound Doppler technique (UDM) became a powerful tool for flow velocity measurements in fluid engineering [1].

The feasibility of velocity measurements in liquid metals using UDM was demonstrated for the first time by Takeda [2], who determined velocity profiles in a T-tube filled with mercury. Further successful applications have been published in different kind of liquid metal flows, see for instance [3–7]. The number of publications concerned with liquid metal flow measurements by means of UDM is still manageable, but, continuously increasing during the last years (for a recent review see [8] and references therein). The purpose of this paper is to provide a brief review with respect to the capabilities and restrictions of the considered measuring technique in liquid metal applications. The UDM technique is capable to deliver valuable insight in miscellaneous flow situations, occurring for instance during electromagnetic stirring [9, 10], during solidification of metallic alloys [11], inside a mercury target for a spallation source [12] or in liquid metal two-phase flows [13].

2 SPECIFIC PROBLEMS ARISING FROM THE APPLICATION OF UDM IN LIQUID METALS

2.1 General Issues

In this chapter we intend to discuss specific problems which have particularly to be taken into account if the Ultrasound Doppler Method is applied for velocity measurements in liquid metal flows. The main issues concern in particular:

- Thermal restrictions of the ultrasonic transducer in hot metallic melts
- Acoustic coupling between different materials along the ultrasonic path transducer – fluid
- Resonance effects arising from transmission through container walls
- Allocation of suitable tracer particles in the fluid

An approach to solve the temperature problem will be presented in the next subsection. Here, we consider especially the wetting, the beam transmission and the reflecting particles.

A good wetting contact between the liquid metal and the active acoustic surface is a prerequisite to guarantee the reception of Doppler signals. The large surface tension of the liquid metals and the almost inevitable existence of oxide layers complicate the wettability significantly. Non-wetted surfaces can cause a sudden change of the acoustic impedance, which obstructs the beam transmission into the fluid to be measured. In many experiments, the liquid metal flow to be measured is enclosed by stainless steel walls. Ultrasonic measurements through such walls require a careful removal of oxide layers at the steel surface by a suitable thermal [14] or chemical treatment [4], respectively. In case of an insufficient acoustic coupling at the inner wall multiple reflections are generated inside the wall material provoking a saturation of the transducer by the wall echoes.

The generation of Doppler signals inside the liquid requires the existence of reflecting particles. We are not aware of any detailed, quantitative studies in liquid metals focussing on the dependence of the signal properties on quantities like the concentration, the morphology (e.g. size and shape) and the acoustic properties of the suspended scatter particles. Difficulties arise if these particles should be added in a well-controlled way to the metallic melts. Such particles have to be homogeneously distributed over the entire fluid volume and their liquid density must approximately be matched in order to prevent a slip between the flow field and the particle motion. Moreover, a wetting of the particles by the liquid metal is necessary: on the one hand, to enable the infiltration into the bulk liquid, on the other hand, to avoid agglomeration effects. Furthermore, for keeping the overall contamination by impurities at an acceptable level an efficient method must be available to separate the particles from the fluid after finishing the measurements. Having all these problems in mind, it is obvious to try to work solely with natural impurities such as oxides or microbubbles which are normally present in metallic melts having a technical purity standard. Noble liquid metals, such as mercury, contain an insufficient amount of natural tracers, whereas in customary alloys such as GaInSn, PbSn or PbBi a distinct and expeditious oxidation can only be

prevented with substantial effort. Here, the situation could arise that the UDM measurements might even be complicated by too many tracers inside the measuring volume [3]. A possible solution for the problem of the insufficient amount of seeding particles in mercury was proposed by Takeda and Kikura [15]. They injected nitrogen bubbles through a capillary tube into the liquid metal. Whereas the larger bubbles are expected to separate quickly from the liquid by the buoyancy force tiny bubbles can persist for a while as suitable reflectors.

2.2 Sensor for high temperature applications

The crucial problem of the high temperatures of the metallic melts impedes the application of standard ultrasonic transducers. The use of the conventional transducer made of PZT based materials confines the range of application of ultrasonic techniques to maximum temperatures of about 150°C (long term load) and 200°C (short term load), respectively. If the measurements have to be performed with a direct contact between the ultrasonic probe and the metallic melt, one has to take care for a sufficient wetting between the probe and the liquid metal in order to guarantee a good acoustic contact, but on the other hand, the sensor has to be saved against a chemical reactions or dissolution in the melt. For this reason a new concept of an ultrasonic transducer with integrated acoustic wave guide has been proposed [5] in order to achieve a thermal as well as a chemical decoupling between the active transducer and the fluid. Stainless steel was proven to work as a dedicated wave-guide material in a temperature range until about 750°C. From the acoustic point of view there are also some ceramic materials as suitable candidates, however, it is difficult to achieve a sufficient wetting between a liquid metal and a solid ceramic surface at moderate temperatures. The integrated ultrasonic probe consisting of the piezoelectric element and the acoustic wave-guide is shown in Fig. 1. The working frequency of the transducer can be chosen between 1 and 4 MHz. The wave-guide is fabricated from a stainless steel foil with a thickness of 0.1 mm which is wrapped axially around a capillary tube. The wave-guide is closed at the front end by means of laser beam welding leading to a flat stainless steel surface. This surface is in direct contact with the melt and has to be prepared before the measurements to obtain a sufficient wetting with the liquid metal. The wave-guide has an outer diameter of 7.5 mm and a length of 200 mm. The half angle δ of the divergence of the ultrasonic beam is about 3.5° for water, 4.2° for PbBi and 5.8° for sodium.

3 APPLICATION EXAMPLES

3.1 Electromagnetic stirring

In the recent past various types of an intermittent or alternate, rotary stirring have been proposed as an

innovative technology for mixing and homogenization of metallic melts. That means that during the process either the magnetic field will be switched on and off several times or the direction of propagation will be inverted frequently. In this way cycles of successive spin-up and -down of the flow will be created, which are accompanied with periodic oscillations of the radial-meridional flow.

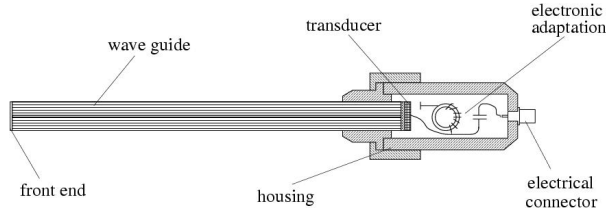


Figure 1: Scheme of an ultrasonic sensor with acoustic waveguide for measurements in hot metallic melts [5]

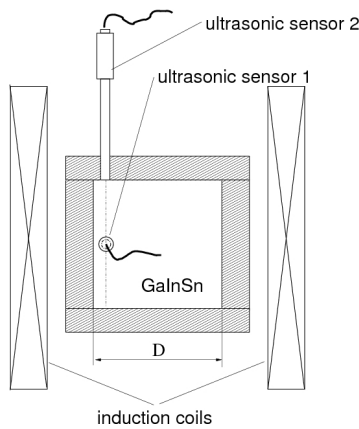


Figure 2: Set-up for UDM flow measurements in a metal cube agitated by electromagnetic stirring (schematic view)

To investigate such flow behaviour in detail, model experiments with low melting point liquids were carried out at FZD using the Ultrasound Doppler Method. We consider here the flow inside a cube with a side length D of 80 mm. A schematic view of the experimental set-up is depicted in Fig. 2. The central point of the cube coincides with the origin of the coordinate system. The experiments were carried out using the ternary eutectic alloy Ga68In20Sn12, which is liquid at room temperature. The cube was positioned inside the magnetic induction system MULTIMAG for generating a rotating magnetic field (RMF). Two ultrasonic sensors were positioned at the side wall (sensor 1) and the lid of the cube (sensor 2) in order to determine the vertical and the horizontal velocity component, respectively. Fig. 3 shows spatio-temporal plots of the vertical velocity obtained for a continuously applied RMF and a sequence of RMF pulses with alternating direction, respectively. The velocity profiles were recorded at a measuring position of $x = 24$ mm and $y = 0$ along the vertical z coordinate. Drawing a sequence of 512 one-dimensional velocity profiles measured consecutively generates such a two-dimensional flow pattern as displayed in Fig. 3. In case of a

continuously applied RMF as shown in Fig. 3(a) the typical double-vortex structure in the meridional plane can be observed. Although the flow is fully turbulent the global structure appears as very stable showing a descending fluid motion in the upper half of the cube and an ascending flow in the lower part. The situation looks different if the rotational direction of the magnetic field is reversed with a frequency f_R of 0.08 Hz. Fig. 3(b) shows that there does not remain any fluid domain with a dominating flow direction. Significant changes of velocity direction and amplitude can be found everywhere, which can be assessed as a serious indication for an enhanced local mixing.

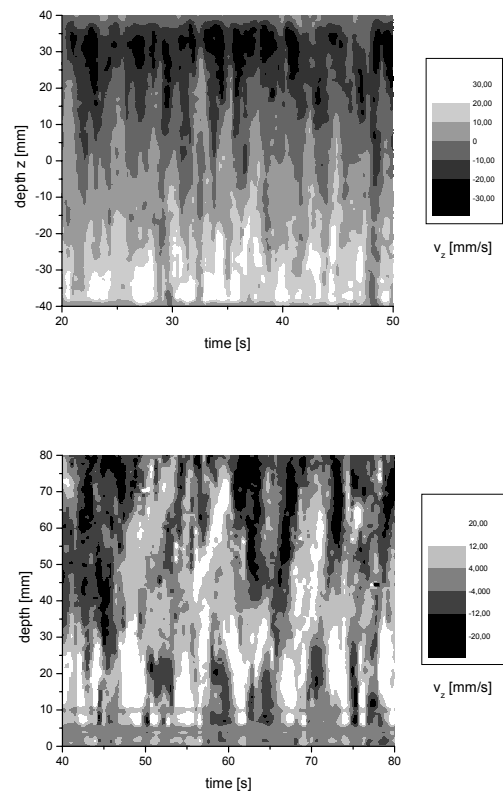


Figure 3: Spatio-temporal distribution of the vertical velocity driven by a rotating magnetic field of 1.9 mT and 50 Hz permanently applied (a), or alternately applied with a frequency of 0.08 Hz (b)

Corresponding measurements of the azimuthal flow in the horizontal mid-plane are depicted in Fig. 4. These time series were obtained at a local position of $x = 24$ mm, $y = 0$ and $z = 0$. At that position the azimuthal velocity shows a mean value of about 50 mm/s if the RMF has been applied continuously. In the case of an alternating RMF the primary flow oscillates around zero with the frequency of the external forcing. The maximum velocity values do not reach the intensity as measured for the continuously applied RMF. Due to the periodic change of flow direction a lower amount of kinetic energy is deposited in the primary flow, but, the intensity of the secondary flow is strengthened.

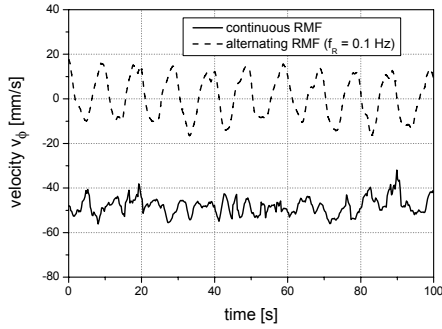


Figure 4: Time series of the local, azimuthal velocity recorded at $x = 24$ mm, $y = 0$ and $z = 0$

It is obvious that the application of an alternating RMF has the capability to enforce the mixing in the metallic melt. The frequency of inversion of the RMF direction f_R appears now as further parameter which should be taken into consideration. A temporary amplification of the secondary flow arises directly from the redirection of the primary flow. Therefore, an increase of f_R should result in a growth of the velocity fluctuations. On the other hand, the inertia of the liquid restricts the fluid motion at higher frequencies. Time-averaged mean values of the vertical velocity U_z^2 can be taken as a representative measure of the flow intensity in the meridional plane [10]. Fig. 5 displays a diagram in which U_z^2 is drawn vs. the frequency f_R for different values of the magnetic field. An optimal range with respect to f_R exists, where a maximum stirring effect can be achieved. Note that such an optimum depends on the geometry under consideration, the properties of the liquid and the strength of the magnetic field.

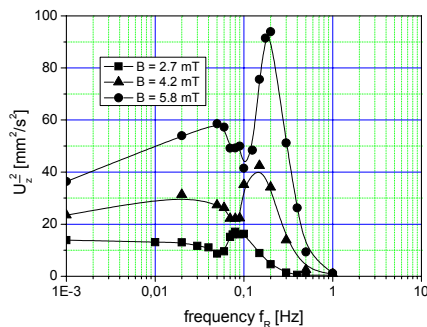


Figure 5: Dependence of the intensity of the meridional flow on the frequency f_R (alternating RMF)

3.2 Liquid metal two-phase flows

Successful applications of the UDM technique in two phase flows have already been reported by Wang et al. [16] or Suzuki et al. [17]. A schematic drawing of our liquid metal two-phase experiment is shown in Fig. 6. Argon bubbles were injected into the eutectic alloy PbBi (Pb44Bi56, $T_{\text{melt}} = 125^\circ\text{C}$) by means of a single orifice ($\varnothing 0.5$ mm). A cylindrical container made of stainless steel with a diameter of 125 mm and a height of 250 mm contains a stagnant pool of

about 2.5 l liquid metal. The experiments were performed at temperatures of 300°C . The ultrasonic probe with acoustic wave guide was positioned at the free surface with a vertical distance of 150 mm from the orifice position. In order to avoid a deterioration of the acoustic contact because of gas bubbles potentially sticking at the front surface of the wave guide, a sensor position outside the bubble swarm was selected resulting in a Doppler angle of 20° with respect to the vertical line. The measurements were restricted to a single bubbly flow regime at small gas flow rates.

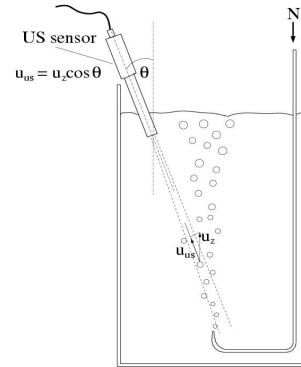


Figure 6: Schematic view of the bubbly flow experiment

A typical velocity profile obtained from the bubbly flow is depicted in Fig. 7. The lower velocity at the small measuring depths corresponds to the liquid metal flow which is driven by the rising bubbles. Two bubble signals were detected showing a higher velocity as the surrounding liquid. Since the ultrasonic pulse is reflected at the bubble interface, the velocity measured can be interpreted as an interfacial velocity. In the region of low gas flow rates it proved to be possible to clearly distinguish between the bubble and the liquid velocities allowing accurate measurements of the bubble velocity and the corresponding wake structure in the liquid [18]. Isolated artefacts caused by multiple reflections of the ultrasonic beam were found to occur in the velocity signal if the gas flow rate was increased until attaining a bubble chain driven flow. Moreover, the so-called shadow effect has to be taken into account that appears to be responsible for the reflection of a considerable amount of ultrasonic energy by the bubbles. As a consequence information from positions behind the bubbles won't reach the sensor or only in fragmentary form, respectively. For bubbly flows at higher gas flow rates an iterative threshold method was developed to obtain correct profiles of the liquid velocity [18]. A comparison regarding time averaged velocity profiles of the liquid phase delivered by UDV and measurements performed with LDA showed an excellent agreement. The frequency of multiple reflections to occur at the gas-liquid interfaces increases with increasing gas flow rate. Thus, one can anticipate serious limitations for measurements at higher gas flow rates. Although it becomes questionable there to distinguish reasonably

between the gas and the liquid phase, information could be obtained with respect to a kind of mixture velocity or the bubble swarm contour.

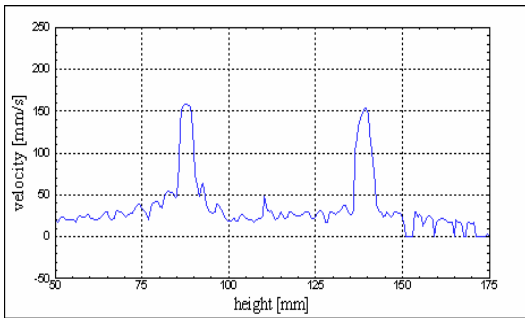
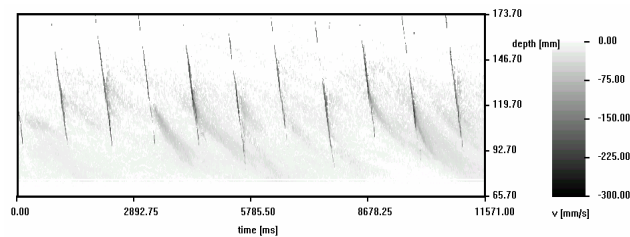
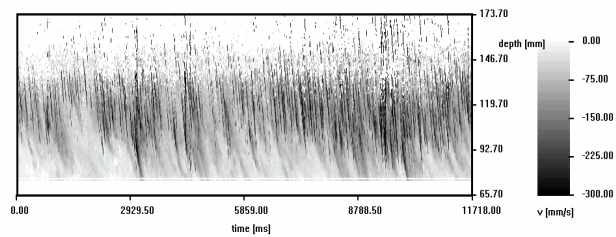


Figure 7: Typical snapshot of the raw velocity profile containing two bubble signals



(a) $Q_{\text{gas}} = 0.04 \text{ cm}^3/\text{s}$



(b) $Q_{\text{gas}} = 1.2 \text{ cm}^3/\text{s}$

Figure 8: Spatio-temporal velocity structure of the bubbly flow at different gas flow rates

Fig. 8 displays the spatio-temporal structure of the bubbly flow based on 700 measured profiles. The sharp signals with the high velocity values coincide with the echoes received from the rising bubbles. Here, a bubble frequency of about 1 Hz is observed for the case of a low gas flow rate in Fig. 8(a). The regular structure of a chain of single gas bubbles is lost if the gas flow rate reaches a value of $1.2 \text{ cm}^3/\text{s}$ as it becomes obvious in Fig. 8(b).

3.3 Solidification of metal alloys

The ultrasound Doppler method can also be applied to measure the bulk flow in a Sn-15wt%Pb alloy solidified directionally from a water cooled copper chill using the experimental configuration as shown in Fig. 9. The stainless steel mould had an internal diameter of 50 mm, a height of 100 mm and a wall thickness of 3 mm. The side walls were covered by a 5 mm heat insulation to prevent a radial heat transfer from the mould. The filling height for each charge was 60 mm. The mould was closed by a stainless steel lid. The volume between the lid and the free surface of the melt was filled with argon gas in order to minimize the oxidation of the melt.

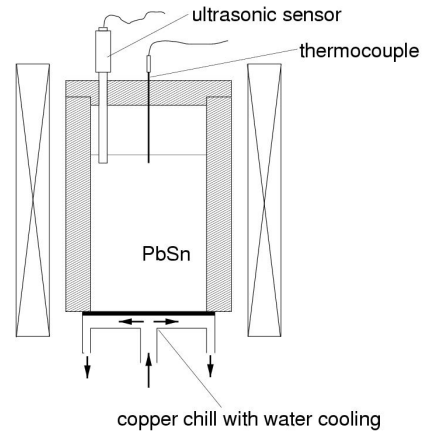


Figure 9: Sketch of the experimental set-up for the solidification experiments

During solidification the convection in the liquid phase was driven by an RMF using magnetic field frequencies of 50 Hz. The alloys were melted and heated until reaching a superheat of 90 K using an electrical furnace. Approaching the terminal temperature the mould was taken from the heater and set immediately on a water-cooled copper chill. Water was circulated through this cooling jacket keeping the copper plate at a constant temperature of about 20°C providing an axial heat transfer from the mould. The agitation of the melt was simultaneously initiated with the cooling at that moment if the stainless steel mould was attached on the cooling system.

The acoustic contact between the ultrasonic sensor and the fluid was realized by dipping the wave guide into the melt 4 mm below the free surface. The sensor was aligned vertically, thus the z-component of the velocity can be measured. Profiles of the vertical velocity were obtained at a radial position of $r = 22 \text{ mm}$. An axial arrangement of thermocouples was used to record the development of vertical temperature profiles in the ingot during solidification.

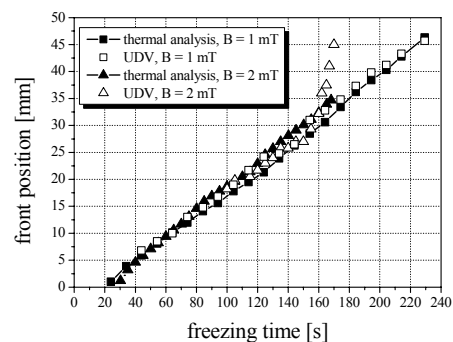


Figure 10: Actual position of the solidification front during unidirectional solidification of Pb-Sn obtained from UDM and temperature measurements, respectively

The bulk flow dissipates at the solid-liquid interface. Therefore, the UDM measurements additionally offer a possibility to track the position of the progressing solidification front. The positions in the UDM profiles where the velocity vanishes are drawn

in Fig. 10. The comparison with corresponding results obtained from thermal measurements shows a satisfying agreement. In the case of the higher magnetic field an accelerated growth of the solidification front can be observed at a height of about 160 mm. The moment where this acceleration starts has been identified to approximately coincide with the transition from a columnar to an equiaxed dendritic growth (CET) [11]. Above the CET position a columnar front does not occur. Here, the solidification proceeds almost simultaneously over the remaining melt volume. Because of a drastic increase of the viscosity the melt flow is damped quickly. This effect becomes obvious in Fig. 11 showing the temporal development of the vertical velocity averaged along the measured profile. It is clear that an increase of the magnetic field strength results in a higher intensity of the bulk flow during the early stages of the solidification process. On the other hand, higher stirring intensities promote the CET and the flow comes earlier to rest after that moment if the CET happened. Further results of velocity measurements during solidification can be found in [11].

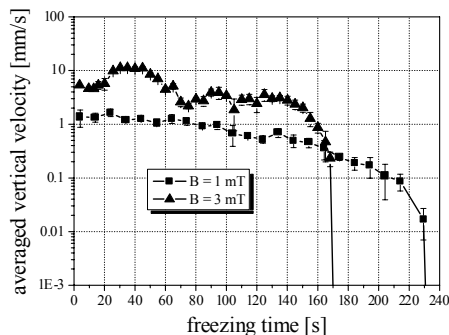


Figure 11: Temporal development of the vertical velocity component averaged along the measuring line during solidification (radial position of the sensor: 22 mm)

4 SUMMARY AND CONCLUSIONS

Because of the capability to measure velocity profiles in opaque melts the Ultrasound Doppler Method becomes very attractive for investigations of liquid metal flows. A growing number of applications and publications concerning UDM measurements in metallic melts can be noticed. Successful measurements especially require a proper acoustic coupling between the transducer and the liquid metal as well as the availability of an appropriate amount of seeding particles. A new type of ultrasonic probe using an acoustic waveguide has been proven for high temperature applications. This approach may open a new field for UDM applications.

ACKNOWLEDGEMENT

This work was financially supported by Deutsche Forschungsgemeinschaft in the framework of the

collaborative research centre SFB 609 "Electromagnetic Flow Control in Metallurgy, Crystal Growth and Electrochemistry".

REFERENCES

- [1] Takeda Y: Development of an ultrasound velocity profile monitor, *Nucl. Eng. Design* 126 (1991), 277-284.
- [2] Takeda Y: Measurement of velocity profile of mercury flow by ultrasound Doppler shift method, *Nucl. Techn.* 79 (1987), 120-124.
- [3] Brito D, Nataf HC, Cardin P, Aubert J, Masson JP: Ultrasonic Doppler velocimetry in liquid gallium, *Exp. Fluids* 31 (2001) 653-663.
- [4] Eckert S, Gerbeth G: Velocity measurements in liquid sodium by means of ultrasound Doppler velocimetry, *Exp. Fluids* 32 (2002), 542-546.
- [5] Eckert S, Gerbeth G, Melnikov VI: Velocity measurements at high temperatures by ultrasound Doppler velocimetry using an acoustic wave guide, *Exp. Fluids* 35 (2003); 381-388.
- [6] Kikuchi K, Takeda Y, Obayashi H., Tezuka M, Sato H: Measurement of LBE flow velocity profile by UDVP, *J. Nucl. Materials* 356 (2006), 273-279.
- [7] Tasaka Y, Takeda Y, Yanagisawa T: Ultrasonic visualization of thermal convective motion in a liquid gallium layer, *Flow Meas. Instrum.* 19 (2008), 131-137.
- [8] Eckert S, Cramer A, Gerbeth G: Velocity measurement techniques for liquid metal flows, in "Magnetohydrodynamics - Historical Evolution and Trends", Molokov S, Moreau R, Moffatt HK (eds), Springer-Verlag (2007), 275-294.
- [9] Cramer A, Zhang C, Eckert S: Local flow structures in liquid metals measured by ultrasonic Doppler velocimetry, *Flow Meas. Instrum.* 15 (2004), 145-153.
- [10] Eckert S, Nikrityuk PA, Rübiger D, Eckert K, Gerbeth G: Efficient Melt Stirring Using Pulse Sequences of a Rotating Magnetic Field: Part I. Flow Field in a Liquid Metal Column, *Metall. Mater. Trans.* 38B (2007), 977-988.
- [11] Eckert S, Willers B, Gerbeth G: Measurements of the Bulk Velocity during Solidification of Metallic Alloys, *Metall. Mater. Trans.* 36A (2005), 267-270.
- [12] Takeda Y, Kikura H, Bauer G: Flow measurement in a SINQ mockup target using mercury, *Proc. of the ASME FED Summer Meeting, FEDSM98-5057* (1998), ASME, Washington DC.
- [13] Zhang C, Eckert S, Gerbeth G: The flow structure of a bubble-driven liquid-metal jet in a horizontal magnetic field, *J. Fluid Mech.* 575 (2007), 57-82.
- [14] Gailitis A: Experimental aspects of a laboratory scale liquid sodium dynamo model, in: Proctor MRE, Mathews PC, Rucklidge AM (eds) *Theory of solar and planetary dynamos*, Cambridge University Press (1993), 91-98.
- [15] Takeda Y, Kikura H: Flow mapping of mercury flow, *Exp. Fluids* 32 (2002), 161-169
- [16] Wang T, Wang J, Ren F, Jin Y: Application of Doppler ultrasound velocimetry in multiphase flow, *Chem. Eng. J.* 92 (2003), 111-122.
- [17] Suzuki Y, Nakagawa M, Aritomi M, Murakawa H, Kikura H, Mori M: Microstructure of the flow field around a bubble in counter-current bubbly flow, *Exp. Thermal Fluid Science* 26 (2002), 221-227
- [18] Zhang C, Eckert S, Gerbeth G: Gas and liquid velocity measurements in bubble chain-driven two-phase flow by means of UDV and LDA, in: *Proc. 5th Int. Conf. Multiphase Flow, Yokohama, ICMF04-260*, (2004).

Ultrasonic velocimetry and the rheological investigation of complex fluids

Sébastien Manneville

Laboratoire de Physique, Université de Lyon - Ecole Normale Supérieure de Lyon, CNRS UMR 5672, 46 allée d'Italie, 69364 Lyon cedex 07, FRANCE (e-mail: sebastien.manneville@ens-lyon.fr)

High-frequency ultrasonic velocimetry is used to explore the rheological behaviour of complex fluids sheared between concentric cylinders. The technique is based on time-domain cross-correlation of speckle signals backscattered either by the fluid microstructure or by contrast agents dispersed in the material. Velocity profiles with a 40 μm resolution can be measured every 0.1-10 s depending on the global shear rate. The technique is applied to various complex fluids that show "shear banding" (i.e. local heterogeneities of the shear rate due to local modifications of the microstructural organization) or shear-induced fractures.

Keywords: velocity profile,

1 INTRODUCTION

Contrary to Newtonian fluids, complex fluids may develop highly *inhomogeneous* flow patterns even under simple shear at low Reynolds numbers. This is due to the coupling between the fluid microstructure and the flow. Examples range from depletion-induced apparent wall slip in concentrated emulsions or fractures in gels to shear-banding in surfactant solutions, colloidal suspensions, foams, or granular materials [1]. In practical applications, such spatial inhomogeneity may be very misleading when interpreting rheological experiments based on the measurement of *engineering* quantities such as the shear stress or the viscosity averaged over the whole sample.

Moreover, spatial inhomogeneity often goes along with complex *temporal* behaviours and instabilities [2-3]. Due to a lack of temporally and spatially resolved instruments coupled to classical rheological tools, such *spatio-temporal* features remain difficult to assess. However, they may have a critical influence on the texture of the final product or on processing rates in industrial applications.

In this paper, we describe how high-frequency ultrasound can be used to measure and follow velocity profiles in sheared complex fluids with a 40 μm spatial resolution and a 0.1–10 s temporal resolution. Such ultrasonic velocimetry is coupled to a standard rheometer in Couette geometry (concentric cylinders). The resulting "ultrasonic rheo-velocimeter" is tested on various complex fluids, which illustrate the wide range of materials accessible to the technique and of possible subsequent characterizations.

2 COMPLEX FLUIDS AND THE NEED FOR LOCAL VELOCIMETRY TOOLS

2.1 Inhomogeneous flows in complex fluids

In complex fluids, the existence of a supramolecular organization (or "micro-structure") at some "mesoscopic" scale can lead to very complicated

behaviours under flow: steady shear modifies the fluid microstructure and may even induce new structures or textures. For instance, shearing an initially isotropic wormlike micelle solution can lead to a nematic phase [4]. In concentrated granular materials and in soft glassy materials, solid-like states are observed that may coexist with shear-induced states [5]. Such transitions between shear-induced states are thus characterized by *inhomogeneous* flows featuring bands of different viscosities and supporting different shear rates. These effects may become crucial in a lot of applications where a good control of the product structure or texture is required.

Moreover, when a complex fluid is confined between two plates and depending on the roughness of the plates, the fluid velocity close to the walls may strongly differ from that of the walls: the fluid *slips*. Such apparent slippage is usually explained by the existence of thin lubricating layers close to the walls in which the fluid structure is very different from that in the bulk. For instance, in concentrated emulsions, apparent wall slip is attributed to the presence of very thin low-viscosity layers where the droplet concentration is much lower than in the bulk (depletion layers) [6].

2.2 Local velocimetry in complex fluids

Accurate time-resolved measurements of *local* velocities are thus crucial to the exploration of complex fluids during processing or quality control through rheological experiments. Since the microstructure of a complex fluid is very sensitive to local deformations, a *non-intrusive* technique is required.

The most popular non-intrusive optical techniques, namely particle imaging velocimetry (PIV), laser Doppler velocimetry (LDV), and dynamic light scattering (DLS), rely on the interaction between light and the microstructure (or seeding particles following the flow). However, many complex fluids, such as emulsions, slurries, or pastes, may not be

transparent enough to allow the use of PIV or LDV. Nuclear magnetic resonance (NMR) offers the possibility to image opaque media [7] but requires the use of powerful magnets and remains expensive and tricky to set up.

On the other hand, ultrasound appears as an efficient, cost-effective tool to measure time-resolved velocity profiles in a large range of fluids. Conventional ultrasound (frequency $f=1-10$ MHz) has been used for in-line flow rate and velocity profile measurements [8-10]. However, “low” frequencies suffer from a poor spatial resolution (0.15–1.5 mm) incompatible with the study of complex fluid flows at the mesoscopic scale. This paper introduces high-frequency ultrasonic velocimetry coupled to a standard rheometer as a powerful characterization tool of the shear flow of various complex fluids.

3 ULTRASONIC RHEO-VELOCIMETRY SETUP

3.1 Apparatus

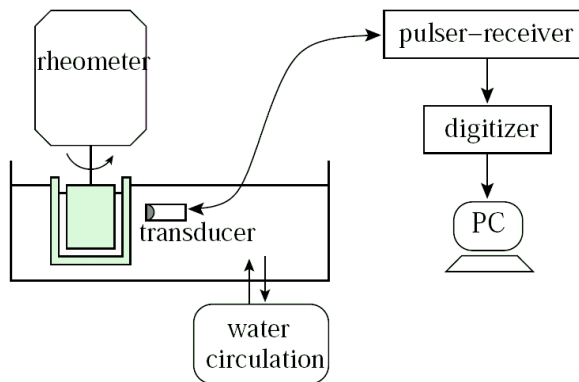


Figure 1: General sketch of the experimental setup.

Our ultrasonic “rheo-velocimeter” consists of two main components sketched in Fig. 1: (i) a commercial rheometer (TA Instruments AR1000N) that allows us to perform rheological measurements in homemade Couette cells and (ii) a high-frequency ultrasonic velocimetry system. The Couette cell is made of Plexiglas and has the following characteristics: inner radius $R_1=24$ mm, outer radius R_2 , gap $e=R_2-R_1=1$ mm, and height $h=30$ mm. The walls of both cylinders can be smooth or sand-blasted. Fig. 2 summarizes the notations used in this paper. The whole cell is surrounded by water whose temperature is kept constant to within 0.1 °C. The rheometer imposes a constant torque Γ on the axis of the inner cylinder, which induces a constant stress σ in the fluid, and measures the rotation speed Ω of the rotor. A computer-controlled feedback loop on Γ can also be used to apply a constant shear rate $\dot{\gamma}$ without any significant

temporal fluctuations.

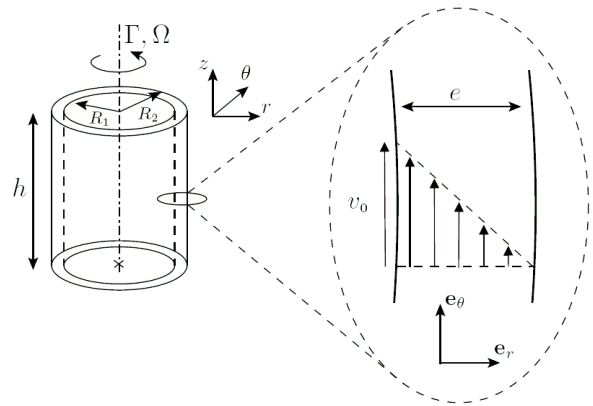


Figure 2: Sketch of the Couette cell used in our experiments and enlargement of the gap between the two cylinders in the case of a homogeneous flow.

High-frequency ultrasonic pulses are generated by a focused PVDF piezo-polymer transducer of central frequency $f=36$ MHz (Panametrics PI 50-2). The focal distance is 11.6 mm and the axial and lateral resolutions are 30 μ m and 65 μ m, respectively over a depth of field of about 1 mm.

The transducer is controlled by a pulser–receiver unit (Panametrics 5900PR) in the transmit-and-receive mode. The pulser generates 220 V pulses with a rise time of about 1 ns. The pulse repetition frequency is tunable from 0 to 20 kHz. The receiver is equipped with a 200 MHz broadband amplifier of maximum voltage gain 54 dB as well as a set of selectable high- and low-pass filters. Ultrasonic signals backscattered by the fluid (see below) are sampled at 500 MHz, stored on a high-speed PCI digitizer with 8 Mb on-board memory (Acqiris DP235), and transferred to the host computer for processing.

3.2 Measurement technique

Ultrasonic pulses are incident on the stator with a given angle $\theta_0 \approx 20^\circ$ relative to the normal to the stator. Pulses travel through Plexiglas and enter the gap with an angle θ that is given by the law of refraction. Once inside the fluid, ultrasonic pulses get scattered by compressibility inhomogeneities that can be either naturally present due to the complex fluid’s microstructure (oil droplets in an emulsion for instance) or artificially introduced to enhance the acoustic contrast. The total round trip for a pulse traveling from the transducer to the rotor and back to the transducer lasts about 15 μ s. The position of the transducer is tuned so that the 1 mm gap lies inside the focal spot. Typical recorded backscattered signals are 1000 point long, which corresponds to a transit time of 2 μ s inside the medium.

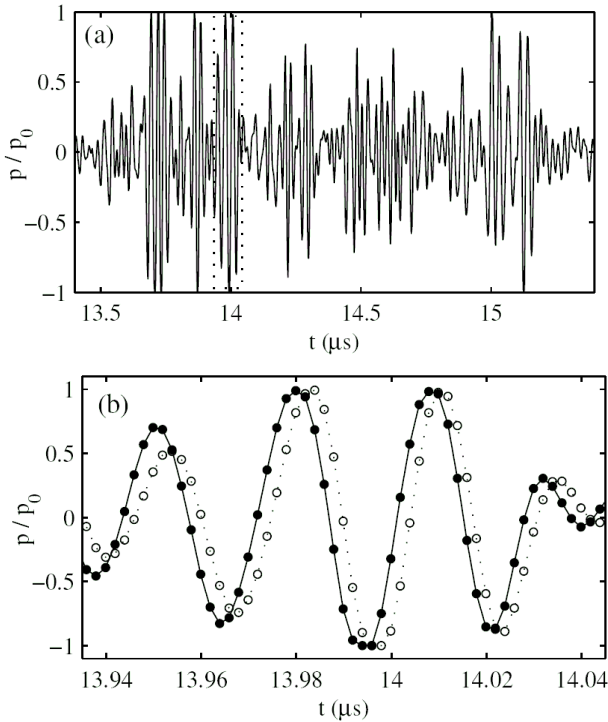


Figure 3: (a) Speckle signal recorded in a sheared Newtonian 1 wt.% suspension of polystyrene spheres of diameter 3–10 μm and normalized by the maximum amplitude p_0 . (b) Zoom over four acoustic periods. •: speckle signal p_T shown in (a) and received after a pulse is sent at time T . o: signal $p_{T+\Delta T}$ recorded over the same time window after a second pulse is sent 1 ms later.

Under the assumption of single scattering, the backscattered signal received at time t on the transducer can be interpreted as interferences of the various echoes from scattering particles located at position $y=c_0(t-t_0)/2$, where y is the distance from the stator along the ultrasonic beam and $t_0 \approx 13.5 \mu\text{s}$ accounts for the fixed contribution of ultrasound propagation through water and Plexiglas. By analogy with optics, such a backscattered signal is called a “speckle” signal. Fig. 3(a) shows a typical speckle signal p_T backscattered by a dilute suspension of polystyrene spheres. When the fluid is submitted to a shear flow, the speckle changes as the scattering particles move along. As shown in Fig. 3(b), two successive pulses separated by ΔT lead to two speckle signals that are shifted in time. The time-shift δt between two echoes received at time t corresponds to the displacement $\delta y=c_0\delta t/2$ along the y -axis of scattering particles initially located at position $y=c_0(t-t_0)/2$. The velocity v_y projected along the y -axis, of the scattering particles located at y is then simply given by $v_y=\delta y/\Delta T$.

The spatial resolution of the “ultrasonic rheo-velocimeter” is given by the acoustic wavelength $\lambda \approx 40 \mu\text{m}$. Its temporal resolution ranges between 0.1 and 10 s per profile depending on the shear rate. More details on the velocimetry technique including data storage, the cross-correlation

algorithm, its accuracy and limitations, and the calibration procedure used to measure c_0 , t_0 , and θ can be found in Ref. [11].

4 APPLICATION TO WORMLIKE MICELLE SOLUTIONS

In this section we show a few results obtained using the above-described experimental setup on solutions of wormlike micelles.

4.1 Shear banding in wormlike micelles

Wormlike micelles solutions are self-assembled surfactant systems constituted of long, cylindrical, semiflexible aggregates (a few nanometers in diameter for lengths up to a few microns) [4]. These solutions undergo a shear-induced transition from a viscoelastic state of entangled, weakly oriented micelles to a state of highly aligned micelles above some critical shear rate. Such a transition is strongly shear-thinning, as the viscosity of the aligned state can be orders of magnitude smaller than the zero-shear viscosity of the system.

Above the critical shear rate, the system spatially separates into coexisting bands of high and low viscosities corresponding, respectively, to the entangled and aligned states. As the shear rate is increased, the shear-induced structure progressively expands along the velocity gradient direction at constant shear stress until the system is fully aligned. This phenomenon, known as “shear banding,” has triggered lots of experimental and theoretical studies in last two decades [12,13].

4.2 Results from ultrasonic velocimetry

We have used ultrasonic velocimetry to confirm the above scenario that was independently established using NMR [14], DLS [15], and PIV [16]. Importantly, the fast temporal resolution of our technique has provided new insights into the dynamics of shear banded flows. As illustrated in Fig. 4, shear banding may involve strong wall slip, oscillations of the interface position between shear bands, and transient nucleation of three-banded flows [17]. Recent flow visualizations have evidenced an instability of the interface between shear bands along the vorticity direction [18]. These experimental results question the validity of the assumption of purely tangential flows. An interesting issue for future research is to explain the origin of the time scales involved in such temporal fluctuations and their order of magnitude (fractions of a second to minutes). A related question is whether such temporal fluctuations and instabilities are inherent to shear-banded flows and whether they may have some “universal” features regarding other shear-induced transitions.

5 APPLICATION TO FRACTURE IMAGING IN GELS

Ultrasound can not only be used to access time-

resolved velocity profiles but also to perform direct imaging of the material microstructure under shear.

An example is shown in Fig. 5 and 6 on an “organogel” that results from the crystallization of *N*-5-hydroxypropyl dodecanamide in toluene at a temperature of 5 °C. The gel is composed of anisotropic branched fibers of typical diameter 10 μm and length 100 μm. In this case, the microstructure is hard enough to scatter ultrasound efficiently and the fluid does not require seeding [19].

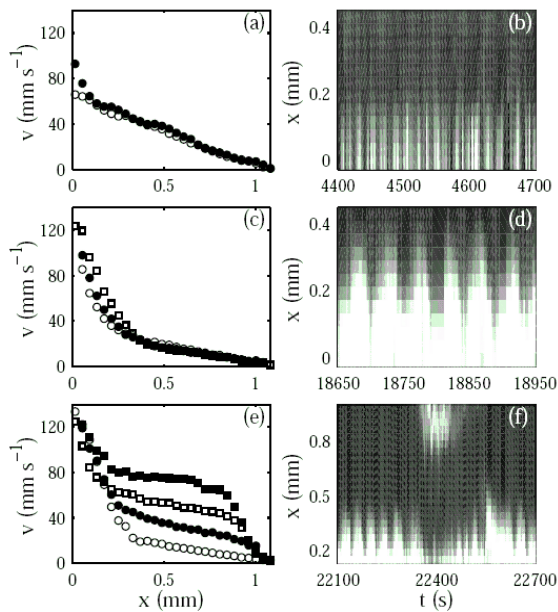


Figure 4: Spatiotemporal behaviors observed in a 20 wt% CTAB solution in D₂O under an imposed engineering shear rate of 186 s⁻¹. (a–b) Intermittent apparition of a highly sheared band at the rotor. (c–d) Oscillations of the position of the interface between shear bands. (e–f) Nucleation of a second highly sheared band at the stator. (a), (c), and (e) present individual velocity profiles, whereas (b), (d), and (f) show spatiotemporal diagrams of the local shear rate inferred from the local velocity measurements. Reprinted from Ref. [17].

The velocity profiles measured in a sand-blasted cell of gap 0.55 mm are strongly inhomogeneous (see Fig. 5(a)): a solid-like region close to the stator extends over about 100 μm. The rest of the fluid is sheared but very large error bars on the time-averaged velocities are recorded in the middle of the gap indicative of huge temporal fluctuations. Such large fluctuations most probably result from *fractures* that occur unevenly in space and time in the central region.

This picture is confirmed by directly looking at the spatiotemporal representation (A-scan) of the ultrasonic echoes shown in Fig. 5(b) and

corresponding to a start-up experiment at a very low shear rate. The solid-like region close to the stator is clearly identified by the fixed vertical echoes. Fractures show up as discontinuities (or even reverse motion) in the ultrasonic echoes, for instance at $t \approx 15, 18, 27,$ or 50 s: some parts of the gel locally translate over typically 20 μm within less than $\Delta T = 0.2$ s.

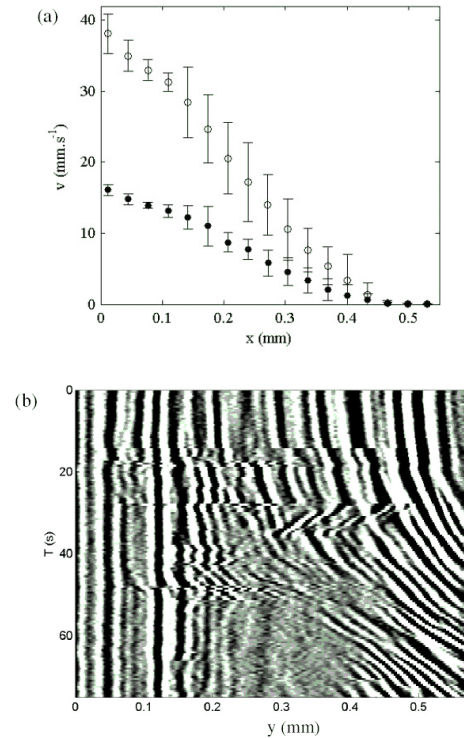


Figure 5: (a) Time-averaged velocity profiles in the organogel at $\dot{\gamma} = 0.05$ s⁻¹ (○) and 70 s⁻¹ (◻). (b) 50 speckle signals with $\Delta T = 0.2$ s recorded during a start-up experiment at $\dot{\gamma} = 0.05$ s⁻¹ and coded in grey levels. Shear is applied at $t = 0$ s. The stator (rotor resp.) is located at $y = 0$ ($y = 0.55$ mm resp.).

6 CONCLUSIONS

Through the above examples, the ultrasonic rheo-velocimeter appears as a promising tool to perform time-resolved measurements of slip velocities and to study shear localization or fractures in complex fluids during rheological experiments. Such measurements are very important in industrial applications where wall slip, slow transients, temporal instabilities, or strong shear-induced effects are involved.

The main perspectives of the present work concern:

- (i) the extension of the technique to *two-dimensional flow imaging* using a transducer array (instead of a single focused transducer) in order to measure the tangential velocity as a function of both radial and vertical positions;
- (ii) its application to *small oscillatory displacements*

during rheological experiments in the linear regime in order to recover a spatiotemporal description of viscoelastic properties of complex materials and investigate the crossover from linear to nonlinear behaviours.

instability in the flow of a triblock copolymer micellar solution, *Phys. Rev. E* 75 (2007) 061502.

ACKNOWLEDGEMENT

The author wish to thank L. Bécu, A. Colin, P. Grondin, S. Lerouge, J.-L. Pozzo, J.-B. Salmon, and F. Schosseler for fruitful discussions and collaborations on the various systems explored in this work.

REFERENCES

- [1] Larson RG: *The Structure and Rheology of Complex Fluids*, Oxford University Press (1999).
- [2] Cates ME, Evans MR, Editors: *Soft and Fragile Matter: Non Equilibrium Dynamics Metastability and Flow*, Institute of Physics Publishing, Bristol (2000).
- [3] Denn MM: Extrusion instabilities and wall slip, *Annu. Rev. Fluid Mech.* 33 (2001) 265–287.
- [4] Berret JF et al.: Isotropic-to-nematic transition in wormlike micelles under shear, *J. Phys. II France* 4 (1994) 1261-1279.
- [5] Möller PCF et al.: Shear banding and yield stress in soft glassy materials, *Phys. Rev. E* 77 (2008) 041507.
- [6] Barnes HA: A review of the slip (wall depletion) of polymer solutions, emulsions and particle suspensions in viscometers: its cause, character, and cure, *J. Non-Newtonian Fluid Mech.* 56 (1995) 221–251.
- [7] Callaghan PT: *Principles of Nuclear Magnetic Resonance Microscopy*, Oxford University Press (1991).
- [8] Takeda Y: Velocity profile measurement by ultrasonic doppler method, *Exp. Therm. Fluid Sci.* 10 (1995) 444–453.
- [9] Ouriev B, Windhab EJ: Industrial application of ultrasound based in-line rheometry: visualization of steady shear pipe flow of chocolate suspension in pre-crystallization process, *Rev. Sci. Instrum.* 74 (2002) 5255–5259.
- [10] Jensen JA: *Estimation of Blood Velocities Using Ultrasound*, Cambridge University Press (1996).
- [11] Manneville S et al.: High-frequency ultrasonic speckle velocimetry in sheared complex fluids, *Eur. Phys. J. AP* 28 (2004) 361-373.
- [12] Olmsted PD: Perspectives on shear banding in complex fluids, *Rheol. Acta* 47 (2008) 283-300.
- [13] Manneville S: Recent experimental probes of shear banding, *Rheol. Acta* 47 (2008) 301-318.
- [14] Mair RW and Callaghan PT: Observation of shear banding in wormlike micelles by NMR velocity imaging, *Europhys. Lett.* 36 (1996) 719-724.
- [15] Salmon JB et al.: Velocity profiles in shear-banding wormlike micelles, *Phys. Rev. Lett.* 90 (2003) 228303.
- [16] Hu YT and Lips A: Kinetics and mechanism of shear banding in an entangled micellar solution, *J. Rheol.* 49 (2005) 1001-1027.
- [17] Bécu L et al.: Spatiotemporal dynamics of wormlike micelles under shear, *Phys. Rev. Lett.* 93 (2004) 018301.
- [18] Lerouge S et al.: Interface instability in shear-banding flow, *Phys. Rev. Lett.* 96 (2006) 088301.
- [19] Manneville S et al.: Wall slip, shear banding, and

Series of Calibration Tests at National Standard Loops and Industrial Applications of New Type Flow-Metering System with Ultrasonic Pulse-Doppler Profile-Velocimetry for Power Plants

Michitsugu Mori

Tokyo Electric Power Co., Inc., R & D Center, 5-1-4 Egasaki, Tsurumi-ku, Yokohama, 230-8510 Japan
(e-mail: michitsugu.mori@tepco.co.jp)

Flow profile factors (PFs), which adjust measuring to real flow rates, also strongly depend on flow profiles. To determine profile factors for actual power plants, manufactures of flowmeters usually conduct factory calibration tests under ambient flow conditions. Indeed, flow measurements with high accuracy for reactor feedwater require them to conduct calibration tests under real conditions, such as fluid conditions and piping layouts. Moreover, as nuclear power plants are highly aging, readings of flowmeters for reactor feedwater systems drift due to the changes of flow profiles. The causes of those deviations are affected by the change of wall roughness of inner surface of pipings. Those changes of flow patterns lead to large errors in measurements with time-of-flight (TOF) ultrasonic flow meters. Therefore, we have to take into account those effects in order to measure the flow rates of feedwater with better accuracy in actual power plants. We proposed the new type of flowmeter called UdFlow/UDF, ultrasonic pulse-Doppler flowmeter, which can measure instantaneously-determined flow-velocity profiles and eliminate the effect of deviated flow profile from expected ideal one in measurements. Calibration tests of UdFlow/UDF were conducted at the national standard loop in Mexico, CENAM (The Centro Nacional de Metrologia) and in USA, NIST (National Institute of Standard and Technology) in order to evaluate the accuracy of the flowmeter. Four ultrasonic transducers are mounted on the surface of stainless steel piping circumferentially with the diameters of 100mm and 200mm to measure four velocity profiles. Flow rates can be obtained by integrating each measuring line and taking the average of them. A small amount of miniaturized air bubbles was injected at the upstream of measuring point for ultrasonic reflectors. Tests were conducted at five different flow rates with the Reynolds numbers between 200,000 and ~1,200,000. Tests were repeated six times at each flow rate to evaluate repeatability. In addition, the put-off and put-back test was carried out at 100mm piping with the flow rate of 3000 L/m to evaluate reproducibility. The values of the CENAM and NIST loops are based on the average of weighing time while those of the ultrasonic-Doppler flow velocity profile flowmeter are based on the time average of instantaneous values. The calibration tests found a deviation better than 0.3% between the two devices in terms of the average of the values recorded by six rounds of each measurement. From the results of measurement conducted with Reynolds number varied, it was found that the overall average deviation between the two devices was better than 0.3%. The UdFlow/UDF system has been applied for the flow rate measurements in the circulation cooling water line of fossil-fired and nuclear power plants, and in the steel penstock of hydro-power plants. We are ongoingly carrying out the development of the UdFlow/UDF system for the application to nuclear feedwater flow rate measurements.

Keywords: ultrasonic-Doppler, velocity profile, flowmeter, industrial application, calibration test

1 INTRODUCTION

With these concerns for accurate measurement of nuclear feedwater flow rates to gain uprated power by measurement uncertainty, time-of-flight (TOF) ultrasonic flowmeters are being introduced to nuclear power plants in the United States and Japan. However, these make it inevitable in quite a few measuring errors for large pipings in nuclear power plants due to unreliability of flow profile factors (PFs), because PFs used for existing nuclear power plants were experimentally obtained at much lower Reynolds Numbers with room temperatures and atmospheric pressures than half of actual ones, which were ~14,000,000 for the feedwater flow under ~7.6MPa and ~220deg-C in existing a boiling water reactor, and because the inner surface roughness of pipings changed by aging has not

been taken into account for PFs used for existing nuclear power plants. Therefore, the measurement accuracy of flow rate by conventional time-of-flight ultrasonic flowmeters is questionable. The general discussion on these errors will be made as Facility Factor ⁽¹⁾.

Figure 1 shows the changes in PFs due to the changes of pipe roughness. These calculations were done using the numerical simulation code, STAR-CD, and logarithmic law under the same hydraulic conditions as 480MW class reactor feedwater system ⁽²⁾. Two kinds of flowmeters were selected for the calculations of PFs, cross flow and transit time (time-of-flight: TOP) types. As the equivalent sand-grain surface roughness, K_s , gets rougher, PFs deviate with a few percentage points against the PFs of smooth pipings in both systems.

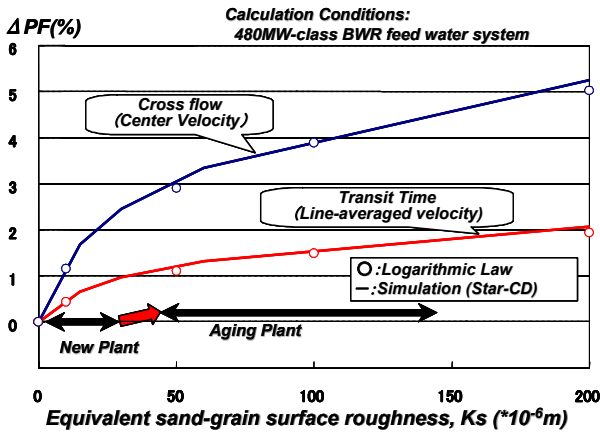


Figure.1 Percentage changes in Profile Factors vs. surface roughness

Up to around 6% deviation is observed in the case of cross flow measurement system that measures the centered-area velocity of pipings. In the case of transit time flowmeter, the PF deviates up to 3% against the smooth pipings. Therefore, if nuclear power plants get aging, we are supposed to experience those PF deviations in both systems. These deviations directly affect to the accuracy of flowmeters.

The feedwater (FW) systems of a power plant are generally exposed to high temperature and/or pressure conditions within large pipes. Therefore, determining the PF under the same flow conditions and configurations as large pipe diameters and curve bends is impractical and results in certain errors in measurement. In fact, it is impossible at the present time to determine PFs by a high-precision calibration loop using a weighing method under such high temperature and pressure conditions as in the FW system. Consequently, the PF has to be determined with a Reynolds number (Re) within one order of magnitude of the actual plant. The conventional ultrasonic flowmeters as described below round off all indeterminate errors by a PF as described in Figure 2⁽³⁾.

To remove these errors, efforts are needed to eliminate the PF by determining flow rates based on the calculation of true flow profiles in the piping^(4,5). In order to achieve a highly accurate flow measurement, the measurement of a flow profile is required to eliminate the PF⁽⁶⁾. We have conducted fields test using the UDF System, the flow-metering system by ultrasonic pulse-Doppler profile-velocimetry⁽⁷⁾ where instantaneous flow profiles and flow rates were widely measured in CW systems and steel penstock of hydro-turbines, etc. The application for the nuclear FW measurement requires further high accuracy within 0.5% to monitor the thermal power and to utilize the measurement uncertainty for a power uprate.

Integration of instantaneously-determined flow velocity profiles, obtained by performing continuous line-measurements over piping, will provide an

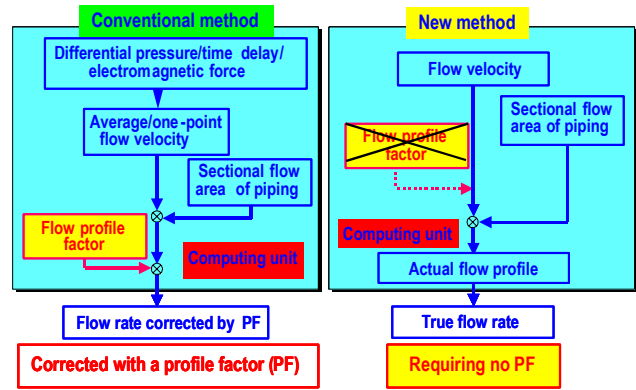


Figure2. Conceptual comparison between conventional flowmeters and the flow-metering system by ultrasonic Pulse-Doppler profile-velocimetry.

accurate flow rate measurement system as an advanced flowmeter, superior to the conventional flowmeter using a PF. The conventional flowmeters based on the time-of-flight (TOF: transit time) method depend largely on the accuracy of a PF as it finally determines the flow rate of a fluid by multiplying it. This is also true of a one-point ultrasonic-Doppler flowmeter. Accordingly, these conventional methods are limited in the scope of application as they are effective only in measuring flows with steady-state developed flow. In other words, the methods have to use an approximation that is applicable only in a narrow flow range⁽⁸⁾.

Calibration tests were performed at the national standard loops in four countries. The UDF is based on the measurement of line velocity profiles, thereby eliminating PFs, resulting in a more accurate determination of flow rates.

2 CALIBRATION TESTS AT NIST, NMIJ, AND NMI

2.1 TESTS AT NIST

The flow rate of water per unit length of time can be determined by accumulating fluid flowing down the measuring test section into the weighing tank in a given period of time and dividing the volume of the fluid thus accumulated by the time elapsed. The layout of the NIST standard loop is shown in Figure 3. The nominal measurement error of the test loop at NIST is 0.12%. In these tests, the flow of water was measured at the point where it reached the stage of full development. The UDF was found to meet the approved values of the standard loop with sufficient accuracy. Table 1 compares the approved values of the NIST standard loop and the corresponding data on the UDF at Re = 400,000. The values of the NIST loop were based on the average of weighing time while those of the UDF were based on the time average of instantaneous values. As indicated in the table, the measuring test found a deviation of 0.03% between the two devices

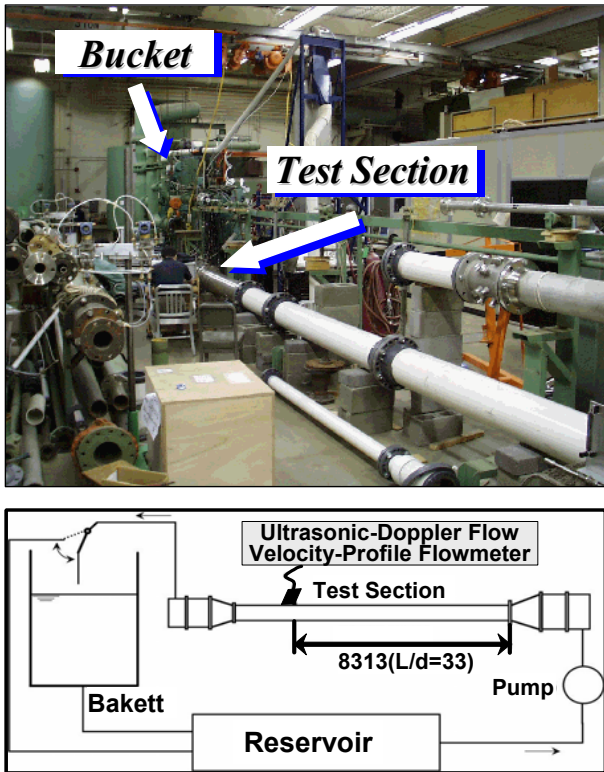


Figure 3. Layout of NIST standard loop

in terms of the average values recorded by five rounds of measurement. From the results of measurement conducted with varied Re numbers, it was found that the overall average deviation between the two devices was determined to be no more than 0.2%⁽⁹⁾.

2.2 TESTS AT NMIJ AND NMI

Further calibration tests were conducted on the UDF by a liquid flowmeter calibration facility, a verification loop shown in Figure 4, at NMIJ in Japan, and NMI in the Netherlands shown in Figure 5 for the water loop and Figure 6 for the kerosene loop.

The calibration tests on the UDF were carried out for water with a measuring instrument attached to the 400A piping section of the loop at NMIJ. At NMI, the calibration tests were carried out for water and kerosene with the 150A piping section of the loop.

Table 2. Comparison of the approved values of the NMIJ standard loop

Reference Flowrate Q_1 (m ³ /h)	Output of Flowmeter under Test Q_m (m ³ /h)	Ratio of Flowrate and Uncertainty	
		Ratio Q_m/Q_1	Expanded Uncertainty (k = 2)
2000.5	2008.9	1.004	0.4%
1512.7	1508.2	0.997	0.1%
986.1	984.6	0.999	0.3%

Table 1. Comparison of the approved values of the NIST standard loop.

Run No.	UdFlow	NIST	Deviation	
			L/s	%
#1	69.760	69.600	-0.161	-0.23%
#2	69.670	69.613	-0.057	-0.08%
#3	69.725	69.612	-0.113	-0.16%
#4	69.444	69.622	0.178	0.26%
#5	69.569	69.609	0.040	0.06%
Average	69.634	69.611	-0.022	-0.03%

Both calibration facilities (made to the national standard loop) have the standard uncertainty set at 0.02% of the reference flow rate. The results of the test at NMIJ and NMI are summarized in Table 2 and Table 3, respectively.

The test findings indicate the uncertainty of the flowmeter examined in terms of the average of the results recorded in 10 rounds of measurement at NMIJ and three rounds at NMI, comparing with the reference flow rate set as a target. The reference meter of NMIJ was based on a weighing method, and that of NMI was a turbine flowmeter. Based on these measuring tests, the UDF was given a calibration certificate showing uncertainty ranges within 0.4% at NMIJ and 0.59% at NMI for water.

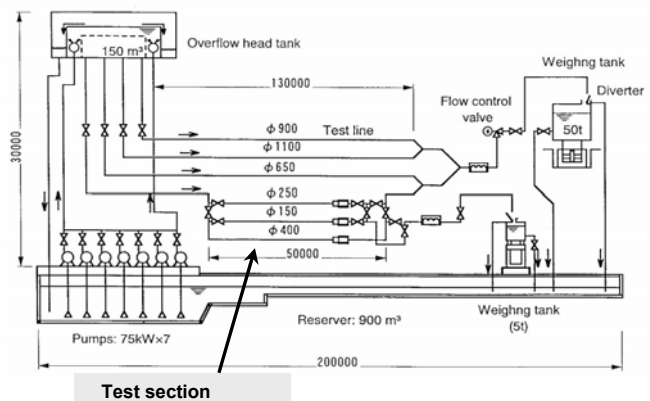
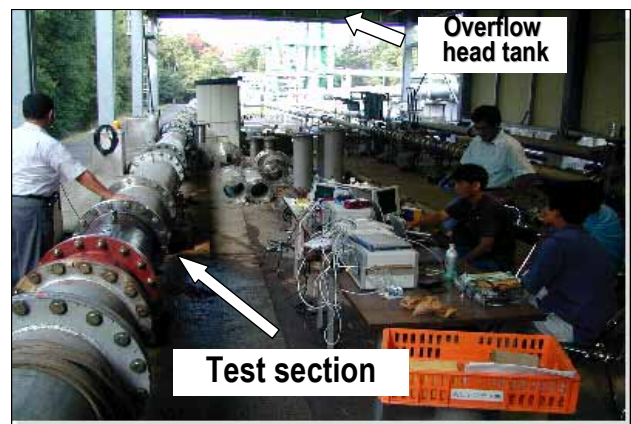


Figure 4. Layout of standard loop and test facility of 400mm pipe test in National Metrology Institute of Japan

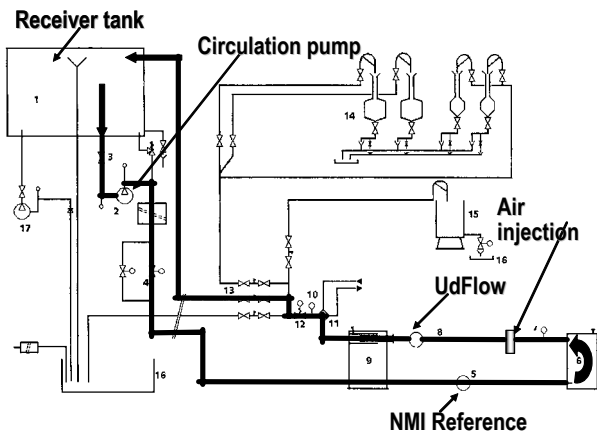


Figure 5. Layout of NMI standard loop for water

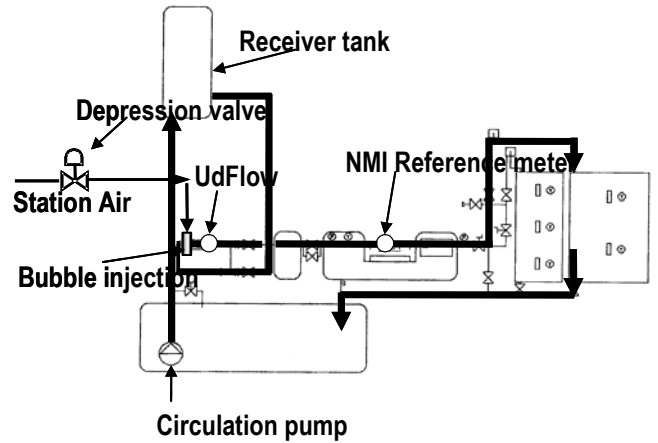


Figure 6. Layout of NMI standard loop for kerosene

3 CALIBRATION TESTS AT CENAM

Following improvements to the UDF System, calibration tests were carried out at CENAM, using ultrasonic transducers clamped on the surface of stainless steel piping having diameters of 100 mm and 200 mm.

Figure 7 shows the pipe arrangement at CENAM. The CENAM loop contains a straight pipe long enough to produce the developed flow condition, an

inlet header and pumps, and weigh systems. CENAM has two weigh systems of 1,500 kg and 10,000 kg.

Air was injected upstream of the measuring point up to ~400 ppm (0.04% as a volumetric fraction.). We confirmed that there was a negligible effect of air injection on the flow rates measured by the weigh systems of CENAM, comparing the flow rate measured without air injection with one using air

Table 3. Comparison of the flow rates measured by UDF with the approved values of the NMI standard loop for water (left) and kerosene (right). NMI - Nederlands Meetinstituut

Reference Flow-rate [l/min]	Reference Velocity [m/s]	Indicated Flow-rate [l/min]	Indicated Velocity [m/s]	Deviation [%]
1276.7	1.2041	1273.1	1.2007	-0.28
1276.6	1.2040	1280.7	1.2079	+0.32
1276.8	1.2042	1271.7	1.1994	-0.40
953.76	0.8995	959.4	0.9048	+0.59
953.41	0.8992	952.8	0.8986	-0.07
953.74	0.8995	949.1	0.8951	-0.49
632.02	0.5961	633.9	0.5979	+0.30
631.82	0.5959	628.5	0.5928	-0.52
632.04	0.5961	630.1	0.5943	-0.30

Reference Flow-rate [l/min]	Reference Velocity [m/s]	Indicated Flow-rate [l/min]	Indicated Velocity [m/s]	Deviation [%]
1276.6	1.2040	1279.5	1.2067	+0.22
1276.4	1.2038	1281.3	1.2084	+0.38
1276.5	1.2039	1281.5	1.2086	+0.39
956.19	0.9018	949.3	0.8953	-0.72
956.54	0.9022	959.1	0.9046	+0.27
955.92	0.9016	955.4	0.9011	-0.06
639.51	0.6032	641.1	0.6046	+0.23
639.49	0.6031	643.6	0.6070	+0.65
639.30	0.6029	643.90	0.6073	+0.73

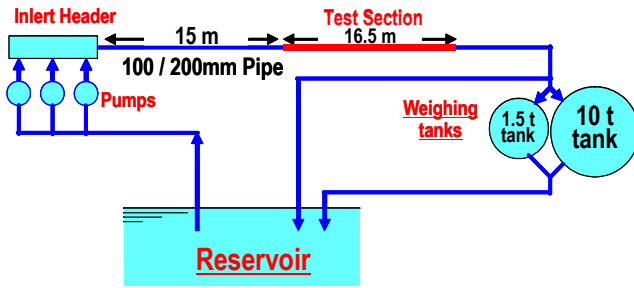


Figure 7 Layout of CENAM standard loop for water and pipe arrangement.

injection.

Tests were conducted at five different flow rates with the Reynolds numbers between 200,000 and 1,330,000. Tests were repeated six times at each flow rate to evaluate repeatability. In addition, the take-off and put-back test was carried out on the 100 mm piping with the flow rate of 3000 L/m to evaluate reproducibility. The values of the CENAM loop are based on the average of weighing time while those of the UDF were based on the time average of instantaneous values. The references 8, 9, and 10 provide the following definitions of each Individual Value:

3.1 RELATIVE ERRORS

The relative error between qv from the reference and qv from the meter is defined by:

$$e = \left(\left[\frac{qv_{meter}}{qv_{primary\ standard}} \right] - 1 \right) 100 \quad (\%)$$

3.2 METER FACTOR

The Meter Factor (MF), $MF_i(q_j)$, for a single measurement i at flow q_j :

$$MF_i(q_j) = \frac{qv_{j\ primary\ standard}}{qv_{j\ meter}}$$

where, :

$qv_{primary\ standard}$ – volumetric flow-rate determined by

the primary standard at line conditions (L/min).

qv_{meter} – time-averaged volumetric flow rate measured for the meter, at line conditions, over the calibration interval (L/min).

The MF arithmetic mean value for a series of measurements at the flow rate q_j :

$$\overline{MF_j}(q_j) = \overline{MF_j} = \frac{1}{n} \sum_{i=1}^n MF_i(q_j)$$

3.3 METER FACTOR UNCERTAINTIES

The experimental variance of $MF_i(q_j) = s^2(MF_j)$, from repeated measurements at flow rate q_j :

$$s^2(MF_j) = \frac{1}{n-1} \sum_{i=1}^n \left(MF_i(q_j) - \overline{MF_j}(q_j) \right)^2$$

The experimental standard deviation of the mean of the Meter Factor, $s_{dm}(\overline{MF_j})$ at each flow, is given by:

$$s_{dm}(\overline{MF_j}) = \frac{1}{\sqrt{n}} s(MF_j)$$

where n is the number of the replicated tests at flow j . The meter Repeatability, i.e., the short term stability can be quantified as the experimental standard deviation of the mean at each test flow; the largest Repeatability is quoted as a bound for the meter for all of the flows tested.

3.4 EXPANDED UNCERTAINTY

The Expanded Uncertainty, U is:

$$U(\overline{MF_j}) = kU_c(\overline{MF_j})$$

The expanded uncertainty U can also be expressed using a coverage factor k based on t-distribution for ν_{eff} degrees of freedom with a level of confidence of approximately 95 %. This uncertainty was evaluated according to Reference 9.

3.5 REPRODUCIBILITY

For specific sets of tests done for the UDF, Reproducibility is defined in terms of the standard deviation of the mean of the multiple sets of runs taken at essentially the same flow condition after specific, typical changes in test conditions are made to assess the meter's performance in these conditions. The specific changes made need to be described. Typical changes needed by most meter users are turning the flow off and then turning it back on, and then repeating the tests; this effect can be quantified by the TOTO (turn-off-turn-on) Reproducibility. For clamp-on type meters, another typical change is quantified by TOPB (take-off-put-back) Reproducibility. The conditions changed in

Table 4 Summary data of the tests on the 100 mm pipe diameter and on the 200 mm pipe diameter in fully-developed flow conditions. The table below lists the mean values of MF -meter factor - and standard deviation calculated from 6 values, the Reproducibility (for a single flow) and the expanded uncertainty of the meter factor.

Primary Standard				UdFlow	Test Result	
Reynolds Number	Average Flow Velocity v (m/s)	Primary Standard Flow Rate qv (L/min)	Relative Standard Deviations (%)	Meter Flowrate Qvm (L/min)	Meter Factor MF	Deviation e (%)
200 mm pipe diameter						
4.46·10 ⁵	2.1	4 000.73	1.59·10 ⁻²	4 010.06	0.997 68	0.23
6.59·10 ⁵	3.1	6 006.78	1.64·10 ⁻²	6 012.02	0.999 13	0.09
8.93·10 ⁵	4.1	8 005.22	1.46·10 ⁻²	7 998.56	1.000 83	- 0.08
1.11·10 ⁶	5.2	9 998.64	1.36·10 ⁻²	9 980.48	1.001 82	- 0.18
1.33·10 ⁶	6.2	12 002.10	5.22·10 ⁻³	12 011.41	0.999 23	0.08
4.46·10 ⁵	2.1	4 000.73	1.59·10 ⁻²	4 010.06	0.997 68	0.23
6.59·10 ⁵	3.1	6 006.78	1.64·10 ⁻²	6 012.02	0.999 13	0.09

these tests include, for a single flow, both TOTO and TOPB and the Reproducibility, i.e., longer term meter stability obtained is quantified by the experimental standard deviation of the mean for these tests:

$$R = sdm [MF_j] = \sqrt{\frac{1}{m(m-1)} \sum_{i=1}^m [MF_i(q_j) - \overline{MF_j}]^2}$$

where “j” is the flow for which the “changed conditions” tests were done again and “m” is the total number of repetitions of data points taken at essentially the same test flow. Table 4 summarizes the test data on the 100 mm and 200 mm pipe diameters in fully-developed flow conditions. The average flow velocities varied from ~2m/s to ~6m/s for both pipes. The Reynolds numbers were set up to 1,330,000 for the case of the pipe diameter of 200 mm, and 641,000 for 100 mm. From the results of measurement conducted with varied Reynolds numbers, it was found that the overall average deviation between the two devices was better than 0.3%. The table lists the mean values of meter factor and standard deviation calculated from 6 values, the Reproducibility (for a single flow) and the expanded uncertainty of the meter factor.

4 INDUSTRIAL APPLICATIONS

4.1 MEASUREMENT TESTS OF NUCLEAR FW CONDITIONS AT HIGH REYNOLDS NUMBER

Measurement tests were carried out to check the performance of the UDF system in elevated temperatures with high Reynolds numbers of

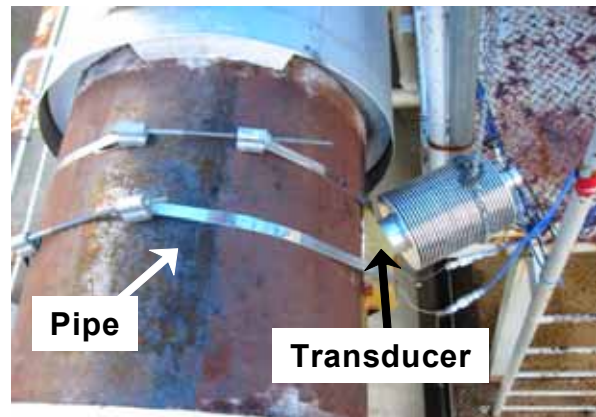


Figure 8 Measurement test section of nuclear feed water Conditions.

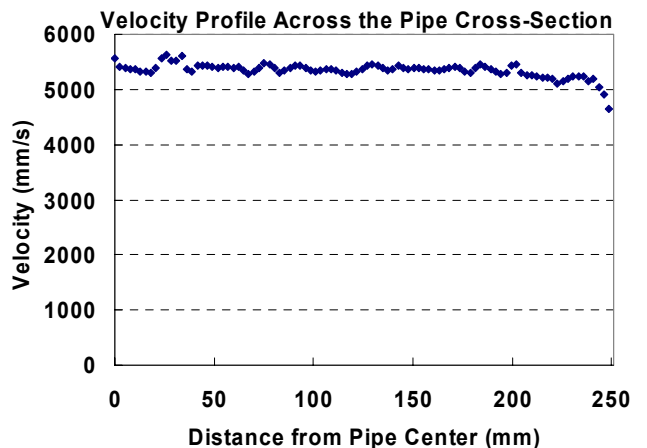


Figure 9 Velocity profile measured at actual nuclear feed water Conditions at high Reynolds number of ~14,000,000.

$\sim 14,000,000$, which are corresponding to ones of feedwater conditions of a boiling water reactor. Figure 8 shows the measurement test section for nuclear reactor feedwater conditions. The ultrasonic transducer was mounted on the carbon steel pipe whose inner diameter of 500mm with the wall thickness of 29.0mm. The volumetric flow rate was $\sim 3200\text{m}^3/\text{h}$ at temperature of 215deg-C and $\sim 7.6\text{MPa}$ in pressure. The miniaturized helium gas bubbles were injected as reflectors with 40ppm in volume. Flow velocity profiles were successfully measured as shown in Figure 9. The averaged velocity was around 5m/s and the profile seemed relatively flat due to the measuring position of $\sim 10D$ from a pipe bend.

4.2 FIELD MEASUREMENT TESTS IN A HYDRO-POWER STATION

Flow velocity profiles were measured to evaluate



Figure 10 Overview of measurement test at a steel penstock in a hydro-power station.

flow rates of a steel penstock in a hydro-power station. Figure 10 shows the overview of the measuring position and steel penstock. Two transducers were installed at the horizontal diameter position of 19D from the inlet of steel penstock, and two simultaneous measurements revealed that non axially-symmetry flow patterns existed at 19D from the inlet of steel penstock as shown in Figure 11.⁽¹⁰⁾. The average of two lines was $1.36\text{ m}^3/\text{s}$ with $1.39\text{ m}^3/\text{s}$ for the transducer A and $1.33\text{ m}^3/\text{s}$ for the transducer B.

4.3 FIELD MEASUREMENT TESTS IN A FOSSIL-FIRED POWER STATION

Figure 12 shows the overview of measuring test section at a sea circulation water pipe in a fossil-fired power station. The pipe diameter is $\sim 1700\text{mm}$ with the wall thickness of 12.8mm. The velocity profile was obtained for the half in diameter, near

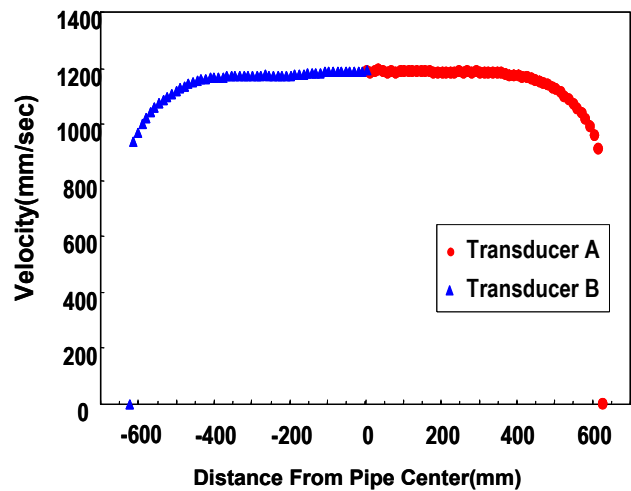


Figure 11 Measured velocity profiles at a steel penstock of $\sim 1250\text{mm}$ in diameter in a hydro-power station.



Figure 12 Overview of measurement test at a sea circulation water pipe in a fossil-fired power station.

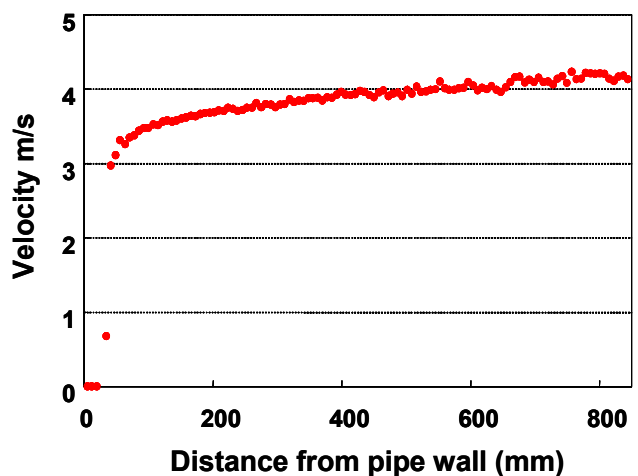


Figure 13 Measured velocity profile at a sea circulation water pipe of ~ 1700 in a fossil-fired power station.

side of the wall on which the ultrasonic transducer was clamped on, since the average velocity was ~4m/s with a flow rate of 10m³/s and the diameter of ~1700mm, as shown in Figure 13, which resulted in constraint by the Nyquist theory.

5 CONCLUDING REMARKS

The calibration tests of the UDF System were conducted at four national standard loops: NIST in the United States, NMIJ in Japan, NMI in the Netherlands, and CENAM in Mexico, in order to evaluate the accuracy of this new type flow-metering system. The test results at NIST, NMIJ, and NMI for the velocity profile measurements exhibited the deviations within ~0.5%. Following improvements to the UDF System, the maximum spreads in individual MF test results in the mean values for the UDF are from -0.17% to +0.14 % for the 100 mm diameter pipe and from -0.18% to +0.23 % for the 200 mm diameter pipe over the range of Reynolds numbers tested at CENAM. At CENAM, the short term stability (Repeatability) and longer term stability (Reproducibility) are both considered good, i.e., better than 0.03 % in these test conditions. Further testing may need to be done to better quantify Reproducibility characteristics.

The expanded uncertainty for the UDF Meter Factor in these tests at CENAM is bounded by ± 0.21 % for the test with 100 mm pipe and by ± 0.16 % for the test with 200 mm pipe; these values are computed for 95% confidence levels. A negligible effect on the CENAM primary standard measurements was found for the air bubble injection used for these tests.

Measurement tests for industrial applications were carried out in the high-temperature loop simulating nuclear reactor feedwater conditions, hydro-power station, and fossil-fired power station. The UDF System of new type flow-metering with ultrasonic pulse-Doppler profile-velocimetry has revealed its high applicability for elevated temperature conditions of nuclear reactor feedwater, the steel penstock of hydro-power, and the circulated water pipe in fossil-fired power plants.

REFERENCES

- (1) Takeda, Y., "ON THE TRACABILITY OF ACCURACY OF ULTRASONIC FLOWMETER", ICONE-14 89803, Proceedings of ICONE 14, July 17-20, 2006, Miami, Florida USA
- (2) Tezuka, K., et. al., "Industrial Applications of New Type Flow-metering System by Ultrasonic-Doppler Profile-Velocimetry, (1) Effects of Surface Roughness and Asymmetric Pipe Flow on Accuracy of Profile Factor", Fourth International Symposium on Ultrasonic Doppler Methods for Fluid Mechanics and Fluid Engineering, Hokkaido University, Sapporo, Japan, September 6-8, 2004
- (3) Mori, M., et.al., "Industrial Application Experiences of New Type Flow-metering System based on Ultrasonic-Doppler Flow Velocity-Profile Measurement," Third International Symposium on Ultrasonic Doppler Methods for Fluid Mechanics and Fluid Engineering, EPFL, Lausanne, Switzerland, September 9 - 11, 2002
- (4) Takeda, Y., et. al., "Development of flow rate measurement using ultrasonic Doppler method [1]Theoretical background," 1998 Fall Meeting of AESJ, [1998] F16, p.343
- (5) Mori, M., et. al., "Development of ultrasonic-Doppler velocity profile method for flow rate measurements of power plant," [1999] ICONE-7, FP7429
- (6) Mori, M., et. al., "EFFECTS OF INNER SURFACE ROUGHNESS AND ASYMMETRIC PIPE FLOW ON ACCURACY OF PROFILE FACTOR FOR ULTRASONIC FLOW METER," ICONE-14 89729, Proceedings of ICONE 14, July 17-20, 2006, Miami, Florida USA.
- (7) Mori, M., et. al., "Development of a novel flow metering system using ultrasonic velocity profile measurement," Experiments in Fluids, 32 [2002] pp.153-160.
- (8) Takeda, Y., "Measurement of velocity profile of mercury flow by ultrasound Doppler shift method," Nuclear Technology, 79 [1987]. pp 120-124.
- (9) Takeda, Y., et. al., "Development of a new flow metering system using UVP, Preliminary performance assessments using NIST flow standards," Proceedings of ASME FEDSM'00, ASME 2000 Fluids Engineering Division Summer Meeting, June 11-15, Boston, Massachusetts.
- (10) Suzuki, T., "Development of New Flow Metering System using Ultrasonic Doppler Method, (2)Flow-rate Measurement for Hydraulic-Turbine Efficiency at Hydroelectric Power Stations", ICEE2008, 90691, July 6-10, 2008, Okinawa, Japan.

Single-shot Doppler Velocity Estimation using double chirp pulse compression

Farès ABDA* and Philippe SCHMITT

Institut de Mécanique des Fluides et des Solides, 2 rue Boussingault, 67000-Strasbourg, France

(*Corresponding author, e-mail: fares.abda@gmail.com).

Coherent ultrasonic Doppler velocimeters provide precise and accurate measurements of velocity profiles in many applications. However, these instruments suffer from the well known range-velocity ambiguity, making this kind of instruments not well suited for velocity measurements in channels of several meters depth and water velocities of some meters per second. On the other side, incoherent ultrasonic Doppler velocimeters don't have such limitations but suffer from reduced spatial and temporal resolution. The known actual solutions to this compromise consist in using phase-coded repeated pulses composing one excitation ping. The performance of such a solution is mainly conditioned by the appropriate choice of the binary coding sequence. While longer codes reduce the variance of the velocity estimate, they limit both spatial resolution and measurable velocity range. We present in this paper an alternative pulse compression scheme using overlapping linear chirps. This method makes it possible to improve the estimation variance with respect to phase coding using minimum peak sidelobe level binary codes. The performances in term of both bias and variance with respect to various parameters including noise level, length of range-gated signal, velocity dispersion within a considered volume and number of particles will be addressed based on a model taking into account the Doppler effect on wideband transmitted pulses. These results will be discussed and compared with experimental measurements and theoretical predictions of performance limits (The Cramér-Rao lower bounds) for both wideband and narrow-band Doppler velocimeters. Furthermore, we will show that it is possible to extend the measurable velocity range without affecting spatial resolution and precision, all parameters otherwise unchanged.

Keywords: pulse-to-pulse coherent sonar, velocity-range ambiguity, pulse compression, precision

1 INTRODUCTION

Ultrasonic Doppler velocity estimation is the measurement of the amount of compression or expansion of the backscattered signal received after the transmission of an arbitrary ultrasonic signal. The principle of such an instrument is based on the existence of backscattering particles within the medium. Such medium consists generally either in oceanic or riverine waters where we need to make the measurement of long range velocity profiles (distribution of the velocity field along the ultrasonic beam) or simply estimating the relative velocity between the instrument referential and the medium for navigation purposes. The Doppler estimation is generally performed along several beams oriented toward the bottom and the projections of the velocity field vector on each ultrasonic beam axis provide a measure of the velocity mean radial vector in the considered range-gated volume. This measure is deduced by linear combination of the total single-beam projections estimated individually where the velocity field is supposed uniform throughout the volume containing all the ultrasonic beams.

We present in this paper a performance analysis by computer simulation based on a point scattering model for reverberation signal synthesis using wideband transmitted pulses. Pulse compression using both *Minimum Peak Sidelobe Level (MPSL)* binary codes and linear chirps will be compared and it will be shown that the latter technique permits the achievement of better performances since it appears to give more flexibility in designing highly

correlated overlapping pulses.

2 PRINCIPLE OF OPERATION

The principle of operation of an instrument using short duration repeated pulses for the estimation of Doppler shift is depicted in figure (1). The excitation signal consists in a sequence of identical pulses of short duration transmitted in a single ping [4]. Like for the case of a coherent system, the problem consists in estimating the phase shift from the reverberation signal resulting from the summation of successive reflections of the two (or more) identical pulses on the ensemble of scatterers contained within the volume of interest.

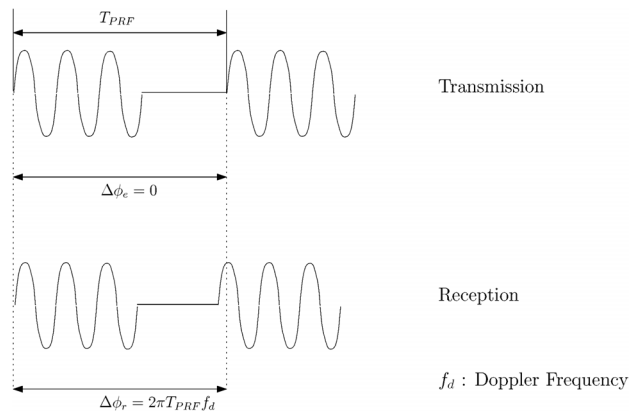


Figure 1: Principle of operation.

To alleviate the notation, we take in the following $T_{PRF} = T$ and the transmitted signal is given by:

$$e(t) = p\left(t - \frac{T}{2}\right) + p\left(t + \frac{T}{2}\right) \quad (1)$$

and

$$p(t) = \Re\left\{\Pi\left(\frac{t}{T_p}\right)e^{2j\pi f_0 t}\right\} \quad (2)$$

where $\Pi(t/T_p)$ is the unity rectangular window of duration T_p and \Re denoting the real part.

The reflection of $e(t)$ on a single scatterer moving with radial velocity v relatively to the transducer will produce $r(t)$. Assuming that the effect of the acoustic backscattering coefficient of the particle as well as the amplitude propagation loss is represented by the coefficient a , the received signal is given by:

$$r(t) = ae\left(\beta\left(t - \frac{2R_0}{c+v}\right)\right) \quad (3)$$

where $\beta = c - v / c + v$ is the Doppler compression/expansion factor and c is the sound velocity in the medium. The relative radial velocity is assumed constant during both the signal duration and the round-trip travel time and R_0 is the distance between the particle and the transducer at the emission instant.

The autocorrelation function argument of the complex baseband signal at a time lag equal to the inter-pulse spacing gives a measure of the Doppler frequency. The autocorrelation of the received signal can be calculated as:

$$\Gamma_r(\tau) = \Gamma_{pp\beta}\left(\tau + \frac{T}{\beta}\right) + 2\Gamma_{pp\beta}(\tau) + \Gamma_{pp\beta}\left(\tau - \frac{T}{\beta}\right) \quad (4)$$

with $\Gamma_{pp\beta}(\tau)$ being the autocorrelation of $ap(\beta t)$.

Therefore, the Doppler effect can be seen as a translation of the lateral peaks of the baseband auto-covariance function by a time delay $\Delta T = (\beta - 1)T / \beta$. An estimate is calculated by evaluating the phase shift equal to the argument of the autocorrelation function at a time lag equal to the pulse pair spacing [2]:

$$\Delta\phi_r = \arg\left[\Gamma_{pp\beta}(\Delta T)\right] = 2\pi(\beta - 1)f_0 T = 2\pi f_d T \quad (5)$$

3 PULSE COMPRESSION

Pulse compression is a widely used technique in RADAR and SONAR technology [3]. The main advantages are an improved spatial resolution and a better immunity to both ambient and electronic noise. In that context, frequency modulated signals and pseudorandomly biphas-modulated signals are the most used methods. Since the former has

gained less attention in the past, the aim of this study is to characterize the performances of each technique both by simulation and experimentation. Phase modulation using binary codes provide the advantage of its simplicity since it consists in simply changing the sign of the carrier frequency, the main drawback is the necessity to find optimal codes whose autocorrelation function have minimized sidelobes. Some of these codes are provided in the literature and the most known among them are the Barker codes with PSL=1 (Peak Sidelobe Level). Longer codes have been discovered but having PSL greater than one. Frequency modulated signals or chirps (linear or hyperbolic) on the other side are more complicated to generate but provide the advantage of being more flexible to adapt by modifying their bandwidth and duration. Furthermore, overlapping two or more chirps gives the possibility to extend the unambiguous velocity range without affecting the estimation variance simply by better filling the transducer bandwidth.

4 REVERBERATION SIGNAL SIMULATION

Performance comparison using various kinds of excitation signals and pulse compression schemes can be compared under the same conditions using a repeatable and easily parameterizable synthetic reverberation signal.

By invoking superposition, the reverberation signal $r(t)$ is the sum of echoes from many discrete scatterers:

$$r(t) = \left[\sum_i a_i D^2(\vec{r}_i)(s * h_T)(\beta_i(t - t_i))\right] * h_T(t) + w(t) \quad (6)$$

with $\beta_i = (c - v_i) / (c + v_i)$. The echo from each scatterer, indexed by i , is delayed by t_i corresponding to the two-way travel time between the scatterer and the transducer as well as the phase of the scatterer acoustic impedance considered to be uniformly distributed random variable on the interval $[0, 2\pi]$. The gain factor $D^2(\vec{r})$ is used to modelize the effect of ultrasonic beam pattern and h_T the transducer transfer function. The individual amplitude factor a_i is representing the modulus of the acoustic impedance of each scatterer as well as the two-way propagation loss. The SNR is adjusted by varying the power of $w(t)$ which is a zero mean additive white Gaussian random noise of variance σ_n^2 . The velocity dispersion is varied as a Gaussian random variable with mean v_m and variance σ_v^2 .

The resulting synthetic reverberation signal is range-gated to obtain the windowed signal corresponding to a cell of arbitrary length. Finally, the signal is passed through an analog quadrature demodulator and subsequently decimated. The output of the simulator is a dual digital data stream representing

the inphase and quadrature components forming together the complex baseband output of the system.

5 SIMULATION RESULTS

The simulations were conducted using a binary code of 51 bits length (4 wavelengths per bit) and PSL=3 repeated two times. The central frequency was $f_0 = 1.25\text{Mhz}$. Two chirps of equal length centered on f_0 and with spectral width equaling two times the equivalent bandwidth of the binary code were used for comparison. One thousand estimations using the same random parameters in each case were performed. The default values were 0dB for the SNR, 100cm for the cell size, no velocity dispersion and 200 particles per a volume equivalent to 200cm range.

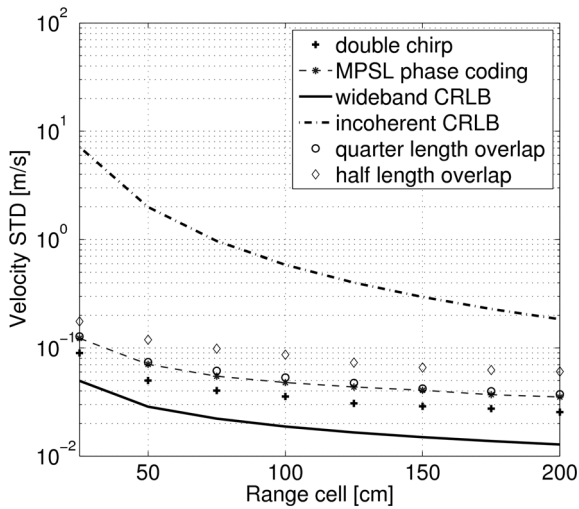


Figure 2: Velocity standard deviation for various cell sizes.

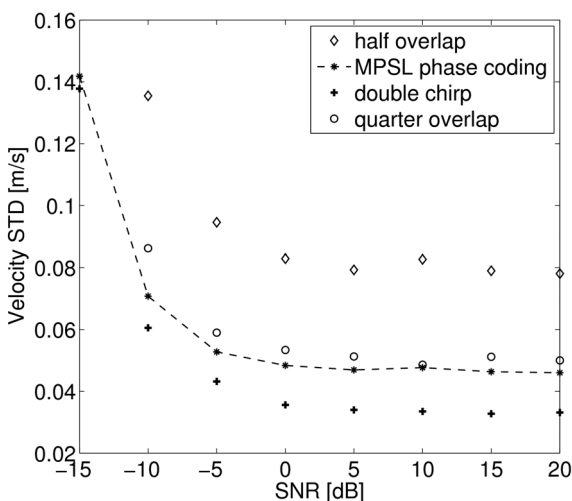


Figure 3: Velocity STD for various SNR values.

The influence of the cell size on the estimation variance is reported in figure (2). For comparison, we give the obtained STDs by using double pulse with MPSL binary phase coding, double chirp with

same duration and inter-pulse spacing (same ambiguity velocity), double half length overlapping chirps with same total duration (ambiguity velocity augmented with 100%), and double quarter length overlapping chirps with same total duration (ambiguity velocity augmented with 50%). Both CRLBs (Cramér-Rao Lower Bounds) for incoherent [5] and wideband [1-2] cases are plotted for reference. In figure (3), the effect of SNR is plotted and using wideband linear chirps is clearly advantageous. Particularly, using double chirp with quarter length overlapping gives almost the same STD (except for very low SNRs), but with the advantage of increasing the maximal unambiguous velocity by 50%. The bias comparison on figure (4) shows no significant difference between the two methods.

As would be expected, the number of particles per volume unit does not have any direct influence on

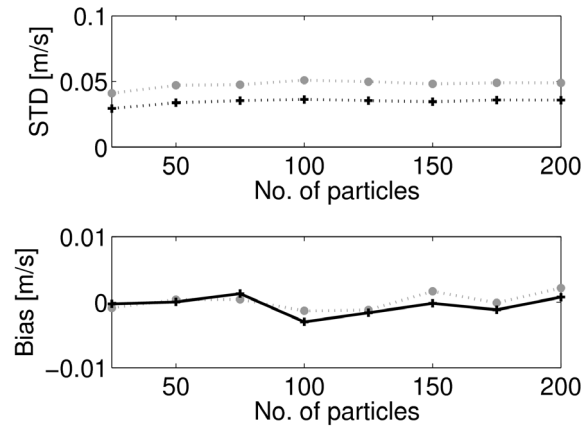


Figure 4: Influence of the number of particles on the measurement precision (Top), and the bias (Bottom). (Grey: Phase Coding, Black: Double chirp).

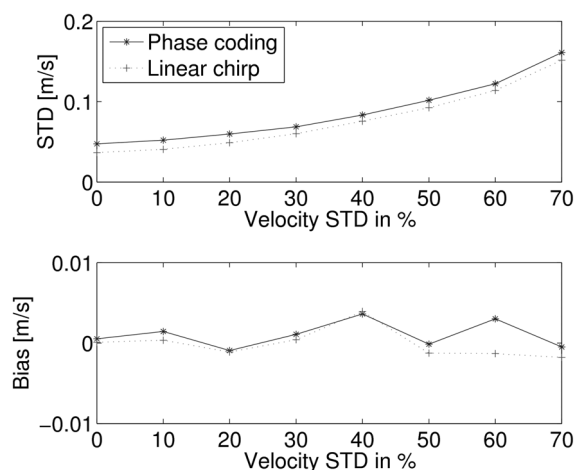


Figure 5: Influence of velocity dispersion on standard deviation and bias of velocity estimate.

the precision of the measurement (see figure (4)), however, in real situations, since the concentration is related to the power of the backscattered signal, the consequence will be a variation in the SNR.

Velocity dispersion was varied and the results on both standard deviation and bias are reported on figure (5). As expected there is a degradation in the estimation of the mean velocity as the dispersion increases. On the other side there is no significant influence on the estimate bias.

6 EXPERIMENTAL VERIFICATION

The comparative results obtained from measurements carried out on a turbulent flow contained in a laboratory channel are presented on figure (6). For the two cases, double chirp pulse compression (top) and phase-coded excitation (bottom), we present the spectrogram of one transmitted and received signals (left), 100 successive velocity profiles (middle), and the mean profile as well as the standard deviation as a measure of the precision in each case.

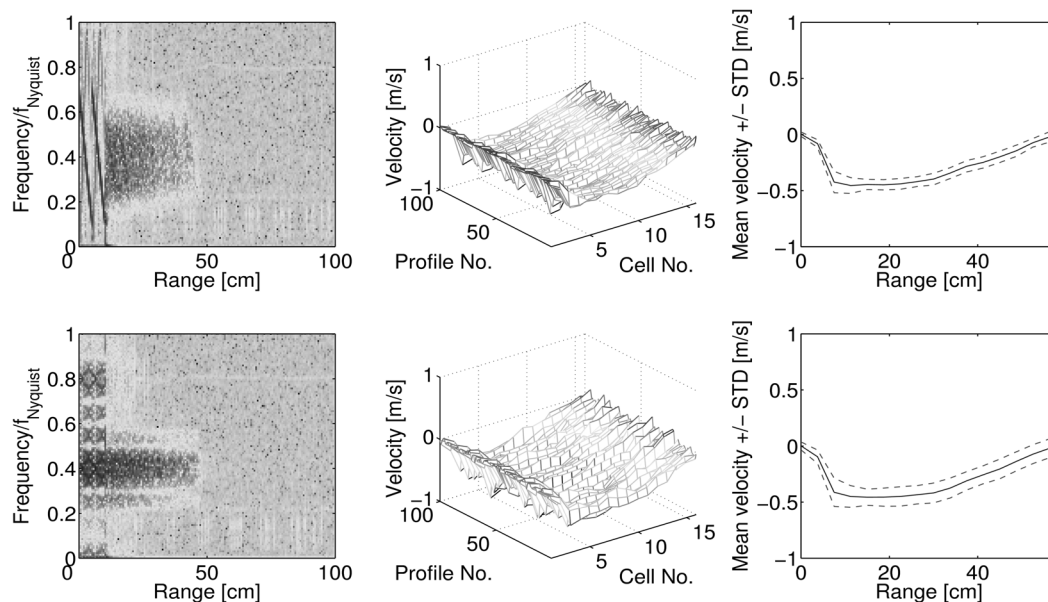


Figure 6: Experimental verification (see text for details).

The excitation signal with central frequency 2Mhz (0.4 as normalized by the Nyquist frequency), is repeated with a frequency equivalent to one meter exploration depth. The phase coded signal was modulated with 51 bits code, 4 wavelengths per bit, and the chirps having 3Mhz bandwidth. By comparing the two spectrograms, it can be seen that while the double chirp have a wide spectrum, the phase-coded signal is characterized by a relatively narrower spectral main lobe despite the fact it have been coded using MPSL binary sequence. The result is a reduced variance using wideband double chirp pulse compression.

7 CONCLUSION

We presented in this paper some comparative results concerning the use of two pulse compression techniques for the improvement of velocity estimation using an hybrid excitation scheme. This method allows the measurement of velocity profiles

along one ultrasonic beam using a single transmit-receive cycle. It has been shown through computer simulation and by measurements conducted in a laboratory controlled water flow that using wideband overlapping chirps permits a valuable improvement in the measurement precision. This achievement is made possible because of a better usage of the transducer bandwidth. Moreover, the flexibility in using frequency modulated chirps also permits the extension of the unambiguously measurable velocity range. This is made possible since overlapping two chirps reduces the inter-pulse duration. Therefore, by augmenting the bandwidth at the same time, it is possible to extend the maximal unambiguous velocity without affecting the estimation variance. The spatial resolution and effective exploration range being unchanged since these quantities are only related to the total transmission duration.

ACKNOWLEDGEMENT

We wish to acknowledge the financial support of the company ULTRAFLUX and the National Association of Technical Research (ANRT).

REFERENCES

- [1] Brumley B. H., Cabrera R. G., Deines K. L. and Terray E. A., Performance of Broad-Band Acoustic Doppler Current Profiler, IEEE Journal of Oceanic Engineering, Vol. 16, No. 4, October 1991, pp 402-407
- [2] Miller K. S., Rochwarger M. M. : A covariance approach to spectral moment estimation, IEEE Transactions on Information Theory 18 (1972) 588-596
- [3] Pintel R. and Smith J. A., Repeat-Sequence Coding for Improved Precision of Doppler Sonar and Sodar, Journal of Atmospheric and Oceanic Technology, April 1992, Vol. 9, pp 149-163
- [4] Rowe F., Deines K. and Gordon R. : High Resolution Current Profiler, Proceedings of the IEEE Third Working Conference on Current Measurement, 3 (1986) 184-189.
- [5] Theriault K. B., Incoherent Multibeam Doppler Current Profiler Performance: Part I-Estimate Variance, IEEE Journal of Oceanic Engineering, Vol. 11, No. 1, 1986.

Open-channel Discharge Measurement based on Ultrasonic Doppler Velocity Profiling – Laboratory Experiments

Vojtech Bares^{1*}, Jan Krajd¹ and Jaroslav Pollert¹

¹Department of Sanitary and Ecological Engineering, CTU Prague, Thákurova 7, 166 29 Prague, Czech Republic (*Corresponding author, e-mail: bares@fsv.cvut.cz).

Presented study deals with the design, the experimental evaluation and the verification of the novel methodology for open-channel discharge measurement suitable especially for the short-term monitoring. The methodology is based on an error-minimized application of ultrasonic velocity profiling method enabling the measurement of instantaneous velocity distribution over the entire flow depth without direct contact with the flowing liquid. The total relative bias of measured and reference values of the discharge from all experiments was 3.2 %. Results show that the relative error increases with the flow depth. The second group of experiments introduces more or less stable results. Besides the total value of discharge, the method also offers detailed information about velocity distribution over the cross section. The influence of side walls on the velocity distribution in verticals close to the channel walls is clearly stated. The neglecting of that effect in classical flow metering techniques contributes to wrong estimation of depth-averaged velocity. The results show high accuracy of presented flow rate measurement methodology and demonstrate its great potential to identify hydraulic singularities in open-channel flows.

Keywords: Discharge measurement; open-channel flow; ultrasonic anemometry; velocity profile

1 INTRODUCTION

The information about the inflow/outflow at the waste water treatment plant (WWTP) is one of the fundamental parameters of performance data to control treatment process and maintenance of the WWTP [1]. Simple measuring devices such as weirs or flumes are accurate enough, however their calibration is needful. The uncertainty of the calibration method often exceeds the uncertainty of the measured flow rate given by measuring weir. The sources of the uncertainty are the human factor, the influence of the velocity field with the measuring device used for calibration (propeller), the flow non-uniformity and unsteadiness, the measuring time and the accuracy of the measuring device (propeller) itself. Presented study deals with the design, experimental evaluation and verification of a novel methodology for open-channel discharge measurement suitable especially for short-term monitoring. The methodology is based on an error-minimized application of ultrasonic velocity profiling method enabling the measurement of instantaneous velocity distribution over the entire flow depth without direct contact with the flowing liquid.

2 EXPERIMENTAL METHODS

2.1 Measuring devices

The methodology was tested under laboratory conditions in a rectangular flume of width of $B=0.525$ m and length of $L=8$ m. The reference values of the total discharge were obtained using MID flowmeter (Krohne Aquaflex DN 200) at inlet pipe of the flume. A calibrated ultrasonic transducer (Pepperl&Fuchs UC2000) was used for

measurement of flow depth. The information about the velocity distribution in the channel was obtained using Ultrasonic Velocity Profiler (Met-Flow SA) together with employing of two ultrasonic transducers (basic frequency $f_0 = 4$ MHz, active diameter $d = 5$ mm, sampling frequency $f = 12.5$ Hz, sampling time of one TDX $t = 120$ sec).

2.2 Hydraulic conditions

Experiments were carried out under different flow conditions in turbulent ($Re = 1.94 \times 10^4 \sim 1.34 \times 10^5$) and subcritical ($Fr = 0.05 \sim 0.54$) flow regime. In the first group of experiments a constant flow depth of $h = 228$ mm was maintained in the channel and the flow rate varied in the range of $Q = 10 \sim 60$ l/s with step of $\Delta Q \cong 10$ l/s. The second series of experiments was carried out with a constant flow rate of $Q = 29.5$ l/s and a varying flow depth $h = 100 \sim 410$ mm with step $\Delta h \cong 80$ mm. Velocity distribution was measured in 11 verticals in each experiment.

2.3 Discharge estimation

The method used for discharge estimation is a modification of the classical hydrometric technique for flow rate measurement, the so-called *area-velocity method*. [2]. In contrast to propeller gauging, the depth-averaged velocity is estimated based on numerical integration of time-averaged velocity profile over flow depth h with spatial resolution of $\Delta y = 2.22 \sim 4.4$ mm.

To minimize possible errors, several critical aspects of UVP method [4] were taken into account. Measurements were made using two independent probes in one vertical with inclination of $\theta = \pm 20^\circ$ to vertical axis [3]. The transducers were placed in a

movable box made of plexiglas (Figure 1). Such positioning can minimize the error originating from non-uniformity of the flow (vertical and horizontal velocity components are identifiable) and the error from wrong setting of the box installation. The box is filled with water and the bottom is made of PVC film (th. 0.1 mm). That allows the positioning of the near field of the US beam out of the flowing liquid.

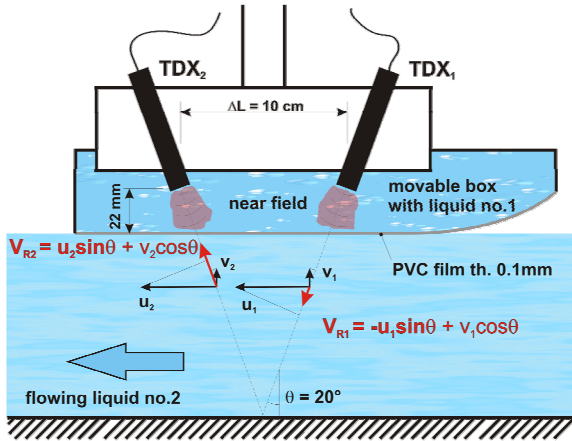


Figure 1: Scheme of transducers position and velocity vector decomposition

Assuming small distance ($\Delta L = 10$ cm) between the heads of transducers compared to the length of the channel, the time-averaged longitudinal velocity components are equal to each other at the same horizontal level.

$$\bar{u}_{1j} \approx \bar{u}_{2j} \approx \bar{u}_j \quad (3)$$

where indexes <1;2> identify a US transducer and index $j = <1;11>$ a given vertical. Based on Figure 1 one can write expressions for time-averaged vectors in direction of radial axis of US probes as:

$$\bar{V}_{R1j} = -\bar{u}_{1j} \sin \theta + \bar{v}_{1j} \cos \theta \quad (4)$$

$$\bar{V}_{R2j} = \bar{u}_{2j} \sin \theta + \bar{v}_{2j} \cos \theta \quad (5)$$

Further, one can easily express longitudinal component of point velocity as:

$$\bar{u}_j = \frac{\bar{V}_{R1j} + \bar{V}_{R2j}}{2 \sin \theta} \quad (6)$$

Integrating the measured values of point velocities over flow depth h and channel width B one can estimate discharge in cross section as:

$$Q = \int_0^B \int_0^h \bar{u}_j \, dy \, dx \quad (7)$$

3 RESULTS

3.1 Velocity profiles

Eleven vertical profiles were measured for each given discharge (Figure 2). It is clearly visible that the velocity distribution in a cross section is highly asymmetrical to vertical axis (Figure 5). The velocity

distribution itself significantly deviates from vertical to vertical and it cannot be described by a general valid formula. Obviously, the velocity profiles in verticals close to side walls are less than in the centerline.

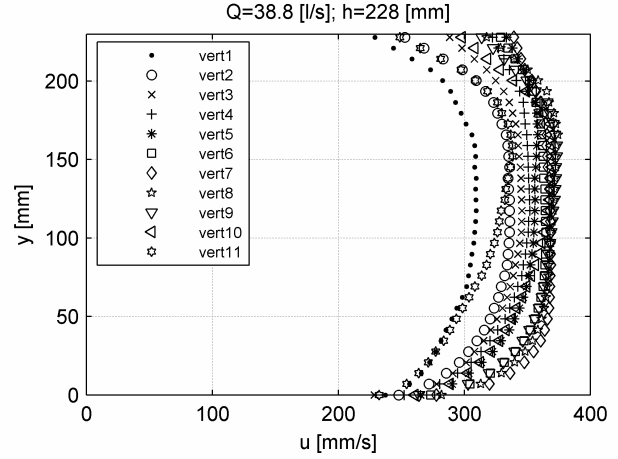


Figure 2: Time-averaged velocity distribution of longitudinal velocity component in given verticals for run Q40_h22 ($Q = 38.8$ l/s; $h = 228$ mm).

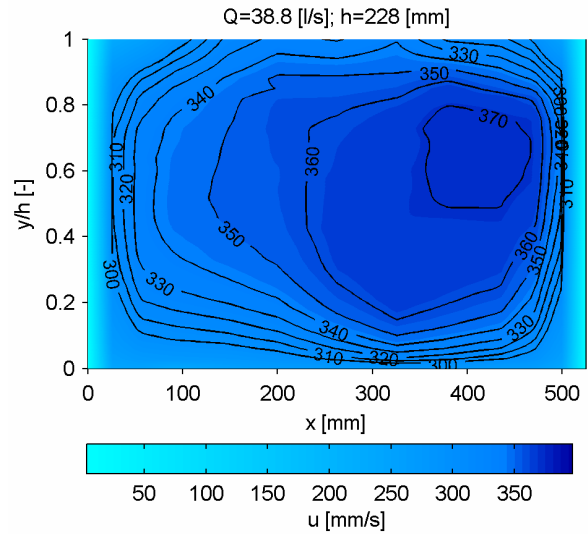


Figure 3: Distribution of longitudinal velocity component in cross section for run Q40_h22 ($Q = 38.8$ l/s; $h = 228$ mm).

3.2 Total discharge

Summarized values of estimated flow rates are presented in Table 1 with values of discharge measured using MID (Q_{KR}) taken as reference values. Absolute and relative errors vary in the range from 0.51% to -5.93%. The average relative error was estimated as -3.22%.

Table1: Results of measured flow rates with absolute and relative errors (100% \approx MID Krohne).

Run	Δy [mm]	h [mm]	U_{Kr} [mm/s]	U [mm/s]	Q_{Kr} [l/s]	Q [l/s]	T [°C]	Fr [-]	Re [-]	abs. error [l/s]	rel. error [%]
Q10_h22	2.22	231	82.48	81.42	9.99	9.87	16.2	0.05	19463	-0.11	-1.12
Q20_h22	2.22	229	168.01	163.13	20.22	19.61	16.2	0.11	39646	-0.61	-2.99
Q30_h22	2.22	229	248.87	241.26	29.98	29.01	16.3	0.17	58874	-0.98	-3.26
Q40_h22	2.22	228	334.11	324.29	40.06	38.82	16.3	0.22	79039	-1.25	-3.11
Q50_h22	2.22	228	416.74	403.33	49.87	48.28	15.9	0.28	97601	-1.59	-3.19
Q60_h22	2.22	228	502.32	483.45	60.11	57.87	15.9	0.34	117643	-2.24	-3.73
Q29_10	1.48	104	543.80	546.57	29.69	29.84	15.6	0.54	126187	0.15	0.51
Q29_18	2.22	194	292.03	282.76	29.69	28.80	15.6	0.21	67843	-0.89	-3.00
Q29_26	2.96	251	222.68	212.64	29.38	28.02	15.8	0.14	52020	-1.36	-4.62
Q29_34	3.7	337	167.62	159.12	29.62	28.15	15.9	0.09	39270	-1.47	-4.97
Q29_41	3.7	411	136.26	128.28	29.42	27.68	15.9	0.07	31928	-1.74	-5.93

Note: Δy = channel distance; h = flow depth; U_{Kr} = average velocity in cross section (MID); U = average velocity in cross section (UVP); Q_{Kr} = discharge (MID); T = water temperature; Fr = Froude number; Re = Reynolds number.

Figure 4 and Figure 5 represent the relationship between rel. error and averaged velocity in the cross section U resp. flow depth h . The relative error seems to be constant ($\approx -3\%$) over a wide range of velocities (150 \div 500 mm/s), with the exception of velocity $U = 80$ mm/s (run Q10_h22). In case of flow depth h (Figure 5), the relative error increases continuously with increasing flow depth up to almost -6%. Comparing two runs (Q30_h22 and Q29_18) with similar flow conditions one can observe a similar relative error of measured flow rate ($\approx -3\%$).

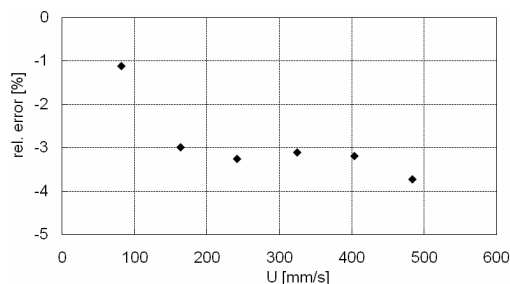


Figure 4: Relationship between the relative error of measured discharge and the average velocity in a cross section.

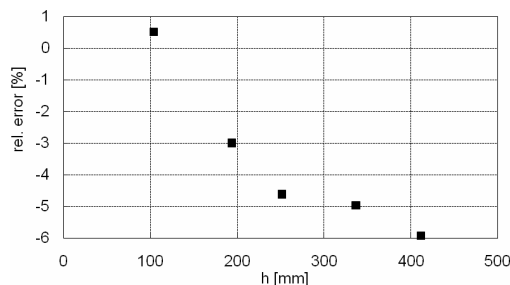


Figure 5: Relationship between the relative error of measured discharge and flow depth.

4 DISCUSSION

4.1 Depth-averaged velocity

The main advantage of UVP measurements related to discharge estimation is the information about vertical velocity profile with high spatial resolution. This contrasts with hydrometric methods, which usually use point measurements with probes, propellers etc. Comparison of measured and estimated depth-averaged velocity is presented in Table 2. The depth-averaged velocity of U was estimated by numerical integration of measured profile using UVP. The averaged velocity in vertical U_v was estimated using the following equation valid for 5 point measurements:

$$\overline{U}_v = 0.1(u_b + 2u_{0.2h} + 3u_{0.4h} + 3u_{0.8h} + u_s) \quad (8)$$

where u_b is velocity on the bottom, u_h is point velocity in a given level h and u_s is the point velocity at water surface.

Table 2 shows that the highest deviation belongs to verticals close to side walls and it decreases towards the centerline of the channel. This corresponds with theoretical considerations.

4.2 Measuring box

The use of the measuring box was found profitable. One doesn't lose velocity data belonging to near field of US beam close to the water surface. Further, the box influences flowing liquid much less than probes placed directly in the water. Moreover, the box minimizes the possibility of clogging of transducer which is a significant difficulty especially in waste water. All experimental runs were made twice (with and without box). Averaged relative error for runs without box was -4.5% , which is more than with the box (Table 1).

Table 2: Deviation between measured and theoretically estimated depth-averaged velocity for given verticals (run Q40_h22).

vertical	U [mm/s]	U _v [mm/s]	rel. error [%]
1	291.0	284.9	2.10
2	317.5	311.8	1.80
3	327.4	320.5	2.13
4	336.5	332.4	1.20
5	344.0	340.8	0.93
6	352.5	348.0	1.26
7	358.8	353.9	1.35
8	358.8	353.4	1.50
9	354.9	348.9	1.68
10	344.9	339.4	1.61
11	307.8	301.4	2.07

4.3 Duration of measurement

When the discharge is measured during a field investigation, one of the important criteria is the duration of the measurement. It is obvious that in systems where the flow rate changes relatively fast (i.e. waste water systems) this can influence the result of hydrometric measurement significantly. Using our experiment as example, the appropriate time for classical hydrometric method using a propeller in 55 positions in the cross section and a measuring time of 1 min per each point would be more than 1 hour. Employing the multiplexer function on UVP Monitor and an appropriate number of US probes one can estimate the flow rate in such channel in 22 minutes (in simplified approach with 1 probe per vertical in 11 minutes), which is significantly shorter.

4.4 Sensitivity to Doppler angle

One of the disadvantages of the UVP method is a high sensitivity of measured mean flow velocity to the setting of correct Doppler angle. The deviation of probe installation by $\theta = \pm 1^\circ$ in presented experiment ($\theta = 20^\circ$) produces an error of $\pm 5\%$ in the estimated discharge. The probability of deviation during in-situ measurement is very high. Therefore, two transducers fixed in steel element were used for velocity measurements. That minimizes the error originating from wrong installation of the whole apparatus.

5 CONCLUSION

Introduced flow metering technique based on non-invasive measuring of velocity distribution in selected verticals provides accurate information about discharge, takes into account specific velocity distribution in verticals, and allows to obtain detailed information about the velocity distribution in a cross

section. Averaged relative error was evaluated as - 3.22%. The error is independent on averaged velocity in cross section U and is significantly influenced by flow depth h .

In respect to classical hydrometric methods it is concluded that even in laboratory rectangular flume the estimation of depth-average velocity using point measurement introduces significant source of error. That would be expected in natural streams as well.

In addition, the experiment revealed a previously unknown asymmetry of measuring flume in the laboratory.

The methodology itself cannot replace classical hydrometric methods for discharge estimation, it would, however, be preferable in specific cases.

ACKNOWLEDGEMENT

This work was supported by the Czech Science Foundation; projects No.103/07/P269 and by the project of the Czech Ministry of Education, Youth and Sport No. MSM6840770002.

REFERENCES

- [1] Harremoes, P. et al: Waste water treatment plants under transient loading – performance, modeling and control. *Wat. Sci. Tech.* 27(12), 71-115, 1993.
- [2] ISO 748: Hydrometry -- Measurement of liquid flow in open channels using current-meters or floats. 2007.
- [3] Lemmin, U. and Rolland, T.: Acoustic velocity profiler for laboratory and field studies. *Journal of Hydraulic Engineering ASCE*, 123(12), 1089-1098, 1997.
- [4] Takeda, Y.: Ultrasonic Doppler method for velocity profile measurement in fluid dynamics and fluid engineering. *Experiments in Fluids*, 26(3), 177-178. 1999.

How can computational fluid dynamics improve measuring in real sewers?

Hossein Bonakdari*, Ali Akbar Zinatizadeh¹

¹Departement of Civil Engineering, University of Razi, Kermanshah, Iran (*Corresponding author, e-mail: bonakdari@yahoo.com).

Flow-rate is an important parameter for the management of sewer networks. One of the most common methods for the evaluation of the discharge consists in measuring the water depth together with the mean velocity in the cross section. The challenge is to obtain an accurate estimation of the mean velocity with available sensors that sample only a limited volume. Computational fluid dynamics (CFD) can be a useful tool for improving the representativeness of measurement: it enables to optimize the position of the sensor in the collector and to determine the processing of the gathered data. This paper presents an application of CFD to calculate the corrective coefficient which must be applied to the measured value of velocity to get the mean velocity for different acoustic Doppler sensors, thus making it possible to improve the accuracy of the calculation of the discharge. The baseline idea is to obtain a good adequacy between an instrument and a measurement section in order to improve the reliability and the accuracy of the measured values. Coherent structures in the near field of a free jet have been studied. Experiments are carried out for the free jets issuing from circular and square nozzles using a water channel. Instantaneous velocity profiles are obtained in the radial directions by using an ultrasonic velocity profiler (UVP). Coherent structures in the radial direction are investigated in terms of the proper orthogonal decomposition (POD). The radial oscillation of the mixing layer is captured by the only first POD mode with about half a total energy. These velocity fields are reconstructed by the only lower-order POD modes and the reconstructed velocity fields by the lower-order and higher-order POD modes demonstrate large-scale and smaller-scale coherent structures, respectively. In the case of circular jet, there is a peak of power spectrum of the random coefficient at the first POD mode.

Keywords: Computational Fluid Dynamics, flow-rate measurement, flow velocity, spatial sampling.

1 INTRODUCTION

Like any industrial process, wastewater collection networks need measuring means for real-time control of flows, as well as for performance evaluation, and this need is supported by European and French regulations. The choice of a measuring section may be difficult as it is necessary to take into account both hydraulic conditions and practical criteria, which are not directly linked to "metrology" such as accessibility, security of staff and equipment, connection to electric and communication networks etc. These parameters determine which measuring sites are possible candidates, provided a suitable measuring method is designed.

From a metrological point of view, it is important to be able to guarantee certain accuracy for the measurement, that means evaluating and limiting uncertainties in a reliable manner, according to the objectives. However, flow-rate measurement is always obtained through an indirect method. Thus some kind of modelling is embedded in every flow-meter in order to transform the measured parameters (water height, sampled velocity in its volume of measurement) into flow-rate. So the inherent uncertainty of in situ measurement combines two uncertainties: (1) the measured parameters and (2) the validity of the applied transformation (or representativeness of

measurement). The former is much related to the apparatus and the latter depends primarily on the site of measurement. Methods relying on a simultaneous measurement of depth and velocity are quite flexible widely used. But it is important to notice that the measured local velocity (either mean velocity U_{meancone} or maximum velocity U_{maxcone} according to the type of sensor) is usually different from the area-averaged mean velocity on the cross section (Hughes *et al.* 1996, [2]). Then special attention has to be paid to the representativeness of the measurement of velocity. In order to get a good evaluation of the mean velocity, a corrective coefficient is needed, and can be defined by considering the measured velocity in the volume explored by the sensor as follows:

$$K_U^{\text{mean}} = \frac{U_{\text{mean}}}{U_{\text{meancone}}} \quad (1)$$

$$K_U^{\text{max}} = \frac{U_{\text{mean}}}{U_{\text{maxcone}}} \quad (2)$$

where U_{mean} is the mean velocity in the whole cross section. The coefficient can be dependent on 4 parameters: (1) geometry of the collector, (2) position of the sensor, (3) type of sensor and (4) hydraulic condition. It is difficult to determine precisely for a particular real case, especially because it may change as condition (4) is variable.

The aim of this study is to show the possible application of the computational fluid dynamics (CFD) for the calculation of corrective coefficients by considering the 4 parameters quoted above. The measurements obtained by various sensors according to their positions and hydraulic conditions (height of water) have been simulated, and made it possible to propose solutions for instrumentation, combining a choice of sensor and its positions in a cross section.

2 EXPERIMENTAL SITE

An experimental site in Nantes (North West of France) has been considered in this study. For this site, the channel is narrow with a channel aspect ratio (width y / height z) between 1.4 and 2.6. As expected in such narrow channels, the maximum velocity is clearly located below the free surface (Larrarte, 2006, [5]) and this phenomenon is called dip phenomenon (Nezu and Nakagawa, 1993, [6]), as shown in Fig. 1a).

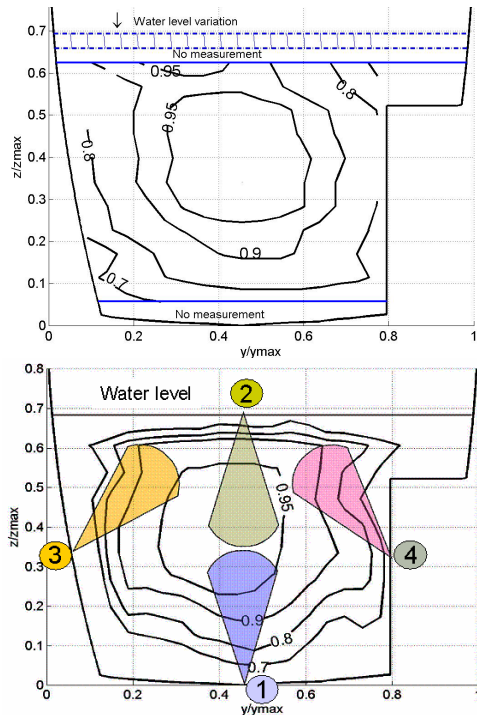


Figure 1: Comparison of experimental velocity measurement and numerical simulation for high water level conditions, a) experimental results b) numerical results with CFX.

3 NUMERICAL STUDY

The numerical procedure uses CFX software package for solving 3D Navier-Stokes equations, and predict distributions of velocity over a cross-section. This study is based on a biphasic modelling (water+air). The numerical simulation gives a good representation of the experimental results as shown in figure 1-b (Bonakdari et al., 2006, [1]).

4 EVALUATION OF THE MEASUREMENTS CARRIED OUT BY SENSORS

Three types of sensors referred as A, C, D were used after being tested by Larrarte *et al.* (2006), [4]. These sensors commonly used in sewers, primarily measure either a maximum or a mean velocity in the sampled volume. These sensors are also different in terms of emission angle, range and beam width as indicated in Table 1.

Table 1: Characteristics of three types of sensors according to Larrarte et al. (2006)ean flow velocities

Emission angle (°)	Range (m)	Beam width (°)
15	3.5	17
31	0.8	10
14	1.3	24

With a velocity field calculated by means of a numerical code, it is possible to determine the theoretical measurement carried out by a sensor by considering its position in the collector, and its own characteristics. According to the type of sensor, we determine either the maximum value or the average value in the scanned volume. This conic volume is deduced from the characteristics of the sensor, by knowing the emission angle, the range and the beam width. It is supposed that the opacity of waste water does not reduce scanned volume. The maximum value ($U_{maxcone}$) is searched among the velocities calculated numerically at the points of the mesh in the cone of measurements. The mean velocity delivered by the sensor is estimated from the weighted average of the velocities, as follows:

$$U_{meancone} = \frac{\sum_{i=1}^n U_{elementi} \times \nabla_{elementi}}{\sum_{i=1}^n \nabla_{elementi}} \quad (3)$$

where $U_{meancone}$ is the mean velocity in the cone of the sensor, $U_{elementi}$ local velocity on the center of the element i , $\nabla_{elementi}$ the volume of the element i

and $\sum_{i=1}^n \nabla_{elementi}$ the sum of n volumes of elements,

that means the volume explored by the ultrasonic cone. Four positions for each sensor was studied in the vertical section of the collector, see figure 1b : position 1 is the usual position at the bottom of the channel, position 2 has been proposed by (Laplace et Deshons, 1998, [3]), position 3 and 4 have been observed in real sewers.

5 RESULTS AND DISCUSSION

3.1 Influence of sampled volume and positions of sensors measuring mean velocity

According to the characteristics of sensors, sampled volume allows a more or less representative

estimation of the mean velocity in the cross section. This phenomenon induces the application of a corrective coefficient to the sampled mean velocity (K_U^{mean}) for the sensors performing this kind of measurement. Figure 2 gives the effects of water level variation and positions of sensors over K_U^{mean} in experimental site for the three studied sensors A, C and D.

For sensor A, it appears that above a height of 1.06 m, the coefficient K_U^{mean} remains constant. In lower part, only position 1 (at the bottom) provides an identical coefficient which corresponds to more important water heights. This sensor is characterized by a large range. When the height of water is sufficient compared to the range, scanned volume can be important. Thus, whatever the position, the measurement deduced from sampled volume remains constant. For the low water level, the sampled volume is smaller, thus the non-uniformity of the velocity field is reflected on the variation of measurement according to the position.

For the sensor C, the coefficient K_U^{mean} varies according to the position, and for all the heights of water. It is advisable to pay attention to the positioning of this sensor. The results show that the coefficients K_U^{mean} are less dependent on the height of water for positions 1 (at the bottom) and 2 (free surface). Concerning sensor D, we note a large variation of the coefficient K_U^{mean} according to the water height. We note a lower variation of this coefficient for the positions 1 and 2, especially for the high water level.

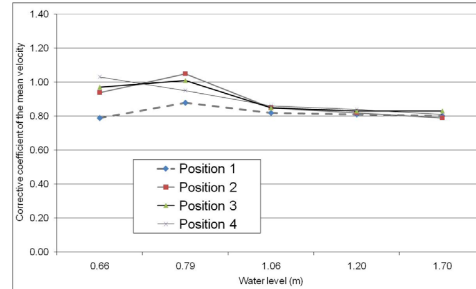
5.2 Influence of sampled volume and positions of sensors measuring maximum velocity

An increase in sampled volume increases the probability to capture maximum velocity in the cross section. But the relationship between the maximum velocity in the cross section and the average value of velocity is still needed. Figure 3 shows the effects of water level variation and positions of sensors over K_U^{max} in experimental site for the three studied sensors A, C and D. The variation of the coefficients K_U^{max} is low according to the height of water and position of sensors compared to the coefficients K_U^{mean} .

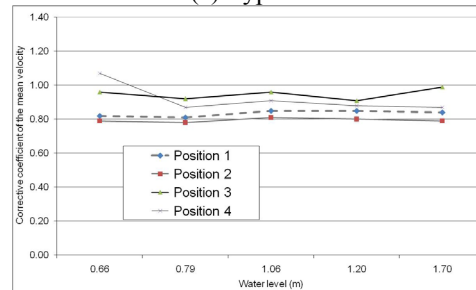
The measurement with sensor A is independent of the position for the high water level, and slightly dependent on the low water level. Other sensors show light variations according to the height of water and the position. As a whole, the maximum velocity measurement is definitely less sensitive than the mean velocity measurement.

5.3 Optimization of the position of sensors in a sewer

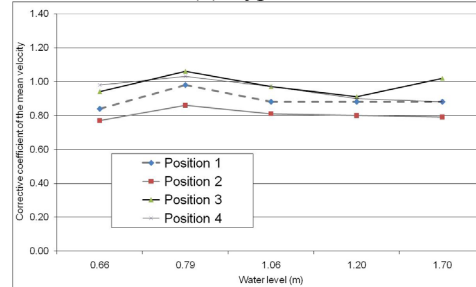
Concerning the optimization of instrumentation, the optimal solution should satisfy the two following criteria: (1) an estimation by the sensor close to mean velocity, which is equivalent to a correction factor near to 1 (2) an independence of the corrective coefficient against the hydraulic conditions (height of water).



(a) Type A



(b) Type C



(c) Type D

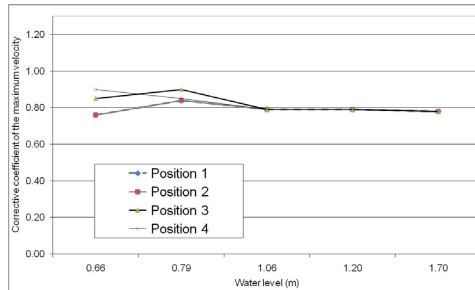
Figure 2: Influence of type and position of sensors on the coefficient K_U^{mean} for 5 water levels.

In the real case, as the first criterion can be difficult to obtain, we focus on the criterion (2) based on the variability of the measurement of a sensor according to the height of water. To evaluate the criterion (2), the coefficient of variation is defined as the ratio of the standard deviation σ to the mean μ :

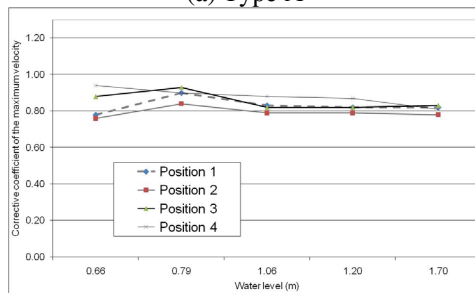
$$Cv = \frac{\sigma}{\mu} \quad (4)$$

Table 2 shows all of the coefficients of variation for the various corrective coefficients, expressed in percentage.

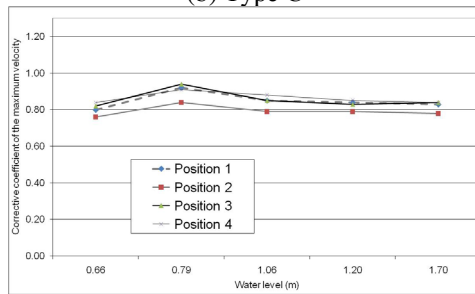
In a general way, for all of the sensors, positions (1) and (2), respectively at bottom and at the free surface, are interesting. In this case, the scanned volume relates to the slice in the central zone of the cross section. This configuration seems optimal to obtain a velocity close to that of the central zone non-disturbed by the walls.



(a) Type A



(b) Type C



(c) Type D

Figure 3: Influence of type and position of sensors on the coefficient K_U^{\max} for 5 water levels.

Table 2: Coefficients of variation of K_U^{mean} and K_U^{\max} for the sensors according to 4 positions.

	Cv (K_U^{mean})			Cv (K_U^{\max})		
	A	C	D	A	C	D
Position 1	4,3%	2,2%	5,8%	3,7%	5,3%	5,2%
Position 2	11,9%	1,4%	4,2%	3,7%	3,7%	3,7%
Position 3	9,5%	3,5%	6,2%	6,3%	5,6%	5,6%
Position 4	10,1%	9,3%	6,4%	6,3%	6,4%	3,5%

The other positions which scan in diagonal the section can appear inadequate for sensors with a small range. Indeed, these sensors are not able to scan the central zone where maximum and mean

velocities are located. If positions (1) and (2) allow an adequate measurement, they can induce practical problem. The position at the bottom can pose problems in term of sedimentation. The position at the free surface makes difficult the fixing of the sensor for installation. If the instrumentation can take place only by fixing the sensors at vertical walls, we can propose to determine the optimal angle allowing the sensor to scan the central zone.

In terms of choice of sensor, it appears that sensor A, which scans an important volume, is selected against the others. This kind of measurement appears less sensitive to the hydraulic conditions and positioning.

6 CONCLUSIONS

The modeling of flows in collectors, combined with a modeling of sampling with Doppler sensors, allow studying the principal parameters influencing measurement. Indeed, errors of measurement are dependent on: the sensor installation, the characteristics and the types of sensors, and the in situ hydraulic conditions. These errors can be corrected with a corrective coefficient of the mean velocity adapted to each case. If the first point depends on the efforts authorized by the building owner at the time of the studies of the project of instrumentation, the second depends on the information provided by the manufacturers of the measurement material. It can be the most difficult point to apprehend correctly today, because the sampling carried out by sensors is certainly not uniform inside the volume of measurement.

REFERENCES

- [1] Bonakdari H., Larrarte F., Bardiaux J. B., (2006), Experimental and computational study of velocity fields in narrow or compound section sewers, Urban Drainage Modeling, Melbourne, Australia, pp 169-176.
- [2] Hughes A.W., Longair I. M., Ashley R. M., Kirby K., (1996), Using an array of ultrasonic velocity transducers to improve the accuracy of large sewer mean velocity measurements, Water Science & Technology, Vol. 33, No. 1, pp 1-12.
- [3] Laplace D., Deshons P., (1998), Le supportage flottant. Une innovation pour la mesure de débit en continu en assainissement, Novatech 1998, 3rd International Conference on Innovative Technologies in Urban Storm Drainage, pp 207-214.
- [4] Larrarte F., Bardiaux J. B., Battaglia P., Joannis C., (2006), Vélométrie Doppler: mise au point d'un protocole d'essai en laboratoire, TSM. Techniques Sciences Méthodes, génie urbain - génie rural, No. 6, pp 58-65.
- [5] Larrarte F., (2006), Velocity fields in sewers: an experimental study, Flow Measurement and Instrumentation, Vol. 17, pp 282-290.
- [6] Nezu I., Nakagawa H., (1993), Turbulence in open-channel flows, IAHR-Monograph, A. A. Balkema Publishers, Rotterdam, The Netherlands, 281 p.

Comparative study of ADV and LDA measuring techniques

Zdenek Chara^{1*} and Vaclav Matousek²

¹Institute of Hydrodynamics ASCR, v. v. i., Pod Patankou 5, 166 12 Prague 6, Czech Republic
(*Corresponding author, e-mail: chara@ih.cas.cz).

²Czech Technical University, Faculty of Civil Engineering, Prague, Czech Republic, Thakurova 7, 166 29 Prague, Czech Republic

The contribution compares measurements of local velocities for water flows of different configurations carried out with the help of the ADV (Acoustic Doppler Velocimeter) and LDA (Laser Doppler Anemometry) measuring techniques. Three different geometrical configurations were tested – open channel flow, flow behind a rectangular cylinder and flow behind a hole in a plate.

Keywords: Flow measurements, turbulent flow, LDA, ADV.

1 INTRODUCTION

Nowadays a lot of experimental techniques exist to measure flow characteristics of complex free surface flows as HWA (Hot-Wire Anemometry), LDA, PIV (Particle Image Velocimetry), UVP (Ultrasonic Velocity Profiler), ADV. However for 3D measurements in a non purely transparent flow a number of suitable experimental methods is limited. An acoustic doppler method represents one of such techniques. This contribution presents a comparison of two measuring techniques - LDA and ADV. Similar study was published in [1] for near-bottom comparison of LDA and ADV; study the mean velocities measured by the ADV techniques were always lower compared to the LDA data. On the other hand the ADV velocity fluctuations were higher than those measured by the LDA.

2 EXPERIMENTAL DETAILS

The measurements were carried out in a hydraulic flume length of which attains 6 m and rectangular cross section 0.25 x 0.25 m. The LDA system consisted of a Dantec two-component system with two BSA processors. The ADV system used was a Nortek 3D side-looking probe (two sensors were oriented parallel with the channel bottom).

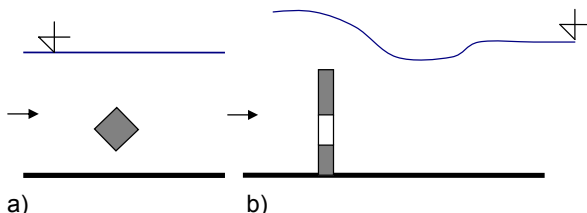


Figure 1: Schematic view of the geometrical arrangements, a) flow behind a rectangular cylinder, b) flow behind a hole in a plate.

Three different configurations were tested, the first one was a pure flow in the hydraulic flume, the flow depth was 110 mm and flow discharge 4.8 l/s. The

second one was the free surface flow behind a rectangular cylinder of the cross section 30x30 mm symmetrically tilted (see Fig. 1, left) where lower edge was 30 mm above the channel bottom. Finally, the third configuration was the free surface flow behind the plate of 80 mm height with a rectangular hole 30x30 mm (see Fig. 1, right). The lower rim of the hole was 20 mm above the bottom. Working frequency of the ADV system was 25 Hz.

3 RESULTS AND DISCUSSION

Fig. 2 depicts velocity profiles of the longitudinal velocity component measured by the both experimental techniques in the open channel. The measuring volume of the ADV system was set to 6 mm and the velocity range was 30 cm/s. As can be seen in Fig. 2 the ADV data compared with the LDA data underestimated the velocity values. The deviation seems to be more or less constant and if the ADV data are multiplied by a factor 1.07 the results fit very well the LDA data. RMS (Root-Mean-Square) values of the horizontal as well as vertical velocity fluctuations are shown in Fig. 3. The RMS values of the horizontal velocity component measured by the ADV method are about 12% lower compared to the LDA data.

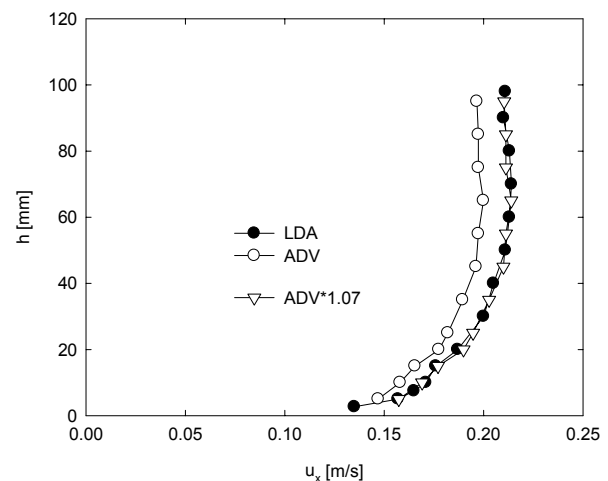


Figure 2: Profiles of the longitudinal mean velocities

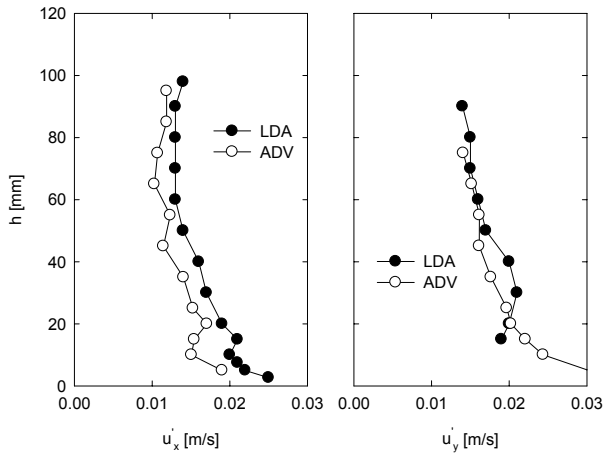


Figure 3: RMS data of horizontal (left) and vertical (right) velocity component

In the upper part of the flow the RMS data of the vertical velocity component measured by the both methods are practically the same, close to the channel bottom the ADV data systematically increased.

The second flow configuration was represented by flow behind the rectangular cylinder. In this case the flow measurements were performed at a distance 40 mm behind the cylinder. ADV velocity range was set to 100 cm/s and a size of the measuring area attained 6 mm. Profiles of the mean velocities in the longitudinal direction are presented in Fig. 4 where a vertical axis shows distances from the channel bottom. A similar tendency as in the previous case was observed - the ADV velocity data are lower compared to the LDA data, but the differences are higher - about 20%.

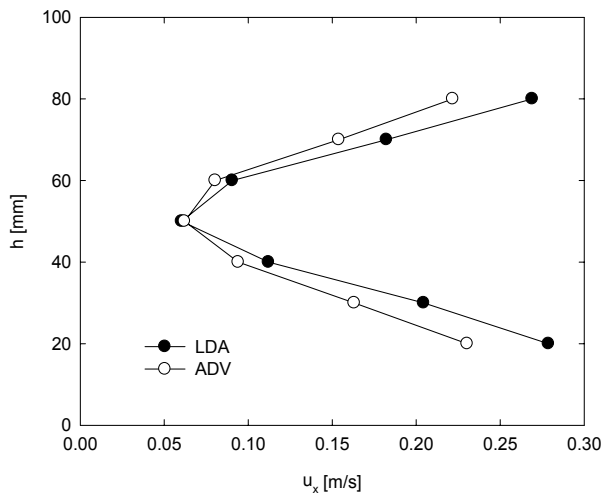


Figure 4: Flow behind the cylinder - mean velocity profiles in the longitudinal direction

Mean velocity profiles in the vertical direction are shown in Fig. 5. Also in this case the ADV data are lower but the discrepancy between the both methods is higher. The RMS values of longitudinal as well as vertical directions are shown in Fig. 6. In the longitudinal direction the RMS

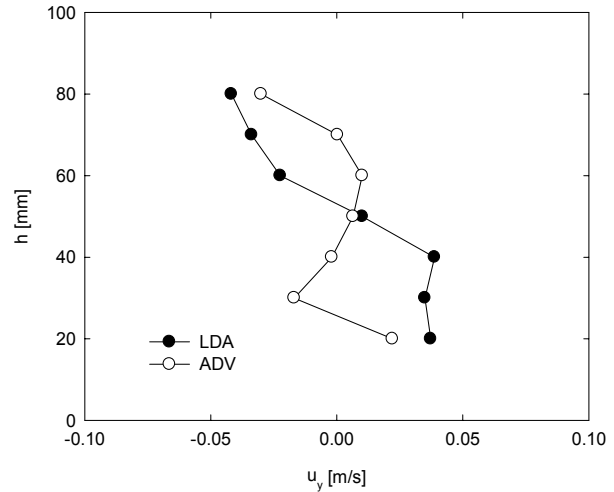


Figure 5: Flow behind the cylinder - mean velocity profiles in the vertical direction

values measured by the ADV are always lower, in the vertical direction the values are lower behind the cylinder, close to the cylinder edges the values are higher.

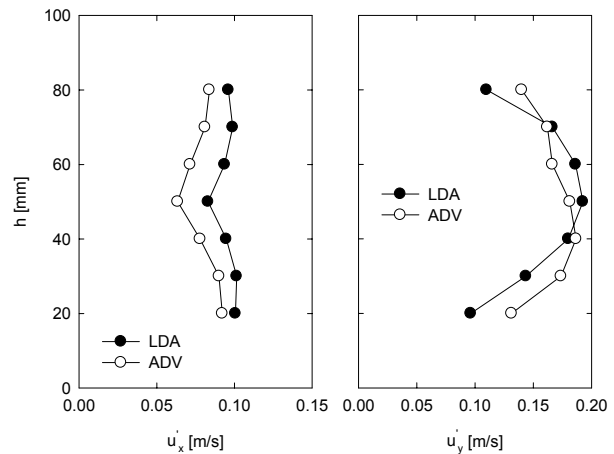


Figure 6: Flow behind the cylinder - RMS data of horizontal (left) and vertical (right) velocity component

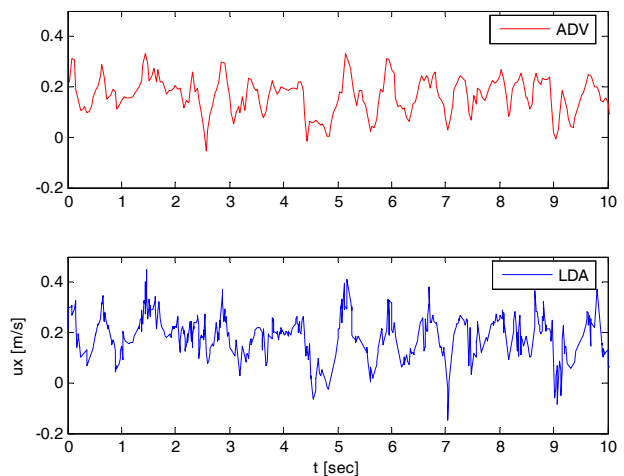


Figure 7: Flow behind the cylinder - time series of the longitudinal velocity component, $h = 70$ mm

Fig. 7 depicts the parts of the time series of the longitudinal velocity component measured simultaneously at a distance 70 mm above the channel bottom where a periodical vortex shedding was observed. As can be expected due to the relatively large measuring volume and low data rate (25 Hz) the ADV method is able to follow quite well only low velocity frequencies. This expectation was confirmed by our measurements. From the time series a FFT analysis was performed and the results are plotted in Fig. 8. The both methods practically indicate the same dominant peak frequency corresponding with the vortex shedding, $f=1.378$ (ADV), $f=1.366$ (LDA).

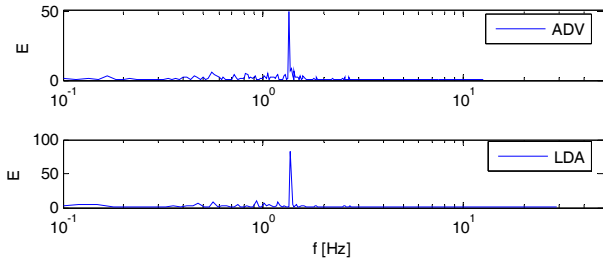


Figure 8: Flow behind the cylinder - FFT analysis of the longitudinal velocity component, $h = 70$ mm

The third experimental run represented flow behind the rectangular hole in the plate. This arrangement was chosen for a comparison of both methods in a region characterized by higher velocities and higher turbulent intensities. The measurements were performed at a distance 45 mm behind and along the vertical axis of the hole. The setting of the ADV measurements was as follows: size of the measuring volume - 6 mm, velocity range - 250 mm/s.

Mean velocity profiles in the longitudinal direction are plotted in Fig. 9. The origin of the vertical axis is placed at the lower rim of the hole. The velocities measured by the ADV are again lower but the ratio of the values of LDA and ADV velocities is no more constant as it was observed in the free surface flow. The ratio is

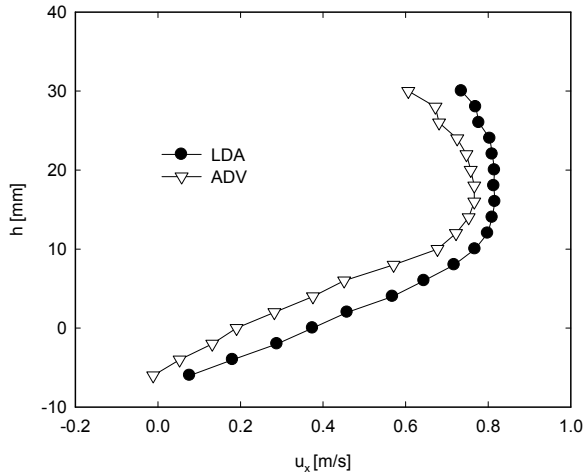


Figure 9: Flow behind the hole - mean velocity profiles in the longitudinal direction

plotted in Fig. 10. In the central part of the hole the velocity ratio is about 1.07 which coincides with the free surface flow but close to the hole rim the ratio is continuously increasing. An example of the time series of longitudinal velocities measured simultaneously at the level of lower rim is shown in Fig. 11. Due to the low data rate of the ADV probe and large measuring volume the ADV technique is unable to measure correctly in an area where a large turbulence level occurs. In such area the ADV has a tendency to smooth the velocity fluctuations as can be seen in Fig. 11. Such inaccuracy was also observed on RMS profiles of the longitudinal velocity component depicted in Fig. 12. At the centre of the hole the RMS values of the ADV probe correspond to the LDA data, but at a distance 7 mm above the hole rim ($u'_x \sim 0.20$ m/s) the ADV data are suddenly decreasing.

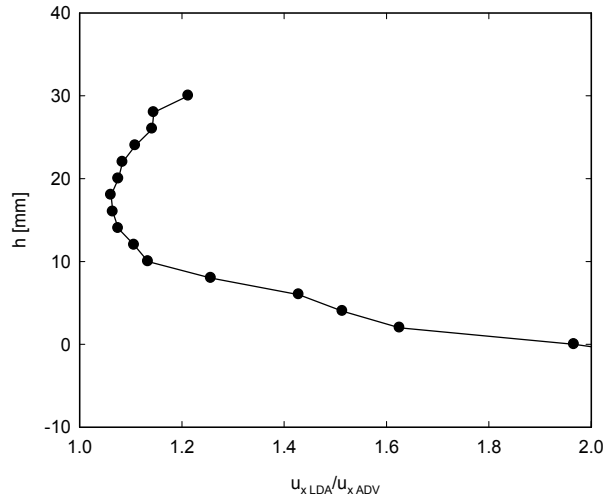


Figure 10: Flow behind the hole - ratio of the LDA mean longitudinal velocities to ADV mean velocities

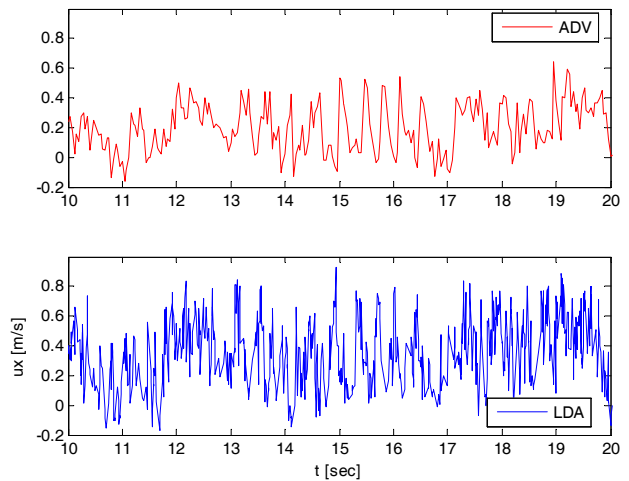


Figure 11: Flow behind the hole - part of the time series of the longitudinal velocities, $h=0$ mm

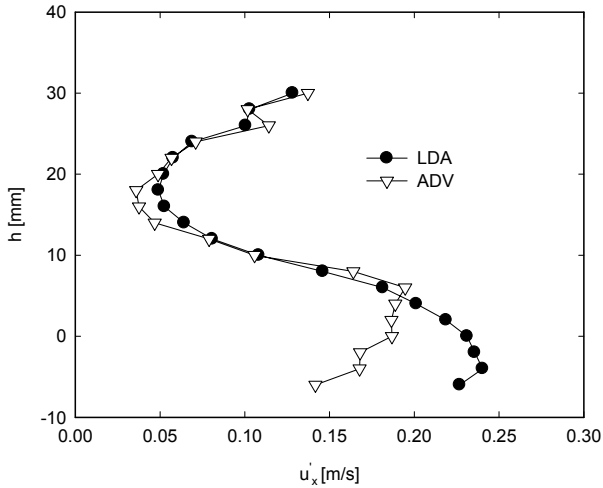


Figure 12: Flow behind the hole - RMS data of the longitudinal velocities

Mean velocity profiles in the vertical direction are shown in Fig. 13. While in the centre of the hole the ADV velocities correspond to the LDA data, close to the hole rim the deviation is strongly increasing. At the lower hole rim the ADV velocities are several times higher than the LDA data. Similar behavior can be seen in Fig. 14 where RMS profiles of the vertical velocity component are plotted.

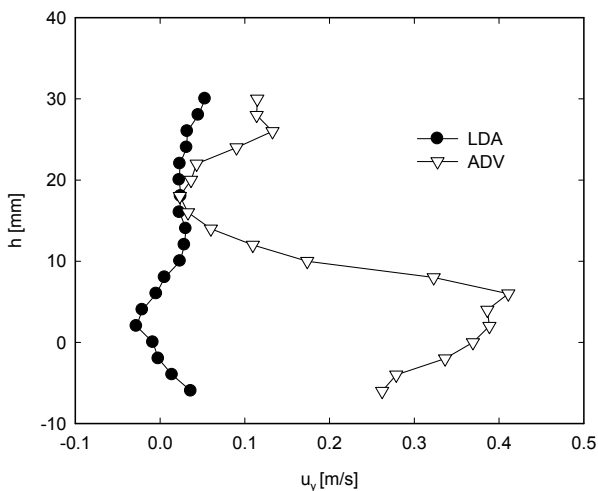


Figure 13: Flow behind the hole - mean velocity profiles in the vertical direction

5 CONCLUSIONS

In this study the comparative study of the ADV and LDA measuring techniques was performed for three different geometrical arrangements of free surface flows. In all tested cases the ADV method underestimated the mean velocities in the longitudinal direction. The deviation attains about 7% for relative simple flow geometry without large disturbances as open channel flow. This conclusion

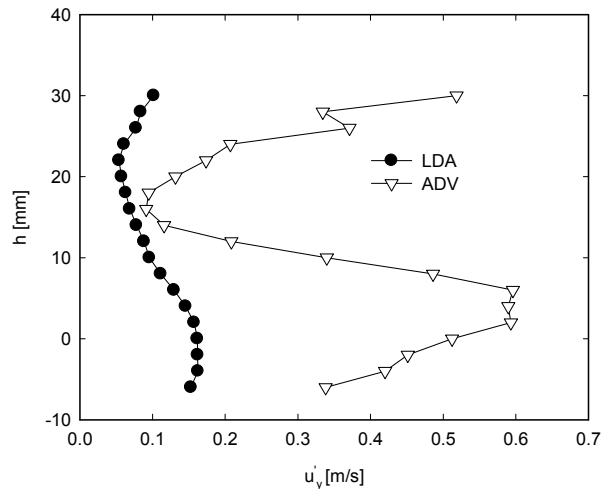


Figure 14: Flow behind the hole - RMS data of the vertical velocities

is consistent with the results published in [1]. But for increasing turbulence level is increasing the deviation between both techniques is also increasing. Mean velocity profiles in the vertical direction were measured for flows behind the rectangular cylinder and behind the hole. In both cases the deviation was larger in comparison to the longitudinal direction and for flow behind the hole the ADV method measured even higher mean velocities. We suppose that the measurement in the vertical direction is affected by one of the ADV probe which seems to be more sensitive.

ADV technique tested is suitable for flow conditions with relatively low turbulence level. In the case of higher turbulence the results have to be carefully analyzed.

ACKNOWLEDGEMENT

The paper was written with the support of the grant GA AS CR No. A200600802 and the Institutional Research Plan No. AV0Z20600510.

REFERENCES

[1] Precht E, Jansen F, Huettel M: Near-bottom performance of the Acoustic Doppler Velocimeter (ADV) - a comparative study. *Aquatic Ecology* 40, (2006), 481-492

Flood discharge measurement Using ADCP

Yen-Chang Chen* Su-Pai Kao and Sheng-Reng Yu

*Department of Civil Engineering, National Taipei University of Technology, 1 Sec. 3 Chung-Hsiao E. Rd. Taipei, Taiwan (*Corresponding author, e-mail:yenchen@ntut.edu.tw).

Discharge measurements not only act as a vital piece of evidence to the national resource database but also become an indispensable source to hydraulic resource planning and developments. Subsequently constant periodical observations need to be made especially to compile crucial high flow data that was laborious and difficult in the past. However, due to the unique characteristics of topography and torrential downpours, Taiwan's rivers and streams inflate instantly during typhoon seasons, becoming quick-water. Combined with strong winds, these conditions may become a threat to hydrologists. To accurately measure discharges during high flow, therefore, an innovative measuring technique and modernized instruments must be introduced and developed.

The unsteady conditions during high flow are unfit to be observed and measured by everyday methods and instruments. Instead, an unorthodox method must be used. The efficient method presented herein uses acoustic Doppler current profilers (ADP hereafter) installed in a 300lb crane system to measure discharges during high flow. The advantages of the proposed equipment are the small and compact size, convenient to relocate and install, efficient to measure velocities and water depths by placing it just below the surface of water, and thus timely enough to complete the observation.

Keywords: ADP, discharge measurement, high flow, probability, velocity distribution

1 INTRODUCTION

The accuracy of conventional discharge measuring instruments and methods becomes venerable to the conditions of surroundings and climates. Methods of the past need longer observation time and are applied only in flows without dramatic changes. For instance, the stage-discharge rating curve resulted from long-term observation is used for establishing water levels and for estimating everyday flow rate within the observed rating curve. However, using it to estimate the unsteady flow conditions of high flow as shown in Figure 1 [1], the stage-discharge rating curve tends to underestimate flows during swells whereas tends to overestimate during retreats. With insufficient instruments and methods of the past, the grasp of flood flow of Taiwan river streams indeed has been enormously challenging and full of uncertainties. The river streams of Taiwan are drastically sloped, and are noticeably disproportioned in terms of water levels. Their cross sections are prone to become silted during discharges and their flow conditions change constantly; and the silt effect on their river beds during high flow varies dramatically. Therefore, the accurate discharge of high flow must be done through immediate first-hand measurements and not through water levels estimated by the stage-discharge rating curve.

The conventional flow measuring instruments all must be placed precisely at the target locations to obtain the needed information. However, during high flow seasons, they cannot be placed exactly at the desired location due to high velocity rapids. The flow conditions of swells, at the height of unsteady

flow that both water level and flow change drastically, must be measured instantly and immediately to seize the accuracy. However, under the difficult conditions of high flow, mostly during typhoon invasions, both hydrologists and measuring instruments will be in danger of rapid flow disasters. Not to mention the cost and labor, it is highly unlikely and impossible to simultaneously obtain the velocity and cross-section area of a river.

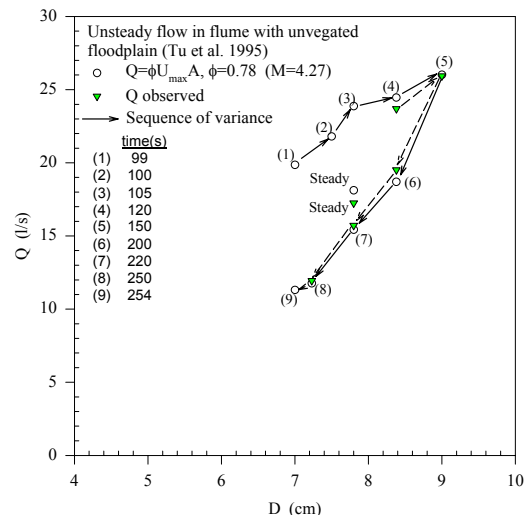


Figure 1: Stage-discharge relation during flood

Using conventional methods and equipments to measure during swells costs more time, thus prolongs hydrologists' time of exposure to danger, and complicates the process of obtaining accurate flow data. Hence, a simple, fast, reliable and accurate flow measurement method for high flow use must be developed.

2 MODERNIZED MEASURING INSTRUMENT

There are several types of flow measuring instruments with advantages and disadvantages or confined within certain limits of usages. Selecting and applying measuring instruments to precisely measure flows during swells vary according to the gauge station's flow field and terrene. Several different types of instruments are tested in this study during high flow to collect flow field data, and the data analysis indicates that the refined Mini ADP of SonTek 1500 kHz coheres with the hydrological characteristics of the Nanshi River and is sufficient to collect the velocity and cross section data. In addition, a unique crane system (Figure 2) is developed to avoid the worst conditions of high flow. The crane system in this study is made of an 300 lb soundings and modified into ADP hanging equipment (Figure 3). It is then carried by a crane truck to be mobilized for observations. As for the immediate data of cross-sectional velocity, wireless equipment is used to transmit the data to the far end computer. The ADP instrument developed for this study is assembled with miniature acoustic Doppler current profilers (Mini ADP hereafter), Electronics Assembly, and necessary accessories.



Figure 2: ADP and sounding hunged by a crane for measuring velocity distribution.



Figure 3: ADP, sounding and wireless communication unit.

3 VERTICAL MEAN VELOCITY AND DISCHARGE MEASUREMENT

Each point velocity on the vertical segment can be obtained through ADP, but the cross-sectional rate is obtained after computation. Hence the velocity-area principle of midsection method [2-4] is applied and with the velocity data from ADP to measure flow rates. A channel cross-section is made of numerous sub-cross-sections. Thus the mean velocity of each sub-cross-section (\bar{v}_n) and sub-cross-section area (a_n) must be estimated to obtain the flow rate q_n , and the summation of each sub-cross-section rate becomes the stream flow rate (Q). Therefore,

$$q_n = \bar{v}_n a_n \quad (1)$$

$$Q = \sum_1^n q_n \quad (2)$$

The data of each sub-cross-section area and mean velocity required for the velocity-area principle are estimated by the water depth and the velocity distribution respectively. The velocity distribution equation by information entropy [5] is applied in here to calculate the mean vertical velocity, which is expressed as

$$u = \frac{u_{max}}{M} \ln \left[1 + (e^M - 1) \frac{\xi - \xi_0}{\xi_{max} - \xi_0} \right] \quad (3)$$

In above, u is the velocity at y ; u_{max} , the maximum velocity; M , the parameter, ξ_{max} and ξ_{min} , the maximum and the minimum ξ respectively; and ξ , the isovel derived after transformation as shown

$$\xi = \frac{y}{D-h} \exp \left(1 - \frac{y}{D-h} \right) \quad (4)$$

where D is the water depth; y , distance from the channel bed; h , the location of u_{max} . By the way of regression analysis, after the velocity distribution equation of most possible cross-sectional velocity has been found, the mean vertical velocity can be obtained by integrating the equation [6-7](Chen , 2005 ; Chen and Chiu , 2002)

4. FLOOD DISCHARGE MEASUREMENT

During 2007, 7 flood discharge measurements were done at the study site. In the process, ADP was submerged only 20cm below water surface to measure velocity profiles. The immediate data by Mini ADP was then to be transmitted through wireless system into the computer for instant calculations of 3D velocity distribution, sonic and depth variations. Under the maximum velocity exceeding 5 m/s and the maximum depth of 5 m, ADP performed well under pressure and was able to provide the required flow field information.

The velocity profiles by ADP were applied to the velocity distribution equation based on probability to obtain the values of mean velocities and rates. Then the complete profiles were used to draw each cross-section's velocity profile segment. Each measurement was the result of the probability distribution equation calculating the mean velocity with the water depth and the midsection method for the flow rate.

Figure 4 displays the cross-section of the Lan-Shan Bridge with gage height being 111.57 m during Typhoon Krosa, and each serial number is shown on the vertical line. 18 water depths are made by ADP with the maximum water depth of 4.47 m. Figure 5 shows the actual measurements of velocity distribution on the 18 verticals, in which the point 15 is the velocity of the maximum vertical depth and the point 7 is of the minimum vertical depth. In addition, the maximum velocity (4.83 m/s) happened on vertical 22, and the flow rate is 447.61m³/s and the maximum cross-section velocity is greater than 5 m/s. The velocity distribution in Figure 5 can be used to draw the isovels, as shown in Figure 6.

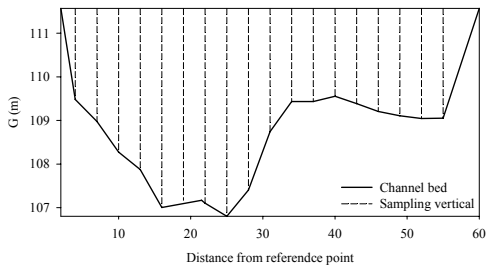


Figure 4: Cross section and sampling verticals during Typhoon Krosa.

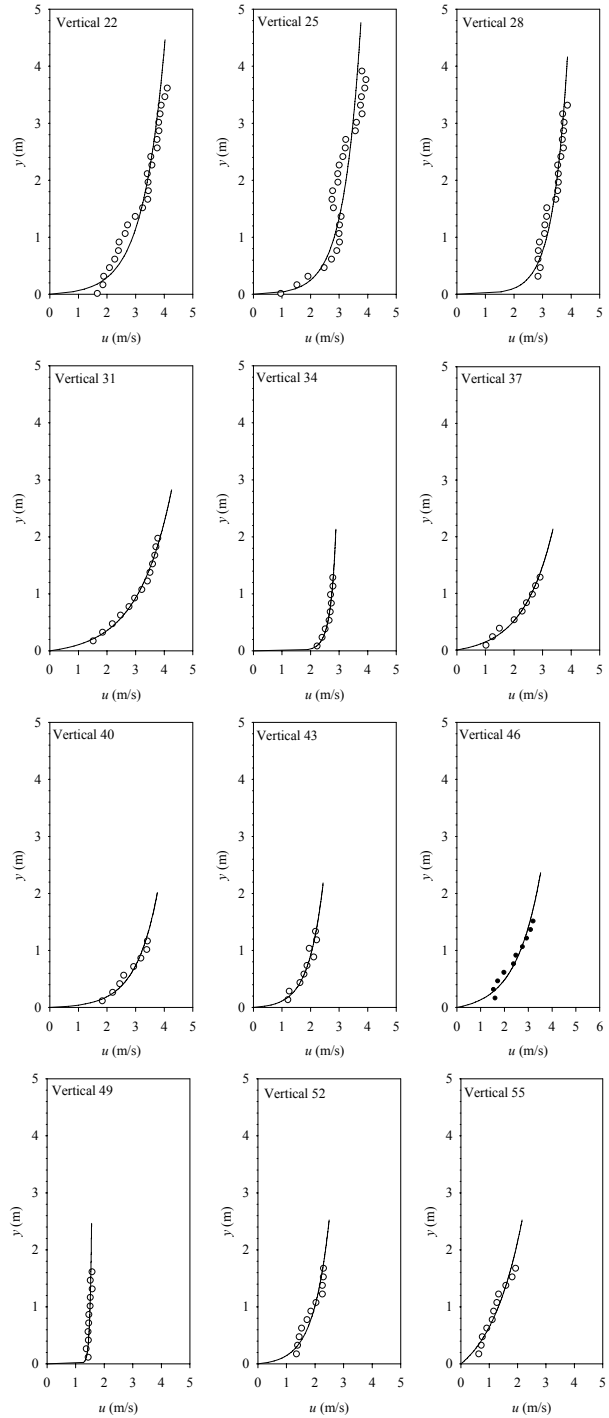


Figure 5: Velocity distribution on the verticals during Typhoon Krosa

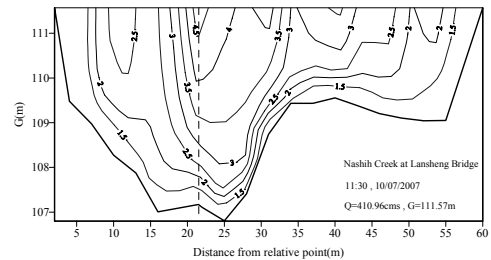
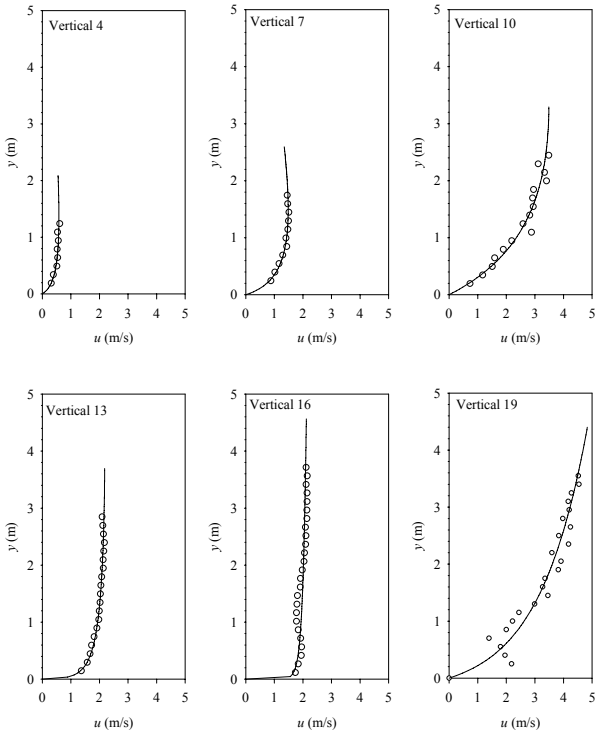


Figure 6: Isovets of the Nanshi River at Lanshan Bridge during Typhoon Krosa

The relationship between gage height and cross-sectional area is established as seen in Figure 7. The data analysis indicates that the maximum velocities occur constantly at the vertical 19. Figure 8 shows the relationship between the maximum and mean velocities, which is the straight segment passing through the origin. Hence, the maximum velocity can be measured hereafter at this location and be multiplied by the cross-section coefficient so to estimate the cross-sectional mean velocity. Consequently the flow rate is the multiplication value of the cross-section area derived from the water level and the estimated mean velocity.

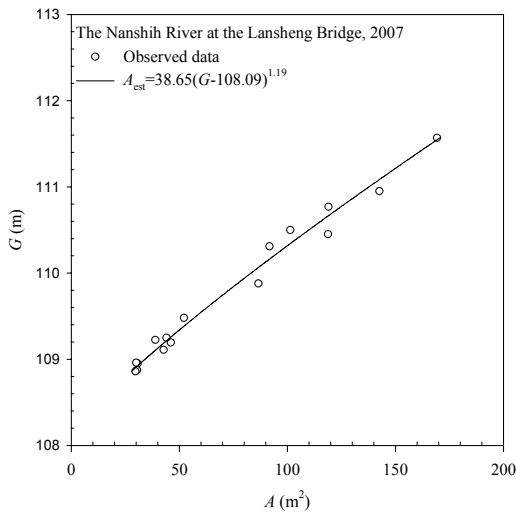


Figure 7: G-A relation of the Nanshi River at the Lanshin Bridge

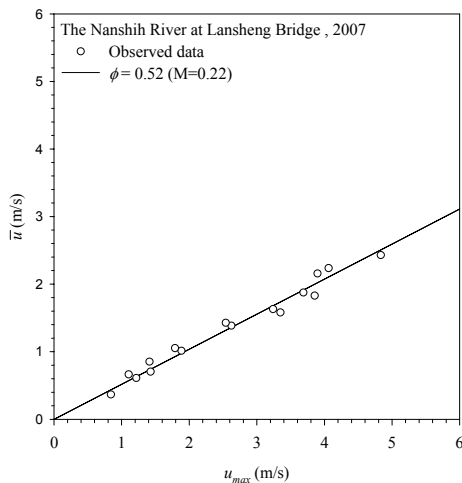


Figure 8: Mean and maximum velocities relation of the Nanshi River at the Lanshin Bridge

5 CONCLUSIONS

By means of the proposed method and modernized instruments, the velocity distribution, flow pattern and water depth during high flows, difficult to obtain in the past, was successfully measured efficiently and accurately. The excellences of the proposed

method are the instant and accurate velocity measurement. This is the most simple calculation with fewer parameter modifications for the mean velocity and the accuracy and efficiency enhancement in measurements. However, the downsides are the high cost of the instruments and the power necessary to operate the crane equipment. Also in shallow waters, there appears to be a blanking at the beginning stage of measuring which causes the point of measure to be insufficient making it impossible to proceed to the cross-section velocity analysis. From the experiment, it is learned that ADP in coordination with the velocity distribution based on probability is suitable for use when the cross-section depth reaches above 1.6m. However, with the high frequency ADP, the blanking can be avoided and the minimum depth can be lowered.

REFERENCES

[1] Chen, Y-C, Chiu, C-L: A Fast Method of Flood Discharge Measurement, Hydrological Processes 18 (2004) 1671-1684.
 [2] Herschy, RW: Hydrometry - Principles and Practices, Wiley, New York (1999).
 [3] Rantz, SE: Measurement and Computation of Streamflow - Volume 1 Measurement of Stage and Discharge, Geological Survey Water-Supply Paper 2175, U.S. Government Printing Office, Washington (1982).
 [4] Rantz, SE: Measurement and Computation of Streamflow - Volume 2 Computation of Discharge, Geological Survey Water-Supply Paper 2175, U.S. Government Printing Office, Washington (1982).
 [5] Shannon, CE: A Mathematical Theory of Communication, The Bell System Technical Journal, 27, (1948) 623-656.
 [6] Chen, Y-C: An Efficient Method Approach to Large Flowmeter Calibration, Journal of Water Supply: Research and Technology – AQUA, 54 (2005) 283-291.
 [7] Chen, Y-C, Chiu, C-L: An Efficient Method of Discharge Measurement in Tidal Streams, Journal of Hydrology, 265 (2002) 212-224.

Experiments on turbidity currents influenced by solid and permeable obstacles and water jet screens

Giovanni De Cesare^{1*}, Christoph D. Oehy² and Anton J. Schleiss¹

¹Laboratory of Hydraulic Constructions (LCH), Ecole Polytechnique Fédérale de Lausanne (EPFL), Station 18, CH - 1015 Lausanne, Switzerland (*Corresponding author, e-mail: giovanni.decesare@epfl.ch).

²formerly at the EPFL-LCH, now at Swiss Reinsurance Company, Mythenquai 50/60, P.O. Box, CH - 8022 Zurich, Switzerland

The sustainable use of reservoirs for irrigation, flood protection, water supply, and hydropower may be endangered due to unavoidable reservoir sedimentation. In many reservoirs turbidity currents are the main process for the transport and deposit of sediments. Besides other measures, turbidity currents can be influenced by means of solid obstacles, permeable geotextile screens or the injection of water jets. Physical experiments and numerical simulations of turbidity currents flowing over an obstacle, against a textile screen or through a water jet screen were carried out. In each experiment vertical velocity profiles in the body of the turbidity current were measured with an ultrasonic velocity profiler (UVP). The velocity measurements were made at three locations upstream of the various obstructions and one location downstream. The investigations showed that turbidity currents could be influenced effectively by properly designed constructive measures. Based on the results of the physical experiments and numerical simulations, some design recommendations for solid and permeable obstacles as well as for a jet screen are proposed.

Keywords: Reservoir, sedimentation, turbidity current, water jet, physical modeling, numerical simulations, velocity profiles, sediment deposits

1 INTRODUCTION

The aim behind the efforts to create reservoirs is storing water, however solid material is carried along by the water and is, as a rule deposited there. Long-lasting operation of reservoirs in terms of sustainable use of available water resources involves the need for sedimentation control and release.

Wise development of hydropower resources regarding sedimentation has frequently not been implemented in the past and the sustainable use of reservoirs is not always guaranteed in the long term. In narrow reservoirs with quite steep bottom slopes, turbidity currents are frequently the main process for the transport and deposit of sediments [1] (Fan and Morris 1992). These turbidity currents with high sediment concentrations mainly occur during floods and follow the thalweg to the deepest zones of the reservoir near the dam. Depending on the slope of the thalweg, density currents reach velocities in the range of 0.5–0.8 m/s, and exceptionally up to 2 m/s during floods [2] (Fan 1986). Sediments, which have already settled down, can therefore be eroded again and transported toward the dam. The resulting introduction of additional suspended sediments into a turbidity current increases its density and consequently its velocity [3] (Parker et al. 1986). On the other hand, turbidity currents slow down on low slopes or after a hydraulic jump, which causes the sediments to settle and the current to die out [4] (Altinakar et al. 1990).

If turbidity currents can be entirely stopped in a reservoir, or influenced in such a way that the sediments are not deposited in critical locations like in front of intakes and bottom outlets, the sustainability of the reservoir operation may be increased considerably. Such technical measures to control reservoir sedimentation due to turbidity currents have in principal the purpose to stop, dilute, or divert the flow influencing the location of major sediment deposits. This can be done by a solid or permeable obstacle [5] (Oehy and Schleiss 2007) or a jet screen placed inside the reservoir (Figure 1).

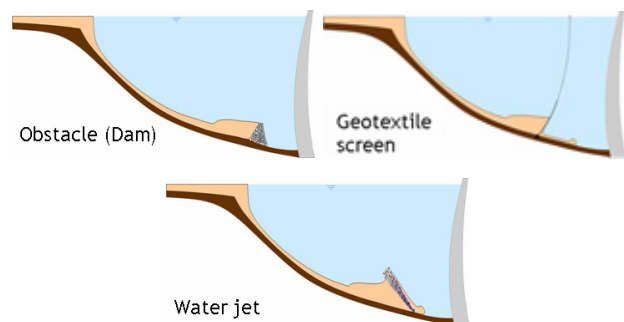


Figure 1: Investigated methods to stop turbidity currents.

2 MODELLING OF TURBIDITY CURRENTS

Turbidity currents have extensively been studied in the laboratory by many investigators [6-9] (Altinakar et al. 1996, De Cesare and Schleiss 1999, Baas et al. 2005, Hosseini et al. 2006). [10] De Cesare et al. (2001) presented three-dimensional numerical simulations of turbidity currents in the Luzzone

Reservoir in Switzerland. The model used in this study is based on the CFX-4 flow solver, where user routines were added to take into account the settling of the suspended sediments and the erosion-deposition at the bottom. The effects of solid obstacles or permeable screens on turbidity currents have been investigated in the case study of Lake Grimsel [11] (Oehy and Schleiss 2001) and Lake Lugano [12] (De Cesare et al. 2006). [13] Bühler et al. (2006) give an excellent overview on the phenomena of flows on inclines passing through water jets directed upstream.

3 EXPERIMENTS

3.1 Experimental set-up

The experiments were carried out in an 8.55 m long, 0.27 m wide and 0.90 m deep multipurpose flume (Figure 2 left). The flume can be tilted in a slope range between 0 and 5%. In the upper part of the flume a stilling box and head tank were installed. A sluice gate allowed the release of the turbidity current in the downstream part simulating a 7.1 m long straight reservoir. An adjacent mixing tank with a capacity of 1.5 m^3 was used to prepare the dense fluid mixture.



Figure 2: Photograph of the experimental flume (left) and the UVP transducer as well as the bottom and reference electrodes (right).

The turbidity current was created by a rapid opening of a sliding gate. Downstream of this gate a tranquilizer composed of small rectangular tubes reduced the scale of the initial turbulence of the released mixture and generated a uniform velocity distribution. A compartment at the downstream end of the flume trapped the turbidity current for withdrawal. For the experiments a cohesionless, fine polymer powder with a density of $\rho_s = 1135 \text{ kg/m}^3$ and a particle diameter of $d_{50} = 90 \mu\text{m}$ was chosen. More details on the experimental set-up can be found in [14] (Oehy 2002).

3.2 Modeling of obstacles (solid and permeable) and of an inclined jet screen

The solid obstacle used in this study was a ridge of

24 cm height, extending across the full width of the flume at a distance of $x = 5 \text{ m}$ from its inlet. It had a Gaussian shape. This particular form is used because it does not have any edges creating flow singularities, and can simulate an embankment dam. Furthermore, [15] Prinos (1999) investigated two-dimensional density currents over semicircular and triangular obstacles and found that there is no significant effect of the obstacle geometry.

Furthermore, five turbidity current runs through a permeable screen made of two different types of Tricopor[®] geotextiles of 0.5 m height, also located at $x = 5 \text{ m}$ from the inlet, were carried out. The respective porosities were 36% and 41%.

In order to investigate the turbidity current flow across an inclined multiport-diffuser, water jets emerged from a rectangular box 60 cm long, 27.2 cm wide and 7 mm thick placed inside the flume on the channel bottom. The jet screen was located $x = 5.15 \text{ m}$ from the inlet gate.

3.3 Measuring devices

In each experiment four vertical velocity profiles in the quasi-steady body of the turbidity current were measured with an ultrasonic velocity profiler (UVP, Figure 2 right). This method was applied successfully in the earlier cited model tests for the monitoring of laboratory turbidity currents, as well as in a laboratory reservoir sedimentation study by [16] (Kantoush et al. 2008). A device to measure the local evolution of sediment layer thickness during the experiments was developed based on the fact that the electrical resistance of a layer of particles depends on its thickness [17] (De Rooij et al. 1999). The thickness of the sediment deposits can thus be determined by measuring its resistance. The resistance was measured between a 6 mm stainless-steel rod, 6.5 m long, mounted 0.5 m above the flume bottom and 62 electrodes on the bottom (Figure 2 right).

4 RESULTS

4.1 Flow over a solid obstacle

When the turbidity current reached the obstacle, it climbed up, decelerating only slightly as can be seen in the photographic sequence in Figure 3.

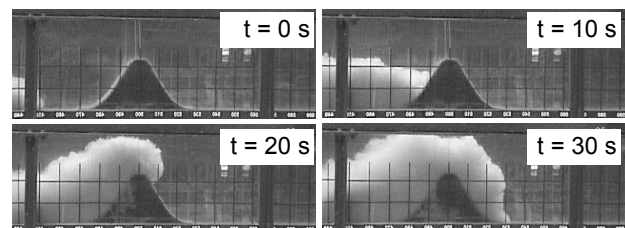


Figure 3: Sequence of a turbidity current flowing over a Gaussian obstacle at time intervals of 10 s. Approach front flow velocity $U_f = 0.039 \text{ m/s}$, height of the current $h = 0.106 \text{ m}$, grid spacing 0.10 m.

The turbidity current head passed over the obstacle, whereas a gap developed behind the head. A less important current followed the head region and kept flowing over the top of the obstacle down the flume. The normal shape of the frontal region was reestablished at some distance downstream of the obstacle. Due to the presence of the obstacle, the flow rate changed and an internal bore traveled upstream. Bores are moving hydraulic jumps and also occur in open-channel flows.

4.2 Flow through a permeable screen

When the turbidity current reached the vertical screen, it was nearly blocked due to the increased flow resistance (Figure 4). The turbidity current then climbed up the screen to a height of 2 - 3 times the height of the oncoming turbidity current, and decelerated as it rose. The turbidity current then started to seep through at the bottom of the screen driven by the pressure gradient. As the interface upstream rises, more fluid passes through the screen, forming a small and slow outgoing turbidity current. Due to the flow resistance of the screen, part of the flow is reflected and moves upstream as an internal bore similar to the experiments with a solid obstacle.

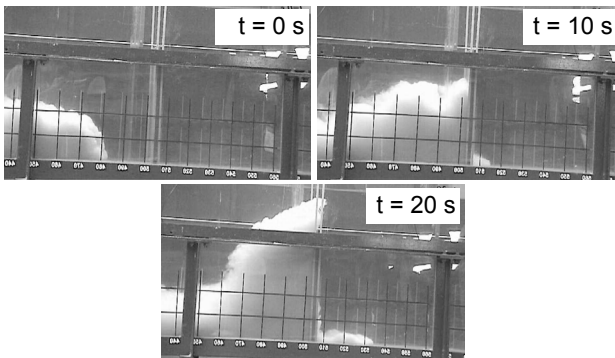


Figure 4: Sequence of a turbidity current flowing through a permeable screen (41% porosity) at time intervals of 10 s. Approach front flow velocity $U_f = 0.051$ m/s, height of the current $h = 0.112$ m.

4.3 Flow through a water jet screen

Figure 5 shows a photographic progression of the turbidity current flowing through the jet screen.

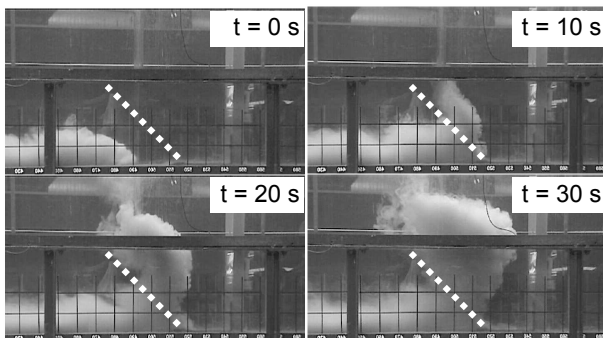


Figure 5: Turbidity current flowing through the 45° inclined jet screen at time intervals of 10 s. Approach flow velocity $U_f = 0.042$ m/s, height of the current $h = 0.106$ m.

The sequence starts just before the turbidity current reaches the inclined jet screen. A small amount of the turbidity current passes through while the major part of it remains upstream and is pushed upwards.

4.4 Velocity profiles of the turbidity currents

Computed profiles of streamwise velocity were compared with the values determined from measurements by UVP using time-averaged profiles in the quasi-steady part of the turbidity current body.

The computed velocity profiles are compared with the experimental results as shown in Figure 6 for the passage over a solid obstacle and through a permeable screen.

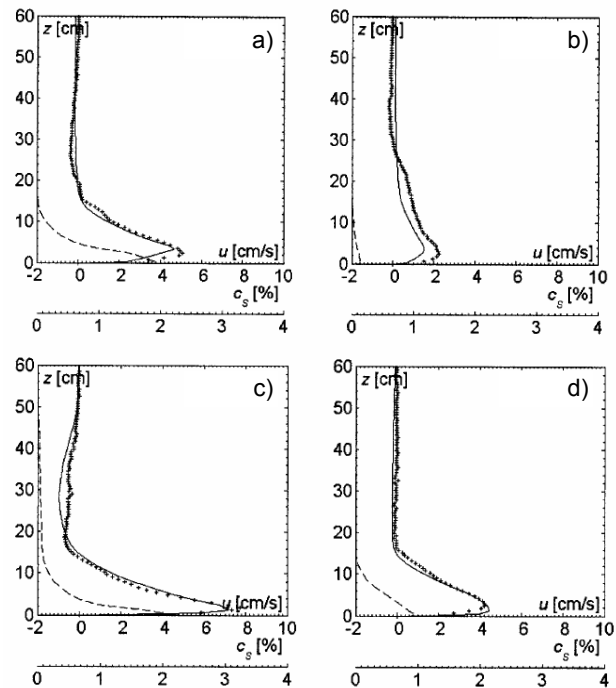


Figure 6: Vertical velocity profiles upstream and downstream of the obstacle a) and b) and of the permeable screen c) and d). Computed velocity, u (thin solid line); measured velocity (plus signs); and computed concentration, c_s (dashed line).

In addition, the computed concentration distribution using CFX-4 is shown on the same graphs. It can be seen that the numerical results agree fairly well with the measured distribution of the streamwise velocity. The height at which the concentration vanishes coincides approximately with the height of zero velocity. Due to the effect of the obstacle and screen, the downstream velocity as well as the concentration is strongly reduced, whereas the height is increased.

4.5 Influence on sediment deposition

The measured evolution of the sediment deposits along the flume is shown in Figure 7 and has been compared to the results from the numerical model. Both approaches showed that sedimentation downstream of the diffuser is significantly reduced

while the upstream deposition is increased due to the flow and sediment retention.

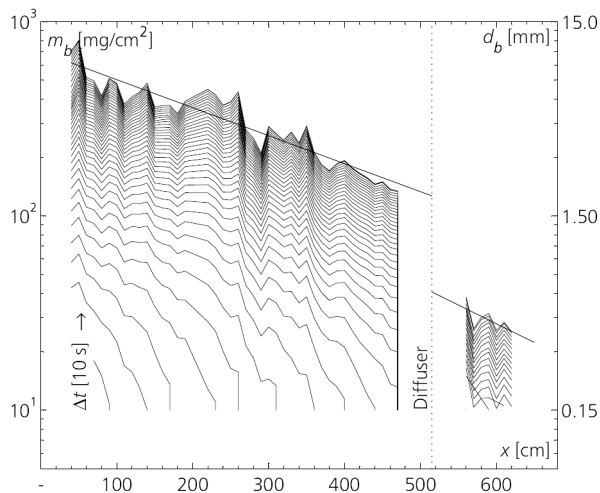


Figure 7: Measured evolution of sediment deposit of the turbidity current partially blocked by the 45° upward inclined water jet screen at time intervals of 10 s.

5 CONCLUSIONS

The long term use of reservoirs for irrigation, flood protection, water supply and hydropower may be endangered due to unavoidable reservoir sedimentation. The challenge for designers and dam operators is to achieve sustainable storage volumes by means of wise reservoir sedimentation management. Very often turbidity currents are the governing process for the transport and deposition of suspended sediments in reservoirs. Physical experiments and numerical simulations of turbidity currents flowing over a solid obstacle and through a geotextile screen as well as through an inclined water jet screen were carried out.

Based on the tests and simulations it can be concluded that solid obstacles with reasonable heights (at least twice the high of the approaching turbidity current) allow for efficient blocking of turbidity currents. The laboratory tests as well as numerical case studies revealed this significant effect of obstacles. The investigations showed also that, in certain configurations, turbidity currents can be considerably slowed down by a geotextile or an inclined water jet screen and therefore most of the sediments can be retained upstream.

The technical measures presented may also be of interest in combination with other traditional methods, such as flushing or turbidity current venting, but also with new concepts of sediment management in reservoirs.

ACKNOWLEDGEMENT

The authors gratefully thank the PSEL foundation of the Swiss Union of Electricity Producers, grant N° 175, the Swiss Committee on Dams (SwissCoD) and Met-Flow for their support of this study.

REFERENCES

- [1] Fan, J., and Morris, G. L. (1992). Reservoir sedimentation I: Delta and density current deposits, *J. Hydraul. Eng.*, 118(3), 354–369.
- [2] Fan, J. (1986). Turbid density currents in reservoirs, *Water Int.*, 11(3), 107-116.
- [3] Parker, G., Fukushima, Y., and Pantin, H. M. (1986). "Self-accelerating turbidity currents." *J. Fluid Mech.*, 171, 145–181.
- [4] Altinakar, M. S., Graf, W. H., and Hopfinger, E. J. (1990). Weakly depositing turbidity current on a small slope, *J. Hydraul. Res.*, 28(1), 55–80.
- [5] Oehy, Ch., and Schleiss, A. (2007). Control of turbidity currents in reservoirs by solid and permeable obstacles, *J. Hydraul. Eng.*, 133(6), 637-648.
- [6] Altinakar, M., Graf, W., and Hopfinger, E. (1996). Flow structure of turbidity currents, *J. Hydraul. Res.*, 34(5), 713–718.
- [7] De Cesare, G., and Schleiss, A. (1999). Turbidity current monitoring in a physical model flume using ultrasonic Doppler method, *Proc., 2nd ISUD*, Villigen PSI, Switzerland, 61-64.
- [8] Baas, J. H., McCaffrey, W. D., Haughton, P. D. W., and Choux, C. (2005). Coupling between suspended sediment distribution and turbulence structure in a laboratory turbidity current, *J. Geophys. Res.-Oceans.* 110 (C11015), doi:10.1029/2004JC002668..
- [9] Hosseini S. A., Shamsai, A., and Ataie-Ashtiani, B. (2006). Synchronous measurements of the velocity and concentration in low density turbidity currents using an Acoustic Doppler Velocimeter, *Flow Measurement and Instrumentation*, 17 (2006), 59-68.
- [10] De Cesare, G., Schleiss, A., and Hermann, F. (2001). Impact of turbidity currents on reservoir sedimentation, *J. Hydraul. Eng.*, 127(1), 6-16.
- [11] Oehy, Ch., and Schleiss, A. (2001). Numerical modeling of a turbidity current passing over an obstacle - Practical application in Lake Grimsel, Switzerland, *Proc., Int. Symp. on Env. Hydr. (CD-ROM)*, Tempe, Ariz.
- [12] De Cesare, G., Boillat, J.-L., and Schleiss A. J. (2006). Circulation in stratified lakes due to flood-induced turbidity currents, *J. Environ. Eng.*, 132(11), 1508-1517.
- [13] Bühler, J., Oehy, Ch., and Schleiss, A. (2006). Jets opposing flow on inclines, *Proc., Int. Conference on Fluvial Hydraulics, River Flow 2006*, Lisbonne, 1617-1622.
- [14] Oehy, Ch. (2002). Effects of obstacles and jets on reservoir sedimentation due to turbidity currents, *Communication No. 15 of the Laboratory of Hydraulic Constructions (LCH)*, Ecole Polytechnique Fédérale de Lausanne (EPFL), Switzerland.
- [15] Prinos, P. (1999). Two-dimensional density currents over obstacles, *Proc., 28th IAHR Congress (CD-ROM)*, Graz, Austria.
- [16] Kantoush, S. A., De Cesare, G., Boillat, J.-L., and Schleiss, A. J. (2008). Flow field investigation in a rectangular shallow reservoir using UVP, LSPIV and numerical modeling, *Flow Measurement and Instrumentation*, Elsevier, 19 (2008), pp. 139–144.
- [17] De Rooij, F., Dalziel, S. B., and Linden, P. F. (1999). Electrical measurement of sediment layer thickness under suspension flows, *Exp. Fluids*, 26, 470–474.

ADCP measurements in a reservoir of a run-of-river Hydro Power Plant

Clemens Dorfmann¹ and Helmut Knoblauch^{2*}

¹ Institute of Hydraulic Engineering and Water Resources Management, Graz University of Technology, Stremayrgasse 10/II, 8010 Graz, Austria

² Institute of Hydraulic Engineering and Water Resources Management, Graz University of Technology, Stremayrgasse 10/II, 8010 Graz, Austria (*Corresponding author, e-mail: helmut.knoblauch@tugraz.at)

The impoundment of the run-of-river hydro power plant Feistritz at the river Drau, Austria, formed a 15 km long reservoir. After 40 years of operation the hydro power plant has to confront severe sedimentation problems. To counteract this problem a special kind of flushing in case of an annual flood should be applied to transport the suspended load into the tail water of the power plant. Both a physical model and a numerical model will be used to simulate different constructive options such as guide walls for a maximal flushing effect. The exact knowledge of the velocity distribution has therefore a crucial influence on the ideal line management and the location of the training structures as well as on their effectiveness. First results of 2-D numerical calculations show that due to the complex reservoir geometry, the flow pattern depends highly on the turbulence model that is applied. Recently performed ADCP velocity measurements (WorkHorse Rio Grande 1200 kHz, RDI) indicate distinct flow patterns of a main stream entering the reservoir with zones of low velocities on the orographic left bank of the reservoir. These results serve as an excellent basis for calibrating both the numerical and the physical model.

Keywords: ADCP measurements, 2-D numerical model, calibration of the constant Eddy Viscosity

1 INTRODUCTION

The hydro power plant Feistritz is part of a chain of hydro power plants, which consists of ten plants. The impoundment created a 15 km long reservoir with maximal water depths of 20 m and a 1000 m wide expanded area upstream of the weir. The large amount of sediment input into the flow represents a severe problem to the power plant. Concepts for the future aim at enabling the transport of suspended load in the case of a flood. To support this project, numeric calculations and related physical model tests will be carried out. As an additional construction measure, guide walls will be installed to prevent disordered movement of suspended load in the reservoir. The goal of the presented ADCP measuring campaign is the analysis of the velocity distributions that occur in nature in the wide area of the reservoir as well as the calibration of the parameter for the Eddy Viscosity in the 2-D numerical simulations.

An ADCP WorkHorse Rio-Grande 1200 kHz[®] of the company RD Instruments was applied. ADCPs (Acoustic Doppler Current Profiler) use as measuring principle the Doppler effect by transmitting sound at a fixed frequency and listening to echoes returning from sound scatterers (small particles) in the water. A key assumption is that these scatterers float in the water and on average they move at the same velocity as the water [1]. RD Instruments ADCP devices use four beams to obtain velocity in three dimensions. One acoustic beam is required for each current component. Currents must be horizontally homogeneous, that is, they must be the same in all four beams. The fourth beam obtains an additional vertical velocity and therefore the

difference between the two estimates of vertical velocity allows to evaluate the assumption of horizontal homogeneity and therefore data quality [2].

2 ADCP VELOCITY MEASUREMENTS

2.1 Measurement procedure and configuration

Previously carried out 1-D numerical calculations showed that the velocities in the measuring area fluctuate between 0.01 and 0.4 m/s that means, they are very low. The water depths in the measuring area are in the range from 6 to 20 m. The ADCP appliance had to be specifically configured for these complicated conditions in order to reduce the large standard deviations that are typical for this type of measurement application. The ADCP WorkHorse Rio-Grande provides different water profiling modes for different water flow conditions. Because of the above described flow conditions, Water Mode 12 was used. This Water Mode is an improved version of the standard Water Mode 1 offering higher sampling rates (up to 20 Hz) and more precise velocity measurement. Contrary to the standard Mode 1 with Water Mode 12 the device transmits and receives a series of sub-pings. The system then averages the sub-pings to produce ping velocity values [3]. Normally the number of sub-pings is 12 and the time between transmitted sub-pings is 40 msec. These values can be adjusted according to the water flow condition. In Water Mode 12 the nominal standard deviation amounts to 6.95 cm/s which is twice as low as in Water Mode 1 [4]. The measurement configuration was additionally improved by changing some default values of Water Mode 12. The WV-command (ambiguity velocity) is

used to adjust the characteristics of the transmission pulse and is set based on the maximum apparent velocity (ADCP motion plus water speed). The lower the value of WV, the lower the single-ping standard deviation. The WV-value was set to 100 cm/s (minimum) for all measurement points according to the 1-D numerical calculations and the predicted ADCP device motion. The BX-command sets the maximum tracking depth used by the ADCP during bottom tracking. This prevents the ADCP from searching too long and too deep for the bottom, allowing a faster ping rate when the ADCP loses track of the bottom. The BX-value was determined based on available echo sounder surveys and adjusted for every measurement point. The default depth cell size (WS-command) of 25 cm was increased according to the water depth to account for the maximal recommended number of depth cells (60 in Water Mode 12) and therefore to achieve high sampling rates.



Figure 1: ADCP measurements with bottom-dump barge

As measuring ship a bottom-dump barge was used to meet the slow flow velocities. The ship was anchored along a cross profile in specific distances and within the 20 m long opened dump gate the ADCP measurements were performed (Figure 1). A GPS was located on the ship to determine the exact position of each single measuring point.

2.2 ADCP measurement results

To maintain the complete flow pattern in the reservoir, the mean flow velocity and its mean flow direction were analysed in every measurement point. The mean horizontal flow velocity (Eq. 1) was computed by averaging all of the ensembles for each bin together to a mean east and north velocity component and computing the mean water speed from the mean velocity components in each bin,

$$|\bar{V}| = \sqrt{\left(\frac{\sum V_e}{n}\right)^2 + \left(\frac{\sum V_n}{n}\right)^2} \quad (1)$$

where $|\bar{V}|$ is the mean flow velocity, V_e is the east component of the water velocity in each bin, V_n is the north component of the water velocity in each bin and n is the number of depth cells with valid water velocity components [5]. The mean flow direction in the measurement points was simply determined by calculating the angle from the two mean velocity components.

In the site chart (Figure 2) the resulting velocity vectors in the measurement points are represented and in Table 1 the corresponding mean flow velocities are depicted.

Table 1: Mean flow velocities

Measuring point	$ \bar{V} $ (m/s)	Measuring point	$ \bar{V} $ (m/s)
100_1	0.063	304_3	0.039
100_2	0.067	304_4	0.026
100_3	0.061	400_1	0.047
100_4	0.038	400_2	0.044
200_1	0.076	400_2_1	0.043
200_2	0.070	400_3	0.038
200_3	0.056	400_4	0.031
200_4	0.031	500_1	0.057
300_1	0.081	500_2	0.102
300_2	0.072	500_3	0.071
300_3	0.040	600_1	0.090
300_4	0.028	600_2	0.141
300_5	0.030	700_1	0.122
304_1	0.071	700_2	0.163
304_2	0.036		

The results represented in the site chart (Figure 2) show that the velocities downstream of the gorge portion are very low and reach values between 2 (measuring point 300_4) and 16 cm/s (700_2). On the basis of the flow directions it is recognizable that the mainstream of the flow is located near the orographic right bank of the reservoir. In the vicinity of the orographic left bank of the reservoir the velocities show the lowest values (measuring points 400_4, 304_4 and 300_5). No clearly determined flow direction could be detected in this part of the reservoir.

All in all it can be said that due to the large device-specific standard deviations for such measurement conditions the values of the velocities are affected by a great imprecision. However, it can be determined that in cases of turbine operation the higher velocities appear on the orographic right side of the reservoir downstream of the gorge portion. On the orographic left side of the reservoir zones with low velocities and light backflow could be detected.

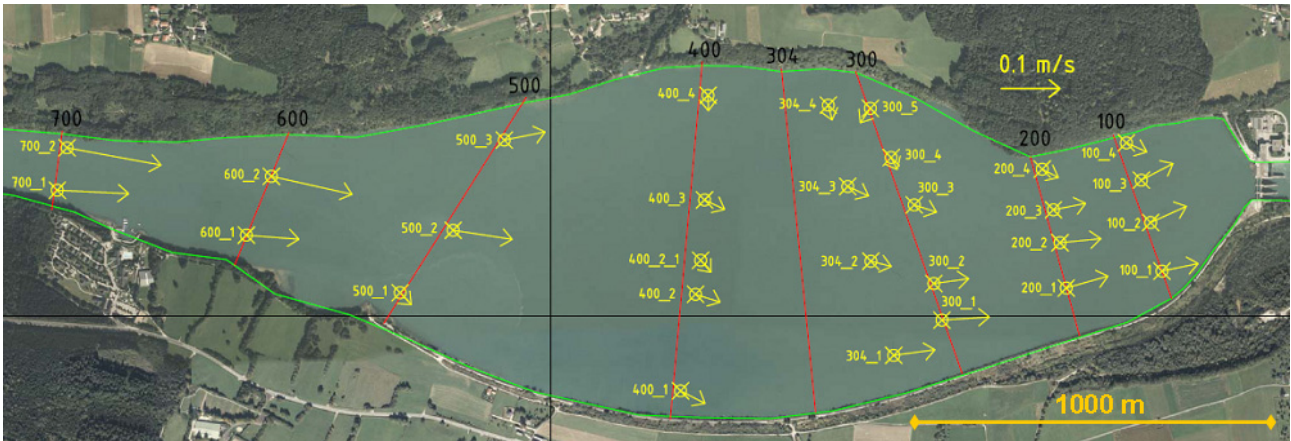


Figure 2: Measuring points with resulting velocity vectors

3 TWO-DIMENSIONAL NUMERICAL MODEL

3.1 Introduction

The results of the numerical models will provide a useful preselection for the measures to be taken in the physical model tests. In a first step, transport and sedimentation behaviour of the suspended load, applied to the cases of turbine operation and weir operation, will be examined in the range between the weir and approximately 5000 m upstream of the weir.

The calculations are executed by the 2-D dimensional hydraulic software MIKE 21C (Danish Hydraulic Institute, DHI), which was especially designed for the calculations of sediment transport respectively bed load and suspended load transport for multiple grain sizes. MIKE 21C solves the vertically integrated equations of continuity and conservation of momentum in two directions by the means of the finite difference method based on structured curvilinear grids [5].

3.2 Constant Eddy Viscosity concept

In MIKE 21C the influence of turbulent stresses on the flow field is parameterised by a one-equation model, respectively a constant Eddy Viscosity formulation. Due to the fact that the Eddy Viscosity depends strongly on the state of turbulence, respectively on the mean velocity gradients and may vary significantly from one point in the flow to another, and also from flow to flow, the value of the constant Eddy Viscosity has to be found directly from available empirical informations or from trial and error calculations to match the observations to the problem considered [6]. On the other hand the Eddy Viscosity does not have a large role to play for most applications in rivers [7], if the model area does not have any abrupt expansions or contractions in the horizontal or vertical direction which would lead to high velocity gradients. Recommended values for the constant Eddy Viscosity formulation range between 0.2 m²/s and 1.0 m²/s [8].

3.3 Calibration of the Eddy Viscosity constant

As mentioned in chapter 1, the reservoir Feistriz is marked by a gorge portion 3500 m upstream of the weir which merges into a 1000 m wide area with change in water depth from 5 to 20 m. For such an irregular geometry the value for the Eddy Viscosity has to be calibrated by field data like ADCP measurements.

Three hydrodynamic steady simulations with a constant inflow of 400.0 m³/s (design flow) as upstream boundary condition and a constant water surface elevation of 461.0 masl (normal operating level) as downstream boundary condition are conducted. For the roughness a constant Strickler-coefficient of $k_{ST} = 45 \text{ m}^{1/3}/\text{s}$ is set within the entire reservoir. The three simulations diverge in the choice of the parameter of the constant Eddy Viscosity (Table 2).

Table 2: Eddy Viscosity values in the 2-D model

Simulation	Constant Eddy Viscosity [m ² /s]
Simulation 1	0.2
Simulation 2	0.5
Simulation 3	1.0

The results of simulation 1 (Figure 3, chart top), downstream the gorge portion, are showing a trend of the main flow direction to the orographic right bank, having back flows mainly at the orographic left bank. In the expanded area of the reservoir there could be seen few back flows at the orographic right bank. In simulation 2 (Figure 3, chart centre) a distinct flow at the orographic right bank can be noticed and, in comparison to simulation 1, a stronger back flow at the left bank can be observed. Simulation 3 (Figure 3, chart bottom) shows nearly the same flow pattern as in simulation 2, whereas the main flow is pushed with even more intensity to the orographic right bank and the back flows are also more intense. The velocity distribution in the zone of the turbine inlet is very similar in all simulations. Upstream of the gorge portion with a

water depth of about 5 m and considerably higher flow velocities, all three simulations have shown nearly identical velocity distributions.

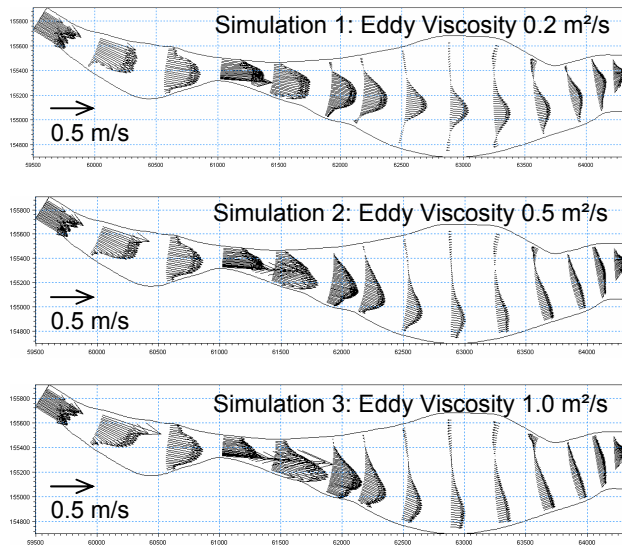


Figure 3: Velocity distributions, 2-D simulations 1, 2, 3

4 COMPARISON BETWEEN NUMERICAL MODEL AND ADCP MEASUREMENTS

The ADCP velocity measurements confirm the results of the numerical simulations. The velocity distributions in all three simulations tend to match the results from the ADCP measuring campaign. The flow field in simulation 2 with the constant Eddy Viscosity of $0.5 \text{ m}^2/\text{s}$ corresponds very well to the measured velocity distributions. The absolute values of the velocities are considerably higher in the numerical simulations. This is due to fact that the calculations were performed for constant discharges of $400 \text{ m}^3/\text{s}$. However, the actual discharge through the turbines varied from 200 to $400 \text{ m}^3/\text{s}$ during the measuring campaign.

5 CONCLUSIONS

The unsorted sedimentation of suspended load in the reservoir should be registered with the help of numerical calculations and a physical model test. The measures at the physical model will start at the beginning of 2009. For a first calibration of the numerical model an ADCP measuring campaign was carried out determining the velocity distribution within the reservoir. The constant Eddy Viscosity value could be determined, which can be applied in further turbine case simulations. Uncertainties in the appearance of the stream patterns downstream of the gorge portion could be solved. The measurements show a good agreement with the results from the numerical calculation according to the qualitative stream patterns. The ADCP measurements and the 2-D numerical simulation results show that the main part of the discharge tends to the orographic right side of the reservoir downstream of the gorge portion. Further planned

measuring campaigns in the case of higher discharges (up to the design discharge) should verify further results of the numerical simulations. In Summer 2008 ADCP measurements in combination with turbidity measurements and sampling of suspended sediments are going to be performed, which in addition to velocity data will provide the basis for the analysis of backscatter data.

ACKNOWLEDGEMENT

We would like to thank the Verbund Austrian Hydro Power Company (AHP) and the Styrian Government of Austria for their help and assistance while performing the ADCP measuring campaign and providing the authors with helpful informations.

REFERENCES

- [1-2] RD Instruments: Principles of Operation - A Practical Primer, 2nd Edition for Broadband ADCPs (1996).
- [3] RD Instruments: High Resolution Water Profiling Mode 12, Application Note FSA-014 (2002).
- [4] RD Instruments: WinRiver II User's Guide (2007).
- [5] Mueller DS, Rehmel M: Determining Mean Velocity for Stationary Profiles using WinRiver, HydroAcoustics, U.S. Geological Survey (2005).
- [6] Danish Hydraulic Institute: MIKE 21C Scientific Reference Manual (2002).
- [7] Rodi W: Turbulence Models and their Application in Hydraulics - a State of the Art Review, 2nd Edition, IAHR, Delft (1984).
- [8] Danish Hydraulic Institute: MIKE 21C Scientific Reference Manual (2002).
- [9] Steffler P, Blackburn J: River2D - Introduction to Depth Averaged Modeling and User's Manual, University of Alberta (2002).

Influence of bank roughness and inclination on straight channel flows

Alexandre Duarte ¹, Koen Blanckaert ¹ and Anton J. Schleiss ¹

¹Laboratory of Hydraulic Constructions, École Polytechnique Fédérale de Lausanne, EPFL-ENAC-ICARE-LCH, GC A* 504 (Bâtiment GC), Station 18, 1015 Lausanne, Switzerland, phone:+41 21 693 6388; fax: +41 21 693 2264, e-mail:alex.duarte@epfl.ch

EPF Lausanne, IGB Berlin, TU Delft and WL Delft are undertaking an ambitious program on open-channel research, which main goal is improving the capabilities of numerical tools for predictions of hydrodynamics and morphodynamics in natural-like rivers. Inserted in the objectives of the above-mentioned cluster program, this paper investigates the influence of bank inclination (vertical, 45° and 30°) and bank roughness (smooth and riprap) on straight open-channel flow characteristics by experimental measurements. The instrumentation used is Acoustic Doppler Velocity Profiler, which enables three-dimensional velocity measurements with high spatial and temporal resolution. The results reveal that the pattern of downstream velocity is influenced strongly by the bank inclination and roughness. The mean and maximum shear stress force values on the wetted perimeter are also influenced by the geometry shape and bank roughness.

Keywords: straight channel, wetted perimeter shear stress, downstream velocity

1 INTRODUCTION

A characteristic feature of straight channel flows is the secondary currents. Due to its convective capacity, it plays an essential role in mixing and transport processes. It also changes the velocity distribution, the shear exerted on the wetted perimeter and as consequence on morphology. A large portion of engineer projects is concerned with the sediment transport and bank erosion. Herewith we report on an experimental study of the dynamics of the streamwise velocity and wetted perimeter shear stress distribution as function of wide channel cross-section shape and wetted perimeter roughness distribution. The lack of experimental data combined with the difficulty to find a theory which explains the secondary currents evolution in wide channel justifies the poor design criteria validity range for trapezoidal cross-section nowadays. It is not found in literature criteria for the influence of different bank/bed roughness ratio on the velocity and shear stress especially on the location and magnitude of maximum shear stresses.

This paper aims at showing the influence of trapezoidal cross sectional shape and roughness distribution on wide channel primary velocity and shear stress. This paper presents measurements from three different wide open-channel cross-section geometries, a rectangular and two trapezoidal with varying bank angle and bank roughness.

The data obtained is from a dense measurement grid, see Figure 1, with a state-of-the-art measuring technique, Acoustic Doppler Velocity Profile (ADVP) developed in LHE [2-3]. ADVP allows resolution measurements of quasi-instantaneous three velocity components. From there it is possible to evaluate all

three mean velocity components, as well as all turbulent stresses components.

2 EXPERIMENTAL SET-UP

Experiments were performed in a $B = 1.3$ m wide laboratory set-up. A horizontal bottom of nearly uniform sand $d_{50} = 2.1$ mm was assembled. Three experiments were performed. Figure 1 shows the cross-section schematic of all three test conditions and Table 1 shows their important parameters. First test condition cross-section is rectangular with smooth banks and rough bed. Second test condition cross-section is trapezoidal. The inner bank is vertical and the outer is 45°-inclined regarding the horizontal bottom. Inner and outer banks are defined based on the n-axis sense shown in Figure 1. The inner bank and bed are smooth. The third test condition is a trapezoidal wherein the inner bank is vertical and the outer bank is 30°-inclined regarding the horizontal bottom. The inner bank is smooth whereas the outer-bank has riprap $d_{50} = 3$ cm elements. The cross-section has been measured on a refined grid with vertical profiles between 50, 25 and 15 mm for central, buffer and near-bank areas, respectively.

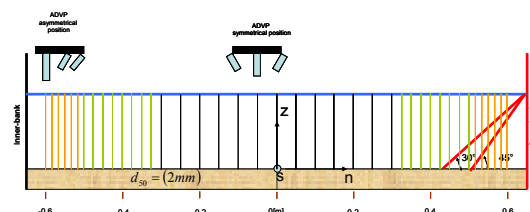


Figure 1: Cross-section measuring grids and shapes

3 RESULTS

Hereafter it is shown streamwise velocity and wetted perimeter shear stress from the three test conditions mentioned above. Figures 3a,b,c show the isolevels

of downstream velocity normalized by U (mean velocity) and normalized wall shear stress by τ_0 over the wetted perimeter where $\tau_0 = \rho g R_h S_s$. R_h is the hydraulics radius and S_s is the downstream water surface gradient at cross-section centerline.

Shear stress is calculated by assuming an equation for the vertical profile of velocity. It is known that even straight channel flows have 3D flows but it is considered negligible in the lowest 20% of water depth. The velocity profile is shown to have the following form in the lowest 20% of water depth, [1].

$$\frac{U}{u_*} = \frac{1}{k} \ln \left(\frac{z}{z_0} \right) \quad (1)$$

where U is the velocity at distance z from the boundary, u_* is the shear velocity or shear stress, k is the turbulent exchange coefficient or von-Kármán constant and z_0 is the distance at which log velocity profile indicates zero velocity.

Figures 3a,b,c do not show velocity-dip phenomenon. It is in agreement with [4] as the aspect ratio B/h is greater than 5.5, its critical value, for all experiments even for the trapezoidal cross-sections.

Experiment F16_90_00, Figure 3a, reveals non-uniform, wavy distributions over width suggesting the existence of circulation cells. This fact is not in agreement with [1]. The maximum velocity, $V_s \max/U$, is equal to $1.2U$ being located at about the free-surface along the cross-section width. Lower downstream velocity zones from where the contour lines bulge towards the free-surface are located at n (m) = [-0.35 -0.1 0.25 0.55]. Higher downstream velocity zones from where the contour lines bulge towards the bed are located at n (m) = [-0.5 -0.2 0.1 0.4]. These "bulges" correspond to upwelling and downwelling, zones of lower and higher velocities, respectively.

Figure 3a also shows that spanwise bed shear stress undulation is of $0.2\tau_0$, being in agreement with [1]. The upwelling and downwelling are also seen in the shear stress distribution. Bank shear is lower than bed shear. Bank shear stress is always lower than the threshold value, $\tau_0 = 1$, and it increases from the bank toe till the mid-depth where the maximum is located.

Figure 3b shows the 45°-bank inclination trapezoidal case with smooth outer-bank, Experiment F16_45_00. The maximum normalized downstream velocity, $V_s \max/U$ is $1.3U$ and it is located at about n (m) = [-0.2 0.2] close to the free-surface contrasting with the rectangular cross-section Experiment F16_90_00 case. The number of upwelling and downwelling is inferior to Experiment

F16_90_00. Three downwelling are located at about n (m) = [-0.6 -0.3 0.3] and three upwelling are located at about n (m) = [-0.5 0 0.5].

Figure 3b also shows that spanwise bed shear stress undulation is $0.2\tau_0$. Bed shear stress evolution shows two maximum at the same downstream velocity maximum spanwise locations. Bank shear is lower than bed shear and always lower than the threshold value. It increases from the bank toe till $z/h=0.3$, where the maximum outer bank shear stress is located, followed by decreasing values till the free-surface.

Figure 3c shows the 30°-bank inclination trapezoidal case with riprap elements on the outer-bank, Experiment F16_30_30. The maximum normalized downstream velocity, $V_s \max/U$, is equal to $1.4U$ and it is located at about channel center and close to the free surface. The number of bulges decreases in comparison with the two-different shape geometries presented before, vertical bank and 45°-inclined bank.

Figure 3c also shows two downwellings at about n (m) = [-0.55 0] and upwelling at n (m) = [-0.4 0.35]. Bed shear stress evolution amplitude range is higher than $0.5\tau_0$. At about channel center the bed shear stress reaches $1.8\tau_0$. Between the channel center and the bank toe a sharp shear stress decrease of $0.7\tau_0$ exists. Bank shear stress is lower than the bed shear stress and lower than the threshold value and its maximum is located at about $z/h=0.2$.

Table 1: Experiments conditions

Label	Q [l/s ¹]	H [m]	U [ms ⁻¹]	u_* [ms ⁻¹]	C [m ^{1/2} s ⁻¹]	Re [10 ³]	Fr [-]	R/B [-]	R/H [-]	B/H [-]	$k_s, bank$ [m]	Θ_{bank} [°]
F16_90_00	90	0.16	0.42	0.029	46	69	0.33	1.31	10.3	7.9	PVC	90
F16_45_00	85	0.16	0.42	0.028	48	69	0.33	1.39	10.3	6.75	PVC	45
F16_30_30	80	0.16	0.42	0.035	38	69	0.33	1.46	10.3	6.24	0.030	30

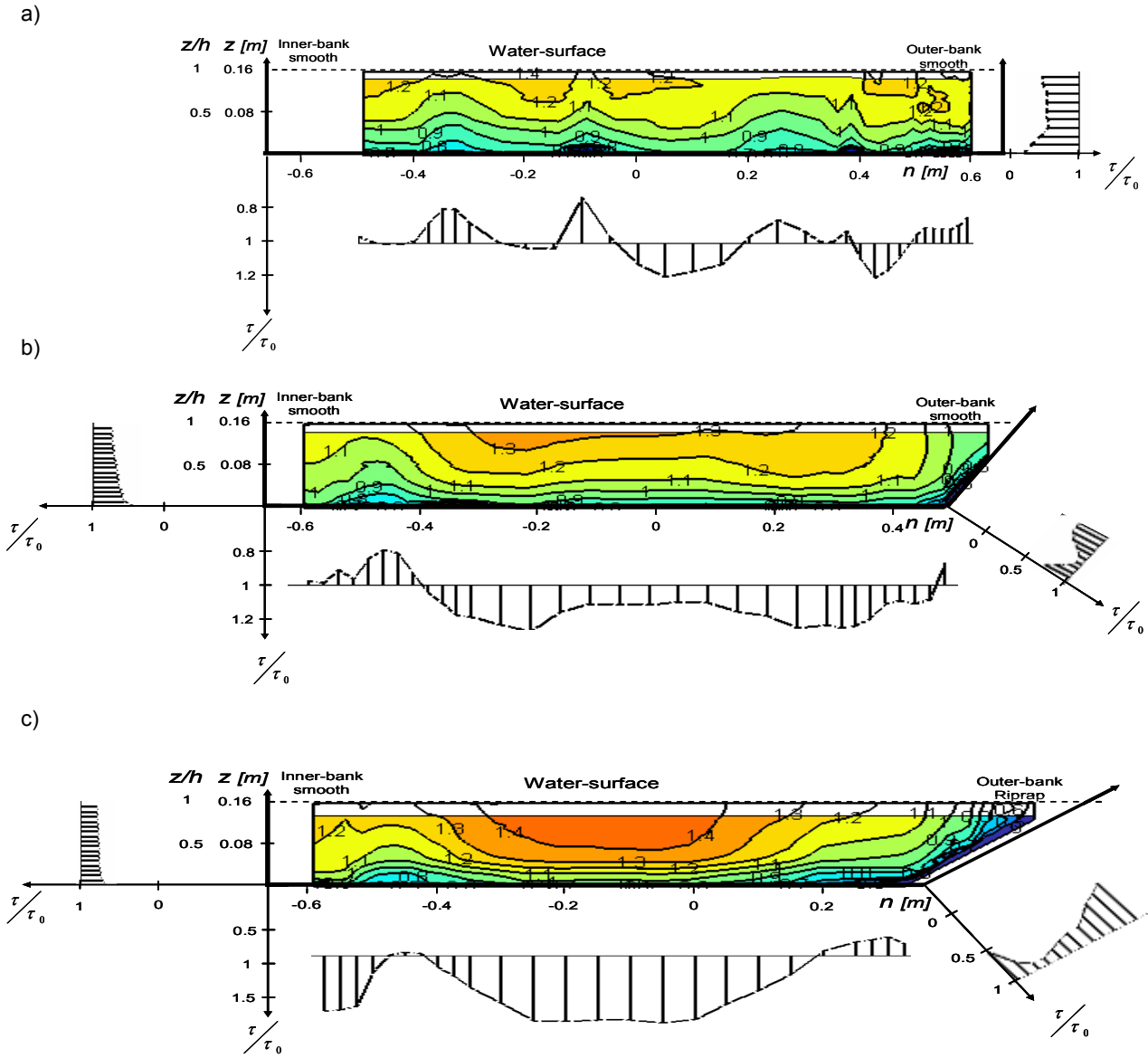


Figure 2: Contour lines of normalized downstream velocity & bed and wall shear stress values:

a) F16_90_00; b) F16_45_00; c) F16_30_30

Table 2: Wall shear stress mean and maximum values

	$\bar{\tau}_{bed} / \tau_0$	$\bar{\tau}_{bank} / \tau_0$	$\max \tau_{bed} / \tau_0$	$\max \tau_{bank} / \tau_0$
F_16_90_00	1.05	0.39	1.3	0.49
F_16_45_00	1.13	0.82	1.31	0.9
F_16_30_30	1.34	0.4	1.8	0.8

4 DISCUSSION

Based on the results obtained, it is possible to analyze the effect of cross-section shape and bank roughness.

F16_45_00 and F16_30_30 results show typical trapezoidal cross-section primary flow characteristics because the maximum downstream velocity is concentrated close to the channel center at the free-surface whereas a rectangular cross-section has typically the maximum downstream velocity spread over the width at free-surface (for wide channel). These differences between rectangular to trapezoidal flow characteristics are well observed when comparing F16_30_30 with F16_90_00.

Bed shear stress spanwise undulation is also affected. Less bulges and higher amplitude range, from $0.2 \tau_0$ (rectangular cross-section) to higher than $0.5 \tau_0$ (trapezoidal cross-section), are observed between F16_90_00 with F16_30_30. Please note that bank shear stress magnitude decreases. The maximum bank shear stress locus becomes closer to the bank toe with decreasing bank angles.

Table 2 shows the normalized mean and maximum bed and bank shear stresses. Table 2 shows that the highest normalized maximum bed shear is obtained for F16_30_30. By contrast, the normalized lowest maximum bank shear is obtained for F16_30_30.

4 CONCLUSIONS

The conclusions of this work are divided in two topics: The primary flow patterns and shear stress distribution on the wetted perimeter.

Primary flow patterns:

- Rectangular and trapezoidal channel flow patterns are different.
- Rectangular velocity patterns reveal several bulges known as upflows and downflows which number agrees well with aspect ratio and Literature
- Trapezoidal channels have less bulges than rectangular channels being in agreement with Literature
- Trapezoidal channels with rougher inclined bank than bed generate higher downstream velocity at about channel center.

Shear stress distribution on the wetted perimeter

- The bed shear stress spanwise evolutions are in agreement with primary velocity patterns

- The normalized bed shear stress oscillates between $0.8-1.2 \tau_0$ for rectangular cross-sections, which is in agreement with Literature.

- The normalized bed shear stress oscillates between $0.8-1.2 \tau_0$ for trapezoidal cross-sections with quasi-homogeneous roughness distribution.

- The normalized bed shear stress oscillates between $0.5-1.5 \tau_0$ for trapezoidal cross-sections with $k_{sbank} / k_{sbed} = 10$.

- The inclined bank shear stress evolution has a maximum in the vicinity of the bank toe for all trapezoidal cross-sections.

- The magnitude of inclined bank shear stress decreases with increasing bank roughness.

ACKNOWLEDGEMENT

The PhD research project is funded by the Swiss National Science Foundation under grant SNF 20020-103932.

REFERENCES

- [1] I. Nezu I, Nakagawa H, A Tominaga: Secondary currents in a straight channel flow and the relation to its aspect ratio, Turbulent shear flows 4, Springer-Verlag. 27 (1985),246-290
- [2] Rolland T.: Développement d'un instrumentation Doppler ultrason adaptée à l'étude hydraulique de la turbulence dans les canaux. Swiss Federal Institute of Technology, Lausanne, (1994), PhD dissertation No.1281
- [3] Shen C.: An acoustic instantaneous particle flux profiler for turbulent flow. Swiss Federal Institute of Technology, Lausanne, (1997), PhD dissertation No.1630
- [4] Tominaga A, Nezu I, Ezaki K, Nakagawa H: Three-dimensional turbulent structure in straight open-channel flows, J.Hydraulic Research. 27 (1989),149-173

Velocity gauging with ADCP in rivers with bedload and sediment transport

Katharina Fiedler¹, Theodor Strobl¹, Franz Zunic^{1*} and Horst Matthes²

¹ Institute of Hydraulic and Water Resources Engineering, Technische Universität München, Arcisstraße 21, 80333 München, Germany (*Corresponding author, e-mail: f.zunic@bv.tum.de).

² E.ON Wasserkraft GmbH, Luitpoldstraße 27, 84034 Landshut, Germany

The ADCP technique is generally accepted as an instrument for velocity gauging in rivers. But still there are many challenges to deal with: (1) In rivers with high sediment transport, like in many streams in the foothills of the Alps, ADCP gauging of velocities is insufficient and sometimes even impossible to be carried out satisfactorily. (2) Rivers with bedload make it difficult to validate the measured data, if the position of the ADCP is fixed by the Bottom-Tracking-Method. (3) Sediment transport is also responsible for inaccurate measurement readings of some gauging stations. Due to streambed erosion during floods, the supposed rating-curve is not valid during peak flow. It has to be adjusted to measured velocity data as well as shape and depth of the riverbed. During a two-year research project, these problems were investigated in detail at two typical rivers in Southern Bavaria: First, the major river *Inn* with high sediment transport rates and considerable erosion and aggradation processes during flood and second, the much smaller river *Tiroler Achen*, flowing into Lake *Chiemsee*. Although no erosion occurs here, considerable bedload requires additional measurement techniques to get exact position data during ADCP measurements.

Keywords: Velocity gauging, flow metering, sediment transport, bedload, differential GPS

1 INTRODUCTION

The knowledge of discharges in rivers is of high importance for many hydrologic tasks and investigations in water resources engineering. Accurate values are the crucial input data for all hydrodynamic-numerical modeling schemes; and in flood frequency analysis, a reliable evaluation of extreme discharges is only possible, if the data from river gauging stations is precise and available in a wide range of different runoffs [1].

In the presented research study the authors tried to detect the supposed erosion processes in the river *Inn*. The original idea was that if the riverbed erodes during flood, the cross section for runoff increases which of course will have a positive effect on the remaining freeboard in the river. While studying the erosion process through ADCP and echo sounder at the river *Inn*, the authors faced some unknown problems, which are described in this article.

The extreme flood in May 1999

The extremely high water in May 1999 was caused by a Vb meteorologic scheme, hitting wide areas in Bavaria, Austria and the Czech republic. Figure 1 shows the hydrograph of this major flood.

While studying the runoff we realized, that the bottom of the river bed at three gauging stations near the city of Rosenheim must have been eroded by several meters during the runoff of the peak of the wave. Using the 1d-model HEC-RAS and assuming a constant river bed before and during the flood event [2], the calculated water levels did not fit to the observed water levels (fig. 1).

The reason for this obviously must lie in the eroded riverbed during flood. Astonishingly, the deviation from measurement and calculation corresponded very closely to the hydrograph. It seemed as if erosion increased with higher discharges, and after the peak the riverbed was filled up with sediments almost simultaneous with the descending discharge.

In this article we will concentrate on our investigations at the river *Inn*. The results we found at the *Tiroler Achen* are presented in detail in [3].

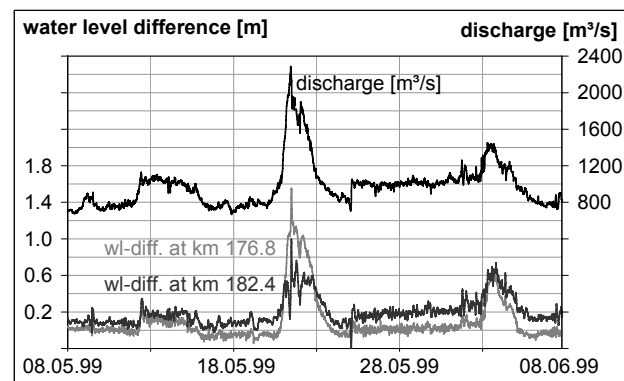


Figure 1: Hydrograph of the flood in May 1999

2 MEASUREMENTS AT THE RIVER INN

Encouraged by this simple insights in the mechanism of erosion processes the authors tried to get more information about erosion and sedimentation coming along with high runoffs. Therefore, during the exceptional flood in August 2005, several measurements have been taken at the *Inn* near the village of Nußdorf using amongst others also the ADCP technique [2].

2.1 ADCP in use

Acoustic Doppler Current Profiler use the well-known Doppler Effect to measure relative velocities between transducer (= measuring device) and reflectors (= particles in water column). For the here presented investigations ADCP model "Workhorse RioGrande", developed by RD Instruments, with a frequency of 1200 kHz was used.

The carrier device is a self made catamaran in aluminium with 20 kilograms of weight. It contains a waterproof box hosting the battery, the modem device and a laptop, and also a GPS antenna used for external recording of position coordinates (fig. 2). Using a second, stationary GPS antenna on the river bank allowed the use of the so-called *differential GPS-technique* and improved the accuracy up to few centimetres.

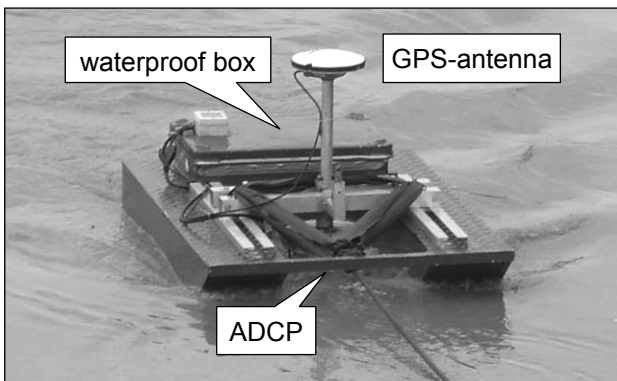


Figure 2: Carrier device with ADCP and onboard GPS

2.2 Situation

The following information is given for better understanding the situation at the gauging station, where the investigations took place.

Geography, catchment area:

The river *Inn* rises in Switzerland, at an altitude of 2484 meters above sea level. After 517 covered river kilometres and 2193 metres of difference in altitude, the river mounts into the Danube near the Bavarian city of Passau. Of its total catchment area of some 26.000 km², about 16.360 km² fall upon Bavarian territory, which the river drains along its final course of 213 kilometers before flowing into the major river *Danube* at Passau. Because of the high alpine catchment area of its upper reaches, the river *Inn* transports heaps of very fine sediment, coming from the glaciers in Switzerland and Austria.

History:

Due to the construction of 16 power plants along the Bavarian Inn during the last 80 years and the declining energy slope of the river, a huge amount of sediment was deposited in the reservoirs and river bed levels ascended up to several metres. Today, these sedimentations already are included in water management studies, but the temporal eroding effect of high floods, often linked with

drawdown of retention water level elevation, is still unknown [2].

Measurement site:

Measurements were carried out at river kilometre 199.2, only 500 metres above the hydro power plant Nußdorf, where a road bridge crosses the river. Water level at retention water level elevation is about 120 metres wide and mean depth is six metres.

Discharge situation:

During the summer months 2005, five measurements could be carried out – three during normal flow conditions and two during high flood (fig. 3).

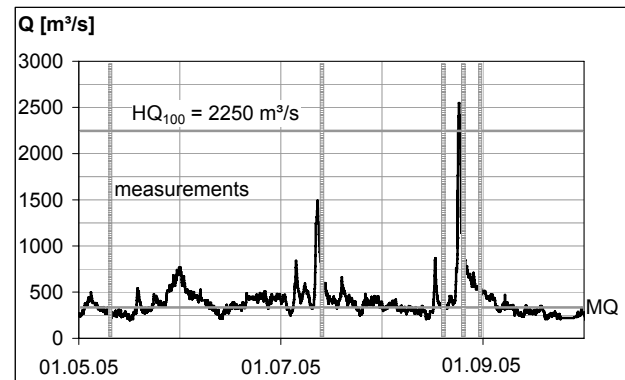


Figure 3: Discharge situation in summer 2005

2.3 Measurements during high flood

Carrying out the measurements was a big challenge for the executing personnel.

Problems:

- A huge amount of branches, trees, parts of wood etc., floating with the current, put the measuring devices at great risk (fig. 4).
- High flowing velocities caused high flow resistance of the ADCP carrying device and great exertion was necessary to keep the boat in position as well as to move it across the river.
- Turbulences at the water surface and stationary waves, induced by the two pillars of the bridge, also made the movement across the river very difficult.
- High suspended sediment concentrations partially made it impossible for the ADCP to collect data.



Figure 4: Driftwood flowing down the river Inn

2.4 Results of the measurements

The following explanations include only the results of the high-flood measurements during August 2005. The Peak of the flood wave occurred from 23rd to 24th of August during night time, which avoided the acquisition of data during peak flow. Measurements were possible not until the following afternoon, while the decelerating branch of the flood wave. Six crossings could be carried out successfully, their data sets were analysed and interpreted [2].

Bottom Track versus dGPS:

Because of sediment transport near the river bed, bottom track was biased upstream (fig. 5).

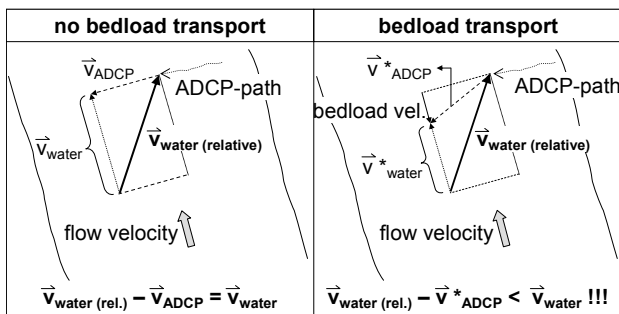


Figure 5: Biased bottom track due to bedload transport

As figure 5 shows, upstream biased bottom track is responsible for underestimating flowing velocities with ADCP measurements [3]. Therefore the calculated discharge is also too small, when referencing ADCP data on bottom track in cross sections with bedload transport. Referencing measurement data on dGPS data produced satisfying results, comparing them with available reference values (fig. 6).

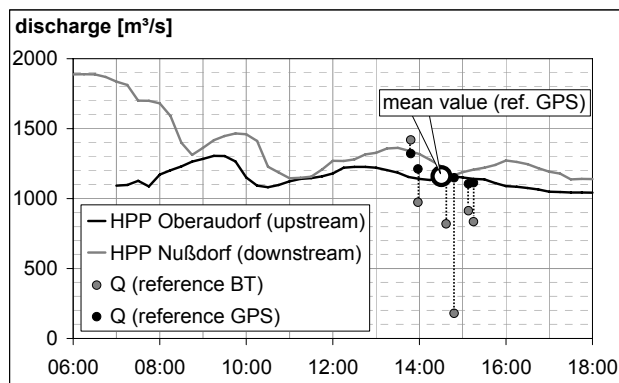


Figure 6: Discharge calculated by the ADCP with reference on bottom track as well as on dGPS

Due to high suspended sediment concentrations, the bottom track signal often lost contact to the river bed. Therefore river width was detected insufficiently, which also could be improved by referencing the data on dGPS information.

Erosion of the river bed:

For the first time known, temporal erosion of the river bed during high flood could be detected with

ADCP measurements. The results show an erosion of up to two metres in comparison with the river profile during normal flow conditions (fig. 7).

Because it was the first time, that the temporal erosion could be detected and documented, this information is very important and is an extremely useful contribution to the ongoing attempts trying to improve the understanding of hydromorphological processes during high floods [2].

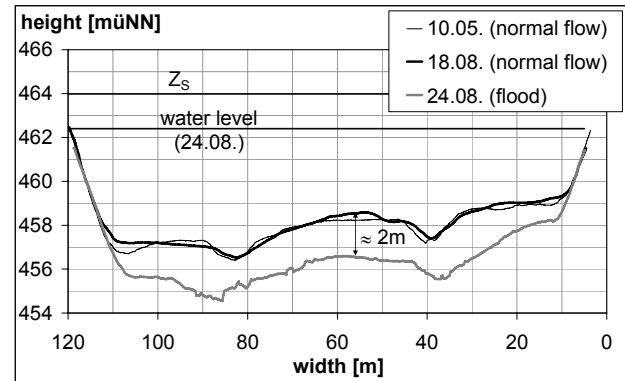


Figure 7: Detected bed erosion during flood

Bedload velocities:

In addition to measuring streambed depths, discharge and flowing velocities, the attempt was made to analyse the ADCP data in respect to bedload velocities [3]. Therefore the phenomenon of upstream biased bottom tracking due to bedload transport was utilised. For each transit, the boat velocities, calculated from the bottom track data of the ADCP, were extracted out of the ASCII files. Using trigonometric relations, the velocities in direction north-south and east-west were transformed into components parallel to the crossing direction and components rectangular to it. Under normal conditions, the components rectangular to the crossing direction should converge to zero. In case of bedload transport these values will be biased, which can be used to estimate the amount of bedload velocity. Figure 8 shows the components of the boat velocities parallel to the crossing direction.

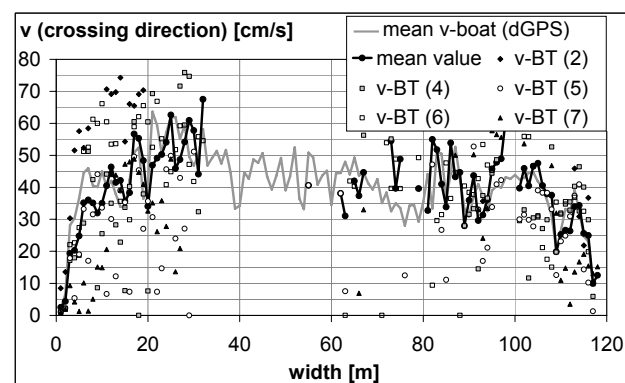


Figure 8: Components of boat velocities parallel to the crossing direction

The grey line represents the mean boat velocity of all five crossings, calculated from the dGPS-data. The huge fluctuations resulted from the manual trailing of the ADCP and the problems faced during the measurements. It can be seen, that despite the scattering of the individual crossings, the mean velocity of the boat calculated from the bottom track data (black line) corresponds well with the actual velocities. The lack of bottom track data in the middle region of the cross section is also eye-catching and emphasizes the need of external positioning data.

Figure 9 contains the illustration of the second components of the boat velocities, in this case rectangular to the crossing direction, which is parallel to the main flow direction.

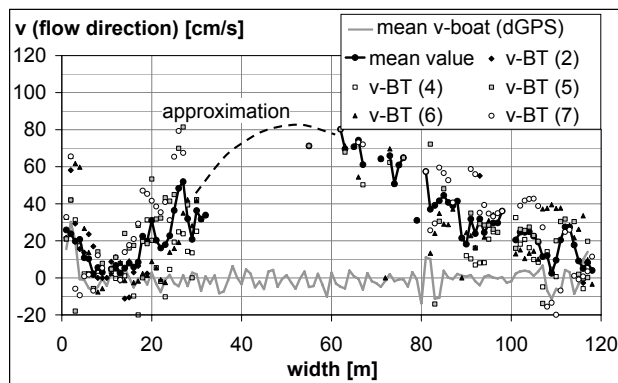


Figure 9: Components of boat velocities rectangular to the crossing direction

The mean value calculated from dGPS-data is fluctuating around zero which means, that besides very small, locally restricted movements up- and downstream the river, there were no components of boat velocities rectangular to the crossing direction. But if you look at the run of the curve, representing the values calculated from the bottom track data, they range between zero and 80 cm/s. That means that bedload moves through the cross section with a velocity up to 80 cm/s.

3 CONCLUSIONS

Various measurements during the extreme flood of August 2005 at the river Inn near the border of Austria and Germany gave us a good insight into a set of problems which can arise, when one tries to use the ADCP technique during high waters.

The challenges in conducting and interpreting the measurements lay in

- extreme driftwood, which compromises the carrier device as well as the expensive measuring devices onboard
- high suspended sediment concentrations, which make it difficult to get sufficient data for interpretation

Consequently, the hydraulic laboratory of the Insti-

tute of Hydraulic and Water Resources Engineering at the Technische Universität München (Oskar-von-Miller Institute in Obernach) will try to improve the carrier device, so that debris and driftwood will be kept away from the ADCP device reliably. Besides, we have plans to investigate the effect of suspension load – in respect of concentrations as well as grain size distributions – on the reflected acoustical signal of the ADCP. The successful interpretation of bottom track data regarding bedload velocities encouraged us to continue this work and to enhance the used procedure.

So our main goal, to describe the erosion process during flood, is still not achieved completely. There is still a lot of investigation to do, but with the aid of the herein presented measurements, we luckily got a lot of important insights, which will help us to reach the original objectives.

ACKNOWLEDGEMENT

The authors of Technische Universität München are grateful to the energy company E.ON and to the Bavarian government for supporting this research project.

REFERENCES

- [1] Fiedler K, Steinbacher F, Strobl T and Zunic F: Sohlen- und Abflussmessungen: Vorteile und Grenzen der ADCP-Technik, *Wasserwirtschaft*, Vol. 98, (2008) 27 - 31.
- [2] Fiedler K, Matthes H and Zunic F: Erfassung des Sohlaustrags während Hochwasser mit Hilfe von ADCP-Messungen. in: *Stauhaltungen und Speicher – Von der Tradition zur Moderne. Schriftenreihe zur Wasserwirtschaft der Technischen Universität Graz*, Vol. 46/1 (2006) 361 - 375.
- [3] Fiedler K: Erfassung hydromorphologischer Vorgänge in Fließgewässern mit Hilfe von ADCP-Messungen, *Berichte des Lehrstuhls und der Versuchsanstalt für Wasserbau und Wasserwirtschaft, Technische Universität München*, Vol. 120 (2008).

Development of Rheometry based on UVP for visco-elastic liquid

Naoki Furuya, Yuji Tasaka, Yuichi Murai and Yasushi Takeda
 Division of Energy & Environmental system, School of Engineering, Hokkaido
 (e-mail: naoki-f@ring-me.eng.hokudai.ac.jp).
 North13-West8, Kita-ku, Sapporo, Hokkaido, Japan

As a method to estimate the property of visco-elastic liquid, UVP is utilized for unsteady flow field which arises during spin-up and spin-down of container. This flow configuration provides necessary information to determine the elasticity and the viscosity of the target fluid. First, a numerical simulation is performed to understand how the velocity profiles along UVP-measurement line is obtained. Secondly, the unsteady flow of PAA solution that is a typical example of visco-elastic fluid is actually measured with UVP. Since the property of PAA solution is characterized by three factors; viscosity, elasticity, and yield stress, these factors are estimated with Maxwell and Bingham models using least square approach. In our study, the least square approach is applied to the spatio-temporal two-dimensional distribution of velocity. The results are validly obtained with this approach, and thus we conclude that the present flow configuration is feasible as a UVP-based rheometry.

Keywords: Rheological properties, Transient shear response, Visco-elasticity, Yield stress

1 INTRODUCTION

Rheology for liquid foods are positioned in highly important research field in a part of life science and food process engineering. They often show very different behavior from ordinary Newtonian fluids. The visco-elastic properties of liquid foods sometimes cause accident in swallowing them, and also relate to quality control of food manufacturing process. In order to estimate these properties in visco-elastic fluids, a high accuracy but convenient method is desired to be built up. Conventional methods for estimating them utilize indirect information obtained from differential pressure in a tube or torque caused by the wall shear stress. In those methodologies, the internal flow structure which will depend sensitively on the visco-elastic properties is consequently kept invisible so that the local flow information cannot be assessed. This problem slows down the scientific understanding of the rheological behavior.

Since ultrasonic velocity profiler (UVP)^[1] can acquire the velocity profiles as a function of time, it has a potential to become a high-performance rheometry. Because of ultrasonic principle, most of liquid foods can be measured regardless the opaqueness, such as milk, yogurt, and chocolates. In this study, our objective is set to develop such a rheometer based on UVP, by choosing the best optimized flow configuration. The best optimizing means that the spatio-temporal two-dimensional velocity information obtained by UVP would be fully utilized to accurately detect the material properties of the target fluid. To this end, the transient shear response of fluid driven by sudden spinning in a container is selected.

In this paper, we describe about the method of UVP-based rheometry, numerical analysis of the visco-elastic fluid in the spinning flow, and the

examination using polyacrylamide (PAA) solution as the demonstration. In the final part of the paper, the algorithm for obtaining the visco-elastic properties from UVP data is proposed and its validity is discussed.

2 FLOW CONFIGURATION

Figure 1 shows general description of the present flow configuration. There are advantages with this flow configuration in comparison to pipe flows that are also utilized as UVP-base rheometry^[2-6]. The key point in spinning flow is that it enables to acquire the transient shear response from quiescent state. Therefore, wall-clinging effect for the elasticity, fluidized behavior departing from the yield point, and shear-thinning effect are all captured simultaneously with a single run of the measurement. Furthermore, the steady state converges to rigid rotation for any type of fluids, we need not to consider the dependence on initial conditions, which often takes place in the case of pipe flow. This is also a important merit for guaranteeing the reproducibility of the measurement. Thus, a small-volume sampling of target fluid pouring into the rotor provides full information of the rheological properties when the spinning flow is utilized.

As shown in Fig. 1, the measurement line is set at the distance of 7mm from center line of a cylindrical container. The container is made of acrylic resin, and has 150mm in diameter and 2mm in thickness. We checked the echo caused on the sidewall of the cylinder to define the range of measurement. As shown in Fig. 2, the temperature of the liquid is controlled to be constant at 20deg C, and an ultrasonic absorber is put on the backside of the transducer. The basic frequency is set at 4MHz. As ultrasonic reflector in fluid, high-porous polymer particles (HP20SS) are mixed. The speed of sound

for 20deg C PAA solution is 1500m/s. Sampling period is 20msec, and the number of profiles is 1024. Spatial resolution is 0.75mm while the number of channels is 230. The flow velocity resolution is 1.95mm/s. The rotational speed of the container can vary from 50 to 150rpm.

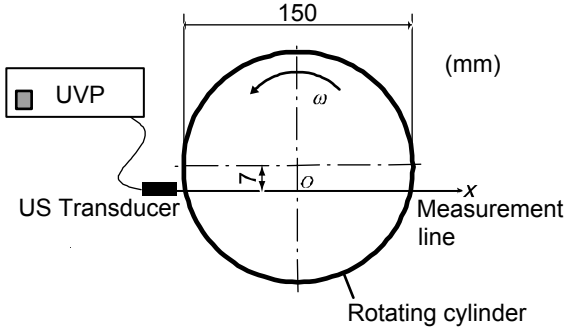


Figure 1: Definition of measurement line in container

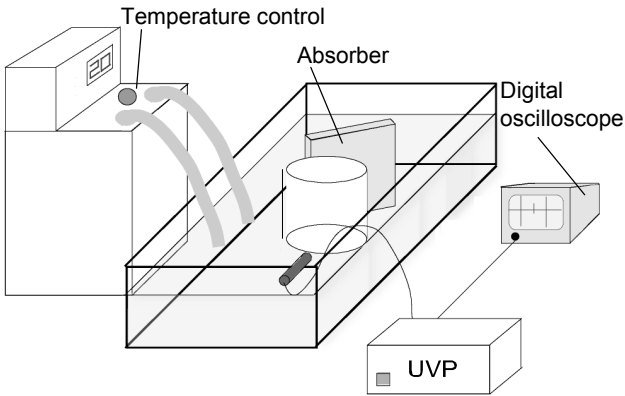


Figure 2: Experimental setup for PAA solution

3 NUMERICAL SIMULATION

Before conducting the experiment, how the velocity profiles are obtained on the measurement line must be evaluated. Ordinary visco-elastic liquid has a yield stress at which the flow is released from the elastic potential to be fluidized and stretched. Therefore we employ Bingham model, which is one of non-Newtonian fluid model in the numerical simulation. The simulation is conducted with axisymmetric cylindrical coordinate system, using the following basic equation.

$$\rho \frac{\partial v}{\partial t} = \frac{1}{r^2} \frac{\partial}{\partial r} (r^2 \tau) \quad (1)$$

Here ρ is density of fluid, t is time, and v is tangential (azimuthal) velocity at the radial position, r . Since there is no pressure gradient in the azimuthal direction as far as any wavy behavior does not appear, the pressure term disappears in Eq.(1). We assume that the radial flow be quiescent so that no equation is required for it. This is valid for a long cylinder in the axial direction (however, the experiments show certain flow in this direction as we mention later). As a model of visco-elastic fluid, we use the following Bingham model.

$$\tau = E\gamma = E \int \frac{\partial \gamma}{\partial t} dt = E \int \frac{\partial v}{\partial r} dt \quad (\tau < \tau_y) \quad (2)$$

$$\tau = \mu \frac{\partial v}{\partial r} + \tau_y \quad (\tau \geq \tau_y)$$

Here, γ stands for shear strain rate, μ the viscosity, and τ_y the yield stress. As shown in eq. (2), the formula of the shear stress switches to be either of two dependent on the local instantaneous shear stress, τ . In the case of the shear stress smaller than the yield stress, the shear stress is caused by the shear displacement that equals to integrated shear rate respect to time. Beyond the yield stress, the shear stress additionally increases linearly to the shear rate similar to Newtonian fluid.

As examples, the following conditions are supposed in the numerical simulation, which approximates the experimental conditions: top rotational speed 50rpm, $\mu=0.05\text{Pas}$, $E=0.05\text{Pa}$, $\tau_y=0.15\text{Pa}$.

Figure 3 shows the results of the numerical simulations. The grayscale bar indicates the flow velocity component along the measurement line (see Fig. 1). In the case of rigid rotation, this velocity component gets uniform on the line, and thus the transient response of the fluid by the spinning is visualized by the change in the grayscale. As shown in Fig. 3 (a), when the rotation suddenly starts at $t=0$, the fluid in the cylinder is accelerated near the sidewall of the container. In the beginning of the spin up, the shear stress exceeds the yield stress for the high shear rate near the wall. Therefore, the high-speed region expands in the container similarly to Newtonian fluid. There is also a certain contribution of the elasticity to the acceleration, which exists in the central region of the container having less shear rate. In fact, a small oscillatory flow is overlapped, however it is hidden in monotonic increase of the velocity. We confirm that changing the three parameters μ , E and τ_y extensively, a number of different spin up responses are obtained.

As shown in Fig. 3(b), the influence of the elasticity is more obviously observed in the process of spin down. Here this sample result is obtained under the following conditions; $\mu=0.15\text{Pas}$, $E=0.10\text{Pa}$, and $\tau_y=0.5\text{Pa}$. After the sudden stop of the cylinder from the steady rotation at $t=0$, the velocity in wide region of the cylinder changes accompanying significant oscillation in time and in space. The shear stress is caused largely near the wall in the beginning, and its effect quickly propagates into the central region to form a wedge typed dark region in the graph. This is Newtonian effect. After that, the slow-speed region involves velocity fluctuation for a long time. Hence a stripe pattern of negative velocity (reverse flow) regions takes place due to the elastic bouncing of the low shear rate fluid. Furthermore, this bouncing behavior converges in the central region as time elapses, and the local amplitude of the oscillation

expands there. Therefore the spin down process is more sensitive to the elasticity when the flow velocity is captured on the measurement line assigned in this study.

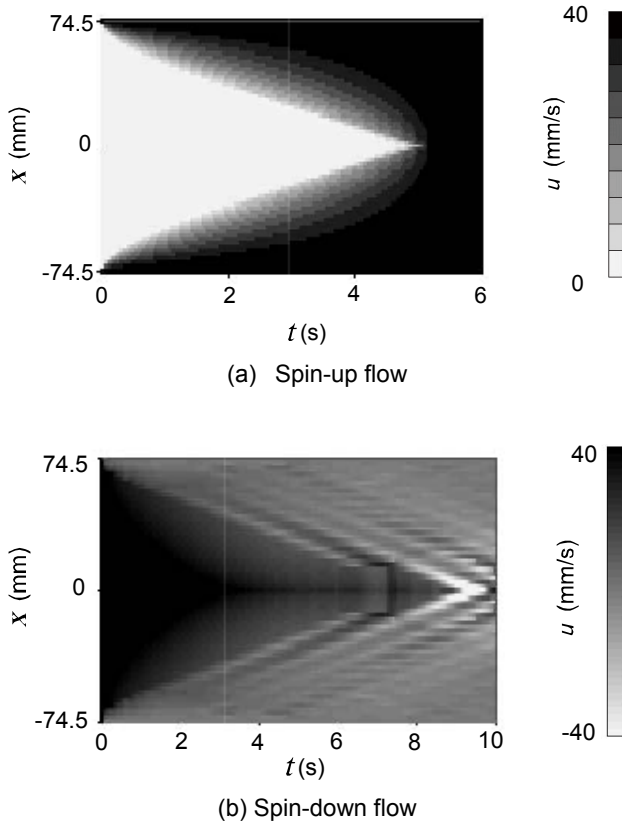


Figure 3: Spatio-temporal two-dimensional velocity distribution of visco-elastic fluid obtained by numerical simulated with Bingham model at 50rpm

4 UVP MEASUREMENT RESULTS

Figure 4 shows a sample of measurement data obtained by UVP for real PAA solution. It shows the spatio-temporal velocity distribution in the same manner as in the last chapter. It is noted that the velocities in the region $-74.5\text{mm} < x < -60\text{mm}$ could not be obtained correctly because of wall interference of the pulsed ultrasound. However, those on the opposite side are validly measured so that it is not a serious lack of the information to determine the rheological properties later.

In general, the measurement result has a good agreement with the numerical simulation in qualitative sense. For instance, we could find reverse flow in the process of spin down for the elasticity of the fluid. The difference from the numerical simulation is that the velocities are obtained asymmetrically for the center of the rotating cylinder. This is due to the flow velocity component induced in the radial direction. In the case of finite cylinder in the axial direction, the spin up causes radial inward flow in the middle part, and the spin down cause radial outward flow there, owing to the difference in centrifugal acceleration.

Namely the finite cylinder forms a secondary flow inside during the sudden spinning. Since UVP detects the velocity component sensitively in the radial direction (see Fig. 1), the data are biased strongly to be asymmetric. However the actual radial velocity component is still ignorable relatively to the tangential one so that the flow itself is approximately axisymmetric. Namely the secondary flow that is detected strongly in UVP can be removed in the post-processing to deduce the rheological properties, as mentioned next.

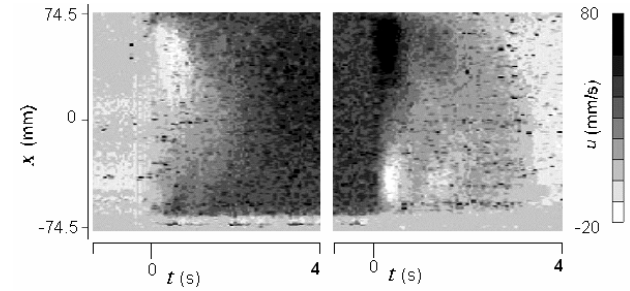


Figure 4: Spatio-temporal velocity distribution of PAA solution, measured by UVP at 50rpm.

5 DATA ANALYSIS AS RHEOMETRY

The radial convection is axisymmetric, and the measurement line of UVP covers the range beyond the center of the cylinder. Thereby the tangential velocity of the flow, v , can be calculated from the single velocity profile of UVP. With this preparation, we can estimate the shear response of the fluid as we explained in the chapter 2.

The data conversion from the raw velocity to the tangential velocity provides another spatio-temporal distribution as shown in Fig. 5. The figure represents the result of a single run that includes both the spin up and the spin down.

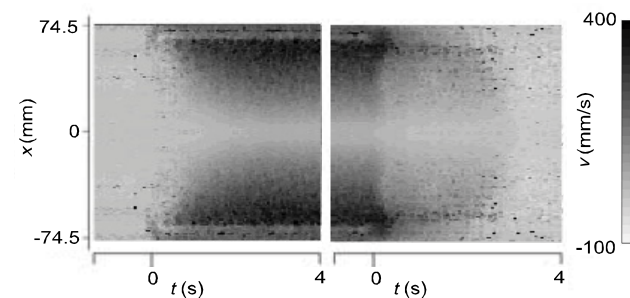


Figure 5: Spatio-temporal distribution of v , tangential velocity component.

The relationship between the local tangential velocity, v , and the local shear stress, τ , is described by the following equation when the flow obeys Maxwell model.

$$\frac{\partial v}{\partial r} = \frac{\tau}{\mu} + \frac{1}{E} \frac{\partial \tau}{\partial t} \quad (3)$$

Coupling this equation with Eq.(1), the tangential velocity must behave with the following equation.

$$\frac{\partial^2 v}{\partial r^2} = \frac{\rho}{E} \frac{\partial^2 v}{\partial t^2} + \frac{\rho}{\mu} \frac{\partial v}{\partial t} \quad (4)$$

In Eq. (4), the elasticity, E , and the viscosity, μ , are treated as unknown constants while the tangential velocity, v , is given by the UVP measurement as spatio-temporal two-dimensional distribution. Here the density, ρ , is treated as known constant because it is easily measured by measuring the mass and the volume.

In mathematical principle, the elasticity and the viscosity are uniquely determined when Eq. (4) is applied two times at arbitrary instants in the UVP data. For ensuring their accuracy, a lot of information from UVP is better applied. Therefore we propose an algorithm based on least square approach as follows. As the error from Eq. (4), the cost function is defined as follows.

$$G(E, \mu) = \iint \left\{ \frac{\rho}{E} \frac{\partial^2 v}{\partial t^2} - \frac{\partial^2 v}{\partial r^2} + \frac{\rho}{\mu} \frac{\partial v}{\partial t} \right\}^2 dr dt \quad (5)$$

The value of the cost function G varies with E , and μ . The best estimates of μ and E are obtained when G is minimized. This condition can be found out by searching the conditions satisfying $\partial G / \partial \mu = 0$, and $\partial G / \partial E = 0$, simultaneously. Deriving mathematically, these conditions are fulfilled when the viscosity and the elasticity are given by the following equations.

$$\mu = \frac{b^2 + ad}{bc + ae}, \quad E = \frac{ae + bc}{cd - eb} \quad (6)$$

Here, a , b , c , d and e are given below.

$$a = -2\rho \iint \left(\frac{\partial^2 v}{\partial t^2} \right)^2 dr dt \quad (7)$$

$$b = -\rho \iint \frac{\partial v}{\partial t} \frac{\partial^2 v}{\partial t^2} dr dt \quad (8)$$

$$c = 2 \iint \frac{\partial^2 v}{\partial r^2} \frac{\partial^2 v}{\partial t^2} dr dt \quad (9)$$

$$d = 2\rho \iint \left(\frac{\partial v}{\partial t} \right)^2 dr dt \quad (10)$$

$$e = \iint \frac{\partial v}{\partial t} \frac{\partial^2 v}{\partial r^2} dr dt \quad (11)$$

These five values become zero in the case of quiescent and rigid rotating conditions. Therefore the integral range for G in Eq.(5) must include the transient response of velocity. In addition, these five values are quite sensitive to the measurement error since all the value is obtained from temporal and spatial derivatives of the velocity. We have applied

some noise reduction filters to the data to overcome this problem.

The estimated properties of the present PAA solution are shown in Table 1. PAA is known as having shear-thinning effect and constant elasticity. The estimated properties are in agreement with them.

Table 1: Properties of 0.24wt% PAA solution assessed by calculation

Rotational Speed	Process	μ (Pas)	E (Pa)
50rpm	Spin-up	2.51	1.39
	Spin-down	2.53	1.31
100rpm	Spin-up	2.49	1.47
	Spin-down	2.56	1.24
150rpm	Spin-up	2.38	1.52
	Spin-down	2.49	1.41

6 CONCLUSIONS

A method to estimate the rheological properties of visco-elastic liquid is proposed. It is enabled by use of UVP that is applied for the line measurement in a sudden spinning of fluid in a cylindrical container. As numerical simulation shows, this configuration provides rich information in terms of shear response. Thereby it is suitable for the inverse analysis that estimates the fluid properties from transient velocity data. A least square approach applied for full spatio-temporal velocity distribution realizes to estimate validly the viscosity and the elasticity of a PAA solution.

ACKNOWLEDGMENT

The authors are grateful for the grant supported by the academic exchanging program between Graduate School of Engineering Hokkaido University Japan and ETH-Zurich Swiss 2008.

REFERENCES

- [1] Y. Takeda, Velocity profile measurement by ultrasonic Doppler method, *Exp. Fluid Sci.* 10-4(1995), 444-453.
- [2] B.H. Birkhofer, Ultrasonic in-line characterization of suspensions, Diss. ETH (No.17331), Zurich (2007).
- [3] I. Fyrippi, I. Owen, M.P. Escudier, Flowmetering of non-Newtonian liquids, *Flow Meas. Instr.*, 15 (2004), 131-138
- [4] H.Xu, C.K.Aidun, Characteristics of fiber suspension flow in a rectangular channel, *Int. J. Multiphase Flow*, 31 (2005), 318-336.
- [5] B.Ouriev, E.Windhah, Novel ultrasound based time averaged mapping method for die entry visualization in flow of highly concentrated shear-thinning and shear-thickening suspensions, *Meas. Sci. Tech.*, 14 (2003), 140-147.
- [6] R.Lombardi, G. Danese, F.Leporati, flow rate profiler an instrument to measure blood velocity profiles, *Ultrasonics*, 39 (2001) 143-150.

Development of a multiphase flow meter by means of multiple ultrasonic velocity profile measurements

S. Roberto Gonzalez A.^{1*}, Yuichi Murai¹, Yuji Tasaka¹, Yasushi Takeda¹

¹Division of Energy & Environmental Systems, School of Engineering, Hokkaido University, N13W8, Sapporo 060-8628, Japan (*Corresponding author, e-mail: roberto@eng.hokudai.ac.jp).

In this paper the liquid phase velocity and gas-liquid interface information are obtained from Ultrasonic Velocity Profile (UVP) measurements. They are used to estimate the liquid phase flow rate of a gas-liquid two phase flow. Three ultrasonic transducers are used simultaneously at different azimuthal locations in the pipe. The gas-liquid interface can be detected with one UVP transducer. However, the curvature of the interface in the cross sectional area of the pipe can not be inferred. By using three ultrasonic transducers the estimation of the gas-liquid interface curvature can be improved. The liquid flow rates in these experiments ranged from 0.6 m³/h to 7.2 m³/h. The gas void fraction ranged from 0 % (pure liquid) to 50 %. Only liquid flow rate calculations are performed, no gas phase calculations are shown in this paper. The estimated liquid flow rate values show good agreement with the actual liquid flow rate values.

Keywords: Multi phase flow, flow meter, Doppler, interface detection

1 INTRODUCTION

Gas-liquid two phase flows are a common occurrence in engineering applications; these types of flow can be encountered in the food industry, oil industry, and power generation processes among others. This paper deals with the liquid flow rate measurement of a gas-liquid two phase flow in a horizontal pipe; although the flow rate measurement in a vertical configuration is more commonly performed [1], the flow rate measurement of a two phase mixture in a horizontal orientation occurs in the transport of oil-gas mixtures from the wells to the reservoirs [1,2,3]. As noted by Oddie and Pearson [1], several devices are available to measure multiphase flows. However, they mostly lack a mechanical understanding of the flow itself. A noninvasive, reliable method to estimate the liquid flow rate of a gas-liquid two phase mixture accurately and in real time is the driving motivation of the present research work; the instantaneous liquid velocity measurements from three ultrasonic transducers are used in the liquid flow rate calculation; no gas flow rate estimations are performed.

With regard to multiphase flow measurement, two of the most commonly used flow meter devices in industry are the Coriolis type and the electromagnetic flow meter. The Coriolis flow meter, although an accurate device, has implicit some assumptions of the actual flow [1], i.e. the phases do not slip with respect to each other when oscillated and the phases are incompressible. Due to these assumptions the Coriolis flow meter is suitable for a liquid-liquid application but not for a solid-gas or gas-liquid application.

On the other hand the electromagnetic flow meters process signals that depend on the electromagnetic

conductivity of the phase of the flow. It is non intrusive and it has no moving parts; but it may need a separate measurement of the liquid phase density to perform the mass flow rate measurements [1]. Approaching the gas-liquid flow metering problem by means of ultrasound offers similar advantages. It is also a non intrusive method and it has no moving parts, therefore maintenance free. In a recent study, Wada et al [4] demonstrated the use of the echo intensity as a way to obtain pattern recognition of a two phase flow. Using the idea presented by Wada et al [4] a method is presented here to calculate the liquid flow rate of a gas-liquid two phase flow by using three simultaneous UVP measurements.

2 EXPERIMENTAL SETUP AND METHOD

2.1 Experimental setup

A schematic diagram of the experimental setup can be seen in Figure 1. It mainly consists of the gas-liquid two phase flow loop and three UVP-DO systems. Water and air are used as the liquid and gas phase respectively. The water is fed into the pump by the water reservoir. It flows through the pipe loop and returns in a horizontal path. At the beginning of the horizontal path the gas phase is added. Before the gas is added to the liquid phase both the gas phase and the liquid phase volumetric flow rates are measured. In this way the desired void fraction for every test is set. The test section that houses the three ultrasonic transducers is located 2.4 m from the entrance of the gas phase. It is a cylinder of 40 mm in inner diameter and 90 mm in length made of an ultrasonic absorbent material. The ultrasonic absorbent material of the test section is selected to avoid interference among the UVP transducers due to the proximity to each other. A schematic diagram of the test section can be seen in Figures 2a and 2b.

The transmitting frequency of the UVP-DUO systems is 4MHz in all the tests performed. The ultrasound wavelength, λ , is 370 μm . 100 μm ion exchange (Diaion) particles are added to the flow. Due to theoretical considerations the size of the flow tracers must be larger than one quarter of the emitted ultrasonic burst [5].

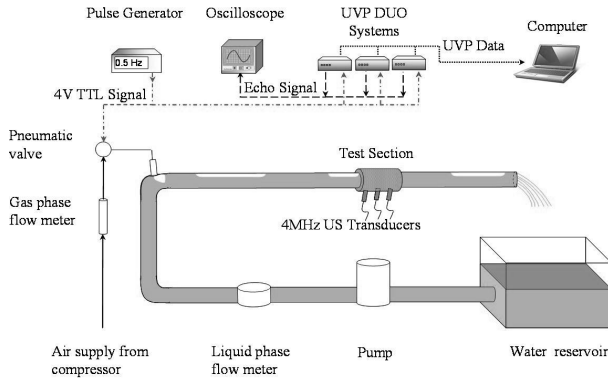


Figure 1. Experimental setup

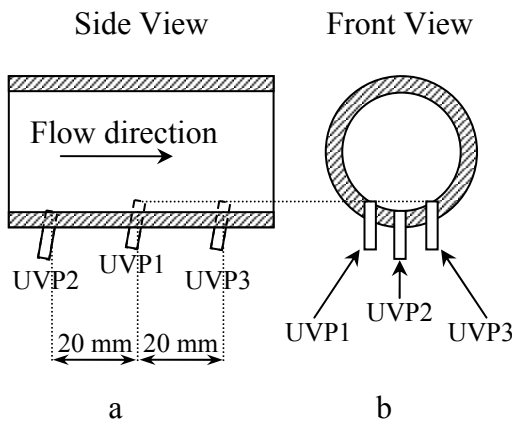


Figure 2. US transducer arrangement in the test section a) Side view b) Front view

2.2 Experimental method

For every UVP file captured one gas-liquid interface height time series, $ht_n(t)$, is obtained; $n = 1, 2, 3$ (one gas-liquid interface height time series for each transducer). The gas-liquid interface height is obtained as follows: each UVP file contains velocity and echo intensity information; from every echo intensity profile the maximum absolute echo intensity value is located and labeled as the location where the gas-liquid interface is found. Due to the location of the transducers the gas-liquid interface height is detected at a different time. This mismatch in the interface height series can be adjusted by finding the maximum correlation coefficient between the series. Then the interface height can be placed as if they are in the same plane, as seen in Figure 3a. After that, the portion of the cross sectional area of the pipe occupied by the liquid phase can be estimated. Consider a square area as that shown in

Figure 3a. This area is divided into 200 elements in both the horizontal and the vertical direction. The locations of transducers 1, 2 and 3 and the location of the gas-liquid interface height are x_1, x_2 and x_3 and $s_1(x_1, y_1)$, $s_2(x_2, y_2)$ and $s_3(x_3, y_3)$ respectively. In the range $x_1 \leq x \leq x_3$ the free surface is calculated by a cubic polynomial function (spline interpolation), [6]. In the ranges $0 \leq x \leq x_1$ and $x_3 \leq x \leq x_f$ the gas-liquid interface is calculated by a linear extrapolation. The slope of the line in these ranges is the slope of the curve at $x = x_1$ and $x = x_3$ respectively.

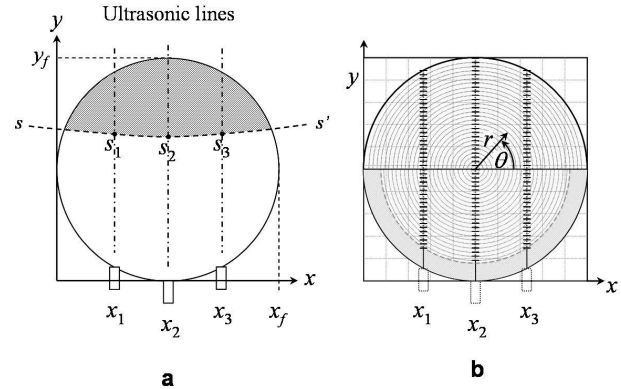


Figure 3. a) Gas-liquid interface height position b) Channel distribution

The velocity values obtained from the three UVP transducers are located as shown on Figure 3b. Next they are distributed radially. At the bottom of the pipe, there are no UVP velocity values (grey shaded region); the first measuring channel (Channel 0) is located at $y = 3.6$ mm from the bottom of the pipe. This is because it takes several microseconds to the UVP DUO system to switch from transmitting to receiving mode, so the echo from the particles closest to the transducer will be lost during the switching time. Consequently, the first measurement is located 3.6 mm away from the bottom of the pipe. In the region $0 \leq y < 3.6$ mm the following liquid velocity values apply.

$$180 \leq \theta < 250 \quad V(r, \theta) = 0.7 \bar{V}_{UVP1} \quad (2.1)$$

$$250 \leq \theta < 290 \quad V(r, \theta) = 0.7 \bar{V}_{UVP2} \quad (2.2)$$

$$290 \leq \theta \leq 360 \quad V(r, \theta) = 0.7 \bar{V}_{UVP3} \quad (2.3)$$

The values \bar{V}_{UVP1} , \bar{V}_{UVP2} and \bar{V}_{UVP3} are the average liquid velocity values of transducers 1, 2 and 3 respectively from channel 0 to the channel where the gas-liquid interface is located. The constant 0.7 is the value obtained in the region $0 \leq y < 3.6$ mm from the power law equation [7]; this equation is used in single phase turbulent flow; the assumption is that the gas phase is located in the upper part of the pipe, then the liquid velocity, not disturbed by the gas phase, develops in the lower part of the pipe as it does in single phase turbulent flow. The position of the velocity values, so far distributed in cylindrical coordinates, are converted

to Cartesian coordinates. With both the liquid velocity distribution and the cross sectional area of the pipe occupied by the liquid phase known, the volume swept out in time dt can be obtained from equation 2.4.

$$vol = \iiint V(x, y, t) dAdt \quad (2.4)$$

Finally, from the instantaneous volumes the time average liquid phase flow rate is calculated from equation 2.5.

$$Q_e = \frac{\iiint V(x, y, t) dAdt}{\int dt} \quad (2.5)$$

3. RESULTS

Experiments were conducted at eight different liquid flow rates: 0.6, 1.8, 2.8, 3.4, 4.5, 5.2, 6.2 and 7.5 m^3/h . The void fraction, α , in the flow is 0 % (liquid phase only), 10 %, 20 %, 30 %, 40 % and 50 %. The void fraction, α , is defined as:

$$\alpha = \frac{Q_g}{Q_a + Q_g} \quad (3.1)$$

Q_g is the actual gas flow rate and Q_a is the actual liquid flow rate. The difference between the actual liquid flow rate, Q_a and the estimated liquid flow rate, Q_e is expressed by δ_e

$$\delta_e = \frac{Q_e - Q_a}{Q_a} \quad (3.2)$$

Before every test is performed both the gas phase and the liquid phase are set to the desired values; then the flow rate is measured pouring the mixture in a bucket for a specific amount of time. The volumetric flow rate of the liquid phase is then calculated and recorded; this is the actual flow rate, Q_a . Next, the UVP measurements are performed.

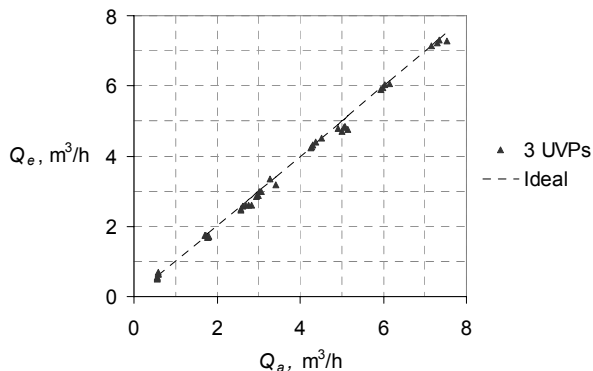


Figure 4. Estimated liquid flow rate, Q_e versus actual liquid flow rate, Q_a

Figure 4 shows the estimated liquid flow rate versus the actual liquid flow rate. The tests of $Q_a = 0.6 m^3/h$ are of the stratified flow type. The tests of $1.8 \leq Q_a \leq$

$7.5 m^3/h$ are of the elongated bubble and slug flow type (depending on the void fraction of the flow) [8]. This figure shows a good agreement between the estimated and the actual liquid flow rate values in the range of liquid flow rates tested. Figure 5 shows the difference between the estimated liquid flow rate and the actual liquid flow rate. The experiments conducted in the range $0.6 \leq Q_a \leq 7.5 m^3/h$ have an average and standard deviation value of -1.9 and 5.1% respectively. The high standard deviation value is mainly due to the tests of lowest flow rate, $Q_a = 0.6 m^3/h$. In the range $1.8 \leq Q_a \leq 7.5 m^3/h$, the average and standard deviation values are -2.6 and 2.6 % respectively. Although the average of these tests decreases, more importantly, the standard deviation of these tests decreases by 49 %.

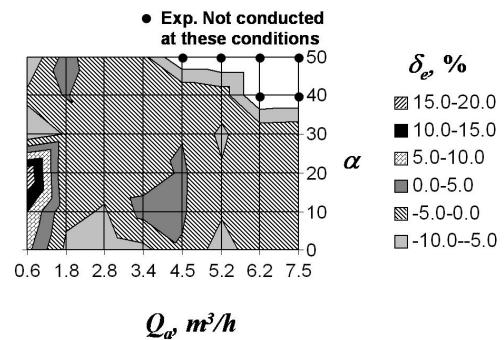


Figure 5. δ_e values of the tests performed

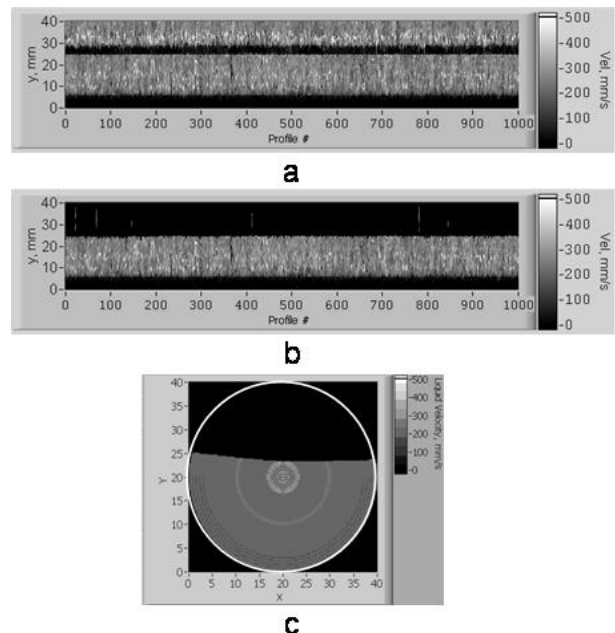


Figure 6. $Q_a=0.6; \alpha=10\%$ a) Raw data b) Processed data c) liquid phase velocity distribution, profile #50

Figure 6 shows the test of $Q_a = 0.6 m^3/h$ and $\alpha = 0\%$; the superficial liquid velocity is 0.13 m/s; only the first 1000 velocity profiles (or 24 %) of the 4096 profiles captured are shown. If all of velocity profiles are displayed important details of the flow may be lost; the upper part of the pipe is occupied by the gas phase. After the UVP file is processed and the

gas-liquid interface detected the data is plotted as in Figure 6b; there are no liquid velocity values in $0 \leq y \leq 3.6$ mm; the liquid velocity values in this region are the liquid velocity values obtained from the power law equation as mentioned in section 2.2. Figure 6c shows a flow map (velocity profile # 50) of the cross sectional area of the pipe. The upper part of the pipe is occupied by the gas phase. The gas-liquid interface height detected by each one of the three transducers has a very similar value; due to it the gas-liquid interface is not flat as expected but instead it shows a small curvature. Liquid velocity values are higher near the center of the pipe. The darker color lines in the lower part of the pipe and near the wall are the values due to the power law equation.

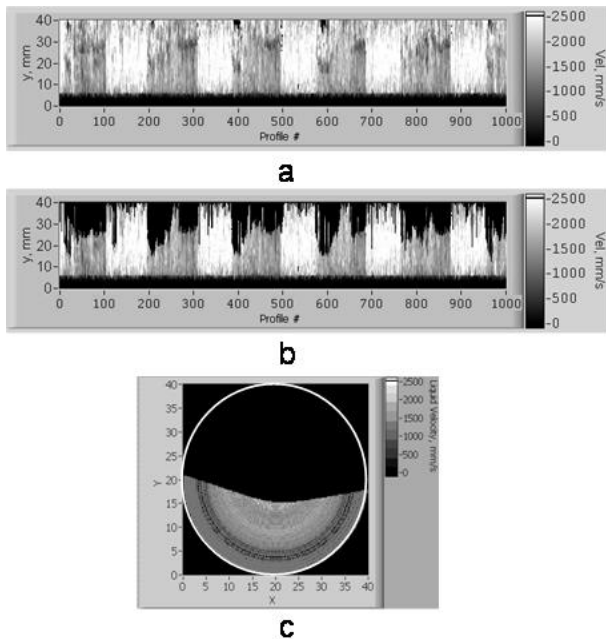


Figure 7. $Q_a=6.2$; $\alpha=30\%$ a) Raw data b) Processed data c) liquid phase velocity distribution, profile #221

Figure 7a shows the raw data of the test of $Q_a = 6.2$ m^3/h and $\alpha = 30\%$, the highest void fraction tested for this liquid flow rate. Figure 7b shows the UVP data processed; at this void fraction the gas-liquid interface can be seen below the middle of the pipe. Figure 7c shows a sample flow map of liquid velocity profile # 221. The gas phase occupies more than 50% of the cross sectional area of the pipe and it is not symmetrically distributed in the upper part of the pipe. This figure also shows higher liquid velocity values near the center of the pipe that decrease radially. The dark (low velocity) values correspond to the near field effect where the transducers output lower liquid velocity values than the actual liquid velocity values. If only one UVP transducer is used, the gas-liquid interface must be assumed to be flat. By using three ultrasonic transducers a more accurate gas-liquid interface shape is obtained.

4. CONCLUSIONS

In this study the liquid flow is assumed to be one dimensional; however, it is acknowledged that this is not true in the vicinity of the bubbles (especially in their leading and trailing edge) where the relative velocity between the bubbles and the liquid phase creates complex liquid motion that is far from one dimensional. Nonetheless, the estimated liquid flow rate values results show good agreement with the actual liquid flow rates. The following conclusions can be inferred from the present study:

- The maximum echo intensity value can be used to estimate the location of the gas-liquid interface. It can be applied to pure liquids as well as gas-liquid two phase flows where the void fraction is as high as 50%.
- The expected average and standard deviation δ_e values are -1.9 and 5.1% respectively in the range $0.6 \leq Q_a \leq 7.5$ m^3/h . The tests of $Q_a=0.6$ m^3/h show a larger variation than the rest of the tests.
- In the range $1.8 \leq Q_a \leq 7.5$ m^3/h the expected average and standard deviation δ_e values are -2.6 and 2.6 % respectively.

ACKNOWLEDGEMENT

The authors wish to thank the New Energy Development Organization (NEDO) of Japan for their support to this study, project number 05A45002d. The technical support of Mr. T. Sampo and support of the LFC members, Hokkaido U. is also appreciated. The assistance of Professor Yasunori Watanabe of the civil engineering department, Hokkaido U. for allowing the use of the third UVP-DUO system to conduct this study is highly appreciated.

REFERENCES

- [1] Oddie G and Pearson J R A: Flow-rate measurement in two-phase flow, *Annu. Rev. Fluid Mech.* 36 (2004) 149-172.
- [2] Shemer L: Hydrodynamic and statistical parameters of slug flow, *Int. J. Heat and Fluid Flow.* 24 (2003) 334-344.
- [3] Cook M and Behnia M: Slug length prediction in near horizontal gas-liquid intermittent flow, *Chem. Eng. Sci.* 55 (2000) 2009-2018.
- [4] Wada S, Kikura H and Aritomi M: Pattern recognition and signal processing of Ultrasonic Echo Signal on Two-phase Flow, *Flow Meas. and Inst.* 17 (2006) 207-224.
- [5] Met-Flow, UVP Monitor User's Guide, Lausanne, Switzerland (2002).
- [6] Kreyszig E: *Advanced Engineering Mathematics*, John Wiley & Sons, New York (1999).
- [7] Munson B R, Young, D F and Okiishi, T H: *Fundamentals of Fluid Mechanics*, John Wiley & Sons (1990).
- [8] Brennen C E: *Fundamentals of Multiphase Flow*, Cambridge University press, (2005).
- [9] Tavoularis S: *Measurement in Fluid Mechanics*, Cambridge university press (2005).

Liquid metal Taylor-Couette experiment on the magnetorotational instability

Thomas Gundrum^{1*}, Frank Stefani¹, Gunter Gerbeth¹, Jacek Szklarski¹, Günther Rüdiger², Rainer Hollerbach³

¹ Forschungszentrum Dresden-Rossendorf, P.O. Box 510119, D-01314 Dresden, Germany, e-mail address: (*Corresponding author, e-mail: th.gundrum@fzd.de)

² Astrophysikalisches Institut Potsdam, An der Sternwarte 16, D-14482 Potsdam, Germany

³ Department of Applied Mathematics, University of Leeds, Leeds, LS2 9JT, United Kingdom

The magnetorotational instability (MRI) plays an essential role in the formation of stars and black holes. By destabilizing hydrodynamically stable Keplerian flows, the MRI triggers turbulence and enables outward transport of angular momentum in accretion discs. We present the results of a liquid metal Taylor-Couette experiment under the influence of helical magnetic fields that show typical features of MRI at Reynolds numbers of the order 1000 and Hartmann numbers of the order 10. The paper focuses on noise reduction in the frequency domain and the wave number domain using standard FFT and shows some preliminary results of selected experiments.

Keywords: Liquid metal, GaInSn, MRI, helical magnetic field, ultrasonic measurement

1. INTRODUCTION

Magnetic fields play a double role in the cosmos: First, planetary, stellar and galactic fields are produced by the homogeneous dynamo effect in moving electrically conducting fluids. Second, magnetic fields can accelerate tremendously the formation of stars and black holes, by enabling outward transport of angular momentum in accretion disks by virtue of the so-called magnetorotational instability (MRI). This instability had been discovered as early as 1959, when Velikhov showed that a Taylor-Couette flow in its hydrodynamically stable regime (i.e. with outward increasing angular momentum) can be destabilized by an applied axial magnetic field [1]. But it was only in 1991 that the relevance of MRI for accretion disks in the vicinity of young stars and black holes was realized in a seminal paper by Balbus and Hawley [2].

The last decades have seen remarkable theoretical and computational progress in understanding the dynamo effect and the MRI. The hydromagnetic dynamo effect has even been verified experimentally in large-scale liquid sodium facilities in Riga, Karlsruhe, and Cadarache, and is presently studied in laboratories around the world [3]. In contrast, attempts to study the MRI in the laboratory have been less successful so far [4]. An MRI-like instability has been observed on the back-ground of a turbulent spherical Couette flow [5], but the genuine idea that MRI would destabilize a hydrodynamically stable flow was not realized in this experiment.-

One of the basic problems for the experimental investigation of the “standard MRI”, with only an axial magnetic field being externally applied, is the

need for flows with large magnetic Reynolds numbers ($R_m = \mu_0 \sigma v L \geq 1$, thereby μ_0 is the permeability of free space, σ the conductivity of the fluid, v its typical velocity, and L is the typical length scale of the flow).

The crucial point is that the azimuthal field, which is an essential ingredient of the MRI mechanism, must be produced from the applied axial field by induction effects proportional to the magnetic Reynolds number Rm . The natural question, why not substitute the induction process by externally applying the azimuthal field as well, was addressed by Hollerbach and Rüdiger [6]. It turned out that the scaling properties for this “helical MRI” are much more comfortable for building laboratory experiments than those of “standard MRI”.

In this paper, we present preliminary results of the PROMISE 2 (Potsdam ROssendorf Magnetic InStability Experiment) experiment. Results of PROMISE 1 were already published in [7-9].

2. THE EXPERIMENTAL FACILITY

The basic part of PROMISE 2 is a cylindrical containment vessel V made of copper cylinders (see fig. 1a). The inner wall of the vessel V is 10 mm thick, and extends in radius from 22 to 32 mm; the outer wall is 15 mm thick, extending from 80 to 95 mm. This vessel is filled with the eutectic alloy $\text{Ga}^{67}\text{In}^{20.5}\text{Sn}^{12.5}$ which is liquid at room temperatures. The vessel V, made of copper cylinders is fixed via a spacer D on a precision turntable T. The outer copper cylinder of the vessel represents the outer cylinder of the Taylor-Couette cell. The inner copper cylinder I of the Taylor-Couette cell is fixed to an upper turntable, and is immersed into the liquid metal from above. It has a thickness of 4 mm,

extending in radius from 36 to 40 mm, thus leaving a gap of 4 mm between this immersed cylinder I and the inner wall of the containment vessel V. The actual Taylor-Couette cell extends in radial direction over a cylindrical gap of width $d = r_{out} - r_{in} = 40$ mm, and in axial direction over the liquid metal height of $z = 400$ mm, resulting in an aspect ratio of 10.

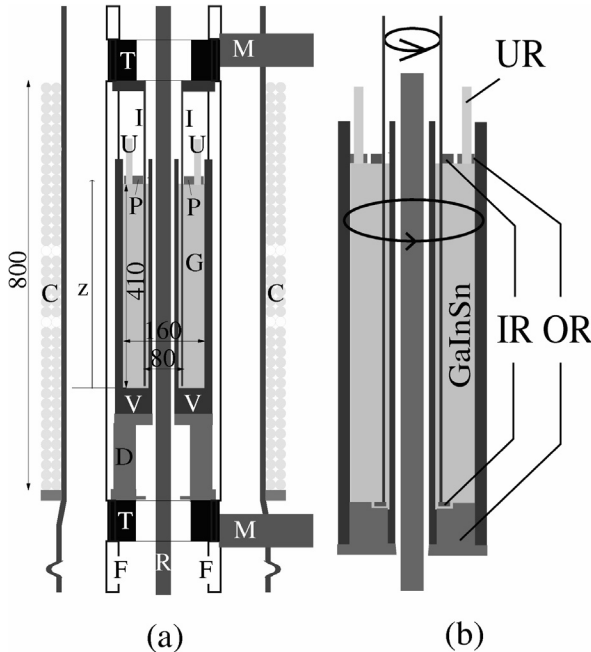


Figure 1. The PROMISE 2 experiment. (a) Sketch. (b) Taylor-Couette cell configuration. V - vessel, OR – Outer cylinder, I /IR – Inner cylinder, G – GalnSn, U/UR – Rotating ultrasonic transducers, P – Plexiglas lid, T - High precision turntables, M – Motors, F – Frame, R – Copper rod for azimuthal field, C – Coil for axial field. The indicated dimensions are in mm.

Figure 1b shows the PROMISE 2 symmetric end cap configuration: Both end caps are made of insulating material in order to avoid short-circuiting of currents along the copper end cap at the bottom. The upper and the lower end caps are split into two rings, the inner rings rotate with the inner cylinder and the outer rings rotate with the outer cylinder. In [10] it had been shown that this splitting yields a minimization of the Ekman pumping if the position of the splitting is at 0.4 of the gap width d . The co-rotation of the two rings with one of the cylinders made it necessary to guide the signal transmission of the ultrasonic transducers via an sliding contact below the vessel. These two transducers provide full profiles of axial velocity v_z along the beam-lines. Data acquisition was carried out with Ultrasonic Doppler Velocimeter (DOP 2000).

An axial magnetic field of order 10 mT is applied by a double-layer coil (C in fig. 1). The coil is fed by currents up to 200 A. The azimuthal field, also of order 10 mT, is generated by a current through a water-cooled copper rod R of radius 15 mm. The

power supply for this axial current is capable of delivering up to 8000 A.

3. DATA PROCESSING

The ultrasonic transducers UR in figure 1b are fixed at the outer ring at $r_{UR} = 68$ mm and shifted by 180° to each other. This configuration was chosen in order to eliminate non-axisymmetric velocity structure. This unwanted velocity structure superimposes the desired MRI signal. Figure 2 shows the time dependent signal of one transducer. The grey scale of the plot represents the axial velocity v_z , from which the z-dependent time average velocity va , plotted on the right hand side of figure 2, was subtracted in order to filter out the two Ekman vortices. These Ekman vortices are characterized by inward radial flows close to the upper and lower endplates.

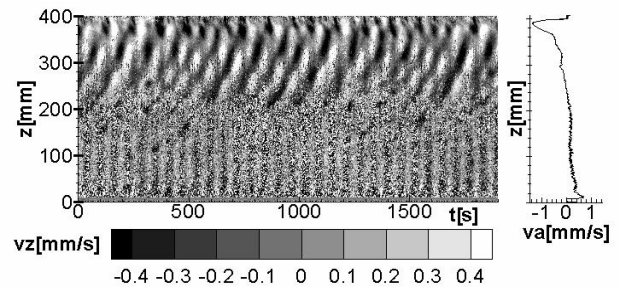


Figure 2: Raw data from one ultrasonic transducer with subtracted z-dependent time average velocity on the right.

The influence of the slight excentricity of the outer cylinder is clearly seen. This excentricity generates a shift of 180° between the two signals from outer rotation. To suppress this signal of the outer rotation we had to average both signals. Instead of doing this in time domain, we transformed both signals with standard FFT into frequency domain, like it is shown in figure 3a for one sensor. For each frequency the average of both signals is calculated. This Average of both channels is shown in figure 3b.

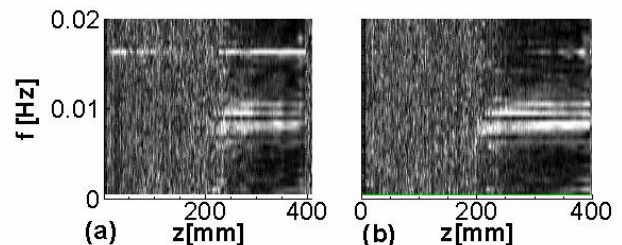


Figure 3: (a) Signal of one channel in frequency domain (b) Average of both channels, where outer rotation is suppressed.

In order to show this improvement (figure 4), we are using standard inverse FFT algorithm for the signal in figure 3b. The vertical stripes on the bottom of figure 2 are reduced, so the signal from outer rotation is suppressed. The quality of the signal can

be improved even more by taking into account, that MRI is expected only in a certain frequency range and a certain wave length, which could clearly be identified in figure 4. This improvement can be done by using a bandpass filter. As simplification we use only a low pass filter cutting off only high frequencies and the short wavelengths.

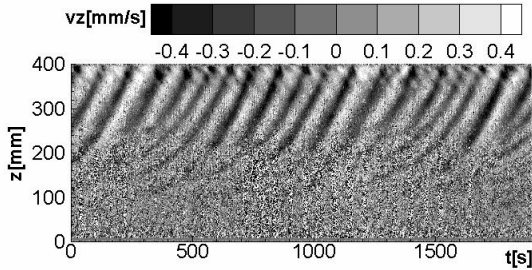


Figure 4: Average of both signals with suppressed signal from eccentricity.

The low pass filtering is again done in frequency domain using the averaged signal shown in figure 3b. A very sharp filter characteristic is used by clearing all frequencies above $f_{LP} = 0.015\text{Hz}$. Figure 5 shows the clearly improved signal after inverse FFT transformation, but the information about the typical MRI wavelength is not yet considered in post processing.

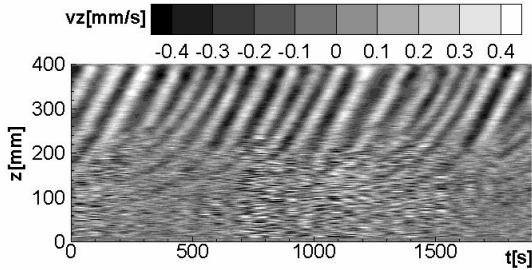


Figure 5: Signal after low pass filtering in frequency domain.

To implement this enhancement the signal is transformed with FFT into wave number domain. All waves with a wavelength below $\lambda_{LP} = 20\text{mm}$ are suppressed by clearing all wave numbers ($k = 2\pi / \lambda$, thereby λ is the wavelength) above $k = 0.31 / \text{mm}$.

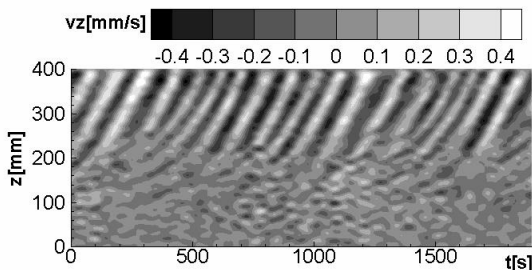


Figure 6: Signal after cutting off short wavelengths in wave number domain.

Figure 6 shows the result of the whole data processing using FFT. Similar results can be produced, by averaging the signal in time domain and using a 2D gauss filter in time domain, but consuming more computation time. The diagrams shown in the next paragraph are processed with the former described algorithm.

4. SOME RESULTS

We have carried out a large number of experimental runs in order to cover a wide range of parameter dependencies. Typically, the duration of an experimental run was 1900 sec, after a waiting time of one hour and more, depending on the distance to criticality and wave velocity. Many details for the first experimental campaign PROMISE 1 can be found in the publications [7-9].

Due to the reflection symmetry breaking under the influence of a helical magnetic field [11], the Taylor vortex flow is replaced by an oscillatory axisymmetric vortex flow that propagates in a unique direction along the vertical axis [5,6]. This direction depends on the sign of the product of rotation direction, axial, and azimuthal magnetic field. The travelling wave appears already with a stationary outer cylinder, i.e. at $\mu := f_{out} / f_{in} = 0$, although with a very low frequency. With increasing μ , the wave frequency increases and typically reaches a value of $(0.1 \dots 0.2) \cdot f_{in}$ at the Rayleigh value $\mu_{Ray} := (r_{in} / r_{out})^2 = 0.25$. While μ_{Ray} would be a sharp boundary between unstable and stable flows in the purely hydrodynamic case, the interesting point is now that under the influence of helical magnetic fields the instability extends beyond $\mu_{Ray} = 0.25$ [6,9]. Typically, this shift of the boundary to higher values of μ becomes larger for increasing values of the ratio of azimuthal field to axial field, $\beta = B_{\phi}(r = r_{in}) / B_z$.

One of the most significant features of the MRI is that, for fixed Re and fixed azimuthal field, it shows up only in a finite interval of the Hartmann number $Ha = B_z(r_{in} d \sigma / \rho \nu)^{1/2}$ (ρ is density, and ν is kinematic viscosity). This appearance and disappearance of a travelling mode is a suitable indicator for the existence of the proper MRI mode and its distinction from other possible flow structures. The results presented in figure 7 are for rotation rates of $f_{in} = 0.06\text{Hz}$ and $f_{out} = 0.0162\text{Hz}$, i.e. for $\mu = 0.27$ which is slightly above the Rayleigh value $\mu_{Ray} = 0.25$. Figure 7 documents a selection of four experimental runs for coil currents I_{coil} of 0, 50, 75 and 120 A. In the present PROMISE 2 case the axial current I_{rod} was fixed to 7000 A. The grey scale of the plots represents the axial velocity v_z .

processed with the algorithm described in section 3 before.

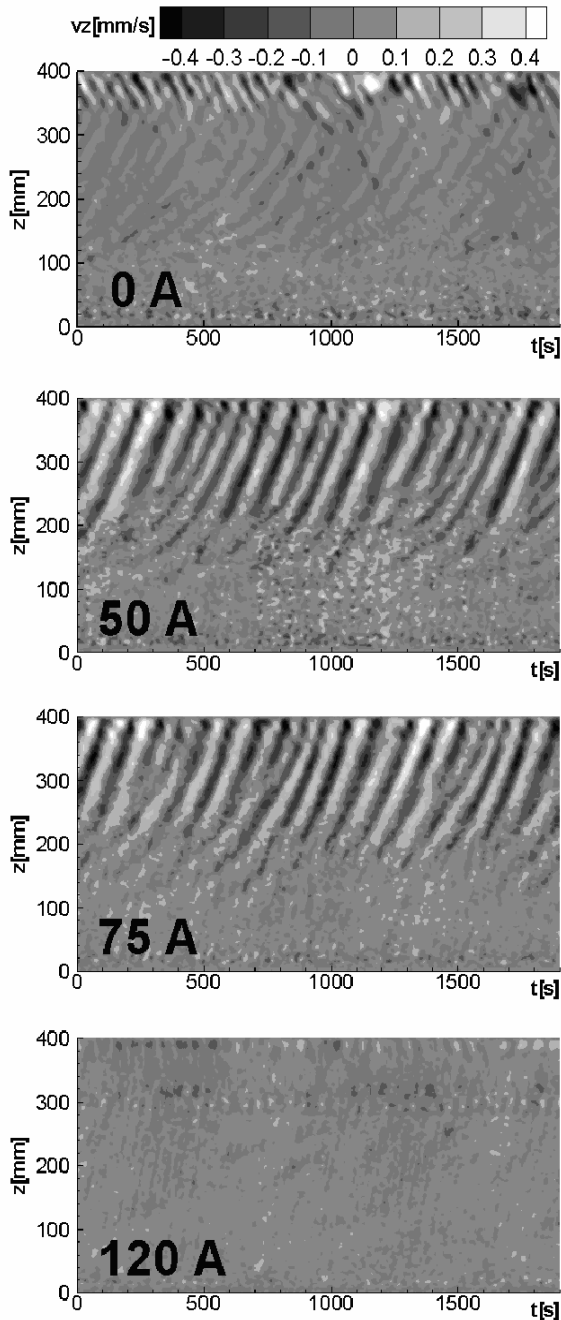


Figure 7. Axial velocity perturbation for differing coil currents during PROMISE 2 experiment at $f_{in} = 0.06\text{ Hz}$ and $f_{out} = 0.0162\text{ Hz}$, i.e. $\mu = 0.27$, $I_{rod} = 7000\text{ A}$.

We observe the typical behaviour that MRI comes up in a finite interval of the coil current (which is proportional to the Hartmann number), the wave growth from the bottom and propagates throughout the total height of the cell. The upward growth of the amplitude is quite typical for an travelling wave instability like the helical MRI for which the absolute instability, in contrast to the convective one, is characterized by a complex wave number [12].

5. CONCLUSIONS

We have obtained experimental evidence for the existence of the MRI in helical magnetic fields, in particular by showing its appearance in a certain interval of the Hartmann number. The symmetrization of the axial boundary conditions and the use of split end caps in PROMISE 2 has led to a strong reduction of the Ekman pumping and hence to a avoidance of artefacts in the radial jet flow region. We could enhance the quality of the visualisation by using standard FFT. Further dependencies of the MRI on parameters like μ , β , and Re , as well as their comparison with numerical predictions will be published elsewhere.

ACKNOWLEDGEMENT

We gratefully thank the Leibniz Association to support this project in the WGL-SAW program. We thank Thomas Wondrak for fruitful discussions during code development and paper preparation.

REFERENCES

- [1] Velikhov, E.P.: Stability of an ideally conducting liquid fluid between cylinders rotating in a magnetic field. Sov. Phys. JETP 9 (1959) 995-998
- [2] Balbus, S.A.; Hawley, J.F.: A powerful local shear instability in weakly magnetized disks. 1. Linear Analysis. Astrophys. J. 376 (1991) 214-222
- [3] Gailitis, A.; Lielausis, O.; Platācis, E.; Gerbeth, G., Stefani, F.: Laboratory experiments on hydromagnetic dynamos. Rev. Mod. Phys. 74 (2002) 973-990
- [4] Rosner, R.; Rüdiger, G.; Bonanno, A. (Eds.): MHD Couette flows: Experiments and Models, AIP Conference Proceedings No. 733 (2004) New York: AIP
- [5] Sisan, D. et al.: Experimental observation and characterization of the magnetorotational instability. Phys. Rev. Lett. 93 (2004) 114502
- [6] Hollerbach, R.; Rüdiger, G.: New type of magnetorotational instability in cylindrical Taylor-Couette flow. Phys. Rev. Lett. 95 (2005) 124501
- [7] Stefani, F. et al.: Experimental evidence for magnetorotational instability in a Taylor-Couette flow under the influence of a helical magnetic field. Phys. Rev. Lett. 97 (2006) 184502
- [8] Rüdiger, G. et al.: The travelling-wave MRI in cylindrical Taylor-Couette flow: Comparing wavelengths and speeds in theory and experiment. Astrophys. J. Lett. 649 (2006) L145-L147
- [9] Stefani, F. et al.: Experiments on the magnetorotational instability in helical magnetic fields. New J. Physics 9 (2007) 295
- [10] Szklarski, J.: Reduction of boundary effects in spiral MRI experiment PROMISE. Astron. Nachr. 328 (2007) 499-506
- [11] Knobloch, E.: Symmetry and instability in rotating hydrodynamic and magnetohydrodynamic flows. Phys. Fluids 8 (1996) 1446-1454
- [12] Gerbeth, G.; Priede, J.: Absolute vs. convective helical MRI in a TC flow. Presentation at the MRI workshop, Catania, 1-3 October 2007

Instantaneous three-dimensional flow structure in a suction sump by 3D-PTV and UVP measurements

Katsuya Hirata^{1*}, Yuki Nakatani¹, Katsuhisa Inagaki¹ and Jiro Funaki¹

¹Department of Mechanical Engineering, Doshisha University, Kyoto 610-0321, Japan (khirata@mail.doshisha.ac.jp).

When we design the suction sumps and the suction pipes, we should know the flow and the air-entrainment mechanism more precisely, to prevent the air entrainment. In the present study, we try to reveal the instantaneous and three-dimensional flow structures in the suction sumps, because the strong unsteadiness and three-dimensionality of such flow. Specifically, we conduct consecutive flow-velocity measurements in a suction sump both by a three-dimensional particle tracking velocimetry (referred to as 3D-PTV) and an ultrasonic velocity profiler (UVP), assisting each other. As a result, we have confirmed a good agreement on time-mean three-dimensional velocity distributions between the 3D-PTV and the UVP. In addition, we reveal some typical flow structures in the sump by the 3D-PTV, which suggest the relationships with the air entrainment.

Keywords: Pump, Water Tank, Two-Phase Flow, Suction Sump, Suction Pipe

1 INTRODUCTION

In power generation plants, irrigations, drainages and so on, the optimum designs of suction sumps have been needed to get low initial/running costs, compact size, high efficiency and high performance. In recent years, we require higher-level solutions for those needs. In such situations, the air entrainment into suction-pipe intakes becomes easy to occur. The air entrainment often induces vibrations, noises, low pumping efficiencies or pumps' collapses at the worst (see ref. [1]). There have existed some systematic studies on the occurrence conditions of the air entrainment (see refs. [2-3]). However, when we design the suction sumps and the suction pipes, we should know the flow and the air-entrainment mechanism more precisely, to prevent the air entrainment.

There have been some investigations concerning the flow observations inside the suction sumps [4-6]. Recently, Funaki et al. [7] reported the quantitative observations using an ultrasonic velocity profiler (referred to as UVP) [8], and they revealed the three-dimensional flow structures. However, their results are time-mean ones due to the characteristics of the UVP.

In the present study, we try to reveal the instantaneous and three-dimensional flow structures in the suction sumps, because of the strong unsteadiness and three-dimensionality of such flow. Specifically, we consider one of the simplest geometries, that is, a straight channel with a rectangular cross section and a simple and vertical suction pipe near the end of the channel. We conduct consecutive flow-velocity measurements in a suction sump both by a three-dimensional particle tracking velocimetry (referred to as 3D-PTV) [9] and an UVP, assisting each other. While the 3D-PTV technique gives us the

information of three-dimensional flow structure, we can measure a velocity profile with high reliability and steadiness by the UVP. In addition, we try to reveal some typical flow structures in the suction sump by the assured 3D-PTV.

2 EXPERIMENTAL METHOD

2.1 Suction Sump and Suction Pipe

Figure 1 shows the present model, which is a simple system of a suction sump and a suction pipe. D and d are the outside and inside diameters of the suction pipe, respectively. A former is used as a characteristic length scale. The latter is fixed to $0.9D$. The suction-pipe intake has a bell-mouth shape. The suction pipe is placed on the center line of the suction sump, taking its axis vertical. B , X and Z denote the breath of the suction sump, the back clearance (namely, the distance from the suction-pipe center to the suction-sump back wall) and the bottom clearance (namely, the distance from the suction-pipe intake to the suction-sump bottom), respectively. H is water level, then, the suction-pipe submergence $S = H - Z$.

A characteristic velocity scale is the mean flow velocity V_i at the suction-pipe intake, which is defined as

$$V_i = 4Q/(\pi D^2). \quad (1)$$

Q is the volumetric flow rate into the suction pipe. Then, we define the Froude number Fr , the Reynolds number Re , the Bond number Bo and the Weber number We as follows.

$$Fr = V_i/(gD)^{0.5}. \quad (2)$$

$$Re = V_i D/\nu. \quad (3)$$

$$Bo = \rho g D^2/\sigma. \quad (4)$$

$$We = V_i(\rho D/\sigma). \quad (5)$$

Here, g , ν , ρ and σ denote the gravitational

acceleration, kinetic viscosity, fluid density and water-to-air surface tension, respectively.

Table 1 shows the present experimental parameters. Tested cases are three, that is, cases A, a and b. The case A is for the accuracy check of the 3D-PTV with the UVP. On the other hand, the cases a and b are for the consecutive observations of instantaneous and three-dimensional flow structures, using the assured 3D-PTV. Precisely speaking, we do not observe the air entrainment in the case a, and we often observe it with "spatially-continuous air strings" in the case b.

In the present coordinate system, the origin O is on the suction-pipe center and on the suction-sump bottom. The x and y axes are horizontal ones. The former and the latter are parallel and perpendicular to the suction-sump channel flow, respectively. And, the z axis is vertical one.

Table 1: Experimental parameters.

	Case A	Case a	Case b
D [mm]	38	32	
d [mm]	34	27	
B/D	3.16	3.15	
X/D	1.58	1.71	
Z/D	0.39	0.71	
S/D	1.19	2.0	1.0
Fr	0.98	1.8	
Re	2.2×10^4	3.2×10^4	
Bo	200	140	
We	14	21	

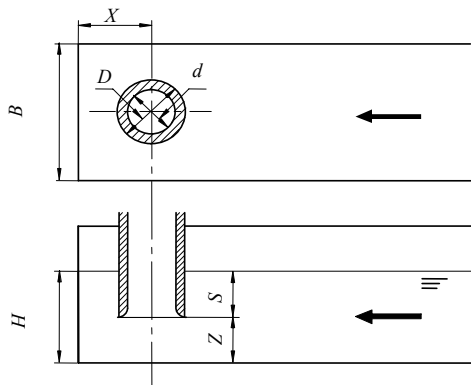


Figure 1: Model; suction pipe and suction sump. B , Sump breath; D , outside diameter of a suction pipe; d , inside diameter of a suction pipe; H , water level; S , submergence depth; X , back clearance; Z , bottom clearance.

2.2 Experimental apparatus

The present experimental apparatus is composed of a closed water-circulation system. A turbo pump feeds working fluid (water) to a suction sump from a reservoir tank. We control the flow rate of the pump by a control valve, and then control the water level H in the suction sump. At the upstream of the suction sump, namely, at 0.84 [m] upstream from the suction-sump back wall, we put a filter to get a uniform flow. The filter consists of unwoven fabric, sandwiched by two wire meshes with a diameter of 0.001 [m] and a grid size of 0.001 [m]. Another turbo pump feeds water up from the suction sump into a suction pipe. We measure the flow rate Q using a flow meter. Water from the flow meter falls into the reservoir tank, then a water-circulation system is closed.

2.3 UVP system

In the present study, we use a UVP monitor of UVP X-2-PS by Met Flow SA with a frequency of 4 [MHz]. The number of measuring points is 128 in one profile, and then, the space resolution on the profile is 0.75 [mm]. As the diameter of the ultrasonic beam is 5 [mm], one measuring volume is a disc with a diameter of 5 [mm] and with a thickness of 0.75 [mm]. We get consecutive 1024 profiles at each measurement with an interval of 32 [ms] or more. When we get time-mean velocities, we average more than 200 profiles, which is previously confirmed to be enough for the present cases. Tracers are bridged polyethylene particles with a mean diameter of 1.2×10^{-5} [m] whose density is controlled to become the same density of water.

2.4 3D-PTV system

Figure 2 shows the experimental apparatus with a 3D-PTV system. As 3D-PTV tracers, we use bridged polyethylene particles with a mean diameter of 1.8×10^{-4} [m], whose density is controlled as well. Tracer particles suspended in water are irradiated by a YAG laser. We take stereo photographs using two high-speed video cameras with a frame rate of 500 [frames/s] fixed outside the back and sidewalls, which are controlled by a PC. For each the 3D-PTV analysis, we use four successive stereo photographs.

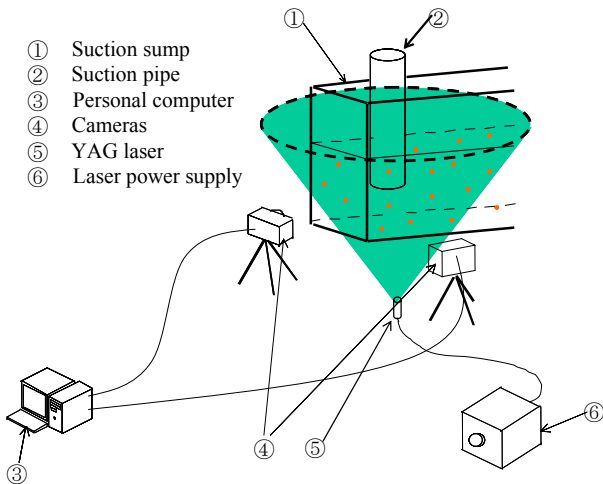


Figure 2: Experimental apparatus with a 3D-PTV system.

3 RESULTS AND DISCUSSION

3.1 Time-Mean Flow Field by 3D-PTV and UVP

In order to confirm the accuracy of the present 3D-PTV measurements, we compare the time-mean velocity distributions in the case A by the 3D-PTV with those by the UVP. Figures 3 and 4 show the velocity vectors on the x - z planes, and Figures 5 and 6 show the velocity vectors on the y - z plane. Here, Figures 3 and 5 are obtained by the 3D-PTV, and Figures 4 and 6 by the UVP.

As a result, we have confirmed qualitative agreements between the 3D-PTV and the UVP results. Namely, in both Figures 3 and 4, we see a downwash just in the downstream of the suction pipe, and a recirculating flow between the suction pipe and the suction-sump back wall. In both Figures 5 and 6, we can see a pair of clear and large longitudinal vortical structures, which induce a strong upward flow near the suction-sump center.

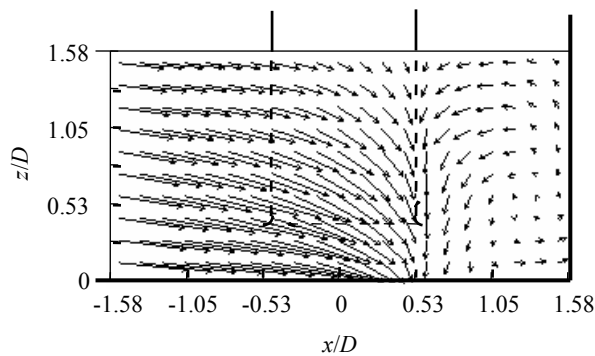


Figure 3: Velocity vectors on the x - z plane by 3D-PTV (case A, $y/D = -0.94$).

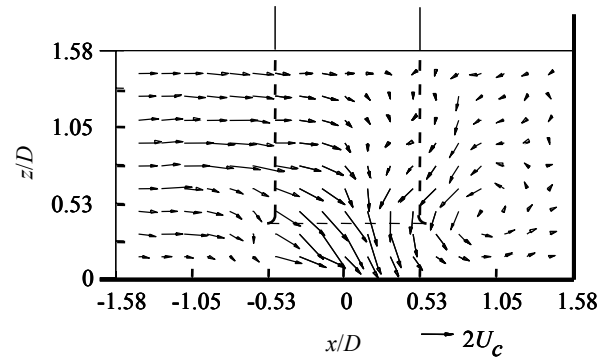


Figure 4: Velocity vectors on the x - z plane by UVP (case A, $y/D = -0.63$).[8]

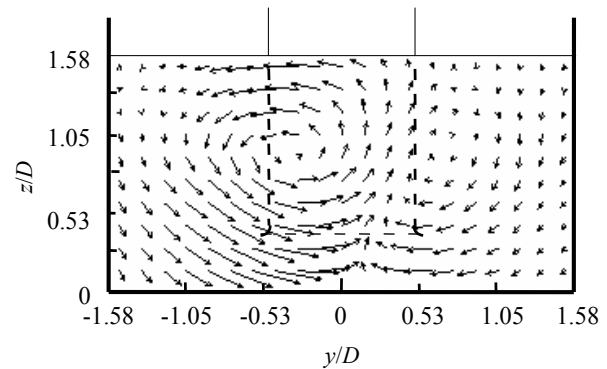


Figure 5: Velocity vectors on the y - z plane by 3D-PTV (case A, $x/D = 1.24$).

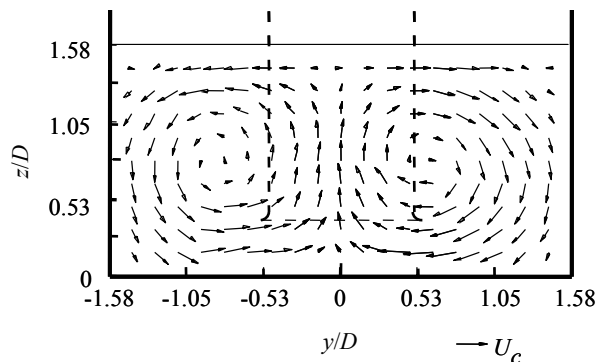


Figure 6: Velocity vectors on the y - z plane by UVP (case A, $x/D = 0.63$).[8]

3.2 Flow Visualization around a Suction Pipe by 3D-PTV

Now, using the 3D-PTV system assured in the above, we show some instantaneous and three-dimensional typical flow structures in the suction sump.

Figure 7 shows a sample result in the case a by the 3D-PTV, that is a set of velocity vectors in the three-

dimensional space at an instant. The obtained vectors seem acceptable everywhere in the visualized whole space. However, it is not easy to understand the three-dimensional structure, owing to the intrinsic limitation of two-dimensional plane maps.

By interpolations and the integrations on Figure 7, we get Figure 8, that is, the streamlines which exist near the free surface in the upstream. Such streamlines are appropriate to consider the air entrainment from the free surface. The streamlines pass over the suction pipe toward the back wall descending down, and reach to the suction-sump intake via the vicinity of the bottom wall. Note that, as we can not obtain the velocity vectors just near walls, some of the streamlines terminate near the back wall. The termination tends to appear for the streamlines near the free surface at the upstream.

Figure 9 shows the streamlines which exist near the free surface in the upstream. As well, the streamlines pass over the suction pipe descending down, and finally reach to the suction-pipe intake. However, we can not find such streamlines as terminate near the back wall, because all the streamlines descend down apart from the back wall. It seems consistent that we observe the air entrainment with the flow structure in Figure 9 more commonly, than that in Figure 8.

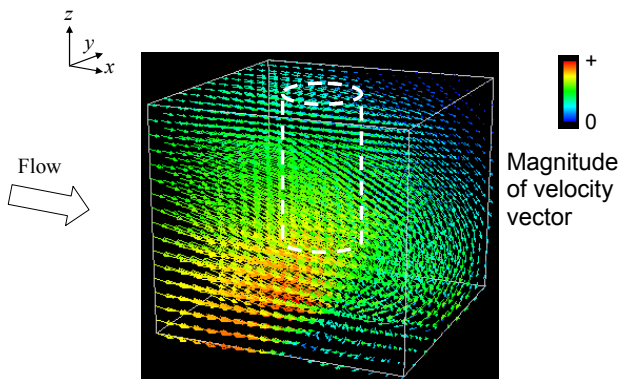


Figure 7: Velocity vectors by 3D-PTV (case a).

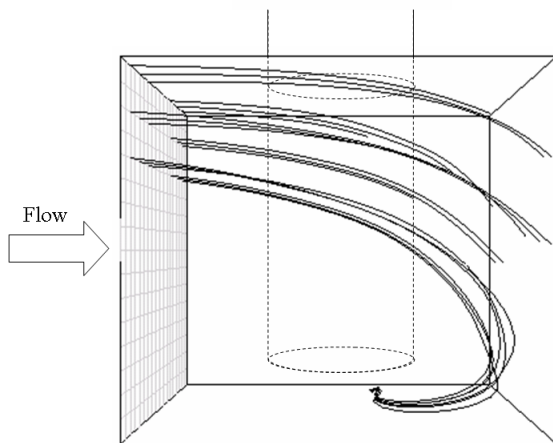


Figure 8: Streamlines by 3D-PTV (case a).

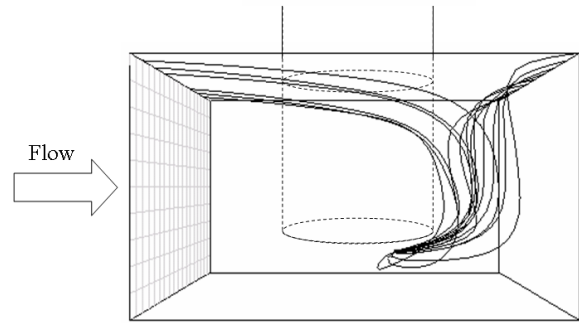


Figure 9: Streamlines by 3D-PTV (case b).

4 CONCLUSIONS

As an accuracy check, we have confirmed a good agreement on time-mean three-dimensional velocity distributions between the 3D-PTV and the UVP. In addition, the authors reveal some typical flow structures in the sump, and discuss the relationship between the flow structures and the air entrainment.

REFERENCES

- [1] JSME standard: standard method for model testing the performance of a pump sump, JSME S 004 (1984) (in Japanese).
- [2] H. O. Anwar, J. A. Weller, M. B. Amphlett: Similarity of free-vortex at horizontal intake, *J. Hydraulic Research*, Vol.16 No.2 (1978) 95-105.
- [3] K. Hirata, J. Funaki, N. Nakajima: On the critical submergence for air entraining vortices in a suction sump, *J. Hydraulic, Coastal and Environmental Engineering*, Proc. JSCE, Vol.65 No.747 (2003) 61-69 (in Japanese).
- [4] R. T. Hattersley: Hydraulic design of pump intakes, *J. the Hydraulics Division*, Proc. ASCE, Vol.91 No.HY2 (1965) 223-249.
- [5] M. Tagomori, H. Ueda: An experimental study on submerged vortices and flow pattern in the pump sump, *Trans. JSME*, Series B, Vol.57 No.543 (1991) 3641-3646 (in Japanese).
- [6] G. S. Constantinescu, V. C. Patel: Numerical model for simulation of pump-intake flow and vortices, *J. Hydraulic Engineering*, Tran. ASME, Vol.4 No.2 (1998) 123-134.
- [7] J. Funaki, M. Neya, M. Hattori, H. Tanigawa, K. Hirata: Flow Measurements in a Suction Sump by UVP, *J. Fluid Science and Technology*, Vol.3 No. 1 (2008) 68-79.
- [8] Y. Takeda: Measurement of Taylor-Couette Flow by the Pulsed Ultrasonic Doppler Method, *J. Phys. Soc. Jpn.*, 49 (2004) 994-1001.
- [9] A. Shintani, J. Funaki, K. Hirata: Measurements of Bubble jets by 3D-PTV and UVP, *Proc. ISUD5* (2006) 139-142.

A comparative study on near-field flow structures in a circular free jet and a square free jet

Yoshihiro Inoue^{1*}, Kunikazu Kondo² and Shintaro Yamashita¹

¹Department of Mechanical and Systems Engineering, Gifu University, 1-1 Yanagido, Gifu 501-1193, Japan (*Corresponding author, e-mail: inouey@gifu-u.ac.jp).

²Department of Mechanical Engineering, Suzuka National College of Technology, Shiroko-cho, Suzuka, Mie 510-0294, Japan

Coherent structures in the near field of a free jet have been studied. Experiments are carried out for the free jets issuing from circular and square nozzles using a water channel. Instantaneous velocity profiles are obtained in the radial directions by using an ultrasonic velocity profiler (UVP). Coherent structures in the radial direction are investigated in terms of the proper orthogonal decomposition (POD). The radial oscillation of the mixing layer is captured by the only first POD mode with about half a total energy. These velocity fields are reconstructed by the only lower-order POD modes and the reconstructed velocity fields by the lower-order and higher-order POD modes demonstrate large-scale and smaller-scale coherent structures, respectively. In the case of circular jet, there is a peak of power spectrum of the random coefficient at the first POD mode.

Keywords: Free Jet, Turbulence Intensity, Flow Structures, Proper Orthogonal Decomposition

1 INTRODUCTION

A study of the jet that is one of a representative flow field of free shear flow has been done a lot so far, and the engineering application field is wide. Investigations of turbulent jets are started for a long time, and Hinze [1] describes the prospects of those days and Rajaratnam [2] writes a monograph on turbulent jets. There are various kinds for a three-dimensional free jet from a difference of shape of an outlet. Of these, a circular jet [3], an elliptical jet [4], a rectangular jet [5-7] are well examined as a simple model.

This study is aimed for elucidation of space-time flow structure of a three-dimensional free jet by water tank experiment using an Ultrasonic Velocity Profiler (UVP). The authors have made experiments on a square and a circular jet and reported the fluctuating flow fields [8-9]. In this report, acquired data are analyzed by the proper orthogonal decomposition, and, from their results, the flow structures are compared between of the circular jet and the square jet.

2 EXPERIMENTAL PROCEDURES

2.1 Apparatus

The outline of flow field and coordinate system are shown in Fig. 1. We take x - and y -axes in the jet-axis and radial directions, respectively. Test section of the water tank used in this experiment is an open channel of 0.7 m wide, 0.64 m deep of water and 3 m long, and jet nozzle is set up at the central portion on the partition of the test section and settling chamber. The exit diameter of the circular nozzle is 85 mm, and the side length of the square nozzle is 100 mm. The contraction shape is a quadrant of a

radius 12 mm added hereafter a straight line. In the experiment, Reynolds number Re_j based on the velocity U_j in the core of the jet and the equivalent diameter of nozzle D_e was set to about 1×10^4 . Then the initial momentum thickness θ_0 of the shear layer at the position of $x/D = 0.2$ for the circular jet was about 1.0 mm, and $Re_\theta = U_j \theta_0 / \nu \approx 10^4$.

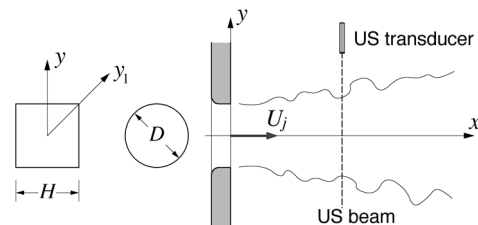


Figure 1: Coordinate system.

2.2 UVP measurement method

In the UVP measurement, ultrasonic transducer comprising a function of transmission and reception is used and velocity component in the traveling direction of ultrasonic beam is detected almost instantaneously for 128 points on the beam. The performance of the UVP measurements should be referred to Takeda [10].

The basic frequency of ultrasonic wave was 4 MHz, and hydrogen bubbles generated from a platinum wire of diameter of 0.03 mm was used for scattering particles. An incidence direction of the ultrasonic beam, namely, the measuring lines were chosen as directions of the y -axis and y_1 -axis as shown in Fig. 1. In working conditions of this experiment, the time interval of velocity data was about 36 - 56 ms, and the space intervals of adjacent measuring point were 2.20 mm for the circular jet, and 2.90 mm for the square jet.

If a flight direction of ultrasonic beam is y , the quantity obtained by this measurement is space-time distribution of y component of the instantaneous velocity, and it is expressed with $V(y) + v(y,t)$. Here $V(y)$ shows time-averaged velocity distribution and $v(y,t)$ space-time distribution of fluctuating velocity. For data set of this space-time distribution, data analysis by the proper orthogonal decomposition is performed as done in the previous report [8], and flow structure is examined.

3 RESULTS AND DISCUSSION

3.1 Mean and fluctuating velocity distributions

In the case of both of nozzle shapes, experiments were performed at the range of $0.5 < x/D_e < 5$ in the axial direction and $-1.5 < y/D_e < 1.5$ in the lateral direction, respectively. RD is used for results of the a circular jet, and for a square jet SQ(s) is corresponding to the direction normal to the side through the jet axis and SQ(d) to the diagonal direction of the nozzle, respectively.

Figure 2 shows the distributions of mean velocity V and Fig. 3 shows the r.m.s. value of fluctuating velocity v . In the case of Fig. 2(a) for the circular jet, the distributions of mean velocity corresponding to the mixing layer formed in the initial region of for $y/D_e = 0.5$ of $x/D_e < 1$ are shown. For $x/D_e > 1.5$, the width of the flow extends outside and the peaks in their profiles move outwardly. It is shown from Fig. 3(a) that the fluctuation in the mixing layer is seen for $x/D_e > 1.5$ and the peak of the fluctuation intensity is located almost same position for the peak of the mean velocity. The peak value becomes $v_{rms}/U_j = 0.15$ and three times the value of $V/U_j = 0.05$. The fluctuation intensity on the jet-axis is augmented as goes downstream.

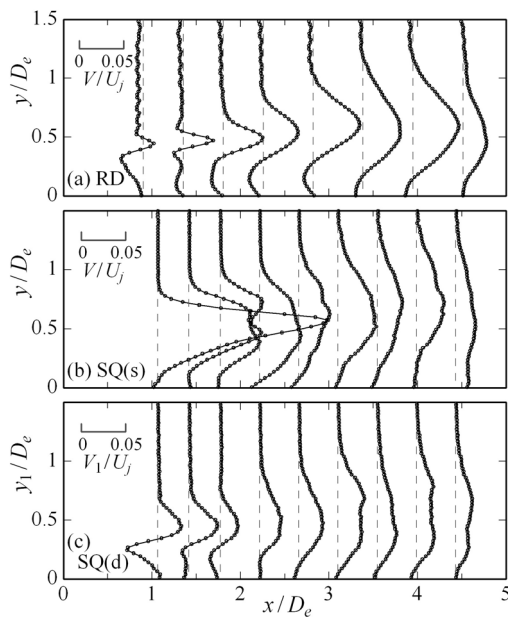


Figure 2: Distributions of the mean velocity component. (a) RD, (b) SQ(s) and (c) SQ(d)

Distribution profile of mean velocity V_1 (Fig. 2(c)) changes in the axial direction in a similar way to RD. It is shown from the mean velocity distributions for $x/D_e < 1.5$ that width of the mixing layer is larger than RD. On the other hand, the distributions of mean velocity of SQ(s), as shown in Fig. 2(b), are different from the others. The positive mean velocity corresponding to an outward flow from the jet axis becomes about 20% of the jet velocity at $x/D_e = 1$. It is indicated that the square jet width more rapidly extends in the y -direction than in the y_1 -direction. Distributions of the fluctuating intensity in the both cases of SQ(s) (Fig. 3(b)) and SQ(d) (Fig. 3(c)) become almost similar to those of RD, but the position where fluctuations start to grow up exists at more upstream position for square jet than RD.

Spatially and temporally averaged intensity of the fluctuating velocity along each measuring line is defined by the following equation,

$$E_v = \frac{1}{T} \iint v^2(y,t) dy dt . \quad (1)$$

Changes of the intensity normalized by U_j in the x -direction are shown in Fig. 4. As shown in the figure, the fluctuating energy increases gradually in the regions of $x/D_e < 3$ for RD and reaches nearly constant value in the downstream of this region. It seems that this change is caused by the distortion behavior of the vortices formed in the mixing layer, and, as shown in the previous report [8], the considerably rapid distortion of vortices are induced in $x/D_e < 1.8$ for square jets, and, as a result, the increasing of fluctuation energy is brought about.

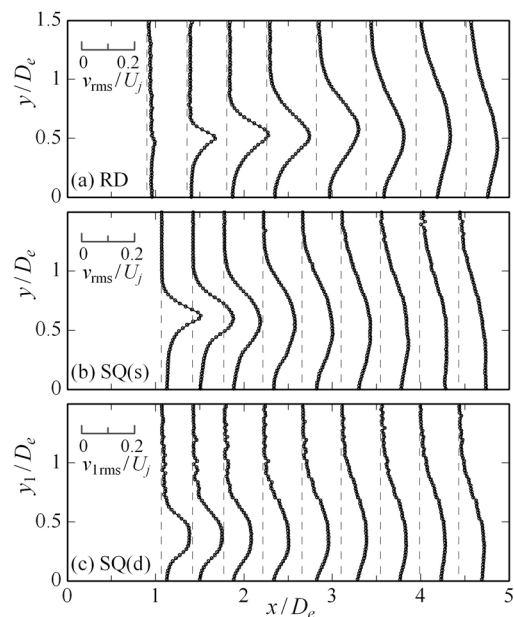


Figure 3: Distributions of the r.m.s. value of fluctuating velocity. (a) RD, (b) SQ(s) and (c) SQ(d)

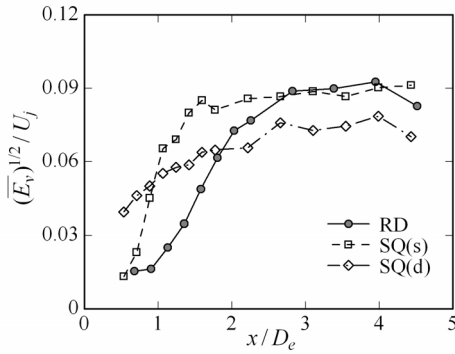


Figure 4: Change in the spatially and temporarily averaged energy of velocity fluctuation.

On the other hand, at the upstream positions, the energy for SQ(d) is most highest, however, the subsequent change of its value is slow in the downstream, and the value don't reach the level of others at $x/D_e = 5$. The averaged energy of velocity fluctuation for SQ(s) rapidly increases and becomes nearly constant for $x/D_e > 1.5$.

3.2 Flow structures

The proper orthogonal decomposition (POD) [11-13] is a method that is expanded empirically and efficiently the fluctuating flow fields in space to any modes, and its details were mentioned in the previous report [8].

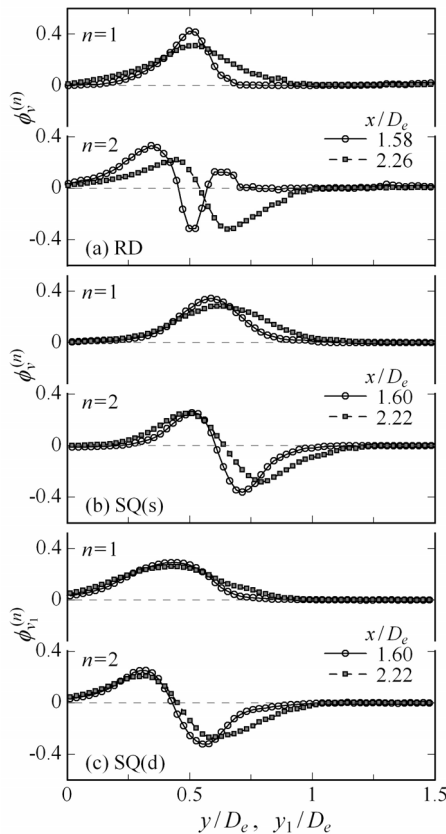


Figure 5: Distributions of the eigenfunction at the first two POD modes. (a) RD, (b) SQ(s) and (c) SQ(d)

Figure 5 shows the distributions of the eigenfunction for $n = 1$ and 2 . There is no conspicuous characteristic of the eigenfunction for all the velocity distributions of RD, SQ(s) and SQ(d). The eigenfunction at first mode indicates fundamental oscillation in transverse direction, and the eigenfunction at second mode indicates its higher-order components. It seems that only second mode at $x/D_e = 1.58$ for RD has a different distribution from the others, however, this shape is similar to the third mode of the others.

The eigenvalue $\lambda^{(n)}$, namely, stock energy at each mode is satisfied following relation,

$$E_v = \sum_n \lambda^{(n)} . \quad (2)$$

Figure 6 shows the changes in the axial direction of energy contribution rate from $n = 1, n = 1$ to 3 and $n = 1$ to 5 to total fluctuating energy. The sum of $n = 1$ to 5 include nearly 80% of energy in any modes, and hence this flow field can be well expressed by the relatively lower-order POD mode only. For $n = 1$, its energy content decreases as goes downstream from a peak of nearly 60 %, the energy included $n = 2$ to 3 relatively increase.

Random coefficients of the fluctuating velocity distributions $v(y,t)$ is defined by the following equation,

$$v^{(n)}(t) = \int v(y,t) \phi^{(n)}(y) dy , \quad (3)$$

and indicates the change in time of the contribution of spatial mode.

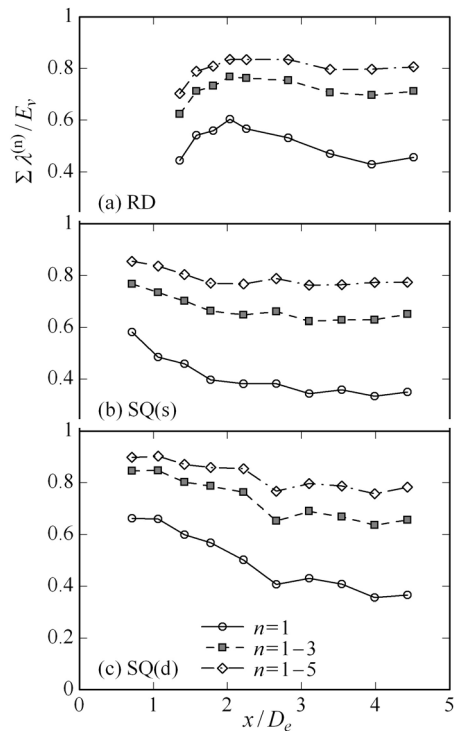


Figure 6: Contributions from several POD modes to the total fluctuating energy. (a) RD, (b) SQ(s) and (c) SQ(d)

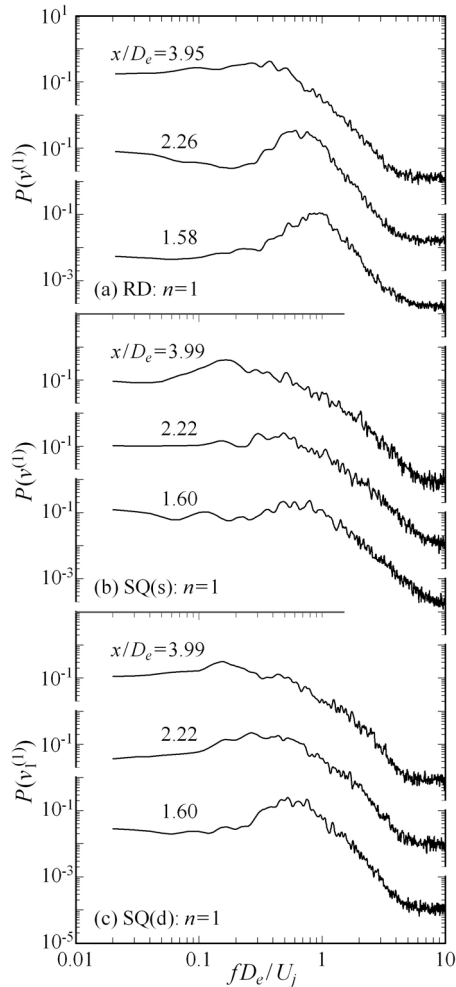


Figure 7: Power spectra of the random coefficient at the first mode. (a) RD, (b) SQ(s) and (c) SQ(d)

The power spectrum obtained from the FFT analysis of random coefficient for $n = 1$ on the three whole cross sections in each direction is shown in Fig.7. From this spectrum, the time periodicity of the spatial variation of mode $n = 1$ can be examined. For RD there exists a clear hill on the distributions of spectra for $x/D_e = 1.58$ and 2.26 , and mean frequency is $f D_e/U_j = 0.94$ at $x/D_e = 1.58$, and this value decreases as goes downstream. On the other hand, the spectrum width for SQ(s) becomes considerably broad, and the spectrum width for SQ(d) is narrow compared with that for SQ(s).

4 CONCLUSIONS

About velocity distributions in the radial direction for circle and square free jet, the fluctuating energy increase in the axial directions in any flow fields, and the value approaches value around 0.09, but the tendency to increase is different respectively, and the increase stopped at nearly $x/D_e = 2$. Also, there was no essential difference of the distribution of each eigenfunction, and any difference between energy contribution rates from lower-order POD mode in space was hardly seen. That is to say, it is

enable to compare the characteristics in time of the flow with the random coefficients that indicates the time contribution of from spatial modes. When this power spectrum was investigated, the different distributions were obtained in each case for $x/D_e < 3$.

REFERENCES

- [1] Hinze JO: Turbulence, An Introduction to its Mechanism and Theory, McGraw-Hill, New York (1959).
- [2] Rajaratnam N: Turbulent Jets, Elsevier Sci. Pub., Amsterdam (1976).
- [3] Wygnanski I, Fiedler H: Some Measurements in the Self-preserving Jet, J. Fluid Mech. 38 (1969) 577-612.
- [4] Husain HS, Hussain F: Elliptic Jets. Part 3. Dynamics of Preferred Mode Coherent Structure, J. Fluid Mech. 248 (1993) 315-361.
- [5] Tsuchiya Y, Horikoshi C, Sato T: On the Spread of Rectangular Jets, Exp. Fluids 4 (1986) 197-204.
- [6] Toyoda K, Hiramoto R: Vortical Structure and Diffusion Mechanism of a Rectangular Jet, Proc. 3rd ASME/JSME Joint Fluids Eng. Conf., San Francisco, USA (1999) FEDSM99-6946.
- [7] Gutmark E, Grinstein FF: Flow Control with Noncircular Jets, Annual Rev. Fluid Mech. 31 (1999) 239-272.
- [8] Inoue Y, Yamashita S, Kondo K: The Ultrasonic Velocity Profile Measurement of Flow Structure in the Near Field of a Square Free Jet, Exp. Fluids 32 (2002) 170-178.
- [9] Inoue Y, Yamashita S, Kondo K: Experiments in an Initial Region of a Circular Free Jet, Proc. 4th ISUD, Sapporo, Japan (1999).
- [10] Takeda Y: Velocity Profile Measurement by Ultrasonic Doppler Method, Exp. Thermal Fluid Sci. 10 (1995) 444-453.
- [11] Arndt REA, Long DF, Glauser MN: The Proper Orthogonal Decomposition of Pressure Fluctuations Surrounding a Turbulent Jet, J. Fluid Mech. 340 (1997) 1-33.
- [12] Berkooz G, Holmes P, Lumley JL: The Proper Orthogonal Decomposition in the Analysis of Turbulent Flows, Annual Rev. Fluid Mech. 25 (1993) 539-575.
- [13] Sirovich L, Kirby M, Winter M: An Eigenfunction Approach to Large Scale Transitional Structures in Jet Flow, Phys. Fluids A2 (1990) 127-136.

Study on ultrasonic velocity profile measurement in vapor-water two-phase flow

Daisuke Ito^{1*}, Hiroshige Kikura¹, Masanori Aritomi¹ and Michitsugu Mori²

¹Research Laboratory for Nuclear Reactors, Tokyo Institute of Technology, 2-12-1-N1-13 Ohokayama, Meguro-ku, Tokyo, 152-8550 Japan (*Corresponding author, e-mail: ito@2phase.nr.ititech.ac.jp).

²Tokyo Electric Power Company, 4-1, Egasaki-cho, Tsurumi-ku, Yokohama, 230-8510 Japan

In the gas-liquid two-phase flow measurement, a number of measuring techniques have been developed and applied to the flow monitoring of the two-phase flow structure. The ultrasonic velocity profile (UVP) measurement is one of the successful measuring techniques, since it is a non-invasive measurement and can obtain the velocity profiles along the measuring line. For the on-site flow monitoring, the clamp-on UVP measurement is required. However a solid wedge is necessary for the installation of an ultrasonic transducer on the pipe without a machining process of the pipe. Because of the use of the wedge, the transmitted sound field in fluid gets complicated, so it is important to clarify the ultrasonic transmission behavior when a wedge is used. Thus the transmission characteristics of the pulse ultrasound transmitted to the flow were investigated using the radiation angle of the ultrasonic beam and the ultrasonic transmission intensity obtained by the sound pressure distribution measurement, and then the optimal incident angle of the ultrasonic pulse was decided. Using the optimal ultrasonic incident condition, the applicability of the UVP measurement to boiling two-phase flow was investigated.

Keywords: Boiling two-phase flow, Velocity profile measurement, Ultrasonic transmission characteristics, Sound pressure distribution, Clamp-on type

1 INTRODUCTION

Gas-liquid two-phase pipe flow is one of the important phenomena for safety operation of industrial plants. They require two-phase flow measuring techniques for monitoring the flow structures (e.g. void fraction distribution, velocity profile, flow rate etc.) in real-time. The ultrasonic velocity profiler (UVP) [1] can measure the flow velocity profiles in opaque pipes. So it can be a very effective tool for on-site flow observation. Furthermore, as an application of UVP technique to gas-liquid two-phase flow, the multi-wave ultrasonic velocity profiling method [2] can measure the velocity profiles of both gas and liquid phases simultaneously. The conventional ultrasonic measurement of gas-liquid two-phase flow has had little applicability to the boiling two-phase flow. The ultrasonic measuring technique to boiling flow has the capability of on-site two-phase flow monitoring. In addition, in the installation of ultrasonic measuring instruments, the clamp-on type is suitable for the two-phase flow monitoring in the plants in operation, because it is not necessary to machine the existing pipes. However the transmitted ultrasonic sound fields get complicated due to the effect of metallic pipes. Hence the transmission characteristics of pulse ultrasound should be examined in detail before the ultrasonic measurement.

In this study, for the purpose of UVP measurement of boiling two-phase flow at high temperatures, the ultrasonic transmission characteristics are clarified by measuring the transmitted sound pressure distributions and comparing them with theoretical analysis, and then the optimal incident angle for

ultrasonic velocity profile measurement is decided. Using the optimal incident angle, the velocity profiles of vapor bubbles in a circular pipe are measured by UVP.

2 ULTRASONIC TRANSMISSION CHARACTERISTICS

2.1 Ultrasonic transmission in clamp-on type

In the clamp-on ultrasonic measurement, an ultrasonic transducer (TDX) is installed on the solid wedge fixed on the pipe wall. So ultrasonic waves emitted from the TDX transmit to the wedge. When the waves pass through the wedge, the wave mode is the longitudinal wave. The reflection, refraction

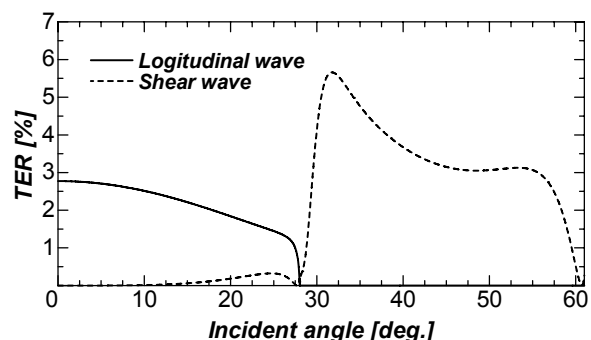


Figure 1: Transmission energy ratio in a case of the transmission between acrylic wedge, stainless steel plate and water.

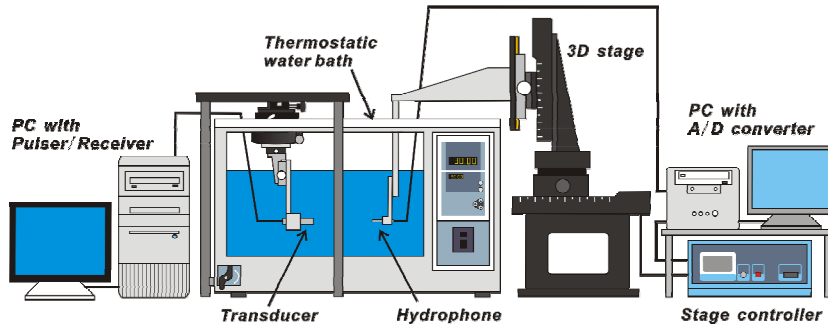


Figure 2: Schematic diagram of three-dimensional automatic USPD measuring system

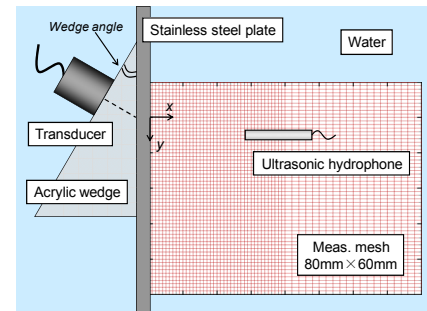


Figure 3: Test section of USPD measurement

and mode conversion occur at the interface between the wedge and the pipe wall, and then, in addition, the shear wave and the plate wave are generated in the pipe wall. These waves are converted into the longitudinal wave again at the interface between the pipe wall and the water. Since each wave mode has a different propagating velocity, the ultrasonic sound field in water contains multiple waves and gets complicated.

2.2 Ultrasonic transmission energy ratio

The transmission energy ratio (TER) [3] of the ultrasonic wave was used to compare the intensity of transmitted ultrasonic wave with the results of the sound field measurement. The TER of the ultrasonic wave transmitted between two mediums can be calculated from the amplitude ratio of displacement potential of each reflection and refraction wave to that of the incident wave. Thus the TERs from acrylic resin to stainless steel and from stainless steel to water were estimated. And then the TER between a wedge, plate and water was obtained from the product of TERs for the longitudinal and shear waves, and the calculated results in the case of transmission between an acrylic wedge, a stainless steel plate and water are shown in Figure 1. The TERs of each wave mode are varied by the incident angle. At an incident angle above 28 degrees, there is no longitudinal wave, since 28.02 degrees is the critical angle of the wave at the interface from acrylic resin to stainless steel. This figure shows the TER has a maximum value at the incident angle of around 30-35 degrees. In this case, the TER is not more than 6 % of the incident wave, so most waves are reflected.

2.3 Sound field measuring method

The ultrasonic sound pressure distributions (USPDs) of transmitted pulse ultrasound were measured by an ultrasonic hydrophone. The measurement system of the USPD and the test section are illustrated in Figure 2 and Figure 3, respectively, and the measurement conditions are shown in Table 1. The pulse signal sent from the pulser/receiver (TB-1000: Matec Inc.) built in a PC was transmitted to the wedge by the TDX. The

Table 1: Measurement conditions of USPDs.

Ultrasonic basic frequency	2 MHz
Ultrasonic beam diameter	10 mm
Wedge material	Acrylic resin
Wedge angle θ_{in}	8-50 degrees
Plate material	Stainless steel
Plate thickness t	1 mm, 2 mm
Water temperature	30°C
Detectable area of hydrophone	1mm x 1mm
Measuring area	80mm x 60mm

signals transmitted into water were received by a movable ultrasonic hydrophone with a detectable area of 1 mm², and the transmitted sound pressure was stored by an A/D converter (NI PCI-5112: National Instruments) in a PC. Then the USPD in the measuring area was obtained.

In the USPD measurement, water temperature was maintained at 30°C by using a thermostatic water bath. The sound velocity in water under such conditions was 1510 m/s. 2 stainless steel plates with 1 and 2 mm thickness were used to estimate the effect of the plate thickness. Through the theoretical analysis, 10 types of wedges whose angles range from 8 to 50 degrees were selected and used to measure the USPDs. A high-temperature TDX (2K10I-H: Japan Probe) with a basic frequency of 2 MHz and an allowable temperature limit of 120°C was used.

2.4 Results of USPD measurement

The typical USPDs are shown in Figure 4. Figures 4(a), (c), (d), (g) and (h) have a single linear beam. On the other hand, there are some different beams in Figures 4(b), (e) and (f) because of the appearance of multiple wave modes. Furthermore, in Figures 4(a), (b) and (e), striped waves are found at different direction from a strong beam. These waves are the leaky plate wave, which is caused by the plate wave generated in the plate. From these figures, the beam formation in fluid can be easily understood, and it is found that the ultrasonic beam

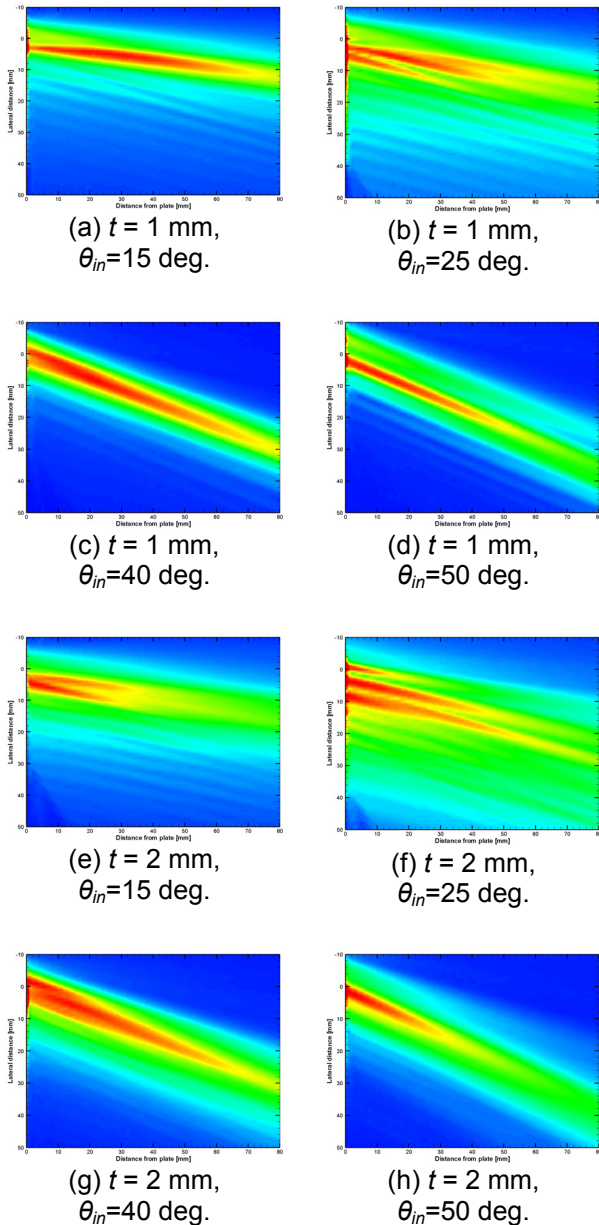


Figure 4: Typical USPDs measured by ultrasonic hydrophone

shapes in the USPDs change depending on the incident angle and plate thickness.

2.5 Ultrasonic transmission characteristics

For the clarification of ultrasonic transmission characteristics when a wedge is used, the radiation angle and the transmission intensity are estimated by using the measured USPDs.

The radiation angles of transmitted beams were evaluated by connecting the beam in USPД, as is shown in Figure 5. Several beams appear at the wedge angles from 15 to 30 degrees, and the radiation angles of each beam were obtained. Under these conditions, these radiation angles show large variations, because the beam characteristics are changed by the overlapping of multiple waves. The

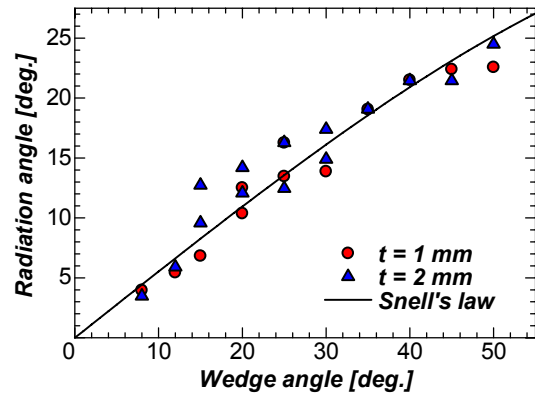


Figure 5: Radiation angle of the ultrasonic beam transmitted to water.

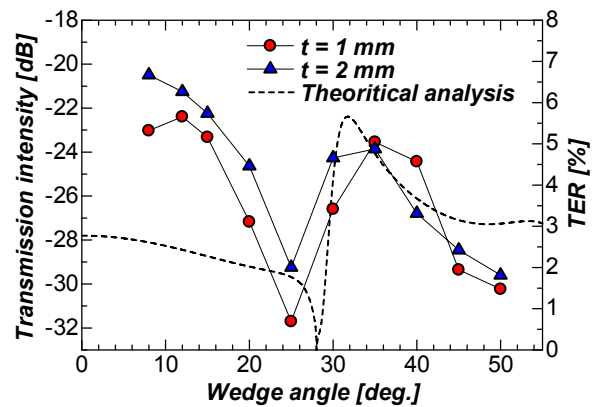


Figure 6: Transmission intensity of the transmitted ultrasonic beam.

radiation angles at the wedge angles of 8, 12, 35 and 40 degrees give close agreement with that of Snell's law, which is calculated by the incident angle and the sound velocity in theory.

The transmission intensity I_T was calculated by the following equation.

$$I_T = 20 \log \left(\frac{V}{V_0 \cos \theta_r} \right) \quad (1)$$

where V is the voltage value detected by the hydrophone, and V_0 is the reference voltage of this TDX. θ_r is the radiation angle of transmitted beam estimated from USPДs. Figure 6 shows the transmission intensity and TER based on by theoretical analysis. The transmission intensity as well as the TER decreases near 25 degrees, because it is the critical angle.

For the velocity profile measurement, the single linear beam with high intensity is better. From the USPД measurement, estimation and comparison with theoretical analysis, it is found that the incident angle (wedge angle) of 40 degrees is well suited for flow measurement in pipe with 1mm thick wall.

3 VAPOR BUBBLE VELOCITY PROFILE MEASUREMENT

3.1 Experimental set-up and method

The experimental set-up for boiling two-phase flow measurement is shown in Figure 7. Water pre-heated by a pre-heater in the storage tank flowed into test pipe by a pump. The flow rate of water was adjusted by the control valve and measured by the orifice flowmeter. The cartridge heater was inserted in the inlet of the test channel and vapor bubbles were generated in the pipe. This heater has a diameter of 12.7 mm, a length of 300 mm and a maximum heat flux of 400kW/m². The heater powers were individually set by the temperature controllers. The overflowed water returned to the storage tank again. The test channel consists of circular pipes made of PYREX glass and stainless steel. PYREX glass pipe was used to visualize the flow field, and stainless steel pipe was used to simulate the ultrasonic measurement in the operating plants. These pipes have an inner diameter *D* of 50 mm.

The UVP monitor (UVP-Duo, Met-Flow) was used for the velocity profile measurement of vapor bubbles in vertical upward flow. The test section of the UVP measurement was placed at 27*D* from the

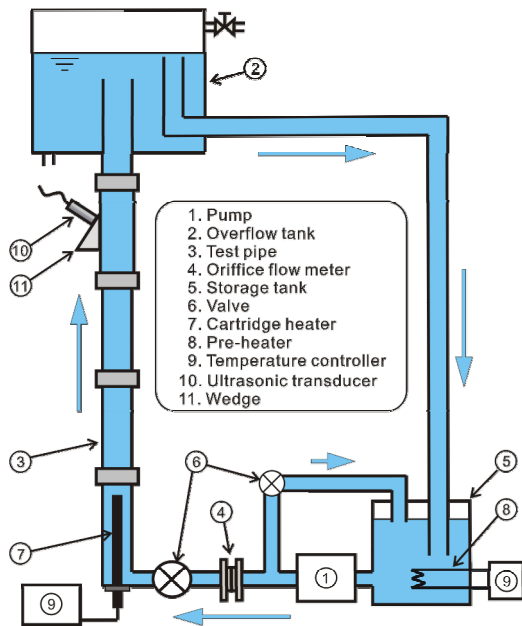


Figure 7: Schematic diagram of experimental loop for boiling two-phase flow measurement

Table 2: Experimental conditions.

Working fluid	Water, vapor
System pressure	Atmosphere
Inlet heat flux	300 kW/m ²
Inlet subcooling temperature	5 K

top of the cartridge heater. The TDX was connected to the UVP monitor and fixed on the surface of the acrylic wedge, which has an incident angle of 40 degrees. The ultrasonic couplant was poured between the TDX and the wedge and between the wedge and the pipe wall surface for transferring the ultrasound into the pipe. This couplant, which is designed for high temperatures, provides the high coupling efficiency and can transmit ultrasound at the temperature up to about 350°C.

3.2 Velocity profiles of small vapor bubbles

The velocity profiles were measured using the small bubbles generated by the heater, as is shown in Figure 8. From this result, it is found that the velocity profiles changed depending on the difference of the liquid flow rate. So the velocity profile of flow field at around 100°C can be obtained by the estimation of the ultrasonic transmission characteristics. However there is a little velocity drop due to the ultrasonic reflection in the wedge. It will be possible to eliminate it by improving the shape of the wedge.

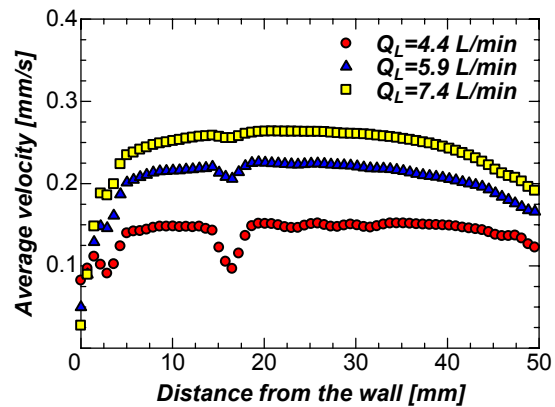


Figure 8: Velocity profiles of small vapor bubbles generated by the heater.

4 SUMMARY

For the clamp-on ultrasonic velocity profile measurement of the vapor-water boiling two-phase flow, the ultrasonic transmission characteristics were investigated experimentally by the ultrasonic sound pressure distribution measurement using the ultrasonic hydrophone. And the possibility of the ultrasonic velocity profile measurement of boiling two-phase flow at high temperatures was verified.

REFERENCES

[1] Takeda Y: Velocity profile measurement by ultrasonic Doppler method, *Exp. Therm. Fluid Sci.* 10 (1995) 444-453.
 [2] Murakawa H, et al.: Application of ultrasonic doppler method for bubbly flow measurement using two ultrasonic frequencies, *Exp. Therm. Fluid Sci.* 29 (2005) 843-850.
 [3] Yamamoto M: *Ultrasonic Fundamental Engineering*, Nikkan Kogyo Shimibun (1981) 70-84. in Japanese.

Effect of standing baffle on the structure of flow in a rectangular open channel

Hamidreza Jamshidnia* and Yasushi Takeda

Division of Energy and Environmental System Engineering, Hokkaido University, Sapporo, Japan

(*Corresponding author, e-mail: hamid@ring-me.eng.hokudai.ac.jp).

Effect of a standing baffle on the spatial and temporal structure of flow in a rectangular open channel has been investigated experimentally by 3D Acoustic Doppler Velocimeter. The flow is observed to be fully developed in the upstream of the baffle and far from the inlet. The presence of baffle causes the spatial structure of flow deviates from uniformity whereas before baffle the flow is fully developed. This effect is reflected in mean streamwise velocity profiles as well as turbulent intensity distribution. By applying a special smoothing method and analyzing the space-averaged power spectra an obvious peak structure is observed in upstream region of baffle whereas in downstream of baffle this peak structure is decreased. Moreover, pattern of flow near the inlet has been investigated. Results showed that due to high inlet velocity a jet of flow is observed near the bed of channel. Accordingly a recirculation zone has been formed upstream of baffle near the inlet.

Keywords: Baffle, power spectrum, turbulence intensity, spatial and temporal structure, ADV

1 INTRODUCTION

Understanding of flows over obstacles is important due to their relevance to many practical and theoretical problems. For example, separated flows produced by an abrupt change in geometry are of great importance in many engineering applications [1]. Also use of baffles or deflectors in settling tanks to improve the flow field has been investigated by several researchers such as Lyn and Rodi who conducted turbulence measurements in a model settling tank and observed the effect of different deflectors [2]. Also Wu and Rajaratnam have investigated the effect of baffles on submerged flows [3]. In this paper due to the lack of quantitative studies and also importance of baffle's application an Acoustic Doppler Velocimeter is used to investigate the structure of flow as well as effect of a standing baffle on spatial and temporal structure of flow in a rectangular open channel quantitatively.

2 EXPERIMENTALS

2.1 Experimental System

A specially designed unit at Fluid Mechanics Laboratory of the Mechanical Engineering Department at Sharif University of Technology (Iran) has been used to demonstrate the hydraulic characteristics and performance of a rectangular sedimentation open channel. A schematic diagram of the experimental setup is presented in Figure 1.

Water from the laboratory main supply was directed by a pump to a cylindrical storage tank and from this tank was pumped to the constant head tank and then was fed to the channel via a flow meter. Experiments were conducted in a glass sided rectangular open channel $8\text{m} \times 0.2\text{m} \times 0.4\text{m}$ in length, width and height (x, y , and z , with $x=0$ at upstream end, $y=0$ in center of channel, and $z=0$ at

the bed), respectively, with a smooth bottom. A rectangular feeding slot with the height of $h_0=0.11\text{ m}$ extending throughout the full width of the channel at the bottom, provided the inlet gate. The depth of water was controlled by a sharp-edged weir of height of 32 cm, located at the downstream end of the channel. The baffle is located at $x=4\text{m}$ and is extended across the full width of the channel. The height of baffle is 8 cm.

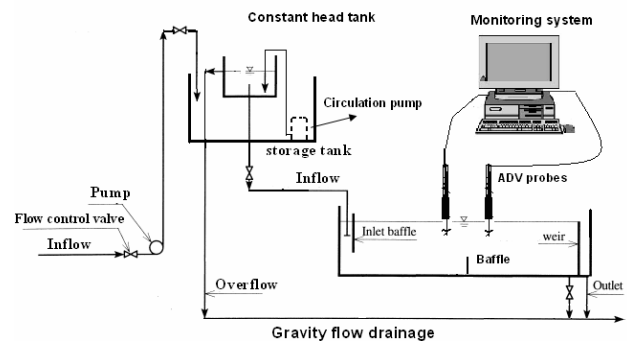


Figure 1: Schematic diagram of experimental setup

2.2 Experimental procedures

The velocities were measured on the central longitudinal plane by a 3D Acoustic Doppler Velocimeter (ADV) which makes it possible to observe the flow field at each point. This device is based on the principles of Doppler shift of a wave reflected from particles suspended in the fluid flow. Data are available at an output rate of 25 Hz. The 3-D velocity range is 2.5 m/s, and the velocity output has no zero-offset. The small sampling volume (0.25 cm^3) is located away from the sensor to provide undisturbed measurements and therefore is able to make accurate velocity measurements. Another advantage of ADV is that the probes of ADV were previously calibrated by the Nortek Company and

the measurements have a relatively high accuracy of 0.1 mm/s. [4]. The data acquisition took 30–40 sec. at each measuring point. Figure 2 illustrates the details of the channel and measured sections. Measurements have been done at 6 stations (sections) along the channel. Because of having only two ADV probes the simultaneous measurement of only two sections at the same time was possible. Therefore measurement at each pair of sections (0.5m, 1.5m), (2.5m, 3.5m) and (4.5m, 5.5m) have been done simultaneously. Also tracer particles were added to water for measurements.

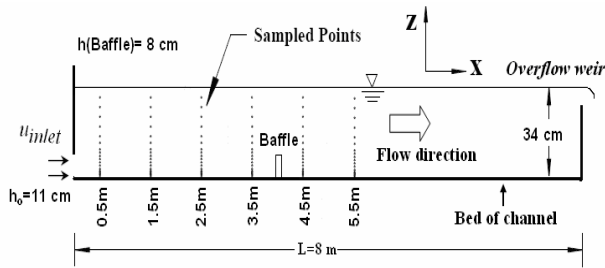


Figure 2: Schematic of channel and measurement sections along the channel

2.3 Conditions of Experiments

The flow conditions as well as the values of non-dimensional parameters such as Reynolds(Re) and Froud(Fr) numbers having the following definitions are represented in Tab.1. Q is the inlet flow rate.

$$Re = \frac{U_0 h_0}{\nu} \quad (1)$$

$$Fr = \frac{U_0}{\sqrt{gh_0}} \quad (2)$$

In equations 1 and 2, h_0 is the opening height of the inlet gate, ν is the kinematic viscosity of the fluid (Water) at $T=20^\circ C$ and U_0 is the inlet bulk velocity.

Table 1: Flow conditions in neutral experiments

Q (lit/min)	h_0 (cm)	Re (inlet)	Fr (inlet)
35.5	11	2946	0.0259

3 RESULTS AND DISCUSSION

The instantaneous velocity has three components in Cartesian coordinate system $U(t), V(t), W(t)$ in streamwise, transversal and vertical direction respectively. A typical example of velocity time series obtained at a specific point is shown in Figure 3.

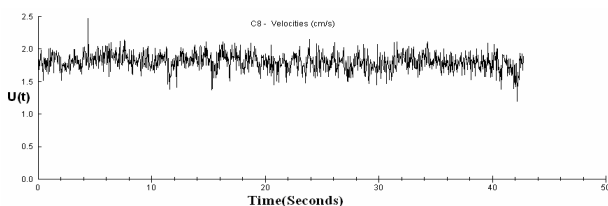


Figure 3: A typical velocity time series at one point

3.1 Spatial structure

3.1.1 Mean Velocities

The high accuracy and the inherent property of zero-drift free velocity measurements make the ADV suitable for accurate measurements of mean flow even at positions close to the boundary ($z=0.75cm$)[5]. In Figure.4 streamwise mean velocity profiles at various streamwise positions are shown. The horizontal axis represents the streamwise velocity (u) which has been made non-dimensional by average velocity based on flow rate. Also vertical axis represents the height relative to the depth of water ($H=34 cm$). It must be noted since a downward-looking ADV probe has been used, the acquisition of data could not cover the free surface because the probe of ADV would be out of water and consequently the variation of sound velocity in air and water would lead to poor quality data.

As shown in the Figure 4, at $x=0.5 m$ which is very close to inlet an obvious jet flow is observed near the bed of channel. Negative velocities at the higher part of the profile indicate the existence of a recirculation region due to high velocity gradient between different layers of fluid. But at $x=1.5 m$ the velocity profile is almost uniform over depth of channel. This is reasonable because this section is far away from inlet and is not under the strong influence of inlet. At $x=2.5m$ and $x=3.5m$ which are located much downstream of inlet region the flow is developed because no difference of mean velocity profile along the streamwise direction appears between $x=2.5m$ to $x=3.5m$. Additionally, as it is observed downstream of the baffle($x=4.5m$) the flow pattern deviates from uniformity. It can be inferred that due to decrease in cross sectional area as a result of presence of baffle at $x=4m$ velocity profile has a maximum value at $x=4.5m$.

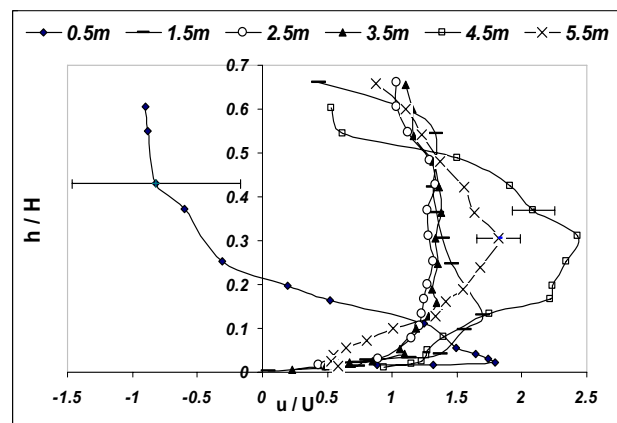


Figure 4: Variation of streamwise velocity profiles along the baffled channel (The error bars represent the dispersion of velocities at some typical points)

At $x=5.5m$ which is located at much downstream of baffle the maximum value of the velocity profile has been decreased compared to the corresponding one at $x=4.5m$. Also the value of velocity near the free

surface at section $x=5.5\text{m}$ is higher than the corresponding one at $x=4.5\text{m}$. This indicates the strong effect of baffle at $x=4.5\text{m}$ which is very close to baffle and also indicates that flow at much downstream of baffle($x=5.5\text{m}$) tends to get more uniform although the effect of baffle is still felt.

3.1.2 Turbulence intensities

The Root-Mean-Square (RMS) of the velocity fluctuations denotes the standard deviation of the samples taken by the ADV and its value relative to mean velocity is equal to the turbulent intensity for the respective velocity component.

3.1.2.1 Effect of inlet

In Figure 5 the value of turbulence intensities near the inlet compared to the next section. At $x=0.5\text{m}$ (very close to inlet) the absolute value of turbulent intensity is very high and varies strongly over height.

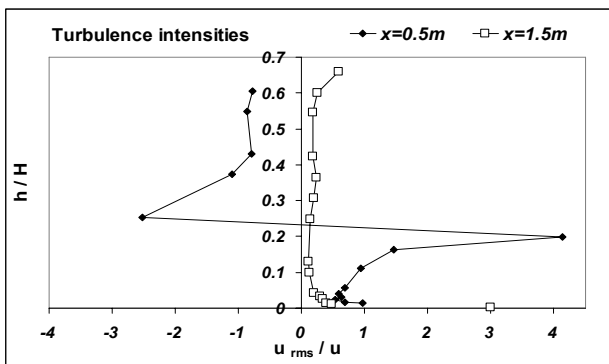


Figure 5: Comparison of turbulence intensities profiles at $x=0.5\text{m}$ and $x=1.5\text{m}$ from inlet

Downstream of the inlet and upstream of baffle the value and the variation of turbulent intensity over height is decreased considerably. Therefore it is concluded that at $x=0.5\text{m}$ the pattern of flow is under the strong influence of inlet flow. The negative turbulent intensity in the upper part of the channel indicates the existence of a recirculation region.

3.1.2.2 Effect of baffle

As shown in Figure 6 before the baffle the variation of turbulent intensity is almost the same over depth

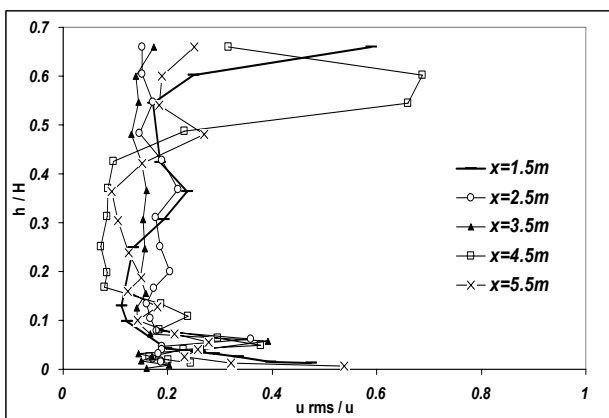


Figure 6: Turbulent intensities along the channel

of channel and flow is calm but downstream of baffle the variation of turbulent intensity over the depth is strong and its value has been increased in the upper part of profiles. These observations indicate the deviation of the spatial structure of flow from uniformity and strong variation of turbulent intensity over depth after baffle due to presence of baffle.

3.2 Temporal structure

3.2.1 Power spectrums

Discrete Fourier Transform (DFT) has been used and a program has been written to extract and analyze the power spectrum from streamwise velocity time series.

3.2.2. Methodology

Usually the power spectrum obtained from raw data of velocity time series contains some noises. Therefore to eliminate the noises to some degree and fare observation of peak structures a special method has been used for smoothing the power spectrum. We denote $u[n]$ as velocity time series at each point in which $n \in \{1,2,3,\dots,N\}$ and N is the number of samples. In this method $u[n]$ has been divided into two time series u_1 and u_2 as follows:

$$u_1[n] : n \in \{1,3,\dots,N-1\}, \quad u_2[n] : n \in \{2,4,\dots,N\}$$

The DFT has been applied separately to each of the subdivided time series to extract their power spectra and then ensemble average of the results has been calculated over frequency to obtain the smoothed power spectrum at each point. In Figure 7 the effect of smoothing is clearly observed for a typical point.

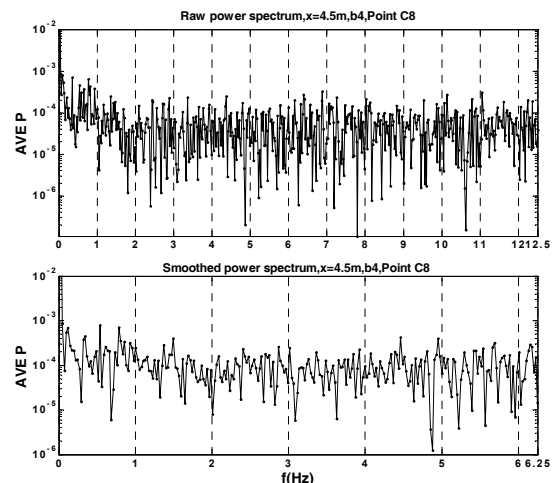


Figure 7: Comparison of raw and smoothed spectra

It is notable that the maximum frequency of the smoothed power spectrum is a quarter of the sampling frequency (25 Hz) that is 6.25 Hz. Although there are special characteristics observed to be space-dependent in the power spectra we focus our attention on space averages of the power spectrum. In fact by taking the space average of power spectra the peak structure could be observed

apparently. Comparison of space averaged power spectra over different ranges in space showed that we are dealing with a local phenomenon and as a result space averaging has been represented in Figures (8, 9 and 10) for three points namely (b6, b7, b8) for upstream sections and (c6, c7, c8) for downstream sections of baffle having the height in the range of $8 \text{ cm} \leq h \leq 12 \text{ cm}$. In these figures the horizontal axis is frequency and vertical axis is the amplitude of space averaged power spectrum.

3.2.3 Effect of baffle on power spectra

In order to observe the effect of baffle the space averaged power spectra over the first half of frequency domain are illustrated in Figures 8 and 9 for upstream and downstream of baffle respectively.

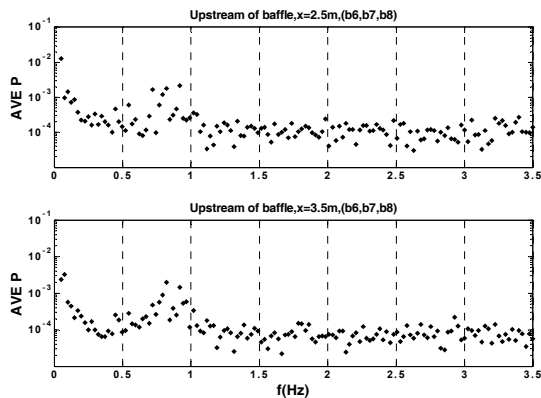


Figure 8: Upstream of baffle ($x=2.5\text{m}$, $x=3.5\text{m}$)

Upstream of baffle a clear peak structure is observed. This peak structure is a natural characteristic of the system because it is observed at $x=2.5\text{m}$ and $x=3.5\text{m}$. On the other hand, in downstream of baffle the amplitude of the peak structure has been decreased.

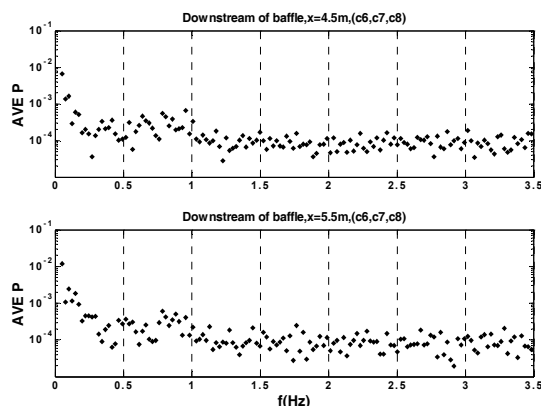


Figure 9: Downstream of baffle ($x=4.5\text{m}$, $x=5.5\text{m}$)

Comparison of the effect of baffle on the power spectra before and after baffle in Figure 10 indicates the destruction of the peak structure due to presence of baffle. As a result clear effect of baffle on temporal structure of flow has been observed by spectral analysis and a special smoothing method.

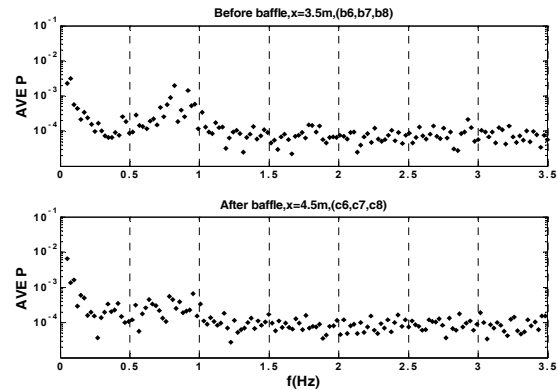


Figure 10: Power spectra before and after baffle

4 CONCLUSIONS

The effect of a standing baffle on spatial and temporal structure of flow in a rectangular open channel has been investigated experimentally using a 3D ADV. Based on the results of this experimental investigation following conclusions can be made:

1. The flow was observed to be fully developed in the upstream of baffle and far from the inlet.
2. Comparison of streamwise velocity profiles and turbulent kinetic energy along the channel shows that existence of baffle causes the flow pattern deviates from uniformity.
3. Importantly, by analyzing and comparing space averaged power spectra it has been found that in the upstream of baffle a clear peak structure is observed whereas in the downstream of baffle the peak structure has been destroyed. This indicates that presence of baffle has caused the inherent periodicity in the temporal structure of flow to be destroyed in the downstream of baffle.

ACKNOWLEDGEMENT

Authors are grateful to Center of Engineering Education Development (CEED) of Hokkaido University for financial support for attending ISUD 2008. Also sincere thanks are expressed to Dr. Bahar Firoozabadi and her valuable inputs during the previous part of work in Iran.

REFERENCES

- [1] Barkley D et al. : Three-dimensional instability in flow over a backward-facing step, *Journal of Fluid Mechanics*, Vol. 473 (2002) 167-190.
- [2] Lyn A and Rodi W: Turbulence measurements in model settling tank, *Journal of Hydraulic Engineering*, Vol.116, No. 1 (1990) 3-21.
- [3]Wu S and Rajaratnum N: Effects of baffles on submerged flows, *Journal of Hydraulic Engineering*, Vol. 121, No. 9 (1995) 644-652.
- [4] Nortek AS., ADV Operation Manual (2000).
- [5] Voulgaris G, Trowbridge JH: Evaluation of the Acoustic Doppler Velocimeter (ADV) for Turbulence Measurements, *Journal of Atmospheric and Oceanic Technology*, Vol. 15, Issue 1(1998) 272-289.

Application of acoustic Doppler Velocimetry in microbubble containing water

Lennart Jönsson

Dep of Water Resources Engineering, Univ of Lund, Sweden

Univ of Lund, P.O.Box 118, S-221 00 Lund, Sweden. Email: Lennart.Jonsson@tvrl.lth.se

Dissolved Air Flotation (DAF) is a method for separating suspended, microscopic particles in water and wastewater treatment. The basic idea is to generate huge amounts of microscopic bubbles, which should attach to the particles whereby less dense aggregates are obtained, rising to the water surface. The flow structure in a flotation tank is important for the separation efficiency. ADV measurements have been performed in a DAF pilot plant for different hydraulic loads and dispersion flows. The bubbles (volumetric fraction < 3-4 ‰) constituted a difficult environment for the ADV (multi-scattering and attenuation): causing noisy signals although the bubbles did not affect the acoustic wave velocity according to direct measurements. It was judged according to different tests that the ADV could be used to map the flow structure qualitatively. A hypothesis of the multi-scattering process was suggested for the operation of the ADV. Studies of the flow structures indicated the importance of bulk water densities and showed that three states existed depending on the magnitudes of hydraulic load and dispersion flow – rotational flow, stratified flow, short-circuit flow. Only the middle one was advantageous for separation. The transition from the first to the second state was studied and physically explained.

Keywords: Dissolved air flotation, bubbles, flow structure, ADV

1 INTRODUCTION

Production of drinking water in water works or the treatment of municipal wastewater involves a very important and central process concerning the separation of suspended, microscopic particles or flocs from the water, for instance generated through biological or chemical treatment but also existing naturally. Dissolved Air Flotation (DAF) is an efficient method for the separation process with a number of advantages compared to the conventional sedimentation technique, for instance having a small footprint and possibility to separate less dense particles. The basic idea with DAF is to generate huge amounts of microscopic air bubbles (size of the order of 50-100 μm), which should attach to the suspended flocs/particles. In this way less dense bubble/floc aggregates are generated, which should rise to the water surface in the flotation tank, where a sludge layer is formed for subsequent removal. DAF is a relatively complex process and in order to utilize the full potential of the process a profound knowledge is required of the process. Thus, it has been shown [1] that the introduction of bubbles in the flotation tank strongly affects the flow structure and that this in turn affects the separation efficiency. Detailed studies and measurements using a laboratory Nortek Acoustic Doppler Velocimeter (ADV) have been performed on a DAF pilot plant, Fig 1, in order to get insight into the detailed characteristics of the flow structure for different hydraulic loadings and different

dispersion flow rates. The presence of bubbles (volumetric proportion up to about 2-4 ‰) constitutes a difficult environment for the ADV. Thus some tests were initially performed in order to assess the applicability of the ADV and a hypothesis was suggested for the operation of an ADV in bubble-containing water based on multiple scattering. Moreover, the paper will discuss different flow structures – rotational flow, stratified flow, breakdown of the stratified flow – basically related to the hydraulic load and the dispersion flow. Finally the mechanism for transition to stratified flow will be discussed.

2 DAF PILOT PLANT

The pilot plant, Fig 1, was 1.2 m long, 0.7 m wide, 1.3 m high with a transparent side. The hydraulic load (0 – 17 m^3/h) was entered (no particles) to the bottom left into a riser shaft (contact zone) ending a few dm:s below the water surface. Huge amounts of micro bubbles were produced by depressurizing water saturated with air at 5 bar via valves into the contact zone where the hydraulic load was entered. The dispersion flow rate was generally about 10 % of the hydraulic load. The hydraulic load together with the bubble flow then entered the separation zone (the main part of the tank), where different flow structures could be obtained. Fig 1 shows the case with a distinct stratified condition with an upper, less dense, bubble-containing layer and bottom layer with more or less clear water. Discharge of (clean)

water took place at the bottom via two perforated pipes. The ADV was mounted on a moveable rig on the top of the tank.



Figure 1. The pilot plant with hydraulic load and dispersion flow (bubbles) entering the riser shaft to the left

ADV PERFORMANCE

In normal circumstances (clean water with few scattering particles) the ADV works very well with the measurement point located 5 cm below the transducer. The ADV operation is dependent on the behaviour of the acoustic waves (speed and attenuation) in the water. Thus, one might expect that the presence of microscopic air bubbles ($\approx 50 \mu\text{m}$, volumetric fraction $\leq 4 - 5 \%$) would affect wave propagation significantly. A number of tests were performed in order to evaluate the ADV performance in such conditions. In the first place a 10 MHz acoustic receiver was placed 5 cm below the ADV transmitter in bubbly water. A digital oscilloscope was triggered each time an acoustic pulse was emitted and the received pulse could be visualized on the scope together with the time passed. This time was constant irrespective of the amount of bubbles (\leq about 4 – 5 %) corresponding to a wave velocity of 1470 m/s, i.e. the same as for pure water. Theory [2] confirms this finding:

$$c^2 = c_0^2 - \frac{4 \cdot \pi \cdot n \cdot a}{(2 \cdot \pi \cdot f)^2} \quad (1)$$

c = real wave velocity, c_0 = wave velocity in pure water, n = number of bubbles/unit volume of water $\approx 6.4 \cdot 10^{10}$, a = bubble radius $\approx 25 \cdot 10^{-6}$ m, f = acoustic frequency = 10^7 Hz. This gives $c \approx c_0$, i.e. no effect of the bubbles.

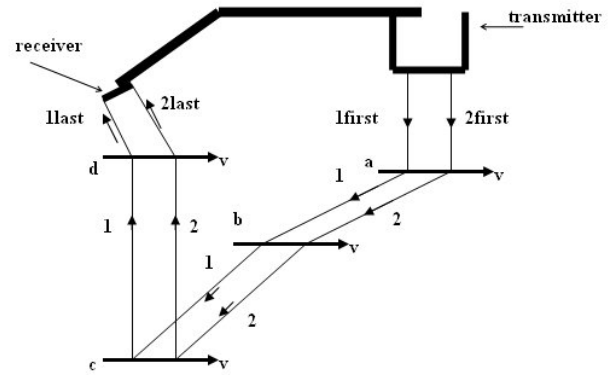


Figure 2. Hypothesis for the assumed multi-scattering process

Another test was performed with the rig and the ADV moved horizontally about 30 cm at a fairly constant speed along the pilot plant with the ADV emerged into the bubbly water. The output from the ADV was recorded giving movement time and the ADV-recorded mean velocity. This latter velocity was corrected for the slow, horizontal water velocity and comparison could then be made with the rig velocity. A clear water test showed that there was almost no difference between the two velocities. A general result was that the ADV velocity was smaller than the rig velocity consistently.

Tests with the ADV in bubbly water strongly indicated that the measurement point was dislocated to a point much closer to the transmitter. However, the operation of the ADV electronics - gating of the receivers to open only during the expected arrival of a pulse in normal conditions - meant that the acoustic waves could not propagate directly from the transmitter to the receiver horizontally (≈ 3 cm) but had to propagate about 10 cm. It was also found that the emitted pulses, although attenuated by the bubbles, were scattered in all directions in the neighbourhood of the transmitter. These facts strongly indicate that multi-scattering on the bubbles takes place for the acoustic waves propagating from the transmitter to the receiver. Fig 2 gives a very simplified illustration of the possible effect of multiple scattering – considering the operation of the ADV using pairs of pulses. Pulses 1 and 2 are emitted consecutively for the determination of the phase difference of the two pulses. Assume a homogeneous velocity field v . Pulse 1 is scattered on a number of single particles, a, b, c, d , and is detected in a direction defined by the very narrow directional properties of the receiver. Pulse 2 is emitted a very short time $\Delta t = 250 \mu\text{s}$ later and is scattered on the same set-up of

particles. During this time period a particle (bubble) with a typical maximum velocity of the order of 20 mm/s will move 5 μm , i.e. an extremely short distance. The very short time scale (250 μs) and the corresponding very small distance (5 μm), that a bubble passes, will most certainly mean, that the velocity for each bubble does not change during this time interval. This will in turn mean that the spatial bubble structure is the same for the two pulses and that the signals at the receiver – emanating from the two emitted pulses - are the result of the same multi-scattering process, i.e. involving the same set of particles/bubbles. Moreover, if the velocity field is exactly homogenous (not necessarily horizontal) the phase difference between the two detected pulses will be independent of the path and is only due to the path difference for the first leg ($1_{\text{first}} - 2_{\text{first}}$) from the transmitter and the last leg to the receiver ($1_{\text{last}} - 2_{\text{last}}$) and will be the same as for a scattering particle in the measurement volume for clear water.

A few factors could be assumed to affect the detected phase difference in reality:

- the velocity field is not homogeneous, which means that the total path difference will be influenced by small variations of velocity magnitudes and directions along the multiple scattering path
- the receiver might be sensitive to variations in the last leg of the path, i.e. the directional sensitivity of the receiver might be broadened

Moreover, if the measurement point is dislocated from 5 cm below the transmitter to only 1 cm from it, the flow velocity in this latter point might be disturbed by the probe, at least in certain flow situations and cause a reduction of the velocity as compared to the undisturbed case.

The general conclusion of the ADV performance, based on tests and mapping of the flow structure in the tank, was that the measurement point seemed to be very close to the transmitter and the horizontal velocities were underestimated but that velocity directions seemed to be more or less correct. As the real velocities were small one has to bear in mind that the ADV measured the movement of the bubbles, which were assumed to move with the water flow in the horizontal direction. Vertical ADV velocities were offset by the rise velocity of the bubbles (≈ 1 mm/s).

3 FLOW STRUCTURE IN THE FLOTATION TANK

The existence of micro bubbles in the flotation tank has two implications – generation of aggregates and influence on the flow structure. The latter aspect is strongly related to the DAF separation efficiency. Detailed ADV measurements were performed in the pilot plant of the average horizontal (v_x) and the vertical (v_z) velocities for different hydraulic loads (Q_i) and different dispersion flows (Q_d) but without particles/flocs in order to study possible flow structures and their characteristics. Flow velocities were mainly in the interval 0 – 2 cm/s (ADV). Averaging time was at least 300 s. The measurements were performed in the longitudinal center plane only. Three significantly different flow structures were identified:

- S1: the case with no bubbles or a sufficiently small Q_d giving a large, clockwise rotating flow, Fig 3
- S2: the case with sufficiently high Q_d but sufficiently small Q_i giving a stratified flow situation, Fig 4
- S3: the case with sufficiently high Q_i where the stratified flow situation broke down.

3.1 Flow structure S1

The flow structure in Fig 3 represents the case with $Q_i = 12$ m³/h, $Q_d = 0$ m³/h, i.e. no bubbles. Inflow takes place horizontally to the left at the top 16 cm.

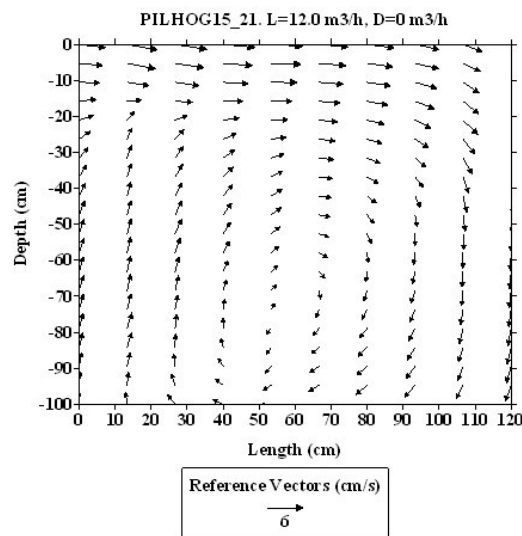


Figure 3. Case S1. ADV-determined flow structure in the pilot plant without any dispersion flow.

Outflow takes place at the bottom. The flow structure could basically be described as a large, clockwise eddy encompassing the entire tank. Particles/flocs entering the tank will be transported horizontally to the downstream wall and then vertically with fairly high velocities to the pipe outlet arrangement on the bottom, i.e. no good separation. The same flow situation will occur for small Q_d (< about 4 % of Q_l). A large amount of bubbles will thus also reach the bottom as the vertical downstream velocity is significantly larger than the bubble rise velocities.

3.2 Flow structure S2

The flow structure in Fig 4 represents the case with $Q_l = 10 \text{ m}^3/\text{h}$, $Q_d = 0.98 \text{ m}^3/\text{h}$, i.e. $Q_d \approx 10\%$ of Q_l . Inflow takes place horizontally to the left at the top 35 cm. Increasing Q_d from 0 to about 4 % of Q_l , maintaining Q_l constant, will abruptly change the flow structure from S1 to a stratified situation, S2, according to Fig 4, due to density differences given by different volumetric air contents. There is an upper, bubble-containing, less dense layer, where water moves horizontally towards the downstream wall. After that a horizontal return flow occurs, containing a less amount of bubbles. Beneath, a downward, bubble-free, denser plug-like flow with

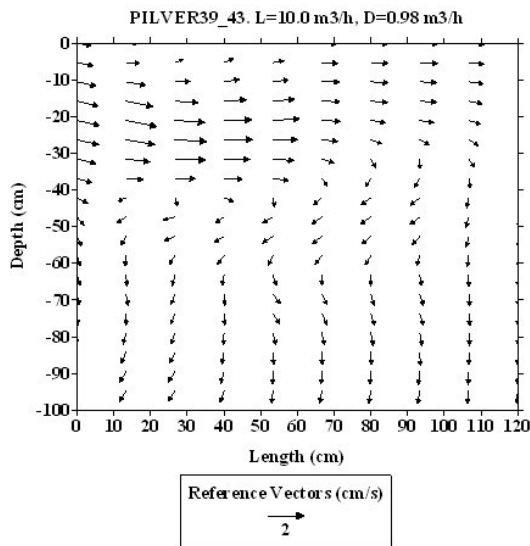


Figure 4. Case S2. ADV-determined flow structure in the pilot plant. $Q_d \approx 10\%$ of Q_l , $Q_l = 10 \text{ m}^3/\text{h}$

low velocities arises towards the outlet. Such a stratified situation is beneficial for the separation efficiency. Aggregates, bubbles and particles entering the tank will tend to stay in the upper layers as the vertical, downward velocities are small as

compared to S1 where a concentrated, vertical high-velocity region existed. Increasing Q_l will tend to extend the upper layer downwards, thus causing aggregates, particles and bubbles to approach the outlet arrangement with possible deteriorating separation.

3.2 Flow structure S3

Increasing the hydraulic load to $Q_l = 16.4 \text{ m}^3/\text{h}$ and with $Q_d = 1.45 \text{ m}^3/\text{h}$, i.e. $Q_d \approx 9\%$ of Q_l causes the stratified structure to break down and a “short-circuit” flow is obtained (not shown here due to lack of space) and aggregates, particles and bubbles will have a high probability of reaching the bottom outlet thus causing a deteriorating separation.

4 TRANSITION TO THE STRATIFIED CASE

The transition from rotational to stratified conditions in terms of hydraulic load and dispersion flow (i.e. the degree of density differences) were studied experimentally. The procedure was as follows. The ADV probe was located at the far end wall of the tank. A constant hydraulic load Q_l was applied with a very low dispersion flow Q_d which did not affect the flow structure. Q_d was then increased gradually to a steady-state value between 2 – 10 % of Q_l . The ADV vertical velocity was recorded simultaneously in order to determine the value of Q_d at the transition. This was characterized by an abrupt change of the vertical velocity. The procedure was repeated for a different Q_l . It was found that transition occurred for $Q_d \approx 4\%$ of Q_l in the studied interval $4.0 \leq Q_l \leq 12.3 \text{ m}^3/\text{h}$.

An explanation for the transition was put forward based on a balance between buoyancy and kinetic energy, Fig 5. In the rotational case a significant

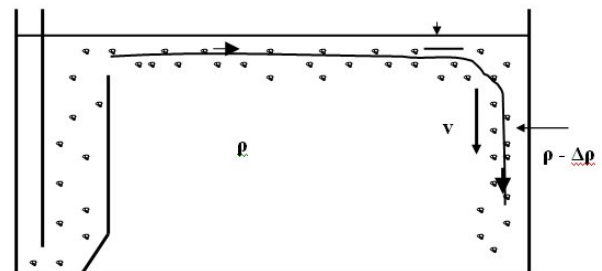


Fig 5. Definition sketch for the explanation of the transition to the stratified flow in the DAF tank

flow velocity v is obtained along the far end vertical wall. This represents a certain kinetic energy

$$E_k = \frac{\rho \cdot vol \cdot v^2}{2} \quad (2)$$

$$y \approx \frac{0.02^2 \cdot 10^3}{2 \cdot 1 \cdot 10} = 0.02 \text{ m}$$

for a water element with volume = vol. Assume that the rotational water contains a small amount of bubbles, volumetric content $m \text{ ‰}$, corresponding to a bulk water density $\rho - \Delta\rho$, and that the ambient water is free of bubbles, Fig 5. The buoyancy force, F_b , on the water element during its downward movement will be

$$F_b = \Delta\rho \cdot vol \cdot g \quad (3)$$

where $\Delta\rho$ is the density difference between the water element and the ambient water. Thus, if the kinetic energy is large enough the water element will be able to overcome the buoyancy force and reach the bottom of the tank. However, if the kinetic energy is not sufficiently large the flow will come to a standstill after some distance y along the vertical wall. Thus, in principle:

$$E_k = F_b \cdot y \quad (4)$$

which gives:

$$y = \frac{v^2 \cdot \rho}{2 \cdot \Delta\rho \cdot g} \quad (5)$$

During the starting phase of the pilot plant the hydraulic load rapidly reaches the steady state flow rate. However, the bubble generation in the dispersion flow is a rather gradual process meaning that the initial volumetric air concentration is very low, for instance of the order of 0.05 ‰ corresponding to $\Delta\rho \approx 0.05 \text{ kg/m}^3$. Assuming $v \approx 0.02 \text{ m/s}$ one obtains:

$$y \approx \frac{0.02^2 \cdot 10^3}{2 \cdot 0.05 \cdot 9.81} \approx 0.4 \text{ m}$$

In reality the buoyancy force will be smaller and probably not constant as the downward moving water element along the wall is not surrounded by clear water but with water containing a small amount of bubbles and consequently with a somewhat lower density, making $\Delta\rho$ smaller and y even larger. This implies that the bubble containing water element will pass along the vertical wall all the way to the bottom (outlet pipes) and the rotational structure will be maintained. When the dispersion water has been flowing for a while, its amount of bubbles increases very significantly and that goes for $\Delta\rho$ too. Thus for $m \approx 1 \text{ ‰}$ ($\Delta\rho \approx 1 \text{ kg/m}^3$) one obtains for y :

i.e. the downward flow will be stopped more or less abruptly, which is in qualitative agreement with visual observations and with ADV measurements of the downward velocity. A density induced barrier with fairly bubble-free water below it is formed, i.e. less dense water elements have not got sufficient kinetic energy to penetrate the barrier. $m \approx 1 - 5 \text{ ‰}$ means that the water elements are stopped almost immediately at the barrier. However, there is of course a continued supply of bubble-containing water to the barrier area, which means that this flow will be diverted horizontally towards the upstream part of the tank and an upper, bubble-containing layer is formed.

CONCLUSIONS

The ADV has been used in micro bubble containing water in a flotation tank, which potentially is a difficult environment for the instrument. However, reasonable velocity data were obtained, at least qualitatively. Direct measurements showed that the acoustic wave velocity was not affected by the bubbles, also confirmed by theory. A number of different tests indicated that velocity directions were fairly correct, whereas velocity magnitudes were underestimated. The measurement point seemed to be located very close to the transmitter. A possible explanation is hypothesized.

Three different kinds of flow structures were identified depending on the hydraulic load and/or the dispersion flow. Beneficial stratified flow conditions occurred for hydraulic loads less than about $16 \text{ m}^3/\text{h}$ and dispersion flow rates larger than 4 % of the hydraulic load.

Transition to stratified flow was studied experimentally and occurred at $Q_d \approx 4\%$ of Q_l . An explanation was provided based on the balance between buoyancy and kinetic energy.

REFERENCES

- [1] Jönsson, L: DAF pilot plant flow structure studies. Dep of Water Resources Engineering, Univ of Lund, Sweden. Report No 3251, 2006
- [2] Urick, R: Principles of Underwater Sound. Mc-Graw-Hill, 3rd ed. ISBN 0-07-066087-5, 1983

Development of ultrasonic streamflow monitoring system using an existing low head broad-crested agricultural small dam

Donggu Kim^{1*}, Chanjoo Lee², Won Kim²

¹ River & Coast Research Division, Korea Institute of Construction Technology, 2311 Daewha-dong Ilsanseo-gu, Goyang-si, Gyeonggi-do, Republic of Korea (*Corresponding author, e-mail: kimdg@kict.re.kr).

² River & Coast Research Division, Korea Institute of Construction Technology, 2311 Daewha-dong Ilsanseo-gu, Goyang-si, Gyeonggi-do, Republic of Korea

In this study, we developed a system of continuous accurate monitoring of streamflow, which is composed of a pair of ultrasonic Doppler velocity sensors installed on an existing low head broad-crested agricultural small dam. In case of using this dam, errors in computing area are minimized due to stability of it, so that discharge can be accurately measured. In addition, by direct measurement of velocity over dam crest, this system can measure discharge not only for modular flow in which free fall occurs, but also for submerged flow affected by downstream as far as depth and velocity are measured. Preliminary results for 15 dam release events display that discharge obtained by this system is in quite good agreement with dam release and with H-Q relationship. Comparison of volumetric discharge is also made and relative difference with dam discharge is 2.7%.

Keywords: Agricultural small dam, ultrasonic, discharge measurement

1 INTRODUCTION

In this study, we developed a system of continuous accurate monitoring of streamflow. This system is composed of stable cross-section provided by small dam and direct measurement of water velocity passing the crest of the dam. Discharge measurement in the natural river section is affected by instability or fluctuation of bed. On the contrary, this system uses pre-existing or newly made concrete finished small dams which give much more accurate cross-section area than normal riverbed. Since up-looking ultrasonic sensors installed upon the crest of the dam provide accurate vertical velocity profile, mean velocity can be computed. Real-time monitoring of discharge is possible by this system [1].

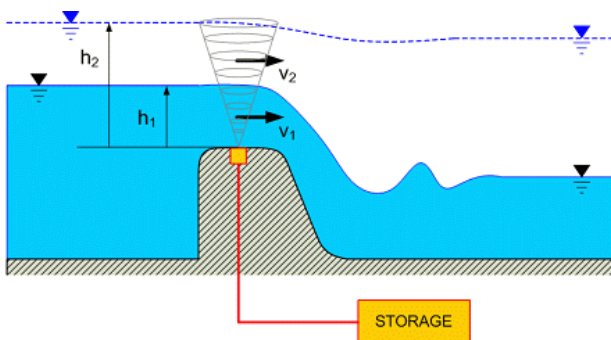


Figure 1: Conceptual view of the automatic velocity measurement system using the low-head broad-crested agricultural dam

2 OUTLINE OF THE SYSTEM

2.1 Composition of the system

The concept of the system is shown in Fig. 1. In the

system, ultrasonic sensors installed upon the dam crest measure both water velocity and depth. With use of separate pressure level sensors, flood flows of depth up to 10 m may be measured. Fig. 2 shows an ultrasonic velocity sensor and a data logger (model Q-Eye PSC made by German company Hydrovision) used in this study. General specification of the system is given in Tab. 1.



Figure 2: Ultrasonic velocity sensor (Q-Eye PSC)

Table 1: General specification of the sensor

Item	Specification
Velocity measurement	Ultrasonic Pulse Doppler
Water level measurement	Ultrasonic method
Sensor Frequency	1.04MHz
Sensor surface material	Polyurethane, Teflon
Range (velocity)	-6 ~ 6m/s
Range(water depth)	0.04~1.5m(~10m, optional)

The system is composed of three elements as below.

- ① A couple of single-beam / single-direction pulse Doppler velocity sensor installed at 20 m and 70 m from the right edge of a 130 m wide Daesu-bo (including water level sensor)
- ② A central controller unit
- ③ A field box (including data loggers, uninterrupted power supply, automatic recovery system, et.al.)

2.2 Installation of the system

This system is installed at the Dalcheon experiment river reach located near the center of South Korea. The experimental river is located near the center of Korea (South). It is about a 3.3 km long and stable cobble-bed river reach downstream of the Goesan dam. Catchment area of the reach is 675.2 km² at the Goesan dam. The river reach is an typical cobble-bed stream and its mean width is about 120 m and its bed slope is about 0.0015. Flow regime of the experiment river reach is entirely controlled by upstream dam other than natural hydrological condition. The dam supplies so wide range of reference discharge up to 1,400 m³/s during the rainy season that the inter-comparison of various kinds of discharge measurement methods is possible [2].

The ultrasonic measurement system is installed upon the Daesu-bo agricultural low-head broad-crested small dam located about 3 km downstream of the Goesan dam. Measured discharge by the system can be easily compared with existing stage (head)-discharge (H-Q) relationship exists. Properties of the Daesu-bo are shown in Tab. 2. Fig. 3 displays existing H-Q relationship [3].

Table 2: Properties of the Daesu-bo

Length	130m
Breadth of crest	1.5m
Type	Concrete type dam
Attachments	1 Fishway an 1 gate

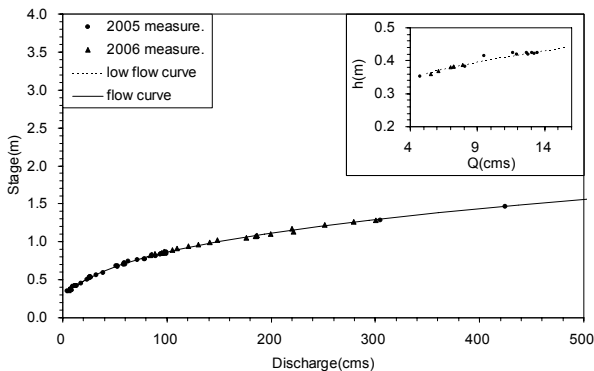


Figure 3: Existing H-Q relationship



Figure 4: Photo of the Daesu-bo viewing from downstream



Figure 5: Photo of the Daesu-bo viewing from upstream

3 RESULTS AND DISCUSSION

Using continuously recorded depth, velocity and discharge by the ultrasonic sensors, various analyses are conducted. At first, in order to test accuracy of depth and velocity measurement, comparison is performed with another water level and ultrasonic velocity meter. Inter-comparison of discharge is made with dam release, conventional velocity-area method and existing H-Q relationship. Since assessment of performance of the system is focused on discharge computation, resultant discharge values are mainly compared. Tab. 3 gives dam release events used for discharge comparison of preliminary test of this system.

Table 3: Dam release events for discharge comparison

Event No.	Dam release time	Peak discharge (m ³ /s)
1	2007-12-11 09:00~11:00	16.2
2	2007-12-11 16:00~19:00	16.3
3	2007-12-12 16:00~20:00	17.0
4	2007-12-13 13:00~19:00	17.0
5	2007-12-14 09:00~12:00	17.3

6	2007-12-15 14:00~17:00	17.2
7	2007-12-16 16:00~18:00	17.0
8	2007-12-18 11:00~13:00	15.8
9	2007-12-20 16:00~20:00	16.5
10	2007-12-21 17:00~19:00	16.4
11	2007-12-24 09:00~11:00	15.9
12	2007-12-24 17:00~19:00	16.5
13	2007-12-26 17:00~19:00	15.6
14	2007-12-27 17:00~19:00	14.9
15	2007-12-28 17:00~19:00	15.6

3.1 Discharge comparison with dam release

For each dam release event, computed discharge by the Q-Eye system is compared with dam discharge. Lag time and peak discharge are also examined. Since the system is located about 3 km downstream of the dam along the river reach, arrival (lag) time occurs according to discharge.

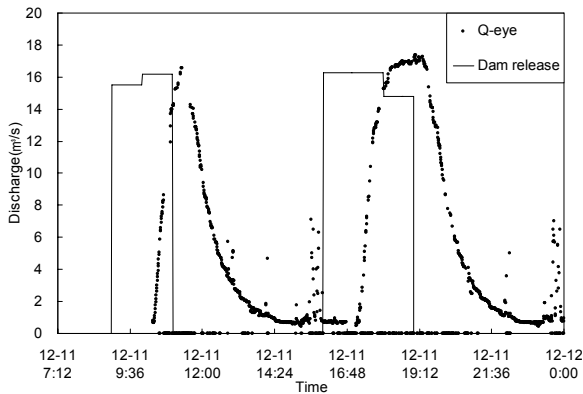


Figure 6: Comparison of discharge hydrograph by the dam and the system (Event 1, 2)

3.2 Discharge comparison with existing H-Q relationship

H-Q relationship upon the small dam is established based on its property as a control and discharge is calculated from the relationship. Consequently, loop phenomenon so hardly occurs that calculated discharge by it becomes more accurate than H-Q relationship of natural river section.

H-Q relationship is only available for free fall modular flow. But direct measurement of velocity over dam crest, this system can measure discharge not only for modular flow in which free fall occurs, but also for submerged flow affected by downstream as far as depth and velocity are measured.

3.3 Comparison of volumetric discharge

Discharge calculated by this system indicates fairly good agreement with dam release and H-Q relationship. In order to compare discharge by three methods more accurately, volumetric discharge for each release event is quantitatively evaluated. Since the Goesan dam releases water for hydroelectric

power generation for several hours and then in turn stops release, it is possible to calculate volumetric discharge for specific periods. Fig. 8 and Tab. 4 show comparison of volumetric discharge for two event occurring from 9 AM Dec. 11th. to 12 PM Dec. 12th. in 2007.

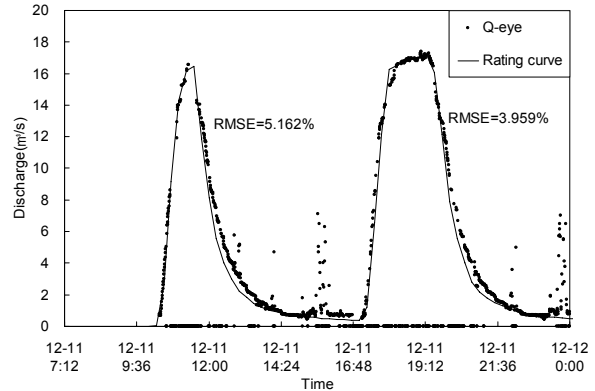


Figure 7: Comparison of discharge hydrograph by H-Q relationship and the system (Event 1, 2)

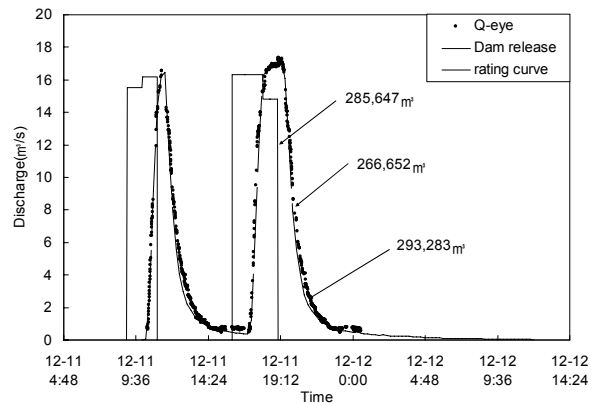


Figure 8: Comparison of volumetric discharge (Event 1, 2)

Table 4: Comparison of volumetric discharge (Event 1, 2)

Method	Volumetric discharge(m ³)	Relative difference (%)
Dam release	285,647	100.0
This system (Q-Eye)	293,283	102.7
H-Q relationship	266,652	93.3

4 CONCLUSIONS

This ultrasonic velocity measurement system is designed to measure wide range of discharge from low flow to high flood flow and it becomes possible by maintaining stable measurement section of dam crest and operating accurate velocity sensors. This system may also be applicable to open-channel sections of little bed change. Consequently, this system will be a practicable and economical method for measuring discharge at many other existing

agricultural small dam widespread in Korea. If the velocity sensor is installed beneath crest surface to reduce blanking distance, it is expected to measure low flow more accurately. Furthermore, if we can measure deep and fast flood flow with this system without any modification, it will be quite suitable solution for discharge monitoring. With a real-time data transfer system, real-time streamflow monitoring will be possible.

ACKNOWLEDGEMENT

This research was supported by a grant from Sustainable Water Resources Research Center (2-1-3) of 21st Century Frontier Research Program.

REFERENCES

- [1] Seo, JW: Ultrasonic Doppler flowmeter for flowmeter for waste drainage system, Monthly Mag. in Auto. Con. Mea. (2007)
- [2] Lee, CJ, Kim W, Kim CY, Kim DG: A comparative study on discharge measurement methods at a river downstream of a dam, Proc. HMEM2007 (2007)
- [3] MOST of Korean Government: Final report for technology for surface water investigation (2007)

Application of Linear Ultrasonic Array Transducer to Two-phase Flow Measurements

Hiroshige Kikura^{1*}, Takuya Hayashida², Daisuke Ito¹, Masanori Aritomi¹ and Michitsugu Mori³

¹Research Laboratory for Nuclear Reactors, Tokyo Institute of Technology, 2-12-1-N1-13 Ohokayama, Meguro-ku, Tokyo, 152-8550 Japan (*Corresponding author, e-mail: kikura@nr.ititech.ac.jp).

²Nomura Research Institute, 2-2-2 Otemachi, Chiyoda-ku, Tokyo, 100-0004 Japan

³Tokyo Electric Power Company, 4-1 Egasaki-cho, Tsurumi-ku, Yokohama, 230-8510 Japan

Velocity measurements using ultrasonic wave have attracted much attention in engineering fields. Especially, Ultrasonic velocity profiling (UVP) technique has been a focus of attention because of its many advantages. The major advantage is that UVP can obtain instantaneous velocity profiles on the beam line. Furthermore, UVP is easy to apply to existing pipes. The authors especially focused on two-phase flow measurements using UVP. This method can measure both the bubble rising velocity and the liquid velocity in bubbly flow. However this method is line measurement, and measuring cross sectional information remains a problem. In this paper, the authors applied an ultrasonic array transducer (array TDX) for two phase flow measurements. Array transducer has many ultrasonic elements on the same surface of the TDX. Using the array TDX, the cross-sectional velocity information was easily measured. In this study, the authors developed 128ch linear array TDX as an initial step. Then the authors applied the array TDX to co-current two-phase flow in a rectangular channel. The averaged bubble rising velocity and liquid velocity are measured on the cross sectional area. Then, the authors proposed the instantaneous velocity measurement method for two-phase flow using the multi-plexer mode of UVP monitor.

Keywords: Ultrasonic linear array transducer, gas-liquid two-phase flow, ultrasonic velocity profile measurement,

1 INTRODUCTION

Velocity measurements using pulse ultrasound have attracted much attention in engineering fields. Especially, Ultrasonic velocity profile (UVP) [1] monitor has been a focus of attention because of its many advantages. The major advantage is that UVP can obtain instantaneous velocity distributions on the ultrasonic beam line by measuring Doppler shift frequencies of echo signals. Furthermore, UVP measurement is easy to apply to existing pipes, because it is non-intrusive measurement. The authors especially focused on gas-liquid two-phase flow measurements using UVP technique. In the previous study, the measuring method of bubbly flow using UVP was proposed [2]. This method can measure both the bubble rising velocity and the liquid velocity. Since the bubble rising velocity is higher than the liquid velocity, the velocity PDF of bubbles is higher than that of liquid at any measuring position. However this method is the measurement along a measuring line, measuring cross-sectional information remained a problem.

In the previous study, it was shown that the UVP measurements with multiple measuring lines increase measuring accuracy. The ultrasonic flow rate measurement using three transducers (TDXs) can achieve higher accuracy than the measurement using one transducer in the asymmetric pipe flow [3]. Furthermore, for the flow rate measurement of the

flow with free surface, UVP measurement of cross-sectional flow was performed by using many TDXs [4]. They have shown that it is possible to do a high accuracy flow rate measurement. However due to the use of many sensors, several problems such as the setting errors of each sensor and limitation of the installation position may be exposed. So the objective of this study is to develop the ultrasonic array transducer (array TDX) for ultrasonic velocity profiling and to apply it to single phase flow and gas-liquid two phase flow measurements.

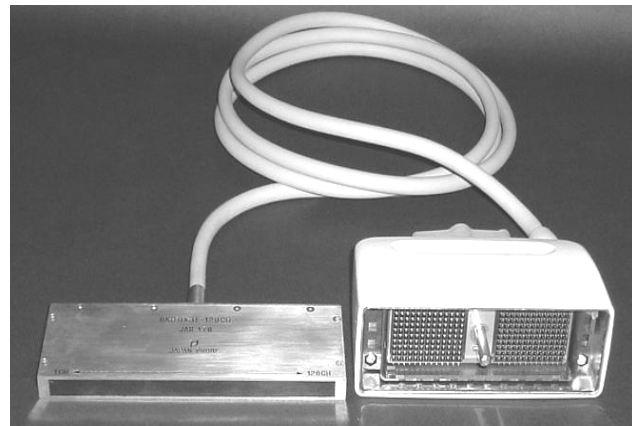


Figure 1: Ultrasonic linear array transducer

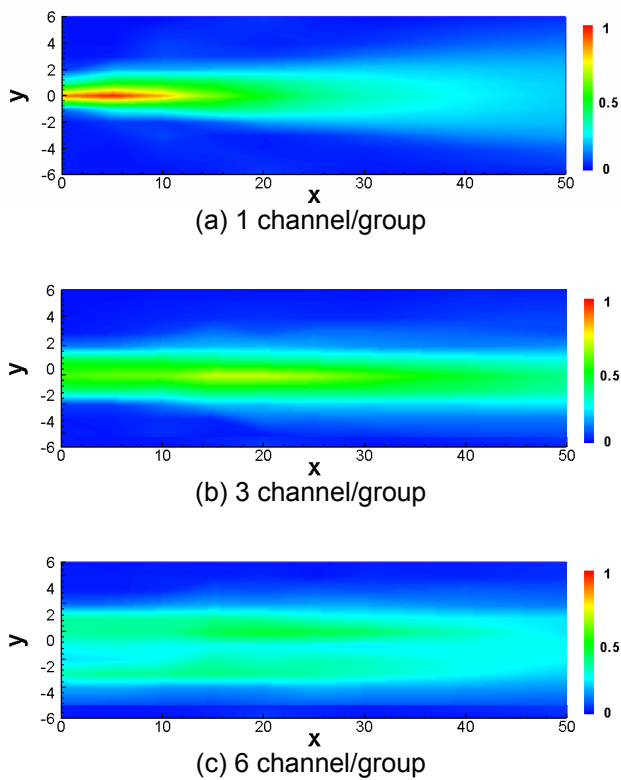


Figure 2: Sound pressure fields of transmitted pulse ultrasound

2 DEVELOPMENT OF LINEAR ULTRASONIC ALLAY TRANSDUCER

2.1 Ultrasonic array TDX for UVP

The ultrasonic array transducers have been applied in the medical diagnosis system and the nondestructive testing system. The authors focus on higher accuracy flow velocity profile measurement using ultrasonic array transducers.

The ultrasonic linear array transducer developed in this study is shown in Figure 1. It has 128 elements with $0.9 \times 3 \text{ mm}^2$, and the pitch of each element is 0.1 mm. So the total length of this TDX is about 128 mm and the spatial resolution of an element has 3 mm^2 . The basic frequency of these elements is 8 MHz.

2.2 Sound pressure field measurement

The sound pressure field of transmitted ultrasound is important from the aspect of the measurement volume, measuring area and reflected intensity. In this study, the sound pressure measurement is performed by the hydrophone technique. A hydrophone is traversed in the test region and it receives the electrical signals emitted from the TDX by the oscillator of the hydrophone. This technique can measure the time change of received signals and can apply to the transmitting path analysis of ultrasonic pulse. The measured

sound pressure

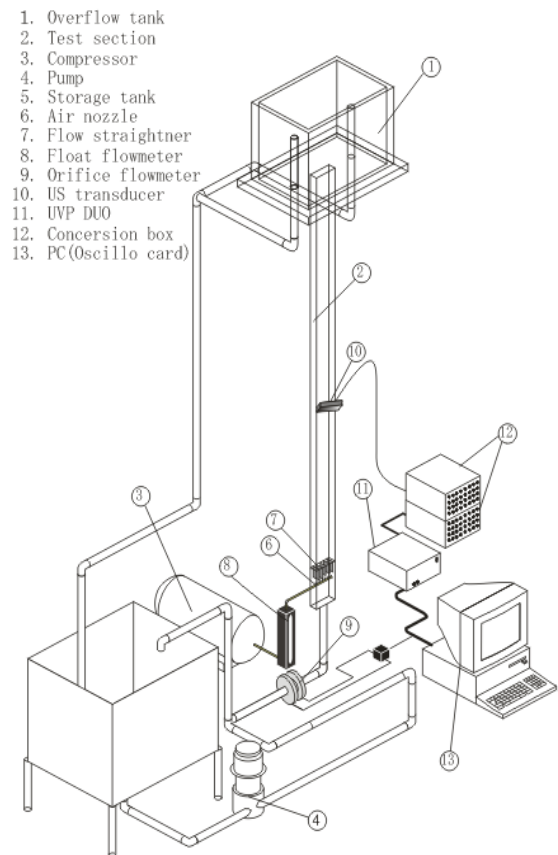


Figure 3: Experimental apparatus

distributions are shown in Figure 2. These figures show the grouping effect of the elements. In Figure 2(a), the sound pressure is higher up to $x = 10 \text{ mm}$ from the TDX surface, and the measuring volume is small. However the decrease of the sound pressure and the spreading of the ultrasonic beam are observed above $x = 10 \text{ mm}$. Thus it is better for the measurement in the near field. Figure 2(b) shows the result in the case of 3 channels per group. In $x = 10\text{-}30 \text{ mm}$, the sound pressure is larger. The spreading of the beam is less than the result of 1 channel/group, so it has good directionality. On the other hand, the measuring volume increases by about 2 mm in Figure 2(c). From this, the spatial resolution for velocity profile measurement decreases. The characteristics of transmitting pulse can be clarified by measuring the sound pressure field.

3 EXPERIMENTAL APPARATUS

The experimental apparatus consists of a water-air circulation system, a test section and a measurement system, as shown in Figure 3. Working fluids are water and air. Water flows into the tank through the valve, orifice flow meter and a flow straightener (0.5mm mesh stainless plate) by the pump. After water flows through the test section,

it overflows and goes back to the storage tank. Water temperature is kept around 20 degrees

hydraulic equivalent diameter is about 33 mm. To increase the ultrasonic transmission, the thickness

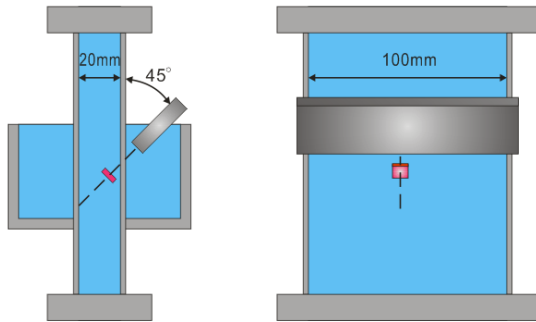


Figure 4: Installation of the transducer

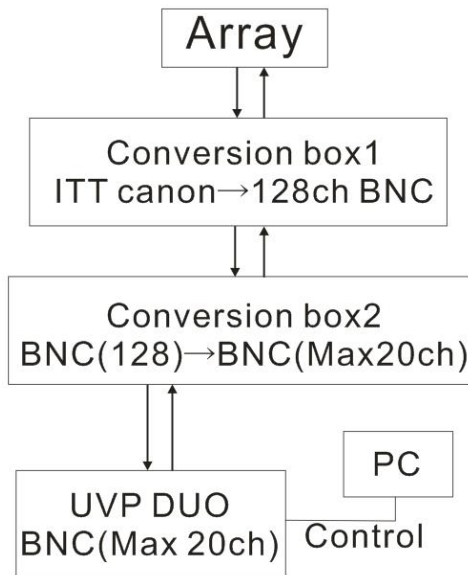
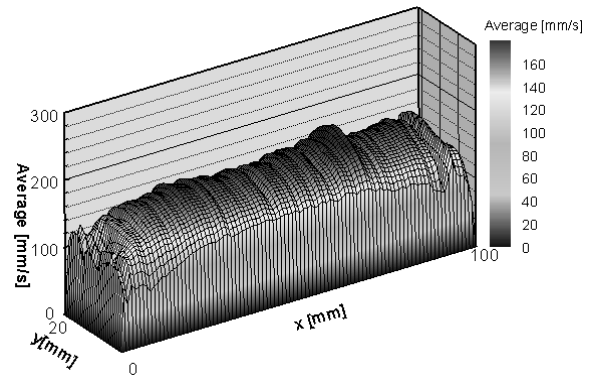


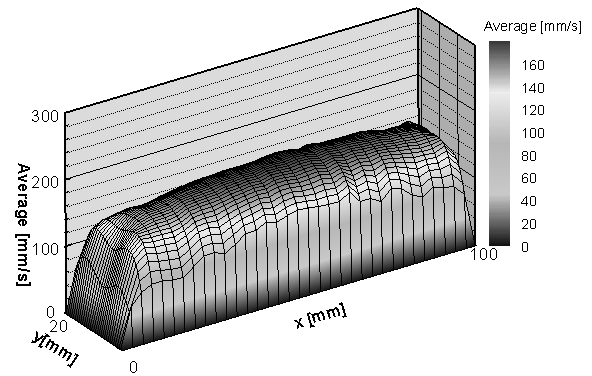
Figure 5: Ultrasonic array velocity profiling system

Celsius by a thermocouple. Air is supplied by a compressor. Air pressure is kept fixed by a control valve. Air flow quantity is measured by a laminar flow flowmeter. The system can supply air at appearance speed 50 mm/s under normal conditions. Air inlet is made of five metal needles set 100 mm below the flow straightener. The outer diameter of a needle is 2 mm and the hole diameter is 1mm. The tip of a needle is round to reduce influence on flow. All the needles are set in parallel to give same performances, and point upswing in mainstream direction of a flow.

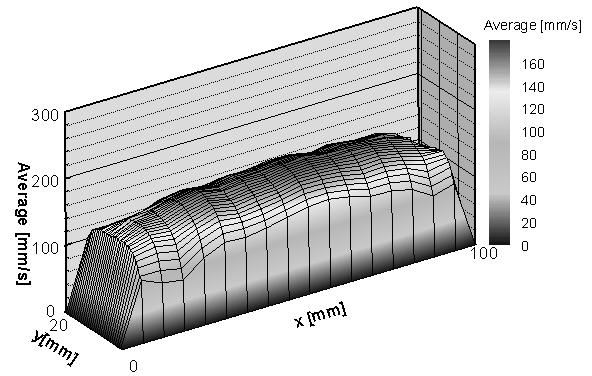
The test section is made of Plexiglas because the acoustic impedance of Plexiglas is almost the same as that of water, and it is also useful for image measurement. Then, we can compare the velocity profiles obtained by UVP with other measurements. The total length of the test section is 1800 mm and the cross section is rectangular, 20x100 mm. The



(a) 1 channel/group



(b) 3 channel/group



(c) 6 channel/group

Figure 6: Cross-sectional averaged velocity profiles in single phase flow

of the wall is 1 mm at the measuring section, and the incident angle of the ultrasonic array transducer is set 45 degrees, as shown in Figure 4. A water box is set next to the test section. Water is filled between the ultrasonic transducer and the wall of the test section. As an ultrasonic reflector, nylon powders with the diameter of 80 μm and specific gravity of 1.02 are used.

The measurement system consists of an

ultrasonic array transducer (Japan Probe Ltd), two conversion boxes, an UVP monitor and a PC, as shown in Figure 5. The array TDX is connected to

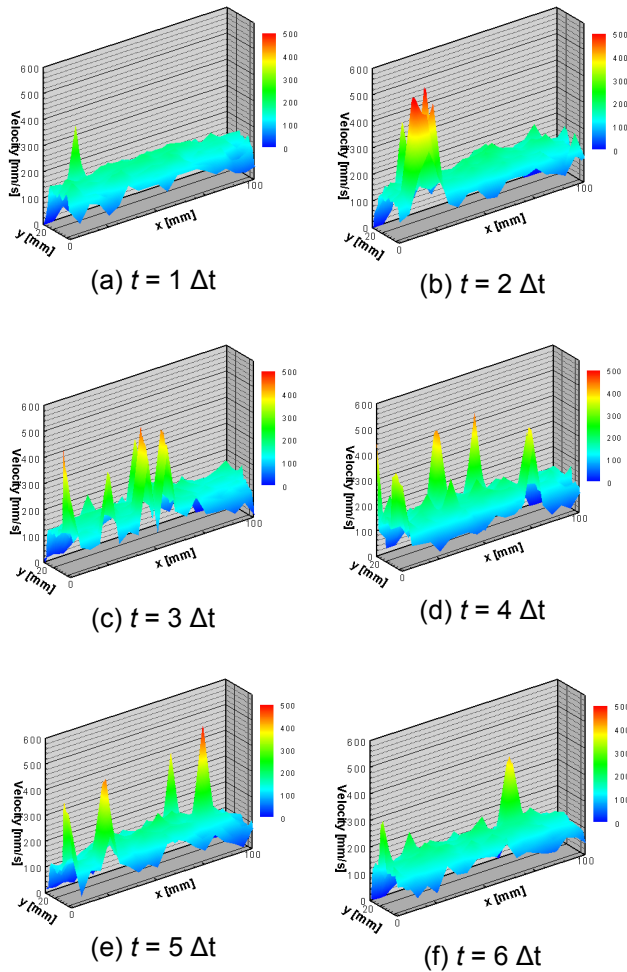


Figure 7: Cross-sectional velocity profiles in bubbly flow

the conversion box1 and all the connectors are converted to the BNC connectors. Then the elements are grouped by conversion box2. The sorted elements are connected to the UVP monitor and the velocity profiles are measured by normal mode for averaged profiles and multiplexer mode for instantaneous profiles.

4 RESULTS AND DISCUSSION

4.1 Single phase flow measurement

The cross-sectional averaged velocity profiles in single phase flow are shown in Figure 6. The grouping effect of elements is examined by measuring the averaged velocity profiles. It is shown that the flow fields can be visualized in the cross-section by using the array TDX. As an effect of grouping at 1 channel/group, the results on some measuring lines have small irregularity, due to the influence of the decrease of sound pressure and presence of noise. The velocity profile of 3channel/group can be understood the flow field.

Since the measurement volume is bigger, the totally averaged profile is obtained in the velocity profile of 6channel/group.

4.2 Two-phase flow measurement

The instantaneous velocity profiles of two-phase flow measurement are shown in Figure 7. Because the UVP monitor has a limitation of 20 channels to the maximum, the cross-sectional measurement of instantaneous velocity profiles needs to make the element grouping 5channel/group. When bubbles come to the measurement area, higher velocity information than the liquid velocity is obtained, and the location of the bubbles can be confirmed in the cross-section of the channel. However the measuring time of a cross-sectional profile (20 channels) is about 1 second, so it is difficult to understand the flow field instantaneously. The improvement of the system is required by faster repetition and using its own algorithm.

5 CONCLUSIONS

The ultrasonic linear array transducer for velocity profile measurement was developed. The array transducer was applied to the averaged velocity profile measurement of single phase flow and the instantaneous velocity measurement of two-phase bubbly flow. The possibility of the high accuracy velocity profile measurement of gas-liquid two-phase flow was shown.

REFERENCES

- [1] Takeda Y.: Velocity profile measurement by ultrasonic Doppler shift method, *Int. J. Heat Fluid Flow* 7 (1986) 313-318.
- [2] Suzuki Y., *et al.*: Microstructure of the flow field around a bubble in counter-current bubbly flow, *Exp. Therm. Fluid Sci.* 26 (2002) 221-227.
- [3] Wada S, *et al.*: Development of pulse ultrasonic Doppler method for flow rate measurement in power plant (Multilines flow rate measurement on metal pipe), *J. Nucl. Sci. Tech.* 41-3 (2004) 339-346.
- [4] Arimatsu T., *et al.*: Development of flow rate measurement on open channel flow using ultrasonic doppler method, *Proc. ISUD4* (2004) 33-36.

Rheological characterisation of highly concentrated mineral suspensions using an ultrasonic velocity profiler

Reinhardt Kotzé*, Rainer Haldenwang and Paul Slatter

Institute for Material Science and Technology (IMST), Cape Peninsula University of Technology, PO Box 652, Cape Town, South Africa (*Corresponding author, e-mail: reinhardtkotze@yahoo.com).

In this research, Ultrasonic Velocity Profiling (UVP), combined with pressure difference (PD) measurement, is experimentally evaluated for the in-line rheological characterisation of different concentrations of opaque non-Newtonian mineral slurries. A unique tube viscometer was designed and constructed. It consisted of four pipes, one of stainless steel and three of PVC, linked to an in-line mass-flow meter and equipped with two different ranges of pressure transducers on each pipe. The stainless steel pipe, with an inner diameter of 16 mm, was equipped with a specially designed flow adapter for in-line rheological characterisation using the UVP-PD method. The three PVC pipes with internal diameters of 9 mm, 13 mm and 16 mm served as a tube viscometer for in-line rheological characterisation of the mineral suspensions. Results determined by the UVP-PD method were compared with results obtained by off-line rheometry and in-line tube viscometry. The agreement between the UVP-PD method, tube viscometry and conventional rheometry was found to be good (within 15 %) for all of the highly concentrated mineral suspensions investigated over a given range of shear rates. This method has been found to have significant potential for the development of new in-line rheometer technology for process control within the mining industry.

Keywords: ultrasound, UVP-PD method, tube viscometry, non-Newtonian, rheology.

1 INTRODUCTION

The rheological behaviour of non-Newtonian, highly concentrated and opaque fluids used in industry have so far been analysed using commercially available instruments, such as conventional rotational rheometers and tube viscometers. Certain authors believe that tube viscometers are best suited for this specific application as they are geometrically similar to a pipeline [1]. However, tube viscometry is time-consuming and design engineers do not have the luxury of unlimited time to entertain the diversities of experimental research [1-2]. The development and adaptation of the UVP-PD technique has given engineers and scientists in the mining engineering field a new tool to investigate the industrial flow process behaviour of these fluids [3-9]. This method was successfully tested on a wide variety of industrial and model suspensions in the food industry [6-9]. It has been shown that ultrasonic propagation through these complex mineral suspensions is indeed possible [10-12]. The main objective of this paper is to evaluate the capabilities of the UVP-PD technique for rheological characterisation of different concentrations of opaque non-Newtonian slurries.

2 LITERATURE STUDY

2.1 UVP-PD technique

Takeda [3] developed a new ultrasonic velocity profile method for mechanical measurements of fluids in physics and engineering. It uses pulsed

ultrasonic echography together with the detection of the instantaneous Doppler shift frequency. This method was originally developed in medical engineering to measure blood flow by means of Doppler sonography during the 1960's [13]. A detailed description and working principle of the UVP monitor can be found in Jensen [14] and Met-Flow SA [15]. The UVP-PD set-up and method was developed in Erlangen, Germany by Steger and Muller [4-5]. This concept is based on the Ultrasound Pulsed Echo Doppler Velocity Profile technique (UVP), in combination with a pressure difference method (PD). Ouriev [6] further developed the in-line ultrasound-based rheometer, which was further modified and optimised by Birkhofer and Wiklund [7-9].

2.2 Tube viscometry

A tube viscometer is in essence a small diameter pipeline and therefore geometrically similar to a pipe [2]. The test fluid flows at a measured flow rate through the tube and the pressure drop ΔP is measured between two fixed points L m apart in the pipe. The relationship between the wall shear stress τ_w and the volumetric flow rate Q and the shear stress τ is as follows [16]:

$$\frac{Q}{\pi R^3} = \frac{8V}{D} \frac{1}{\tau_w^3} \int_0^{\tau_w} \tau^2 f(\tau) d\tau, \quad (1)$$

where $\tau_w = \frac{R}{2} \left(-\frac{\Delta P}{L} \right)$ and $\left(-\frac{\Delta P}{L} \right)$ is equal to the pressure drop per unit length of tube. The shear

stress at any radius r is:

$$\tau = \frac{r}{2} \left(-\frac{\Delta P}{L} \right). \quad (2)$$

A plot of $8V/D$ vs τ_w will give a unique line for a given material for all values of R and $\left(-\frac{\Delta P}{L} \right)$ in laminar flow. This also provides confirmation of the assumption that the time dependent properties of the fluids tested are not significant. The problem with tube viscometry is that $8V/D$ is not the true shear rate but the wall shear rate for a Newtonian fluid, therefore this “pseudo” shear rate has to be transformed to the true shear rate at the wall, $\dot{\gamma}_w$, by using the Rabinowitsch-Mooney transformation procedure for tube viscometer data [16].

2.3 Rheological characterisation

The equation for the Herschel-Bulkley model is as follows:

$$\tau = \tau_y + K(\dot{\gamma})^n, \quad (3)$$

where K , n and τ_y are three empirical curve-fitting parameters and are known as the fluid consistency index, the flow behaviour index and the yield stress respectively [16]. Eqs. 2 and 3 can be combined and integrated to give the radial velocity profile:

$$v = \left(\frac{n}{1+n} \right) \left(\frac{\Delta P}{2LK} \right)^{\frac{1}{n}} \dots \left((R - R_{plug})^{1+\frac{1}{n}} - (r - R_{plug})^{1+\frac{1}{n}} \right), \quad (4)$$

where $R_{plug} = \frac{2L\tau_y}{\Delta P}$ is the plug radius [9]. It will be noted that the Herschel-Bulkley model can easily be modified to describe the power-law and Bingham plastic models.

3 EXPERIMENTAL PROCEDURES

3.1 UVP-PD setup

The schematic layout of the experimental UVP-PD flow loop is shown in Fig. 1. A special flow adapter for repeatable and stable positioning of ultrasound transducers was designed and manufactured. The flow adapter cell was designed for simultaneous measurements of velocity profiles and velocity of sound in-line. More information on this particular design of flow adapter and transducer setup can be found in Birkhofer [7] and Wiklund [8]. Ultrasound transducers (TN and TX-line, Imasonic, France) together with the latest UVP instrument (UVP-Duo-MX, Met-Flow SA, Lausanne, Switzerland) were used for velocity profile measurements. Special software was developed in MATLAB® to fit theoretical velocity profiles to experimental data and determine

rheological parameters.

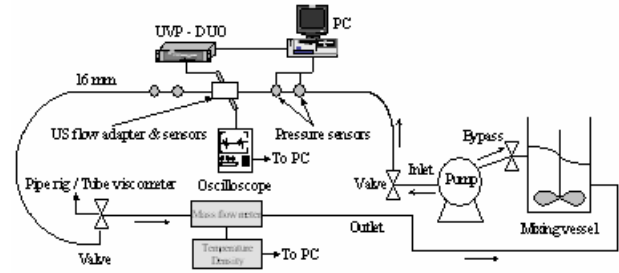


Figure 1: Schematic illustration of the UVP-PD flow loop

The experimental UVP-PD flow loop forms part of a specially designed tube viscometer.

3.2 Tube viscometer

A unique portable pipe rig was constructed at the IMST and is described in detail by Kotzé [17]. The pipe rig consisted of a progressive cavity positive displacement pump with variable speed drive which was fed through a damper to minimize pump pulsations to three PVC tubes and one stainless steel pipe. Three PVC tubes were used as an in-line pipe viscometer. The stainless steel pipe (16 mm) was used to measure rheological parameters in-line by using the UVP-PD method. The PVC tubes were in parallel and had 16, 9 and 13 mm inner diameters respectively. All of the pipes were linked to an in-line mass-flow meter (Danfoss, Cape Town, South Africa), which also measures fluid temperature and density. The mixing tank had a capacity of 250 l and was fitted with an electrically driven mixer that ran continuously during tests. Differential pressure was measured by two high range (0-10 bar) and low range (0-1 bar) point pressure transducers (S-11, WIKA, Cape Town, South Africa).

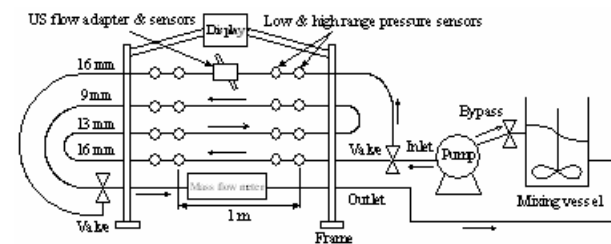


Figure 2: Pipe rig layout

All the outputs of the pressure transducers and the mass-flow meter were connected to a data acquisition unit (μ DAQ, Eagle Technologies, Cape Town, South Africa) linked to a personal computer (PC). The schematic layout of the above is shown in Fig. 2.

3.3 Rotary Viscometer

Rheological parameters were also obtained from flow curves measured with a Paar Physica MCR300 rheometer equipped with an air bearing. The cup and roughened bob geometry was used for testing.

3.4 Materials tested

Two model mineral suspensions were tested namely bentonite (Protea Chemicals, Cape Town, South Africa) and kaolin (Serina Kaolin, Cape Town, South Africa). Water was selected for calibration purposes. Bentonite 7 % w/w with a d_{85} of about 25 μm was selected as the Bingham plastic model fluid. The yield pseudoplastic mineral suspension selected was kaolin clay 12 % v/v with a d_{85} of about 35 μm .

4 RESULTS AND DISCUSSIONS

4.1 Bentonite 7 % w/w

An experimental velocity profile along the pipe diameter for bentonite 7 % w/w (density $\rho = 1044 \text{ kg/m}^3$, velocity of sound $c = 1560 \text{ m/s}$) measured by the in-line UVP-PD method is shown in Fig. 3. These are represented by the theoretical profile obtained by fitting the experimental data and pressure drop using the Bingham plastic model. The flow is laminar, since the value of the Reynolds number is equal to 742 [18], validating the use of the theoretical point velocity distribution equations. The volumetric flow rate obtained from integration of the measured velocity profile equals 0.456 l/s and differs by 11 % when compared to the flow rate obtained from the mass-flow meter (0.411 l/s).

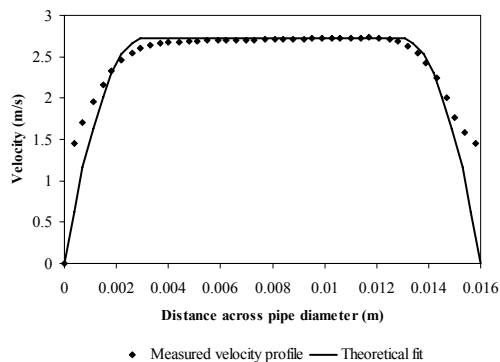


Figure 3: Experimental and theoretical velocity profile for bentonite 7 % w/w

Bentonite suspensions showed little attenuation and absorption of ultrasonic energy and thus the acoustic energy could penetrate across the whole pipe diameter. The end results or flow curves obtained from off-line conventional rheometry and in-line tube viscometry, as well as determined by the in-line UVP-PD rheometric method, are displayed in Fig. 4. Error curves are $\pm 15\%$ error deviations from the UVP-PD flow curve. Results obtained from the tube viscometer and conventional rheometer show good agreement when compared with each other over the shear rate range. The UVP-PD method shows lower apparent viscosities when compared to those determined from the other two rheological methods. However, results show a 15 % agreement when apparent viscosities obtained from all three methods, are compared.

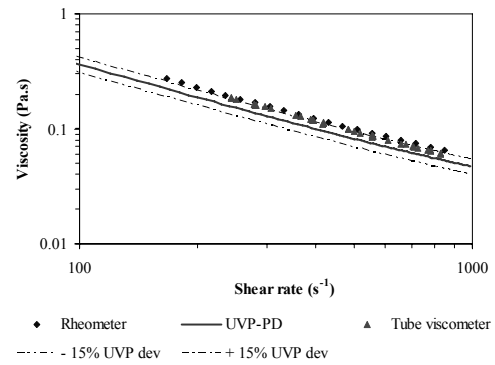


Figure 4: Variation with shear rate in viscosity for bentonite 7 % w/w

4.2 Kaolin 12 % v/v

Experimental and theoretical velocity profile for kaolin 12 % (density $\rho = 1198 \text{ kg/m}^3$, velocity of sound $c = 1555 \text{ m/s}$) is shown in Fig. 5. The flow is laminar (Reynolds number = 601) validating the use of theoretical Herschel-Bulkley models.

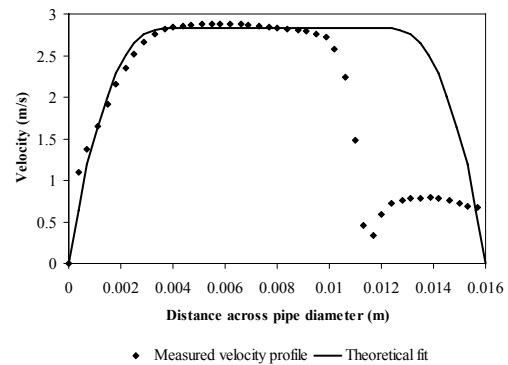


Figure 5: Experimental and theoretical velocity profile for kaolin 12 % v/v

The volumetric flow rate determined by integration is equal to 0.471 l/s and differs by 7 % when compared to the measured flow rate (0.44 l/s). Kaolin mineral suspensions attenuated the ultrasonic energy significantly more than when compared to bentonite suspensions. The effect of ultrasonic attenuation on velocity profile measurements can be observed in Fig. 5. Here the experimental profile starts to distort after the pipe radius (8 mm). In this case the penetration depth was significantly reduced due to ultrasonic attenuation. However, only half of the velocity profile is required for obtaining rheological parameters. The attenuation and absorption of ultrasound energy increased as the solids concentrations of the kaolin mineral suspensions increased and was also observed by Chen et al. [12] and Kotzé [17]. Fig. 6 shows the summary of rheological results obtained from three different methods. Results are in good agreement (within 15 %) with each other across the whole shear rate region (100 to 1000 s^{-1}).

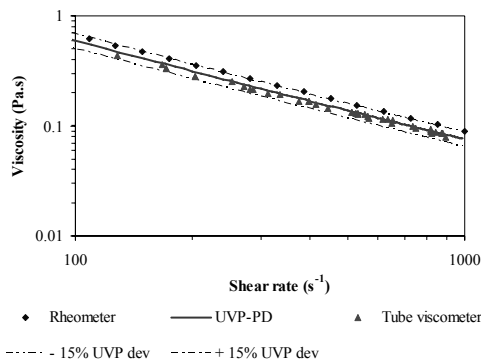


Figure 5: Variation with shear rate in viscosity for kaolin 12 % v/v

Tab. 1 shows mathematically determined rheological parameters from curve fitting for the above model mineral suspensions.

Table 1: Rheological parameters obtained from three different methods for bentonite and kaolin

Fluid	Parameters	UVP-PD	Tube viscometer	Rheometer
Bentonite 7 %	K (Pa.s)	0.0116	0.0089	0.0145
	n	1	1	1
	τ_y (Pa)	35.15	43.14	42.86
Kaolin 12 %	K (Pa.s)	1.32	0.62	3.52
	n	0.43	0.57	0.36
	τ_y (Pa)	49.94	46.15	47.30

5 CONCLUSIONS

The capabilities of the UVP-PD technique for the rheological characterisation of different concentrations of non-Newtonian slurries have been evaluated. Results were found to be in good agreement (within 15 %) when compared with those obtained by off-line rheometry and in-line tube viscometry. The UVP-PD rheometric method can be used effectively for in-line rheological characterisation of highly concentrated mineral suspensions and has been found to have significant potential for the development of new in-line rheometers for process control within the mining and minerals industry.

ACKNOWLEDGEMENT

The National Research Foundation of South Africa (NRF) and the Cape Peninsula University of Technology (CPUT) for funding.

REFERENCES

[1] Lazarus, J.H. & Slatter, P.T. 1988. A method for the rheological characterisation of tube viscometer data. *Journal of pipelines*, V7:165-176.
 [2] Haldenwang, R., Slatter, P., Alderman, N., Kotzé, R., Sery, G. & George, N. 2006. Balanced Beam Tube

Viscometry vs Rotary Viscometry: A Comparison. *12th International Conference on Transport and Sedimentation of Solid Particles*, Tbilisi, Georgia. 12:145-156.

[3] Takeda, Y. 1986. Velocity Profile Measurement by Ultrasound Doppler Shift Method. *Int. J. Heat Fluid Flow*, 7(4):313-318.

[4] Steger, R. 1994. *Optisch und Akustische Methoden in Der Rheometrie*. Erlangen: University of Erlangen: 1-100.

[5] Müller, M., Brunn, P.O. & Wunderlich, T. 1997. New Rheometric Technique: the Gradient-Ultrasound Pulse Doppler Method. *Applied Rheology*, 7:204-210.

[6] Ouriev, B. 2000. *Ultrasound Doppler Based In-Line Rheometry of Highly Concentrated Suspensions*. ETH dissertation No. 13523, ISBN 3-905609-11-8. Zurich, Switzerland.

[7] Birkhofer, B. H. 2007. *Ultrasonic In-Line Characterization of Suspensions*. Laboratory of Food Process Engineering, Institute of Food Science and Nutrition, Swiss Federal Institute of Technology (ETH), Zurich, Switzerland. ISBN 978-3-905609-34-7.

[8] Wiklund, J. 2007. *Ultrasound Doppler Based In-Line Rheometry: Development, Validation and Application*. SIK – The Swedish Institute for Food and Biotechnology, Lund University, Sweden. ISBN 978-91-628-7025-6.

[9] Wiklund, J., Shahram, I. & Stading, M. 2007. Methodology for in-line rheology by ultrasound Doppler velocity profiling and pressure difference techniques. *Chemical Engineering Science*, 62(16), August 2007:4159-4500.

[10] Besq, A., Monnet, P. & Pantet, A. 2001. Flow situations of drilling muds: effects of thixotropic property. *Proceedings of the 6th Triennial International Symposium on Flow Control, Measurement and Flow Visualization*, Sherbrooke (Qc), Canada, 13-17 August 2000.

[11] Haldenwang, R., Kotzé, R., Slatter, P.T. & Mariette, O. 2006. An Investigation in Using UVP for assisting in Rheological characterisation of Mineral Suspensions. *Proceedings of the 5th International Symposium on Ultrasonic Doppler Methods for Fluid Mechanics and Fluid Engineering*, Zurich, Switzerland, 12-14 September 2006. ISUD5:77-79.

[12] Chen, A.Q., Freear, S. & Cowell, D.M.J. 2007. Measurement of Solid in Liquid Content Using Ultrasound Attenuation. *5th World Congress on Industrial Process Tomography*, Bergen, Norway, 3-6 September 2007. 5:820-826.

[13] Kuttruff, H. 1991. *Ultrasonics: Fundamentals and Applications*. London and New York: Elsevier Applied Science.

[14] Jensen, J.A. 1996. *Estimation of Blood Velocities Using Ultrasound: A Signal Processing Approach*. Great Britain: Cambridge University Press. ISBN 0-521-46484-6.

[15] Met-Flow SA. 2002. UVP Monitor – Model UVP-DUO User's Guide. Software version 3. Met-Flow SA, Lausanne, Switzerland.

[16] Chhabra, R.P. & Richardson, J.F. 1999. *Non-Newtonian Flow in the Process Industries*. Oxford, Great Britain: Butterworth-Heinemann.

[17] Kotzé, R. 2008. Rheological Characterisation of Highly Concentrated Mineral Suspensions using an Ultrasonic Velocity Profiler. Unpublished M. Tech thesis. Cape Peninsula University of Technology, Cape Town, South Africa.

[18] Slatter, P.T. 1999. The role of rheology in the pipelining of mineral slurries. *Min. Pro. Ext. Met. Rev.* 20:281-300.

Numerical prediction of compound channel flow in comparison with ultrasonic Doppler method measurement

Jan Krupicka^{1*}, Vojtech Bares², Jakub Jirak², Petr Sklenar¹

¹Department of Hydraulics and Hydrology, CTU Prague, Thakurova 7, 166 29 Prague, Czech Republic (*Corresponding author, e-mail: jan.krupicka@fsv.cvut.cz).

²Department of Sanitary and Ecological Engineering, CTU Prague, Thakurova 7, 166 29 Prague, Czech Republic.

Determination of cross section flow capacity and depth-averaged velocity distribution are prevailing tasks of river hydraulics. Lateral Distribution Method (LDM) is one of the more sophisticated approaches proposed during the last few decades and belongs to the so-called 1,5D methods. Numerical solution of governing equation using FEM leads to the depth averaged velocity profile. The subject of our study is to evaluate potential benefit of the LDM applied under the circumstances of non-uniform flow using data obtained by Ultrasonic Velocity Profiling (UVP) method. Experiments were undertaken on the model of river reach with the non-prismatic compound channel. UVP was used to determine point velocities in selected gauging cross-sections. Three inclined probes enabled estimation of all three velocity vector components. Depth averaged velocities and total discharge were obtained integrating the point velocities. Discharge exchange between main channel and flood plains was identified as the prevailing source of the secondary currents with the clear effect on the main flow velocity distribution. Comparison of experimental and numerical simulation results showed great potential of LDM for the practical calculations of compound channel flow even under non-uniform flow conditions. UVP seems to be highly reliable and applicable to velocity field measurement in open channels.

Keywords: Velocity profile, compound channel flow, ultrasonic Doppler method, numerical simulation.

1 INTRODUCTION

For practical purposes, one dimensional modeling is still the prevailing approach to the tasks of river mechanics. As a component of the classical step-by-step method, cross section flow capacity has to be evaluated. Moreover, accurate prediction of the velocity distribution over a channel cross section is essential for flood risk assessment as well as for sediment transport and channel stability evaluation. Predictions of the usual computational methods are fallible especially in the case of heterogeneous velocity distribution which is typical of the compound channels. Better results can be obtained if momentum transfer in transverse direction is involved in numerical model. This is the case of so-called 1,5D or 1D+ methods which Lateral Distribution Method (LDM) belongs to.

LDM was introduced more than twenty years ago, but it has not become widely employed in practical computations yet. Benefit of LDM applied under the uniform flow condition is clear (see e.g. [1,2]). The object of presented study was to verify usability of LDM for depth-averaged velocity profile computation if non-uniform flow occurs.

2 NUMERICAL SIMULATION

As mentioned previously, LDM deals with momentum transfer in direction transversal to the main flow. Governing equation can be derived (see [3] for details) from depth-averaged Reynolds

equation assuming uniform flow. Empirical or semi empirical model has to be adopted for turbulent stress and secondary currents term. According to [4], governing equation of the LDM can be written in the form of:

$$gHI_0 - \frac{f}{8}U^2\sqrt{1+I_{y0}^2} + \frac{\partial}{\partial y}\left(H^2\frac{\lambda}{2}\sqrt{\frac{f}{8}}\frac{\partial U^2}{\partial y}\right) = \Gamma. \quad (1)$$

Here y is the lateral direction coordinate, U is the depth-averaged velocity in the main flow direction, H is the depth, f is the friction factor, I_0 is the bottom slope in the main flow direction, I_{y0} is the bottom slope in the lateral direction and λ and Γ are the model parameters. The first term on the left side is gravity term followed by bottom shear term and turbulent shear term in vertical. The right side represents secondary flow term. Finite element method was employed to solve Eq. (1) (to find $U(y)$).

3 EXPERIMENTAL SETUP

3.1 Physical model

Experiments were performed on the model of left-handed reach of the Trebovka River (Fig. 1). The Thomson weir with a stilling box and the model were integrated into the hydraulic circuit of laboratory of CTU in Prague. The length of model was 8,2 m and width 1,2 – 2,0 m (scale 1:40). Compound channel cross section consisted of two flood plains with variable width and main channel of trapezoidal and rectangular shape. Roughness of concrete surface of the model was increased in floodplains to ensure

heterogeneous velocity distribution. Discharge of 48.8 l/s was hold for all experiments, corresponding water depth was 50 ± 150 mm.

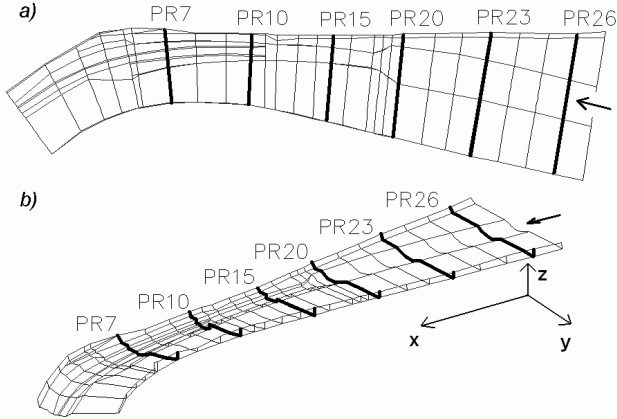


Figure 1: Physical model of Trebovka River. Gauging cross sections highlighted. a) Plan. b) Axonometric view.

3.2 Velocity measurement

Detail velocity distribution was investigated in six gauging cross sections (Fig. 1) using UVP monitor [6]. As UVP monitor provides only radial velocity component V_R (i.e. in direction of ultrasonic transducer axe), three independent probes P_1 , P_2 and P_3 were employed to enable all three velocity component evaluation. Probes were fixed in special movable box and inclined from vertical at an angle $\theta = 25^\circ$ (Fig. 2). Inner space of the box was filled with water and separated from flow by PVC foil 0,1 mm thin. As there is a minimum distance from probe, where measuring window can start, spacing of 25 mm was set between probes and foil. Thus, if the box was vertically positioned to foil just touched water surface, minimal disturbance was introduced into measured velocity field and measurement window covered entire water depth. To improve signal/noise rate, PVC reflection solids ($\rho = 1350 \text{ kg/m}^3$, $d = 100 \mu\text{m}$) were supplied to the flow.

After the box with probes was positioned at the required vertical in actual cross section, velocity profiles in the probes axes direction were measured (sampling period $t = 60 \text{ ms}$, number of samples $n = 1000$). Then, the box was moved to next vertical in 50 mm distance.

3.3 Other measurements

Thomson weir was used to discharge measurement. Model geometry and water surface profile were obtained using point gauge.

4 EXPERIMENTAL DATA EVALUATION

Equations relating velocity vectors components measured in probes axes direction V_{Rj} ($j = 1, 2, 3$) and components u_j, v_j, w_j in x, y, z direction can be derived from (Fig 2.):

$$V_{R1} = u_1 \sin \theta - w_1 \cos \theta \quad (2a)$$

$$V_{R2} = -u_2 \sin \theta - w_2 \cos \theta \quad (2b)$$

$$V_{R3} = -v_3 \sin \theta - w_3 \cos \theta \quad (2c)$$

Following assumptions are necessary for evaluation of velocity vector components u, v, w :

- Only time averaged velocity is evaluated.
- Longitudinal slope of water surface and probes distance $\Delta L = 51 \text{ mm}$ are so small, that for u and v at the same vertical position it is possible to write:

$$\bar{u}_1 \equiv \bar{u}_2; \bar{w}_1 \equiv \bar{w}_2 \quad (3)$$

In fact, Eqs. 3 are satisfied only for the point of the probes axes intersection.

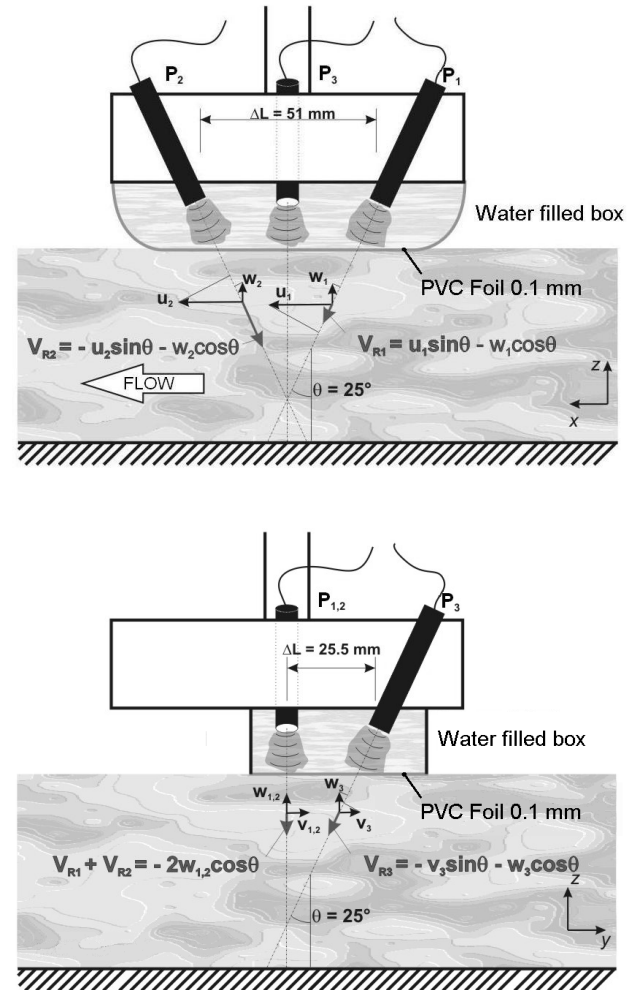


Figure 2: Scheme of probe fixation in movable box filled with water. Velocity vector decomposition. Up – vertical section in the plane normal to y axe ($u(z)$ and $w(z)$ evaluation). Down – vertical section in the plane normal to x axe ($v(z)$ evaluation).

Relations for time averaged velocity vector components than read:

$$\bar{u} = \frac{\bar{V}_{R1} - \bar{V}_{R2}}{2 \sin \theta} \quad (4a)$$

$$\bar{w} = -\frac{\overline{V_{R1}} + \overline{V_{R2}}}{2 \cos \theta} \quad (4b)$$

$$\bar{v} = \frac{\frac{1}{2}(\overline{V_{R1}} + \overline{V_{R2}}) - \overline{V_{R3}}}{\sin \theta} \quad (4c)$$

After numerical integration of point velocities evaluated from Eqs. 4, depth averaged velocities in gauging verticals and total discharge in gauging cross-section can be obtained.

5 RESULTS

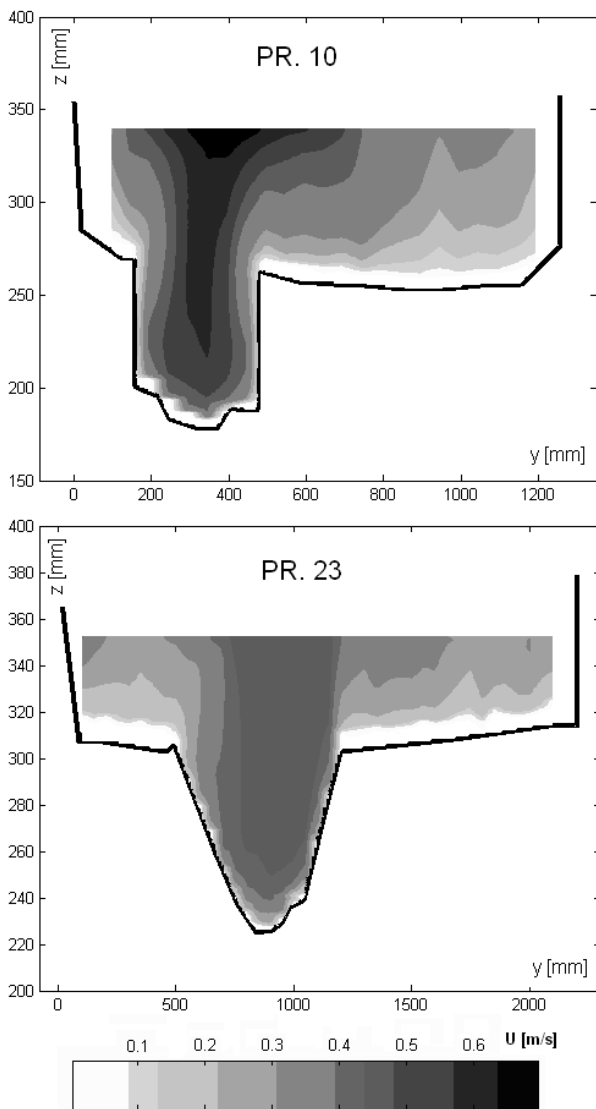


Figure 3: Main flow velocity distribution $u(y,z)$ in cross sections PR. 10 and PR. 23. White space at the left and right side is out of measured area.

5.1 Total discharge evaluation

In each of six gauging cross sections total discharge was evaluated from UVP time averaged point

velocities and compared with discharge deduced from Thomson weir. Excellent agreement was achieved between these two methods. Average relative error was only 0.21 %. Relative errors were less than 1% except of PR. 23 (error -2.95%).

5.2 Flow visualization

Distribution of velocity vector component in main flow direction can be seen in Fig 3. Flow is concentrated in the main channel. High roughness of floodplains causes lower velocity gradient near channel bottom than in the main channel, as can be also seen in Fig. 4. There is an apparent flow in the direction from right flood plain (from the left in Fig. 3 – upstream view) to main channel in cross section PR. 23. This observation is confirmed by Fig 5, where projection of velocity vectors into yz plane is plotted. This is an effect of changing channel geometry resulting in non-uniform flow. Figs. 3, 4 and 5 give clear demonstration of secondary flow influence on main flow near the flood plain and main channel interface.

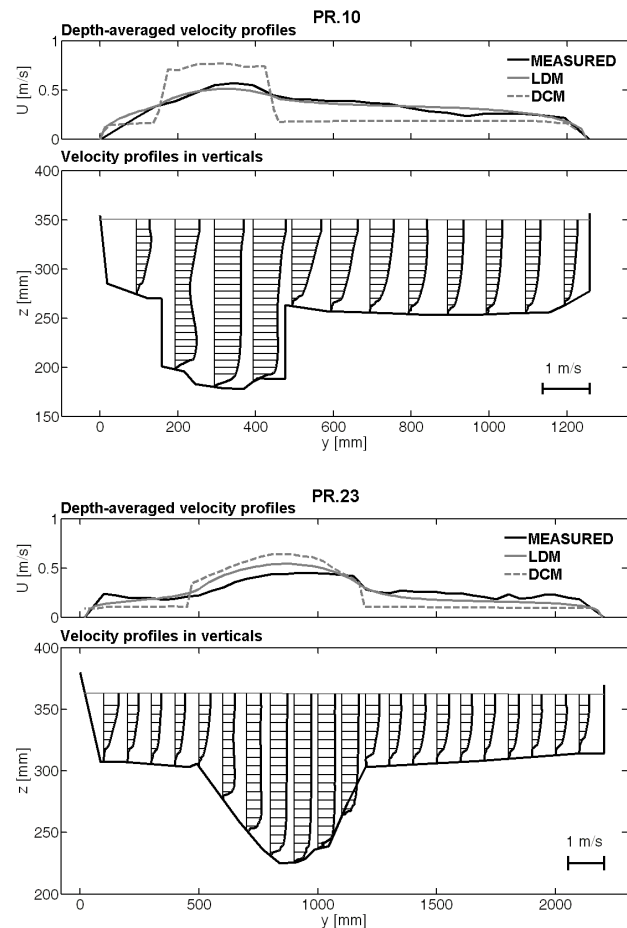


Figure 4: Main flow velocity components in verticals for cross section PR. 10 and PR. 23. Upper part – depth-averaged velocity profiles $U(y)$. Comparison of experiment and numerical simulation (LDM, DCM). Bottom – profiles of velocity component $u(y, z)$ measured in verticals.

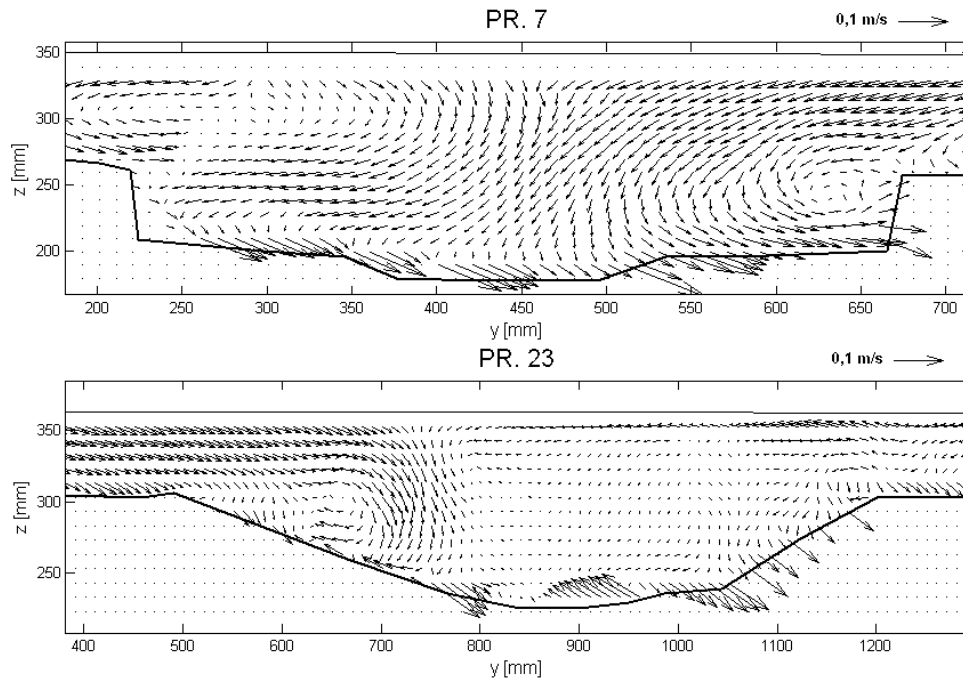


Figure 5: Projection of velocity vectors into yz plane. Upstream view. Unrealistic velocity vectors arise from problematic assignment of points measured by probe P_1 to points measured by probe P_2 near channel bottom.

5.3 Comparison of depth-averaged velocities

Comparison of numerical simulation and measurement proves that LDM provides very good prediction of the shape of the depth-averaged velocity profiles (Fig. 4). This is not the case of usual method based on dividing of compound channel to section (DCM). Significant deviation of LDM computed profile from measured one was observed only in cross section PR. 23 and 26. Water entered the model there and therefore flow in compound channel was not fully developed.

6 DISCUSSION

Accordingly to Hersberger [3], three probes inclined in angle θ were employed to 3D flow investigation in open channel. Accuracy in the estimation of velocity components v and w was reduced because of considerably smaller absolute value of these components. Discrepancy in vertical component (Eq. 4b) affects evaluation of transversal component (Eq. 4c). Visualization of secondary currents was not the main objective of our experiments. Usage of fourth vertical probe P_4 seems to be more appropriate for this purpose.

7 CONCLUSIONS

The potential of LDM for compound channel flow computations was evaluated using UVP method. Our experiments demonstrated high reliability of LDM depth-averaged velocity profile prediction in contrast to methods based on more simplified approach. Further, it can be concluded, that UVP is able to describe this type of flow with high accuracy.

The discrepancy between discharge evaluated from UVP and reference discharge measurement was 0.21%. Visualization of secondary currents has shown that UVP is sensitive enough to be able to describe three-dimensional vortex structures. Fixation of ultrasonic probes above water surface allows measurement in whole water depth with negligible disturbance of flow.

ACKNOWLEDGEMENT

This study was supported by grant GACR 103/04/1328, research center CIDEAS – project 1M0579 MSMT CR and Research task MSMT CR MSM 6840770002.

REFERENCES

- [1] Shiono K, Knight DW: Turbulent open-channel flows with variable depth across the channel, *J. Fluid Mech.* Vol. 222 (1991), 617–646.
- [2] Abril JB, Knight DW: Stage-discharge prediction for rivers in flood applying a depth-averaged model, *Journal of Hydraulic Research* Vol. 42, No. 6 (2004), 616–629.
- [3] Bousmar D: Flow modeling in compound channels, PhD thesis, (2002).
- [4] Conveyance User Manual (2004). DEFRA and HR Wallingford, www.river-conveyance.net (2004)
- [5] Hersberger DS: Wall roughness effects on flow and scouring in curved channels with gravel bed. PhD thesis, EPFL Lausanne (2003).
- [6] Lemmin U, Rolland T: Acoustic Velocity Profiler for Laboratory and Field Studies, *J. Hydr. Engrg., ASCE*, Dec 1997, 1089-1098.
- [7] Takeda Y: Ultrasonic Doppler method for velocity profile measurement in fluid dynamics and fluid engineering, *Experiments in Fluids* 26 (1999), 177-178.

Suspended solids and attenuation of ultrasonic beams

Frédérique Larrarte^{1*}, Pierre François²

¹Laboratoire Central des Ponts et Chaussées, Water & Environment Department,

Route de Bouaye BP4129 44341 Bouguenais Cedex, France, (*Corresponding author, e-mail: frederique.larrarte@lcp.fr).

²Institut de Mécanique des Fluides et des Solides de Strasbourg, 4 rue Boussingault, 67000 Strasbourg, France

Acoustic flow-meters are gauging devices commonly used in urban hydrology. Many of them are based on the Doppler principle and their use is based on the hypothesis that the velocity of suspended particles is equal to the flow velocity. Thus, at least a small amount of backscattering particles (or bubbles) is required for the use of acoustic Doppler velocimeters. In the same time, due to thermal conduction and viscosity effects, the intensity of an ultrasonic wave propagating in an homogeneous medium decreases. In suspensions an additional attenuation due to scattering and absorption by particles contribute to intensity decay. This term depends on the particles nature and concentration. There is a complete lack of data for runoff and wastewaters. Moreover the density of the particles ranges between 1.03 and 1.3 and their granulometry is roughly known,... In order to quantify the attenuation by wastewaters solids, an experimental set-up has been developed. The attenuation measurement for various types of particles is presented.

Keywords: : ultrasonics, suspended solids, instrumentation

1 INTRODUCTION

Flow measurement accuracy is a major concern in waste water management. Acoustic flow-meters are gauging devices commonly used in urban hydrology [1]. The Doppler principle, mostly used for these devices, assumes that the velocity of suspended particles is equal to the flow velocity. Thus, at least a small amount of backscattering particles (or bubbles) is required for the use of acoustic Doppler velocimeters. In the same time, due to thermal conduction and viscosity effects, the intensity of an ultrasonic wave propagating in an homogeneous medium decreases. In particles laden flows an additional attenuation due to scattering and absorption by particles contribute to intensity decay. This term depends on the particles nature and concentration. There is a complete lack of data for runoff and wastewaters which density, granulometry, nature are roughly known,... An experimental study has been conducted to quantify the attenuation effect different kinds of particles. A set-up was specifically developed. It is presented before the results obtained with various kinds of particles. Then, it is now possible to estimate the attenuation parameters.

2 THEORY

The tension U received by an ultrasonic transducer located in front of another one at a distance r can be written in far-field :

$$U(r) = U_o \frac{K}{r} e^{-\alpha r} \quad (1).$$

where K depends on electro-acoustics properties of

the transducers, U_o is the emission tension, r is the distance between the two transducers, α is the attenuation factor such as $\alpha = \alpha_w + \alpha_p$ with α_w the clear water factor and α_p the particles factor. The term $1/r$ arises from the spherical divergence of the ultrasonic beam in far-field .

Particle attenuation factor can easily be isolated from others intensity decay factors by using :

$$\text{Ln}\left(\frac{U_{with\ particles}(r)}{U_{without\ particles}(r)}\right) = -\alpha_p \cdot r \quad (2)$$

For spherical particles of radius a , the attenuation coefficient is expressed as following:

$$\alpha_p = \frac{3\chi C_m}{4a \rho_p} \quad (3)$$

where C_m is the concentration in kg.m^{-3} and the mass per volume ratio in kg.m^{-3} .

A literature review shows that, by fitting experimental results, a relatively simple expression of coefficient χ has been established for sand rigid particles [2]:

$$\chi = \frac{4}{3} \frac{1.1k_a x^4}{1 + 1.3x^2 + 4/3k_a x^4} \quad (4)$$

with $k_a=0.18$ and $x=2\pi a/\lambda$. where a is the particles radius and λ the wave length The ultrasounds celerity into water is equal to 1480 m/s at 20° C.

The attenuation coefficient of a mixture of n classes of particles is then calculated by:

$$\alpha_p = \sum_1^n \alpha_{p,i} \quad (5).$$

Let's consider various mixtures of particles having attenuation behaviour similar to sand and a density corresponding to suspended solids commonly encountered in wastewater $d=1.03$. It can be seen that this estimated attenuation at a frequency of 0.5 MHz is in any case very low (Table 2). It corresponds in worst case to a tension decay of about 3.6% at a distance of 1 meter. This estimated attenuation has to be compared to tension decay resulting from the spherical divergence of the ultrasonic beam of the order of 70 % at the same distance.

Table 1 : Particles diameters

Name	P1	P2	P3	P4	P5	P6	P7
Diameter (microns)	50	75	100	125	500	1000	2000

Table 2 : Attenuation coefficient of various particle mixtures

Mixture	Composition	$\alpha_p(m^{-1})$
M1	100 P1+ 100 P5 = 200 mg/l	$4.5 \cdot 10^{-3}$
M2	300P1 + 200 P2 + 100 P3 + 100 P4 + 100 P5 = 800 mg/l	$4.7 \cdot 10^{-3}$
M3	100 P1 + 50 P6 + 50 P7 = 200 mg/l	$1.7 \cdot 10^{-2}$
M4	200 P5 = 200 mg/l	$9 \cdot 10^{-3}$
M5	200 P6 = 200 mg/l	$3.6 \cdot 10^{-2}$

For a Doppler flowmeter, the important data is the backscattered tension :

$$U(r, C_m) = U_0 K^2 K_1 f(r) \sqrt{C_m} \exp(-2\beta_m \frac{C_m}{\rho_p} r) \quad (6)$$

where r is the distance between the transducer and the particle, β_m the mean value of β for a given granulometric distribution, f(r) a function depending on the distance. The coefficient K is the same than in equation (1). The coefficient K_1 depends upon the particles characteristics in term of density, size or acoustic impedance. As we focus in the present paper on attenuation effects, the evolutions of this retro diffusion coefficient are not taken into account in what follows. At a given distance and a given particle size distribution the tension exhibits a maximum in function of concentration. This maximum is found at a concentration:

$$C_m = \frac{\rho}{4\beta_{moy} r} \quad (7)$$

Figure 1 shows the theoretical tension evolutions in function of concentration at a distance of 1m under various conditions in term of frequency and particle diameter. As can be seen at a frequency of 0.5 MHz and for a particle size distribution commonly encountered in waste waters, attenuation has little influence up to 5000 mg/l . Under the usual conditions of use of the flow-meters average particle diameter is to be at least 1mm for attenuation to cause a substantial decrease of the backscattered tension. Note that we estimate in the present paper the attenuation by solid particles. In case of large bubble concentration a much higher attenuation coefficient is to be expected.

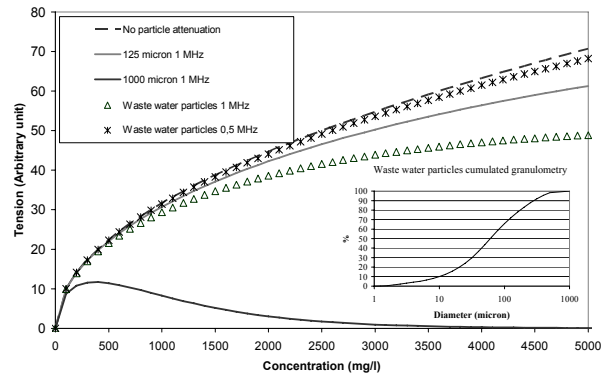


Figure 1 : evolution of the backscattered tension for particles of density 1.03

3 EXPERIMENTAL SET-UP

Industrial acoustic Doppler flowmeters designed for operating in real networks are inconvenient devices for our purpose because the signal can not be trig and monitored. Then a set-up has been built (figure 2), it is made of:

A Plexiglass water column with an height of 1.3 m and a diameter of 0.24 m. The height of the column was defined by reference to technical characteristics of flowmeters [3]:

- Two piezoelectric transducers which frequency is 0.5 MHz. This frequency is among those commonly used in wastewaters acoustic Doppler flowmeters . The emitter is located at the bottom of the column, the receiver is moved vertically with a metallic rod,
- A micro-table that controls the receiver position with 0.5 μ m alignment accuracy,
- A frequency generator provides the emission tension
- An numerical oscilloscope that allows :

- To visualize the emitted and received waves,
- To measure the frequency, transit time and amplitude of the ultrasonic waves
- To record those data.

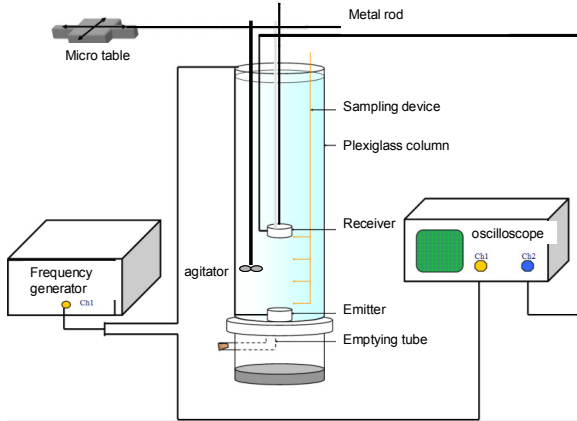


Figure 2: Experimental set-up

For each experiment, the column is full of clear water and the received intensity is measured at given distances between the emitter and the receiver. Then two experimental procedures were used following the nature of particle:

- dry sediments are melt to clear water and the received intensity is measured at given distances between the emitter and the receiver. The concentration is increased from 250 to 1000 mg.L⁻¹ corresponding to usual range of suspended solids concentrations in waste-waters,
- Raw waste-water is poured into the column after removing clear water and the received intensity is measured

4 RESULTS

Basin sediment

The sediment was sampled in a retention-infiltration basin receiving highway runoff of the main bridge, close to Nantes (France). Opened in 1991, the Cheviré bridge supports on present time an average daily traffic of 90000 vehicles, with 8% of trucks. The sediment comes in the form of aggregates composed of mineral phases (quartz, feldspaths) and organic matters, deeply mixed. [4] has measured the sediment granulometry in three locations (Table 3) and determined that the x% of the particles are smaller than dX. About 80% of the particles are smaller than 100 microns. The density is equal to 2.33.

Figure 3 shows the evolution of the ratio of the received tension by the emitted tension at a distance r between the two transducers. The ratio

decreases with the distance but the influence of the sediment concentration remains negligible. The intensity decay is mainly due to the spherical divergence of the ultrasonic beam.

Table 3 : Cheviré basin sediment granulometry

	D10 microns	D50 microns	D90 microns	< 100 microns
Cheviré entrance	7,40	37,40	193,40	0,80
Cheviré middle	5,00	27,20	997,30	0,79
Cheviré exit	3,90	24,00	611,90	0,83
Mean value	5,43	29,53	600,87	0,81

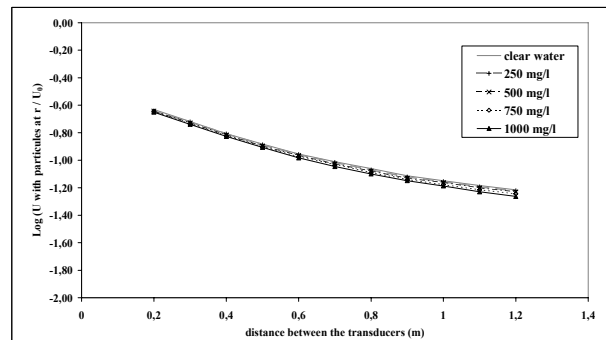


Figure 3 : Evolution of the tensions ratio with the distance between the transducers for pond sediment.

Figure 4 shows the evolution of the ratio of the received tension at a given concentration by the received tension in clear water at the same distance r between the two transducers. The evolution can be represented for example by an $\exp(-0,05 r)$ function at 750 mg/l. The attenuation coefficient α can therefore be estimated at 0.05 m^{-1} . Note that the tension decrease at low distance can not be attributed to attenuation in the bulk of fluid and reveals rather the settling of a few particles on the lower transducer. In consequence the attenuation coefficient is probably overestimated. Generally speaking this phenomenon of particle settling on the transducer is much more likely to cause a decrease of velocimeter range than attenuation in the bulk of fluid.

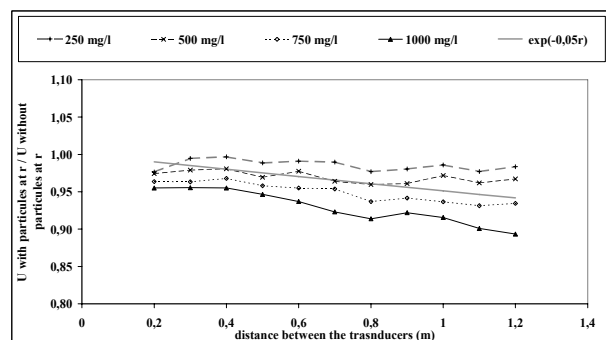


Fig. 4: evolution of the ratio of the received tension at a

given concentration by the received tension in clear water.

Waste waters

The sampling point is located in the urban combined network of Nantes (north-western part of France). All the waste waters of the northern part of the urban district are transported there, that means the effluents from the area with 600,000 equivalent-inhabitants.

Figure 5 shows the evolution of the ratio of the received tension by the emitted tension at a distance r between the two transducers. The ratio decreases with the distance but the influence of the sediment concentration remains negligible.

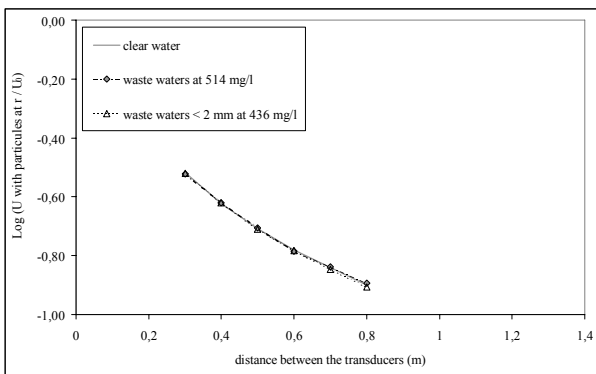


Figure 5 : Evolution of the tensions ratio with the distance between the transducers waste-waters.

Figure 7 shows the evolution of the ratio of the received tension at a given concentration by the received tension in clear water at the same distance r between the two transducers. There is not any decay of the ratio that means that the attenuation coefficient can be taken equal to zero. In other words the attenuation of the ultrasonic beams by the particles in suspension within the wastewaters, at the common wastewaters concentrations, is negligible. Those results correspond to those of [5, 6].

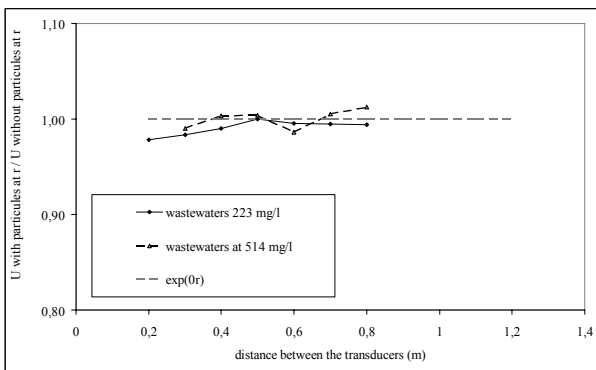


Figure 6 : evolution of the ratio of the received tension at a given concentration by the received tension in clear water.

5 CONCLUSIONS

Due to diffusion, the intensity of an ultrasonic wave propagating in a suspension of solid particles within water decreases. The order of magnitude of this decrease has been estimated theoretically for particles having the same attenuation behavior than sand and proved to be negligible.

The experimental investigation has shown that pond sediment are slightly attenuating the propagation of ultrasonic beams. On the other hand, the attenuation of the ultrasonic beams by the particles in suspension within the wastewaters, at the common wastewaters concentrations, is negligible. And then those particles are not influencing the range of the flow meters. In cases when a decrease of the velocimeter range is actually observed it is rather to be attributed to particle settlement on the transducer or to a high bubble concentration in the flow .

ACKNOWLEDGEMENT

The authors wish to acknowledge Jean-Pierre Legendre, technician at the Water & Environment Department of the Laboratoire Central des Ponts et Chaussées, for his valuable contribution to this project.

REFERENCES

- [1] Joannis C., (2001), La mesure de débits en assainissement, La Houille Blanche, 2001-5, pp. 58-62
- [2] Thorne, P.D., Hanes, D.M., (2002) A review of acoustic measurement of small-scale sediment processes. Continental Shelf Research, 22, 603-632
- [3] Larrarte F., Bardiaux J-B., Battaglia P., Joannis C., (2008), Acoustic Doppler flow-meters : a proposal to characterize their technical parameters, in press at Flow Measurement and Instrumentation.
- [4] Durand C, (2003), Caractérisation physico-chimique des produits de l'assainissement pluvial : Origine et devenir des métaux traces et des polluants organiques, Thèse de doctorat de l'Université de Poitiers, 214 pages + annexes.
- [5] Bouye J-M., Moreau S., (1996), Piézométrie et débitmétrie sur déversoir avec les ultrasons immergés. Journées application des ultrasons aux mesures dans les écoulements, p. 27-38.
- [6] Burgert C., (1996), Applications des ultrasons immergés, Journées application des ultrasons aux mesures dans les écoulements, p. 20-26.

Discharge estimation using partially measured ADVM data

Chanjoo Lee^{1*}, Won Kim², Chiyong Kim², Donggu Kim²

¹River & Coast Research Division, Korea Institute of Construction Technology, 2311 Daewha-dong Ilsanseo-gu, Goyang-si, Gyeonggi-do, Republic of Korea (*Corresponding author, e-mail: c0gnitum@kict.re.kr).

²River & Coast Research Division, Korea Institute of Construction Technology, 2311 Daewha-dong Ilsanseo-gu, Goyang-si, Gyeonggi-do, Republic of Korea

This study shows some results from streamflow monitoring operation of side-looking ADVM installed at lower part of cross-section to meet the hydrologic situation of highly variable natural rivers which have much longer period of low flow than short flood season. To estimate sectional velocity distribution and discharge with partially measured ADVM data, Chiu's formulae are used. Calculated velocity data are roughly similar with measured ones. Calculated discharge by 10-cell scheme gives fairly good agreement with reference discharge of the dam below 800 m³/s, while 5-cell scheme seems more suitable for higher discharge estimation. These characteristics are also shown in the plot of coefficient of determination and seem related with acoustic signal attenuation in high sediment concentration flow.

Keywords: Velocity, discharge, ADVM(acoustic Doppler velocity meter), Chiu's formulae

1 INTRODUCTION

In order to continuously monitor streamflow in highly variable natural rivers which have far longer period of low flow than short flood season, a fixed side-looking acoustic Doppler velocity meter (ADVM) is required to be installed at lower part of cross-section. In this condition, wide-shalowness and bed irregularity confines aspect ratio related to acoustic beams, then high frequency transducers of short reach length are used. Consequently, the ADVM only measure the relatively low-velocity outskirts rather than high-velocity core (Fig 3).

Though velocity data measured partially in the cross-section are not able to be used for discharge calculation by itself, they can be used practically either for index velocity rating, or with formulae simulating two-dimensional sectional velocity distribution. The latter may be the more cost-effective of the two in that it does not need many direct discharge measurements to develop rating.

A few two-dimensional sectional velocity distribution formulae have been reviewed [1, 2]. Among them, the formulae proposed by Chiu [1] are applied in this study. Calculated discharges are compared with ones by index-velocity rating and dam release discharges, and the results are discussed.

2 CHIU'S FORMULAE AND APPLICATION

2.1 Basic theory and formulae

Chiu [1, 3] proposed entropy-based two-dimensional probabilistic velocity distribution function for simulation in the river cross-section. His formulae are theoretically capable of reproducing maximum velocities occurring below water surface. By using Chiu's formulae, estimation of velocity distribution and discharge is possible with at least three

measured point velocity data in the cross-section.

Two-dimensional velocity distribution formulae proposed by Chiu [1, 3] are composed of 1) isovelline-based coordinate (Fig. 1, Fig. 2) velocity distribution function based on the principle of maximum entropy, 3) relationship about hydraulic parameter M .

The first thing is isovelline-based $\xi - \eta$ coordinate in the cross-section (Fig 1). Of ξ and η , only ξ is necessary for calculation of velocity distribution and equation is written as follows.

$$\xi = Y(1 - Z)^{\beta_1} \exp(\beta_1 Z - Y + 1) \quad (1)$$

where, $Y = (y + \delta_y) / (D + \delta_y + h)$, and $Z = |z| / (B_i + \delta_i)$.

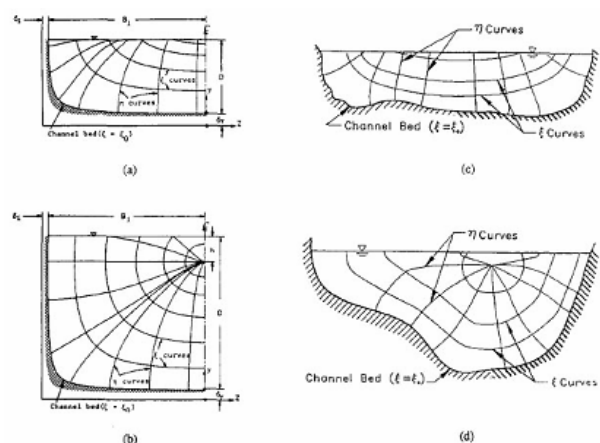


Figure 1: $\xi - \eta$ coordinates in open-channels

The second is general velocity distribution function and is expressed by Eq.(2).

$$u = \frac{u_{\max}}{M} \ln \left[1 + (e^M - 1) \frac{\xi - \xi_0}{\xi_{\max} - \xi_0} \right] \quad (2)$$

Thirdly, entropy parameter M which shows relationship between maximum and mean velocities is described as Eq.(3).

$$\phi(M) = \frac{\bar{u}}{u_{\max}} = e^M (e^M - 1)^{-1} - \frac{1}{M} \quad (3)$$

2.2 Determination of parameters

There are four parameters in Eq. (1). They are related to the shape of isovel (contour). Of them, h has physical meaning in the range of $-D < h \leq 0$ and represents vertical location below water surface along maximum velocity axis. Others (β_L , δ_x , δ_y) are variables relevant to shape of zero-velocity isovel and isovels near the boundary [4]. Considering range of values in [4], δ_x and δ_y are treated as zero, but β_L is determined in the range from 0 to 1. Parameter h and β_L are determined in two ways. First, h and β_L are determined according to a previous study by Lee et.al.[5] (Model_1). Second, h and β_L are considered as 0 and 1, respectively (Model_2). In case of $h=0$, it assumes that maximum velocity along the vertical axis occurs at water surface. The latter will be used for simple prediction for sites which do not have any hydraulic information in the cross-section. β_L is determined individually for the left (β_L) and right (β_R) half of the cross-section.

Parameter M in Eqs. (2) and (3) is an entropy one. It is only parameter related to hydraulic characteristics of the channel. It is related to maximum and mean velocity in the cross-section. M is also determined in two ways. It is determined either by Lee et.al. [5], or as 2.13 considering the study by Kim et.al. [6] and Moramarco et.al. [7].

Table 1: Applied parameters and discharge for cases in this study

Cases	Parameters (for Model_1)				Dam discharge (m ³ /s)
	h	β_L	β_R	M	
C200707161806	0.05	0.58	1.0	2.36	16.8
C200707201900	0.00	0.58	1.0	2.36	39.1
C200707240839	-0.07	0.59	1.0	2.36	61.0
C200707241329	-0.52	0.59	1.0	2.36	321.2
C200707242130	-0.29	0.71	1.0	2.36	175.0
C200707250730	-0.17	0.64	1.0	2.36	106.1
C200708050429	-0.67	0.57	1.0	2.36	407.7
C200708050029	-0.77	0.55	1.0	2.36	626.6
C200708082229	-0.69	0.56	1.0	2.36	480.4
C200607161929	-1.13	0.47	1.0	2.36	830.2
C200607170229	-1.41	0.45	1.0	2.36	1,093.9
C200607162359	-1.56	0.44	1.0	2.36	1,307.3

2.3 Calculation of velocity distribution and discharge

Before calculating velocity distribution for discharge estimation by Chiu's formulae, four different schemes are individually treated according to settings of parameters and the ADVm multi-cell

settings (Tab. 2).

Table 2: Applied parameters and discharge for cases in this study

Model	Parameter determination	Multi-cell scheme (ADVm setting)
Model_1	by Lee et.al.[5]	10 whole cells
		proximate 5 cells
Model_2	$h=0$, $\beta_L=0$, $\beta_R=0$, $M=2.13$	10 whole cells
		proximate 5 cells

Velocity distribution in the cross-section is substantiated by using both Eqs. (1) and (2), and rectangular grid network. Since simulated grid velocity values are non-dimensional, it is necessary to correlate them with real velocity values measured by ADVm. 10 or 5 observed multi-cell velocity data are used to establish linear correlation with non-dimensional velocity data calculated by Chiu's formulae. In this linear correlation relationship, slope of the fit line becomes maximum velocity and correlation coefficient presents index between calculated and measured velocity distribution. After determination of maximum velocity, all the non-dimensional grid velocity values are converted to real ones by Eq. (2). Total sectional discharge is computed by summation of all the grid discharge. For precise calculation of velocity distribution, size of each grid cell is 1 m in spanwise direction and 0.05m in vertical direction.

3 STUDY SITE AND ADVm SYSTEM

Streamflow monitoring system has been being operated at the reach of the Dalcheon river located near the center of South Korea. The river reach is an approximately 110 m wide and straight stable cobble-bed stream (Fig 2). There is the Goesan dam about 800 m upstream of the study reach. Its discharge release ranges from 5 m³/s during low flow season, up to 1,700 m³/s at severe flood. In this study, dam discharge is a reference for discharge comparison.



Figure 2: A view of the study site

The cross-section for streamflow monitoring is

shown in Fig 3. Low water level ranges from 110.0 to 110.5 m above sea level and is maintained by the riffle crest located 450 m downstream from the cross-section, while high water level comes up to 115.0 m.

The ADVM is a Sontek's Argonaut-SL of 1.5MHz frequency. It is set up to measure 10 cells in the range from 10 to 20 m from the transducers. In order to unceasingly measure water velocity even during dry low flow season, the ADVM is installed near the lower right edge of the cross-section. Consequently, it can partially measure the velocity of the outskirts of the cross-section.

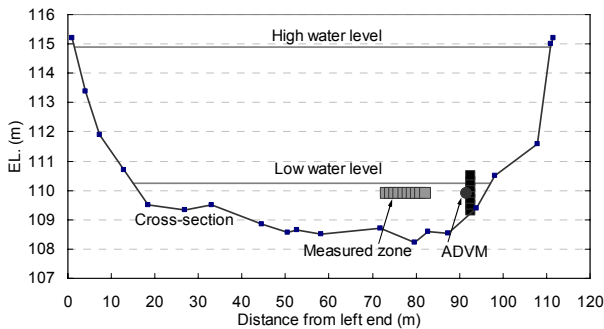


Figure 3: Cross-section and ADVM installation

4 RESULTS AND DISCUSSION

4.1 Velocity comparison

Fig. 4 shows lateral velocity distribution calculated by Chiu's formulae compared with measured by ADVM for the C200708050429 case (407.7 m³/s). Upper plots are for 10-cell data, while lower ones for 5-cell data. For both scheme (10-cell and 5-cell), calculated velocity shows more gradual increase in magnitude than measured distribution. In general (including other cases), this discrepancy is similar, but for higher discharge cases (> 800 m³/s), measured velocity of outer cells in the 10-cell scheme shows decrease in spite of discharge increase. It is likely to be attributed to acoustic signal attenuation caused by high suspended concentration [8].

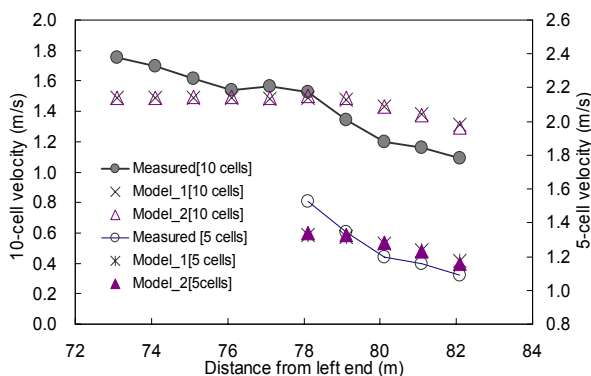


Figure 4: Comparison of velocity calculated by Chiu's formulae with measured velocity

There are very slight velocity differences calculated by model_1 and model_2. It is likely to be caused by similarity of parameters, especially hydraulic parameter *M*. In addition, it seems to be a cause that velocity is not measured near core, but in the outskirts.

4.2 Discharge comparison

Since streamflow monitoring in natural rivers depends on accuracy of discharge, more interest is focused on discharge. For range from 10 to approximately 800 m³/s, calculated discharge by Chiu's formulae for 10-cell scheme shows roughly good agreement with dam discharge except a case of discharge 626.6 m³/s (Fig. 5). Mean absolute relative differences with dam discharge are 5.7%, 7.0% for model_1 and model_2 of 10-cell scheme, respectively. On the contrary, for 5-cell scheme, they are 12.6% and 15.1% for model_1 and model_2, respectively. Consequently, discharge calculation using 10-cell data gives more accurate results. Mean absolute relative differences with index method are 5.6% and 8.2% for 10-cell scheme, 14.3% and 16.5% for 5-cell scheme.

For most cases, relative discharge differences with dam discharge show negative bias (-3.9%, -6.7% for 10-cell scheme, -12.6%, -15.1% for 5-cell condition). That is, 10-cell scheme can provide less negative bias than 5-cell condition. This is because the 10-cell condition has more possibility to get higher velocity by distant cells so that it estimates higher maximum velocity than in the 5-cell scheme. According to the results above, it can be inferred that if higher velocity near core is measurable, then estimated maximum velocity will be larger and negative bias in discharge calculation may decrease.

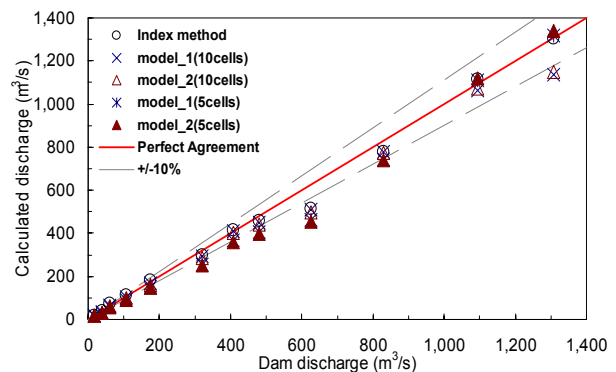


Figure 5: Comparison of discharge calculated by Chiu's formulae and index method with dam discharge

4.3 Coefficient of determination

C200607162359 case (discharge=1,307.3 m³/s) for 10-cell scheme displays abrupt discharge decrease (Fig. 5). It seems to be attributed to abnormal velocity decrease in the distant cells, which is probably caused by signal attenuation just as occurs in lateral velocity distribution. Fig. 6 shows abrupt

decrease of coefficient of determination between 800 and 1,100 m³/s for 10-cell scheme. Since calculated maximum velocity by Chiu's formulae depends on linear correlation with partially measured 10-cell data by ADVN, this low coefficient of determination depreciates reliability of the calculated data. Therefore it is desirable that 10-cell scheme should be used at discharge below 800 m³/s and above this discharge, another method is required to simulate velocity distribution and estimate reliable discharge.

In contrast to 10-cell scheme, coefficient of determination in the proximate 5-cell scheme presents more constant values because measuring cells are closer to the transducers in the 5-cell scheme. In addition, for discharge above 800 m³/s, relative error compared with dam discharge becomes much smaller (1.1% for model_1 and 2.3% for model_2, respectively) than for discharges below 800 m³/s. On the ground of both less erroneous discharge estimation and high coefficient of determination, it seems desirable to use calculated discharge by 5-cell scheme for discharge above approximately 800 m³/s.

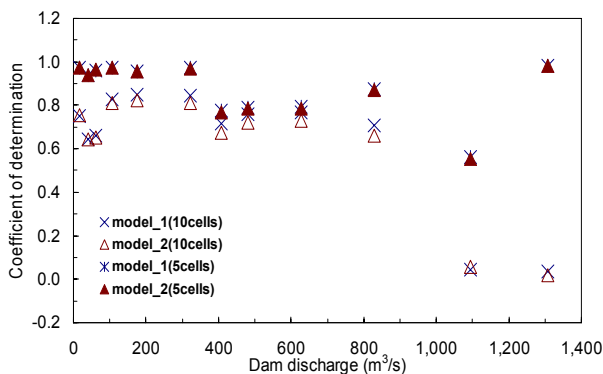


Figure 6: Coefficient of determination between calculated and measured velocity for 4 different conditions

5 CONCLUSIONS

In this study, we estimate lateral velocity distribution and discharge by using Chiu's entropy-based formulae with partially measured ADVN cell velocity data. The main outcome of this study is as follows:

For lateral velocity distribution, calculated values are roughly similar with measured data. But for higher discharge cases (> 800 m³/s), discrepancy between calculated and measured velocity increases in outer cells.

Calculated discharge by 10-cell scheme gives fairly good agreement with reference discharge of the dam below 800 m³/s, while 5-cell scheme seems more suitable for higher discharge. These characteristics are also shown in the plot of coefficient of determination.

This study shows another method for estimating velocity and discharge in natural rivers of irregular

bed configuration. In addition, if a target river section has similar value for entropy parameter M , it is possible to estimate discharge for wide range without troublesome effort for developing conventional H-Q or index-velocity rating. But due to dampening of acoustic signal in water of high suspended sediment concentration, complementary method is necessary to meet higher flood condition.

ACKNOWLEDGEMENT

This research was supported by a grant from Sustainable Water Resources Research Center (2-1-3) of 21st Century Frontier Research Program.

REFERENCES

- [1] Chiu, CL: Entropy and 2-D velocity distribution in open channels, J. of Hydraulic Eng., ASCE, 114 (1988) 738-756
- [2] Nihei Y, Kimizu, A: A new discharge monitoring system with an H-ADCP measurement and numerical simulation, Proc. 32nd IAHR Conf. in Venice (2007) CD-ROM
- [3] Chiu, CL: Entropy and probability concepts in Hydraulics, J. of Hydraulic Eng., ASCE, 113 (1987) 583-599
- [4] Chiu, CL, Chiou, JD: Structure of 3-D flow in rectangular open channels, J. of Hydraulic Eng., ASCE, 112 (1986) 1050-1068
- [5] Lee, CJ, Seo, IW, Kim, CW, Kim, W: Application of Chiu's two dimensional velocity distribution equations to natural rivers, Korean J. of Wat. Res. Ass. 40 (2007) 957-968 (*in Korean*)
- [6] Kim, CW, Lee, MH, Jung, SW, Yoo, DH: Discharge estimation using non-dimensional velocity distribution and index-velocity method in natural rivers, Korean J. of Wat. Res. Ass. 41 (2008) *in press (in Korean)*
- [7] Moramarco, T, Saltalippi, C, Singh, VP : Estimation of mean velocity in natural channels based on Chiu's velocity distribution equation, J. of Hydrologic Eng., ASCE, 9, (2004) 42-50
- [8] MOST of Korean Government: Final report for technology for surface water investigation (2007)

Turbulence and free surface flow at relevant Froude number

Sandro Longo

Department of Civil Engineering, University of Parma, Viale G.P. Usberti, 181/A, 43100 Parma, Italy, e-mail: sandro.longo@unipr.it

This work concerns the analysis of experimental instantaneous fluid level and three-component fluid velocity measurements in a stationary flow field generated by a Crump weir in a laboratory flume. The tests are characterized by different and increasing Froude numbers ($Fr = 0.10-0.38$), with the free surface of the fluid ranging from flat (low Froude number) to almost aerated (high Froude number). The data are elaborated obtaining the macro-turbulence Reynolds tensor, even using conditional averages based on free surface fluctuation statistics. A free surface boundary layer was detected having a thickness proportional to the root mean square of the free surface height series and with a velocity scale well related to the free surface elevation time gradient. The correlations between free surface elevation and the underlying flow velocities allow the evaluation of the time lag between turbulence and free surface. The results show that free surface motion is delayed with respect to turbulence at low Froude numbers (turbulence acts on the free surface) but is in advance at higher Froude numbers (free surface triggers turbulence). A specific regime occurs with an optimal tuning between free surface and turbulence. In this regime, the length scales are raised and the eddy viscosity assumes larger values.

Keywords: Free surface turbulence, turbulence intensity

1 INTRODUCTION

Many important transfer phenomena take place near the interface between air and water in the rivers, sea and lakes. Gas, chemicals, heat can be transferred in both directions depending also on turbulence level near the interface. Several attempts to quantify the effects of the free surface on turbulence have been successfully completed using numerical methods and experimental techniques, but in our knowledge no attention has been paid to the effects of turbulence on the free surface elevation. In literature no results have been presented with a quantification of the statistics of the free surface.

There are a great variety of free surface patterns and several mechanisms of energy transfer at a free surface such as capillary and gravity waves. In particular, the presence of waves requires the separation of their contribution in the flow field. The problem of separating waves and eddies, essentially a potential and a rotational component of the flow field (even though vorticity is not always turbulent, but turbulence is always vortical), is still unsolved. In the present experiments, we used the filtering method, with a cut-off frequency based on the observation of the energy spectra.

In the present experiments, we use Ultrasound to measure fluid velocity and fluid level in a spilling type breaker generated on a steady current by a Crump weir.

The Ultrasound technique is not new, but its application and recent evolution provide a new system to study velocity measurements in complex flows. The technique is well suited for giving information in a complex flow field, especially if spatial distribution is a main concern (e.g., [1]).

2 PROCEDURE FOR THE EXPERIMENTS

The present analysis refers to experiments in a flume, with free surface turbulence generated by a Crump weir (Figure 1).

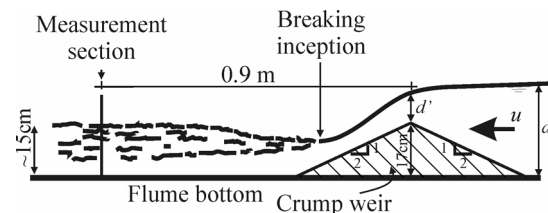


Figure 1: Scheme of the Crump weir set-up.

The flume was 15 m long, 0.30 m wide and 0.47 m high, and was supplied by a pump feeding a small tank at one end. The Crump weir was made with PMMA and was symmetric with an upstream and downstream slope 1:2 and a crest height of 17 cm with respect to the bottom of the flume. The crest was 7.1 m from the tank and the approaching flow had a flat surface with limited turbulence. The measurement section was 0.9 m past the weir, where the mean level was maintained at ~ 150 mm and was controlled by a bottom-hinged flap gate in the exit section of the flume. In all tests, a modular flow condition was obtained, with a head over the weir crest varying from ~ 20 mm (minimum discharge in the tests) to ~ 90 mm (maximum discharge in the tests). The approaching flow has a Froude number in the range 0.02-0.14, while a supercritical flow develops on the downstream face of the weir. Then, it turns to subcritical flow ($Fr = 0.10-0.38$) after a weak jump located well behind the measuring section.

2.1 Surface elevation and fluid velocity measurements

Free surface elevations were measured using an ultrasonic sensor based on flight-time having a carrier at 10 MHz, with temperature compensation and a sensing range of 50 to 250 mm (distance from the emitter/receiver). The response time was 10 milliseconds and the overall error (including non-linearity and repeatability) was assessed to be equal to 0.3 mm. Fluid velocity measurements below the free surface were taken using an array of three probes of an Acoustic Doppler Velocity Profiler, with a carrier frequency of the probes equal to 8 MHz (the arrangement of the probes is shown in Figure 2). The transducers had an active element diameter of 5 mm in a cylindrical plastic housing 8 mm in diameter. The arrangement of the three probes was chosen in order to guarantee an overlap of the measurement volume in the area of interest, just below the mean free surface, with the aim of mapping out the near surface flow field. In order to increase the S/N ratio, the water was seeded with clay, which proved to be an excellent seeding.

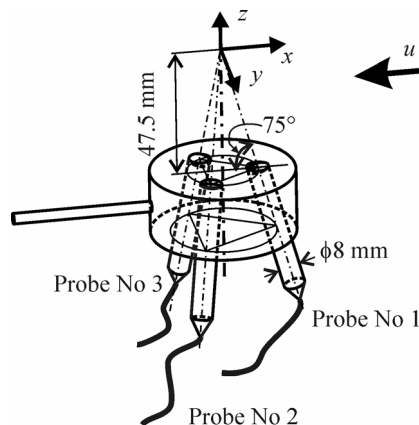


Figure 2: Arrangement of the velocity probes.

The acquisition was multiplexed, with a circular scanning of a single profile for each probe. The time lag between two different probe profiles was equal to 0.03 s on average, whereas the time lag between two subsequent gates was equal to $k \times \delta z / c$, where k is a coefficient roughly equal to two, δz is the distance between two gates and c is the ultrasound celerity in water. The resolution was equal to 1/128 (1 LSB) of the velocity range. For most tests, the resolution was equal to 0.5 cm/s (velocity measured along the probe axis). The presence of the moving interface generates a Doppler shift, which is highly energetic and can persist in the flow field as a stationary signal. The elimination of these stationary components by high-pass filtering implies an increase in the dynamic of the analyzed echoes and a reduction in the sensitivity in the measurement of low velocities. The Doppler frequency shift induced by these movable interfaces cannot be removed if their values have the same values as the flowing

particles. In order to balance all these effects, the presence of some artifacts is tolerated, which essentially influence the mean values, but not the statistics of the fluctuations (these artifacts determine a shift of the measured value of the velocity).

2.2 Data acquisition and analysis

Free surface elevation data was acquired at 100 Hz and velocity measurements were stored independently by a second dedicated PC triggered to free surface elevation data by an external cable. The frequency of acquisition of the velocity depends on the ADVP set-up and cannot be forced to a specific value. For a proper timing of free surface elevation (higher data rate) and velocity measurements (lower data rate), free surface data was sub-sampled at the lower rate. Then, velocity data was elaborated in order to obtain the mean values of fluid velocity and of the Reynolds tensor in an Eulerian frame with a coordinate system having its origin at the mean water level.

Free surface elevation was also statistically analysed in the time domain with a zero-crossing analysis in order to extract the root mean square height (H_{rms}) and several zero(-up) crossing statistical estimators.

3 ENERGY SPECTRA

The one dimensional energy spectrum for the vertical component of velocity at various levels and at large-scale normalization is shown in Figure 3.

The velocity scales derive from the turbulent kinetic energy and all variables are time averaged. The large-scale Reynolds number, Re_Λ , varies from $\sim 4 \times 10^3$ well below the mean water level to $\sim 2 \times 10^2$ in the crest of the free surface fluctuations; Λ is the integral scale. At small wave numbers, the spectrum tends to become flat and is coherent with the energy renewal model of the energy-containing eddies reported in [2]. The exponent of the spectrum in the intermediate wave numbers and at the zero level is slightly higher than the classical Kolmogorov spectrum exponent equal to $-5/3$. Moving below the zero level, the exponent tends to reduce and to reach the classical value. There are several phenomena to account for when interpreting the measured shape of the spectrum. The assumption of the existence of an inertial subrange relies on the existence of a Reynolds number larger than 4×10^3 [3], which is not the case of the present experiments (the maximum Reynolds number is ~ 1000). That means that the effects of production and dissipation, which usually appear for $k\Lambda < 10$ and $k\Lambda > 1000$, also modify the shape at intermediate wave numbers. Another important phenomenon is intermittency. Turbulence generation is an intermittent phenomenon, but also dissipation seems to be organised in patches, instead of being uniformly present in the flow field.

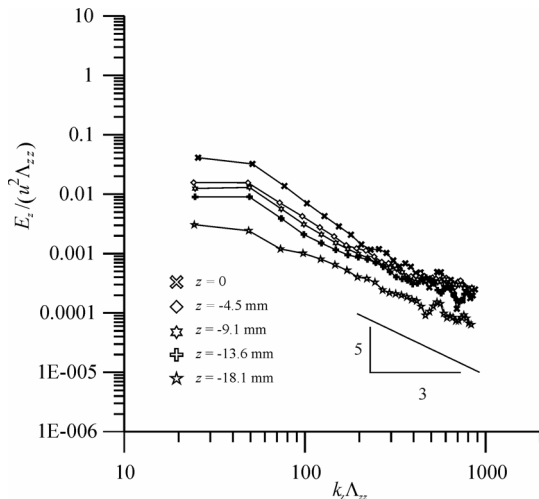


Figure 3: Normalized wave number energy spectra of velocity fluctuations. Energy spectrum vertical velocity fluctuations. Test No 66, $H_{rms} = 12.09$ mm.

Chorin [4] analysed in detail the possible corrections of the exponent in the Kolmogorov spectrum, and indeed found that the correction proposed should not be addressed directly to intermittence, even though using different arguments also justifies an exponent equal to -2 derived by a cascade construction as a better candidate for a model where fluctuations due to intermittency are ignored. In the present experiments, in the domain below the mean water level, the intermittency is due to the free surface fluctuations and also to the presence/absence of fluid. Its effects should possibly be reduced or disappear far from the free surface. It gives a plausible interpretation of the observed spectra.

At a low wave number, the vertical spectrum E_z shows larger values at $z = 0$ with respect to the spectra below the free surface (Figure 3). That means that no suppression of the eddies larger than the depth occurs and that eddies are strictly responsible of the free surface fluctuations. Instead, the two other spectra show larger values below the $z = 0$ level, reaching a maximum at z roughly equal to $-H_{rms}$.

4 THE EDDY VISCOSITY

Using a phenomenological approach, the eddy viscosity can be expressed as

$$\nu_e = \Lambda_{zz} w' \quad (2)$$

Λ_{zz} is the integral scale in the vertical and w' is the vertical velocity fluctuation. This description seems much more appropriate than the classical expression related to the mean velocity gradient in flow fields characterised by the presence of coherent structures. In fact, according to many researchers, coherent structures generate most of the turbulent shear stress, even in homogeneous turbulence. The main effect of disregarding the presence (or the effects) of these families of eddies,

is the poor adherence to the reality of some common assumptions, as eddy viscosity to express the behaviour of the turbulence stresses in terms of the mean velocity gradients.

Figure 4 presents the eddy viscosity profiles for all tests. u_s is the free surface velocity scale based of the time derivative of the instantaneous free surface elevation. The tests with $Fr_s > 0.19$ show a maximum at $z = H_{rms}$, where the mean shear also has a maximum (not shown) and a fast damping towards the free surface. The damping is mainly associated with the reduction of the velocity scale, because the length scale even increases near the free surface.

The eddy viscosity profiles refer to different Reynolds numbers and do not collapse to a single curve.

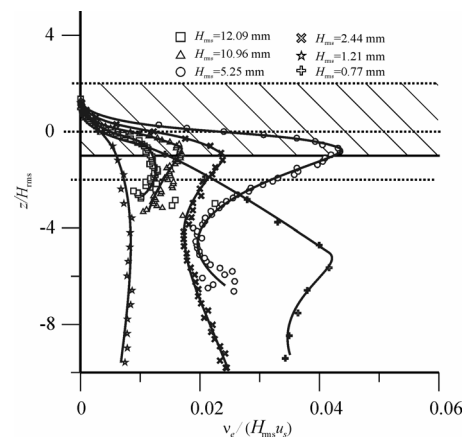


Figure 4: Eddy viscosity profiles.

Rather, the mean value of eddy viscosity generally increases with the Reynolds number up to a maximum, reached at an intermediate level of fluctuation ($H_{rms} = 5.25$ mm), which also showed the highest values for the macroscale Λ_{zz} ; then decreasing once more. This is another consequence of an optimal tuning between free surface oscillations and macrovortices, which also improves the efficiency in momentum transfer between the external region and the boundary layer. As usual, the tests at low levels of fluctuation show an anomalous behaviour due to the fact that other scales are significant in this condition.

5 THE CORRELATION BETWEEN FREE SURFACE AND FLUID VELOCITY

The analysis of the correlation between free surface and vertical velocity fluctuations is shown in Figure 5. The upper box is the coherence map for the vertical velocity component, the lower box is the phase lag map, with positive values of the phase indicating that the free surface elevation has a delay with respect to the velocity fluctuations. The coherence between the two variables a and b ranges between 0 and 1 and is defined as

$$c = \frac{P_{ab}^2}{P_{aa}P_{bb}} \quad (3)$$

where P_{ab} is the power cross-spectral density and P_{aa} and P_{bb} are the power auto spectral densities. Similar maps for the spanwise velocity component show a negligible coherence value and will not be further considered. In the present tests, the coherence generally has a maximum value immediately below the mean water level and at frequencies from 3.3 Hz to slightly less than 2 Hz for decreasing H_{rms} . For all tests, the maximum coherence has a value less than 0.3 and decreases with H_{rms} . The maximum lies at higher frequencies or near the main peak of the free surface elevation power spectrum (not shown). Occasionally, two peaks can be found with the second at twice the main frequency. At high H_{rms} (Test No66), we can observe that the phase lag between the free surface fluctuations and the vertical velocity fluctuations is generally negative in the free surface layer, i.e. the free surface fluctuations are advanced with respect to the vertical velocity fluctuations; it happens that where the coherence is maximum, the phase lag changes from 0° to -90° at the zero level, then increases again (see the dashed and the dotted thick curves in Figure 5). The phase lag is positive below the free surface layer, i.e. the free surface fluctuations have a delay with respect to the vertical velocity fluctuations. In the same test, the phase lag between the free surface fluctuations and the stream wise velocity fluctuations is positive in the domain where the maximum coherence occurs. Note that while two separate curves connecting the maxima can be drawn for the vertical velocity fluctuations (ranging between 1 Hz and 3.5 Hz), a single curve can be drawn for the stream wise velocity fluctuations (not shown). A model of interpretation of the data assumes that the stream wise velocity fluctuations act as forcing term for the free surface fluctuations, with maximum efficiency near the observed peak of 2 Hz; the free surface fluctuations, in turn, force the vertical velocity fluctuations with maximum efficiency in two bands centred at 2 Hz and at nearly twice the peak frequency of 2 Hz. The superharmonic of the response is due to the fact that both crests and troughs excite the eddies and hence, the velocity fluctuations. The mechanism of wave generation by turbulence in the water could be that analysed by Teixeira & Belcher [5] with a forcing dominated by turbulent pressure fluctuations. This scenario can also be recognised for the other tests at lower values of H_{rms} .

6 CONCLUSIONS

The presented results show the characteristics of free surface turbulent flows at low, but not negligible, Froude numbers without air inception.

- The eddy viscosity profile depends on Reynolds number, is damped in the free surface boundary layer, has a maximum at the edge of the free surface boundary layer, and assumes larger values in optimal tuning tests.

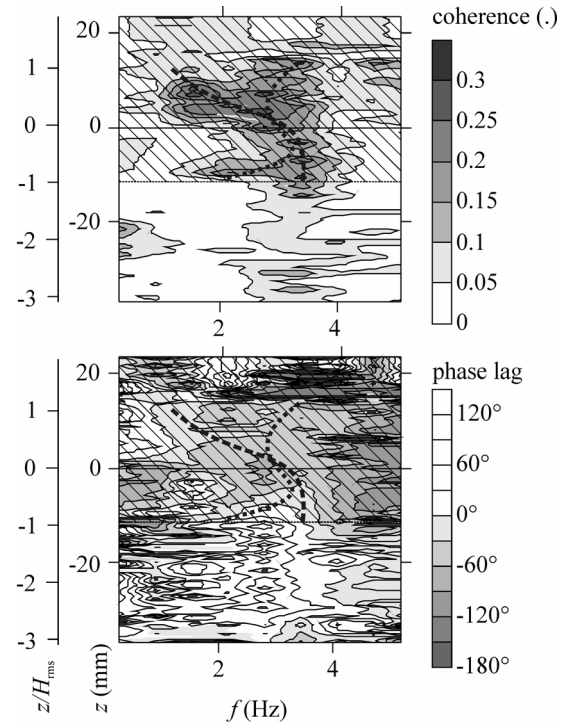


Figure 5: Coherence and phase lag. Test No 66, $H_{rms} = 12.09$ mm.

- The analysis of correlation between free surface instantaneous elevation and the vertical component of fluctuating velocity reveals that the free surface is generally delayed with respect to fluid velocity, except at high H_{rms} . We can infer that free surface fluctuations are generally triggered by turbulence, but strong fluctuations of free surface can easily invert the roles. The triggering mechanism could be that inferred by Teixeira & Belcher [5], with pressure fluctuations related to turbulence and generating the free surface fluctuations.

REFERENCES

- [1] Takeda Y: Quasi periodic state and transition to turbulence in a rotating Couette system, *Journal of Fluid Mechanics* 389 (1999), 81-89.
- [2] Komori S, Murakami Y, Ueda, H.; The relationship between surface-renewal and bursting motions in an open-channel flow, *Journal of Fluid Mechanics* 203, (1989) 102-123.
- [3] Tennekes H, Lumley JL: *A first course in turbulence*, The MIT Press, pp. 300 + xii, ISBN 0-262-20019-8 (1972).
- [4] Chorin AJ: *Vorticity and turbulence*, Springer-Verlag, ISBN 0387941975, pp.174+VII (1994).
- [5] Teixeira MAC, Belcher SE: The initial generation of surface waves by turbulent shear flow, submitted.

Vortices at intake works of pump-storage schemes

Rémi Martinerie², Michael Müller¹, Giovanni De Cesare^{1*} and Jean-Louis Boillat^{1*}

¹Laboratory of Hydraulic Constructions (LCH), Ecole Polytechnique Fédérale de Lausanne (EPFL), Station 18, CH-1015 Lausanne, Switzerland

(*Corresponding author, e-mail: giovanni.decesare@epfl.ch).

²formerly at the EPFL-LCH, now at e-dric.ch Sàrl, Grand Chemin 73, CH-1066 Epalinges, Switzerland

Physical model testing for two new major pump-storage hydropower scheme projects were performed at the Laboratory of Hydraulic Constructions (LCH) of the Ecole Polytechnique Fédérale de Lausanne (EPFL). One, the 600 MW Nant-de-Drance pump-storage scheme between the Emosson and Vieux-Emosson reservoirs, is located in the Valais Alps. The other one, the 1'000 MW Linth-Limmern pump-storage scheme between the Limmernsee and Muttssee reservoirs, is located in the Glarner Alps. Pump-storage schemes, like ordinary hydropower schemes, are equipped with water intakes. Secondary flow and vortex formation above the intakes were investigated according to the operation conditions in generating mode for the upper basin, respectively in pumping mode for the lower basin for various discharges and water levels. The detailed velocity fields around and inside the vortices were measured using ultrasonic velocity profilers UVP. The geometry of the intake structures could be optimized through minor structural modifications in order to keep the intake operations outside the critical limit of air entrainment. Vertical velocity profiles along the vortex cores were also measured using ultrasonic velocity profilers. The velocity measurements highlighted the risk of frazil ice crystal entrainment, which could lead to the obstruction of the metallic intake grid.

Keywords: pump-storage hydropower scheme, water intake, vortex, frazil ice entrainment, velocity field, ultrasonic velocity profiler UVP

1 INTRODUCTION

In January 2008, the total installed capacity of hydropower schemes greater than 300 KW in Switzerland amounted to 14'200 MW. Today some 1'610 MW are available for pump-storage [1].

Within the frame of major upgrading of existing hydropower schemes with storage reservoirs in Switzerland, two distinct new projects are currently under final investigation: the Nant-de-Drance and the Linth-Limmern pump-storage schemes. These two projects, once completed, will practically double the existing pump-storage capacity in Switzerland.

Physical model testing for these pump-storage hydropower scheme projects were performed at the Laboratory of Hydraulic Constructions (LCH) of the Ecole Polytechnique Fédérale de Lausanne (EPFL) [2-5]. Pump-storage schemes, like ordinary hydropower schemes, are equipped with water intakes. Secondary flow and vortex formation above the intakes were investigated in both physical model studies considering the operation conditions in generating (turbining) mode for the upper basin, respectively in pumping mode for the lower basin for various discharges and water levels.

2 CASE STUDIES

2.1 Nant-de-Drance pump-storage scheme

The Nant-de-Drance pump-storage scheme, located in the Valais Alps (Figure 1), consists of the installation of an underground pump-turbine plant between the existing reservoirs of Emosson

(1'930 m a.s.l.) and Vieux-Emosson (2'205 m a.s.l.). The power station is composed of four production units with a total power of 600 MW and is fed by two pressure tunnels of 6.5 m in diameter.

2.2 Linth-Limmern pump-storage scheme

The existing Linth-Limmern hydropower scheme, located in the Glarner Alps (Figure 1), has at present an installed capacity of 340 MW.

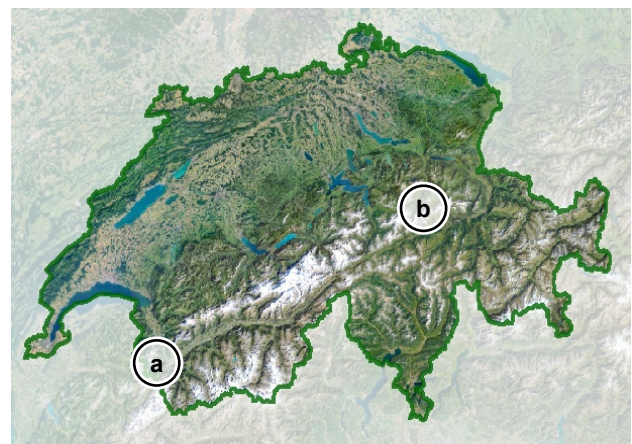


Figure 1: Location of the Nant-de-Drance (a) and the Linth-Limmern (b) pump-storage schemes projects.

The extension project "Linthal 2015 KW Limmern" foresees a new underground pump storage powerhouse able to pump water from the lower basin (Limmernsee, 1'857 m a.s.l.) into the upper basin (Muttssee, at present at 2'446 m a.s.l.). During peak hours, the stored water can again be used for

generating energy. The single upper basin intake guides the water into a conduit of 8 m in diameter, which feeds the power station composed of four units with a total power of 1'000 MW. The lower outlet (in generating mode) is composed of two separate works.

3 THEORETICAL CONSIDERATIONS

3.1 Vortices on water intakes

Referring to their intensity, vortices on water intakes can be classified into six types, reaching from non coherent surface swirls to eddies with continuous core and air entrainment. A vortex is considered to be critical when the air core reaches the intake. In order to avoid such situations, a minimal submersion has to be guaranteed. For a first approach, Knauss (1987) [6] proposes an empirical formula to calculate this critical water depth above the intake:

$$\frac{h_t}{D} > 2.3 \cdot F_p + 1 \quad (1)$$

$$F_p = V / \sqrt{g \cdot D} \quad (2)$$

With F_p the Froude number of the intake, V the mean velocity in the conduit, D the hydraulic diameter of the conduit, and h_t the water depth referred to the conduit axis.

The values of V , h_t and D vary according to the position within the intake structure due to intake inclination, vertical and lateral contraction and finally change of the conduit cross section from rectangular to circular. Thus, the verification of the critical water depth over intake structures has to be carried out for several cross sections (Figure 2), namely at the end of lateral (A) and vertical (B) contractions and at the entrance into the circular conduit (C).

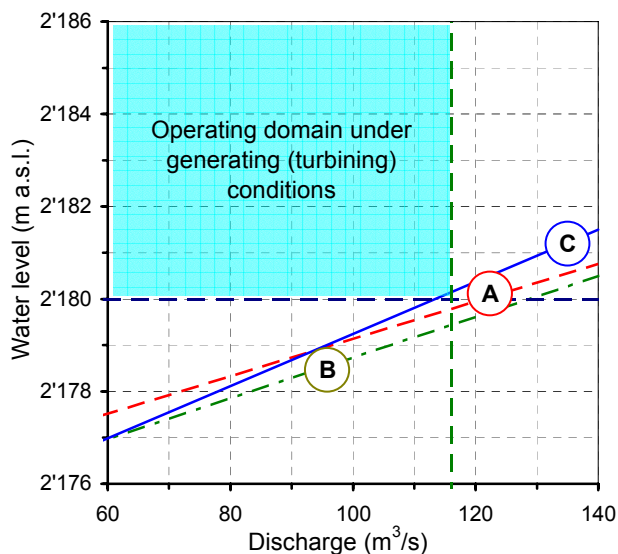


Figure 2: Relation between discharge and critical submersion depth for three cross sections (A), (B), and (C) of the Vieux-Emosson intake structure.

The theoretical considerations reveal the existence of a critical minimal water depth that has to be maintained during generating mode at full capacity. This condition will thus be verified experimentally.

3.1 Frazil ice particle entrainment

If water temperature falls below the freezing point and no ice layer covers the lake surface, frazil ice can form. If wind or currents agitate the water, these ice crystals can be entrained vertically along the water column and transported towards the intake [7].

Frazil ice can easily adhere to the metal bars of the trash rack that have high thermal conductivity, not only on their contact surfaces but also between them [8]. The accumulation of frazil ice and their growing can lead to rapid and complete blocking of the entrance section [9].

The lake of Vieux-Emosson is situated at 2'200 m a.s.l. where extreme climatic conditions can occur. In particular negative temperature peaks of -10 to -15 °C and clear, cold nights favour frazil ice formation. Furthermore, primary and secondary flow conditions due to generating and pumping modes contribute to thermal mixing of the water and therefore to frazil ice production.

In order to define whether frazil ice can be entrained by vertical flow, the different forces applying on an ice particle have to be analyzed. Ice crystals usually form disks of less than 1 mm in diameter, but after growing these disks can reach 15 mm and also coalesce to near spherical shapes [8].

The ice disk thickness is 5 to 10 times smaller than its diameter. A one-dimensional model allows equilibrating active and resisting forces, that is to say disk weight P , buoyant force F_A and drag force F_T .

$$P = \rho_i \cdot g \cdot \bar{V} \quad (3)$$

$$F_T = \frac{1}{2} \cdot C_T \cdot S \cdot \rho_w \cdot V_z^2 \quad (4)$$

$$F_A = \rho_w \cdot g \cdot \bar{V} \quad (5)$$

with \bar{V} the ice particle volume, S the projected section of the disk in flow direction, C_T the drag coefficient, V_z the relative velocity, g the gravity acceleration, ρ_i and ρ_w the volumetric mass of the ice particle respectively of water.

The theoretical approach admits that the disks are positioned perpendicularly to the vertical flow velocities. This conservative hypothesis can be justified by the fact that the ice disks will orientate parallel to major horizontal velocities in the eddy. This model allows calculating critical velocities for frazil ice particle entrainment, for disks with a thickness/diameter ratio of 0.1 and for spheres

(Figure 3).

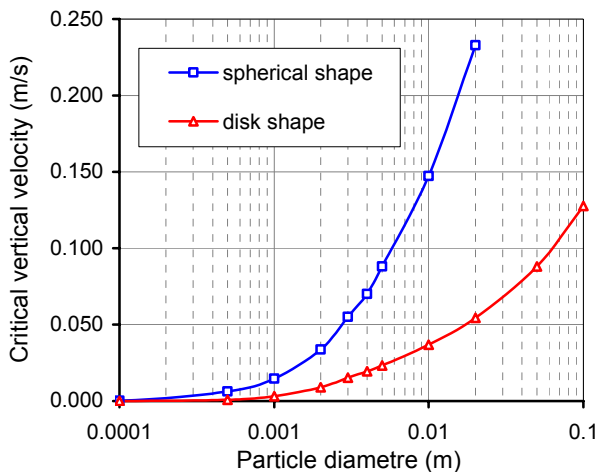


Figure 3: Critical velocity for frazil ice particle entrainment.

Physical modelling thus consists in quantifying the limits of the vertical velocity range for frazil ice entrainment.

4 PHYSICAL MODELING

4.1 Experimental set-up

The physical models of the Nant-de-Drance and the Linth-Limmern intake structures have been built at scales ranging from 1:36 to 1:42. This scale range allows representing the behaviour of swirling flow in an adequate way [11], [12], [13]. In order to reveal possible model effects and to evaluate the robustness of the results, supplementary test series have been run with higher flow rates.

The limits of the physical model were selected in a way that the substantial influences of the topography on the flow conditions can be considered and the model delimitation leads to no substantial influences. The intake works have been built in PVC and the reservoir topography with a rigid cement covered structure (Figure 4). Every conduit can be run individually and independently in generating, as well as in pumping mode. The reservoir level is controlled by an overflow weir.

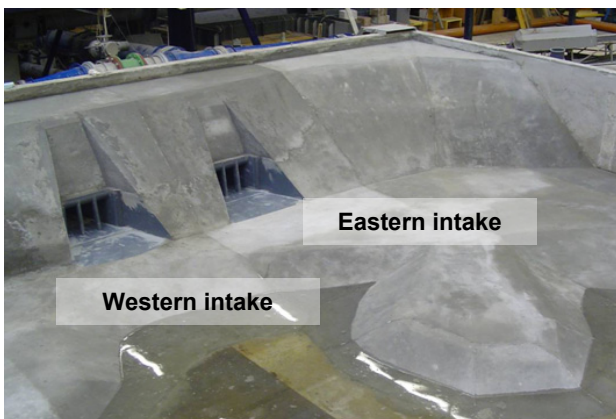


Figure 4: Hydraulic model of the two adjacent intakes inside the lower Limmernsee basin of the Linth-Limmern

pump-storage scheme project.

The models have been exploited considering Froude similarity. The Reynolds number is considered only for head losses at the intake entrance.

4.2 Measuring technique

For the quantitative evaluation of eddies, 2D velocity measurements have been carried out using UVP (Ultrasonic Velocity Profiler). Two rows of four sensors have been placed perpendicularly in order to obtain a network of 16 measuring points (10 cm x 10 cm, Figure 5). A hydrogen bubble generator installed upstream the measurement area allowed to trace the flow [14], [15].



Figure 5: Measurement frame with 4x4 US transducers for vortices flow field mapping. A hydrogen bubble generator (in the back) was used for local hydrogen seeding supply.

Vertical velocity measurements have been carried out with UVP as well, this time perpendicular to the water surface in the center of vortices. Flow velocities have been recorded only when eddies were highly developed.

5 EXPERIMENTAL RESULTS

The following results concern exclusively vortices in front of the intake structures. Two problems are analyzed: the first deals with eddy formation and potential air entrainment, and the second reveals the risk relative to frazil ice entrainment.

5.1 Assessment of vortex formation

Vortices above the intakes have been analyzed qualitatively, considering eddy type, dimension and persistence. Observations have been made for possible operation conditions (discharges and reservoir water levels).

Based on these results, critical configurations have been selected and analyzed quantitatively by 2D UVP measurements.

An example of such observations and measurements results are given for the Vieux-Emosson reservoir in Figure 6. Technical solutions allowing an improvement of the swirling flow behaviour have been proposed and optimized

thanks to the hydraulic model tests.

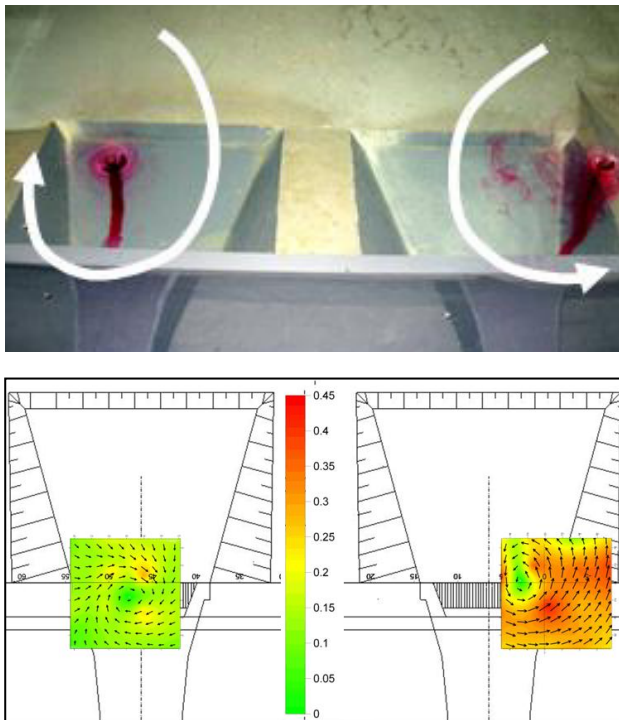


Figure 6: Formation of vortices in generating mode at the water intakes of Vieux-Emosson. Top: dye injection. Bottom: horizontal measured flow field at an intermediate level.

5.3 Evaluation of frazil ice entrainment

Figure 7 shows an example of the vertical velocities measured in the core of the vortices for several reservoir water levels. Velocities of 0.05 to 0.10 m/s can easily entrain frazil ice disks of some 5 cm in diameter. The frazil ice forming on the water surface, with a size of 1 mm, can therefore be entrained towards the trash rack of the intake structure. Solutions to reduce the risk of blocked trash racks must be considered.

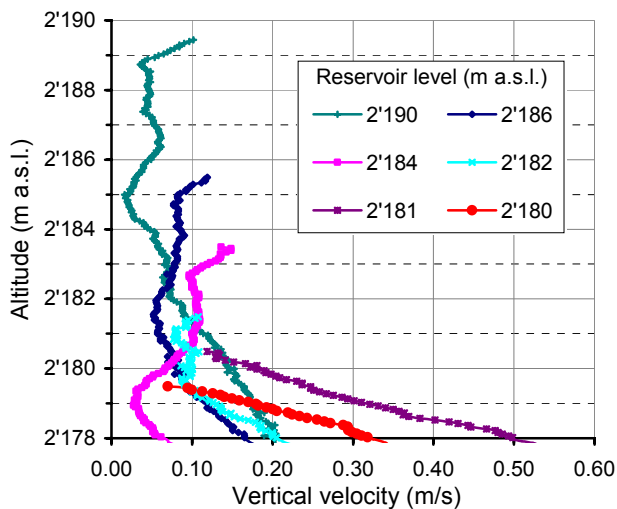


Figure 7: Vertical velocity inside the vortex core to assess

frazil ice entrainment in the Vieux-Emosson model.

6 CONCLUSIONS

UVP measurements applied to physical models of the intake structures of the pump-storage schemes Nant-de-Drance and Linth-Limmern allowed exploring the velocity fields associated with vortex formation. Based on the detailed results of these tests, problems have been identified and solutions have been proposed and optimized.

In order to reduce the frequency and persistence of eddies, the excavation niches have been enlarged. The vortex intensity could be reduced by implementing small walls above the intake platform (Nant-de-Drance) or by placing a concrete crossing beam over the intake (Linth-Limmern).

The risk of trash rack blocking due to frazil ice has been revealed and both constructive solutions (spacing between bars, protection layers or coatings, possible heating) and exploitation measures (potential underwater frazil ice detection, flushing by reverse current) have been proposed.

ACKNOWLEDGEMENT

The Nant-de-Drance study has been entrusted by Aare Tessin AG für Elektrizität (Atel) and the Swiss Federal Railway (SBB). The Linth-Limmern study was performed on behalf of the Krafterke Linth-Limmern (KLL).

REFERENCES

- [1] BFE (2008). Statistik der Wasserkraftanlagen der Schweiz, Swiss Federal Office of Energy (SFOE).
- [2]-[5] EPFL-LCH, unpublished reports concerning hydraulic model tests of Nant-de-Drance and Linth-Limmern projects, Ref. LCH 25/06, 9/07, 19/07, 1/08.
- [6] Knauss, J. (1987). Textbook: Swirling flow problems at intakes, Hydraulic Structures Design Manual No 1, IAHR.
- [7] Osterkamp, T. E. (1978). Frazil ice formation: A review, J. Hydraul. Div., Am. Soc. Civ. Eng., 104(9), 1239-1255.
- [8] Ashton, G. D. (1988). Textbook: "Intake design for ice conditions." Advances in Hydraul. Eng., P. Novak, ed., Vol. 5, Chp. 2, Elsevier Appl. Sc., London, 107-138.
- [9] Daly S. F., Ettema R., (2006). "Frazil ice blockage of water intakes in great lakes." J. Hydr. Eng., 132, 814-824.
- [10] Carriveau, E. C., Baddour, R. E, Koop, G. A. (2002). The entrainment envelope of dye-core vortices at submerged hydraulic intakes, Can. J. of Civil Eng. 29, 400-408.
- [11] Odgaard, A. J. (1986). "Free-surface air core vortex." J. Hydr. Div., ASCE, 112(7), 610-620.
- [12] Daggett, L. L., Keulegan, G. H. (1974). "Similitude conditions in free-surface vortex formation." J. Hydr. Div., ASCE, 100(11), 1565-1580.
- [13] Padmanabhan, M., Hecker, G. E. (1984). "Scale effects in pump sump models." J. Hydr. Div., ASCE, 110(11), 1540-1556.
- [14] Met-Flow SA. (2002). UVP Monitor Model UVP-DUO users guide. Metflow SA, Lausanne, Switzerland.
- [15] Meile T., De Cesare G., Blanckaert K., Schleiss A. J. (2007). Improvement of Acoustic Doppler Velocimetry in steady and unsteady turbulent open-channel flows by means of seeding with hydrogen bubbles, Flow Meas. and Instrumentation, Elsevier, 19 (2008), pp. 215-221.

Flume flows between boundaries of very different roughness: evaluation of friction using ADV measurements

Vaclav Matousek* and Tomas Picek

Department of Hydraulics and Hydrology, CTU Prague, Thakurova 7, 166 29 Prague, Czech Republic

(*Corresponding author, e-mail: v.matousek@fsv.cvut.cz).

Two ADV probes (one side-looking probe and one down-looking probe) were used for measurements of the local velocities and turbulence characteristics in a boundary layer of a flume flow in order to determine friction conditions at the flow boundaries. Three configurations of the top of the flow were tested and mutually compared: the flow with free water surface (open channel flow), the flow with water surface covered by a smooth solid plate, and the flow with water surface covered by a very rough solid plate. The tests carried out for various installed flow rates and water depths showed that the presence of a solid plate (1-m long) at the top of the flow significantly affected the longitudinal-velocity distribution and turbulence characteristics in the flow. Hence the presence of the water-surface cover considerably increased the shear velocity at the bottom of the flow. This would increase a danger of the bottom erosion if the bottom was a mobile bed. The paper comments on the test results and quantifies the effects of the velocity-profile deformation on the friction conditions at the bottom of the flow.

Keywords: Bed shear stress, velocity distribution, turbulence characteristics, flume test

1 INTRODUCTION

A solution of many problems associated with flow of water through conduits of different geometries requires information on the distribution of local velocities (all three components) and turbulence characteristics throughout the flow.

At present, the most often used instrument for the measuring of local velocities in open-channel flows is a propeller velocity meter, or an electromagnetic probe. These instruments are capable to measure just one component of the local velocity. Moreover, the obtained value of the local velocity is time averaged and do not allow to take care of turbulence characteristics. Furthermore, the instruments have a large control volume and the sensed value of the velocity may be influenced by a deformation of the velocity field caused by the submerged volume of the probe itself.

The ADV (Acoustic Doppler Velocimeter) enables a measurement of all three components of the local velocity and determination of their time-averaged and fluctuating parts. The instrument is robust enough to be used in the field conditions. Experiences published in the technical literature [e.g. 1-4] suggest that the instrument may be used successfully in both field and laboratory flows. For the lab tests the ADV technique can be a financially attractive alternative to the more sophisticated techniques as LDV (Laser Doppler Velocimeter), PIV (Particle Image Velocimetry) or UVP (Ultrasonic Velocity Profiler).

The investigation described in this paper was set to analyze an applicability of the ADV for the purposes of laboratory tests simulating flows influenced by irregularities (e.g. flows under barriers of floating

debris developed at the water surface of an open channel and accumulated in front of hydraulic objects like bridges during a flood event).

2 EXPERIMENTAL FACILITIES

2.1 Laboratory flume

The laboratory flume used for our ADV tests is rectangular, 0.25 m wide, and 6.3 m long. The bottom and side walls of the flume are hydraulically smooth. The probe was positioned to the vertical axis of the flume cross section.

2.2 ADV probe

The entire experimental program was carried out using the Nortek 3-D side-looking probe with the sampling frequency 25 Hz and the control volume positioned 50 mm in front of the probe transmitter (Fig. 1). Since this was our first experience with the ADV probe, its measuring abilities were tested first by comparison with other measuring techniques before carrying out the actual experiments. The comparison of velocity profiles measured using the side-looking probe with the down-looking probe [5], the LDA [6], and the series of different propellers [5], confirmed that after elimination of a certain systematic error in the longitudinal-velocity measurement the side-looking probe produces velocity profiles in undisturbed channels with a satisfactory accuracy. Thus it was suitable to use for a mutual comparison of profiles of longitudinal velocity in flows of three different geometries of a boundary at the top of the flow through a laboratory flume.

The comparison of the local turbulence characteristics (fluctuating components of local velocities) showed a reasonable agreement between the LDA and the side-looking ADV probe in

flows through undisturbed channels. Surprisingly bad match was found for the down-looking ADV probe that tended to underestimate heavily the values of the vertical fluctuating velocity. This was in accordance with the experience that others [7] had gained with this particular probe. Thus the down-looking probe in our possession is not suitable for turbulence-characteristics tests. The side-looking probe is acceptable for channels flows. However, its comparison with LDA revealed also that due to its relatively low sampling frequency the ADV probe is not suitable for measuring at locations of high intensities of turbulence in a flow (e.g. within wakes behind obstacles) [8]. Since such measurements are not included in our experimental program this finding does not disturb our tests.

A sensitivity analysis of the probe operating parameters suggested that the length of the control volume of 6 mm is the most suitable for the tests (the probe offers a choice of 3-, 6-, and 9-mm length). The sampling time of at least 40 second is required to collect representative data for both the time-averaged- and the fluctuating components of the local velocity. Our data were collected with the 90-second sampling time. An application of seeding particles is mandatory.

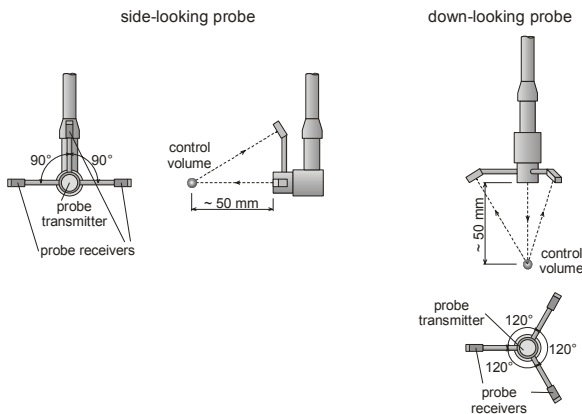


Figure 1: The side-looking probe used for experiments and the down-looking probe used for a comparison.

2.3 Different boundaries at water surface during tests

Three configurations of the top of the flow were tested and mutually compared: the flow with free water surface (open channel flow), the flow with water surface covered by a smooth solid plate, and the flow with water surface covered by a very rough solid plate. The smooth plate was a 1-m long plastic plate of the thickness of about 1 cm. The very rough solid plate was actually the smooth plate, used for the smooth-boundary tests, covered by the mattress Enkamat 7010 made of synthetic polyamide fiber of the diameter of about 0.7 mm. The mattress is 10 mm thick, thus the fibers penetrate the flow down to the 10-mm depth below the water surface.

3 RESULTS AND DISCUSSION

3.1 Methods for determination of bottom shear velocity

The main objective of the experiments is to determine the shear velocity at the bottom of the flow (u_{*b}) and to evaluate its variation with the changing boundary conditions at the top of the flow. Basically, there are two methods for the shear velocity determination from the measurements of local velocities along the vertical axis of the flow:

- the comparison of measured- and theoretical distribution of longitudinal velocity across the flow,
- the comparison of measured- and theoretical distribution of Reynolds shear stress across the flow.

ad a. the method is based on the assumption that there is the logarithmic distribution of the time-averaged longitudinal velocity u_y across a certain part of the boundary layer above the bottom of the flow. If the bottom is hydraulically smooth, the distribution can be expressed using the relation between two dimensionless parameters:

$$z^+ = \frac{z \cdot u_{*b}}{\nu_f}, \quad \text{and} \quad u^+ = \frac{u_y}{u_{*b}}.$$

The relationship is given e.g. by the Prandtl-Karman equation

$$u^+ = 2.5 \cdot \ln z^+ + 5.5 \quad (1).$$

Considering that u_y is measured at various vertical positions z above the bottom of the flow, and the kinematic viscosity (ν_f) of the flowing water is known, Eq. 1 can be exploited to determine the u_{*b} value required to fit the measured velocity profile with the theoretical one.

ad b. the method is based on the assumption that the vertical distribution of the Reynolds shear stress ($\tau_{zy} = \rho_f \cdot \overline{u'_y \cdot u'_z}$) is linear across the most part of the turbulent flow (except the viscous sub-layer and the lower portion of the buffer layer) with the zero value at the hydrodynamic axis of the flow and the maximum value near the bottom of the flow. The distribution equation reads

$$\tau_{zy,b} = \tau_{zy} \cdot \frac{h_a}{h_a - z} \quad (2),$$

in which h_a is the height of the hydrodynamic axis above the bottom of the flow. The bottom shear

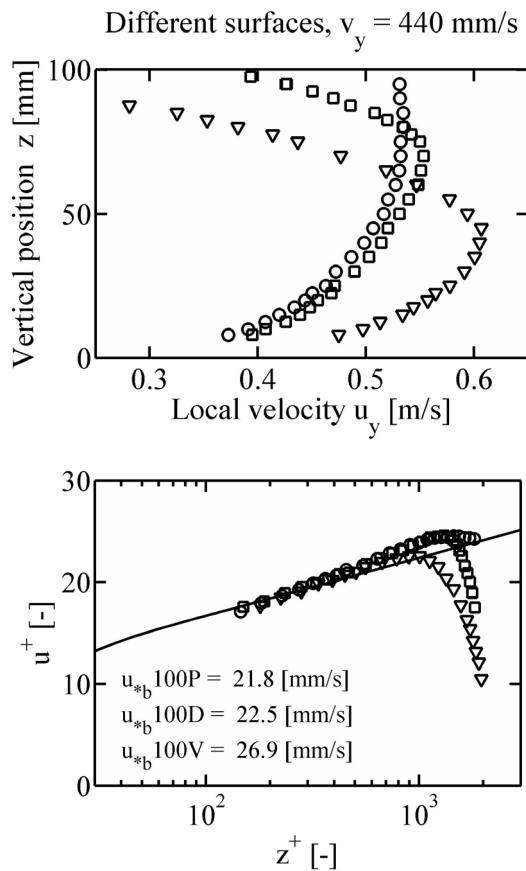
$$\text{velocity, } u_{*b} = \sqrt{\frac{\tau_{zy,b}}{\rho_f}}.$$

Considering that the fluctuating components of the longitudinal-, and vertical local velocities (u'_y , and u'_z) are measured, and the density (ρ_f) of the flowing water is known, Eq. 2 can be exploited to determine the u_{*b} value required to fit the measured shear-stress profile with the theoretical one.

3.2 Bottom shear velocity from distribution of longitudinal velocity

Table 1: Positions of hydrodynamic axis (h_a) and values of bottom shear velocity (u_{*b}) for flows of constant depth H and flow rate Q (average velocity $v_y \approx 440$ mm/s); code P = free water surface, D = surface covered by smooth plate, V = surface covered by rough plate; see also Fig. 2.

Run code	H (mm)	Q (lit/s)	h_a/H (-)	$u_{*b(u)}$ (mm/s)
H100Q1100P	100	10.92	0.85	21.8
H100Q1100D	100	11.04	0.7	22.5
H100Q1100V	100	10.92	0.45	26.9

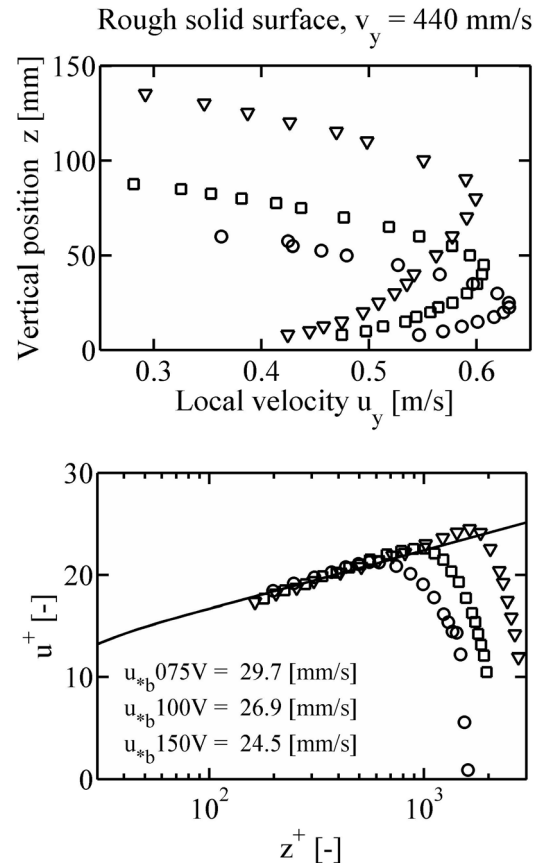


Legend:
 ○ - flow with free water surface, water depth $H = 100$ mm,
 □ - flow below smooth solid plate, water depth $H = 100$ mm,
 ▽ - flow below rough solid plate, water depth $H = 100$ mm,
 line - Prandtl-Kármán log law, Eq. 1.

Figure 2: Comparison of measured velocity profiles with Eq. 1 (flow properties are given in Tab. 1).

Table 2: Positions of hydrodynamic axis (h_a) and values of bottom shear velocity (u_{*b}) for flows of constant average velocity $v_y \approx 440$ mm/s but different Q and H below the rough plate, see also Fig. 3.

Run code	H (mm)	Q (lit/s)	h_a/H (-)	$u_{*b(v)}$ (mm/s)
H075Q0825V	74.7	8.15	0.30	29.7
H100Q1100V	100	10.92	0.45	26.9
H150Q1650V	150.6	16.40	0.53	24.5



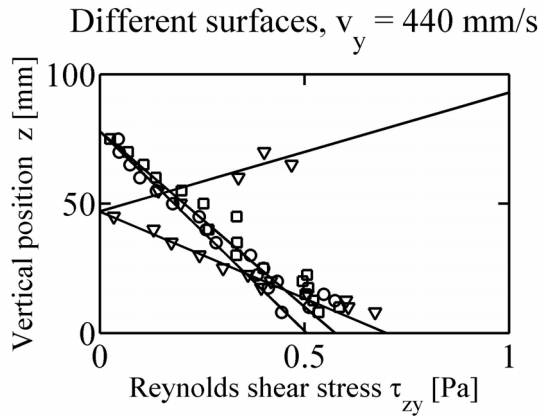
Legend:
 ○ - flow below rough solid plate, water depth $H = 75$ mm,
 □ - flow below rough solid plate, water depth $H = 100$ mm,
 ▽ - flow below rough solid plate, water depth $H = 150$ mm,
 line - Prandtl-Kármán log law, Eq. 1.

Figure 3: Comparison of measured velocity profiles with Eq. 1 (flow properties are given in Tab. 2).

3.3 Bottom shear velocity from distribution of Reynolds shear stress

Table 3: Positions of hydrodynamic axis (h_a) and values of bottom shear velocity (u_{*b}) for flows of constant depth H and flow rate Q (average velocity $v_y \approx 440$ mm/s); code P = free water surface, D = surface covered by smooth plate, V = surface covered by rough plate; see also Fig. 4.

Run code	H (mm)	Q (lit/s)	h_a/H (-)	$u_{*b(r)}$ (mm/s)
H100Q1100P	100	10.92	0.78	22.5
H100Q1100D	100	11.04	0.78	24.0
H100Q1100V	100	10.92	0.47	26.5



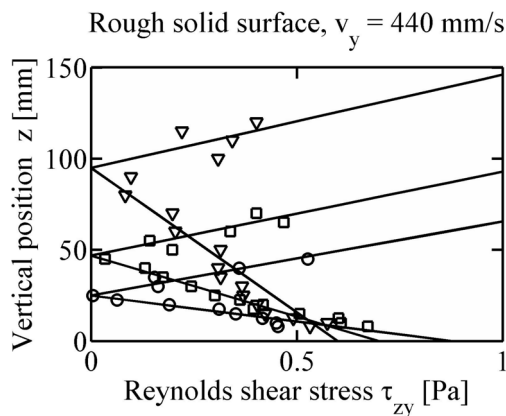
Legend:

- - flow with free water surface, water depth $H = 100$ mm,
- - flow below smooth solid plate, water depth $H = 100$ mm,
- ▽ - flow below rough solid plate, water depth $H = 100$ mm,
- line - linear distribution of Reynolds shear stress, Eq. 2.

Figure 4: Comparison of measured τ_{zy} profiles with Eq. 2 (flow properties are given in Tab. 3).

Table 4: Positions of hydrodynamic axis (h_a) and values of bottom shear velocity (u_{*b}) for flows of constant average velocity $v_y \approx 440$ mm/s but different Q and H below the rough plate, see also Fig. 5.

Run code	H (mm)	Q (lit/s)	h_a/H (-)	$u_{*b(r)}$ (mm/s)
H075Q0825V	74.7	8.15	0.33	29.7
H100Q1100V	100	10.92	0.47	26.5
H150Q1650V	150.6	16.40	0.63	24.5



Legend:

- - flow below rough solid plate, water depth $H = 75$ mm,
- - flow below rough solid plate, water depth $H = 100$ mm,
- ▽ - flow below rough solid plate, water depth $H = 150$ mm,
- line - linear distribution of Reynolds shear stress, Eq. 2.

Figure 5: Comparison of measured τ_{zy} profiles with Eq. 2 (flow properties are given in Tab. 4).

4 DISCUSSION

The values of the bottom shear velocity acquired from the distribution of the longitudinal velocities differ with less than 7 per cent from the values obtained from the Reynolds shear stresses. The position of the hydrodynamic axis (h_a) differs with less than say 20 per cent.

The comparison of the processed ADV data with the corresponding theories indicates that the match is tighter for the longitudinal velocity profiles (the measured profiles compared with the theoretical logarithmic profiles using Eq. 1), than for the measured Reynolds shear stress profiles (the measured profiles compared with the theoretical linear profiles using Eq. 2).

5 CONCLUSIONS

The tests confirmed that covering an originally free water surface with debris or an ice cover (during the tests simulated by solid plates of different roughness) deforms the velocity distribution across the flow, changes the turbulence characteristics and increases the shear velocity at the bottom of the flow. The roughness of the covering plate influences considerably the value of the shear velocity.

Furthermore, the tests revealed that, for the particular ADV probe used, the determination of the bottom shear velocity was less accurate if derived from measurements of the turbulence characteristics than from measurements of vertical profiles of the time-averaged longitudinal velocity.

ACKNOWLEDGEMENT

The work was supported by the CIDEAS VS project 1M0579 of the Czech Technical University.

REFERENCES

- [1] Strom BK, Papanicolaou AN: ADV measurements around a cluster microform in a shallow mountain stream, *J. Hydr. Engrg.* 133(12) (2007)1379-1389.
- [2] Stone MC, Hotchkiss RH: Evaluating velocity measurement techniques in shallow streams, *J. Hydr. Res.* 45(6) (2007) 752-762.
- [3] Meftah BM et al.: Experimental study of flexible and rigid vegetation in an open channel, *Proc. River Flow 2006* (2006) 603-611.
- [4] Carollo FG et al.: Analyzing turbulence intensity in gravel bed channels, *J. Hydr. Engrg.* 131(12) (2005) 1050-1061.
- [5] Píček T, Matoušek V: Comparison of flow characteristics measured using horizontal- and vertical-oriented ADV probes, *Proc. The 22nd Symposium on Anemometry, Holany-Litice* (2008), in press (in Czech).
- [6] Matoušek V: Determination of bed shear stress from velocity profiles and turbulence characteristics measured using ADV probe, *Proc. seminar VC CIDEAS -VS Nejistoty modelů a přístupů aplikovaných v říčním inženýrství, povrchové a podpovrchové hydrologii*, (2007) 47-54, ISBN 978-80-01-03924-3 (in Czech).
- [7] Jiráček J, Bareš V: Comparison of ADV and UVP method for turbulent characteristic measurement of free surface flow in circular pipe, *Proc. The 20th Symposium on Anemometry, Holany-Litice* (2006) 53-58 (in Czech).
- [8] Chára Z, Matoušek V: A possibility of ultrasonic method to measure flow characteristics, *Proc. The 21st Symposium on Anemometry, Holany-Litice* (2007) 59-66, ISBN 978 80 87117 019 (in Czech).

Contact measurement of turbulent intensity of the pipe flow using UVP

Hisato MINAGAWA^{*}, Tomoki ISHIDA and Takahiro YASUDA

Department of Mechanical Systems Engineering, The University of Shiga Prefecture, Hassaka 2500, Hikone, Shiga 522-8533 (*e-mail: minagawa@mech.usp.ac.jp)

In this study, the authors directly inserted the transducer of the UVP with an accurate movable device into the flow parallel to the flow axis. We investigate the measurement accuracy of the velocity and the possibility of the velocity fluctuation measurement concerning with turbulent intensity using this method. This method is free from the effects of reflection and refraction at the pipe wall unlike the UVP measurement through the pipe wall, although this method has the demerit of contact with liquid. In addition, we adopted micro bubbles as the reflector of the ultra sound. They are environment-friendly compared with fine solid particles which may pollute the environment, and they are economy. These bubbles are generated by the pressurized dissolution method. As the results of the measurement, the time-averaged velocity profiles measured by the UVP contact measurement agreed well with the calculated results by the $(1/n)$ power's law. The deviations are smaller than those measured by the UVP measurement through the pipe wall. RMS values of velocity fluctuation divided by the cross-sectional averaged flow velocity U are presented by the UVP contact measurement. The results agreed with the tendencies of Hosokawa et al.'s and Laufer's data.

Keywords: Pipe flow, Velocity profile, Ultrasonic Velocity Profile monitor, Micro bubble

1 INTRODUCTION

Piping is used in various industrial fields and the flowing characteristics have been researched by a lot of researchers. However, in the case the opaque piping and/or the opaque fluid, it is difficult to measure the flow using light such as the laser beam or the PIV. The ultrasonic velocity profile monitor (UVP) can be applied to such a case.

The measurement of the flow in pipes using the UVP is usually carried out through the pipe wall. However, because the ultrasonic wave is reflected and refracted complexly through the pipe wall with the curved surface, it may be difficult to obtain the high signal to noise ratio data in a round pipe. In addition, only the transducer direction component of the velocity can be measured because of setting up the transducer at a certain acute angle to the radial axis.

Then, in this study, the authors directly inserted the transducer of the UVP with an accurate movable device (it moves from the pipe wall to the center) into the flow parallel to the flow axis. We investigate the measurement accuracy of the velocity and the possibility of the velocity fluctuation measurement concerning with turbulent intensity using this method.

This method (UVP contact measurement) is able to be used for the opaque piping and/or opaque liquids unlike the LDV, not necessary to calibrate before the experiment unlike a heat-wire airflow meter, and free from the effects of reflection and refraction at the pipe wall unlike the UVP measurement through the pipe wall, although this method has the demerit of contact with liquid. In the near future, the authors

plan to make a precise measurement of the flow around a large bubble using this method.

In addition, we adopted micro bubbles as the reflector of the ultra sound. As for the first reason, they are environment-friendly compared with fine solid particles which may pollute the environment. Secondly, they are economy. Once we have a micro bubble generator, we don't have to pay any more than the electricity expense. These bubbles are generated by the pressurized dissolution method.

In order to verify the validity of this method, we measured the velocity distribution and computed the root-mean-square value of the velocity fluctuation in turbulent flow of the water single phase in a vertical pipe of 53.5mm I.D.

2 EXPERIMENT

2.1 Experimental apparatus and experimental method

Figures 1 and 2 show the experimental apparatus and transducer installed at the exit part of the pipe, respectively. In this study, water single phase turbulent flow is measured with the pipe made from the acrylic resin of 53.5mm in inside diameter. We prepare the water tank kept about 20 degree Celsius and generate micro bubbles in the tank. The average bubble diameter is $30\mu\text{m}$. The micro bubbles produced in the water tank flow to the vertical pipe by a Mohno pump with water. The pipe length L , from the elbow to the measuring section is 3.1m, and it is equivalent to 57 times pipe diameter, D . The UVP we used is type X-3-PSi (1999).

We attached the transducer at the pipe exit with an accurate movable device. The frequency of the transducer is 4MHz, the beam diameter 5mm, and

measuring range 5~100mm from the transducer tip. The time resolution of the UVP in this measurement

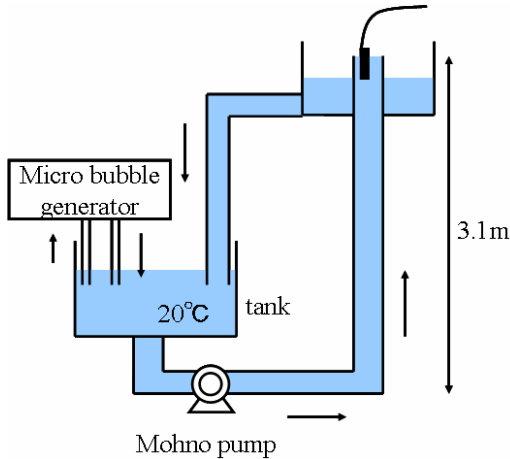


Figure 1: Experiment apparatus

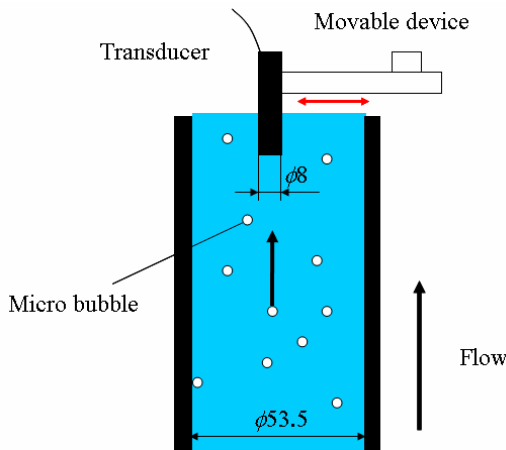


Figure 2: Setting of transducer

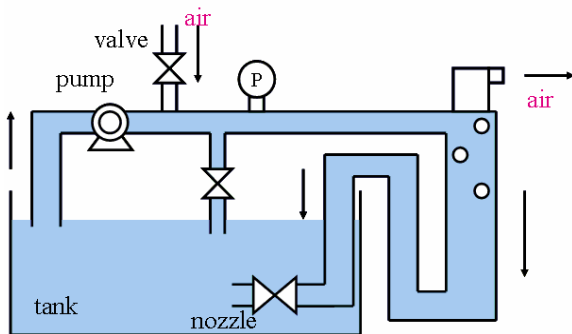


Figure 3: Micro bubble generator

is about 18~23msec, the velocity resolution 0.90~1.73mm/s, and the space resolution 0.74mm in the beam direction. This velocity resolution is 2.92 times smaller than the case setting transducer outside of the pipe at 20 degrees to the horizon.

Figure 3 illustrates a schematic of the micro bubble

generator. The pressurizing dissolution system to produce micro bubbles consists of a pump (Swirl chamber pump, 20KED04S, 560W, Nikuni Co., Ltd.), a water tank (tank in Fig.1), a pressurizing pipe with an air vent, and some pipe arrangements. The back pressure valve is adjusted to create an adequate pressure in the pressurizing pipe beforehand. The pump suctions water from the water tank. This pump also aspirates air through the air valve simultaneously, and mixes water and air in its swirl chamber. The air-water mixture is then pressurized up to 0.2MPa (gauge) and sent to the pressurizing pipe.

According to the Henry's law, more air is dissolved in water in this pressurized condition than under atmospheric pressure. Extra gas, which is not dissolved in the water still exist as bubbles, is exhausted to the atmosphere through air vent. Then the flow is apparently water single phase flow. After the pressurizing pipe, the flow proceeds to the main tank of the experimental apparatus.

2.2 Data procession

To remove the noise in the obtained velocity profiles, we carried out the calculation of root-mean-square (RMS) value of the velocity fluctuation u' and time-averaging of the velocity data after excluding zero or negative velocity data.

Figure 4 shows the relation between the time-averaged velocities and the distance from the transducer tip under the condition of flow rate $Q=8.89\text{ l/min}$, cross-sectional averaged flow velocity $U=65.9\text{ mm/s}$, and Reynolds number, $Re=3500$. The symbols exhibit the difference of the radial direction distance r from the pipe wall. The velocity near the transducer was affected by the existence of the transducer. It shows almost constant values within the range of 40~60mm. So that, we cut out the data from the transducer tip (0mm) to about 40mm. The data beyond about 60mm from the tip were also cut out because of the unreasonable decrease of time-averaged velocities probably because of the spreading of the ultrasonic beam. Therefore, data from about 40 to 60mm is used.

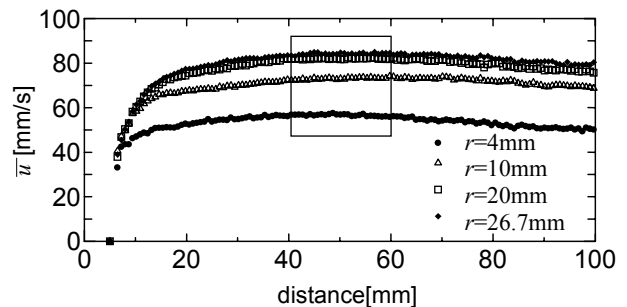


Figure 4: Plot of \bar{u} vs. distance from the transducer tip

Because the space resolution in this measurement is 0.74mm, there are 29 data points in this range. When we obtain the time-averaged velocity profile, the velocity values at each data point are arithmetical averaged. Therefore, the obtained velocity profiles are both time- and space-averaged ones. Similarly, the RMS value of the velocity fluctuation $\sqrt{u'^2}$ is first obtained locally and averaged in this range.

2.3 Adjustment of velocity profiles

As the ratio of the beam diameter ($\phi 5$) to the pipe diameter ($\phi 53.5$) is relatively large, the measured velocity by the UVP may be deviate from the local velocity at the transducer's center, especially near the pipe wall. This is because the beam-area averaged velocity differs from the transducer's center velocity. Its modification coefficient is not easily estimated analytically. Therefore, we used the Monte Carlo method to adjust this influence.

More than 50000 random numbers are generated in the range of the ultrasonic beam. The velocities at the random numbers' positions are calculated using the $(1/n)$ power's law, and averaged. This average is compared with the velocity at the transducer's center is calculated using the $(1/n)$ power's law, and the modification coefficient is obtained.

Considering the effect of the flotation of micro bubbles, the measured velocity includes the floating velocity of bubbles. Therefore, in order to obtain an actual velocity, 0.5mm/s is subtracted from the measured velocity data since their average diameter is about $30\mu\text{m}$, and the mean floating velocity is 0.5mm/s.

3 EXPERIMENTAL RESULTS AND DISCUSSION

3.1 Time-averaged velocity profiles

The time-averaged velocity profiles measured by the UVP contact measurement are shown in Fig.5. The velocity profiles almost agree well with the curve lines drawn using the $(1/n)$ power's law, where the value of n was calculated using Eq.(1)[1].

$$n = \log_{10}(\text{Re}) + 2 \quad (1)$$

The mean value of the deviation from the measured and the calculated values using the $(1/n)$ power's law is 2.84, 2.12, 1.98 and 0.799% respectively for $\text{Re}=3500, 4200, 5200$ and 7700 , and their average is 1.94%.

On the other hand, the corresponding measured data by the UVP through the pipe wall with setting transducer outside of the pipe at 20 degrees to the

horizon is shown in Fig.6. Although the number of data point for each velocity profile is larger than Fig.5, the deviations seem larger. The mean value of the deviation from the measured and the calculated values using the $(1/n)$ power's law is 5.52, 5.69, 3.51, 2.56 and 1.67% respectively for $\text{Re}=3500, 4200, 5000, 6000$ and 9000 , and their average is 3.79%. From these values, it is obvious that the UVP contact measurement is more effective than the UVP measurement through the pipe wall based on the perspective of the precision of the time-averaged velocity measurement.

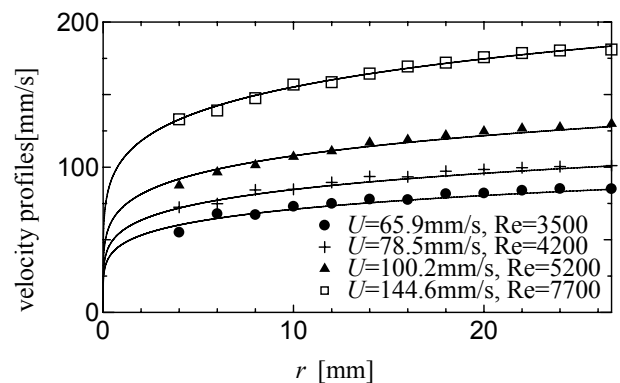


Figure 5: Time-averaged velocity profiles by the UVP contact measurement ($D=53.5\text{mm}$)

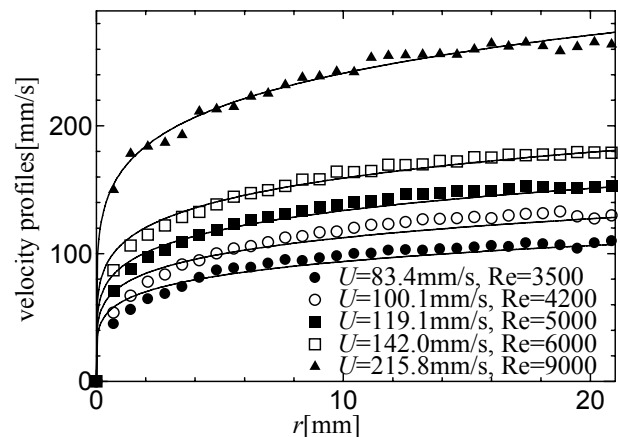


Figure 6: Time-averaged velocity profiles by the UVP through the pipe wall ($D=42\text{mm}$)

3.2 RMS value of velocity fluctuation

According to the experimental results of Hosokawa and Tomiyama [2], the turbulent length scale is about $0.2D$ except for the neighborhood of the pipe wall ($r/R < 0.2$) regardless of Re in the pipe flow. Hence, the turbulent length scale is estimated about 10.7mm in this study. Under the assumption that the scale propagates at the time-averaged velocity, the frequency can be estimated at most from 7.9Hz ($\text{Re}=3500$) to 16.8Hz ($\text{Re}=7700$). The time

resolution of the UVP contact measurement in this study is about 18~23msec, which correspond to 56 to 43Hz. Thus, the time resolution is satisfied in these conditions, and we try to measure the velocity fluctuation relating to the turbulent intensity. The measured results of RMS value of velocity fluctuation $\sqrt{u'^2}$ divided by the cross-sectional averaged flow velocity U are presented in Fig.7 with Hosokawa et al.[2]'s data measured by a LDV and Laufer[3]'s data measured by a heat-wire airflow meter. According to Fig.7, the values of $\sqrt{u'^2}/U$ are larger near the pipe wall. It decreases to the pipe center. This tendency agrees with the existing data [2-3]. The smaller Re is, the larger the values of $\sqrt{u'^2}/U$ especially near the pipe wall similarly to the existing data. These tendencies prove the data obtained by the UVP contact measurement in this study are validated.

On the other hand, Figure 8 shows the corresponding data measured by the UVP through the pipe wall. The tendencies of the data presented in Fig.7 are not recognized. The values are much larger. Therefore, these RMS values measured by the UVP through the pipe wall in this study are confirmed to be useless. This is probably because of the insufficient velocity resolution and the shortage of signal to noise ratio.

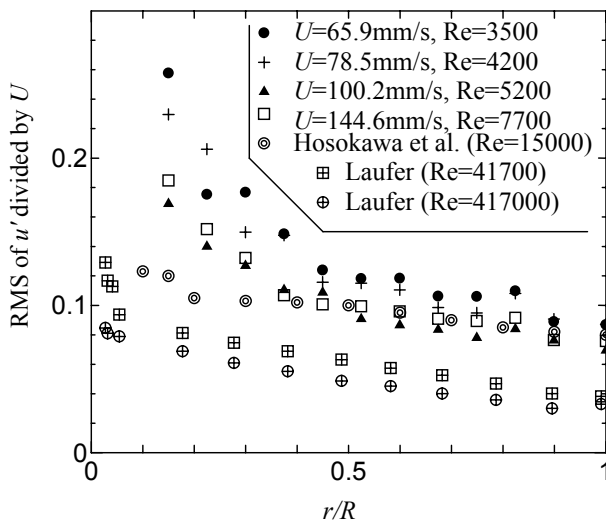


Figure 7: RMS value of velocity fluctuation $\sqrt{u'^2}$ divided by the cross-sectional averaged flow velocity U measured by the UVP contact measurement ($D=53.5\text{mm}$) together with existing data

4 CONCLUSIONS

In this study, we directly inserted the transducer of the UVP with an accurate movable device into the

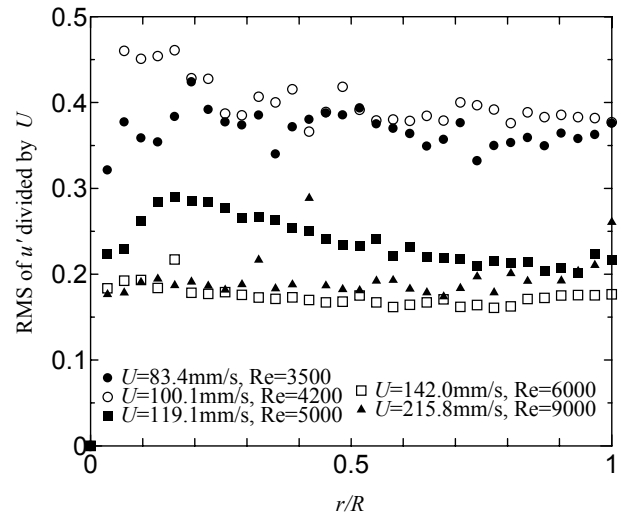


Figure 8: RMS value of velocity fluctuation $\sqrt{u'^2}$ divided by the cross-sectional averaged flow velocity U measured by the UVP through the pipe wall ($D=42\text{mm}$)

flow parallel to the flow axis. In order to verify the validity of this method, we measured the velocity distribution and computed the root-mean-square value of the velocity fluctuation in turbulent flow of the water single phase in a vertical pipe of 53.5mm I.D.

As the results of the measurement, the conclusions are obtained as follows:

1. The time-averaged velocity profiles measured by the UVP contact measurement agreed well with the calculated results by the $(1/n)$ power's law. The deviations are smaller than those measured by the UVP measurement through the pipe wall.
2. RMS values of velocity fluctuation $\sqrt{u'^2}$ divided by the cross-sectional averaged flow velocity U are presented by the UVP contact measurement. The results agreed with the tendencies of Hosokawa et al.'s and Laufer's data. In this case, the measured results by the UVP measurement through the pipe wall were also insufficient.

REFERENCES

- [1] Watanabe, K., Fluid mechanics, flow and loss (in Japanese), Maruzen, Tokyo (2002).
- [2] Hosokawa, S. and Tomiyama, A., Turbulence modification in gas-liquid and solid-liquid dispersed two-phase pipe flows, Heat and Fluid Flow, 25 (2004), 489-498.
- [3] Laufer, J., The structure of turbulence in fully developed pipe flow, NACA Report No.1174 (1954), 417-434.

Non-Newtonian fluid flow in elastic tubes

S. Nahar^{1*}, B.H. Birkhofer^{1,2}, S.A.K. Jeelani¹ and E.J. Windhab¹

¹Laboratory of Food Process Engineering, Institute of Food Science and Nutrition, Swiss Federal Institute of Technology, Schmelzbergstrasse 7, 8092 Zurich, Switzerland (*Corresponding author, e-mail: samsun.nahar@ilw.agrl.ethz.ch).

²Present address: Tüffenwies 16-22, Sika Services AG, 8084 Zürich, Switzerland.

The knowledge on the non-Newtonian fluid flow behavior in inflatable and collapsible elastic tubes is important to applications such as biofluid mechanics in human body and the transport of food and liquids in pharynx (throat), esophagus and intestines. The ultrasound Doppler based velocity profiles are measured at a fixed position from the outlet of a horizontal collapsible elastic tube immersed in a liquid filled chamber, whose pressure is maintained at a constant value during steady laminar flow of a shear thinning xanthan aqueous solution. For a given volume flow rate and a critical external chamber pressure, the tube is buckled. The shape of the deformed cross section visually observed has two lobes, above and below the horizontal axis through the tube center, with no contact between tube's two vertical planes. As the external chamber pressure increased, the width at the tube center and area of cross section of the two lobed-shaped deformed tube decreased. Consequently, the measured maximum flow velocity at the center of the tube width increased. The shear rate dependent viscosity of xanthan solution was measured using a rheometer.

Keywords: Elastic tube flow, non-Newtonian liquid flow, shear thinning fluids, ultrasound Doppler Velocity profile.

1 INTRODUCTION

The flow of non-Newtonian fluids in elastic inflatable and collapsible tubes is important to biofluid mechanics encountered in human body and other applications; for instance, transport of food and liquids in human throat (pharynx), the tube (esophagus) connecting the throat and stomach, and intestines. The knowledge on the mechanisms of pharyngeal, esophageal and intestinal transport of food and liquids is very useful for the treatment of patients with malfunctioning of these transport processes. The physiology of these applications in human body is very complex, which is not fully understood. The flow behavior (rheology) of the food and liquids through the throat or esophagus or intestines could be broadly characterized in terms of parameters related to: (i) food composition, physico-chemical properties, interaction and microstructure, (ii) mechanical properties (elastic modulus, Poisson ratio, strain and bending stresses) of the elastic tube and its lining (mucus) and (iii) external applied (pressure or compressive) stresses to induce and sustain flow. The food and liquids could have viscous Newtonian or viscous non-Newtonian or viscous and elastic non-Newtonian flow behavior; the latter may be due to the presence of viscoelastic biopolymers.

Although the Stokes laminar flow structure of Newtonian fluids in an elastic tube was numerically investigated [1], there exists no published experimental information on the corresponding

velocity distribution in the collapsed tube. Hasegawa et al. [2] experimentally investigated the velocity profiles during swallowing of food in pharynx using ultrasound Doppler velocimetry. In contrast, there are several publications on the velocity profiles measured using this technique during steady and unsteady laminar flow of non-Newtonian fluids and particulate suspensions [see for example reference 3] in non-collapsible pipes. Consequently, the present paper investigates the measurement of the ultrasound Doppler based velocity profiles during steady laminar flow of a non-Newtonian shear thinning xanthan (polysaccharide) solution through a partially collapsed elastic tube immersed in the liquid of a pressure chamber called Starling Resistor [4] set up. The influence of the external chamber pressure on the deformation of the elastic tube and the velocity profiles are also measured.

2 EXPERIMENTAL

2.1 Starling Resistor setup for non-Newtonian fluid flow in elastic tubes

The Starling Resistor setup shown in Figure 1 consists of a cylindrical Plexiglass (PG) pressure chamber (111 mm inner diameter, 5.66 mm thick and 300 mm long) with two side PG flanges through each of which an aluminum pipe is fixed. A 20 mm inner diameter, 1 mm thick and 200 mm long silicone elastic tube (Lindemann GmbH, Germany) is mounted between the two aluminum pipes. The left pipe is connected to a rotor pump and a PVC

tank containing the non-Newtonian liquid. Two pressure sensors (Honeywell, Type: 40PC-030G2A) are installed in both the inlet and outlet aluminum pipes to measure the pressures of liquid. Two additional pressure sensors are connected to the pressure chamber to measure the externally applied pressure to deform the elastic tube. The four pressure transducers are connected to a data acquisition board (type USB-6221, National Instruments) with a resolution of 16 bits. Sony DFW-V500 Camera with a resolution of 640X480 is used to obtain images of deformed elastic tube. The Camera is mounted on a aluminum arm, which can be rotated to obtain images of the deformed tube at different angles. The steady flow of a shear thinning non-Newtonian aqueous solution of 0.1 % xanthan (and 0.02 M NaCl) at a constant volume flow rate and different values of the external chamber pressure P_e is carried out at 22°C.

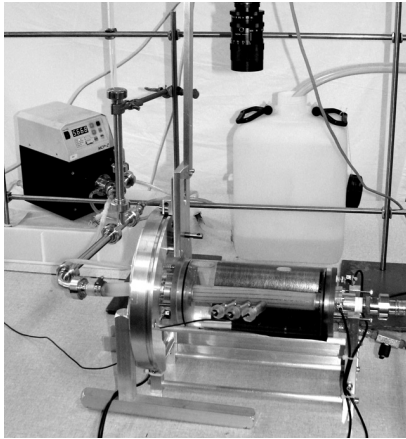


Figure 1: Ultrasound Doppler velocimetry for flow through collapsible silicone elastic tube in Starling resistor setup.

2.2 Ultrasound Doppler based velocity profile measurement in elastic tube

A UVP-Duo (Met-Flow SA, Lausanne, Switzerland) instrument is used to measure the velocity profiles of xanthan solution flowing through the deformed elastic tube in the Starling Resistor setup. A 4 MHz base frequency ultrasound transducer of 5 mm active diameter and 8 mm diameter housing (Met-Flow SA, Lausanne, Switzerland) is used as transmitter and receiver. The Perspex cylindrical pressure chamber is provided with a side tube to house an ultrasound transducer at an angle of 20° with respect to the normal to the horizontal axis. The transducer submerged in water in the pressure chamber is in direct contact with the elastic tube and is positioned at 75 mm from the tube outlet. The transducer is so positioned that it does not contribute to tube deformation. The communication with the UVP-Duo is made with an active X Library from Met-Flow SA. The number of cycles per pulse is 2 and the channel width is 0.37 mm. Each profile

is obtained by averaging 100 profiles, which is represented by the full line. The measured velocity of sound in the xanthan solution at 22°C is 1492 m/s.

3 RESULTS AND DISCUSSION

The velocity profiles obtained for undeformed and deformed silicone elastic tube under different external chamber pressures at constant volume flow rate of 33.2 ml/s of xanthan solution are presented below. The corresponding images of the deformed tubes are also shown.

3.1 Velocity profiles in elastic tube

Fig. 2 shows the velocity profile along the tube diameter (expressed as a function of channel number, the channel distance being 0.37 mm) measured during steady flow of xanthan solution in the undeformed silicone elastic tube of circular cross-section when the external chamber pressure P_e is zero and the inlet pressure $P_i = 76.6$ mbar and $P_o = 73.4$ mbar. The profile is flat at the center of the tube, indicating shear thinning behavior of xanthan solution.

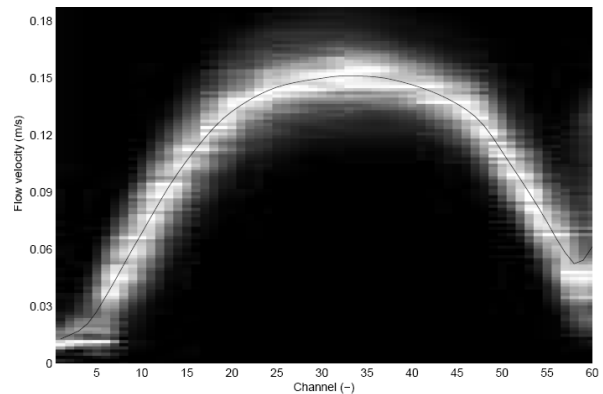


Figure 2: Velocity profile (full line: average profile) in undeformed elastic tube at 0 mbar external chamber pressure.

The profiles in the collapsed tube due to 85 mbar external chamber pressure are shown in Fig.3 (with channel distance of 0.56 mm) for which the inlet pressure is about 73 mbar. The corresponding two images taken from the top and after rotating the camera 110° anticlockwise around cylinder are shown in Fig.4. The length of the deformed tube is 55 mm from the transducer in addition to 20 mm long undeformed tube towards the tube outlet. The shape of the cross section (see Fig.5) along the length of the deformed tube seem to have two lobes above and below the horizontal axis with no contact between the two 39 mm tall vertical planes of the tube. The widths of the deformed tube at the center and top are about 9 mm and 11.4 mm respectively.

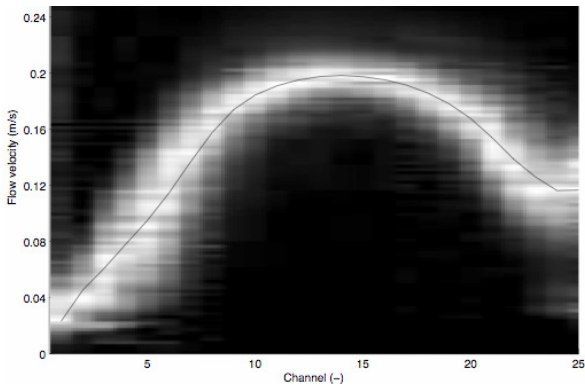
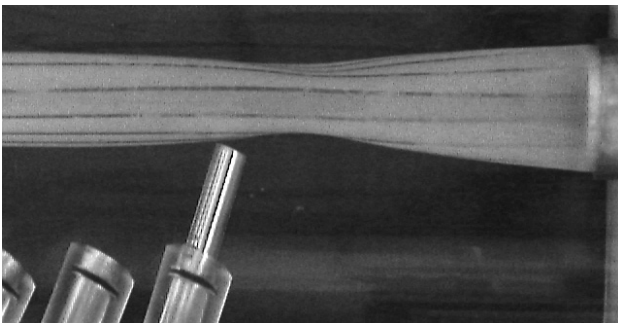
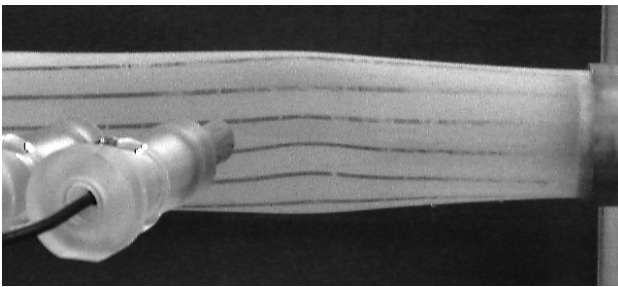


Figure 3: Velocity profile (full line: average profile) in collapsed elastic tube at 85 mbar external chamber pressure.



(a)



(b)

Figure 4: Images of deformed tube at 85 mbar external chamber pressure: (a) top view (b) front view.

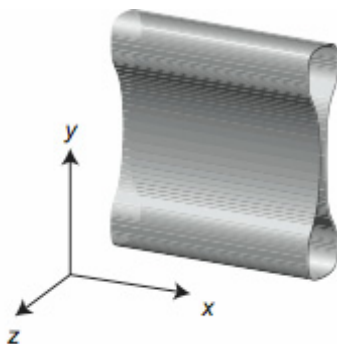


Figure 5: Schematic front view of a partially buckled elastic tube.

Fig.6 shows the velocity profile (with channel distance of 0.56 mm) in the more collapsed flattened silicone tube at 90 mbar external chamber pressure, $P_I = 73.1$ mbar and $P_O = 72.8$ mbar. The images

of deformed tube from top and after rotating the camera 140° anticlockwise around cylinder are shown in Fig.7.

The deformed tube length from the transducer to the tube outlet is 80 mm. Its shape is similar to that for 85 mbar external chamber pressure shown above although the dimensions of the cross section are reduced. The deformed tube widths are 5.6 mm and 6.6 mm at the center and top respectively with a height of 18 mm. In contrast, as the chamber pressure increased from 85 mbar to 90 mbar, the area of the two lobed shaped cross section of deformed tube decreased.

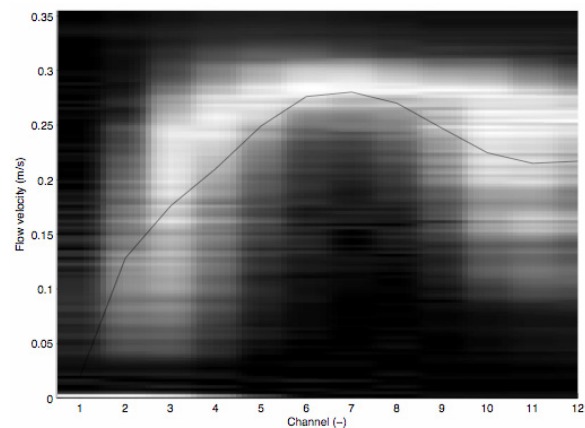
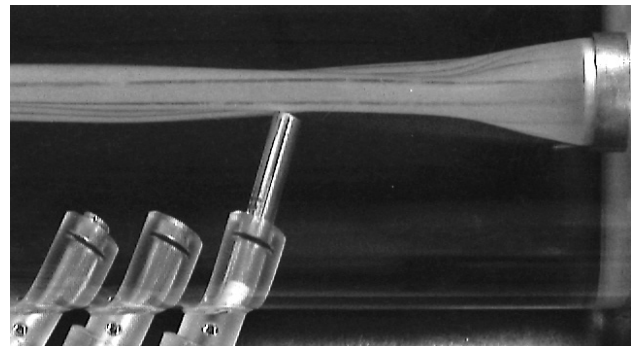
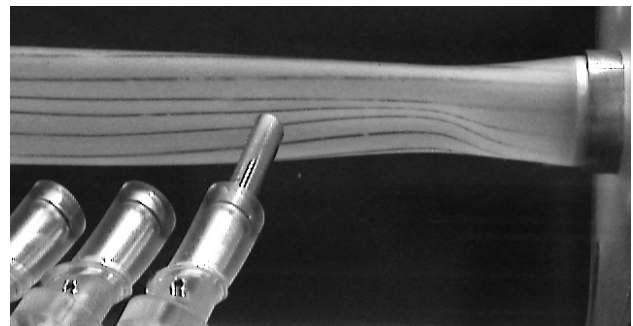


Figure 6: Velocity profile (full line: average profile) in collapsed elastic tube at 90 mbar external chamber pressure.



(a)



(b)

Figure 7: Images of deformed tube at 90 mbar external chamber pressure: (a) top view (b) front view.

Consequently, the corresponding maximum velocity

at the center of the tube width can be seen from Figs. 3 and 6 to increase from about 0.2 m/s to 0.28 m/s. The velocity profile in undeformed tube shown in Fig.2 is more symmetric than those at the center of deformed tube width with the two lobed shaped cross section in Figs. 3 and 6. The asymmetry at the center of the tube width could be due to multiple echoes from the tube walls, which are closer to each other. The sensitivity of measured velocity profiles depends on the refraction associated with different sound velocities of the elastic tube, xanthan solution and water in pressure chamber, and the thickness of the tube.

The shear rate, $\dot{\gamma}$ dependent viscosity, η measured using the Physica (MCR300, CC27) rheometer with Couette geometry is shown in Fig.8. It can be seen that the xanthan solution is a shear thinning solution, which is well represented (full line) by the Carreau model:

$$\eta = \eta_0 \left[1 + (\lambda \dot{\gamma})^2 \right]^{(m-1)/2} \quad (1)$$

where η_0 is the viscosity at zero shear rate, λ is the time constant describing the transition from constant shear rate to the shear thinning power law behavior described by the value of m . The values of the constants obtained by fitting the viscosity data are $\eta_0 = 0.063$ Pa.s, $\lambda = 1.09$ and $m = 0.603$ (regression coefficient=0.983).

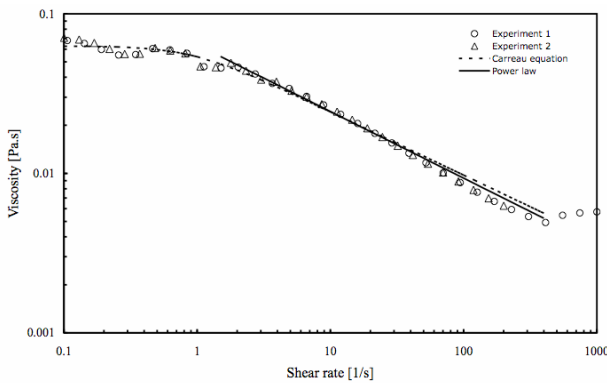


Figure 8: Variation in viscosity with shear rate of xanthan solution measured (symbols) using rheometer at 19°C. Experiments 1 and 2 are replicates carried out for testing reproducibility.

In contrast, the power-law model

$$\eta = K \dot{\gamma}^{n-1} \quad (2)$$

represented (dashed line) the data well for shear rates higher than 1 1/s in the shear thinning region with the fitted values of $K = 0.064$ Pa.sⁿ and $n = 0.582$ (regression coefficient=0.996). However, this model enables [5] the estimation of maximum velocity:

$$v_m = 4(3n+1)Q / \pi(n+1)d^2 \quad (3)$$

which agreed reasonably well with the measured

value using the ultrasound Doppler method during the flow of shear thinning xanthan solution volume flow rate of Q (Fig.2) through undeformed tube of diameter d . The calculated average shear rate is 6.7 1/s for the velocity profile. The corresponding viscosity is about 0.03 Pa.s so that the Reynolds number is about 70 based on average velocity of 0.11 m/s. Thus the flow of shear thinning xanthan solution in the elastic tube is laminar.

5 CONCLUSIONS

It is demonstrated that the velocity profiles during steady laminar flow of non-Newtonian shear thinning aqueous xanthan solution in undeformed and deformed elastic tube can be measured using ultrasound Doppler velocimetry. A critical external chamber pressure in Starling resistor setup caused the collapse of the elastic tube to form a two lobe-shaped cross-section with a narrow width at the center through which the pulsed ultrasound beam penetrates. The width at the center and area of cross section of the partially collapsed tube decreased with increase in external chamber pressure. Hence the velocity profile is distributed over a narrow width resulting in a higher maximum velocity at a constant volume flow rate. Further investigation of flow field over whole length of the buckled elastic tube for different flow rates, external chamber pressures, non-Newtonian fluids and tube material will enable better understanding of the flow structures relevant to several applications.

ACKNOWLEDGEMENT

We would like to thank Swiss National Science Foundation for the financial support, and P. Bigler, J. Corsano, D. Kiechl, B. Koller and B. Pfister for the experimental setup installation and instrumentation.

REFERENCES

- [1] Heil M: Stokes flow in collapsible tubes – Computation and experiment, *J. Fluid Mech.* 353 (1997) 285-312.
- [2] Hasegawa A, Otaguro A, Kumagai H, Nakazawa F: Velocity of swallowed gel food in the Pharynx by ultrasonic method, *Nippon Shokuhin Kagaku Kogaku Kaishi* 52(10) (2005) 441-447.
- [3] Birkhofer BH, Jeelani SAK, Windhab EJ, Ouriev B, Lisner KJ, Braun P, Zeng Y: Monitoring of fat crystallization process using UVP-PD technique, *Flow Meas. Instrumen.* 19 (2008) 163-169.
- [4] Knowlton FP, Starling EH: The influence of variations in temperature and blood-pressure on the performance of the isolated mammalian heart. *J. Physiol (Lond)* 44 (1912) 206-219.
- [5] Wiklund J, Johansson M, Shaik J, Fischer P, Windhab E, Stading M, Hermansson AM: In-line ultrasound based rheometry of industrial and model suspensions flowing through pipes, In: papers of the 3rd International Symposium on Ultrasonic Doppler Methods for Fluid Mechanics and fluid Engineering. EPFL Lausanne, Switzerland, 2002, p.69-76.

Experimental study for thermal striping in LBE loop by using UVP with high-temperature ultrasonic transducer

Hironari Obayashi* and Kenji Kikuchi

Japan Atomic Energy Agency (JAEA), 2-4, Tokai-mura, Naka-gun, Ibaraki-ken, Japan
(*Corresponding author, e-mail: obayashi.hironari@jaea.go.jp)

Japan Atomic Energy Agency (JAEA) has been proceeding with the research and development on accelerator-driven system (ADS) for the transmutation of long-lived radioactive nuclides. The ADS proposed by JAEA utilize the Lead-Bismuth Eutectic (LBE) as a spallation target and core coolant. Understanding and precise prediction of the flow condition in spallation target is one of the important items for estimate the soundness of materials for beam window, flow guides and irradiation samples. To examine the feasibility and applicability of the LBE to accelerator-driven transmutation systems, JAEA has an experimental lead-bismuth loop for investigate the problems caused by LBE flow. As a result of the experimental surveys, LBE flow is connected closely with a lot of serious problems in development of ADS. Therefore, the development of the high-temperature transducer that can be used at the high temperature condition (over 150 degrees Celsius) is a pressing need because it establishes the velocity measurement techniques for LBE flow. We adopted the wave guide method. And we conducted a survey of the suitable guide material for LBE flow by using the wave equation. As a result, it is forecast that Al and Si are excellent materials in the present situation.

Keywords: Liquid metal, High temperature, UVP, Erosion, ADS

1 INTRODUCTION

Japan Atomic Energy Agency (JAEA) has been proceeding with the research and development on accelerator-driven system (ADS) for the transmutation of long-lived radioactive nuclides. The ADS proposed by JAEA utilize the Lead-Bismuth Eutectic (LBE) as a spallation target and core coolant. The conceptual design study on the Transmutation Experimental Facility (TEF) to study the basic science and engineering of the transmutation technology was continued under a framework of Japan Proton Accelerator Research

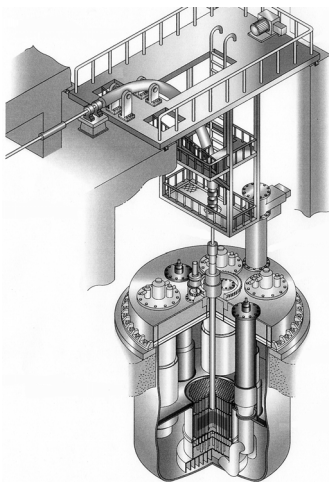


Figure 1: Image of a target for Accelerator Driven System

Complex (J-PARC) project. Understanding and precise prediction of the flow condition in spallation target is one of the important items for estimate the soundness of materials for beam window, flow guides and irradiation samples. To examine the feasibility and applicability of the LBE to accelerator-driven transmutation systems, there are three experimental LBE loop.

The measurement of the flow of the high temperature liquid metal is extremely difficult, and there are no practical measurement techniques other than neutron radiography [1-4] and ultrasonic velocity profiling.[5-7] Therefore, UVP measurement techniques that can be equivalent to high temperature liquid metal are studied in JAEA.

The objective of this study is measurement of the LBE flow related to the thermal characteristic of the beam window and the problem of erosion-corrosion. In the process of this study, various problems caused by the flow of LBE were clarified by the experiment that used the three LBE loop. This paper introduces the clarified problem caused by the LBE flow, and shows the result of examining the validity of the technique for applying UVP to the high temperature LBE flow.

2 EXPERIMENTAL SURVEYS

2.1 Erosion of materials

In the experiment with the LBE loop operation, it has been found that corrosion-erosion of materials

would be caused by flowing LBE. In this report, “corrosion” points at a phenomenon caused by the chemical action on the boundary surface of materials and LBE. And “erosion” points at a mass loss phenomenon caused by LBE flows on the surface of corroded material. The experiments of corrosion-erosion were conducted by using a LBE loop. In this loop, a test pipe (see. Figure 2) was installed at the test section. The total length of the test pipe was 420 mm, and nominal inside diameter of the diffuser section was 15 mm. And the straight section was 9.8 mm. Temperature of the test section was kept at 350 degrees Celsius. The operating time was 3000-3600 hours. Table 1 shows the result of erosion-corrosion test. When SUS304 stainless steel was used for the material of test pipe, the decrease of material caused by erosion was about 100 μm at the straight tube section. In the diffuser section, decrease of material was 500 μm. on the other hand, when F82H Ferritic steel was used for the material of test pipe, decrease of material was 50-100 μm at the diffuser section. In the straight tube section, the extremely little mass loss was observed.

SUS304 stainless steel and F82H Ferritic steel are contained in the materials proposed for the target

Table 1: Result of the mass loss thickness caused by erosion in LBE loop

Materials	Straight tube section	Diffuser section
SUS304	100 μm	500 μm
F82H	< 20 μm	50 μm

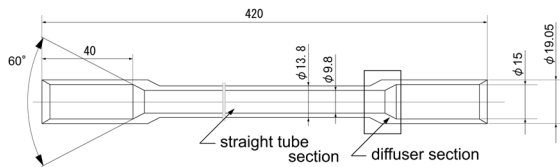


Figure 2: Illustration of the test pipe for corrosion-erosion test in LBE loop

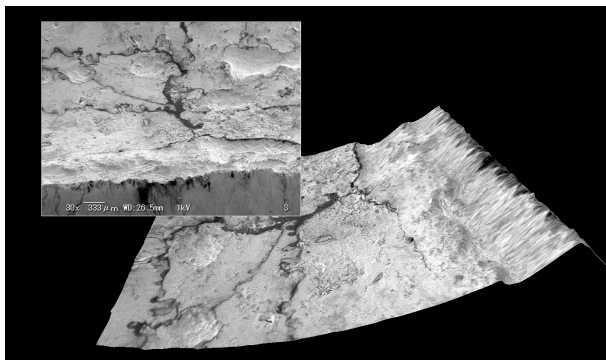


Figure 3: SEM image of the erosion on the surface of straight tube section (SUS304 stainless steel)

beam window and the flow path of ADS. Because the thickness of beam window under the examination is 2 mm, the decrease in the thickness of 25 % (Maximum) gives a serious bad influence to the safety of target system.

2.2 Thermal striping

In an experiment of the thermal characteristic on the surface of the mock up model of beam window, an unnatural phenomenon was observed. This experiment was conducted by using the other LBE loop that installed a mock up in a model of target vessel filled with LBE. Thermo-couples were installed at the surface of the hemispherical mock up model. A result of the temperature data measured by a thermo-couple (TC8) is Figure 5. In this experimental condition, LBE inlet boundary flux at test section was 500 l/min and reference temperature was 330 degrees Celsius. In this figure, the horizontal axis represents the measurement time, and vertical axis represents temperature measured by a thermo-couple. This result shows a typical temperature fluctuation at a tip of the model. The gap between the maximum temperature and the minimum temperature was about 15 degrees Celsius and the fluctuation shifted to the high temperature side. In this condition, it was forecast that the huge thermal stress (about 50 GPa) attacked the beam window. And thus, the beam

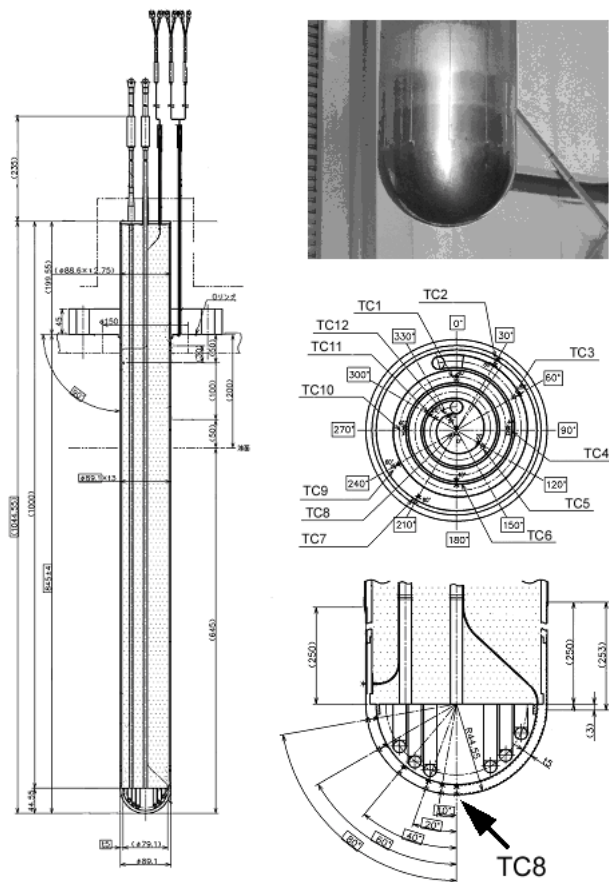


Figure 4: Mock up model of beam window

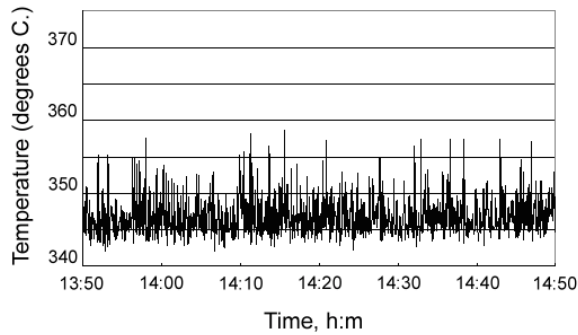


Figure 5: Typical temperature fluctuation at a tip of the mock up model of the target beam window

window would get the serious damage by the thermal striping phenomenon.

It is necessary to measure the temperature and the velocity profiles simultaneously, because it is thought that this phenomenon originates in the fluctuation of the stagnation region of LBE flow at the tip of mock up model.

2.3 UVP measurement of LBE flow

LBE would be enclosed as a neutron source and a coolant in the target vessel of ADS. It is impossible to confirm the cooling performance of the target loop without knowing of the LBE flow. And the flow structure and erosion of the materials of the loop are closely related. And thus, it is necessary that the development of velocity measurement techniques could be applied to LBE flow.

An experimental measurement of LBE loop was successfully realized by using UVP at low temperature condition (at 150 degrees Celsius).

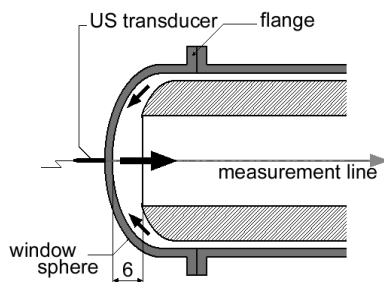


Figure 6: Flow passage of LBE loop

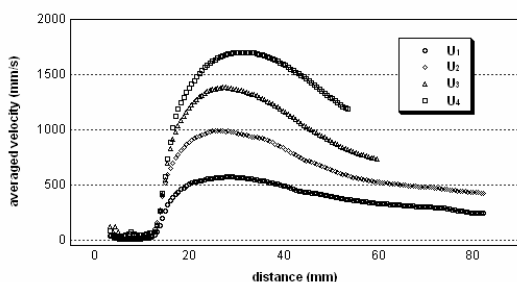


Figure 7: Averaged velocity profile in LBE loop; where velocity conditions are U₁, U₂, U₃, U₄=0.25, 0.50, 0.75, 1.00 m/sec

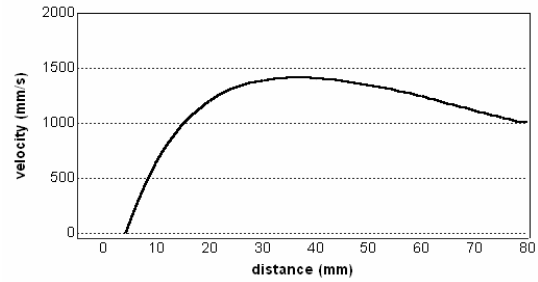


Figure 8: velocity profile given by numerical calculation; where velocity condition is U₃=0.75 m/sec

4 FUNDAMENTAL STUDIES FOR HIGH-TEMPERATURE TRANSDUCER

In operating ADS, the temperature of the LBE is expected to reach 500 degrees Celsius. Therefore, it is indispensable that the ultrasonic transducer which could apply to a high temperature condition. Lithium niobate (LiNbO₃) element and the other piezo elements used for the ultrasonic testing for materials could work at a high temperature condition. LiNbO₃ element is used for measurement of sodium flow in Fast Breeder Reactor (FBR); however, the voltage of about 1000 V is required for operating the transducer because the sensitivity is too bad.

In this study, a technique to attach the signal guide to the conventional ultrasonic transducer is developed. This idea was given by S. Eckert and others.[8-10] Their "acoustic wave guide" succeeds in a velocity profile measurement of CuSn flow at 620 degrees Celsius. Therefore, we conducted a survey of the suitable guide material for LBE flow by using the wave equation.

4.1 Formation of Ultrasonic beam

To estimate the beam formation in LBE and the permeability in guide materials, the sound field was calculated by wave equation.

$$\frac{\partial^2 P(t, x, y)}{\partial t^2} = c(x, y)^2 \left\{ \frac{\partial^2 P(t, x, y)}{\partial x^2} + \frac{\partial^2 P(t, x, y)}{\partial y^2} \right\} \quad (1)$$

A result of wave calculation for a continuous wave signal is shown in Figure 9. The mesh size was 0.02×0.02mm, and time step was 0.1 nsec. The diameter of was 5 mm, and the frequency of signal was 4 MHz. As for the shape of the guide, the column type was selected. The diameter of the guide was 10 mm, and the length was 30 mm. The material of this guide was SUS304 stainless steel. The target medium was LBE. In this result, it was confirmed that the ultrasonic beam was formed without trouble after the guide material had been penetrated. The comparable result is obtained for other materials.

4.2 SURVEY OF TRANSMITTANCE FOR MATERIALS

To know the permeability in guide materials, the

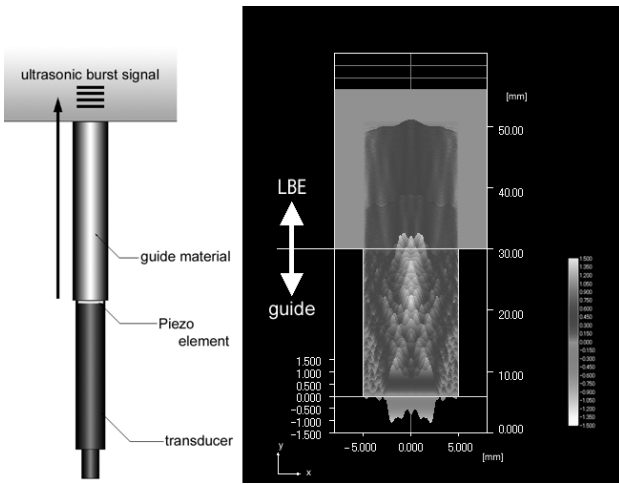


Figure 7: Simulation result of beam formation (continuous signal)

simulations of wave propagation were conducted by using the pulse signal. The length of guide cylinder was 25 mm. The other parameters were set to the same condition as the previous calculation. The number of cycles was 4. A simulation result is shown in Figure 7. The transmittances for each material obtained by dividing the amplitude of signal that immediately passed through the guide by the amplitude of initial signal were shown in Table 2. In these result, Al and Si showed the good permeability because the acoustic impedance of LBE($Z=19.6$) is a value close to these materials.

Table 2: Transmittance of pulse signal for each material

Materials	Z [MRayl]	Transmittance [%]
Ti	27.3	35
W	100.9	19
Zr	30.1	33
Mo	63.0	28
SUS304	45.7	30
Al	17.1	48
Si	17.5	52

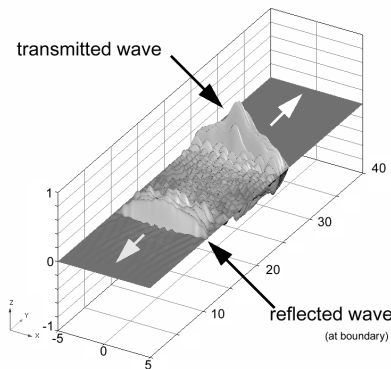


Figure 7: Simulation result of beam formation (pulse signal)

5 CONCLUSIONS

As a result of the experimental surveys, LBE flow is connected closely with a lot of serious problems in development of ADS. The development of the high-temperature transducer that can be used at the high temperature condition (over 150 degrees Celsius) is a pressing need because it establishes the velocity measurement techniques for LBE flow. We adopted the wave guide method. And we conducted a survey of the suitable guide material for LBE flow by using the wave equation. As a result, it is forecast that Al and Si are excellent materials in the present situation.

REFERENCES

[1]Sito, et al.: Visualization and Measurements of Liquid Phase Velocity and Void Fraction of Gas-Liquid Metal Two-Phase Flow by Using Neutron Radiography, Proc. 9th International Symposium on Flow Visualization (2000)
 [2]N.Takenaka, et al.: Visualization of Streak Lines in Liquid Metal by Neutron Radiography, Neutron Radiography Vol.4, Gordon and Breach (1993) 355-362.
 [3] N.Takenaka, et al.: Liquid metal flow measurement by neutron radiography, Nucl. Instrum. Methods. Phys. Res. A. Vol.377 (1996) 156-160.
 [4]H.Umekawa, et al.: Visualization of bed material movement in a simulated fluidized bed heat exchange by neutron radiography, Nucl. Instrum. Methods. Phys. Res. A. Vol.424 (1999) 77-83.
 [5]Y.Takeda: Measurement of velocity profile of mercury flow by ultrasound Doppler shift method, Nucl. Tech. Vol 79 (1987)120-124.
 [6]Y.Takeda, et al.: Flow measurement in a SING mockup target using mercury, ICANS XIV (1998) 321
 [7]K.Kikuchi, et al.: Measurement of LBE flow velocity profile by UDVP, J. Nucl. Materials 356 (2006) 273-279
 [8]S.Eckert, et al.: Velocity measurement at high temperatures by ultrasound Doppler velocimetry using an acoustic wave guide, Exp. in Fluids 35 (2003) 381-388.
 [9]A.Cramer, et al.: Liquid metal model experiments on casting and solidification processes, J. Materials Sci. 39 (2004) 7285-7294.
 [10]S.Eckert, et al.: Velocity measurements in metallic melts, Proc. FEDSM2005-77089 (2005).

Boundary layer measurement of a vessel sailing over the sea

Shoko OHTA^{1*}, Akinari SHIGETOMI¹, Yuji TASAKA¹, Yuichi MURAI¹,
Yasushi TAKEDA¹, Munehiko HINATSU² and Yoshiaki KODAMA²

¹ Graduate School of Engineering Hokkaido University, N13, W8, Kita-ku, Sapporo, Hokkaido 060-8628 Japan (*Corresponding author, e-mail: shoko-o@ring-me.eng.hokudai.ac.jp).

² National Maritime Research Institute, 6-38-1, Shinkawa, Mitaka-shi, Tokyo 181-0004, JAPAN

Friction drag of a large ship accounts for 80 % of the total drag, and hence drag reduction caused by bubbles is expected because of less environmental impact and easy installation. As a method to assess the bubble-originated alternation of the boundary layer structure beneath actual moving ship, we have designed a ship-mounting type of ultrasound probe and applied for ultrasound velocity profiler (UVP). The measurement performance is examined by a 50m-long flat bottom ship in NMRI 400m-long towing tank. After the measurement system is verified and improved for high-speed seawater environment, the system is applied to the measurement of the boundary layer beneath a moving vessel on the sea around Japan for five days. The vessel is 127 long and the local seawater velocity profiles at three position of the vessel are measured. With the results, the alternation of the profiles due to injection of bubbles is detected by the present UVP instruments.

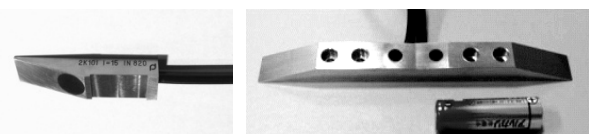
Keywords: ship engineering, drag reduction, turbulent boundary layer, velocity profile

1 INTRODUCTION

Energy-saving is severely requested for recent jump in oil prices. The merchant service is also affected with it considerably. Around 80% of the fuel for a large ship is consumed only for the friction drag that the ship receives on the sea. Thus the drag reduction has been a long and hot topic in this area. In particular the use of bubbles is expected at present as the most feasible way to reduce the friction drag because of less negative impact to the sea environment, and easy installation to existing ships^{[1][2]}. A great deal of laboratory scale experiments^[3] has been carried out to date to have confirmed the great effect of bubble-provided drag reduction. Now the stage is moving to the examination on the sea so that the practical usefulness is directly evaluated.

In Japanese NEDO-grant project, our UVP^[4]-team is assigned to the measurement of the velocity profiles at plural positions around the ship under the sea. Several demands must be satisfied for the ultrasonic transducers in the high-speed natural seawater environment, which is available for long days. To this end, we design and manufacture a number of transducers in various points of view. Fig. 1 shows two samples of the transducers among them, which are actually employed for the measurement.

In this paper, we report on the design of the transducers, the examination by mounting them on 50m-long flat bottom ship at NMRI 400m-long towing tank, and also the application to 127m-long vessel moving on the sea. In addition, the effect of bubble injection on the turbulent velocity profiles is focused on as the measurement results are discussed.



(a) Single Beam Type (b) Double Beam Type
Figure 1: Ultrasonic Transducers Employed for Ship

2 TOWING SHIP TEST

2.1 Design of transducer

The ultrasonic transducer that we newly designed for the ship is shown in Fig. 1.

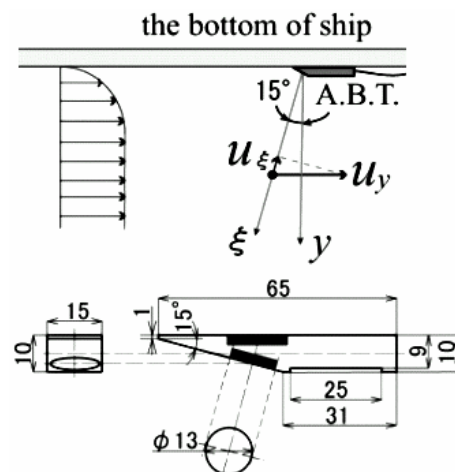


Figure 1: Angled Beam Transducer (2MHz)

It has inclined head relative to the flow-perpendicular direction at angle of 15 degree. We call this angled beam transducer (ABT) in this paper. The head of ABT constitutes of hundreds of vibrating semi-conductor elements, i.e. composite

type transducer, being adjusted to have 2MHz in resonance frequency. A thin sheet of ultrasonic absorber is inserted on the backside of the head to avoid the internal multiple reflection. In addition, the wire connected with the transducer is covered with electromagnetic double shield to prevent from noise inclusion through 100m-long transfer. The streamwise velocity profile along the measurement line is obtained as

$$u_y(\xi, t) = u_\xi(\xi, t) / \sin \theta. \tag{1}$$

2.2 Experimental conditions

The towing ship test is carried out in NMRI(National Maritime Research Institute of Japan)'s 400m-long towing tank that is 18m in width and 8m in depth. The towing ship of 50m in total length runs at constant velocity for around 10s. In this towing ship, ABT is mounted at 27.5m from the ship head. The sampling frequency, the spatial resolution in the beam direction, the velocity resolution, and the depth of the measurement of UVP are, 9ms, 1.5mm, 7.9mm/s, and 130.6mm, respectively. Bubbles are injected from the bottom of the ship at mean diameter of around 0.5 to 2.0mm. The towing speed is varied from 1.0m/s to 7.2m/s(14knwt), stepwise. The UVP measurement is conducted twice for the same speed to compare the velocity profiles that change with the bubble injection.

2.3 Experimental Results

As shown in Fig. 2, ultrasound reflects on the first bubble interface near the transducer. Thus it cannot transmit further to measure the flow beyond the bubble. This is because bubble size is larger than the effective diameter of the ultrasound beam. At near the first bubble position, UVP outputs locally low velocity. This does because a local standing wave is formed within a half-length of the pulsed ultrasound from the gas-liquid interface when it reflects on the interface. As the result, Doppler shift disappear near the bubble interface to provide very low velocity locally. With this principle, the bubble position that is located near the ship wall is measured, and the velocity of liquid and the bubble distribution are measured from the single data set of UVP measurement.

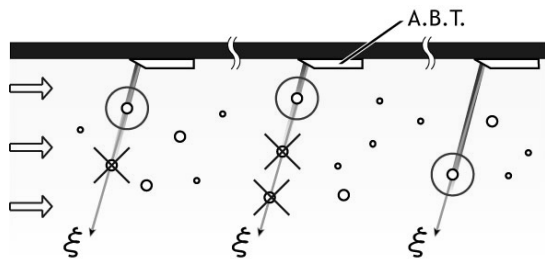


Figure 2: Ultrasonic beam reflection on nearest bubble

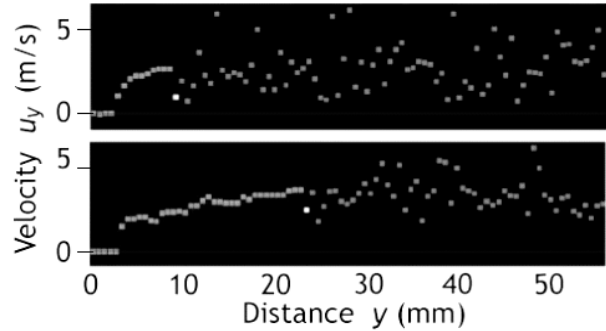


Figure 3: Instantaneous velocity profiles including bubbles: White point corresponds with position of bubble

3 APPLICATION TO ACTUAL SHIP

3.1 Improvement of transducer

In the application of UVP to actual ship, a coupled type of ABT is designed and manufactured so that the full information of turbulent flow characteristics in the boundary layer^[6] is captured. The details are shown in Fig. 4. Since two ultrasonic beams form a Y-shape for measuring velocity vector profiles, we call this Y-type angled beam transducer (YABT). Depending on demands for UVP in measuring different location of the ship, three types of YABT are made as listed in Table 1.

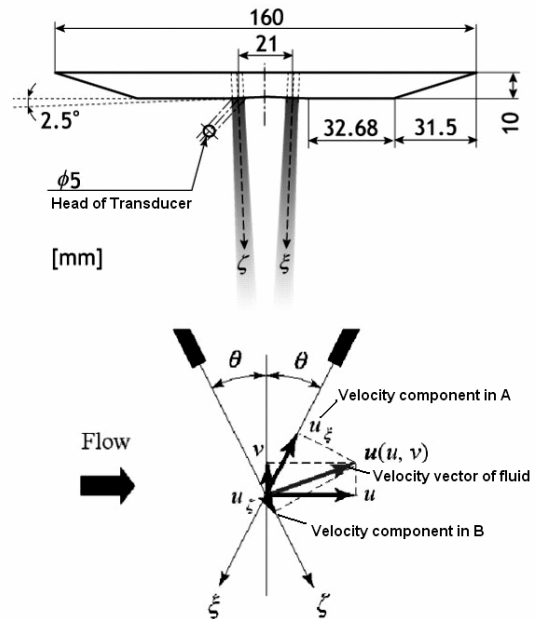


Figure 4: Y-type Angle Beam Transducer (2MHz)

Table 1: Specification of YABT

Basic Frequency	f_0	[Hz]	1	0.5	2
Wavelength	l	[mm]	1.53	3.06	0.765
Oscillator Diameter	D_0	[mm]	10	20	5
Measuring Range	X	[mm]	958.3	1916.7	479.2
Spatial Resolution	Dx	[mm]	3.06	6.12	1.53
NF length	x_{NF}	[mm]	8.170	16.340	4.085
Spread Angle	g_0	deg	4.475	4.475	4.475

The YABT is fabricated as a single unit in which a pair of transducers is tightly fixed with metal matrix. The relative angle of them is rigidly determined so that the velocity vector is obtained accurately despite to a narrow angle that is set so for handling high-speed flow conditions. When the velocity component of u_{ξ} , u_{ζ} are measured with each transducer, not only the time averaged velocity vector but also Reynolds shear stress is obtained by the next equation^[5]. Therefore, the process of drag reduction caused by bubbles is deduced as well.

$$-\rho \overline{u'v'} = \rho \frac{u_{\xi}'_{rms} - u_{\zeta}'_{rms}}{2 \sin \theta} \quad (2)$$

3.2 Experimental conditions

The flow around actual moving ship [Pacific Seagull, Azuma Shipping Co.ltd., see Fig. 5] is measured for five days in January 2008, around the mainland of Japan. The ship is 127m in total length and runs at around 13knot (6 to 7m/s). The measurement conditions are classified into two cases; ballast and loaded conditions of liquid cement. The measurement positions are as shown in Fig. 6. Here YABT(1MHz) near the bow is for measuring the ship velocity relative to seawater, YABT(2MHz) at the center of the ship is for visualizing the boundary layer structure, and YABT(0.5MHz) at the stern is for investigating the inflow velocity profile upstream of the screw.



Figure 5: Experimental vessel "Pacific Seagull"

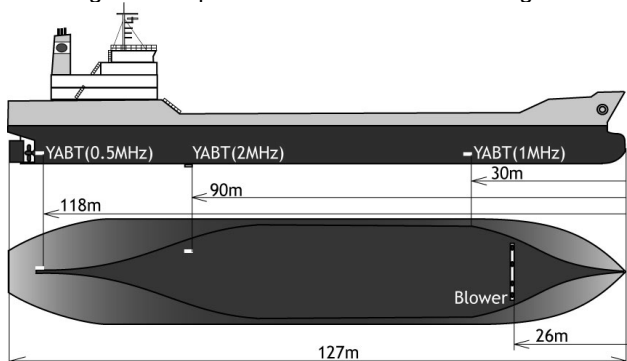
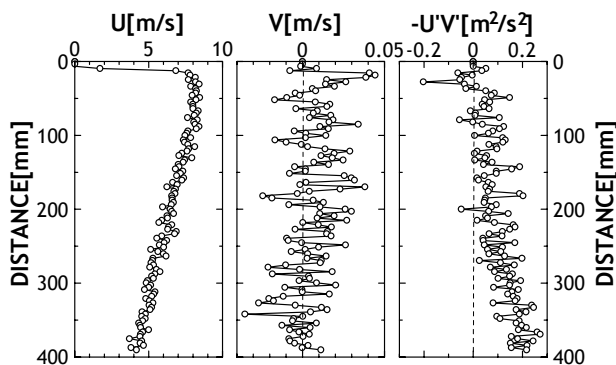


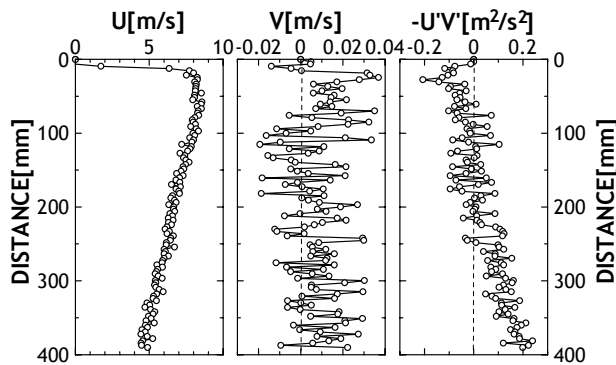
Figure 6: Mounting position of three different YABTs

3.3 Measurement results and discussion

The tracer of the present UVP measurement is naturally included contamination in the sea, but not intentionally mixed. In the case of ballast experiment, small bubbles created by the breaking surface at the bow are suspended long under the ship to be the tracer of UVP. Contrary, no significant echo is obtained in the loaded experiment due to deep distance from the seawater surface. The results shown below are limited to the ballast conditions.

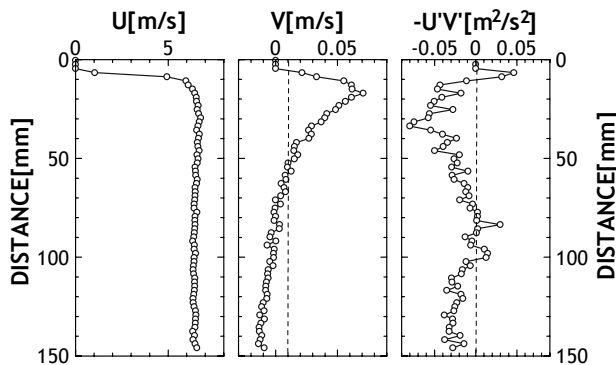


(a) Velocity profile in the case without bubble

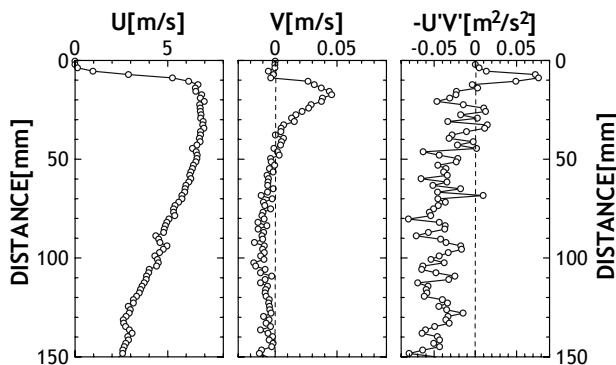


(b) Velocity profiles in the case with bubbles

Figure 7: Velocity profiles (YABT-1MHz) at bow



(a) Velocity profile in the case without bubble



(b) Velocity profiles in the case with bubbles

Figure 8: Velocity profiles (YABT-2MHz) beneath the ship
Figure 7 shows the velocity profiles measured by YABT near the bow of the ship. The thickness of

boundary layer is found to be around 15mm, matching well the one estimated by the boundary layer theory. The main flow velocity profile has the highest velocity at 20mm and decreases with the distance from the wall to have a gentle negative velocity gradient. This is because the fluid exclusion effect downstream the bow remains there. In terms of bubble injection effect, there is no significant alternation seen in the results. This is explained by the fact that the flow near the measurement position does not interact with bubbles.

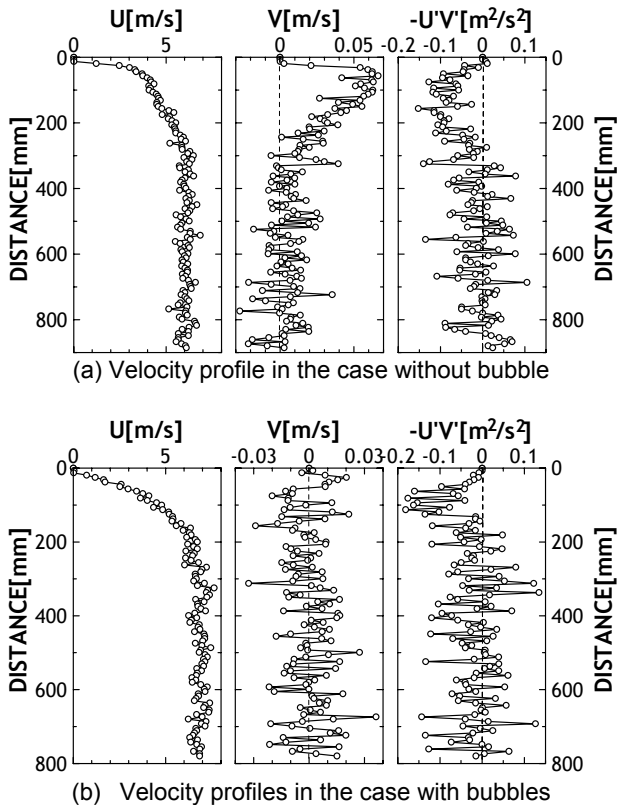


Figure 9: Velocity profiles (YABT-0.5MHz) at stern

Figure 8 shows the same set of results measured in the central part where bubbles can migrate through. The injection of bubbles changes the main flow velocity profile to be dumped at the far region from the wall ($y > 50$ mm). This change is caused by the reflection of ultrasound on densely suspended bubbles within $y < 50$ mm, but not the alternation of liquid velocity. However we can see an increment of the velocity near the wall in the case with bubbles. This is consistent to the general knowledge, i.e. the velocity gradient of logarithmic layer increases when drag reduction occurs with bubbles^[6]. On the other hand, Reynolds shear stress increases near the wall. This means that bubbles generate additional turbulence in the boundary layer while total drag is reduced mainly by the wall-contact area of bubbles. This is known as bubble-covering effect that is similar to air-film method of drag reduction. In fact,

the mean bubble size estimated from the bubble's echo signal ranges from 15mm to 25mm. This range of bubble has no function to damp the turbulence of liquid phase but rather activate the momentum transfer. Consequently the present data well describe the actual situation of drag reduction provided by large bubbles^[7].

Figure 9 shows the same results measured at the stern of the ship. This point is located inside the wake region of the ship and the flow is affected by the long friction from the bow. Thereby the main flow velocity decreases thickly from the wall. In the case of bubble injection, the main flow velocity increases due to reduced average density before the screw. In the NEDO project, the influence of bubbles on the screw performance is also investigated, which is reported in another publication.

4 SUMMARY

In order to understand how the boundary layer is altered with injection of bubbles in actual moving ship on the sea, we have designed and utilized several types of ultrasonic transducers that are applicable to seawater environment. The final form of the transducer we applied for it is Y-type angled beam transducer (YABT) that can capture the velocity vector profile as a function of the distance from the ship wall. In the stage of towing ship test, bubble distribution is measured from the first bubble reflection in the direction of the ultrasonic beam. The application of the YABTs to three positions around the ship reveals for the first time that the seawater velocity in the logarithmic layer is accelerated with presence of bubbles.

ACKNOWLEDGMENT

The authors are grateful for the financial support by Japanese NEDO grant titled "development of energy-saving technology for ships by means of microbubbles", and also for Japan Probe. Ltd, which cooperates with manufacturing ultrasonic transducers.

REFERENCES

- [1] Kodama Y: Int. J. Heat Fluid Flow, **21** (2000) 582-588.
- [2] Kato H *et al.*: J. Marine Sci. Tech., **4** (1999) 115-162.
- [3] Chen J Chang C: Ocean Eng., **33** (2006) 2025-2046.
- [4] Takeda Y: Int. J. Heat & Mass Flow, **7** (1986) 313-318.
- [5] Taishi T, Kitaura H and Aritomi M: Exp. Fluids, **32**(2002) 188-196
- [6] Murai Y *et al.*: J. Fluid Sci. Tech., **1** (2006) 12-23.
- [7] Murai Y, Fukuda H, Oishi Y, Kodama Y, Yamamoto F, Int. J. Multiphase Flow, **33** (2007) 147-163.

Application of the Ultrasound Doppler method for velocity measurements in an electromagnetically-stirred liquid metal

Dirk Rübiger, Sven Eckert* and G. Gerbeth

Forschungszentrum Dresden-Rossendorf, MHD Department, P.O: Box 510119, 01314 Dresden, Germany (*Corresponding author, e-mail: s.eckert@fzd.de).

This experimental study considers the transient liquid metal flow which is generated inside a cylindrical container by discontinuously applying a rotating magnetic field (RMF). The focus is on the fluid motion arising from the impulsive spin-up from the resting state, a single pulse or a sequence of RMF pulses. The ultrasonic Doppler velocimetry (UDV) has been used to determine profiles of the fluid velocity in the ternary alloy GaInSn. The azimuthal and vertical velocity components have been measured allowing for an analysis of both the primary, swirling flow and the secondary flow in the radial-meridional plane. The experimental results show an excellent agreement with recently published numerical results. The investigations reveal that the recirculating flow in the radial-meridional plane undergoes characteristic oscillations. Periodic reversals of the meridional flow direction can be observed for a specific length of the RMF pulses.

Keywords: Liquid metal, electromagnetic stirring, rotating magnetic field, velocity profile, Ultrasound Doppler method

1 INTRODUCTION

Alternating current (AC) magnetic fields are commonly used in industrial practice for melt stirring. The requirements arising from the particular metallurgical or casting operation can be manifold. For instance, the electromagnetic stirring is applied to provide an efficient mixing of metallic melts, to control the flow at the mold region in the continuous casting process or to achieve a purposeful alteration of the microstructure of casting ingots.

We consider here the standard case of electromagnetic stirring by means of a rotating magnetic field (RMF). For a liquid metal inside a cylindrical vessel, the imposition of an RMF creates a primary motion in form of a swirl. A secondary recirculating flow in the r-z plane, which consists of a double vortex structure for the laminar case, results from the Ekman pumping at the horizontal walls [1]. Although the amplitude of the primary motion is several times higher than the secondary flow, its contribution to an efficient bulk mixing is marginal, because it consists mainly of an almost rigidly rotating core. The convective transport in vertical and radial direction is mainly achieved by the secondary flow. An amplification of the secondary flow causes an intensification of the mixing rate, which can be realized in the simplest way by increasing the magnetic field. At sufficiently high field intensities so-called Taylor-Görtler vortices occur, moving along the sidewalls of the cylinder and dissipate inside the Bödewadt layers. Such vortex structures are very efficient with respect to melt mixing [2]. On the other hand, an increase of the magnetic field also accelerates the primary, swirling flow, which results in an increasing deflection of the free surface. Instabilities at the

meniscus region should be strictly avoided in many applications, because they can lead to surface defects or the entrainment of gas. In addition, specific problems arise if the rotary stirring is applied during directional solidification. The double-vortex structure of the secondary flow results in a radial inward flow along the solidification front, which transports the solute towards the axis of the ingot and is therefore responsible for typical segregation pattern [3, 4]. A mitigation of the problem could probably be achieved if the flow in the mushy zone can be oriented by turns in different directions.

A possible approach to overcome the handicaps of rotary stirring is the use of a time-modulated RMF. The goal is to amplify the secondary, recirculating flow, but to limit the amplitude of the swirling flow at the same time. A purposeful practice of melt stirring requires suitable flow measurements which deliver a detailed knowledge of the magnetic field impact on the flow. Therefore, this study is concerned with the experimental investigation of specific flow pattern arising from an impulsive change in the magnetic field strength, known as the spin-up or spin-down, respectively. In detail, we present velocity measurements arising from an RMF spin-up, a single pulse and a pulse sequence, respectively.

2 EXPERIMENTAL SET-UP

The flow measurements have been carried out using the ternary eutectic alloy Ga68In20Sn12, which has a melting point of about 10°C and shows the following properties at room temperature: electrical conductivity $\sigma = 3.2 \times 10^6 \text{ Sm}^{-1}$, density $\rho = 6.36 \times 10^3 \text{ kgm}^{-3}$ and viscosity $\nu = 3.4 \times 10^{-7} \text{ m}^2\text{s}^{-1}$. A schematic view of the experimental set-up is depicted in figure 1. The fluid vessel is a closed cylinder made from Perspex with a radius R_0 of

30 mm. The height of the liquid metal column H_0 was chosen to be 60 mm ensuring an aspect ratio $2R_0/H_0$ of unity. The experiments were performed in the magnetic induction system KOMMA at FZD. Six coils are arranged in one pole-pair connection to create the rotating magnetic field. The fluid vessel was placed concentrically inside the bore diameter of the magnetic system. In order to preclude flow artifacts arising from symmetry deviations of the experimental configuration (vertical alignment, conformity of both the cylinder and magnetic field axis), special care was necessary to ensure a precise positioning of the cylinder inside the magnetic system. The homogeneity of the magnetic field was checked using a 3-axis Gauss meter (Lakeshore model 560, sensor type MMZ2560-UH). Within the container diameter of 60 mm the variance of the magnetic field strength was found to be smaller than 3%.

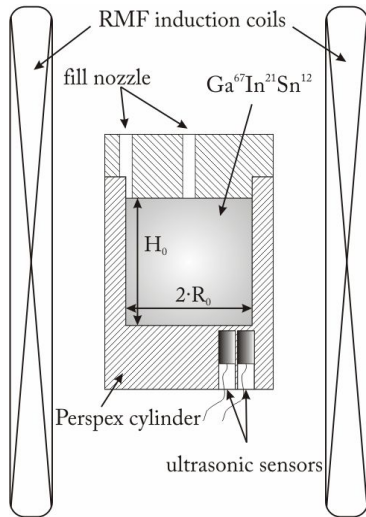


Figure 1: Schematic view of the experimental set-up

In the last twenty years the UDV technique became an accepted method for flow investigations in various liquid metals [5-8]. In the present study we used an 8 MHz transducer, which was attached to the plane-parallel bottom wall of the fluid container having a thickness of 2.5 mm. The vertical alignment of the transducer allowed for recording axial profiles of the vertical velocity between the bottom and the lid of the fluid cylinder. All velocity measurements presented in this paper have been obtained at radial positions of $r/R_0 = 0.6$ and 0.9 , respectively. Because of the divergence of the ultrasonic beam the lateral size of the measuring volume increases with the distance from the transducer. Hence, the spatial resolution in lateral direction varies from 5 mm at the sensor to approximately 7.5 mm at the lid of the fluid vessel. In axial direction a spatial resolution of about 1.4 mm was achieved. The velocity data were acquired with sampling frequencies ranging from 2 to 25 Hz. The accuracy of the velocity data can be assessed to be better than 0.15 mm/s. The geometrical restrictions of the experimental configuration,

namely the small bore diameter of the coil system, did not permit for the determination of the azimuthal velocity component.

3 RESULTS

3.1 RMF spin-up

The spin-up of a fluid in a rotating axisymmetric container is a classical problem in fluid dynamics which has been reviewed by Benton and Clark [9]. The problem concerns a fluid being at rest or in the state of steady rotation, which experiences an increase of the angular velocity. Analytical and numerical studies concerning the spin-up of an RMF-driven flow have been published recently [10, 11]. In case of an RMF spin-up from the rest the azimuthal Lorentz force initiates a rotating motion of an electrically conducting liquid. The resulting imbalance between the centrifugal forces and the radial pressure gradient in the horizontal Ekman layers drives the fluid radially inwards. Required by continuity, a secondary circulation occurs in the meridional plane. Unlike the rotational direction, the sense of secondary circulation in the steady state is such that the interior fluid near the cylinder mid-plane is moving towards the side walls. In contrast to the case of a rotating container the secondary flow is an inherent feature of the steady state RMF flow. Nikrityuk et al. [11] divided the RMF-driven spin-up into two phases: a so-called initial adjustment time in which the secondary flow is firstly established in form of two toroidal vortices and a subsequent inertial phase showing distinct inertial oscillations until the flow reaches a steady state after the spin-up time.

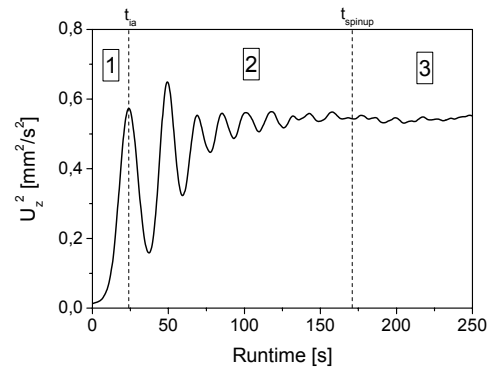


Figure 2: U_z^2 averaged over the vertical velocity profile, obtained at a radial position of $r/R_0 = 0.9$ and a magnetic field strength of $B_0 = 0.42$ mT (1 – initial adjustment phase, 2 – inertial phase, 3 – steady state).

Figure 2 displays the evolution of the square value of the vertical velocity U_z averaged along the vertical measuring line at

$$U_z^2 = \frac{1}{H_0} \int_0^{H_0} u_z^2 dz \quad (1)$$

This quantity can be considered as a qualitative measure describing the intensity and kinetic energy

of the secondary circulation in the meridional plane. The curve in figure 2, which has been obtained from an ensemble average of five miscellaneous reruns, reveals an oscillatory raise of the vertical velocity before a steady state is reached. Following the suggestions given by Nikrityuk et al. [11] we can identify the so-called initial adjustment phase and the inertial phase, respectively. We determined the duration of the initial adjustment phase, t_{ia} , as a function of the applied magnetic field strength B_0 from our experimental data (see figure 2). Figure 3 shows a satisfying agreement between experiment and numerical calculations [11] in the subcritical Ta number range although in the case of the numerical analysis the initial adjustment time was derived from the time history of the volume-averaged meridional velocity U_{rz} . A further increase of the magnetic field intensity reveals that t_{ia} follows a $1/B$ -dependency in the turbulent range.

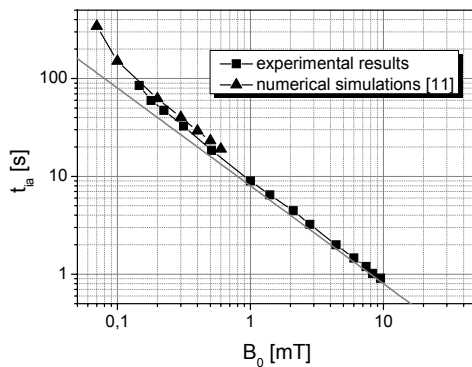


Figure 3: Influence of the magnetic field B_0 on the initial adjustment time t_{ia}

3.2 RMF single pulse

The flow arising from the application of a single RMF pulse is governed by an impulsive spin-up from the rest state followed by a spin-down phase due to the inertia of the fluid. Nikrityuk et al. [12] found that the recirculating flow in the meridional plane becomes especially pronounced if the pulse length t_p of the electromagnetic forcing is consistent with the initial adjustment time. Figure 4 shows a transient flow pattern using an RMF pulse with the amplitude B_0 of 2.8 mT and the pulse length t_p of 3.6 s, which corresponds to the duration of the initial adjustment phase t_{ia} for the case considered here. At the beginning an ascending flow appears in the upper part of the container and a descending motion in the lower part, which indicates the formation of two toroidal vortices usually appearing during the initial adjustment phase. The shutdown of the RMF does not extinguish the secondary flow immediately. The double vortex structure undergoes oscillations, the double vortex decays temporarily and will be displaced by another vortex pair emerging at the horizontal endwalls and spreading towards the mid-plane. It is important to note that the velocity shows a reversal of its direction. At the mid-plane a short-

time erasement of the flow structure seems to occur before the vortices expand over the other half of the container.

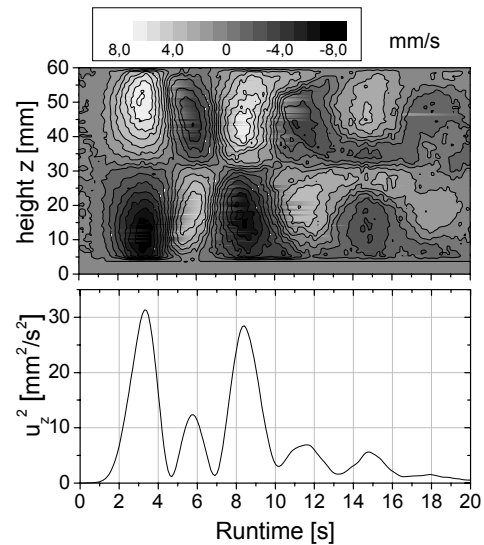


Figure 4: Spatiotemporal plot of the vertical velocity and corresponding temporal development of U_z^2 (RMF pulse with $B_0 = 2.8$ mT and $t_p = 3.6$ s, $r/R_0 = 0.9$)

3.3 RMF pulse sequence

As a next step we consider a succession of RMF pulses. As shown in figure 5 additional parameters emerge, namely, the pulse length t_p and the time between two subsequent pulses t_D , also called as dormant period. If equal periods of driving and inactive phases are chosen, the respective pulse frequency $f_p = 1/(2 \cdot t_p)$ appears as new important control parameter. Recent results demonstrated the occurrence of a distinctive double-vortex structure with high velocity values and periodic inversions of the vorticity only in a very narrow range of pulse frequencies [13].

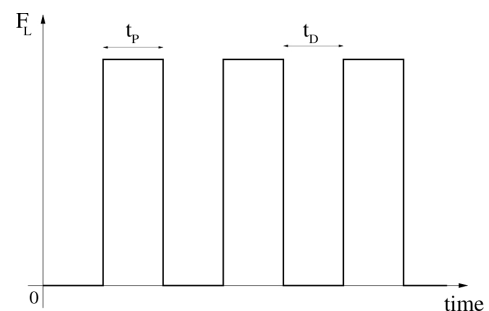


Figure 5: Temporal scheme for the modulation of the electromagnetic force F_L

An explanation of this phenomenon requires an understanding of the interaction between the primary and the secondary flow. The energy transfer between the rotary motion and the meridional flow is governed by inertial waves [11, 14]. Preliminary results [13] reveal that a characteristic flow pattern will be achieved if the pulse frequency f_p corresponds to the eigenperiod of inertial waves in a developed regime as given by Greenspan [15]. This

is confirmed by figure 6 in which the square values of the vertical velocity averaged over both the measuring line and the total measuring time are drawn vs. the frequency f_p . It becomes obvious that pronounced maxima occur at selective frequencies, varying for different values of the magnetic field B_0 . These maxima correspond to values of the frequency where distinct periodic reversals of the secondary flow have been observed [13]. As expected, the excitation of different modes becomes more pronounced with increasing B_0 .

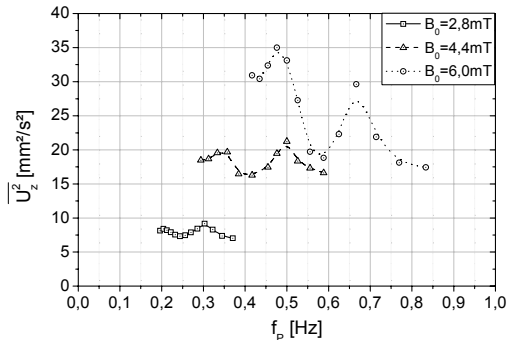


Figure 6: Intensity of the secondary flow vs. frequency f_p , ($\overline{U_z^2}$ - average over velocity profile and measuring time)

4 DISCUSSION AND CONCLUDING REMARKS

We presented velocity measurements in a cylindrical liquid metal column with a flow which is driven by an application of an intermittently applied RMF. Thereby, the focus was especially directed on generic situations such as the spin-up, a single pulse or a sequence of equidistant pulses. By delivering both the instantaneous velocity profiles and the resulting spatiotemporal flow structure the ultrasound Doppler method provides a valuable insight into the vortex dynamics of such nontransparent, oscillating flows. Our experimental results show a very good agreement with previous numerical predictions [11-13].

The flow measurements show the capability of intermittently applied RMF to overcome the limited mixing character of conventional rotary stirring. A suitable choice of parameters provides high mixing intensities by a distinct intensification of the secondary flow, which can reduce the mixing time for industrial applications. Moreover, it becomes possible to control the direction of the secondary circulation. The outcome of the present study demonstrates that a preferential intensification of the secondary flow requires the careful adjustment of the respective frequencies f_p for pulsing the rotational direction of the RMF. The respective optimum for f_p depends on the magnetic field strength B_0 , the material properties of the liquid and the geometry under consideration. A mismatch of the relevant parameters may prevent an

improvement of the mixing intensity, actually, the results may become worse compared to the situation of a continuously applied RMF.

ACKNOWLEDGEMENT

This work was financially supported by Deutsche Forschungsgemeinschaft in the framework of the collaborative research centre SFB 609 "Electromagnetic Flow Control in Metallurgy, Crystal Growth and Electrochemistry".

REFERENCES

- [1] Davidson PA: Swirling flow in an axisymmetric cavity of arbitrary profile driven by a rotating magnetic field, *J. Fluid Mech.* 245 (1992), 669-699.
- [2] Nikrityuk PA, Eckert K, Grundmann R: Axisymmetric modelling of the mixing of two miscible liquid metals driven by a rotating magnetic field, *Proc. Conf. Turbulence and Interactions TI2006* (2006), Porquerolles, France, CD-ROM.
- [3] Priede J, Gerbeth G: Breakdown of Burton-Prime-Slichter approach and lateral solute segregation in radially converging flows, *J. Crystal Growth* 285 (2005) 261-269.
- [4] Nikrityuk PA, Eckert K, Grundmann R: A numerical study of unidirectional solidification of a binary alloy under the influence of a rotating magnetic field, *Int. J. Heat Mass Trans.* 49 (2006) 1501-1515.
- [5] Takeda Y: Measurement of velocity profile of mercury flow by ultrasound Doppler shift method, *Nucl. Technol.* 79 (1987), 120-124.
- [6] Brito D, Nataf HC, Cardin P, Aubert J, Masson JP: Ultrasonic Doppler velocimetry in liquid gallium, *Exp. Fluids* 31 (2001) 653-663.
- [7] Eckert S, Gerbeth G: Velocity measurements in liquid sodium by means of ultrasound Doppler velocimetry, *Exp. Fluids* 32 (2002), 542-546.
- [8] Eckert S, Gerbeth G, Melnikov VI: Velocity measurements at high temperatures by ultrasound Doppler velocimetry using an acoustic wave guide, *Exp. Fluids* 35 (2003); 381-388.
- [9] Benton ER, Clark C: Spin-up, *Ann. Rev. Fluid Mech.* 6 (1974), 257-280.
- [10] Ungarish M: The spin-up of liquid metal driven by a rotating magnetic field, *J. Fluid Mech.* 347 (1997) 105-118.
- [11] Nikrityuk PA, Ungarish M, Eckert K, Grundmann R: Spin-up of a liquid metal flow driven by a rotating magnetic field in a finite cylinder: A numerical and an analytical study, *Phys. Fluids* 17 (2005), 067101.
- [12] Nikrityuk PA, Eckert S, Eckert K: Spin-up and spin-down dynamics driven by a single rotating magnetic field pulse, *Eur. J. Mech. B-Fluids* 27(2008), 177-201.
- [13] Eckert S, Nikrityuk PA, Rübiger D, Eckert K, Gerbeth G: Efficient Melt Stirring Using Pulse Sequences of a Rotating Magnetic Field: Flow Field in a Liquid Metal Column, *Metall. Mater. Trans.* 38B (2007) 977-988.
- [14] Davidson PA, Boysan F: Oscillatory recirculation induced by intermittent, rotary stirring, *Ironmaking and Steelmaking* 18 (1991), 245-252.
- [15] Greenspan HP: *The Theory of Rotating Fluids*, Breukelen Press, Brooklin (1990)

Uncertainty of ADCP spatial velocity distributions

Colin D. Rennie^{1*}

¹Department of Civil Engineering, University of Ottawa, 161 Louis Pasteur St., Ottawa, Canada
(*Corresponding author, e-mail: crennie@genie.uottawa.ca).

Uncertainty is assessed for the spatial distribution of depth averaged velocity estimated from a four-beam Acoustic Doppler Current Profiler (ADCP) asynoptic spatially intensive survey of a 6 km river reach. Kriging was used to interpolate the irregular data on to a uniform grid. Uncertainty due to ADCP single-ping error, macroturbulent velocity fluctuations, and kriging interpolation is evaluated. Specifically, the uncertainty of an estimate of mean streamwise velocity from a single-ping velocity measurement in a single bin (σ_v) is evaluated using ADCP error velocity (σ_ϵ) for error, and an empirical predictor for root-mean-square turbulence intensity (σ_s) for real fluctuation: $\sigma_v^2 = \sigma_\epsilon^2 + \sigma_s^2$. Average σ_ϵ and σ_s in the reach were 0.22 m/s and 0.17 m/s, respectively. The resulting average single-ping single-bin σ_v was 0.30 m/s, and corresponding average uncertainty of depth average velocity (σ_U) was calculated to be 0.089 m/s. Depth average velocity interpolation uncertainties, as represented by kriging standard deviations, ranged from 0.38 m/s to 0.68 m/s in the reach, thus interpolation uncertainty far exceeded estimated measurement uncertainty. Finally, shear velocity uncertainty (σ_{U^*}) was also estimated. For $\sigma_v = 0.30$ m/s and depth equal to the mean channel depth of 5.7 m, σ_{U^*} was 0.045 m/s.

Keywords: ADCP uncertainty, spatial distribution, river, acoustic noise, turbulence intensity

1 INTRODUCTION

Spatial distributions of velocity in rivers have been mapped based on four-beam Acoustic Doppler Current Profiler (ADCP) survey throughout a large river reach [1]. The data were asynoptic, in that an irregular spatial survey with closely spaced sections was collected over a period of time. It was assumed that flow was stationary. Kriging was used to interpolate the irregular data on to a uniform grid. However, a mean velocity spatial distribution from an asynoptic survey is subject to errors associated with single-ping ADCP errors and the fact that instantaneous measurements represent both the mean velocity and macroturbulent velocity fluctuations. In other words, instantaneous data display variance due to both measurement error and real fluctuations, thus an instantaneous measurement may be a poor realization of the local mean velocity. It was previously assumed [1] that kriging would provide sufficient spatial smoothing to overcome this variance. Alternatively, [2] suggested that repeat transects are necessary to reduce ADCP velocity uncertainty. However, repeat transects will necessarily limit the spatial range of the survey, particularly if flow is sufficiently unsteady to limit survey time. In this paper a more rigorous assessment of uncertainty in the spatial velocity maps generated from asynoptic ADCP surveys is presented.

2 METHOD

2.1 Measurements

An RD Instruments 1200 kHz Rio Grande ADCP operated in Water Mode 1 was utilized to survey nearly 6 km of river. ADCP positions were recorded

using a Real Time Kinematic Differential Global Positioning System. A total of nearly 30000 vertical profiles were collected using individual pings in 25 cm depth bins, a sampling frequency of 2 Hz, and a radial ambiguity velocity of 3.59 m/s. Depths ranged from 1.5 m to 17 m and depth average velocities ranged from zero to greater than 3 m/s (Figure 1). Refer to [1] for more details on measurement methods.

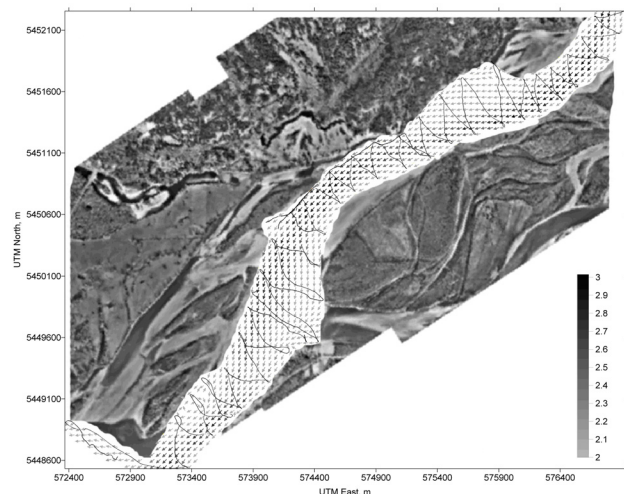


Figure 1: Depth average water velocity (m/s) in 6 km reach of Fraser River, June 24-25, 2006. Spatial distribution kriged to 25 m grid spacing, every second vector shown. Model variogram was fit to observed variogram. Black line shows boat track, where raw data were collected. Air photo from early spring 2006, courtesy Michael Church.

2.2 Uncertainty Assessment

Velocity measurement uncertainty was evaluated using estimates of both measurement error and

turbulent velocity fluctuations. Specifically, the uncertainty of an estimate of mean streamwise velocity from a single-ping velocity measurement in a single bin (σ_v) was evaluated using ADCP error velocity (σ_ε) for error, and an estimate of root-mean-square turbulence intensity (σ_s) for real fluctuation:

$$\sigma_v^2 = \sigma_\varepsilon^2 + \sigma_s^2 \quad (1)$$

where σ denotes standard deviation, and σ_ε and σ_s are assumed independent. ADCP error velocity is based on the difference between two redundant measurements of vertical velocity in a depth bin, and accounts for both Doppler noise and heterogeneity of actual velocities between beams. Turbulence intensity was estimated using the empirical equation presented by [3]:

$$\sigma_s = 2.04u_* \exp\left(-0.97\frac{y}{h}\right) \quad (2)$$

where u_* is the shear velocity, y is the elevation above the channel bed, and h is the flow depth. Equation 2 was developed for uniform flow conditions, thus its application requires an assumption of reasonably uniform flow. Furthermore, application of Equation 2 requires a prediction of local u_* , which was obtained from a log-law fit to the velocity measurements themselves (see [1]).

The validity of Equation 2 for the present conditions was tested using a 7 minute (>800 pings) stationary profile located in the centre of the reach, for which $u=0.120 \pm 0.035$ m/s. The mean σ_s from Equation 2 over all bins in all pings was 0.22 m/s. Alternatively, σ_s was estimated directly as

$\sigma_s = \sqrt{\sigma_v^2 - \sigma_\varepsilon^2}$, using the observed measurement variance in each bin for σ_v and observed average σ_ε in each bin. Observed σ_s averaged across all bins was 0.27 m/s, which compared reasonably well with the prediction from Equation 2.

Finally, the uncertainty of depth average velocity (σ_U) was calculated from single-bin uncertainty, utilizing the dubious assumption that N measured velocities in each vertical profile were independent:

$$\sigma_U = \frac{1}{N} \sqrt{\sum_{i=1}^N \sigma_{v_i}^2} \quad (3)$$

In fact, measured velocities at adjacent bins are correlated due to the fact that each bin employs Doppler backscatter from a triangularly weighted window with a width equal to two bins. In other words, neighbouring bins employ overlapping measurement volumes.

2 RESULTS

The ADCP error velocity (σ_ε) was recorded for every bin of every ping. Average σ_ε in the reach was 0.22 m/s, with a standard deviation of 0.18 m/s. Values of σ_ε tended to increase towards the bed in deeper profiles, presumably due to greater velocity heterogeneity between beams. The expected root mean square error in single bin, single ping velocity due to Doppler noise alone (σ_D) can be estimated for a given water mode (signal transmission and processing algorithm), bin size, and ambiguity velocity using the RD Instruments software PlanADCP. For the current deployment, σ_D was predicted to be 0.18 m/s, suggesting that error was increased due to beam heterogeneity by an average of 0.13 m/s.

The single bin, single ping estimate of σ_s from Equation 2 averaged 0.17 m/s in the reach, with a standard deviation of 0.07 m/s. As can be seen from Equation 2, estimated turbulent fluctuations were greatest near the channel bed in areas of high shear stress.

The resulting average single-ping single-bin σ_v was 0.30 m/s, with a standard deviation of 0.16 m/s. Given that both σ_ε and σ_s increased towards the bed, σ_v was greatest near the channel bottom.

The uncertainty of depth average velocity σ_U was calculated throughout the reach from the distribution of σ_v using Equation 3. The average value of σ_U was 0.089 m/s, with minimum and maximum values of 0.023 m/s and 0.386 m/s, respectively (Figure 2). Values of σ_U were least in deeper areas of the river, due to increased averaging from multiple bins.

Depth average velocity interpolation uncertainties were evaluated using the kriging standard deviations (σ_k). Kriging variance is calculated as the difference between the kriging model variance and the weighted covariance between adjacent points and the estimate location. In effect, σ_k is an estimate of the degree of spatial autocorrelation in the data that could be utilized during kriging. If there is little spatial autocorrelation, then σ_k approaches the standard deviation of the raw spatially distributed data. Values of σ_k ranged from 0.38 m/s to 0.68 m/s in the reach (Figure 3). Kriging standard deviations were least in locations near available raw data, and greatest in interpolated areas. The standard deviation of the spatially distributed depth average velocity data was 0.73 m/s, thus kriging variance approached the variance of the data in locations without data. This implies that spatial correlation in the data was of insufficient range to allow for accurate kriging interpolation between transects, particularly if transects were widely spaced. It appears that interpolation uncertainty exceeded estimated measurement uncertainty.

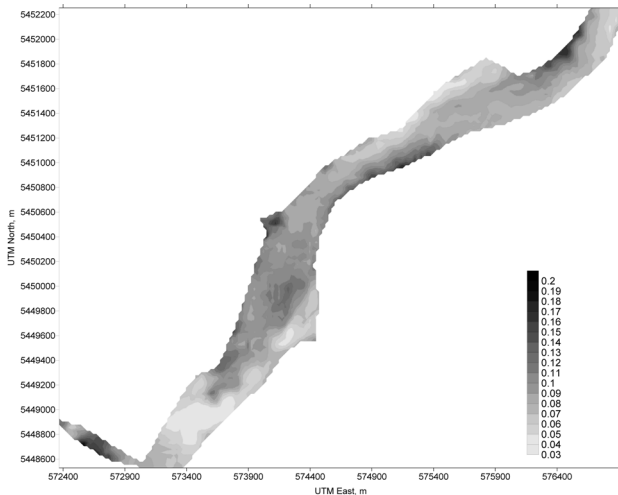


Figure 2: Calculated uncertainty of depth average water velocity (σ_U) (m/s). Spatial distribution interpolated by kriging to 25 m grid spacing using modeled variogram fit to observed variogram.

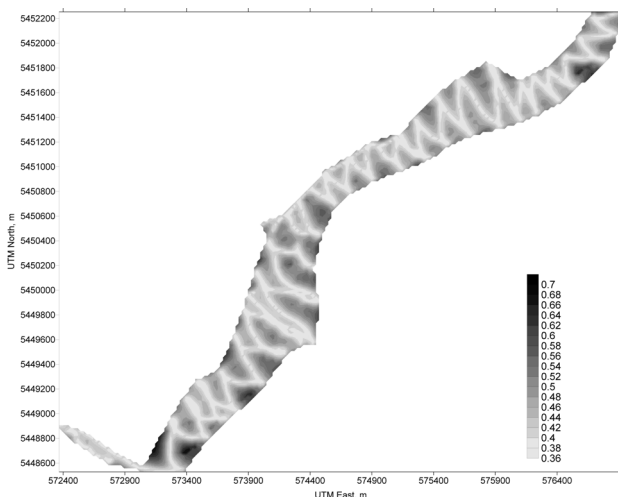


Figure 3: Kriging standard deviation (σ_k) of interpolated depth average water velocity (m/s). Spatial distribution interpolated by kriging to 25 m grid spacing. The standard deviation of observed depth velocity throughout the reach was 0.73 m/s, and kriging standard deviations ranged from 0.38 m/s to 0.68 m/s.

Finally, shear velocity (u_*) was estimated from a log-law fit to the velocity profile, with values ranging from 0.03 m/s to 0.18 m/s. Uncertainty of shear velocity (σ_{u^*}) is independent of u_* and roughness, but σ_{u^*} does depend on depth and the associated number of bins in the vertical profile. For $\sigma_v = 0.30$ m/s and depth equal to the mean channel depth of 5.7 m, σ_{u^*} was 0.045 m/s. Averaging at least 10 pings for each velocity profile reduces σ_{u^*} to < 0.02 m/s for all depths (Figure 4).

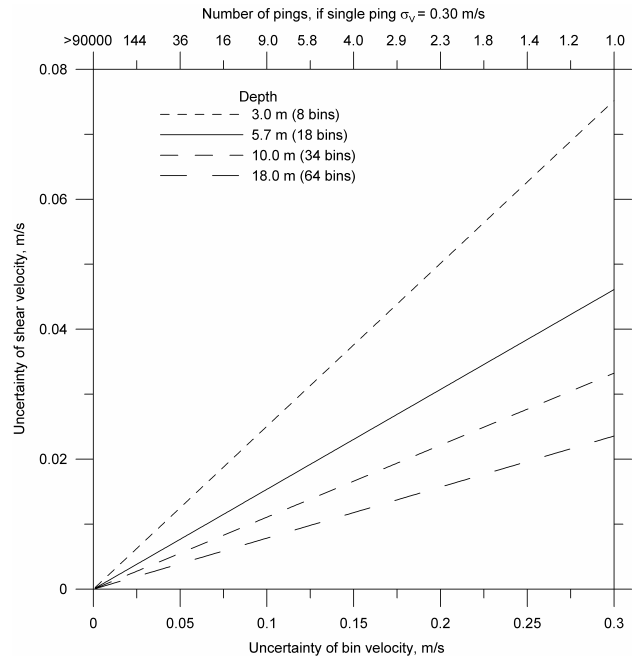


Figure 4: Uncertainty in estimated shear velocity (m/s), depending on number of bins in the vertical profile (depth), and number of pings in an ensemble average of pings (assuming single ping, single bin $\sigma_v = 0.30$ m/s).

3 DISCUSSION AND CONCLUSIONS

Uncertainty of spatial velocity distributions measured by asymptotic ADCP survey appears to be dominated by interpolation. For the present data:

- Estimated mean uncertainty due to turbulence = 0.17 m/s
- Mean uncertainty due to ADCP measurement error = 0.22 m/s
- Resulting mean single ping single bin uncertainty = 0.30 m/s
- Corresponding depth average velocity uncertainty = 0.09 m/s
- The standard deviation of measured depth average velocities = 0.73 m/s, and the kriging standard deviations approached this value in locations devoid of measurements.

In order to minimize this uncertainty, more spatially intensive measurements would be required, with reduced spacing between transects. The relative advantages of repeat transect surveys versus spatially dense asymptotic surveys for accurate estimation of spatial distributions requires further investigation.

ACKNOWLEDGEMENT

The author wishes to thank Professor Michael Church of the U. British Columbia for continued collaboration and support for the present research. The research was funded by the Natural Sciences and Engineering Research Council of Canada and the Canadian Foundation for Innovation.

REFERENCES

- [1] Rennie CD, Church M: ADCP shear stress and bedload transport in a large gravel bed river, 32nd IAHR Congress (2007), 10 p.
- [2] Dinehart RL, Burau JR: Averaged indicators of secondary flow in repeated acoustic Doppler current profiler crossing of bends, Water Resources Research 41 (2005) W09405, doi:10.1029/2005WR04050.
- [3] Kironoto BA, Graf W: Turbulence characteristics in rough uniform open-channel flow, Proc. Inst. Civ. Engrs. Wat., Marit. & Energy 106(Dec.) (1994) 333-344.

Instrumental development and characterization for loaded liquid flow measurement

Philippe Schmitt^{1*}, Farès Abda¹, Anne Pallarès¹, Stéphane Fischer¹, Denis Ensminger¹ and Pierre François¹

¹Institut de Mécanique des Fluides et des Solides, ULP, 2 rue Boussingault, 67000 Strasbourg, France (*Corresponding author, e-mail: schmitt@convergence.u-strasbg.fr).

Real-time sewer networks survey becomes a major key in wastewater regulation. Needs for continuous and precise information, especially in wastewater discharge, increase in importance. In the frame of a technological research and innovation network in water and environment technologies (RITEAU), our research group, in collaboration with industrial partners and other research institutions, has been in charge of the development of a suitable flowmeter: an ultrasonic device measuring simultaneously water flow and concentration of size classes of suspended particles. This paper will focus on velocity. After the description of the instrument and the utilized velocity principle, representative experimental results obtained in an experimental laboratory channel will be shown. Velocity profiles will be given and analysed, correspondance with theory and quality criterions will be discussed.

Keywords: Acoustic, velocity, estimator, profile.

1 INTRODUCTION

There are several methods for flow velocity profile evaluation. One of the commonly used is the pulsed ultrasound technique: the estimation of the flow velocity at different depths along a profile can be obtained by Doppler evaluation from the backscattered acoustic signal. The measured ultrasonic signal at each depth is the result of the reflection of the emitted beam by moving scatterers in a volume defined by the ultrasonic beam geometry and the range-gated echo duration [1].

Also several techniques can be used to extract Doppler information from the volumes [2]. They are classified in two main categories, the incoherent and the coherent Doppler methods. Incoherent Doppler is a narrowband method and consists in estimating the Doppler shift from echoes of single-pulse pings. Every ping generates a single estimation of velocity profile. This method is robust and allows long measurement ranges, but the velocity resolution error requires long averaging times. Coherent Doppler includes narrowband and broadband methods. For this technique, phase changes from successive pings are observed for each insonified volume [3]. Good spatial resolution and low variance are obtained with this method, but its main disadvantage consists in the well-known "range-velocity" limit.

Our research group has developed an acoustic device, designed for real time sewage supervision, which allows simultaneous measurement of velocity profile based on pulsed Doppler coherent method in monostatic mode, and concentration of different size classes of suspended particles. The current instrument's prototype is made of two distinct parts: a submersible part containing transducers and acquisition electronics and an external processing

part in charge of data analysis and storage.

After the description of the developed device, the paper will focus on velocity profiles estimations obtained on a hydraulic channel in the laboratory. The instrument's velocity profile measurements will be discussed in order to evaluate the influence of secondary flows on discharge calculation [4]. Finally, a criterion to evaluate quality of the measurements will be discussed. Aim is to increase the precision of the instrument.

2 INSTRUMENT DESCRIPTION

The initially required specifications of our instrumental development were the combined possibility of flow rate measurements in open channels with diameters going from 0.3 to 1 m and velocities up to 3 m/s and concentration measurements of suspended solids with granulometric estimation.

From the design point of view, the instrument is split in two distinct parts: an immersed frame which is placed in the flow and a data management platform which remains on shore. Its schematic representation is shown figure 1.

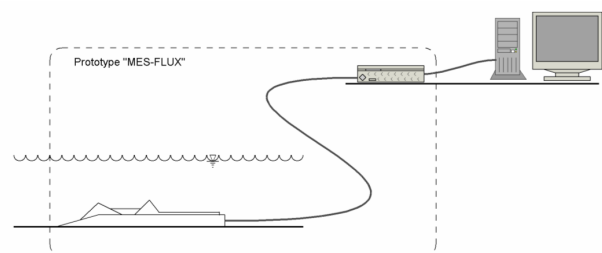


Figure 1: Schematic layout of the MES-FLUX.

Both parts are connected by a power supply and communication wire. The immersed frame contains

the transducers and electronics for emission-reception sequencing and digitalisation. The management platform, in charge of data treatment and storage can be accessed by a personal computer or can be directly connected to a network.

Figure 2 shows the open data management platform with the frame on the right. Global dimensions of the frame are about 260x75x45 mm³. The 3 specifically oriented transducers are used for velocity, water height and suspended solids concentrations measurements on the well known pulsed ultrasound principle.



Figure 2: Picture of frame and open data management platform.

The biggest broadband transducer of mean frequency 1.8 MHz is used for velocity and water height measurements. When the instrument is placed on the channel bottom, which is its conventional position, this transducer makes a 75° angle with the flow direction. This transducer orientation allows higher velocity values for a given Doppler frequency. This first transducer and a second one, equally oriented, of mean frequency 9.2 MHz, are also used for suspended solids concentration measurements. The third and last transducer, centred on 4.5 MHz, makes an angle of 70° with the direction of the other transducers. It is used for collecting complementary data at another diffusion angle for granulometric measurements. Concentration measurements are made on frequencies ranging from 1 to 14 MHz and carrier frequency for velocity can be chosen between 0.9 and 2.3 MHz.

3 VELOCITY PROFILE ESTIMATION

3.1 Pulsed ultrasound principle

Instruments working on pulsed principle potentially provide measurement profiles. Their working principle allows precise knowledge of position in the flow of a given data at a given time stamp. Periodically an ultrasonic pulse is emitted in the medium. This signal is backscattered by the particles suspended in the flow (figure 3). Received

by the transducer, the signal is conditioned, amplified and sampled in order to extract the information on velocity and concentration of suspended solids. Values are estimated on a succession of measurement volumes by windowing the backscattered signal in several blocs related to several measurement depths.

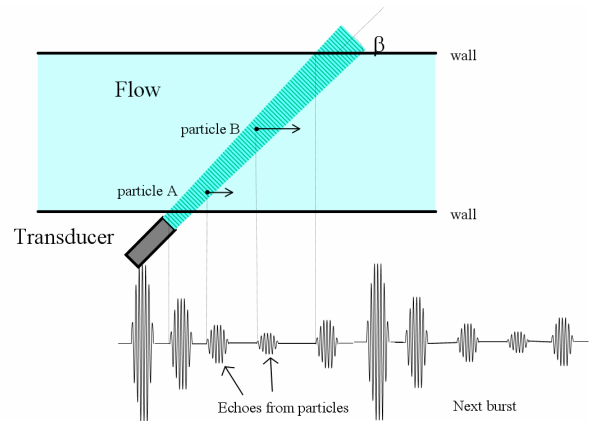


Figure 3: Pulsed ultrasound principle.

The Doppler signal frequency only depends on the particles velocity. Several methods are used to extract the Doppler information from the volume's signature. Our instrument uses the coherent Doppler method. This method uses the observed phase shift of the acoustic signal in a same volume during consecutive emission-reception cycles [3]. Each cycle generates a data sample by volume. This method allows good spatial resolution with low variance. Its major disadvantage is the "range-velocity" limit due to the signal sampling.

An estimator allows the calculation of mean Doppler frequency f_D , thus the flow velocity v in the corresponding volume according to:

$$v = \frac{c \cdot f_D}{2f_0 \cdot \cos \beta} \quad (1)$$

where c is the speed of sound in the medium, f_0 the carrier frequency and β the angle between flow and ultrasonic beam. Thus, velocity profile is obtained along the ultrasonic beam and its integration over the flow section gives the flow rate.

3.2 Doppler frequency estimation

Calculation of the first order moment of the signal (samples of the complex envelope with in-phase and quadrature components) gives the Doppler frequency in a given volume. Several methods may be used for Doppler frequency estimation. The Pulse-Pair method is commonly used [5]; another approach may be spectral analysis of the signal [6]. With the Pulse-Pair method, the estimated value of Doppler frequency is given by:

$$f_D = \frac{1}{2\pi T_{PRF}} \arctan \frac{\text{Im}(R(T_{PRF}))}{\text{Re}(R(T_{PRF}))} \quad (2)$$

$R(\tau)$: Autocorrelation function, T_{PRF} : sampling repetition period.

The Coherent Pulsed Doppler method ensures good temporal and spatial resolution and low variance on velocity estimation. Unfortunately this method is limited by its sampling principle (so called "range-velocity" limit):

$$v_{\max} P_{\max} = \frac{c^2}{8f_0} \quad (4)$$

v_{\max} : maximum detectable velocity, P_{\max} : maximum depth, f_0 : carrier frequency.

To override this limit, several methods have been tested. Among them, the most popular ones uses interlaced pulse repetition frequencies [7] or relies on several carrier frequencies [8]. Thus, a factor 3 might be gained on the « range-velocity » limit.

3.3 Estimation of variance and S/N ratio

The second order moment of the signal gives access to the variance of the Doppler spectrum. Good representation of various turbulent media is given by a Gaussian shaped power spectrum [7]. Assuming that the signal is hidden in white noise, the evaluation of Doppler signal variance is given by [9]:

$$\sigma_S^2 = \frac{\ln(|R(T_{PRF})|/|R(2T_{PRF})|)}{2\pi^2((2T_{PRF})^2 - T_{PRF}^2)} \quad (5)$$

σ_S : standard deviation of the Doppler signal

In case of large signal to noise ratios, the variance of the Doppler signal can be related to the standard deviation of mean Doppler frequency [7]:

$$\sigma_{f_D} = \frac{1}{2\pi} \sqrt{\frac{\sigma_S}{MT_{PRF}}} \quad (3)$$

σ_{f_D} : standard deviation on Doppler frequency estimation; σ_S : Doppler spectrum width, T_{PRF} : pulse repetition period; M : number of samples used for a velocity estimation in a bloc.

Note that the signal-to-noise ratio related to this approach is given by [9]:

$$SNR = \frac{|R(T_{PRF})|}{|R(0)|e^{(-2\pi^2\sigma_S^2 T_{PRF}^2)} - |R(T_{PRF})|} \quad (6)$$

4 EXPERIMENTAL RESULTS

4.1 Open Channel setup

Measurements were done on the canal of the

hydrologic platform of Alsace. This canal has a length of 16m, a width of 60 cm and a maximum water height of 80 cm. Its slope is adjustable. The instrument is centred in the flow, put in a zone where the hydraulic regime is well established. Its measurement beam goes from canal bottom to water surface (figure 4).

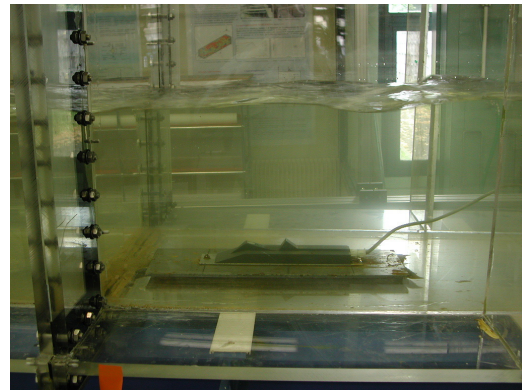


Figure 4: Experimental setup.

4.2 Doppler mean and variance measurement

The results shown below were obtained in a channel configuration with a flow of 253 m³/h. The instrument's configuration is given in Tab.1. Several estimations of instantaneous profiles are depicted on figure 5. This figure represents the velocity profile and the standard deviation of the Doppler spectrum converted to velocity dimension. Water height is situated at 0.29m.

Each instantaneous profile corresponds to a estimation performed on a single data bloc, i.e. for a temporal resolution of 100 ms, giving the possibility to observe a turbulence phenomenon along the profile. Velocity profile observed beyond the water surface corresponds to multiple echoes and is not representative.

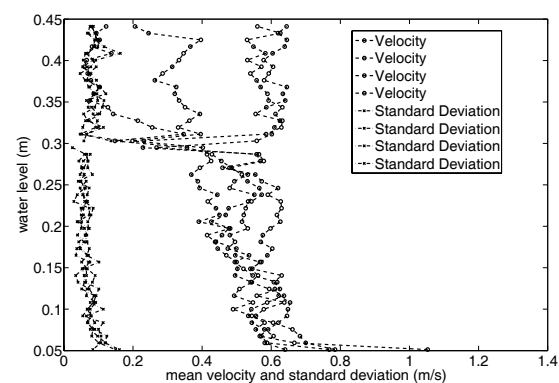


Figure 5: Instantaneous velocity profiles.

4.3 Distorsion in the profile

Figure 6 represents a mean profile scaled with its standard deviation. Water height level is characterized by a strong increase in standard deviation, because of the velocity gradient and

turbulence in this volume. Good agreement between spectral variance and velocity standard deviation leads to the conclusion that the instrument brings weak electronic noise.

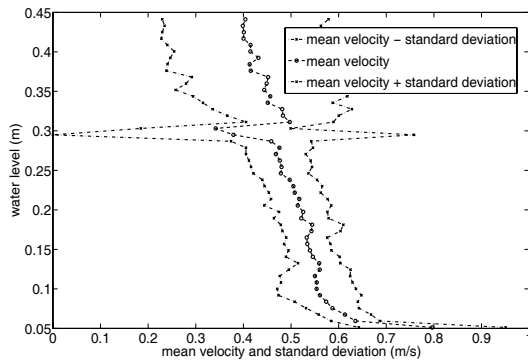


Figure 6: Mean profile with standard deviation.

Increase in velocity can be observed near to the transducer. This phenomenon is due to the velocity vector projection on the ultrasonic beam. Indeed, the instrument's topology induces changes in the velocity field in his near environment.

4.4 Measurement performance

Figure 7 represents the correlation coefficient, proportional to the ratio between mean Doppler frequency and spectral standard deviation, and the signal to noise ratio (SNR) for the whole profile.

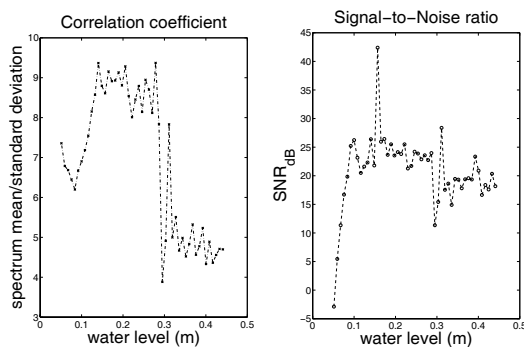


Figure 7: Correlation coefficient and SNR.

The correlation coefficient gives an estimation of the quality of the correlation, which can be decreased by turbulence, velocity gradient or presence of bubbles. Low correlation coefficient increases the variance of the Doppler estimates, but doesn't introduce bias.

We can observe a good signal to noise ratio all along the profile and a good correlation coefficient from bottom to water height. This coefficient decreases strongly after this level, indicating a loss in measurement quality. Combination of the two variables might be an interesting validation criterion for the quality of the measurement and might allow the filtering out of degraded data in measurement campaigns.

Table 1: Instrument configuration.

Variable	Symbol	Value
Carrier frequency	f_0 (MHz)	1.56
Number of periods/pulse	N_P	14
Pulse repetition frequency	PRF (Hz)	650
Number of volumes	N_{vol}	60
Distance between volumes	Δt (μs)	9.6
Number of samples/bloc	M	64
Number of blocs	N_{blocs}	24

5 CONCLUSIONS

Two prototypes of the described instrument exist. Both are used for various laboratory and in situ measurement campaigns. They showed good coherence for velocity measurements versus imposed flow. The influence of velocity field perturbation due to presence of the frame has still to be evaluated by comparison between the instrument's velocity profile measurement and its scanning obtained with a single-point Acoustic Doppler Velocimeter. A second investigation point would be Dual-PRF measurements and the evaluation of the possible quality criterion in these conditions.

REFERENCES

- [1] Yu A.C.H. et al.: Transit-time broadening in pulsed Doppler ultrasound: a generalized amplitude modulation model, IEEE Transactions on Ultrasonics, Ferroelectrics, and Frequency Control, Vol. 53-3(2006) 530- 541.
- [2] Brumley B. H. et al.: Performance of a Broad-Band Acoustic Doppler Current Profiler, IEEE Journal of Oceanic Engineering, Vol. 16, NO. 4, October 1991.
- [3] Takeda Y.: Velocity profile measurement by ultrasonic Doppler Method, Experimental Thermal and Fluid Science, 10 (1995) 444-453.
- [4] Yokoyama K.: Flow Measurement in an Open Channel by VVP, Fourth International Symposium on Ultrasonic Doppler Method for Fluid Mechanics and Fluid Engineering, 2004.
- [5] Miller, K.S., Rochwarger, M.M.: A covariance approach to spectral moment estimation, IEEE Transactions on Information Theory, 18(1972) 588-596.
- [6] Fischer, S. et al.: A New Velocity Estimation Method using Spectral Identification of Noise, Flow Measurement and Instrumentation. Under Press (2008).
- [7] Zrnica, D.S.: Spectral Moment Estimates from Correlated Pulse Pairs, IEEE Transactions on Aerospace and Electronic Systems, Vol. AES-13 (1977), NO. 4.
- [8] McCormick, W.S. et al.: Resolution of a 2π Ambiguity Problem in Multiple Frequency Spectral Estimation, IEEE Transactions on Aerospace and Electronic Systems, VOL. 31(1995), NO. 1.
- [9] Lhermitte, R., Serafin, R.: Pulse-to-Pulse coherent Doppler sonar signal processing techniques, Journal of Atmospheric and Oceanic Technology, Vol.1(1984),NO. 4.

A basic study on sound-field characteristics around an Ultrasonic Oscillator and Acoustic Streaming

Hirochika TANIGAWA¹, Hiroaki TAKEDA², Jiro FUNAKI² and Katsuya HIRATA^{2*}

¹Maizuru National College of Technology, Maizuru 625-8511, Japan

²Department of Mechanical Engineering, Doshisha University, Kyoto 610-0321, Japan
(khirata@mail.doshisha.ac.jp).

The sound fields produced by ultrasonic oscillators are useful for applications in various industrial aspects, such as measurements, heat/mixture enhancements, cleanings and so on. Recently, according to the development of the UVP measurement, their importance has been increasing. In this research, the authors develop a simple and high-speed computational technique to simulate the sound fields produced by oscillators with arbitrary and complicated geometries, and investigate the optimum conditions for various oscillators, numerically. Moreover, the authors simulate the acoustic streaming in a cylindrical tank, using the simulated sound field. Such numerical results are compared with experiments.

Keywords: *oscillator, sound field, ultrasonic, cylindrical container, acoustic streaming*

1 INTRODUCTION

Ultrasonic waves, strictly speaking, linear compressional waves with comparatively high frequencies, are useful for applications in various industrial aspects, such as measurements and cleaning, together with remote manipulations and non-contact transport technologies. Recently, according to the development of the ultrasonic velocity profiler (hereinafter referred to as UVP), their importance has been increasing. Moreover, ultrasonic waves can produce not only sinusoidal motions of fluid particles, but also the flow of fluid particles, even with small amplitudes. The flow is called as the acoustic streaming [1-3]. The acoustic streaming is useful as well, especially for the enhancements of heat transfers and material mixings.

Such recent increasing needs for ultrasonic waves are promoted by manufacturing cheap and robust ultrasonic oscillators such as piezoelectric actuators. The piezoelectric actuators have high flexibility in their geometries, by which we can expect widely-applicable potentials in other fields. So, we still further demand the understanding of their detailed and precise sound fields, and faster and more efficient simulation techniques.

In this research, we develop a simple and high-speed computational technique to simulate the sound field produced by ultrasonic oscillators with arbitrary and complicated geometries. Namely, we consider the sound field around an oscillator, as an ensemble of spherical waves from many point sources. Concretely speaking, we calculate the sound-pressure distributions for circular-plate, annular-plate and semi-spherical oscillators at several driving frequencies, in order to reveal the optimal frequencies and geometries. Moreover, we

simulate the acoustic streaming in a cylindrical tank, using the simulated sound field. Such numerical results are compared with experiments, by which we can confirm the present numerical accuracy. Incidentally, the tested range of the non-dimensional dominant parameter $k \times a$ (for its definition, see later) is from 10-60, which is close to the value of the most common UVP probes in use.

2 COMPUTATIONAL METHOD

2.1 Velocity potential

(a) A circular-plate oscillator and other plate-type oscillators

Figure 1 shows a circular-plate oscillator, which is an oscillating-circular plate, on an infinite baffle, together with the definitions of geometrical parameters and the present coordinate system (r, φ, z). A point B denotes an arbitrary measuring point. Note that the B is on the r - z plane at $\varphi = 0$.

From a theoretical point of view, in order to obtain Φ , we should integrate the potential $d\Phi$ corresponding to a minute area dS on the oscillator

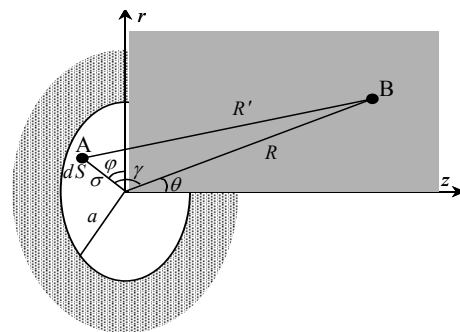


Figure 1: A circular-plate oscillator (an oscillating-circular plate) on an infinite baffle.

surface, all over the oscillator- surface areas. However, this procedure is not so easy even for simple-geometry oscillators.

Instead, we divide the oscillator into many minute sections. For example, we divide a circular-plate oscillator into $L \times M$ sections, where L and M denote the division numbers in the azimuthal and radial directions, respectively. Next, at each section, we put a point source, which is weighted by the corresponding section area. Then, we approximately regard the whole oscillator as an ensemble of $L \times M$ point sources.

As shown in Figure 1, we consider the velocity potential Φ in the complex form at the B. An arbitrary point source A with a weight of dS yields a velocity potential $d\Phi$ at the B, which are given by

$$d\Phi = \frac{\xi_0 dS}{2\pi R'} e^{j(\omega t - kR')}, \quad (1)$$

where R' denotes the distance between the A and the B. ξ_0 , ω , t and j represent velocity amplitude of the oscillator, excitation angular frequency, wave number, time and the imaginary-number unit, respectively.

Using Φ , acoustic pressure p_a is given by

$$p_a = \rho \frac{\partial \Phi}{\partial t}, \quad (2)$$

where ρ denotes the density of fluid.

As well as the circular-plate oscillator, by the present method, we can easily calculate the sound fields produced by the oscillators with other geometries such as annuli and rectangles, if the oscillators are two-dimensional plates. For example, we merely divide an annular-plate oscillator to many minute sections in the azimuthal and radial directions, as well.

(b) A semi-spherical oscillator

We may consider three-dimensional non-plate-type oscillators, expecting the control of acoustic-wave

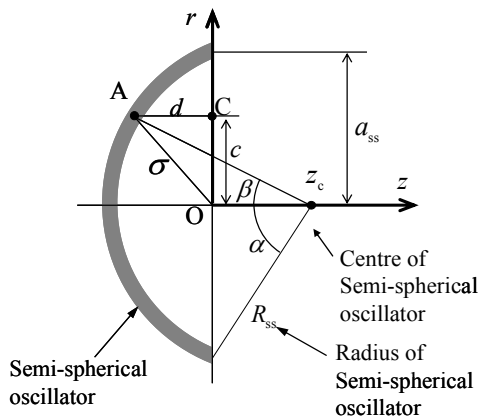


Figure 2: Sectional view of a semi-spherical oscillator.

convergence at a restricted space. Even in such cases, we can easily compute the sound field by the present method.

Figure 2 shows one of the non-plate-type oscillator, specifically speaking, the cross section on the r - z plane of a semi-spherical oscillator. z_c and a_{ss} represent the centre and the projected radius of the oscillator. The origin O of the coordinate system is at the centre of the oscillator's circumference. As a characteristic length scale, we consider the equivalent radius a , which defined by the radius of the circle with the same area as the oscillator surface. Then, a_{ss} is always less than a .

As well as the circular-plate oscillator, we divide the oscillator into many minute sections of $L \times M$. And, at each section, we put a point source weighted by the corresponding section area. The distance between a point source A and an arbitrary measuring point B is given by

$$R' = \sqrt{\sigma^2 + R^2 + 2R(d \cos \theta - c \sin \theta \cos \varphi)}. \quad (3)$$

Under the linear approximation, we should consider one non-dimensional governing parameter $k \times a$ on the produced sound field, together with some geometrical parameters. k denotes the acoustic wave number, which is equal to $2\pi f / c_0$, where f and c_0 represent the excitation frequency and the sound speed, respectively. Then, $k \times a$ is proportionate to the ratio of the oscillator size to the acoustic wave length.

2.2 Acoustic streaming

When we consider the acoustic streaming, the governing equations are the compressible-viscous-unsteady Navies-Stokes equations. In the present study, we suppose only the two-dimensional r - z plane, assuming the axi-symmetrical flow in a cylindrical tank. Moreover, we assume that U/c_0 , u_a/c_0 and ρ_a/ρ_0 are constant values much less than unity, and that the third and the higher order terms are negligible. Then, we get the governing equations using the vorticity ζ and the stream function ψ , as follows. [2]

$$\frac{\partial \zeta}{\partial t} - \frac{1}{r} \frac{\partial \psi}{\partial z} \frac{\partial \zeta}{\partial r} + \frac{1}{r} \frac{\partial \psi}{\partial r} \frac{\partial \zeta}{\partial z} + \frac{\zeta}{r^2} \frac{\partial \psi}{\partial z} = \nu \left(\frac{\partial^2 \zeta}{\partial r^2} + \frac{1}{r} \frac{\partial \zeta}{\partial r} + \frac{\partial^2 \zeta}{\partial z^2} - \frac{\zeta}{r^2} \right) + \left(\frac{\partial F_r}{\partial z} - \frac{\partial F_z}{\partial r} \right), \quad (4)$$

and

$$\frac{1}{r} \frac{\partial^2 \psi}{\partial r^2} - \frac{1}{r^2} \frac{\partial \psi}{\partial r} + \frac{1}{r} \frac{\partial^2 \psi}{\partial z^2} = -\zeta, \quad (5)$$

where ν denotes the kinematic viscosity of fluid. A vector $\mathbf{F}(F_r, F_z)$ represents the force par unit mass driven by the acoustic waves. \mathbf{F} is given by

$$\mathbf{F} = -\overline{(\mathbf{u}_a \cdot \nabla) \mathbf{u}_a} - \overline{\mathbf{u}_a (\nabla \cdot \mathbf{u}_a)}, \quad (6)$$

where a superscript “ $\overline{\quad}$ ” represents the time-mean operation. We get the velocity vectors of fluid particle driven by acoustic waves as follows.

$$\mathbf{u}_a = -\nabla \phi, \quad (7)$$

where the velocity potential ϕ is the real part of Φ . Time-mean flow velocity $\mathbf{U}(U_r, U_z)$ is given by

$$\mathbf{U} = \mathbf{u}_0 + \frac{\rho_a \mathbf{u}_a}{\rho_0}, \quad (8)$$

where a subscript “0” represents the time-mean value [4].

When we consider the acoustic streaming, we need another governing parameter in addition to kxa . Then, we define the acoustic Reynolds number Re_a as

$$Re_a = \frac{\xi_0 c_0}{\delta_0 \omega}, \quad (9)$$

where δ_0 denotes acoustic diffusivity. We solve the equations (4) and (5) by a finite difference method with Crank-Nicolson semi-implicit discretisation in time and 2nd-order central discretisation in space, using the SOR algebra solver.

3 EXPERIMENTAL METHOD

In the present experimental apparatus, a cylindrical tank has such dimensions as 60mm in diameter and 150mm in length. The Working fluid is glycerin aqueous solution, suspending many but small-amount-of aluminum flakes of 2-3 μ m inside for flow visualisation.

4 RESULTS AND DISCUSSION

4.1 Accuracy of computed sound field

At first, we check the numerical accuracy of computed sound fields, by means of comparing them with the analytical ones obtained by Stenzel [5].

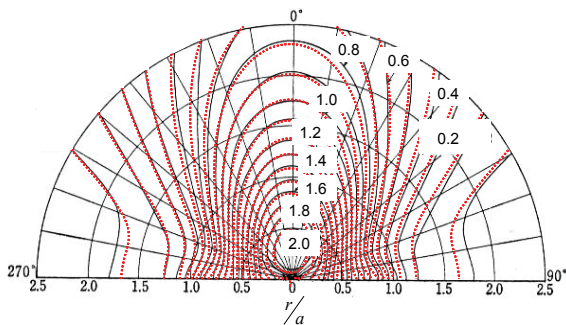


Figure 5: Contours of non-dimensional acoustic pressure amplitude $p'_a / (\rho c_0 \xi_0)$, for a circular-plate oscillator at $kxa = 4$. \cdots , Computational ; — , analytical (Stenzel, 1958).

Figure 5 shows contours of non-dimensional acoustic pressure amplitude $p'_a / (\rho c_0 \xi_0)$ at $kxa = 4$, where $p'_a \equiv |p_a|$. Dotted and solid lines correspond to the computational and the analytical results, respectively. We can see a good agreement between them. At other $kxa = 6$ and 10, we also confirm good agreements.

4.2 Sound field around a circular-plate oscillator

Figure 6 shows the computed distributions of instantaneous acoustic pressure p_a (in figure (a)) and sound-pressure level $SPL \equiv 20 \log_{10}(p_e/p_0)$ (in figure (b)) for a circular-plate oscillator at $kxa = 55.1$, where p_e denotes the effective value of acoustic pressure p_a . In Figure 6(a), we see acoustic waves

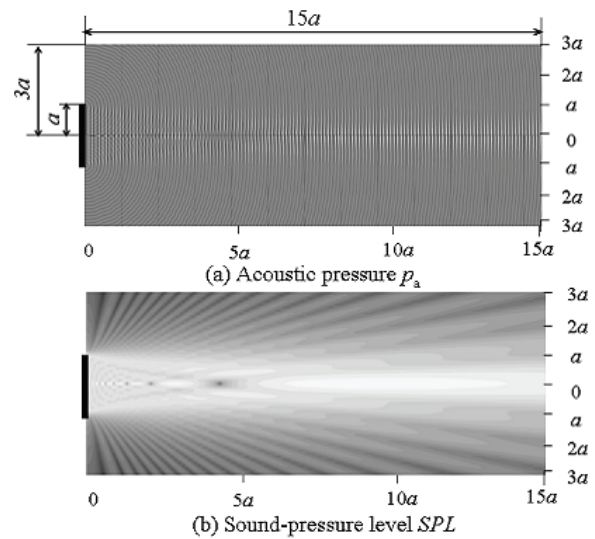


Figure 6: Distributions of p_a and SPL , for a circular-plate oscillator at $kxa = 55.1$ ($a = 10$ mm, $f = 1600$ kHz).

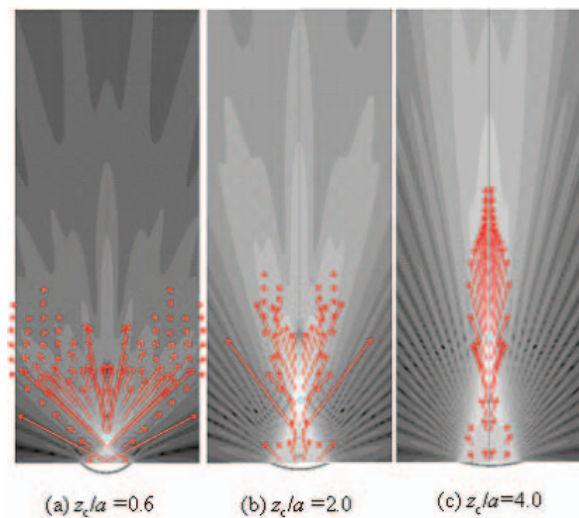


Figure 7: Distributions of sound-pressure level SPL and driving force vectors \mathbf{F} , for around a semi-spherical oscillator at $kxa = 55.1$ and $Re_a = 0.36$ ($a = 10$ mm, $f = 1600$ kHz).

traveling from the oscillator, and see clear parallel stripes near the centre axis of the oscillator. The wave lengths shown by the stripes' intervals are almost equal to the plane wave theory.

Because, higher contrasts of the stripe mean larger amplitudes of p_a , we expect the strong directivity of the produced acoustic waves. In Figure 6(b), we can confirm the strong directionality.

In addition, closer to the oscillator we see, more non-uniform SPL is. Even on the centre axis, the maximum and minimum SPL s appear one after the other, with going apart from the oscillator.

4.3 Sound field around a semi-spherical oscillator

Figure 7 shows the distributions of SPL for a semi-spherical oscillator at $kxa = 55.1$, together with the produced driving force vectors at $Re_a = 0.36$. We show only the vectors with larger magnitudes than 2% of the maximum. Figures (a), (b) and (c) are at $z_c/a = 0.6, 2.0$ and 4.0 , respectively, where z_c/a is a geometrical parameter of the oscillator. Note that the oscillator with $z_c/a = \infty$ is a circular-plate one. We can see that the directivity becomes weak with

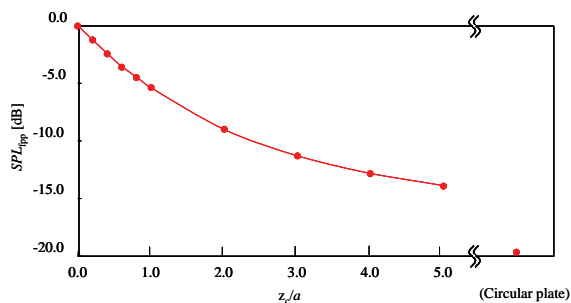


Figure 8: Sound-pressure level SPL_{fpp} at focus peak point against z_c/a , for a semi-spherical oscillator at $kxa = 27.6$ and $Re_a = 0.36$ ($a = 10\text{mm}$, $f = 800\text{kHz}$).

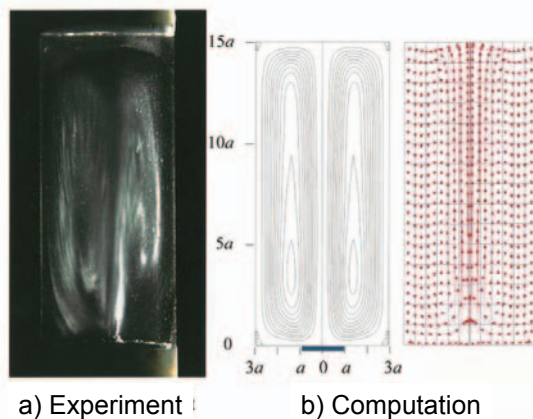


Figure 9: Comparison between experiment and computation, for a circular-plate at $kxa = 27.6$ and $Re_a = 0.36$ ($a = 10\text{mm}$, $f = 800\text{kHz}$).

decreasing z_c/a . At each z_c/a , the maximum driving force and one of the largest SPL s exist near the oscillator's focus point. Figure 8 shows the sound-pressure level SPL_{fpp} at the focus peak point plotted against z_c/a , at $kxa = 27.6$ and $Re_a = 0.36$. Here, SPL_{fpp} is defined as the point where SPL attains the largest value near the oscillator's focus point. As a result, smaller z_c/a is, stronger and nearer the acoustic convergence becomes.

4.4 Computations of acoustic streaming

In order to confirm the numerical accuracy of the acoustic streaming, we investigate the mesh effect upon the maximum value of stream function ψ , at $kxa = 13.8$ and $Re_a = 0.36$. For example, a 301×61 mesh means a mesh system with 301 and 61 meshes in the azimuthal and radial directions, respectively. As the relative error of the 201×41 mesh to the 301×61 mesh is 6.4%, we use the 301×61 mesh for the other main calculations.

Figure 9 shows an acoustic streaming at $kxa = 27.6$ and $Re_a = 0.36$, both by experiment (in figure (a)) and by computation (in figure (b)). We can confirm that these results are qualitatively similar with each other.

5 CONCLUSIONS

We have developed a simple and high-speed computational technique to simulate the sound fields around complicated-geometry oscillators. The computations for a circular-plate oscillator shows a good agreement with analytical ones. Considering a semi-spherical oscillator, we have revealed the following. With decreasing z_c/a the directivity becomes weak. On the other hand, smaller z_c/a is, stronger and nearer the acoustic convergence becomes. Moreover we have simulated the acoustic streaming, and compared it with an experiment. Both are qualitatively similar with each other.

REFERENCES

- [1] C. Eckert: Vortices and streams caused by sound waves, Phys. Rev., 73-1 (1948), pp.68-76.
- [2] H. Mitome: Study of the generation mechanism of an acoustic jet through visualization experiments, Jpn. J. Appl. Phys. Supp., 30-1 (1991), pp.60-62.
- [3] K. Matsuda, T. Kamakura and Y. Kumamoto: Theoretical study on acoustic streaming generated in a focused Gaussian beam, J. Acoustical Soc. Jpn., 50-12 (1994), pp.997-1005 (in Japanese).
- [4] L. D. Rozenberg: High-intensity ultrasonic fields, Plenum Press New York (1971), pp.135-199.
- [5] H. Stenzel and O. Brosze: Leitfaden zur berechnung von schallvorgängen, Zweite Auflage, S. 77, Springer, Berlin (1958).

Ultrasonic investigation of flow transition in surface switching of rotating fluid

Yuji Tasaka^{1,2*}, Kanako Yano¹ and Makoto Iima³

¹ Graduate School of Engineering, Hokkaido University, N13 W8, 060-8628 Sapporo, Japan

² Center for Nonlinear Dynamics, The University of Manchester, Oxford road, M1 3BS Manchester, UK

(*Corresponding author, e-mail: tasaka@eng.hokudai.ac.jp).

³ Research Institution for Electric Science, Hokkaido University, N12W6, Sapporo, 060-0812, Japan

We have investigated the effect of surface tension in the recently reported phenomenon called "surface switching"; it occurs in the flow driven by a rotating disk in an open cylindrical vessel [1]. The deformed free surface abruptly changes from an axisymmetric to a non-axisymmetric shape accompanying with a change of typical height at irregular intervals. Ultrasonic velocity profiling (UVP) was utilized to measure the spatio-temporal fluid motion in three kinds of liquid; water, 10 cSt silicone oil and liquid gallium. The measurement and observation of the free surface indicate: (a) The silicone oil allows the breaking of axisymmetric flow and surface deformation even in the laminar region, but distinct surface switching is not observed. (b) The liquid gallium sustains the flow axisymmetry even in the turbulent region and the surface elongation does not occur. These results suggest that the surface tension as well as the viscosity play an important role in the mechanism of the surface switching.

Keywords: Rotating flow, Free surface, Flow transition, Instability, Surface tension, Liquid metal

1 INTRODUCTION

1.1 Background & Objective

Rotating flow accompanying with large-deformed free surface such as bathtub vortex is ubiquitous. The recently reported phenomenon called "surface switching" that occurs in the flow driven by a rotating disk in an open cylindrical vessel is one of the most interesting phenomena among them. Suzuki *et al.* [1] reported a temporally-irregular switching phenomena: the free surface shape changes the symmetry irregularly in time from axisymmetric to non-axisymmetric and vice versa while the height of the surface at the center of the vessel changes in the vertical direction. This "surface switching" is observed at $Re \sim 1.3 \times 10^5$, which is near the critical Reynolds number for the laminar-turbulent transition of the boundary layer on a rotating disk, $Re \sim 10^5$ [2]. They suggested that the mechanism of the switching is the decrease/increase of the pressure in the central region caused by the laminar-turbulent transition of the flow. Tasaka *et al.* [3] studied the transition to surface switching using flow visualization. As mentioned above, the critical Re for the switching is close to the turbulent transition of the boundary layer on a rotating disk [2]. Therefore the turbulent transition may be a trigger for the large scale deformation of the surface. However, there are other possibilities that the centrifugal instability and/or the inertial instability induce the large-scale deformation. Tasaka & Iima [4] studied the flow transition in the region below the critical Reynolds number of surface switching to investigate the qualitative fact about the flow characteristics that may lead to the surface switching. They find that the fluid-air interface becomes unstable at a smaller

Reynolds number than the critical Reynolds number for the surface switching.

This phenomenon has at least four control parameters; Reynolds number, Froude number, Weber number and aspect ratio. This study aims to clarify the effects of the Weber number using various liquids; water, 10 cSt silicone oil and liquid gallium.

1.2 Process of the temporally irregular switching

Figure 1 shows a typical sequence of the switching. (a) The bottom of an axisymmetric surface elongates and attaches to the rotating disk. (b) The shape of the surface changes into non-axisymmetric shape. (c) Deformation of the surface becomes large and finally the surface detaches from the bottom. (d) The surface with two humps rotates. (e) The free surface restores axisymmetry and then elongates to the bottom.

The detailed dynamic process consists of the

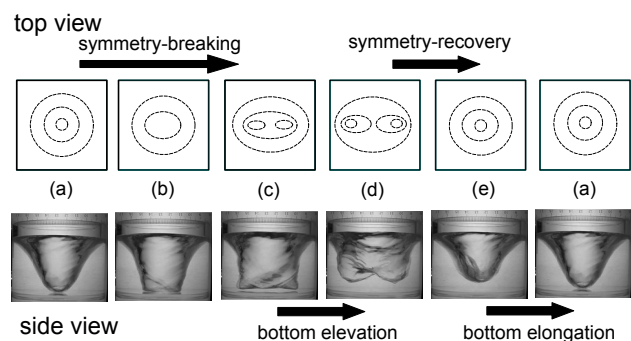


Figure 1: Visualization of the shape of the free surface during the switching process; top view (above, schematic) and side view (bottom, visualization). The free surface repeats its deformation from (a) to (e)

following three states; surface switching (SW), regular oscillation (RO) and flat rotation (FR) [4]. Figure 2 shows a temporally expanded image extracted from snapshots of a movie taken from a side by constructing their middle lines. Rectangles indicate each state; (a) SW, (b) RO and (c) FR. SW shows the large depression of the surface due to the flow transition from turbulent to laminar. RO sustains a periodic oscillation of the surface with keeping the non-axisymmetric shape with clear humps (see figure 1 (d)). In FR the bottom of the surface looks flat and it has no clear humps.

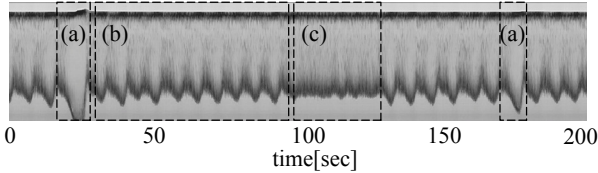


Figure 2: Typical variation of the surface height in the temporally irregular surface switching extracted from a movie at the vertical center line of the cylinder, where labels (a), (b) and (c) represent surface switching (SW), regular oscillation (RO) and flat rotation (FR) respectively.

2 EXPERIMENTAL SETUP AND METHOD

Figure 1 (a) shows a coordinate system and a schematic diagram of the experimental setup. The open end cylindrical vessel is made of acrylic resin for water and silicone oil or tin for liquid gallium; its inner radius is $R = 42$ mm. A disk is also made of two kinds of material; glass for water and oil, and tin for gallium because of wetting properties. The disk was driven by a stepping motor through a shaft. A gap between the disk and the side wall of the vessel, $\Delta R = 0.3$ mm, was set to reduce a vibration due to the friction. The height of the liquids at rest was $H = 40$ mm; and the aspect ratio $\Gamma = H/R = 0.95$. Particles of porous resin or ZrB₂, which are 50 to 60 μm in diameter, were mixed into the fluids as tracers for the velocity profile measurement. The liquid gallium layer was surrounded by Argon gas to prevent oxidization. The physical properties of the working fluids are specified in table 1. Reynolds number in this system is defined as $Re = 2\pi\Omega R^2/\nu$ (here Ω and ν are the rotating speed [rad/s] of the disk and kinematic viscosity of the fluid respectively).

Ultrasonic velocity profiling (UVP) was used to determine instantaneous velocity profiles. It is capable of measuring the spatio-temporal motion of fluid even in opaque fluid such as liquid metal [5, 6]. An ultrasonic transducer was mounted at the side wall of the vessel perpendicular to the wall at a height of 8 mm from the disk ($z/H = 0.2$). Instantaneous profiles of the radial velocity component along the horizontal center line of the cylinder, $u(r, t)$, were measured through the side wall. The contact face of the vessel with the transducer was flattened to improve transmission of the ultrasonic wave through the cylinder wall. The

basic frequency of the ultrasonic wave was set to 4 MHz; the spatial resolution of the velocity profile, which is determined from the wavelength of the ultrasound, is 0.74 mm for water, 0.5 mm for silicone oil and 1.43 mm for liquid gallium. The number of the velocity profile is 4096.

The free surface of the water was illuminated by a back light (Halogen lamp scattered by tracing paper) from a side of the cylinder, and its motion was captured by a digital video camera.

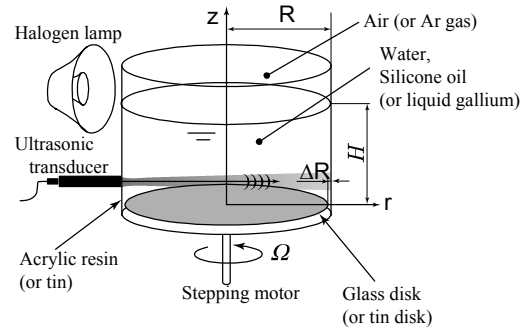


Figure 3: Experimental setup for the UVP measurement and the surface height measurement; Materials of the vessel are acrylic region and glass for water and silicone oil or tin for liquid gallium.

Table 1: Comparison of physical properties (kinematic viscosity ν , surface tension σ and speed of sound c) in working fluids, water, 10 cSt silicone oil and liquid gallium

Liquid	ν [m^2/s]	σ [N/s]	c [m/s]
Water	1.0×10^{-6}	0.073	1480
Silicone oil	10.0×10^{-6}	0.021	995
Gallium	0.32×10^{-6}	0.715	2860

3 RESULTS AND DISCUSSIONS

3.1 Silicone oil (low surface tension & high kinematic viscosity)

In the silicone oil, the rotating fluid loses axisymmetry even at small rotating speed because of small surface tension (see Table 1). Such symmetry-breaking is reported by Lopez *et al.* [7], but it is not distinct in the case of water. Figure 4 shows mean velocity profiles on the horizontal line through the center of the cylinder; (a) the silicone oil and (b) water. Error bars in the figures represent the standard deviation of the velocity fluctuation. The rotating speed is 300 rpm in the both cases and corresponding Reynolds numbers are 0.55×10^4 for the oil and 0.55×10^5 for the water. In water a local circulation forms a central region of the cylinder but the radial velocity is small in other area when rotating speed is small [3]. Figure 4 (b) follows this: There are large mean velocity and large velocity fluctuation around the center. In the silicone oil, mean velocity is small but the fluctuation is quite large (up to around 60 mm/s) from the center to $r/R \sim 0.75$. Mean velocity near the wall has a relatively large value. It is caused by a local circulation near

the wall. Figure 5 shows typical surface shape for the silicone oil, where the schematics attached on the pictures indicate the shooting angle for the surface. The free surface has certain non-axisymmetric shape but it has never taken the humps which are observed in the water (cf. Fig.1 (d)). In this sense, this state looks as flat rotation (FR) observed for the case of water (cf. Fig. 2 (c)). Rotation of this surface causes the oscillation in the fluid flow. The surface also has a stair-like shape near the side wall corresponding to the boundary of the local-circulation region near the wall. Such the shape has never observed in water.

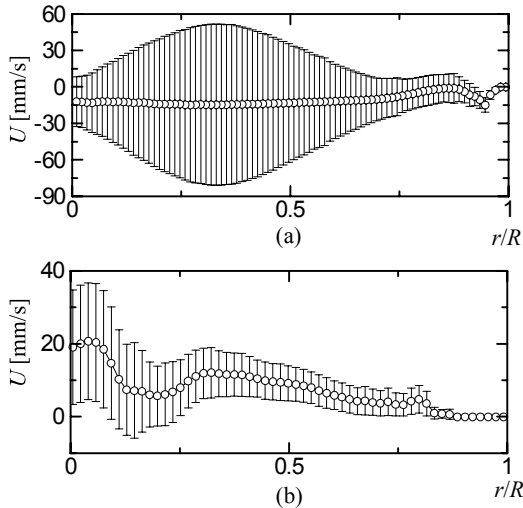


Figure 4: Mean velocity profile on the center line of the cylinder; (a) 10 cSt Silicone oil and (b) water, where the error bars represent the standard deviation of the velocity fluctuation (rotating speed is 300 rpm in the both cases.)

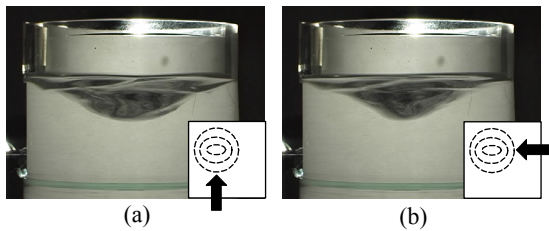


Figure 5: Typical pictures of the surface shape in 10 cSt silicone oil, where the schematics attached on the pictures indicate angle for the non-axisymmetric surface (300 rpm)

Figure 6 shows the spatially averaged intensity of the velocity fluctuation for the silicone oil and water [4] as the function of (a) rotating speed (proportional to the Froude number, defined as $Fr = 2\pi\Omega R / (gH)^{1/2}$) or (b) the Weber number ($We = \rho U^2 R / \sigma$, where g , U , ρ and σ are gravity acceleration, characteristic velocity, density and surface tension of the fluids. We choose here the rotating velocity at the edge of the disk, $2\pi\Omega R$, as U for simplicity). In the water the intensity decreases with respect to the rotating speed until the surface attaches to the bottom (around 500 rpm). It greatly increases at the onset of the switching (around 760 rpm). In the silicone oil, the intensity rises sharply at a small rotating speed,

around 200 rpm, by the surface deformation (cf. Fig. 5). It sustains a constant value until 350 rpm, and after that, it is roughly proportional to the rotating speed. In this region, the height of the free surface gradually decreases as the rotating speed increases. But it should be noted that the rate is smaller than the water because it is prevented by an increment of the pressure at the central region of the cylinder due to the flow mixing by non-axisymmetric surface. The visualization of the surface shows that it attaches to the bottom around 650 rpm, which is substantially larger than the case of water; however, there is no data larger than 600 rpm because of the measurable velocity range of UVP. It also shows that the surface never detached from the bottom even at 850 rpm. The surface is also deformable in this condition. But it cannot produce large velocity fluctuation enough to detach from the bottom against the pressure gradient; because the Reynolds number is much smaller than water due to the large kinematic viscosity.

Figure 6 (b) shows the Weber-number dependency of the spatially averaged velocity fluctuation intensity. Appearance of the surface deformation is in the same order of We in the both cases. But the flow phenomenon is quite different as explained follows.

Figure 7 (a) shows the apace averaged power spectrum of the velocity fluctuation in the silicone oil; the averaging area is $0.49 \leq r/R \leq 0.67$. There are

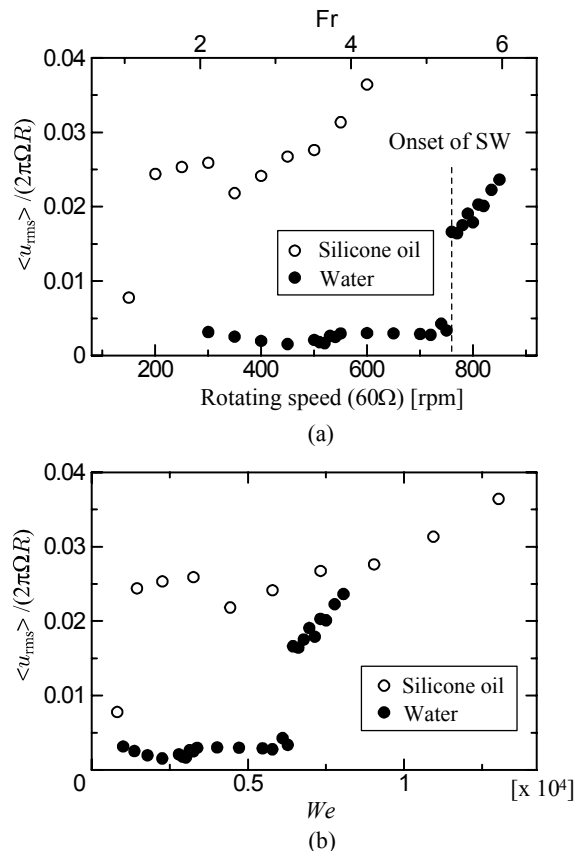


Figure 6: Spatially averaged intensity of the velocity fluctuation for 10 cSt silicone oil and water versus (a) rotating speed and Froude number or (b) Weber number

clear peaks of f_1 and its harmonics. f_1 corresponds to the rotation of the non-axisymmetric surface. In comparison with the spectrum for the temporally irregular switching in water (Fig. 7 (b), 850 rpm), there are no other frequency components than f_1 , f_2 or f_3 in the Fig. 7 (b), which corresponding to the vertical oscillation of the surface or irregular switching. We observe such a regular oscillation appears in the silicone oil around 500 rpm, where the surface is close to the bottom, but its amplitude is substantially smaller than the surface switching.

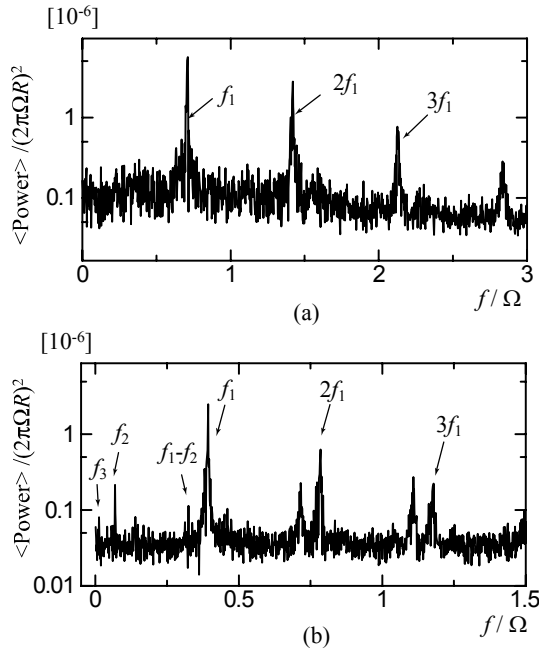


Figure 7: Space averaged power spectra of the velocity fluctuation; (a) in 10 cSt silicone oil with 300 rpm in the rotating speed and (b) in water with 850 rpm

3.2 Liquid gallium (high surface tension & low kinematic viscosity)

Figure 8 shows the mean velocity profile in the liquid gallium; (a) on a line, ξ , parallel to the line through the center of the cylinder, with a distance Δy and (b) the line through the center. A schematic in Fig. 8 indicates the relation between the measurement lines. Figure 8 (b) shows that value of the radial velocity is very small along the line through the center of the cylinder except several negative values around $r/R = 0.5$; it may be due to the measurement error. It means that the fluid motion is fully axisymmetric. The velocity profile on the measurement line ξ provides that the velocity has an azimuthal component as shown in Figure 8 (a). Comparing with Fig. 4 (b), we observe that in the water case the local circulation at the central part of the cylinder causes the velocity fluctuation. Such a large fluctuation is not observed in the gallium case, because the surface tension is so large (around ten times larger than water) that the symmetry-breaking of the surface deformation is depressed. The height of the free surface gradually decreases with respect

to the rotating speed. It should be noted that the rate is smaller than the water because the large surface tension prevents the elongation of the free surface. It does not attach to the bottom even at 700 rpm.

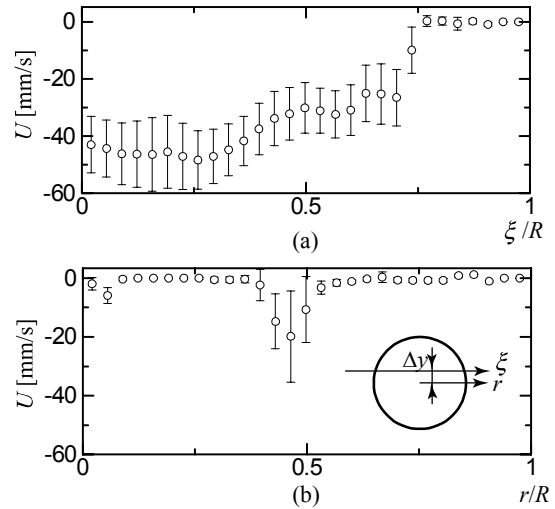


Figure 8: Mean velocity profile of the rotating liquid gallium (a) on a line parallel to the center line with a distance and (b) on the center line

4 CONCLUSIONS

It was shown that the surface tension greatly influences the temporally irregular surface switching using three kinds of liquids. 10 cSt silicone oil allows the surface deformation even at a small rotation speed. But the surface switching is not observed even at the critical rotating speed of the switching in the water because of large kinematic viscosity. Large surface tension of the liquid gallium sustains the flow axisymmetry and prevents the surface elongation.

ACKNOWLEDGEMENT

This work is supported by Grant-Aided Research for Science of the Japanese Ministry of Education & Science: No.18760116 and No.18204038. The authors express thanks for this support.

REFERENCES

- [1] SUZUKI T, *et al.*: Surface switching of rotating fluid in a cylinder, *Phys. Fluids* 18 (2006) 101701.
- [2] REED HL, SARIC WS: Stability of three-dimensional boundary layers, *Ann. Rev. Fluid Mech.* 21 (1989)235-284.
- [3] TASAKA Y, *et al.*: Visualization of a Rotating Flow under large-deformed Free Surface using anisotropic Flakes, *J. Visualization* 11(2008) 163-172.
- [4] TASAKA Y, IIMA M: Flow transition in surface switching of rotating fluid, in progress.
- [5] TAKEDA Y: Measurement of velocity profile of mercury flow by ultrasound Doppler shift method, *Nuclear Tech.* 79 (1987) 120-124.
- [6] MASHIKO T, *et al.*: Instantaneous measurement of velocity fields in developed thermal turbulence in mercury, *Phys. Rev. E* 69 (2004) 036306.
- [7] Lopez JM, *et al.*: Symmetry breaking in free-surface cylinder flows, *J. Fluid Mech.* 502 (2004) 99-126.

Acoustic Doppler Velocity Profiler for velocity and turbulence measurements in a large amplitude meandering flume

Donatella Termini¹ and Mafalda Piraino^{1*}

¹Dipartimento di Ingegneria Idraulica ed Applicazioni Ambientali, University of Palermo, Viale delle Scienze, 90128 Palermo, Italy (*Corresponding author, e-mail: piraino@idra.unipa.it).

Flow over deformed bed of a meandering laboratory channel is experimentally investigated. The velocity components have been obtained using an Ultrasonic Doppler Profiler (DOP2000) that measures the instantaneous flow velocity profile along the probe direction. In this work, some results obtained in peculiar sections along the channel are reported. A refined mesh of the measurement points has been used for each considered cross-section. The analysis of the collected data essentially confirms that when the aspect ratio is small the secondary circulation assumes great importance and, in accordance with previous findings, a second counter-rotating secondary circulation cell appears near the free surface of the outer bank of the apex section. Such second circulation cell initiates at the bend entrance.

Keywords: Acoustic instrument, flow velocity field, secondary circulation, Reynolds stresses

1 INTRODUCTION

Accurate flow field measurements are necessary to analyze many stream processes, such as interaction flow-sediments, exchanges mechanism of sediments, nutrients and contaminants.

Because of the difficulty to obtain detailed flow velocity data by using traditional flow velocity meters, the analysis of turbulent structure of flow has been often limited. During the last decades, by developing laser and PIV sampling techniques, intensive experimental researches on the mechanism of turbulence production have been carried out [3-4]. But, very few experimental works have been conducted in order to analyze the secondary motion and the flow turbulence structure along a meandering bend.

In the present work detailed measures of flow velocity field in some sections of a large amplitude meandering channel have been carried out using an Acoustic Doppler Velocity Profiler (DOP 2000) by Signal Processing S.A. The instrument functioning is based on Doppler effect and consists of a probe that is simultaneously emitter and receiver of acoustic pulses; thus it allows to measure instantaneously the flow velocity profile along the probe direction. In order to analyze the interaction flow-sediment, from the instantaneous measured flow velocity vectors the turbulent fluctuation components as well as the turbulent stresses have been estimated.

The analysis has substantially confirmed the formation, in each apex section of the flume, of two circulation cells: the main circulation cell occurring in the central-region and a second counter-rotating circulation cell occurring near the free surface of the

outer bank. This second circulation cell strongly affects the turbulent activity and the distribution of the Reynolds stresses [1-2].

2 MEASUREMENT TECHNIQUE

The experimental installation has been constructed at the Dipartimento di Ingegneria Idraulica ed Applicazioni Ambientali, University of Palermo (Italy). The meandering channel follows the sine-generated curve with a deflection angle at the inflection section of 110°. The length of the meandering channel is of almost 27 m, i.e. equal to two meander wavelengths. The channel cross-section is rectangular with width $B=0.50$ m; the banks are rigid and the bed is of quartz sand, with medium sediment diameter $D_{50}=0.65$ mm and standard deviation $\sigma_g=1.34$. The initial longitudinal bed slope at the channel axis is of 0.371%. Other details of the experimental apparatus can be found in previous works [5-6].

The experiment has been conducted until the equilibrium bed topography was reached. The water discharge was $Q=0.012$ m³/s and the average water depth at the channel centerline was $h=5.5$ cm. At the end of the experiment the deformed bed was fixed by using cement dust. Then, the flow velocity measurements were carried out using the DOP 2000 in sections distant each other 50 cm or so. The acquisition frequency was of 4MHz and the pulse repetition frequency was variable in the range 5900-15600 Hz, depending on the local water depth and flow velocity. The distance between the center of adjacent sampling volumes was set equal of 0.75 mm; consequently, the number of emitted profiles

was included in the range $500 \div 800$. The acquisition time varied between 16.51 sec and 43.25 sec.

In order to obtain simultaneously the flow velocity components along the vertical (z), the transverse (r) and the longitudinal (s) directions, three probes inclined of 60° with respect to the horizontal direction have been used.

Because each probe measures the instantaneous velocity vectors along its direction, the aforementioned velocity components have been determined through the vectorial composition of the measured vectors. For such purpose, a refined measurement mesh has been considered (see Figure 1). In the central area of the examined section (radial abscissa variable in the range 5 cm $<r<$ 45 cm) a measurement mesh with a step of 1.5 mm was used. As an example, Figure 2 shows the transverse and the vertical velocity components, V_r and V_z , obtained at the measurement point P of a cross-section.

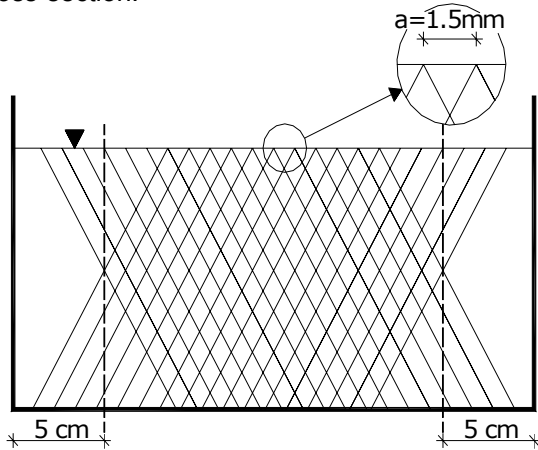


Figure 1: Measurement mesh

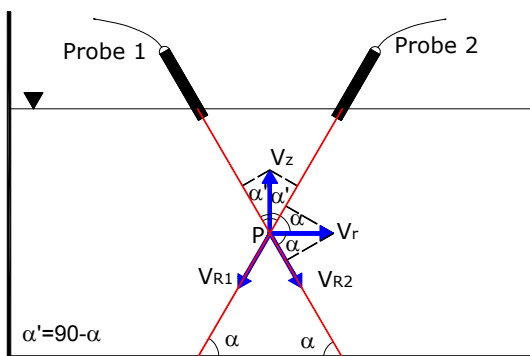


Figure 2: Measurement point P in the central zone of the cross-section.

V_{R1} and V_{R2} are the velocity vectors measured at time t by probe 1 and probe 2, respectively. Thus, at point P, V_r and V_z have been obtained by solving the following system of equations:

$$V_{R1} = V_r \cdot \cos(\alpha) - V_z \cdot \sin(\alpha) \quad (1)$$

$$V_{R2} = -V_r \cdot \cos(\alpha) - V_z \cdot \sin(\alpha) \quad (2)$$

After simple passages it is:

$$V_r = \frac{V_{R1} - V_{R2}}{2 \cdot \cos(\alpha)} \quad (3)$$

$$V_z = -\frac{V_{R1} + V_{R2}}{2 \cdot \sin(\alpha)} \quad (4)$$

In the near-bank area, i.e. for a distance of 5 cm from each bank (see Figure 1), the probe nearest the bank was placed in vertical position as shown in Figure 3. In this case, the following system of equations has been solved:

$$V_{R1} = -V_z \quad (5)$$

$$V_{R2} = -V_r \cdot \cos(\alpha) - V_z \cdot \cos(\alpha) \quad (6)$$

The components V_r and V_z at point P has been obtained as:

$$V_r = -\frac{V_{R1} \cdot \sin(\alpha) - V_{R2}}{\cos(\alpha)} \quad (7)$$

$$V_z = -V_{R1} \quad (8)$$

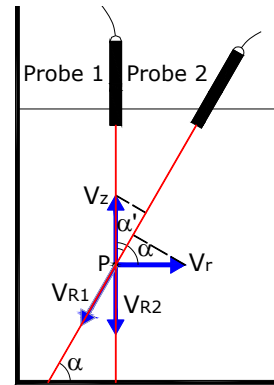


Figure 3: Measurement point in the near-bank area.

3 REYNOLDS STRESS DISTRIBUTION

In this paper the measurement sections reported in Figure 4 have been considered for the analysis.

For each measurement point, the Reynolds stresses $\tau_{rZ} = -\rho \overline{v'_r v'_z}$, $\tau_{rS} = -\rho \overline{v'_r v'_s}$, $\tau_{zS} = -\rho \overline{v'_z v'_s}$, (being v'_i $i=r, z, s$ the instantaneous fluctuation velocity component and the over-bar indicating the time-averaged values) have been estimated.

The contour lines of the estimated Reynolds stress components, normalized with respect to the mean shear stress $\tau = -\rho u_*^2$ (being u_* the shear flow

velocity), are reported in Figures 5-7.

It can be observed from these figures that in both the apex sections (sections A and E) the cross-sectional Reynolds stress τ_{rz} assumes different sign in the central region and in the outer bank region showing two peak values: one near the center of the cross-section and one near the free surface of the outer bank region. The component τ_{zs} , that represents the shear stress acting on the vertical plane parallel to the banks, assumes a peak value near the free surface of the outer bank region. The component τ_{rs} , that represents the shear stress acting on the horizontal plane, presents an alternance of sign inside the cross-section. It assumes the same sign (that is negative for section A and positive for section E) in the outer bank region and in the central region of the cross-section; such behaviour could be related to the evolution of turbulent structures in stream-wise direction. Furthermore, the maximum value of τ_{rs} is found near the free surface of the outer region. Then, moving toward the outer bank it decreases in value assuming very low values very close to the outer bank.

As the curvature increases, i.e. passing from section A to section B, it can be observed that the distribution of each considered Reynolds stress component seems to be similar to that observed in the apex section A, but in section B the peak values of both the Reynolds components τ_{rz} and τ_{rs} occurring in the outer region seem to go away from the free surface and to decrease in magnitude.

In the inflection section (section C), where the channel curvature is maximum, all the three considered Reynolds stress components do not show evident peak values.

Passing from section C to section D, i.e. as the channel curvature decreases, it can be observed that for both the components τ_{rz} and τ_{rs} the contour-lines initiate to thicken in the outer bank region. Such behavior suggests that the outer bank circulation cell could initiate in this section.

4 CONCLUSIONS

Acoustic Doppler Velocity Profiler has used to obtain detailed measures of flow velocity field in some sections of a large-amplitude meandering channel. From the measured flow velocity vectors, the Reynolds stresses τ_{rz} , τ_{zs} and τ_{rs} have been estimated. The analysis of the contour lines of these components has highlighted the formation of a counter-rotating outer-bank circulation cell near the free surface of each apex section. It seems that such circulation cell initiates at the bend entrance and decays approaching to the inflection section downstream.

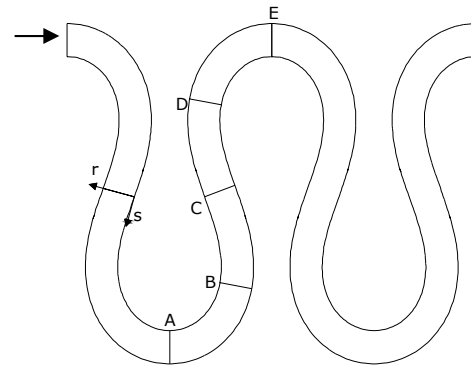


Figure 4: Measurement sections

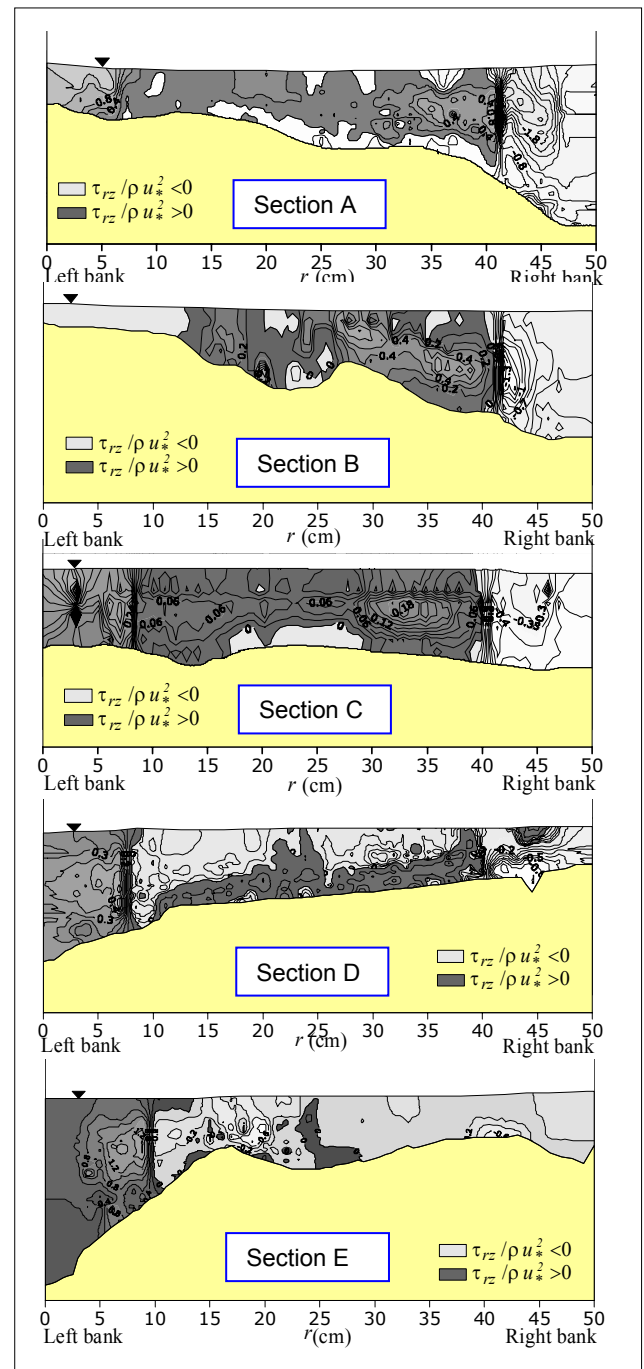


Figure 5: Normalized contour lines of τ_{rz}/u_*^2

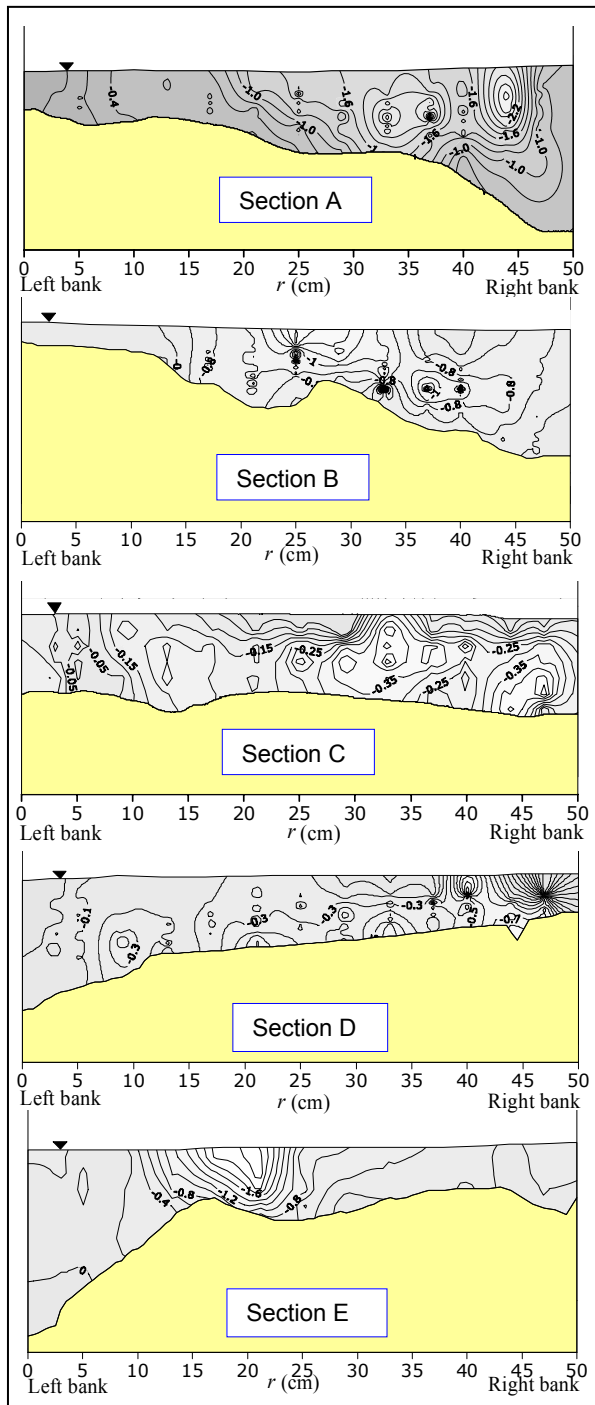


Figure 6: Normalized contour lines of τ_{rs}/u_*^2

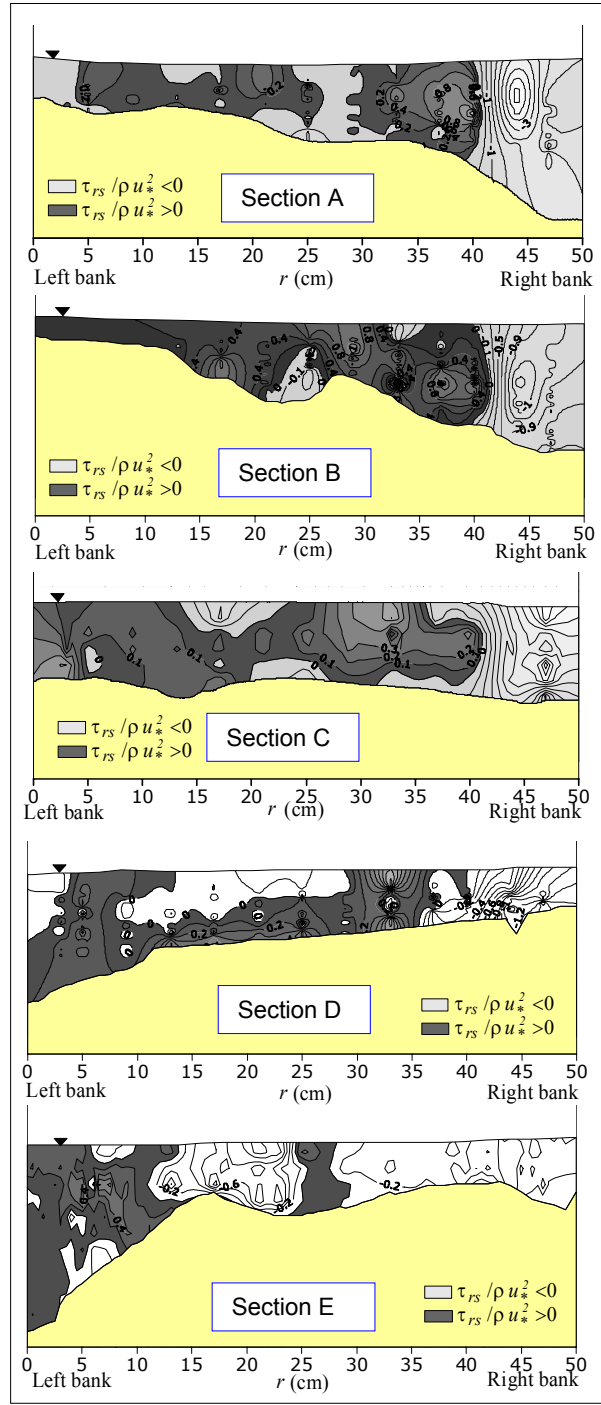


Figure 7: Normalized contour lines of τ_{rs}/u_*^2

REFERENCES

- [1] Blanckaert K: Secondary currents measured in a sharp open-channel bends, International congress River Flow 2002, 4-6 September, Belgium (2002) 117-127.
- [2] Booij R: Modelling of the secondary flow structure in river bends, International congress River Flow 2002, , 4-6 September Belgium (2002) 127-133.
- [3] Cellino M, Lemmin U: Influence of coherent flow structures on the dynamics of suspended sediment transport in open-channel flow, Journal Hydraulic Engineering (2004) 1077-1088;

- [4] Nino Y, Garcia M H: Experiments on particle-turbulence interactions in the near-wall region of an open channel flow: implications for sediment transport, Journal Fluid Mechanics. 326 (1996) 285-319.
- [5] Termini D, Bonvissuto G, Piraino M: Analisi sperimentale delle caratteristiche cinematiche della corrente in un canale meandriforme di elevata ampiezza: primi risultati, XXIX Convegno di Idraulica e Costruzioni Idrauliche, Trento, 7-10 Settembre (2004) 555-562.
- [6] Termini D, Piraino M: Secondary circulation motion in the apex section of a large amplitude meandering flume, 32nd congress of IAHR, Venice, 1-7 July (2007).

Cross correlation – the better Ultra Sonic Doppler – technique

Michael Teufel^{1*} and Milan Suchánek²

¹ NIVUS GmbH, Im Tále 2, D-75031 Eppingen, GERMANY (*Michael Teufel, e-mail: Michael.Teufel@nivus.com)

² DHI Hydroinform a.s., Na Vrších 5, 100 00 Prague 10, CZECH REPUBLIC (Milan Suchánek, e-mail: M.Suchanek@dhi.cz)

The acoustic Doppler effect is used since years to carry out velocity and flow rate measurements in liquids and gases. To determine the flow rate in waste water first versions were realized with continuously working (cw) acoustic sources and separate detectors. Stochastic considerations together with assumptions of the velocity profile allow the determination of the mean velocity, but with usually quite poor accuracy for the volume flow rate. To improve the accuracy the required spatial resolution was realised with Pulse Doppler technique. This ADCP technique offers the determination of velocity profiles with spatial resolutions of some decimetres as minimal dimensions. Therefore it is mainly used in larger dimensions such as oceanographic investigations. The cross correlation technique offers much higher accuracy for the velocity determination and also for the spatial resolution, resulting in an accurate flow profile estimation. It can be used for small dimensions as well, for the spatial resolution may be as small as 1-2 cm. To measure in larger dimensions too, chirp coded pulse can be used. This technique is therefore used for applications with a demand of high accuracy for open channel flows. Some of this applications will be described.

Keywords: flow rate measurement, velocity profile, cross correlation technique, float system

1 INTRODUCTION

Since years ultra sound is used for velocity and flow rate measurements of water and waste water in pipes, open channels and water courses. There are mainly two techniques; transit time and Doppler. Here only Doppler technology is considered. A minimum of pollution is required to use this Doppler echo technique due to the fact, that the velocity of small particles or air bubbles is measured. Generally this is a very good approach as this velocity is approximately the same as the real flow velocity. Signals can be evaluated in the time or the frequency domain; usually Doppler and Puls Doppler devices work in the frequency domain; they are described in section 2.1. Evaluation in the time domain by cross correlation is explained in section 2.2.; also a brief comparison is given there. Section 3 describes some applications.

2 ULTRASONIC ECHO DEVICES

2.1 Doppler technology

There are many simple ultrasonic devices on the market for flow rate measurements. These normally use continuously working piezo-ceramic electric sensors and separate detectors [2]. The detector measures the flow velocity by use of the reflected and Doppler shifted ultrasonic echoes of scattering particles; i.e. air bubbles or any solid particles. The flow rate is then calculated from this velocity. With no spatial resolution the accuracy of this instruments as flow rate meter is quite poor.

To obtain a spatial resolution, too, the pulse Doppler technology is used. Here short pulse bundles are sent into the medium. This kind of sensor does not

require a separate detector; normally only one ceramic is used as sending and receiving unit. Knowing the sound velocity c , it is easy to determine a spatial resolution (l = distance to the detector) by measuring the time T between sending and receiving the echo. This can be seen in figure 1.

$$l = \frac{c \cdot T}{2} \quad (1)$$

Usually the echoes are collected in time frames resulting in spatial windows which are used to determine the velocity; see figure 1.

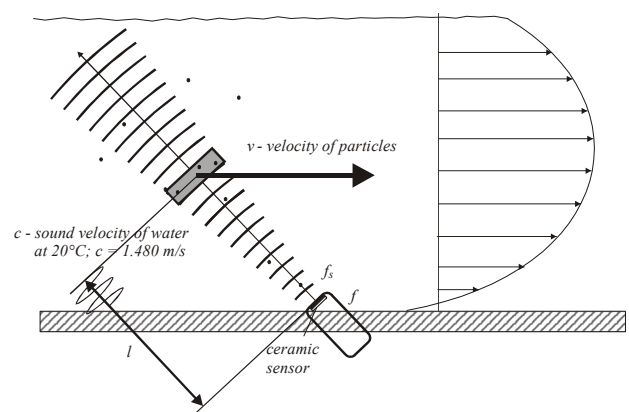


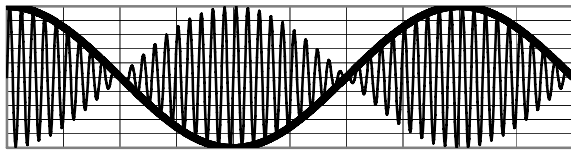
Figure1: Doppler system

The direct measurement of the Doppler shifted frequency f_s with v as particle velocity is difficult:

$$f_s = \frac{f \cdot c}{c - 2 \cdot v \cdot \cos \alpha} \quad (2)$$

Some numbers may explain this; for a sending frequency of 1,000,000 Hz the typical shift is about 100 to 1,000 Hz. It is more difficult to determine this frequency directly than overlapping the echo frequency with the basic frequency and determining the beat frequency $\Delta f = (f_s - f)$. Figure 2 shows the beat frequency. The resulting formula is:

$$v = \frac{(f_s - f) \cdot c}{2 \cdot f \cdot \cos \alpha} \quad (3)$$



Picture 2: Beat frequency

The determination of the beat frequency is possible only if there are enough cycles of the basic frequency within the beat frequency. Due to this, the spatial resolution of this Doppler devices is restricted to a minimum of typically 0.30 to 0.40 m. Usually an easy frequency determination is implemented; it is indirectly calculated by measuring the time between the zero crossings of the beat frequency. This measurement fails at low velocities and it becomes impossible at 0 m/s, where the corresponding frequency is 0 Hz, too ($1/T \rightarrow \infty$).

2.2 Cross correlation technology

Correlation is more and more used as a mathematical tool for flow rate measuring especially for signal evaluation since fast and powerful microprocessors have become available. Used in stand-alone flow rate meters, it is meanwhile used for measurements in two-phase fluids, too.

The figure 3 shows the acoustic cross correlation sensor OCM *Pro* CF of the NIVUS [3]. The sensor at the bottom sends a short ultrasonic pulse into the water with an angle of 45° towards the flow direction. The echoes are then collected in time frames. Then a second pulse is sent into the water and the echoes of this sensor are collected in the same time frames. The correlation of both echoes enables the calculation of the temporal movement in each frame/window; the velocity profile can be calculated. The method offers a spatial resolution of the length of a single oscillation, but to achieve a better mean the minimal window length is set to about 0.01 m. The maximal size is variable and may reach up to 0.10 m.

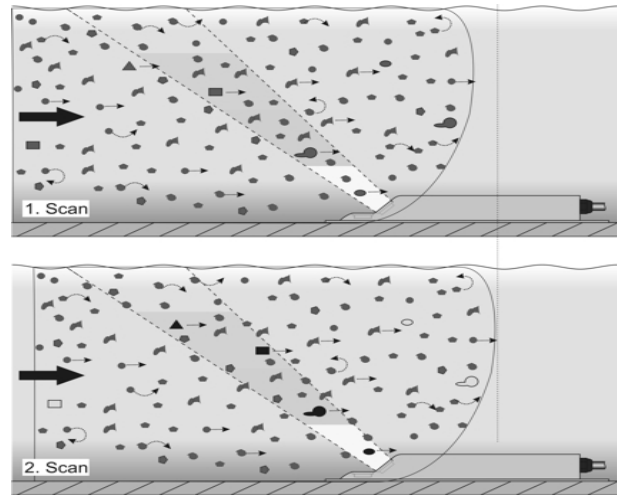


Figure 3: Acoustic cross correlation method

The formula 4 gives the mathematic expression:

$$\varphi_{f,g}(\tau) = \lim_{T \rightarrow \infty} \frac{1}{T} \int_{-\frac{T}{2}}^{+\frac{T}{2}} f(t) \cdot g(t + \tau) dt \quad (4)$$

or as digital expression:

$$\varphi(\Delta T) = \frac{\sum_{i=1}^N f_i \cdot g_i(\Delta T)}{\sqrt{\sum_{i=1}^N f_i^2 \sum_{i=1}^N g_i^2}} = \frac{\sum_{i=1}^N f_i \cdot g_i(\Delta T)}{N^2} \quad (5)$$

with

f = echo function of digital picture 1

g = echo function of digital picture 2

The velocity is calculated in maximal 16 windows (time frames) and can be used to determine a velocity profile. The velocity values and the profile can be used to calculate the flow rate in full pipes and open channels as well. The velocity profiles in full filled pipes are well known and the flow rate determination is straightforward [1].

For part filled open channel flows an additional height measurement is required. Therefore an ultrasonic height sensor as well as a hydrostatic sensor are integrated. Using an external sensors is possible, too. The height fixes the position of the 16 velocities. The calculation of the flow rate from this velocities will not be discussed here, some information about this topic can be found in [3].

There is one major limitation for cross correlation used by the OCM *Pro* CF. The maximum height in which velocities are measured is 1.00 m or 1.5 m along the ultrasonic beam. For larger distances only

empirical or numerical calculations can be used taking into account the measurements along the first meter.

This limitation is caused by a de-correlation between the 2 pulses. Before the second pulse is sent into the water, all echoes from the first echo need to be collected in advance. Therefore the time between the 2 pulses is getting longer while the distance to the sensor increases. As the distance to the ceramics is growing, the ultra sonic intensity of the reflected echoes decreases due to the normal propagation of waves; this two effects lead to a poorer correlation.

The OCM *Pro* LR overcomes both problems. It uses ceramics with a larger diameter. As a result the lower spreading angle keeps the intensity of the ultrasonic beam higher. This first step neglects explosion requirements (ATEX), too; with more ultrasonic power the intensity problem of the echoes could be ignored.

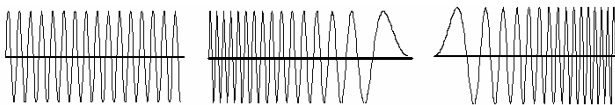
Reducing the time between the two pulses was done by using a chirp coding of the “normal” ultra sonic burst:

$$U = U_0 \cdot \sin(\omega \cdot t) \quad (6)$$

where U is the amplitude of the ultrasonic wave, ω the frequency and t the time. For chirp coded signals ω is not longer a constant but depending on time. A linear chirp e.g. utilizes

$$\omega = \omega_0 + k \cdot t \quad (7)$$

with k as a constant. We did not consider other chirps, thus as exponential. Picture 4 shows linear up and down chirp coded pulses in comparison to a “normal” pulse:



Picture 4: “Normal” burst, up-burst, down-burst

To use chirps ceramic oscillators are required that can be excited in a larger frequency range. Under ideal conditions the 2 bursts are orthogonal and do not interfere with each other. The ideal orthogonality is not possible and also disturbed due to the interaction of the ultra sonic pulse in the $3/4 \cdot \lambda$ coupling plate and in the water. Beside the good correlation of this pulses a higher energy can be involved with larger bursts. This results in larger distances that can be measured.

3. Applications

Meanwhile the OCM *Pro* is used for many different applications. In the following there will be three different ones.

Flow rate measurements are difficult in the sludge return with up to 3-5% solid content. If there is fat as well magnetic inductive instruments cant be used. Figure 5 shows the sludge pipe from the digestion tank to the sludge incineration.



Figure 5: Flow rate meter in the sludge return

The right picture shows at the display of the transmitter a well developed velocity profile; therefore a good accuracy can be assumed. A fast removal of the pipe sensor during cleaning is realised with a special fitting.

Especially in the influent to the waste water plants you may have sedimentation in the channel. The sensor may still work at low sedimentation, but it will fail finally. Secondly usually a wrong cross section, the complete big one is taken to calculate the flow rate. A float system (figure 6) can help to solve this problem. A wedge sensor is mounted below the float.



Figure 6: Float system by use of surf boards

A ultra sonic height sensor measures the sludge level to calculate the correct cross section. The velocity sensor measures from the surf boards to the bottom; there is no need to consider a sedimentation, but fat is removed from time to time.

Flow monitoring is a significant part of operating of a sewer system. The presented example comes from Prague sewer network, where a system of permanent flow monitoring includes all main collectors, which collect waste water for the CWWTP (Central Waste Water Treatment Plant), and also at important CSO structures.

In 2006 one of the most complicated permanent flow sites, called "ACK", was equipped with an OCM Pro flow meter. It replaced the former Doppler device with a Correlation system. The data measured by OCM PRO are implemented into the telemetry system to enable remote access to them. Figure 7 shows a sketch of the site

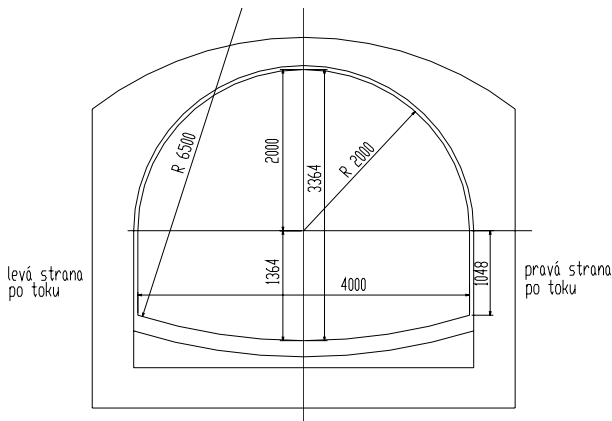


Figure 7: Sketch of "ACK"

The shape is a mouth profile made of reinforced concrete; channel height is 3.35 m, the width 4.0 m. With a slope of 0.2 % there is no sedimentation. To mount this devices in the channel special brackets were used that can be seen in figure 8. Also the ultra sonic level meter is visible at the ceiling.

To reach high accuracy a calibration was carried out. The calibration was performed with a grid measurement with a hydrometric propeller; the uncertainty of the calibration was within about 5%. The analysis of the measured data show very stable readings of the flow meter.

After two years of operation it is obvious, that that the flow meter OCM Pro has brought a significant improvement of the flow measurement at this site. Based on this experience two other permanent measurement profiles "F1" and "K1" were equipped by the same technology in 2007.

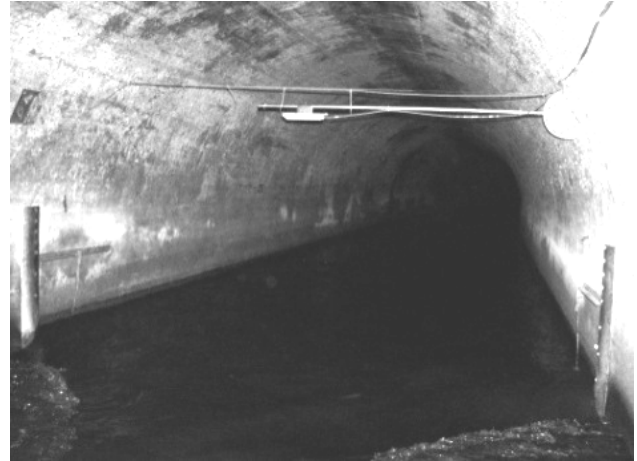


Figure 8: Measuring site "ACK"

4 CONCLUSIONS

Other successful applications meanwhile indicate the potential of the cross correlation instrument. The applicability in different degrees of pollution covers a range from very high pollution (see above) up to very clean water in the effluent of waste water treatment plants with nearly drinking water quality. The dimension rage from 0.1 m up to several meters; resulting in flow rates from about 1 l/s to about 1000 m³/s

ACKNOWLEDGEMENT

Beside the theory here the complete application know how of the company NIVUS is involved. The description of more applications can of course be found in other documentations of NIVUS.

REFERENCES

- [1] Fiedler O.: Strömungsmesstechnik und Durchflussmesstechnik, Oldenburg, München, 1992
- [2] Teufel M.: Doppler-Verfahren, Pulsdoppler und Kreuzkorrelation bei Ultraschallmessungen; Seminar: Neue Entwicklungen in der Durchflussmessung in natürlichen und künstlichen Gerinnen; TU München, März 2004
- [3] Teufel M.: Durchflussmessung mit Kreuzkorrelation; KA – Abwasser, Abfall 2006 (53) Nr. 7

Near wall studies of pulp suspension flow

Johan Wiklund^{1*}, Helena Fock², Anders Rasmuson² and Mats Stading^{1,3}

¹ SIK - The Swedish Institute for Food and Biotechnology, P.O. Box 5401, SE-402 29 Göteborg, Sweden (*Corresponding author, e-mail: johan.wiklund@sik.se).

² Department of Chemical and Biological Engineering, Chalmers University of Technology, SE-412 96 Göteborg, Sweden

³ Materials and Manufacturing Technology, Chalmers University of Technology, SE-412 96 Göteborg, Sweden

Understanding the flow behaviour of pulp suspensions is very important in the design and operation of process equipment and paper mills. Pulp suspension flow is an opaque two-phase flow system, consisting of water and pulp fibres that aggregate and form coherent networks, resulting in very complex flow behaviour above a certain concentration. An Ultrasound Velocity profiling (UVP) technique was used in this study to investigate pipe flow of pulp suspensions in the near wall region. The study was performed at two concentrations and at four bulk velocities. The results showed that the mean velocity profiles exhibit a distinct plug at the centre of the pipe surrounded by a sharp velocity gradient. The plug size increases when the concentration increases or the bulk velocity decreases. The demodulated echo amplitude profile indicates a concentration profile in the near wall area, with a decreasing amount of fibres close to the pipe wall.

Keywords: Velocity profile, ultrasound, Doppler, pulp, wall layer

1 INTRODUCTION

1.1 Background

Detailed knowledge of the flow behaviour of pulp suspensions is important in the design and operation of process equipment and paper mills. This study focuses on the flow of concentrated fiber suspensions near the wall in a square pipe.

A pulp suspension flow is a two-phase flow system consisting of pulp fibres and water that tends to aggregate and form coherent networks above a certain fibre concentration. Since the shearing mechanisms are not the same throughout the suspension it is misleading to use a non-Newtonian flow model with a yield stress, [1]. Pulp suspension flow in pipes exhibits some extra flow regimes in the area between the pipe walls and the pulp network besides the usual laminar and turbulent flow regimes of common Newtonian and non-Newtonian fluids. The flow regimes originate in the different shearing situations occurring in the suspensions, mainly in the region close to the wall. These flow effects are of great importance for the frictional behaviour of the pulp suspension flow as well as for the pressure drop in the system. Flow phenomena, such as forming of flocs and water annulus occur in this region. Extensive reviews of pulp suspension flow in pipes have been published by for example [2].

The Ultrasound Velocity profiling (UVP) technique is well suited for opaque non-Newtonian fluid systems, but UVP has only been used in few studies on pulp suspension flow, [3-5]. The pulp consistencies were however below 2% (w/w). In a previous comparative

study between UVP and LDA, velocity profiles were successfully measured with good agreement between the two techniques in pipe flow of pulp suspensions with consistencies as high 7.8% (w/w), see [6]. Recent studies, e.g. [7] have also indicated a concentration gradient within the pulp suspension flow in pipes in the near wall region. In recent publications, [8, 9] it is shown that direct access to Demodulated Echo Amplitude (DMEA) data from a customized UVP instrument provides information on the quality of acquired data but also that new information can be extracted from spectral analysis. Ultrasound echo energy dependence can e.g. be used to measure the variation in bulk concentration of solids in fluid systems.

1.1 Aim of the study

Velocity profile and demodulated echo amplitude measurements were performed at four different bulk velocities and for two pulp consistencies. By investigation of the variations in echo amplitude and velocity gradient in the near wall layer related the demodulated echo amplitude to a concentration gradient or profile.

2 MATERIALS

A fully bleached kraft pulp from Södra Cell Värö was used in this study. The pulp had an average fibre length of 2.65 mm and an average diameter of 30 μm . The pulp was diluted from the original concentration, around 20 % (w/w), to two consistencies, 1.9 and 4.8 % (w/w). Approximately 150 L of pulp suspension was used in each test.

3 EXPERIMENTAL SET-UP & EQUIPMENT

3.1 Experimental flow loop

The experiments were carried out in a specific test facility at Chalmers University of Technology. A schematic view of the experimental flow loop is shown in Figure 1.

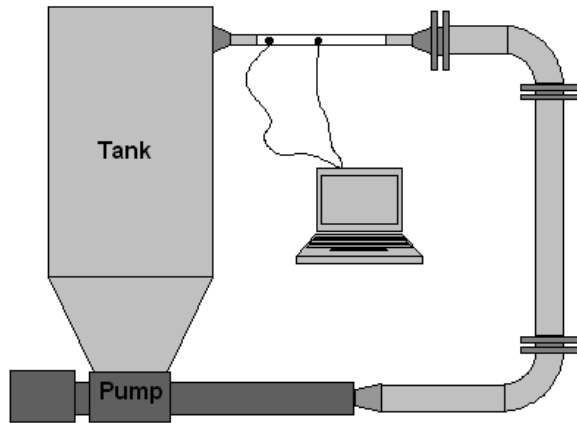


Figure 1: Experimental pulp flow loop.

The set-up consists of a 300 L open tank that supplies pulp suspension to a progressive cavity pump, which produces a maximum bulk velocity of 180 L/min. The pump is connected to a stainless steel pipe of a larger diameter than the downstream test section in order to reduce the pressure load on the pump. The pulp flows from the larger cylindrical pipe 100 mm in diameter through a contraction, designed for pulp suspensions, into a smaller cylindrical pipe 40 mm in diameter and then into the UVP test section. The test section, shown in Figure 2, is a 40 mm square Plexiglas conduit. The velocity profiles were measured at the location shown in Figure 2 using two 4 MHz TX-TN type transducers (Imasonic, Bensacon, France). The wall thickness was optimized for maximum transmission of ultrasound energy and transducers were installed at a distance from the wall interface to avoid measurements within the near-field. More details are given in [11].

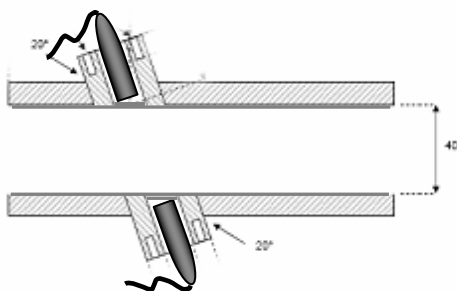


Figure 2: Experimental transducer set-up.

3.1 UVP-PD method and data acquisition system

The UVP-PD method and data acquisition system for in-line viscometry, developed at SIK, has been presented in e.g. [8, 9]. A customized Doppler-based ultrasound velocity profiling instrument equipped with a Multiplexer and modified firmware that allowed direct access to the demodulated echo amplitude (DMEA) was used for data acquisition (UVP-Duo-MX, Met-Flow SA, Lausanne, Switzerland). The instrument was connected to a master PC and communication was implemented with an Active X library, supplied by Met-Flow SA Lausanne, Switzerland. Versatile Matlab (Math Works, Natick, MA, USA) based software with a user-friendly GUI was developed and used to control data acquisition, for real-time data processing of DMEA raw data, visualization and analysis. The Doppler shift frequency and velocity profiles were determined using time-domain or frequency domain based signal processing, [8, 9, and 10]. A digital oscilloscope, Agilent Technologies, model 54624A, USA was an integral part of the set-up and was used for measuring the acoustic properties of the suspensions. Experimental UVP parameters are given in Table 1.

Table 1: Experimental UVP parameters

Frequency	4 MHz
Cycles per pulse	2-4
Repetitions	256 and 512
No. profiles	50
Sound velocity	~1490 (1.9 %) ~1505 (4.8 %) m/s
Doppler angle	70±0.5°
Spatial resolution	~0.37-0.74 mm
Time resolution (single profile)	55 ms/profile
Velocity resolution	6.5-22 mm/s

4 RESULTS & DISCUSSION

4.1 Measured velocity profiles and gradient

Figures 4 and 5 show the measured arithmetic mean velocity profiles, averaged over 30 profiles, from both transducers (TX and TN) for the two pulp suspensions of consistencies 1.9 and 4.8 % (w/w) respectively. Figures 4 and 5 shows a distinct plug region at the centre of the pipe that was found to stay intact and move as a solid body. The size of the plug was found to decrease with an increasing bulk velocity but also to increase with increasing consistency. A small difference in measured plug velocity was observed, at the right and the left side of the profile respectively, which can be seen in Figures 4 and 5. The measurements were made sequentially in different directions relative to the flow direction and started with the TX-transducer

followed by the TN- transducer for each bulk velocity. The temperature of the pulp suspension increased during the run of the flow loop but the sound velocity was only measured and updated at the beginning of the measurements of each bulk velocity. However, the most likely explanation for the small difference in measured velocities is that the pump has a tendency to loose effect after a while, thus giving lower flow velocities at the same frequency setting. Both effects were found to be more pronounced when the consistency was increased. A stationary echo is visible in Figure 4 for the highest and lowest bulk velocity at the 1.9 % consistency. This is indicated by local dips in velocity, in the plug flow area, and was most likely caused by multiple reflections in the pipe interface wall material. Measured velocity profiles are in good agreement with previous studies [4, 6].

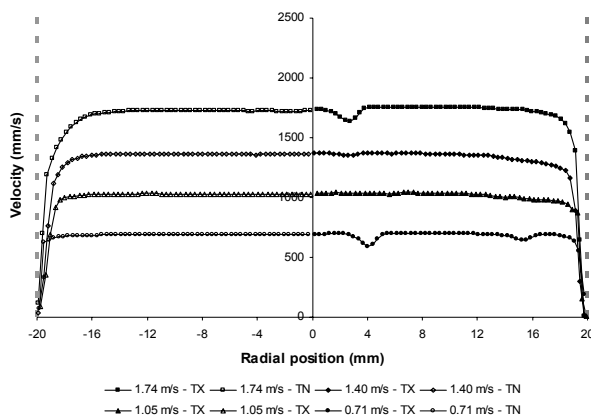


Figure 4: Measured velocity profiles at 4 different bulk velocities for a 1.9% (w/w) pulp suspension.

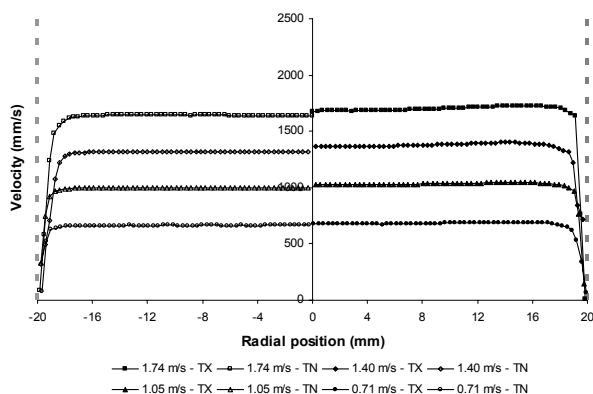


Figure 4b: Measured velocity profiles at 4 different bulk velocities for a 4.8% (w/w) pulp suspension.

Obtained results indicate an area close to the wall with a shear layer with a velocity gradient, thus indicating also a possible fibre concentration gradient. This is in accordance with previous studies

by [4, 6, and 7]. Even though the trends are the same in the different studies the width of the gradient layer differs between the studies. These differences could originate from the different measurement techniques used, e.g. if comparing for example LDA and UVP measurements. The gradient layer measured with LDA is reported to be around 0.2 mm, which is much thinner compared to the ones measured with UVP (around 2 mm). The difference in the measured width of the gradient layer between the UVP based studies in literature is probably due different experimental UVP parameter settings. However, the velocity resolution along the measurement axis in the near wall region was significantly higher in this study, 0.37mm.

4.2 Relating demodulated echo amplitude and fibre concentration

In this study, an attempt was made to relate the demodulated echo amplitude to a concentration gradient or profile. The general trend for the echo amplitude curve is to have low amplitude close to the wall interface and to slowly rise to a maximum due to the migration of particles from the wall area towards the centre of the pipe. The echo amplitude then decreases with increasing distance from the transducer due to attenuation of ultrasound energy. This trend can be seen, e.g. in water seeded with a small amount of particles. The shape of the demodulated echo amplitude curve can thus be used to indicate the width of a concentration gradient layer.

Figures 4 and 5 shows a distinct plug region at the centre of the pipe that was found to stay intact and move as a solid body. An increase in echo amplitude closer to the plug front indicates an increase in concentration of fibres (since more fibres give a stronger echo). Theoretically, the location of the maximum received demodulated echo amplitude in the radial direction thus indicates the point at which the plug starts since the plug front generates the strongest echo. This is since the maximum received echo amplitude in the radial direction theoretically occurs at the position where the difference in acoustic impedance is the largest. Two examples of measured DMEA vs. radial position are presented in Figures 6 and 7.

When compared to the demodulated echo amplitude curve for water we observe that the echo amplitude peak is very sharp for the pulp suspensions and then quickly drops due to the attenuation of ultrasound energy, as shown in Figure 6 and 7. It also clearly indicates a decrease in plug size when bulk velocity is increased. This is in agreement with previous studies for softwood pulp suspension flow at lower consistencies, 2.0-3.1% (w/w), [7].

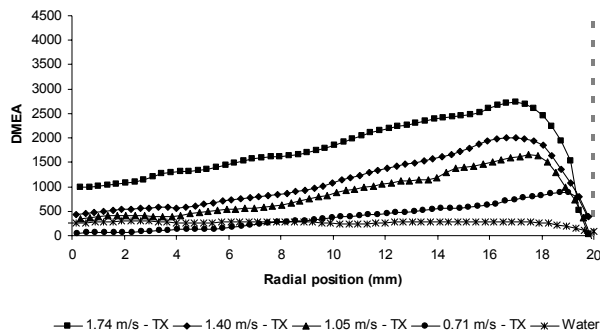


Figure 6: DMEA profiles for water and a 1.9 % (w/w) pulp suspension measured at 4 different bulk velocities.

Another interesting observation for the 1.9 % consistency is that the size of the plug for velocity profiles and thickness of the concentration gradient seems to more or less the same. This contradicts the results from a previous study where the width of the concentration gradient was larger than the width of the velocity gradient, [7].

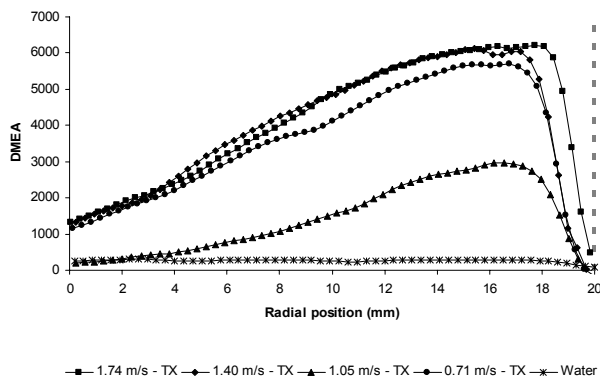


Figure 7: DMEA profiles for water and a 4.8 % (w/w) pulp suspension measured at 4 different bulk velocities.

For the 4.8 % consistency, shown in Figure 7, the trends are not as clear as in the 1.9 % case. Here, it appears that the size plug increases when the bulk velocity increases. The width of the concentration gradient also seems to be larger than the size of the velocity gradient. This can be explained by the fact that the DMEA profiles for the 4.8 % consistency were most likely affected by the flow situation. The measurements were performed in the so called rolling friction regime for all the bulk velocities at the 4.8 % consistency. In the rolling friction regime there are flocs present between the plug and the pipe wall and the size of the flocs reduces with an increase in velocity, [4]. This could explain why the width of the velocity gradient increases with decreasing bulk velocity.

5 CONCLUSIONS

- (1) Velocity profiles were successfully obtained in pipe flow of pulp suspensions at four different bulk velocities and at two different consistencies. The obtained mean velocity profiles are in good agreement with results from previous studies, both in terms of profile shape and in width of the velocity gradient.
- (2) Higher spatial and velocity resolution in the near wall region was achieved compared to previous studies presented in the literature.
- (3) Higher spatial and velocity resolution in the near wall region was achieved compared to previous studies presented in the literature.
- (4) The demodulated echo amplitude curve can be used to indicate the start of a moving fiber plug as well as the width of a concentration gradient layer.

ACKNOWLEDGEMENT

The financial support of Södra Cell is gratefully acknowledged. A. G. Gogniat and O. Mariette at Met-Flow SA, Switzerland are acknowledged for their support. Beat Birkhofer from ETH, Switzerland is acknowledged for fruitful discussions.

REFERENCES

- [1] Duffy G, Titchener, A, Lee, P, Moller K: The mechanisms of flow of pulp suspensions in pipes, APPIA J. 29 (1976) 363-370.
- [2] Duffy G: The significance of Mechanistic-Based Models in Fibre Suspension Flow, Nord. Pulp Paper Res. Jour. 18(2003) 74-80
- [3] Hirsimäki, O: Determination of radial velocity profile and flow disturbance of pulp suspensions by ultrasonic echo correlation, Paperi ja Puu 60 (1978) 95-97.
- [4] Dietemann P, Rueff M: A study of fibre suspension flow by means of Doppler ultrasound velocimetry and image analysis, in PAPTAC 90th Annual Meeting, Montreal, Que., Canada (2004).
- [5] Hanjiang X, Aidun C: Characteristics of fiber suspension flow in a rectangular channel, Int. Journ. of multiphase flow. 31(2005) 318-336.
- [6] Wiklund J, Pettersson J, Rasmuson A, Stading M: A Comparative Study of UVP and LDA Techniques for Highly Concentrated Pulp Fibre Suspensions in Pipe Flow, AIChE J. 52 (2006) 484-495.
- [7] Pettersson J, Wikström T, Rasmuson A: Near Wall Studies of Pulp Suspension Flow Using LDA, Can. Jour. Chem. Eng. 84 (2006) 422-430.
- [8] Wiklund J "Ultrasound Doppler Based In-Line Rheometry – Development, Validation and Application", Ph.D. Thesis, Lund University, Lund, Sweden, 2007.
- [9] Wiklund J, Sharam I, Stading M: Methodology for In-line rheology by ultrasound Doppler velocity profiling and pressure difference techniques, Chem. Eng. Sci. 62 (2007) 4277-4293.
- [10] Wiklund J, Stading M: Application of in-line ultrasound Doppler-based UVP-PD rheometry method to model and industrial suspensions, Flow Meas & Instr. 19 (2008) 171-179.
- [11] Fock H. et al.: Ultrasound Velocity Profile (UVP) Measurements of Pulp Suspension Flow near the Wall, J. Pulp & Paper Sci. XX (2008), in press.

Measurement of turbulent thermal convection in liquid metal under uniform magnetic field

Takatoshi Yanagisawa^{1*}, Yasuko Yamagishi¹, Aataru Sakuraba², Yuji Tasaka³, Kanako Yano³, Yasushi Takeda³, and Yozo Hamano¹

¹ Institute for Research on Earth Evolution (IFREE), Japan Agency for Marine-Earth Science and Technology (JAMSTEC), 2-15 Natsushima-cho, Yokosuka, Kanagawa 237-0061, Japan
(*Corresponding author, e-mail: yanagi@jamstec.go.jp).

² Department of Earth & Planetary Sciences, University of Tokyo, 7-3-1 Hongo, Bunkyo-ku, Tokyo 113-0033, Japan

³ Division of Energy & Environmental Systems, Hokkaido University, Kita-13, Nishi-8, Kita-ku, Sapporo 060-8628, Japan

UVP is used to visualize the flow of liquid gallium for Rayleigh-Benard convection. Measuring the horizontal component of the flow velocity for several lines, organized roll-like structure with many fluctuations is observed at Rayleigh number $10^4 \sim 10^6$, and the roll shows clear periodic oscillatory behavior. The typical period of the oscillation is comparable to the circulation time of the mean flow. Our numerical simulation with the same setting and material properties confirms these features. When the uniform magnetic field is imposed on this convecting system, drastic changes of the flow are observed depending on the direction and intensity of the magnetic field. Horizontal magnetic field enhances the two-dimensionality of the roll-like structure, and vertical magnetic field reduces the velocity of the mean flow.

Keywords: Liquid metal, thermal convection, magnetic field, turbulence, velocity profile

1 INTRODUCTION

Thermal convection under the vertical temperature gradient is described by two non-dimensional parameters, Rayleigh number (Ra) and Prandtl number (Pr). The onset of the convective motion is controlled by critical Ra and independent of Pr , but after the convection occurs, the behavior of the system is strongly dependent on Pr [1]. It easily becomes turbulent for lower Pr . Molten metals are used for the study of low Pr region. Molten metals, however, are opaque fluids, so any optical methods for the flow measurement cannot be applied. Some works have been done by tracing the particle at the surface of mercury, and some have utilized the temperature dependence of sound velocity in liquid gallium and reconstructed roll pattern [2]. These works have been performed near the critical Ra where steady rolls exist. At higher Ra with extremely turbulent flow region ($Ra \sim 10^{10}$), temperature is measured at some points in the convective cell, and the statistical features are discussed in the view of turbulence and heat transport in many studies [3], but direct measurement of convection pattern has been strongly desirable. The Ultrasonic Velocity Profiler (UVP) method [4] is a powerful tool to measure the flow occurring in the liquid metal. By using the UVP, *Mashiko et al.* succeeded in the direct measurement of convective velocity at high Ra region and found out a kind of large-scale flow existing in the cell [5], but their apparatus is a large tall cylinder in which only one main circulation occurs. The organization process to large-scale flow

is not understood, so it is necessary to focus on the moderate Ra region.

On the other hand, liquid metals have large electric conductivity and the magnetic field affects the behavior of the flow. It is also important to study Rayleigh-Benard convection under various types of magnetic field. There are many experimental studies on this topic from critical to moderate Ra [6-8], but most of them are based on the measurement of temperature. Simultaneous measurement of velocity profile is also desirable to clearly grasp the characteristics of the flow.

Our aim of this study is to achieve a direct velocity measurement for Rayleigh-Benard convection in liquid metal and to look at the characteristic pattern at moderate Ra ($10^4 \sim 10^6$), whether there exists any mean flow with large-scale structure or not, and furthermore, in which way the external uniform magnetic field deforms the structure and nature of the turbulence of the flow. The container for our experiment is horizontally long one to realize the intrinsic convection pattern.

2 APPARATUS AND METHOD

We use UVP to measure the fine-scale velocity field of the flow occurring in the liquid metal. Liquid gallium is used as the working fluid in our experiment. The container for convection is made of glass whose thickness is 10 mm. We choose Pyrex-glass because of its affinity to gallium and its impedance. Top and bottom plates are made of copper to keep the temperature constant by

circulating water. The horizontal scale of the container is 200 mm, the other horizontal length is 50 mm, and height is 50 mm. The transducer for ultrasonic measurement is fixed on a sidewall, so the length of the measurement line is 200 mm. The horizontal component of the flow velocity at each line is measured in this system (Figure 1). The system we used for the measurement is UVP-Duo (Met-Flow inc.), and the basic frequency of the transducer is 4 MHz.

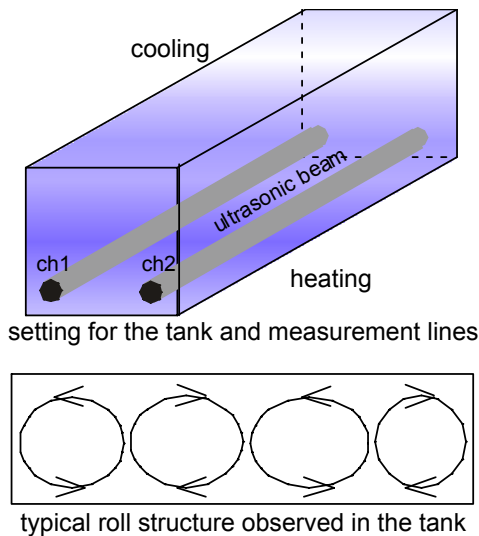


Figure 1: Schematic of the container and measurement lines by UVP (top). Liquid gallium is filled in the container. The typical convective flow pattern by vertical temperature difference has the roll like structure (bottom).

Powder of ZrB_2 is used as tracer particles because it has neutral buoyancy in liquid gallium. The typical diameter of the particles is 50 micrometer. To reduce the surface tension and to promote dispersion of the particles into liquid gallium, once we heated up the gallium up to 700 K. Gallium is easily oxidizable, so we handle it in argon gas. The melting temperature of gallium is 29.8 °C, so the upper plate cooling temperature is fixed at 32.0 °C, and lower plate heating temperature is raised up to 70.0 °C. In the calculation of Ra , we used the material properties of gallium same as [9]. Pr of gallium around this temperature is 0.03. There is a small density difference between the tracer particles and liquid gallium; hence, the particles are gradually sinking even in convecting gallium. Then the reflection signals become weak, so we cannot continue UVP measurements for more than couple of hours.

Helmholtz coil system is used to impose uniform magnetic field on the container. We can set horizontal or vertical magnetic field, whose intensity is up to 20 mT. The diameter of the coil is 700 mm, and uniformity of the magnetic field is assured around the container. The maximum Hartmann number realized in this system is about 30. Three component of the magnetic field is monitored

outside of the container by a magnetometer. Temperature is measured at some points inside of the liquid gallium by small-sized thermistors.

3 RESULT

3.1 Thermal convection without magnetic field

First, we report the result of simple Rayleigh-Benard convection, without magnetic field. We set the Ra one to three orders above the critical value, because the flow velocity is too small to be measured by UVP near the critical. Measuring the horizontal velocity at several sites in the container, many fluctuations are observed, that reflect turbulent behaviors of the flow. When we see the long-term tendency, we can reconstruct two-dimensional roll-like pattern (Figure 2). This roll-like pattern is supposed to be a kind of mean-flow which is the organized structure in the turbulence, and the small fluctuations may show the behavior of small vortices. The roll-like pattern shows clearly regular periodic behavior. This means that the roll structure gets longer and shorter sideways, and the axis of the rolls is swinging periodically. We found out that its period is comparable to the circulation time of the mean-flow, and gets shorter with the increases of Ra .

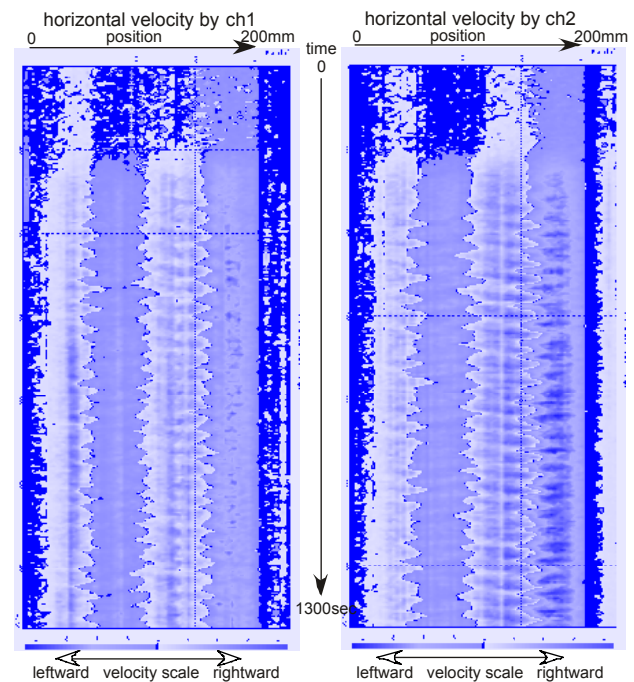


Figure 2: An example of the time series of the horizontal flow velocity. The measurement lines ch1 and ch2 are shown in Figure 1. Horizontal axis is the position, and vertical axis is the time. The magnitude of the velocity is displayed in grayscale. The top is the onset of convection, and four rolls are developed. The result clearly shows the periodic oscillations of the convective roll structure. $Ra=1 \times 10^5$ for this case.

3.2 Numerical simulation for the same setting

We made up a code for numerical simulation of thermal convection to compare and evaluate our

results obtained by laboratory experiments. The numerical simulation is for three dimensional rectangular box, with no-slip boundary conditions at all boundaries, fixed temperature at the top and bottom, and insulating at side walls. The material properties of the working fluid are those of liquid gallium. We used enough grid points to resolve the small-scale behavior without any assumption for the turbulence. Our numerical result reproduced oscillatory convection patterns as observed in the experiments (Figure 3). Some statistical values, such as the relation of the circulation time and oscillation period, Ra dependence of the mean velocity, are in good agreement in both laboratory and numerical studies. This confirms that our laboratory experiment and numerical simulation are reliable ones.

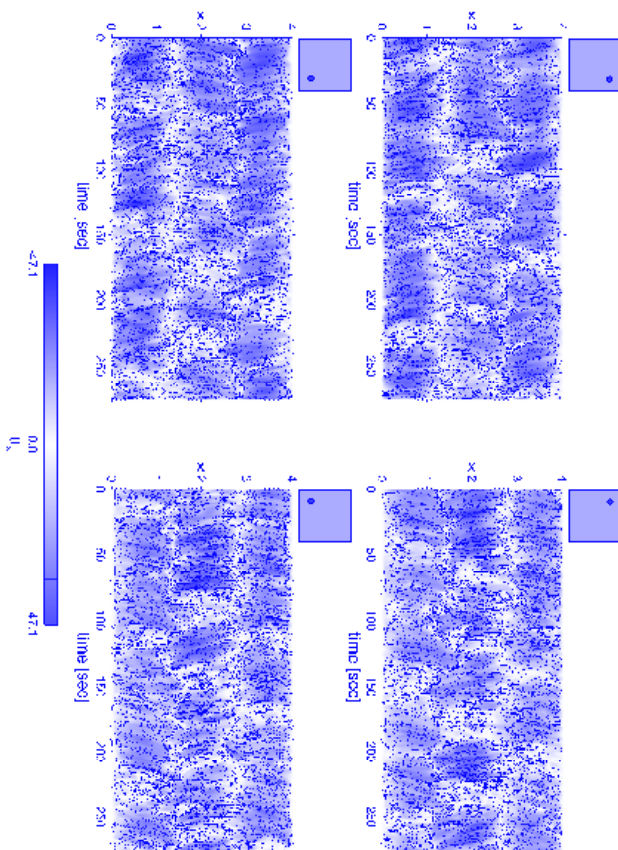


Figure 3: An example of the numerical simulation for the same setting as our laboratory experiment. Time series of the horizontal flow velocity is shown in the same way as UVP measurement. The features observed in Figure 2 (roll-like structure with small fluctuations, periodic oscillations of the rolls) are reproduced well. $Ra=1 \times 10^5$, $Pr=0.03$.

3.2 Thermal convection under horizontal magnetic field

We measured the horizontal flow velocity in liquid metal with stepwise increase of the external magnetic field. We observed obvious change of the flow characteristics depending on the direction and intensity of the magnetic field.

Figure 4 shows the simultaneous measurement of velocity and temperature under horizontal magnetic field. The direction of the applied magnetic field is parallel to the mean roll axis of this convecting system, and its intensity is increased step by step. The basic flow structure, that is, the number of the rolls and its flow direction is not changed, but the fluctuating components of the flow are reduced remarkably and the mean velocity of the roll-like flow pattern is increased. The reduction rate of the fluctuation depends on the intensity of the applying magnetic field.

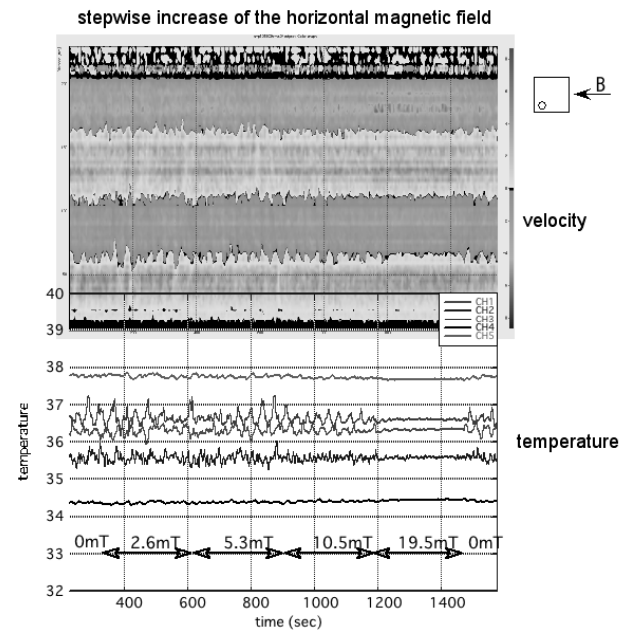


Figure 4: The behavior of the flow with stepwise increase of the horizontal magnetic field. $Ra=1 \times 10^5$. Simultaneous measurement of horizontal velocity (top) and temperature (bottom) is displayed. Horizontal axis is the common time. In the bottom graph, three lines with large fluctuation are the signal from the thermistors inside of the liquid gallium. 0 mT, 2.6 mT, 5.3 mT, 10.5 mT, 19.5 mT, and again 0 mT, is the intensity of the imposed horizontal magnetic field. The reduction of fluctuating component is observed for both velocity and temperature from 5.3 mT, and the flow is almost steady for 19.5 mT.

3.3 Thermal convection under vertical magnetic field

Figure 5 is the result for the stepwise increase of vertical magnetic field. The basic flow pattern for 0 mT consists of four fluctuating rolls as in Figure 4, but the behavior with the increase of the magnetic field shows obvious difference. The typical flow velocity decreases with the increase of the magnetic intensity. At the same time, the typical period of the roll's fluctuation gets longer gradually. And little reduction of the fluctuation is observed except for 19.5 mT. The drastic reduction of random fluctuation is observed for this intensity, but periodic oscillation is survived.

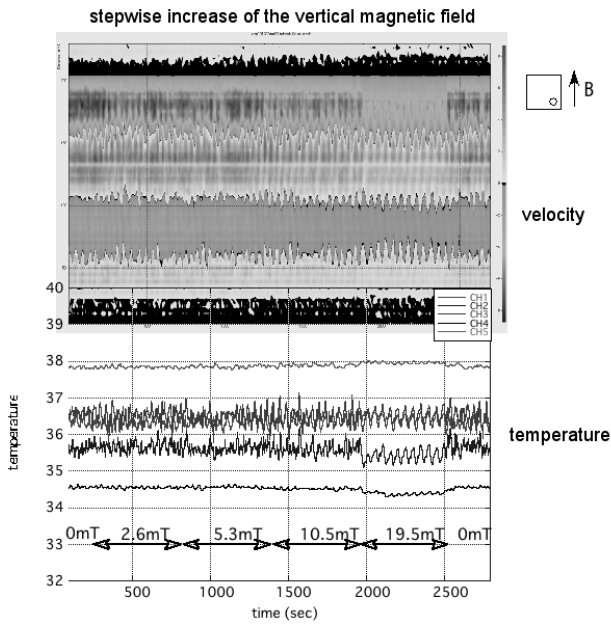


Figure 5: The behavior of the flow with stepwise increase of the vertical magnetic field. $Ra=1 \times 10^5$. 0 mT, 2.6 mT, 5.3 mT, 10.5 mT, 19.5 mT, and again 0 mT, is the intensity of the imposed vertical magnetic field. Typical flow velocity is decreasing with the increase of magnetic field, though it is not clear in this grayscale. Note that the total time in this series is longer than in Figure 4.

4 DISCUSSION

We succeeded in the measurement of velocity profile for the Rayleigh-Benard convection at low Pr with moderate Ra . Measuring the horizontal velocity at several sites of the container with the UVP, we can reconstruct two-dimensional roll-like pattern coexisting with small fluctuations. This roll-like pattern is supposed to be a kind of mean-flow, that is the organized structure in the turbulence, and the small fluctuations may show the behavior of small vortex. The periodic behavior of the roll-like structure is very important; it might show the interaction between the small vortex and the mean-flow. The velocity of the mean-flow becomes higher with the increase of Ra . At the same time, temporal fluctuation of the mean-flow field becomes faster. In the range of Ra $10^4 \sim 10^6$, the UVP measurement shows that the typical velocity of the mean-flow U is proportional to $Ra^{1/2}$. The dependence of the typical period of the roll oscillation is $Ra^{-1/2}$, which suggests close relation between the mean-flow and the oscillation.

When we apply horizontal magnetic field along the roll axis of this convecting system, the fluctuating components are reduced and two-dimensionality of the roll structure is enhanced. The reduction rate of the fluctuation depends on the intensity of the applying magnetic field. We think that the criterion for the reduction is described by the comparison of two time scales, Joule dissipation time (t_{JD}) and circulation time (t_U). If $t_{JD} < t_U$, then strong reduction of the fluctuation may occur. This can explain the Ra

dependence of our result that stronger magnetic field is necessary to stop the fluctuation of the roll for higher Ra (for larger U).

When we apply vertical magnetic field, the flow velocity and frequency of the periodic behavior reduces as the apparent Ra of the system becomes smaller. This is easily understandable because the critical Ra increases with the intensity of vertical magnetic field, then effective Ra for the fluid decreases.

5 CONCLUSIONS

Rayleigh-Benard convection with liquid metal is characterized by the organized roll-like structure and its fluctuation. This feature is confirmed both by UVP measurements and numerical simulations.

Horizontal magnetic field along the mean roll axis enhances the two-dimensionality of the flow structure, and decrease the fluctuation.

Vertical magnetic field reduces the effective Ra of the convective system.

ACKNOWLEDGEMENT

Numerical simulations were executed using the Earth Simulator, Japan Agency for Marine-Earth Science and Technology. This work is supported by the JSPS Grant-in-Aid for Scientific Research.

REFERENCES

- [1] Krishnamurti R: On the transition to turbulent convection, *J. Fluid Mech.* 42 (1970) 295-320.
- [2] Fife S, Andereck CD, Rahal S: Ultrasound thermometry in transparent and opaque fluids, *Experiment in Fluids* 35 (2003) 152-158.
- [3] Segawa T, Naert A, Sano M: Matched boundary layers in turbulent Rayleigh-Benard convection of mercury, *Phys. Rev. E* 57 (1998) 557-560.
- [4] Takeda Y, Instantaneous velocity profile measurement by Ultrasonic Doppler Method, *JSME International Journal, series B* 38 (1995) 8-16.
- [5] Mashiko T, Tsuji Y, Mizuno T, Sano M, Instantaneous measurement of velocity fields in developed thermal turbulence in mercury, *Phys. Rev. E* 69 (2004) 036306.
- [6] Aurnou JM, Olson P: Experiments on Rayleigh-Benard convection, magnetoconvection and rotating magnetoconvection in liquid gallium, *J. Fluid Mech.* 430 (2001) 283-307.
- [7] Burr U, Muller U: Rayleigh-Benard convection in liquid metal layers under the influence of a horizontal magnetic field, *J. Fluid Mech.* 453 (2002) 345-369.
- [8] Burr U, Muller U: Rayleigh-Benard convection in liquid metal layers under the influence of a vertical magnetic field, *Phys. Fluids* 13 (2001) 3247-3257.
- [9] Aubert J, Brito D, Nataf HC, Cardin P, Masson JP: A systematic experimental study of rapidly rotating spherical convection in water and liquid gallium, *Phys. of Earth and Planet. Int.* 128 (2001) 51-74.

Ultrasonic investigation on coupling of flows between liquid and liquid metal layers

Kanako YANO^{1*}, Yuji TASAKA¹, Yuichi MURAI¹, Yasushi TAKEDA¹,
and Takatoshi YANAGISAWA²

¹ Graduate school of Engineering, Hokkaido University, Kita-13, Nishi-8, Sapporo 060-8628, Japan
(*Corresponding author, e-mail: kanako-y@ring-me.eng.hokudai.ac.jp)

² Japan Agency for Marine-Earth Science and Technology, Yokosuka 237-0061, Japan

This study aims to clarify coupling of flows between liquid metal and other usual liquids, e.g. water or oil, in fluid dynamical systems. In past studies for two-layer Rayleigh-Bénard system where the immiscible two liquids are layered, two types of coupling were observed; these are called as “mechanical coupling” and “thermal coupling”. We investigate which type of the coupling is dominant when one of the layers is liquid metal by changing a ratio of the height of the layers and viscosity, and how the oscillation of cells in the liquid metal layer propagates to the upper liquid layer and vice versa. First we attempt to observe ideal mechanical coupling with forced rotating flow, in which the rotating motion and fluctuation in a liquid Gallium layer propagates to the upper layer via the interface by visualization and UVP measurement. And we also investigate how two types of coupling occur in this system by using water and oil for comparison.

Keywords: Ultrasonic measurement, Liquid metal, Coupling of flows, Rayleigh-Bénard convection, Two layers

1 INTRODUCTION

An experiment of thermal convection using liquid metal in a laboratory has great importance for physical and industrial purposes, e.g. geo-science and manufacturing technology of steel or silicon. Earth's core consists of molten Iron, and its convective motion generates the earth's magnetic field. Oscillating convective motion in crystal growth process reduces the quality of products. We have to observe fluid motions in molten metals including molten Iron to understand its properties and mechanism. However, we have never seen fluid motions by ordinary way, e.g. optical visualization, because these are opaque. Ultrasonic Velocity Profiling, UVP, is a useful measuring technique for investigating opaque liquids [1]. UVP gives an instantaneous velocity profile and then it makes possible to observe a spatiotemporal motion of opaque liquids including molten metal [2,3]. We have investigated natural convection, especially Rayleigh-Bénard system, in a liquid Gallium layer by using UVP. The ultrasonic visualization of liquid Gallium flow confirmed that there are convective cells in this layer as a large scale motion of the convection and these cells oscillate in a horizontal direction [4].

Two-layered thermal convection has been studied for fluid dynamical interests and also for industrial applications. Some experimental and theoretical works mentioned that there are two kinds of coupling between the layers, thermal coupling (TC) and mechanical coupling (MC) [5]. Alternation between the couplings depends on the height ratio

of the layers, viscosity and thermal diffusivity of fluids. Figure 1 shows a schematic motion in each coupling. In the thermal coupling (TC) the flow of the upper layer is driven by a horizontal temperature gradient at the interface between the layers induced by the convective motion in the lower layer. So the convective cells have the same rotating direction with the lower layer. The flow of the upper layer is driven by viscous effect in the mechanical coupling (MC), namely momentum transportation beyond the interface is the source of the convective motion in the upper layer. So the cells have opposite rotation for the lower layer cells.

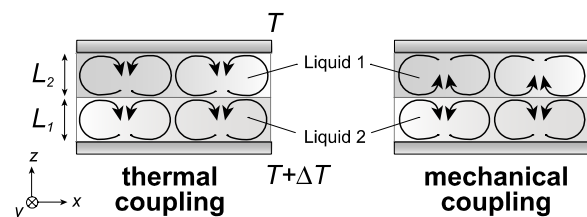


Figure 1: (Left) Thermal coupling: The upper layer fluid is driven by horizontal temperature gradient due to the convective motion in the lower layer fluid. (Right) Mechanical coupling: Motion of the upper layer fluid is induced by momentum transfer from the lower layer motion.

This study provides observations of two-layered convective motion in liquid liquid-metal layers at comparably large Rayleigh number at which the oscillating motion appears in the liquid metal layer. Liquid Gallium and ordinal transparent liquids, glycerol solution and silicone oil, were chosen as the lower layer and the upper layer fluids respectively. We investigate the alternation of the coupling and

how the oscillating motion in the liquid Gallium layer affects the fluid motion in the upper layer. Particle Image Velocimetry, PIV, was utilized to determine the 2D velocity field in the transparent fluids in the upper layer. UVP and PIV measurements at each layer were done simultaneously. Flow pattern in the layers were observed for several settings of the height ratio and viscosity of the upper transparent liquid layer.

We also provided a simple experiment to clarify effects of an oxidized film on the mechanical coupling.

2 PRERIMINARY EXPERIMENT – ROTATING TOW-LAYERED FLOW –

Liquid Gallium we use is easier to treat on experiment in a laboratory than other liquid metals, e.g. Sodium or Mercury. But it quickly oxides in ordinal atmosphere and then oxidized film at the interface between the Gallium and other fluid may affect momentum transfer. We attempt here to clarify the effect of the oxidized film by a simple experiment of a rotating two-layer flow. Table 1 shows a specification of physical properties of liquid Gallium and water. The sound speed in liquid Gallium which is required for UVP measurement is around 2860 m/s at working temperature. There is small temperature dependence and it does not affect accuracy of the measurement [4].

Table 1: Physical properties of water and liquid Gallium, each symbol indicated as density, kinematic viscosity and thermal diffusivity

	Water	Gallium
ρ [kg/m ³]	0.9982×10^3	6.095×10^3
ν [m ² /s]	1.004×10^{-6}	1.96×10^{-3}
κ [m ² /s]	1.44×10^{-7}	1.18×10^{-5}

2.1 Experimental setup and method

Figure 2 shows an experimental setup. It consists of a glass beaker put on a magnetic stirrer (0.2 T magnet). The glass has similar acoustic impedance with liquid Gallium and makes easy to propagate ultrasonic wave. The diameter of the beaker is around 90 mm. The working fluids, water and liquid Gallium, are poured into the beaker. The height of liquid Gallium layer is about 50 mm, and that of water is about 20 mm. A 4 MHz ultrasonic transducer was mounted at the side wall of the beaker with almost half height of the Gallium layer. The measurement line corresponding to the propagation line of ultrasonic wave was parallel to the horizontal center line of the beaker with small distance. UVP monitor model Duo (Met-Flow S.A.) was used for the signal processing. Fine powder of ZrB₂ was used as tracer particles; these are 50 μ m in diameter and have a density of 6.17 kg/m³. This

kind of powder has also been used in other work of UVP measurements in liquid Gallium and provided good results [2]. A white light sheet created by a metal halide lamp with a cylindrical lens illuminated the upper layer close to the interface for visualization. A digital video camera was fixed above the beaker to record a movie of the illuminated layer. Drops of hydrochloric acid were poured into the rotating fluids to remove an oxidized film. Influence of removing the film on the mechanical coupling was observed by UVP and the video camera.

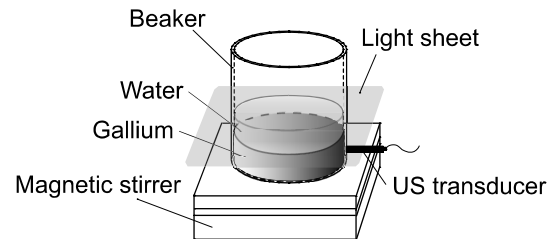


Figure 2: Schematic diagram of experimental apparatus for two-layer rotating flow

2.2 Summary of the results

Figure 3 shows a spatiotemporal velocity distribution of the liquid Gallium layer measured by UVP; at 5 seconds past the start of the measurement, drops of the acid were added into the fluid. The horizontal axis is time and the vertical axis is distance from the transducer in the measurement line. The gray scale shows the instantaneous velocity and the positive value are indicated the velocity of a direction getting away from the transducer.

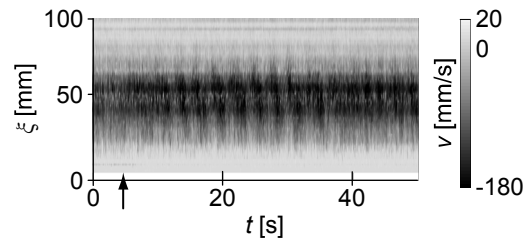


Figure 3: Spatiotemporal velocity distribution of the liquid Gallium layer; adding drops of the acid into the fluid after a lapse of 5 seconds indicated by arrow

Before adding the acid the surface of the liquid Gallium layer is covered with the oxidized film. The film is stationary and there is no momentum transmission from the liquid Gallium layer to the upper water layer. Strong shear waves are observed on the film and it may dissipate the kinematic energy. Therefore the velocity in the liquid Gallium layer is generally smaller than that after adding the acid. When we pour the acid into water the oxidized film is dissolved by deoxidization and the water layer starts to rotate by propagation of the momentum from the liquid Gallium layer. We omit here to show this behavior of the upper layer because of the lack of space, but it will be shown as movie in the presentation. Periodic oscillation with 3 sec in the

period appears after adding the acid around 20 seconds. The rotating liquid Gallium originally has such the oscillating motion due to the eccentricity of the rotating magnetic field [4]. The oxidized film, however, prevents the oscillation. Dissolving the film therefore allows a deformation and a stagger of the interface between the layers. Because of small amount of the adding the acid, the oxidized film forms again. It also prevents the periodic oscillation and the amplitude of the oscillation decreases (cf. around 40 sec in Fig. 3).

We confirmed that an oxidized film at the surface of the liquid Gallium layer fully prevents the diffusion of momentum from the lower layer to the upper layer. This condition is not suitable to investigate the mechanical coupling, but is useful to realize the perfect thermal coupling.

3 TWO-LAYER THERMAL CONVECTION

3.1 Experimental setup

A 200×50×60 mm rectangular vessel was used for the experiment of the two-layer Rayleigh-Bénard convection. Top and bottom plates are made of copper and the thickness of these plates is 5 mm. The plate was cooled or heated by flowing water through the surface provided by a constant temperature bath. All of the side plates are made of Pyrex glass and the thickness of the shorter sides at which the ultrasonic transducer is mounted is 5 mm for the penetration of the ultrasonic wave, other 10 mm.

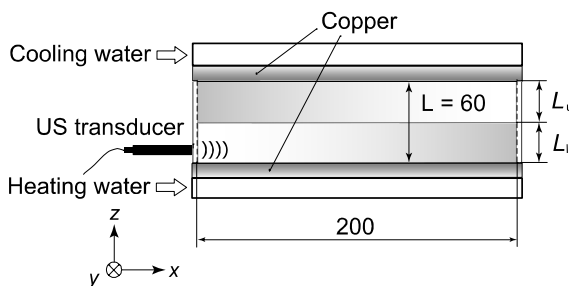


Figure 4: Schematic diagram of experimental apparatus for Rayleigh-Bénard convection

First water-oil two-layer experiment was made for understanding both of the flow pattern and the coupling phenomenon in usual fluids. 100 cSt Silicone oil and 80 % glycerol solution were used as working fluids. The physical properties of these fluids are shown in Table 2. Different tracer particles were mixed into each fluid for visualization. Particles are porous resin (1020 kg/m^3 in density and $50 \mu\text{m}$ in diameter) for water and spherical powdered resin (981 kg/m^3 in density and $180 \mu\text{m}$ in diameter) for Silicone oil. Temperature difference between the plates, defined as ΔT , was changed as 0.5, 1, 2, 4, 8, 16 degrees Celsius. A green laser light sheet created by a 50 mW Nd YAG Laser with a cylindrical lens illuminated the vertical cross section of the layers. Several pictures of the visualized motion

were taken by a digital camera and PIV analysis was made on the pictures.

Subsequent measurement of liquid Gallium-liquid two-layer flow used 50 % glycerol solution. UVP and PIV measurements were done simultaneously. The transducer was put at the side wall near the bottom of the vessel, and the picture of the upper transparent layer was taken as the same way of water-oil experiments. A height ratio of the layers, $\Gamma = L_u/L_l$ (here L_u and L_l are height of the upper and the lower layer.), was varied for several values but results in the case of $\Gamma = 2/3$ are shown here.

PIV analysis was utilized to determine the motion in the transparent liquids. Fundamental PIV algorithm, cross correlation between two particle images, was used. It generally has a disadvantage on the spatial resolution in contrast with its easy handling. But it does not affect this study because the phenomenon observed here is still laminar. The velocity is calculated from particle moving distance and time interval of these pictures, 1 sec in this study.

Table 2: Physical properties of glycerol solution (GS) and Silicone oil

	80% GS	50% GS	Silicone oil
ρ [kg/m^3]	1.208×10^3	1.125×10^3	0.965×10^3
ν [m^2/s]	49.57×10^{-6}	5.364×10^{-6}	100.0×10^{-6}
κ [m^2/s]	7.82×10^{-8}	10.4×10^{-8}	10.94×10^{-8}

3.2 Results and discussions

The experiment with transparent liquids shows a typical flow pattern of the coupling. Figure 5 shows an instantaneous velocity vector field calculated by PIV. Temperature difference is 4 degrees Celsius and height ratio is 0.5. In velocity vector field gray scale shows the amplitude of velocity; a darker arrow shows a larger velocity. In each layer certain convective cells exist. The direction of the horizontal flows is opposite in both sides of the interface, and the vertical flow has the same position and direction. This therefore shows the thermal coupling (cf. Fig.1). The horizontal length of the cells in such a system usually becomes smaller than the height of the fluid layer. The cells in the upper layer, however, have larger horizontal length than the height.

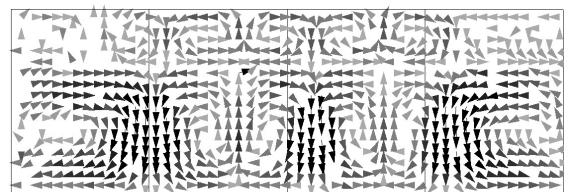


Figure 5: Instantaneous velocity vector field calculated by PIV analysis; temperature difference $\Delta T = 4 \text{ K}$ and height ratio of the layers $\Gamma = 0.5$

The upper layer cells near the side walls are unclear than the other cells because there is no clear

horizontal temperature difference due to the influence of the side boundary. These indicate that the fluid motion in the upper layer is dominated by the convective motion in the lower layer.

Figure 6 shows (a) instantaneous velocity vector field of the upper glycerol solution layer and (b) spatiotemporal velocity distribution of the liquid Gallium layer. This state is before adding the acid into the upper fluid, i.e. the momentum transfer from the lower to the upper layer is prevented by the oxidized film. The horizontal scales of the figures roughly correspond. In the liquid Gallium layer, the velocity changes from negative to positive or vice versa at the positions around 50, 120 and 160 mm. These positions roughly correspond to the positions at which the boundary of the cells exists in the upper layer. The flow direction of the liquid Gallium layer at the boundary estimated from the velocity distribution is the same to that of the upper layer (see Fig.6 and Fig.7). This therefore mentions that the thermal coupling is there as our expectation (see Fig. 7). Furthermore the spatiotemporal velocity distribution in the liquid Gallium layer shows periodic oscillation of the cells, and this layer behaves as the liquid Gallium single layer [4].

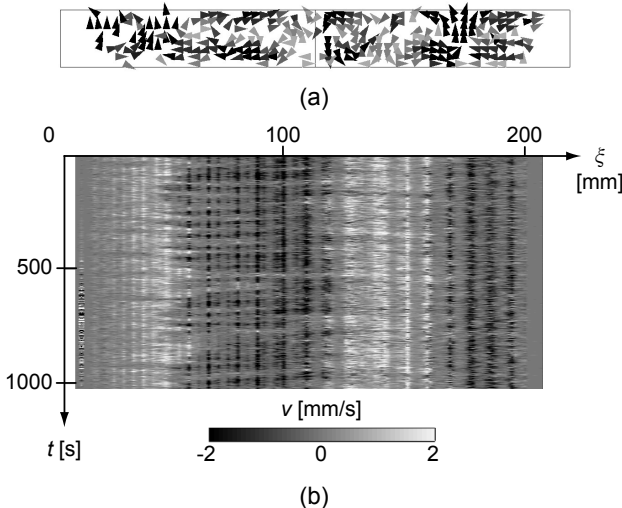


Figure 6: (a) Instantaneous velocity vector field in the glycerol solution layer; (b) spatiotemporal velocity distribution in the liquid Gallium layer before adding the acid, where the temperature difference is $\Delta T = 10$ K

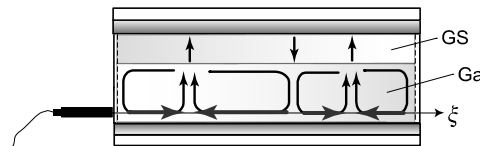


Figure 7: Schematic illustration of the flow pattern in the liquid Gallium layer

Figure 8 shows the fluid motions in the layers after adding the acid. In both layers, the velocity becomes small in comparison with that before adding the acid. It is confirmed that the several convective cells exist in the upper layer but the flow near the interface weakens independently from the convective motion. Dissolution of the oxidized film allows the

momentum propagation: It reduces rotating velocity of the cells in the liquid Gallium layer and the horizontal temperature gradient. Finally the motion due to the thermal coupling is prevented. The cells in the upper layer may not be driven by the couplings, because the motion of the cells seems independent from the motion in the lower layer.

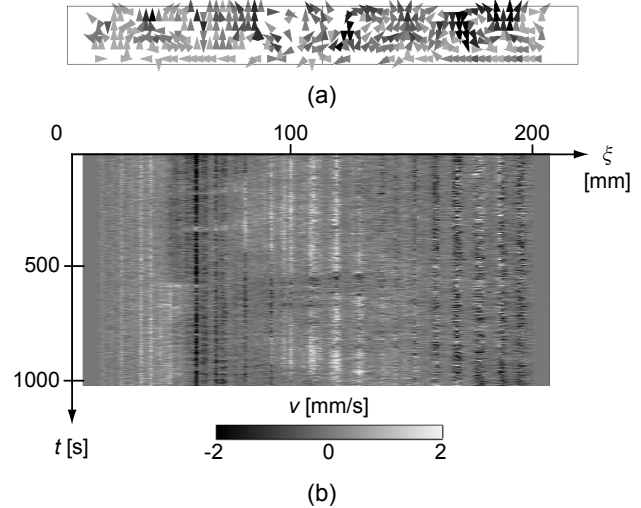


Figure 8: (a) Instantaneous velocity vector field in the glycerol solution layer; (b) spatiotemporal velocity distribution in the liquid Gallium layer after adding the acid

CONCLUDING REMARKS

We investigated the coupling of flows between liquid and liquid metal layers. It was confirmed in the two-layer rotating flow that the oxidized film formed on the liquid Gallium layer fully prevents the momentum transmission between the layers. We realized and observed the perfect thermal coupling utilizing the oxidized film. Effects of the momentum transmission in the thermal coupling were observed by dissolving the film using the acid. The transmission weakens the motion in the lower layer and allows the independent motion in the upper layer from the lower layer.

REFERENCES

- [1] Takeda Y: Measurement of velocity profile of mercury flow by ultrasound Doppler shift method, Nuclear Tech. 79 (1987) 120-124.
- [2] Brito D, *et al.*: Ultrasonic Doppler velocimetry in liquid gallium, Exp. in Fluids 31 (2001) 653-663.
- [3] Mashiko T, *et al.*: Instantaneous measurement of velocity fields in developed thermal turbulence in mercury, Phys. Rev. E 69 (2004) 036306.
- [4] TASAKA Y, *et al.*: Ultrasonic visualization of thermal convective motion in a liquid gallium layer, Flow Meas. Inst. 19 (2008) pp.131-137.
- [5] Michael M. Degen, *et al.*: Time-dependent patterns in the two-layer Rayleigh-Bénard system, Phys. Rev. E 57 (1998) 6647- 6659